Modelling and Attenuation Feasibility of the Aeroelastic Response of Active Helicopter Rotor Systems During the Engagement/Disengagement Phase of Maritime Operation

by

F. Khouli, B.Eng., M.Eng.

A thesis submitted to the Faculty of Graduate Studies and Research
in partial fulfillment of the requirements for the degree of

Doctor of Philosophy

Ottawa-Carleton Institute for Mechanical and Aerospace Engineering

Department of Mechanical and Aerospace Engineering
Carleton University
Ottawa, Ontario

May, 2009

Your file Votre référence
ISBN: 978-0-494-60113-6
Our file Notre référence
ISBN: 978-0-494-60113-6

Abstract

An aeroelastic phenomenon, known as blade sailing, encountered during maritime operation of helicopters is identified as being a factor that limits the tactical flexibility of helicopter operation in some sea conditions. The hazards associated with this phenomenon and its complexity, owing to the number of factors contributing to its occurrence, led previous investigators to conclude that advanced and validated simulation tools are best suited to investigate it. A research gap is identified in terms of scaled experimental investigation of this phenomenon and practical engineering solutions to alleviate its negative impact on maritime helicopter operation. The feasibility of a proposed strategy to alleviate it required addressing a gap in modelling thin-walled composite active beams/rotor blades. The modelling is performed by extending a mathematically-consistent and asymptotic reduction strategy of the 3-D elastic problem to account for embedded active materials. The derived active cross-sectional theory is validated using 2-D finite element results for closed and open cross-sections. The geometrically-exact intrinsic formulation of active maritime rotor systems is demonstrated to yield compact and symbolic governing equations. The intrinsic feature is shown to allow a classical and proven solution scheme to be successfully applied to obtain time history solutions. A Froude-scaled experimental rotor was designed, built, and tested in a scaled ship airwake environment and representative ship motion. Based on experimental and simulations data, conclusions are drawn regarding the influence of the maritime operation environment and the rotor operation parameters on the blade sailing phenomenon. The experimental data is also used to successfully validate the developed simulation tools. The feasibility of an open-loop control strategy based on the integral active twist concept to counter blade sailing is established in a Mach-scaled maritime operation environment. Recommendations are proposed to improve the strategy and further establish its validity in a full-scale maritime operation environment.

Acknowledgements

Firstly, I would like to sincerely thank and praise the foremost one who inspired, guided, and steered this research into completion. Secondly, the inspiration, guidance, advice, and supervision of my two supervisors: Prof. Fred F. Afagh and Prof. Robert G. Langlois, are sincerely valued and appreciated. Without their support and extensive expertise, none of this research would have been possible. Also, the support of my immediate family, especially my mother, is equally appreciated and acknowledged. Special thanks are extended to the genuine friendship and support of my peers and other professors and the staff in the Department of Mechanical and Aerospace Engineering at Carleton University. Finally, the support and help provided by the National Research Council, Institute for Aerospace Research are acknowledged and appreciated.

Fidel Khouli, 2009

List of Symbols

Chapter 2

a	characteristic dimension of cross-section of beam-like structure
l	characteristic length of beam-like structure
ℓ	wavelength of global elastic deformation along the beam
h	characteristic thickness of the wall of the cross-section
$\frac{a}{\ell}$	small parameter, slenderness ratio
$\frac{h}{a}$	small parameter, thinness ratio
ς	small parameter inherent to the structure
$\mathcal{F}(\Gamma, \varsigma)$	3-D elastic energy functional
Υ	energy terms that do not involve unknown warping functions
z_j	the j^{th} perturbation of the 3-D elastic displacement field
w_{ji}	the j^{th} unknown perturbation/warping function along the i^{th} Cartesian direction
$\bar{\mathcal{C}}_i$	the i^{th} constraint on the warping field
$\mathcal{O}(\varsigma^i)$	the i^{th} order terms in the elastic energy functional expansion
$\mathcal{U}_{\text{classical-like}}$	classical-like elastic energy per unit length
$\bar{S}_{4\times4}$	4×4 classical-like stiffness matrix
$\bar{\epsilon}$	4×1 vector containing the classical strain measures at the beam reference line
$\mathcal{U}(\bar{\epsilon})^{(a)}_{\text{classical-like}}$	classical-like energy per unit length due to embedded smart structures
$\bar{S}_{6\times6}$	6×6 Timoshenko-like stiffness matrix
$\bar{S}_{5\times5(Vlasov)}$	5×5 Vlasov-like stiffness matrix
$\mathcal{U}_{\text{refined}}$	refined elastic energy per unit length
F_1	axial force at the beam reference line
F_2	transverse force at the beam reference line in the x_2 direction
F_3	transverse force at the beam reference line in the x_3 direction

M_1	twisting moment at the beam reference line
M_2	bending moment at the beam reference line about the x_2 direction
M_3	bending moment at the beam reference line about the x_3 direction
$F_1^{(a)}$	Active axial force at the beam reference line
$F_2^{(a)}$	Active transverse force at the beam reference line in the x_2 direction
$F_3^{(a)}$	Active transverse force at the beam reference line in the x_3 direction
$M_1^{(a)}$	Active twisting moment at the beam reference line
$M_2^{(a)}$	Active bending moment at the beam reference line about the x_2 direction
$M_3^{(a)}$	Active bending moment at the beam reference line about the x_3 direction
x_1, x_2, x_3	Length measures along the Cartesian axes
u_1, u_2, u_3	Displacements along the cartesian dextral triad at beam reference line
$\hat{u}_1, \hat{u}_2, \hat{u}_3$	Displacements along the cartesian dextral triad at a point on the shell mid-surface
v_1, v_2, v_3	Displacements along the shell dextral triad at a point on the shell mid-surface
ξ	through the thickness shell coordinate
$(\dot{\ })$	derivative along the shell contour coordinate s
$(\ )'$	derivative along the shell axial coordinate x_1
$\vec{\mathbf{r}}$	position vector of the shell mid-surface
$\vec{\tau}$	tangential vector to the shell mid-surface
$\vec{\mathbf{n}}$	normal vector to the shell mid-surface
r_τ	component of $\vec{\mathbf{r}}$ along the tangent to the shell mid-surface
r_n	component of $\vec{\mathbf{r}}$ along the normal to the shell mid-surface
R	curvature of shell mid-surface
$\breve{\varepsilon}_{ij}^{(a)}$	induced piezoelectric strain tensor
$\varepsilon_{\alpha\beta}$	shell total strain tensor
d_{kij}	electromechanical coupling tensor of the piezoelectric material
E_k	applied electric field vector

$\mathcal{R}(\vartheta)$	strain transformation operator
$D^{\alpha\beta\gamma\delta}$	the plane-stress reduced material elastic constants
$E^{\alpha\beta\gamma\delta}$	the 3-D elastic material constants
$\gamma_{\alpha\beta}, \rho_{\alpha\beta}$	Koiter and Sanders shell strain measures
$\tilde{\mathcal{U}}^{(m)}$	shell mechanical strain energy per unit length
ψ^{T}	vector of shell strains containing no unknown warping functions
ϕ^{T}	vector of shell strains containing the unknown warping functions
$\aleph(E_1)$	energy density in a quadratic form of the electric field
Q	cross-sectional material and geometry matrix
S	cross-sectional material and geometry matrix
P	cross-sectional material and geometry matrix
H	cross-sectional electro-mechanical and geometry matrix
G	cross-sectional electro-mechanical and geometry matrix
$\parallel \epsilon \parallel$	maximum amount of small strain
E^{T}	cross-sectional geometry matrix
$\hat{T}$	cross-sectional geometry matrix
$\bar{\lambda}$	vector containing the Lagrange multipliers of the constraints
λ_i	Lagrange multiplier of the i^{th} constraint
T	cross-sectional geometry matrix
K	cross-sectional electro-mechanical and geometry matrix
F	cross-sectional material and geometry matrix
J	cross-sectional material and geometry matrix
η	sectorial coordinate of the open thin-walled cross-section
$\mathbb{F}^{(\mathrm{a})}$	actuation force and moments vector
$\mathbb{F}^{(\mathrm{m})}$	mechanical force and moments vector
$\mathbb{M}_{\omega}^{(\mathrm{a})}$	active bi-moment

S_{11}	cross-sectional axial stiffness constant
S_{22}	cross-sectional torsional rigidity constant
S_{33}	cross-sectional bending stiffness constant about x_2 axis
S_{44}	cross-sectional bending stiffness constant about x_3 axis
S_{55}	cross-sectional Vlasov stiffness constant
S_{12}	cross-sectional stiffness constant of coupling between stretch and twist
S_{13}	cross-sectional stiffness constant of coupling between stretch and bending
S_{14}	cross-sectional stiffness constant of coupling between stretch and bending
S_{15}	cross-sectional stiffness constant of coupling between stretch and Vlasov mode
S_{23}	cross-sectional stiffness constant of coupling between twist and bending
S_{24}	cross-sectional stiffness constant of coupling between twist and bending
S_{25}	cross-sectional stiffness constant of coupling between twist and Vlasov mode
S_{34}	cross-sectional stiffness constant of coupling between the two orthogonal bendings
S_{35}	cross-sectional stiffness constant of coupling between bending and Vlasov mode
S_{45}	cross-sectional stiffness constant of coupling between bending and Vlasov mode

Chapter 3

$(\dot{\ })$	derivative of a quantity in time
$\mathbf{r}(x_1)$	position vector of the undeformed beam reference line
$\hat{\mathbf{r}}(x_1, x_2, x_3)$	position vector of a material point on the undeformed cross-section
$\mathbf{b}_i$	dextral triad of the undeformed beam cross-section
$\mathbf{u}(x_1)$	elastic deformation vector of the beam cross-section
$\mathbf{B}_i$	dextral triad of the deformed beam cross-section
$\mathcal{C}^{lr}$	transformation operator from the broken frame, r, to the unbroken frame, l
$\mathbf{k}$	initial twist and curvature vector of undeformed beam
k_1	initial twist of the undeformed beam

k_2	initial curvature about the x_2 axis
k_3	initial curvature about the x_3 axis
$\mathcal{C}^{\mathbf{ba}}$	transformation operator to the twisted and curved frame
$\mathbf{g}_i$	the covariant base vectors at a material point of the undeformed cross-section
$\mathbf{g}^i$	the contravariant base vectors at a material point of the undeformed cross-section
g	the metric scaling factor
ε_{ijk}	the cyclic permutation tensor
$\mathbf{G}_i$	the covariant base vectors at a material point of the deformed cross-section
$\mathcal{C}^{\mathbf{Bb}}$	transformation operator of from the undeformed frame to the deformed one
$\mathfrak{A}$	the elastic deformation gradient
$\mathcal{R}$	deformation rotation operator at a material point
$\mathfrak{U}$	right stretch tensor
$\mathfrak{V}$	left stretch tensor
$\mathbf{\Gamma}^*$	the symmetric Jaumann-Biot-Cauchy strain tensor
$\mathbf{I}$, $\underline{\Delta}_{3\times3}$	the 3×3 identity matrix
ζ_2	nondimensionalized cross-sectional coordinate
ζ_3	nondimensionalized cross-sectional coordinate
$\boldsymbol{\epsilon}$	the generalized/average strains at the beam reference line
$\boldsymbol{\gamma}$	the average cross-sectional extensional strain measure
$\boldsymbol{\kappa}$	the twist/curvature (moment) strain measures
$\mathfrak{Z}$	the Jaumann-Biot-Cauchy stress tensor at a material point
$\mathbb{D}$	the symmetric 6×6 material elastic constants
$\mathbf{K}$	the total twist/curvature measure vector
$\mathbf{e}_0^{\mathrm{T}}$	$\begin{bmatrix} 0 & 0 & 0 \end{bmatrix}$
$\mathbf{e}_1^{\mathrm{T}}$	$\begin{bmatrix} 1 & 0 & 0 \end{bmatrix}$

$\mathbf{e}_2^{\mathrm{T}}$	$\begin{bmatrix} 0 & 1 & 0 \end{bmatrix}$
$\mathbf{e}_3^{\mathrm{T}}$	$\begin{bmatrix} 0 & 0 & 1 \end{bmatrix}$
$\mathcal{T}$	the beam kinetic energy per unit length
$\mathcal{U}$	the beam strain energy per unit length
$\bar{\mathcal{W}}$	the beam virtual work of applied loads per unit length
$\bar{\mathcal{A}}$	the beam virtual action term
$\mathbf{F}$	internal cross-sectional forces at beam reference line
$\mathbf{M}$	internal cross-sectional moments at beam reference line
$\overline{\delta\boldsymbol{\psi}}$	virtual rotations
$\overline{\delta\mathbf{q}}$	virtual displacements
$\mathbf{V}$	the linear inertial velocity at the reference line of the deformed frame
$\mathbf{v}$	the total inertial velocity of the undeformed frame
$\boldsymbol{\omega}$	the inertial angular velocity of the undeformed frame
$\boldsymbol{\Omega}$	the inertial angular velocity of the deformed cross-section
$\mathbf{V}^{\breve{m}}$	The inertial velocity of a material point on the cross-section
$\boldsymbol{\xi}$	the position vector of the material point, $\breve{m}$
$\rho(x_2, x_3)$	the material density
$\bar{m}$	the beam mass per unit length
$\overline{m\xi}$	the first mass moment of inertia per unit length
$\bar{i}$	the second mass moment of inertia per unit length
$\mathbf{P}$	the cross-sectional linear momentum
$\mathbf{H}$	the cross-sectional angular momentum
$\mathbf{f}$	external body forces per unit volume
$\mathbf{m}$	external body moments per unit volume
$\hat{\mathbf{P}}$	beam boundary cross-sectional linear momentum

$\hat{\mathbf{H}}$	beam boundary cross-sectional angular momentum
$\hat{\mathbf{F}}$	beam boundary cross-sectional forces
$\hat{\mathbf{M}}$	beam boundary cross-sectional moments
R	3×3 sub-matrix of the asymptotically correct cross-sectional stiffness matrix
S	3×3 sub-matrix of the asymptotically correct cross-sectional stiffness matrix
T	3×3 sub-matrix of the asymptotically correct cross-sectional stiffness matrix
D	3×3 sub-matrix of the cross-sectional inertia matrix
Q	3×3 sub-matrix of the cross-sectional inertia matrix
I	3×3 sub-matrix of the cross-sectional inertia matrix
$\bar{x}_2$	the x_2 location of the centre of mass of the beam
$\bar{x}_3$	the x_3 location of the centre of mass of the beam
$\bar{I}_1$	cross-sectional moment of inertia per unit length about the x_1 axis
$\bar{I}_2$	cross-sectional moment of inertia per unit length about the x_2 axis
$\bar{I}_3$	cross-sectional moment of inertia per unit length about the x_3 axis
$\bar{I}_{23}$	cross-sectional product of inertia per unit length
$\mathbf{f}_d$	damping forces per unit volume
$\mathbf{m}_d$	damping moments per unit volume
$\mathbb{C}$	damping proportionality matrix
$\bar{\eta}$	parameter that controls damping level of low frequency modes
$\bar{\delta}$	parameter that controls damping level of high frequency modes
J	3×3 sub-matrix of the cross-sectional damping matrix
N	3×3 sub-matrix of the cross-sectional damping matrix
B	3×3 sub-matrix of the cross-sectional damping matrix
W	3×3 sub-matrix of the cross-sectional damping matrix
$\mathcal{X}_1$	state vector of beam element
$\mathcal{X}_2$	state vector of articulation mechanism

m_i	mass of the i^{th} rigid body in a multibody system
$\mathbb{I}_i$	inertia tensor of the i^{th} rigid body in a multibody system
$\breve{\mathbf{C}}$	inertia coefficient matrix of rigid bodies in a multibody system
c_{flap}	flap hinge viscous damping coefficients
$c_{lead-lag}$	lead-lag hinge viscous damping coefficients
$\mathbb{I}_1$	mass inertia tensor of flap link
$\mathbb{I}_2$	mass inertia tensor of lead-lag link
$\mathbf{\Omega}_{ship}$	ship angular velocity in the ocean frame
$\mathbf{\Omega}_{hub}$	rotor hub angular velocity
$\mathbf{\Omega}_{flap}$	flap link angular velocity
$\mathbf{\Omega}_{lead-lag}$	lead-lag link angular velocity
$\mathcal{C}^{SI}$	transformation matrix from inertial ocean frame I to the ship frame S
$\mathcal{C}^{\mathcal{R}_0 S}$	transformation matrix from the ship frame S to the rotor hub frame $\mathcal{R}_0$
$\mathcal{C}^{\mathcal{R}_1 \mathcal{R}_0}$	transformation matrix from the rotor hub frame to the flap link frame $\mathcal{R}_1$
$\mathcal{C}^{\mathcal{R}_2 \mathcal{R}_1}$	transformation matrix from the flap link frame to the lead-lag link frame $\mathcal{R}_2$
$\mathbf{R}_{cm1}$	centre of mass position vector of the flap link in the $\mathcal{R}_1$ frame
$\mathbf{R}_{cm2}$	centre of mass position vector of the lead-lag link in the $\mathcal{R}_1$ frame
$\mathbf{R}_{l1}$	lead-lag joint position vector in the flap link frame
$\mathbf{R}_{l2}$	blade root position vector in the lead-lag link frame
$\mathbf{V}_{ship}$	ship linear velocity in the ocean frame
$\mathbf{R}_{HR}$	position vector of the helicopter in the ocean frame
$\mathbf{R}_{HB}$	position vector of the rotor hub in the ship frame
$\mathbf{R}_{N1}$	position vector of the beam reference line relative to the blade point of attachmen
$\mathcal{C}^{\mathcal{N} \mathcal{R}_2}$	transformation matrix from the $\mathcal{R}_2$ frame to the blade root frame $\mathcal{N}$
$\mathbf{V}_{N1}$	blade root linear velocity in the blade root frame
$\mathbf{\Omega}_{N1}$	blade root angular velocity in the blade root frame

χ	augmented state vector of articulation mechanism
$\mathbf{F}_{impact}$	phenomenological forces of impact between articulation links and blade stops
a	penetration distance of impact
k	elastic stiffness constant of blade stops
c	viscoelastic damper constant of blade stops
$D_{\S}$	length setting of blade stops/limiters
$\phi_{flap/droop}$	angular setting of blade stops/limiters

Chapter 4

$\overline{\mathbf{X}}_k^j$	midpoint value of state variable of beam element k at time index j
Δx_k	length of beam element
Δt	size of time step
α_m	first parameter of the first order generalized-α method
α_k	second parameter of the first order generalized-α method
γ	third parameter of the first order generalized-α method
λ^∞	spectral radius at infinity of the first order generalized-α method
ρ_∞	eigenvalue at infinity of the first order generalized-α method
δ	blade tip sweep angle

Chapter 5

$\bar{\mathcal{K}}$	aerodynamics reduced frequency
c	airfoil chord length
ω	frequency of the airfoil varying phenomenon
V	incoming air free-stream velocity
M	flow Mach number
C_l	quasi-steady lift coefficient
C_d	quasi-steady drag coefficient
C_m	quasi-steady moment coefficient

α	angle of attack
V_{app}	apparent wind velocity as seen by the airfoil
$y_{3c/4}$	location of the three-quarter chord point relative to beam reference line
$y_{c/4}$	location of the quarter chord point relative to beam reference line
ρ	flow medium density
L	the normal aerodynamic force per-unit-length
D	the drag aerodynamic force per-unit-length
$m_{c/4}$	the aerodynamic twisting moment per-unit-length
Φ	incoming flow skew angle
s	aerodynamic time
$w_{3/4}(t)$	airfoil vertical velocity at the three-quarter chord point
$\phi(s)$	indicial step response function of the airfoil
$C(k)$	Theodorsen function in the frequency domain
$w_{3/4,eff}$	effective airfoil vertical velocity at the three-quarter chord point
A_1	constant of Jones approximation of Theodorsen function in the time domain
A_2	constant of Jones approximation of Theodorsen function in the time domain
b_1	constant of Jones approximation of Theodorsen function in the time domain
b_2	constant of Jones approximation of Theodorsen function in the time domain
X	unsteady aerodynamics deficiency function
Y	unsteady aerodynamics deficiency function
α_{eff}	effective angle of attack
C_l^c	unsteady circulatory lift coefficient
C_n^c	unsteady normal lift force coefficient
C_c^c	unsteady chord-wise force coefficient
C_n^{nc}	non-circulatory lift coefficient
C_m^{nc}	non-circulatory moment coefficient

C'_{n}	corrected quasi-steady normal lift coefficient
$D^{\mathrm{p}}_{\mathrm{n}}$	deficiency function of quasi-steady normal lift coefficient
T_p	experimentally determined airfoil constant (critical leading edge pressure)
f'	uncorrected trailing edge separation point (dynamic stall)
α'_1	experimentally determined critical airfoil angle (trailing edge separation)
f''_{j}	corrected trailing edge separation point
$D_{f'_{\mathrm{j}}}$	deficiency function of trailing edge separation
T_f	experimentally determined airfoil constant (trailing edge separation)
C^f_{n}	normal force coefficient due to the trailing edge separation
C^f_{m}	moment coefficient due to the trailing edge separation
C^f_{d}	chord-wise drag coefficient due to the trailing edge separation
C^v_{n}	uncorrected normal force coefficient due to vortex shedding
$C^v_{N_{\mathrm{n}}}$	corrected normal force coefficient due to vortex shedding
T_v	experimentally determined airfoil constant (vortex shedding)
T_{vl}	experimentally determined airfoil constant (vortex shedding)
τ_v	non-dimensional vortex time
CP_v	location of centre of pressure of vortex along the airfoil
$C^v_{N_{\mathrm{m}}}$	corrected moment coefficient due to vortex shedding
$C^{\mathrm{dynamic-stall}}_{\mathrm{n}}$	total normal force coefficient due to dynamic stall
$C^{\mathrm{dynamic-stall}}_{\mathrm{m}}$	total moment coefficient due to dynamic stall
$\breve{C}^{\mathrm{dynamic-stall}}_{\mathrm{n}}$	total normal force coefficient due to dynamic stall in airfoil frame
$\breve{C}^{\mathrm{dynamic-stall}}_{\mathrm{d}}$	drag force coefficient due to dynamic stall in airfoil frame

Chapter 6

λ_f	rotor blade frequency scaling factor
γ_l	rotor blade lock number
μ	rotor blade tip advance ratio

F_r	Froude number
f^*	scaled frequency of turbulence in the flow
n_{Fr}	length Froude-scaling factor
$\epsilon_{\text{Gauge}i}$	experimental strain value of the i^{th} gauge
$\alpha_{\text{Gauge}i}$	i^{th} strain gauge proportionality factor
Θ_{Hinge}	experimental flap angle from the Hall-effect sensor
α_{He}	Hall-effect proportionality factor
ΔV_{He}	voltage difference measured by the Hall-effect sensor
v	aluminum beam half-thickness
z	experimental flap elastic displacement measured from the beam reference line
β_{He}	experimental angular offset of Hall-effect sensor
V_{offset}	experimental voltage offset of strain gauge

Chapter 8

$D(t)$	ship degree of freedom
$\dot{D}(t)$	time rate of change of ship degree of freedom
$\ddot{D}(t)$	second time rate of change of ship degree of freedom
A_i	amplitude of the i^{th} frequency component of the ship degree of freedom
f_i	i^{th} linear frequency component of the ship degree of freedom
ϕ_i	phase shift of the i^{th} frequency component of the ship degree of freedom

Chapter 9

κ	gust factor of ship airwake linear deterministic model
$\mathbf{t_{electrodes}}$	distance between electrodes
Ω_{max}	maximum angular speed of rotor hub
t_{engage}	rotor engagement time
$t_{disengage}$	rotor disengagement time
$V(t)$	applied voltage signal at time t

f_i	frequency of the i^{th} frequency component of the applied voltage signal
N	number of applied voltage components
V_{wind}	free stream wind velocity
Ψ_{wod}	wind over the deck angle
Ψ_{yaw}	ship yaw angle
Φ_{roll}	ship roll angle
$\|u_3\|$	maximum total tip flap displacement
R	total rotor blade span
Ω_{critical}	angular rotor hub speed at which actuation mode is switched
t_{critical}	engagement time at which actuation mode is switched
$t_{\text{d/critical}}$	disengagement time at which actuation mode is switched
$V_{\text{wind\_x}}$	x-component of free stream velocity in ship frame
$V_{\text{wind\_y}}$	y-component of free stream velocity in ship frame
$V_{\text{wind\_z}}$	z-component of free stream velocity in ship frame
$V_{\text{wind\_Y}}$	beam wind velocity seen by a ship in motion
α	variable wind over the deck angle
$\bar{V}_z$	rotor disc total gust wind velocity
σ	rotor hub azimuthal angle
φ	lead-lag hinge angle of articulated rotor system
$\vec{V}(x,y,z,t)$	airwake total wind velocity at grid point in space and time
$\bar{\vec{V}}(x,y,z)$	airwake steady wind velocity in space
$\breve{\vec{V}}(t)$	airwake fluctuating wind velocity of perfectly correlated turbulence model

Contents

Acceptance ii

Abstract iii

Acknowledgements iv

List of Symbols v

Contents xviii

List of Figures xxv

List of Tables xlv

1 Introduction 1

1.1 Overview of Chapter 1 1

1.2 Maritime Helicopter Operation 1

1.2.1 Overview of Hazards and Challenges 1

1.2.2 Overview of Helicopter Ship Dynamic Interface 4

1.2.3 Aeroelastic Response of Rotor Systems During Engagement and Disengagement Operational Phases (The Blade Sailing Phenomenon) . 6

1.3 Review of Experimental Investigations and Modelling Techniques of the BSP 10

1.3.1 Early Investigations 12
1.3.2 Recent Investigations 13
1.4 Review of Control and Attenuation Strategies 21
1.5 Overview of Present Research 23

2 Cross-Sectional Analysis of Active Rotor Blades **26**
2.1 Overview of Chapter 2 26
2.2 Motivation 26
2.3 The Integral Active Twist Concept 28
2.4 Overview of Analysis Techniques 32
2.5 Structural Idealizations of Active Rotor Blades 35
2.6 The Variational Asymptotic Method (VAM) 37
2.6.1 General Description 38
2.6.2 Application of the VAM to Active Thin-Wall Beams 42
2.7 Advantages and Limitations of the Developed Theory 78
2.8 Future Recommendations 83

3 Intrinsic and Geometrically-Exact Modelling of Maritime Active Rotor Systems **84**
3.1 Overview of Chapter 3 84
3.2 Review of Available Rotorcraft Comprehensive Analysis Codes 85
3.3 Nonlinear Beam Kinematics Preliminaries 87
3.4 Intrinsic Dynamics Equations of Moving Active Beams 96
3.4.1 Intrinsic Structural Damping 106
3.4.2 Intrinsic Conservation Laws 108
3.5 Intrinsic Multibody Formulation of Active Rotor Systems in a Non-Inertial Frame 113

3.5.1 Backlash Modelling 119
3.6 Implementation 120
3.7 Future Recommendations 121

4 Solution of the Intrinsic and Geometrically-Exact Model of Active Rotor Systems 123

4.1 Overview of Chapter 4 123
4.2 Overview of Numerical Solution of Nonlinear Elastodynamics Models of Multibody Systems 124
4.3 Setting up the Problem 126
4.4 Problem Discretization (Shape Functions) 128
4.5 The Proposed First Order Generalized-α Scheme 132
4.6 Validation and Numerical Investigation 133
4.6.1 Active Beam Element Validation 148
4.7 Future Recommendations 149

5 Nonlinear Quasi-Steady and Unsteady Aerodynamics Modelling 150

5.1 Overview of Chapter 5 150
5.2 Nonlinear Quasi-Steady Model of NACA0012 with Stall Effects 150
5.3 The Arbitrary Motion Theorem (Dynamic Wake Modelling) 156
5.3.1 Unsteady Circulatory Aerodynamic Loads 157
5.4 Leishman and Beddoes Dynamic Stall Model 162
5.5 Future Recommendations 168

6 Design and Manufacture of a $1/12^{th}$ Froude-Scaled Flap-articulated Rotor System 170

6.1 Overview of Chapter 6 170
6.2 Experiment Motivation and Goals 171

6.3 Design Evolution of the Hardware 173
6.3.1 Froude Scaling 173
6.3.2 Rotor Blades 175
6.3.3 Rotor Hub 177
6.3.4 Instrumentation 177
6.3.5 Identified Challenges and Limitations 181
6.4 Design Evolution of the Software 183
6.4.1 Identified Challenges and Limitations 183
6.5 Calibration and Data Reduction 184
6.6 Future Recommendations 186

7 Aeroelastic Response of the 1/12th Froude-scaled Flap Articulated Rotor System in the NRC-IAR 2×3 Meter Wind Tunnel 190

7.1 Summary of Chapter 7 190
7.2 Overview of Experimental Setup and Runs 191
7.3 Experimental and Simulated Aeroelastic Response 197
7.3.1 Analysis of Experimental Results 197
7.3.2 Simulation of Experimental Runs 201

8 Dynamic response of the 1/12th Froude-scaled Flap Articulated Rotor System to Representative Scaled Ship Motion 222

8.1 Overview of Chapter 8 222
8.2 Overview of Experimental Setup and Runs 223
8.3 Experimental and Simulated Dynamics Response 227
8.3.1 Sub-phase(I) 227
8.3.2 Sub-phase(II) 232
8.4 Future Recommendations 234

9 Feasibility Study of Open-Loop Integral Active Twist Actuation Strategies for Countering the Blade Sailing Phenomenon **245**

9.1 Overview of Chapter 9 245

9.2 The $1/6^{th}$ Mach-scaled Integral Active Twist CH-47D Rotor 246

9.2.1 Design Parameters 248

9.2.2 Design Modifications 249

9.2.3 Cross-Sectional Analysis 251

9.2.4 Simulation Model Setup 253

9.2.5 Relevant Dynamic Active Twist Study 255

9.3 Aeroelastic Response of the IATR During Engagement and Disengagement Operation Using the Linear Deterministic Airwake Model 258

9.3.1 Investigation of Two Open-Loop Control Strategies 263

9.3.2 Effect of Ship Motion and Turbulence 278

9.4 Future Recommendations 295

10 Conclusions **301**

References **305**

Appendices **326**

A **327**

A.1 The Plane-Stress Reduced Constants $D^{\alpha\beta\gamma\delta}$ 327

A.2 The Shell Energy Per Unit Length Material and Electromechanical Matrices 328

A.3 Convergence of the Displacement Field of Closed Cross-Sections 330

A.4 Mathematical Implications of the Constraints on the Displacement Field of Closed Cross-Sections 332

A.5 Material and Geometry Matrices of Single- and Two-Cell Cross-Section . . 334

B **337**

B.1 Properties of the Skew-Symmetric Operator 337

B.2 Intrinsic Beam Dynamic Relations 338

B.3 Intrinsic Conservation Laws Relations 341

C **343**

C.1 Cross-Sectional Properties Used in Numerical Examples 343

C.2 Post-Processing to Obtain Rotation and Displacement Parameters 344

D **347**

D.1 Quasi-steady Constants of the NACA64A010 347

D.2 Leishman and Beddoes Dynamic Stall Model Constants 348

E **350**

E.1 Basic Properties of NACA 64A010 Blade Cross-Section 350

E.2 Elastic and Inertial Properties of the $1/12^{th}$ Froude-Scale Rotor Blade . . . 351

E.3 Engagement and Disengagement Profile of the $1/12^{th}$ Froude-Scale Rotor Blade 353

F **354**

F.1 Predicted Time Histories of Total Tip Displacement, Elastic Tip Displacement, and Flap Hinge Angle of Experimental Runs of Phase (I) 354

G **370**

G.1 Sample Time History of Representative $\mathbf{1/12^{th}}$ Froude-Scaled Ship Motion 370

H **374**

H.1 Static Actuation 374

H.2 Dynamic Actuation 379

H.2.1 Test Temporal Points 379
H.3 Effect of Ship Motion 390
H.4 Effect of Turbulence 391

List of Figures

1.1 Formation of Canadian Navy ships with the helicopter flight decks highlighted [Courtesy of the Canadian Navy]. 2

1.2 Heavy seas encountered by a navy ship [Courtesy of the Canadian Navy]. . 3

1.3 Typical maritime operation of a Sea King helicopter by the Canadian Navy [Courtesy of the Canadian Navy/Airforce]. 3

1.4 Hypothetical SHOLs for shipborne helicopter operation. Safe operation points are shaded. 4

1.5 Phases of a typical helicopter ship operation [Photos courtesy of the Canadian Air Force]. 5

1.6 Examples of the BSP [10]. 6

1.7 (a) Computational airwake using FLUENT 6.1 CFD [2], (b) Experimental airwake visualization over -20° ship deck. 9

1.8 Six ship motion degrees of freedom (DOF). 10

1.9 Sikorsky H-19 fully articulated rotor head with important components highlighted [Courtesy of Sikorsky/United Technology Company]. 10

1.10 Eurocopter 135 hingeless rotor head [Courtesy of Eurocopter]. 11

1.11 Early deterministic models of ship airwake [17]. 12

1.12 Kamov Ka-29TB coaxial rotor head [Courtesy of Kamov Helicopters]. . . . 13

1.13 Linear deterministic model of the ship airwake. 15

1.14 Normalized vertical velocity of the linear deterministic model of a ship airwake over the rotor disk. 16
1.15 Sample $1/120^{th}$ scaled transverse velocity contours of the experimental airwake model at $-5°$ and $20°$ deck roll angle [44]. 17
1.16 Trailing edge concept for vibration and noise reduction [Courtesy of the Boeing Company]. 23
1.17 Pictorial overview of present research. 25

2.1 Isometric view of Bell 429 rotor system. 27
2.2 Typical laminate design of a rotor blade with the IAT concept. 28
2.3 Positive fibre orientation convention indicating local and global coordinate systems respectively. 29
2.4 A monolithic piezoelectric material block undergoing mechanical deformation due to the application of an electric field. 30
2.5 Section of an AFCs ply undergoing axial extension due to an applied electric field in the fibre poling direction. 31
2.6 Generic MFCs ply design components. 31
2.7 Generic IAT concept with an active airfoil undergoing positive active twist due to AFCs/MFCs subjected to an electric field with appropriate polarity. 32
2.8 Finished MFCs package and its geometric dimensions. 33
2.9 Isometric view of a generic helicopter rotor blade. 36
2.10 (a) Cross-sectional spar design of the Active Low Vibration Rotor (ALVR), (b) Geometric idealization of two-celled rotor blade cross-section. 37
2.11 Geometry of active thin-wall slender anisotropic beam structure. 45
2.12 (a) Contour of two-cell closed cross-section with surface normals, (b) Contour of three-cell closed cross-section with surface normals 61
2.13 Three-cell isotropic box beam. 72

2.14 Active anisotropic single-cell box beam. 73
2.15 Example of open cross-section beams (a) C-channel, (b) I-beam. 75
2.16 Rotating frequencies for an example rotor blade;solid lines with shear flexibility, dashed lines without. 81

3.1 Kinematics of general beam deformation. 89
3.2 Illustration of blade tip (a) sweep and (b) anhedral and associated frames. 90
3.3 Top view of hingeless rotor system. 114
3.4 Top view of fully articulated rotor system. 115
3.5 Simple and representative multibody dynamics model of the hub system in the non-inertial frame of a moving ship. 115
3.6 Articulation point of attachment relative to the beam reference line. 117
3.7 Droop/flap stops mechanism attached to the flap link, and the stops viscoelastic model used to evaluate impact forces. 120
3.8 Detailed block diagram of the implementation of developed models to simulate active rotor systems. 122

4.1 Space-time discretization of the blade into n beam elements. 129
4.2 Time history of: (I) The blade normalized total mechanical energy and its difference after the loading is ceased, (II) The second intrinsic conservation law of the blade after the loading is ceased of case 2(a). 136
4.3 Time history of: (I) The axial force F_1, (II) The flapping shear force of the blade F_3 of the 25^{th} beam element after the loading is ceased of case 2(a). . 137
4.4 Time history of: (I) The normalized total mechanical energy of the blade during the initial steps of the simulation, (II) The normalized total mechanical energy of the blade during the final steps of the simulation of cases 2(b), (c), and (d). 138

4.5 Time history of the second intrinsic conservation law of the blade after the loading is ceased of cases 2(b), (c), and (d). 139
4.6 Size of the time step used by the solver during the initial stages of the simulation of case 2(c). 140
4.7 Time history of the total mechanical energy of the fully articulated rotor system of case 3. 142
4.8 Time history of: (I) The flapping shear force F_3, (II) The tip flap displacement u_3, (III) the flap hinge angle ϕ_{flap} of case 3. 143
4.9 Normalized relative error based on the signal RMS of: (I) Cases 4 using the linear flap velocity V_3, the tip displacement u_3, and the shear flapping force F_3 of the 25^{th} beam element, (II) The second intrinsic conservation law. . . 144
4.10 (I) Normalized FFT of the tip displacement u_3 of cases 5(a), (b) and (c), (II) Time history of the twisting moment of the second beam element of cases 5(a) and (c). 145
4.11 Time histories of: (I) The experimental/theoretical flap hinge angle, (II) The Experimental/Theoretical strain at 40% blade length station of the drop test/droop stop impact from 9.7°. 147

5.1 NACA0012 airfoil with the relevant aerodynamic frames and points. 154
5.2 Nonlinear quasi-steady aerodynamic coefficients of NACA0012 at a Mach number of 0.3. 154
5.3 Blade frame view and incoming wind. 156
5.4 Unsteady circulatory aerodynamic coefficient of an airfoil pitching with a functional form of $\alpha = 2.1° + 8.2° \sin(wt)$, $\bar{K} = 0.074$, $M = 0.383$. 162
5.5 Illustration of dynamic stall and relevant physical quantities. 163
5.6 Normal lift and moment coefficients of a NACA0012 airfoil pitching with $\alpha = 10.3° + 8.1° \sin(wt)$, $\bar{K} = 0.075$, and $M = 0.379$. 168

5.7 Flow chart illustration of the L-B dynamic stall algorithm. 169

6.1 Top view of the blades with and without the airfoil segments. 176
6.2 Rotor hub components of the Froude-scaled rotor system. 178
6.3 Wired strain gauge. 179
6.4 Voltage node V-Link and top view of the DAQ. 180
6.5 Rotor hub shaft and base casing. 181
6.6 Neoprene bumper behaviour characterization. 182
6.7 Motion control software and hardware. 187
6.8 Experimental and theoretical optical encoder signal. 188
6.9 Blade static deflection under gravitational loading. 189

7.1 Downstream view of the rotor system on the two ship decks considered inside the 2×3[m] wind tunnel. 192
7.2 The steady airwakes of the 0° and −20° decks. 193
7.3 System components and their interaction in the 2×3[m] wind tunnel. . . . 194
7.4 Reference/Initial azimuthal orientation of the rotor system in the wind tunnel. 194
7.5 Experimental and simulated drop test of the blade on the neoprene stops with and without aerodynamic forces 195
7.6 Illustration of positive and negative collective pitch setting. 196
7.7 Raw signals received blade 705 for the experimental run of deck roll angle of −20°, wind speed 7.66 [m/s], collective pitch setting of -4°, engage/disengage time of 8 [sec]. 197
7.8 Datum of the tip displacement and sign convention used. 198
7.9 Registered downward extremum of blade 705 as a function of engage/disengage time for 0° deck roll angle; wind speeds of:(1) 4, (2) 6, and (3) 8 [m/s]; collective pitch setting of: (I) 0°, (II) 4°, (III) 6°, (IV) 8°, (V) −4°, (VI) −8°. 198

7.10 Registered upward extremum of blade 705 as a function of engage/disengage time for 0° deck roll angle; wind speeds of:(1) 4, (2) 6, and (3) 8[m/s]; collective pitch setting of: (I) 0°, (II) 4°, (III) 6°, (IV) 8°, (V) −4°, (VI) −8°.199

7.11 Registered downward extremum of blade 705 as a function of engage/disengage time for −20° deck roll angle; wind speeds of:(1) 4, (2) 6, and (3) 8[m/s]; collective pitch setting of: (I) 0°, (II) 4°, (III) 6°. 200

7.12 Registered upward extremum of blade 705 as a function of engage/disengage time for −20° deck roll angle; wind speeds of:(1) 4, (2) 6, and (3) 8 [m/s]; collective pitch setting of: (I) 0°, (II) 4°, (III) 6°. 201

7.13 The maximum downward tip displacement predicted by the three aerodynamic models considered in this investigation versus experimental data, Run12, P3 (Deck Angle: 0°, Collective Pitch Setting: 0°, Wind Speed: 4[m/s]). 202

7.14 The maximum downward tip displacement predicted by the three aerodynamic models considered in this investigation versus experimental data, Run12, P10 (Deck Angle: 0°, Collective Pitch Setting: 0°, Wind Speed: 6[m/s]). 203

7.15 The maximum downward tip displacement predicted by the three aerodynamic models considered in this investigation versus experimental data, Run13, P3 (Deck Angle: 0°, Collective Pitch Setting: 4°, Wind Speed: 4[m/s]). 203

7.16 The maximum downward tip displacement predicted by the three aerodynamic models considered in this investigation versus experimental data, Run16, P16 (Deck Angle: 0°, Collective Pitch Setting: 6°, Wind Speed: 8[m/s]). 204

7.17 The maximum downward tip displacement predicted by the three aerodynamic models considered in this investigation versus experimental data, Run17, P10 (Deck Angle: 0°, Collective Pitch Setting: 8°, Wind Speed: 6[m/s]). 204
7.18 The maximum downward tip displacement predicted by the three aerodynamic models considered in this investigation versus experimental data, Run19, P3 (Deck Angle: 0°, Collective Pitch Setting: −4°, Wind Speed: 4[m/s]). 205
7.19 Time histories of the engagement for Run 12,P 3 produced by the quasi-steady and the unsteady model. 206
7.20 Simulated versus experimental maximum downward total and elastic tip displacement, 0° deck roll angle case. 208
7.21 Simulated versus experimental maximum upward elastic tip displacement and hinge angle, 0° deck roll angle case. 209
7.22 Simulated versus experimental maximum downward total and elastic tip displacement, −20° deck roll angle case. 211
7.23 Simulated versus experimental maximum upward elastic tip displacement and hinge angle, −20° deck roll angle case. 212
7.24 Engagement of Run (19, P9); total tip displacement. 213
7.25 Engagement of Run (19, P9); tip elastic displacement. 213
7.26 Engagement of Run (19, P9); hinge angle. 214
7.27 Engagement of Run (20, P5); total tip displacement. 214
7.28 Engagement of Run (20, P5); tip elastic displacement. 215
7.29 Engagement of Run (20, P5); hinge angle. 215
7.30 Engagement of Run (27, P4); total tip displacement. 216
7.31 Engagement of Run (27, P4); tip elastic displacement. 216

7.32 Engagement of Run (27, P4); hinge angle. 217
7.33 Disengagement of Run (13, P3); total tip displacement [Uncorrected]. . . . 218
7.34 Disengagement of Run (12, P18); total tip displacement. 219
7.35 Disengagement of Run (12, P18); tip elastic displacement. 219
7.36 Disengagement of Run (12, P18); hinge angle. 220
7.37 Disengagement of Run (16, P16); total tip displacement. 220
7.38 Disengagement of Run (16, P16); tip elastic displacement. 221
7.39 Disengagement of Run (16, P16); hinge angle. 221

8.1 Isometric schematic of the MOOG 6DOF2000E motion platform [Courtesy of MOOG MOTION SYSTEMS DIVISION]. 223
8.2 Froude-scaled rotor system attached to the motion platform while: (I) being stationary (II) moving with the platform and engaged. 224
8.3 Rotor system reference orientation for Phase (II) of the experimental work. 227
8.4 Maximum downward and upward tip deflection as a function of ship roll frequency and hub angular velocity [0° collective pitch setting], sub-phase(I). 228
8.5 Maximum downward and upward tip deflection as a function of ship roll frequency and hub angular velocity [4° collective pitch setting], sub-phase(I). 228
8.6 Maximum downward and upward tip deflection as a function of ship roll frequency and hub angular velocity [8° collective pitch setting], sub-phase(I). 229
8.7 Maximum downward and upward tip deflection as a function of ship roll frequency and hub angular velocity [−4° collective pitch setting], sub-phase(I). 229
8.8 Maximum downward and upward tip deflection as a function of ship roll frequency and hub angular velocity [−8° collective pitch setting], sub-phase(I). 230
8.9 Time history of the tip displacement of Run 1 of sub-phase(II). 233
8.10 Time history of the tip displacement of Run 2 of sub-phase(II). 234
8.11 Time history of the tip displacement of Run 3 of sub-phase(II). 235

8.12 Time history of the tip displacement of Run 4 of sub-phase(II). 236
8.13 Time history of the tip displacement of Run 5 of sub-phase(II). 237
8.14 Time history of the tip displacement of Run 6 of sub-phase(II). 238
8.15 Spectrum of the tip displacement during steady-state for Run 1 of sub-phase(II). 239
8.16 Spectrum of the tip displacement during steady-state for Run 2 of sub-phase(II). 240
8.17 Spectrum of the tip displacement during steady-state for Run 3 of sub-phase(II). 241
8.18 Spectrum of the tip displacement during steady-state for Run 4 of sub-phase(II). 242
8.19 Spectrum of the tip displacement during steady-state for Run 5 of sub-phase(II). 243
8.20 Spectrum of the tip displacement during steady-state for Run 6 of sub-phase(II). 244

9.1 Close up of H-46 Sea King on USS Midway. 246
9.2 Cross-section and top view of the IATR [all dimensions are in inches]. . . . 247
9.3 Top view of the elastic portion of the adopted IATR blade. 249
9.4 Linear initial twist of the IATR. 251
9.5 Cross-section of the modified IATR. 251
9.6 (a) Side view of the generic IATR system, (b) Top view of the generic IATR system. 253
9.7 Percentage error of the tip deflection relative to the reference solution of the cantilevered generic IATR in the gravitational field versus number of beam elements. 254

9.8 Comparison of simulation CPU time using three different time stepping strategies. 255
9.9 Time-domain tip twist response of the active rotor blade subjected to the signal in Eq. 9.7 at 0[Hz] hub frequency. 256
9.10 Frequency-domain tip twist response of the active rotor blade subjected to the signal in Eq. 9.7 at 0[Hz] hub frequency. 257
9.11 Frequency-domain tip twist response of the active rotor blade subjected to the signal in Eq. 9.7 at 2.865[Hz] hub frequency. 257
9.12 Frequency-domain tip twist response of the active rotor blade subjected to the signal in Eq. 9.7 at 5.730[Hz] hub frequency. 257
9.13 Definition of Wind Over the Deck (WOD) angle, ψ_{WOD}. 259
9.14 Time history of the adopted IATR engagement under the wind conditions of 60[kn], 270°WOD for:(a) Total tip displacement, (b) Flap hinge angle, (c) Lead-lag hinge angle, (d) Flap-link transverse force. 260
9.15 Time history of the adopted IATR disengagement under the wind conditions of 45[kn], 60°WOD for:(a) Total tip displacement, (b) Flap hinge angle, (c) Lead-lag hinge angle, (d) Flap-link transverse force. 261
9.16 Maximum downward and upward tip deflection of the engagement of the adopted IATR. 262
9.17 Maximum downward and upward tip deflection of the disengagement of the adopted IATR. 263
9.18 Maximum downward and upward tip deflection of the engagement of the adopted IATR with DC actuation of the integrated AFCs. 264
9.19 Maximum downward and upward tip deflection of the disengagement of the adopted IATR with DC actuation of the integrated AFCs. 265

9.20 Maximum downward and upward tip deflection of the engagement of the adopted IATR with DC actuation of the integrated MFCs. 266
9.21 Maximum downward and upward tip deflection of the disengagement of the adopted IATR with DC actuation of the integrated MFCs. 267
9.22 Time history of the adopted IATR engagement with MFCs static DC actuation under the wind conditions of 60[kn], 270°WOD for:(a) Total tip displacement, (b) Flap hinge angle, (c) Lead-lag hinge angle, (d) Flap-link transverse force. 268
9.23 Time history of the adopted IATR disengagement with MFCs static DC actuation under the wind conditions of 45[kn], 60°WOD for:(a) Total tip displacement, (b) Flap hinge angle, (c) Lead-lag hinge angle, (d) Flap-link transverse force. 269
9.24 Top view of a proposed variable actuation strategy with the proposed twist polarity indicated. 270
9.25 Scaled first component of voltage signal of the proposed dynamic actuation strategy for $2\Omega_{\text{critical}}$, WOD of 270°, and 60 [kn] wind speed. 274
9.26 Scaled second component of voltage signal of the proposed dynamic actuation strategy for $2\Omega_{\text{critical}}$, WOD of 270°, and 60 [kn] wind speed. 274
9.27 Application of the proposed actuation strategy for $2\Omega_{\text{critical}}$, WOD of 270°, and 60 [kn] wind speed for the engagement phase. 275
9.28 Twist command of the first component of the actuation voltage signal as a function of the rotor azimuthal angle. 275
9.29 Maximum downward and upward tip deflection of the engagement of the adopted IATR with dynamic actuation of the integrated MFCs for Ω_{critical}. 276
9.30 Maximum downward and upward tip deflection of the disengagement of the adopted IATR with dynamic actuation of the integrated MFCs for Ω_{critical}. 277

9.31 Maximum downward and upward tip deflection of the engagement of the adopted IATR with dynamic actuation of the integrated MFCs for $0.5\Omega_{\text{critical}}$. 278
9.32 Maximum downward and upward tip deflection of the engagement of the adopted IATR with dynamic actuation of the integrated MFCs for $1.25\Omega_{\text{critical}}$. 279
9.33 Maximum downward and upward tip deflection of the engagement of the adopted IATR with dynamic actuation of the integrated MFCs for $2\Omega_{\text{critical}}$. 280
9.34 Time history of the adopted IATR engagement with MFCs dynamic actuation under the wind conditions of 60[kn], 270°WOD for:(a) Total tip displacement, (b) Flap hinge angle, (c) Lead-lag hinge angle, (d) Flap-link transverse force. 281
9.35 Time history of the adopted IATR disengagement with MFCs dynamic actuation under the wind conditions of 45[kn], 60°WOD for:(a) Total tip displacement, (b) Flap hinge angle, (c) Lead-lag hinge angle, (d) Flap-link transverse force. 282
9.36 Time history of the tip twist angle of the adopted IATR engagement with MFCs dynamic actuation under the wind conditions of 60[kn], 270°WOD. . 283
9.37 Analysis of ship motion effect on the experimental airwake model (a) top view, (b) back view. 283
9.38 Flight deck of the aircraft carrier HMSOcean [Courtesy of the Royal Navy]. 284
9.39 Maximum downward and upward tip deflection of the engagement of the adopted IATR, sea state 4_000_10, experimental airwake. 286
9.40 Maximum downward and upward tip deflection of the disengagement of the adopted IATR, sea state 4_000_10, experimental airwake. 287
9.41 Maximum downward and upward tip deflection of the engagement of the adopted IATR, sea state 4_060_10, experimental airwake. 288

9.42 Maximum downward and upward tip deflection of the disengagement of the adopted IATR, sea state 4_060_10, experimental airwake. 289
9.43 Maximum downward and upward tip deflection of the engagement of the adopted IATR, sea state 4_000_10, deterministic airwake. 290
9.44 Maximum downward and upward tip deflection of the disengagement of the adopted IATR, sea state 4_000_10, deterministic airwake. 291
9.45 Maximum downward and upward tip deflection of the engagement of the adopted IATR, sea state 4_060_10, deterministic airwake. 292
9.46 Maximum downward and upward tip deflection of the disengagement of the adopted IATR, sea state 4_060_10, deterministic airwake. 293
9.47 Time history of the adopted IATR engagement under the wind conditions of 50[kn], 270° WOD with 4_060_10 sea state using the experimental airwake model for:(a) Total tip displacement, (b) Flap hinge angle, (c) Lead-lag hinge angle, (d) Flap-link transverse force. 294
9.48 Time history of the adopted IATR engagement with the actuation strategy employed under the wind conditions of 50[kn], 270° WOD with 4_060_10 sea state using the experimental airwake model for:(a) Total tip displacement, (b) Flap hinge angle, (c) Lead-lag hinge angle, (d) Flap-link transverse force. 295
9.49 Time history of the adopted IATR engagement under the wind conditions of 50[kn], 180° WOD with 4_000_10 sea state using the linear deterministic airwake model for:(a) Total tip displacement, (b) Flap hinge angle, (c) Lead-lag hinge angle, (d) Flap-link transverse force. 296

9.50 Time history of the adopted IATR engagement with the actuation strategy employed under the wind conditions of 50[kn], 180° WOD with 4_000_10 sea state using the linear deterministic airwake model for:(a) Total tip displacement, (b) Flap hinge angle, (c) Lead-lag hinge angle, (d) Flap-link transverse force. 297
9.51 Maximum downward tip deflections for various deck roll angles when the perfectly correlated turbulence is considered. 298
9.52 Maximum upward tip deflections for various deck roll angles when the perfectly correlated turbulence is considered. 298
9.53 Percent change in the maximum downward tip deflections for various deck roll angles with the perfectly correlated turbulence model and the actuation strategy. 299
9.54 Percent change in the maximum upward tip deflections for various deck roll angles with the perfectly correlated turbulence model and the actuation strategy. 299

E.1 Cross-section of the $1/12^{th}$ Froude-scale rotor based on NACA64A010. . . . 350
E.2 Lift-curves for the NACA 64A010 at two Reynolds numbers of interest [167]. 351
E.3 Elastic properties of the $1/12^{th}$ Froude-Scale Rotor Blade. 352
E.4 Inertial properties of the $1/12^{th}$ Froude-Scale Rotor Blade. 352

F.1 Time histories of Run 12, P10 [Simulation: dashed line, Experiment: solid line]. 355
F.2 Time histories of Run 15, P8 [Simulation: dashed line, Experiment: solid line]. 355
F.3 Time histories of Run 15, P18 [Simulation: dashed line, Experiment: solid line]. 356

F.4 Time histories of Run 16, P4 [Simulation: dashed line, Experiment: solid line]. 356
F.5 Time histories of Run 16, P10 [Simulation: dashed line, Experiment: solid line]. 357
F.6 Time histories of Run 17, P3 [Simulation: dashed line, Experiment: solid line]. 357
F.7 Time histories of Run 17, P10 [Simulation: dashed line, Experiment: solid line]. 358
F.8 Time histories of Run 19, P3 [Simulation: dashed line, Experiment: solid line]. 358
F.9 Time histories of Run 19, P17 [Simulation: dashed line, Experiment: solid line]. 359
F.10 Time histories of Run 22, P3 [Simulation: dashed line, Experiment: solid line]. 359
F.11 Time histories of Run 22, P10 [Simulation: dashed line, Experiment: solid line]. 360
F.12 Time histories of Run 25, P9 [Simulation: dashed line, Experiment: solid line]. 360
F.13 Time histories of Run 25, P15 [Simulation: dashed line, Experiment: solid line]. 361
F.14 Time histories of Run 26, P3 [Simulation: dashed line, Experiment: solid line]. 361
F.15 Time histories of Run 26, P9 [Simulation: dashed line, Experiment: solid line]. 362
F.16 Time histories of Run 26, P15 [Simulation: dashed line, Experiment: solid line]. 362

F.17 Time histories of Run 27, P10 [Simulation: dashed line, Experiment: solid line]. 363
F.18 Time histories of Run 27, P17 [Simulation: dashed line, Experiment: solid line]. 363
F.19 Time histories of Run 28, P3 [Simulation: dashed line, Experiment: solid line]. 364
F.20 Time histories of Run 28, P9 [Simulation: dashed line, Experiment: solid line]. 365
F.21 Time histories of Run 28, P14 [Simulation: dashed line, Experiment: solid line]. 365
F.22 Time histories of Run 30, P4 [Simulation: dashed line, Experiment: solid line]. 366
F.23 Time histories of Run 30, P22 [Simulation: dashed line, Experiment: solid line]. 366
F.24 Time histories of Run 31, P6 [Simulation: dashed line, Experiment: solid line]. 367
F.25 Time histories of Run 31, P12 [Simulation: dashed line, Experiment: solid line]. 367
F.26 Time histories of Run 31, P22 [Simulation: dashed line, Experiment: solid line]. 368
F.27 Time histories of Run 33, P5 [Simulation: dashed line, Experiment: solid line]. 368
F.28 Time histories of Run 33, P17 [Simulation: dashed line, Experiment: solid line]. 369

G.1 Scaled sway and sway velocity of ship motion file 4_045_25. 370
G.2 Scaled pitch and pitch velocity of ship motion file 4_045_25. 371

G.3 Scaled roll and roll velocity of ship motion file 4_045_25. 371
G.4 Scaled heave and heave velocity of ship motion file 4_045_25. 372
G.5 Scaled yaw and yaw velocity of ship motion file 4_045_25. 372
G.6 Scaled surge and surge velocity of ship motion file 4_045_25. 373

H.1 Maximum downward and upward tip deflection of the engagement of the adopted IATR with DC actuation of the integrated AFCs. 375
H.2 Maximum downward and upward tip deflection of the disengagement of the adopted IATR with DC actuation of the integrated AFCs. 376
H.3 Maximum downward and upward tip deflection of the engagement of the adopted IATR with DC actuation of the integrated MFCs. 377
H.4 Maximum downward and upward tip deflection of the disengagement of the adopted IATR with DC actuation of the integrated MFCs. 378
H.5 Maximum downward and upward tip deflection of the engagement of the adopted IATR with dynamic actuation of the integrated AFCs for Ω_{critical}. 380
H.6 Maximum downward and upward tip deflection of the disengagement of the adopted IATR with dynamic actuation of the integrated AFCs for Ω_{critical}. 381
H.7 Maximum downward and upward tip deflection of the engagement of the adopted IATR with dynamic actuation of the integrated MFCs for Ω_{critical}. 382
H.8 Maximum downward and upward tip deflection of the disengagement of the adopted IATR with dynamic actuation of the integrated MFCs for Ω_{critical}. 383
H.9 Maximum downward and upward tip deflection of the engagement of the adopted IATR with dynamic actuation of the integrated MFCs for $0.5\Omega_{\text{critical}}$. 384
H.10 Maximum downward and upward tip deflection of the engagement of the adopted IATR with dynamic actuation of the integrated MFCs for $0.75\Omega_{\text{critical}}$. 385
H.11 Maximum downward and upward tip deflection of the engagement of the adopted IATR with dynamic actuation of the integrated MFCs for $1.25\Omega_{\text{critical}}$. 386

H.12 Maximum downward and upward tip deflection of the engagement of the adopted IATR with dynamic actuation of the integrated MFCs for $1.5\Omega_{\text{critical}}$. 387
H.13 Maximum downward and upward tip deflection of the engagement of the adopted IATR with dynamic actuation of the integrated MFCs for $1.75\Omega_{\text{critical}}$. 388
H.14 Maximum downward and upward tip deflection of the engagement of the adopted IATR with dynamic actuation of the integrated MFCs for $2.0\Omega_{\text{critical}}$. 389
H.15 Maximum downward and upward tip deflection of the engagement of the adopted IATR, sea state 4_030_10, experimental airwake. 390
H.16 Maximum downward and upward tip deflection of the disengagement of the adopted IATR, sea state 4_030_10, experimental airwake. 391
H.17 Maximum downward and upward tip deflection of the engagement of the adopted IATR, sea state 4_090_10, experimental airwake. 392
H.18 Maximum downward and upward tip deflection of the disengagement of the adopted IATR, sea state 4_090_10, experimental airwake. 393
H.19 Maximum downward and upward tip deflection of the engagement of the adopted IATR, sea state 4_030_10, deterministic airwake. 394
H.20 Maximum downward and upward tip deflection of the disengagement of the adopted IATR, sea state 4_030_10, deterministic airwake. 395
H.21 Maximum downward and upward tip deflection of the engagement of the adopted IATR, sea state 4_090_10, deterministic airwake. 396
H.22 Maximum downward and upward tip deflection of the disengagement of the adopted IATR, sea state 4_090_10, deterministic airwake. 397
H.23 Time history of the adopted IATR disengagement under the wind conditions of 50[kn], 300° WOD with 4_090_10 sea state using the experimental airwake model for:(a) Total tip displacement, (b) Flap hinge angle, (c) Lead-lag hinge angle, (d) Flap-link transverse force. 398

H.24 Time history of the adopted IATR disengagement with the actuation strategy employed under the wind conditions of 50[kn], 300° WOD with 4_090_10 sea state using the experimental airwake model for:(a) Total tip displacement, (b) Flap hinge angle, (c) Lead-lag hinge angle, (d) Flap-link transverse force. 399
H.25 Time history of the adopted IATR disengagement under the wind conditions of 25[kn], 270° WOD with 4_060_10 sea state using the linear deterministic airwake model for:(a) Total tip displacement, (b) Flap hinge angle, (c) Lead-lag hinge angle, (d) Flap-link transverse force. 400
H.26 Time history of the adopted IATR disengagement with the actuation strategy employed under the wind conditions of 25[kn], 270° WOD with 4_000_10 sea state using the linear deterministic airwake model for:(a) Total tip displacement, (b) Flap hinge angle, (c) Lead-lag hinge angle, (d) Flap-link transverse force. 401
H.27 Maximum downward tip deflections for various deck roll angles when the perfectly correlated turbulence is considered. 401
H.28 Maximum downward tip deflections for various deck roll angles when the perfectly correlated turbulence is considered. 402
H.29 Percent change in maximum downward tip deflections for various deck roll angles with the perfectly correlated turbulence model and the actuation strategy. 402
H.30 Percent change in maximum upward tip deflections for various deck roll angles with the perfectly correlated turbulence model and the actuation strategy. 403

H.31 Time history of the adopted IATR engagement with the actuation strategy employed under the wind conditions of 45[kn], beam wind, -5° deck roll angle, experimental airwake model with perfectly correlated turbulence for:(a) Total tip displacement, (b) Flap hinge angle, (c) Lead-lag hinge angle, (d) Flap-link transverse force. 404

H.32 Time history of the adopted IATR engagement with the actuation strategy employed under the wind conditions of 45[kn], beam wind, 5° deck roll angle, experimental airwake model with perfectly correlated turbulence for:(a) Total tip displacement, (b) Flap hinge angle, (c) Lead-lag hinge angle, (d) Flap-link transverse force. 405

List of Tables

2.1 The elements of the stiffness matrix obtained using the thin-wall anisotropic beam theory and VABS for Fig. 2.13. 72

2.2 Elastic parameters of the plies used in the active box beam examples. . . . 73

2.3 Laminate design of the active box beam cases. 73

2.4 Actuation DC voltage of active plies. 74

2.5 The nonzero classical stiffness constants and actuation vector elements for the BB1 case. 74

2.6 The nonzero classical stiffness constants and actuation vector elements for the BB2t case. 74

2.7 The nonzero classical stiffness constants and actuation vector elements for the BB2st case. 75

2.8 Material and geometric properties of the passive C-channel. 75

2.9 The elements of the stiffness matrix for the isotropic C-channel. 76

2.10 Percentage difference between the prediction of the present implementation, VABS, and UM/VABS for the isotropic C-channel. 76

2.11 Geometry of active open cross-sections depicted in Fig. 2.15. 76

2.12 Laminate design of the active open cross-section beam cases. 76

2.13 Laminate actuation of the active open cross-section beam cases. 77

2.14 The significant elements of the stiffness matrix and the actuation vector of the active I-beam (I). 77
2.15 The significant elements of the stiffness matrix and the actuation vector of the active I-beam (II). 78
2.16 The significant elements of the stiffness matrix and the actuation vector of the active C-channel. 78

4.1 Predicted first mode natural frequencies versus the experimental ones for examined hingeless aluminum blade cases. 134
4.2 Tip deformation due to embedded active material. Active beam element implementation validation example. 149

6.1 Scaling laws for Froude aeroelastic scaling. 174
6.2 Relevant $1/12^{th}$ Froude-scaled parameters of the experimental rotor system. 175
6.3 Rotor system operation parameters at 33% full rotor speed. 177

7.1 Experiment parameters of Phase[I]. 196
7.2 Experimental runs examined using the three different aerodynamic models. 202
7.3 Simulated experimental runs of the 0° deck case[C:collective pitch setting,W:wind speed]. 207
7.4 Simulated experimental runs of the $-20°$ deck case[C:collective pitch setting,W:wind speed]. 210

8.1 Ship motion files used in the test matrices of Phase [II]. 226
8.2 Elements of the test matrix of sub-phase (I). 226
8.3 Elements of the test matrix of sub-phase (II). 226
8.4 Elements of the test matrix of sub-phase (III). 226
8.5 Simulated experimental runs of sub-phase (II). 232

9.1 Laminate design and cross-sectional geometry of the IATR from Reference [168]. 248
9.2 Elastic and electromechanical properties of the IATR plies. 248
9.3 Inertial and geometric properties of the articulation links of the IATR. . . 249
9.4 $1/6^{\text{th}}$ Mach-scaled operation parameters of the adopted IATR. 250
9.5 Selected rotor speeds for system identification study and the first flap fundamental. 255
9.6 Ω_{critical} and t_{critical} for a set of wind speeds and a gust factor of 0.25. 270
9.7 $0.5\Omega_{\text{critical}}$ and t_{critical} for a set of wind speeds and a gust factor of 0.25. . . 271
9.8 $1.25\Omega_{\text{critical}}$ and t_{critical} for a set of wind speeds and a gust factor of 0.25. . . 271
9.9 $2\Omega_{\text{critical}}$ and t_{critical} for a set of wind speeds and a gust factor of 0.25. . . . 272
9.10 Sea states selected to examine the effect of ship motion on the proposed strategy to counter the BSP. 285
9.11 Experimental airwake conditions selected to examine the effect of the perfectly correlated turbulence. 293

C.1 Sectional stiffness constants, sectional mass/inertia constants, and beam length of the Aluminum blade in [147]. 343
C.2 Sectional stiffness constants, sectional mass/inertia constants, and beam length of the Aluminum blade in [150]. 343
C.3 Sectional stiffness and actuation constants. Active beam element implementation validation example [121]. 344

D.1 L-B dynamic stall model constants at $M = 0.3$. 349

H.1 $0.75\Omega_{\text{critical}}$ and t_{critical} for a set of wind speeds and a gust factor of 0.25. . . 379
H.2 $1.5\Omega_{\text{critical}}$ and t_{critical} for a set of wind speeds and a gust factor of 0.25. . . 379
H.3 $1.75\Omega_{\text{critical}}$ and t_{critical} for a set of wind speeds and a gust factor of 0.25. . . 379

Chapter 1

Introduction

1.1 Overview of Chapter 1

A brief overview of the hazards associated with operating helicopters from ship decks is presented. A specific problem, known as the Blade Sailing Phenomenon, that occurs during the engagement and the disengagement phase is highlighted. Past and recent investigations of this phenomenon and the factors contributing to its occurrence are reviewed in addition to the limited research devoted to its reduction/control. Finally, a high level overview of the present research is presented.

1.2 Maritime Helicopter Operation

1.2.1 Overview of Hazards and Challenges

The unique flight capabilities of helicopters, unattainable with fixed-wing aircraft, offer advantages in terms of maritime operation. However, maritime helicopter operation involves challenges and hazards that are not normally encountered in land-based operations. These challenges stem largely from the unusual aerodynamic environment present over the ship

deck due to the interaction of the free stream airflow over the ocean with the ship bluff body sharp edges and superstructures like the hangar and the towers. This is depicted in Fig. 1.1, where the flight deck of the helicopter is highlighted to show the complexity of its structural environment.

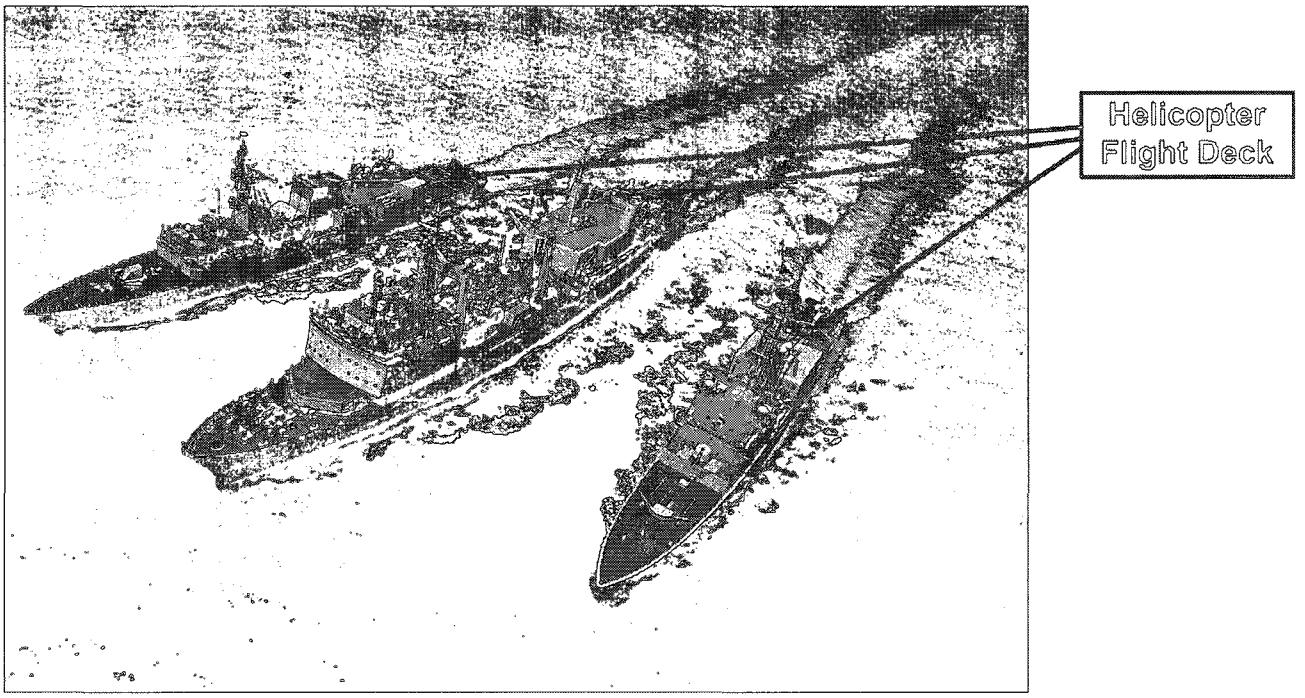

Figure 1.1: Formation of Canadian Navy ships with the helicopter flight decks highlighted [Courtesy of the Canadian Navy].

Additionally, rough sea states, like the one shown in Fig 1.2, cause significant ship motion and add another dimension to the hazards of shipborne helicopter operation through influencing the airwake over the ship deck and generating inertial forces on the helicopter and other support systems prior to it being secured, rotor blades folded, and traversed to the hangar. The aforementioned hazards coupled with poor visibility and adverse climatic conditions associated with rough weather and sea states may render the most skilled helicopter pilots, the support crew, and the infrastructure powerless against accidents. Other factors, like sea water, may also play a role in damaging subsystems essential for safe maritime operation of helicopters. An example of a typical Sea King helicopter operation

by the Canadian Navy is shown in Fig. 1.3, where the complexity of the operation can be qualitatively seen.

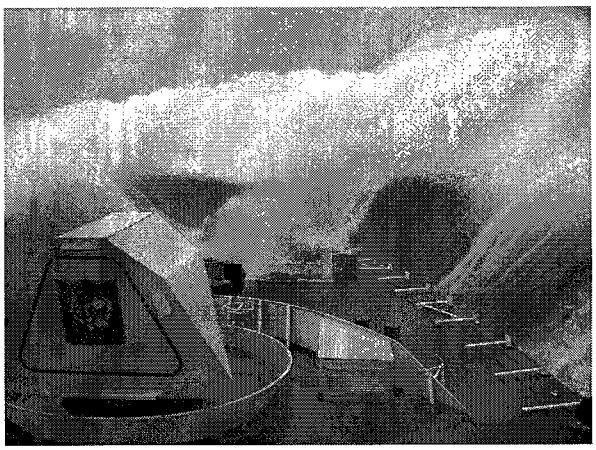

Figure 1.2: Heavy seas encountered by a navy ship [Courtesy of the Canadian Navy].

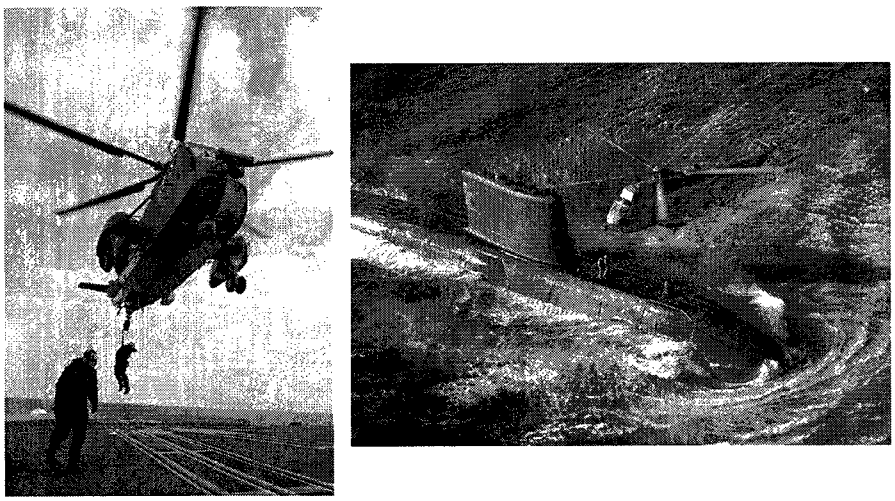

(a) (b)

Figure 1.3: Typical maritime operation of a Sea King helicopter by the Canadian Navy [Courtesy of the Canadian Navy/Airforce].

Given the operational hazards, Safe Helicopter Operating Limits (SHOLs) are established by specialists using a combination of field experiments, analytical models, and quantitative assessment. These SHOLs are usually functions of relative wind speed and direction, which indicate the severity of the aerodynamic environment and often the sea state.

Hypothetical SHOLs for a shipborne helicopter operation are shown in Fig. 1.4, where the radial and the azimuthal coordinates represent wind speed and direction respectively. The shaded region represents safe shipborne helicopter operation points. It is clear from this illustration that the safe zone available for operation can be quite limited.

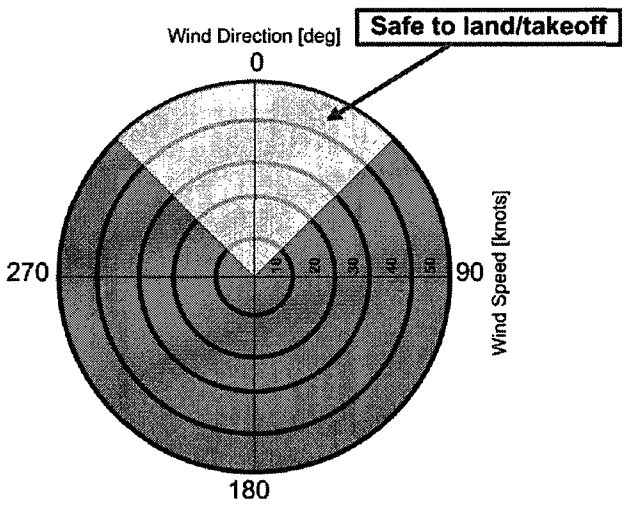

Figure 1.4: Hypothetical SHOLs for shipborne helicopter operation. Safe operation points are shaded.

These restrictions set limits on the tactical flexibility of the helicopter and impede its availability in emergencies including sea rescue and relief operations. Expanding the SHOLs to include more operational points using certain control strategies is certainly an attractive idea. However, the cost-effectiveness and feasibility of any such strategy must also be evaluated.

1.2.2 Overview of Helicopter Ship Dynamic Interface

As depicted in Fig. 1.5, Helicopter Ship Dynamic Interface (HSDI) encompasses all phases and aspects of Helicopter Ship Operation (HSO), that are summarized in Fig. 1.5, and include predicting the forces acting on the helicopter and the supporting systems for investigating components' fatigue life and failure [1], storm lashing (securing the helicopter

during sea transport in storms) [2], on-deck stability, and even ergonomic factors concerning the crews and helicopter landing/take-off/securing aids [3, 4]. In summary, in addition to the important factors contributed by the ship airwake and motion mentioned earlier, HSDI is a broad multidisciplinary field that spans many engineering disciplines including mechanical, aerospace, electrical, and human factors [5, 6]. Obviously, providing a comprehensive survey of HSDI is a challenging task that is beyond the scope of this brief overview.

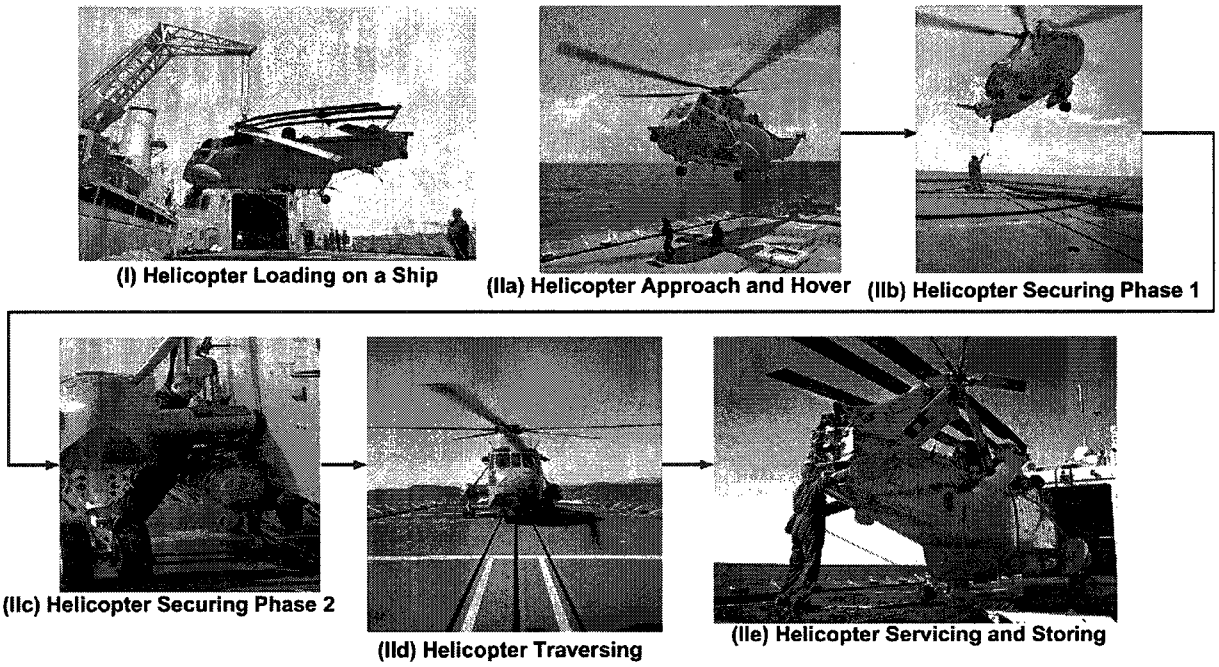

Figure 1.5: Phases of a typical helicopter ship operation [Photos courtesy of the Canadian Air Force].

Validated tools developed for HSDI are used to predict and generate SHOLs for envisioned HSO, which sometimes can be the only means available due to the difficulties, if not the impossibilities, associated with conducting actual field experiments. With the advent of advanced computational tools, generating SHOLs based solely on validated simulation packages has become more reliable [7, 8, 9].

One of the critical phases of HSO is the rotor system engage and disengage prior to

take-off or upon landing. During this phase, large rotor blade elastic deflections and bending moments may occur. The phenomenon is considered a major limiting factor in HSO that negatively impacts the SHOLs, which limits the tactical flexibility of maritime operation of helicopters [10]. Investigation, characterization, and reduction of this phenomenon becomes paramount since helicopter take-off and recovery is an unavoidable part of HSO.

1.2.3 Aeroelastic Response of Rotor Systems During Engagement and Disengagement Operational Phases (The Blade Sailing Phenomenon)

The phenomenon of large tip deflection/root bending moment of rotor blades during rotor engage and disengage operations on ship decks is known as the Blade Sailing Phenomenon (BSP), as shown in Fig. 1.6

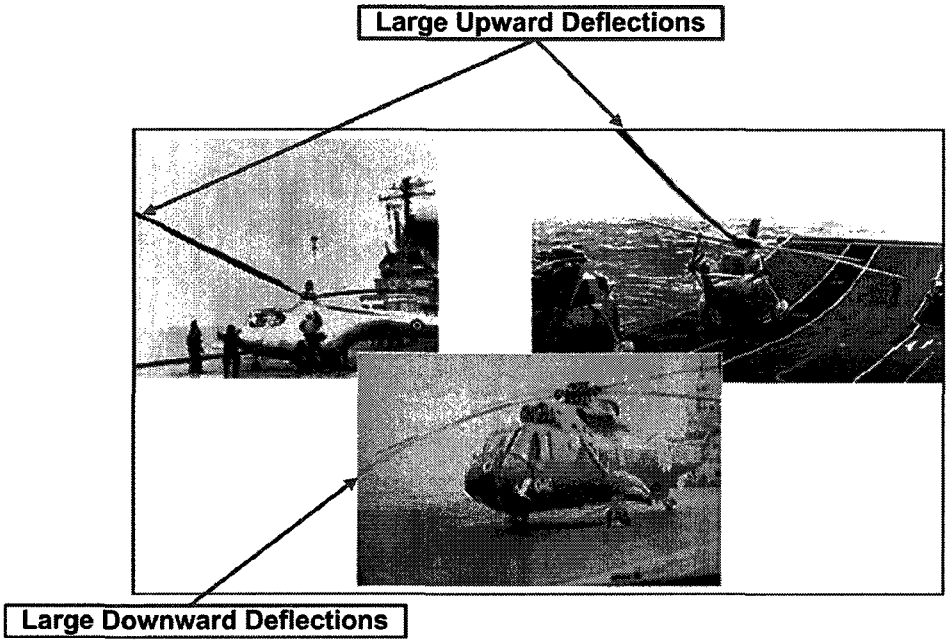

Figure 1.6: Examples of the BSP [10].

The major factors contributing to the occurrence of the BSP can be summarized as

follows:

1. Blade Centrifugal Stiffening: Unlike their fixed-wing counterparts, helicopters rely on the inertial centrifugal force to stiffen their rotor blades. Therefore, during the early/late stages of the rotor system rotational acceleration/decelaration the blades are relatively very flexible and large elastic deflections can be induced with relatively low external loading. This design characteristic is more profound for modern rotor blades that are made exclusively of composite materials.

2. Ship Airwake: The unusual airflow that is present over the flight deck is a major contributing factor to the BSP as alluded to above. The ship hull and its superstructures can create a complex flow field that gives rise to an unusual loading of the rotor disc. Examples of complex flow fields over ship decks are shown in Fig. 1.7 based on a computational model and an experimental study.

3. Ship Motion: Ship motion in any of its six degrees of freedom (6-DOF): roll, pitch, yaw, surge, sway, and heave (identified in Fig. 1.8) will influence the airwake over the flight deck in general. Additionally, inertial forces generated by ship motion in heavy seas will also influence the behaviour of the rotor blades.

4. Rotor System Articulation: The two most common types of rotor system hub design are the articulated and the hingeless ones. The articulated design, like the one shown in Fig. 1.9, seeks to prevent the flap (transverse vertical blade motion) and the lead-lag (transverse edgewise blade motion) moments from being transferred to the helicopter. Consequently, at low rotational speeds blade limiters in the flap degree of freedom, and sometimes in the lead-lag one, are needed to restrict the rigid body motion of the rotor blade about its hinges. These limiters are retracted when a certain rotational speed is reached (corresponding to sufficient centrifugal blade stiffening). Modern hingeless rotor blades like the one shown in Fig. 1.10 do not

require these limiters since they employ strong elastomeric dampers at their root. The type of rotor system and its design affect mostly how the BSP manifests itself. For articulated rotor blades (including the Sea King maritime helicopter currently used by the Canadian Navy), larger transverse deflections compared to hingeless rotors are observed due to the blade cuff striking the deployed droop/flap stops as in Fig. 1.6. For modern hingeless rotors, larger root bending moments are transmitted to the hub and they are expected to be severe.

The BSP is an aeroelastic phenomenon that is overwhelmingly undesirable from every point of view [10, 11]. The negative impact on the HSO and its SHOLs can be summarized as follows:

1. The large downward tip deflections can be severe enough to cause an impact between the blade tip and the helicopter fuselage or tail. This is the reason for referring to the BSP in the U.S. Navy as tunnel/boom strike. More dangerously, the blades can strike the support crew during the securing procedure shown in Fig. 1.5 and fatalities have been reported [12].

2. The large bending moments transmitted to the hub for hingeless blades (large transverse forces for articulated blades) can severely fatigue the components reducing their service life, or lead to in-flight accidents due to component failure.

3. The aforementioned perils of the BSP can limit the tactical flexibility of the helicopter, and in some instances prevent its deployment when it is urgently needed.

The highest environment of concern for the BSP to occur is when operating helicopters from ship decks, but there are reported blade sailing accidents for helicopters operating from offshore oil rigs as well [13]. With the foreseen increase in offshore helicopter operations, the BSP is expected to continue to be of a major concern in the future. Furthermore,

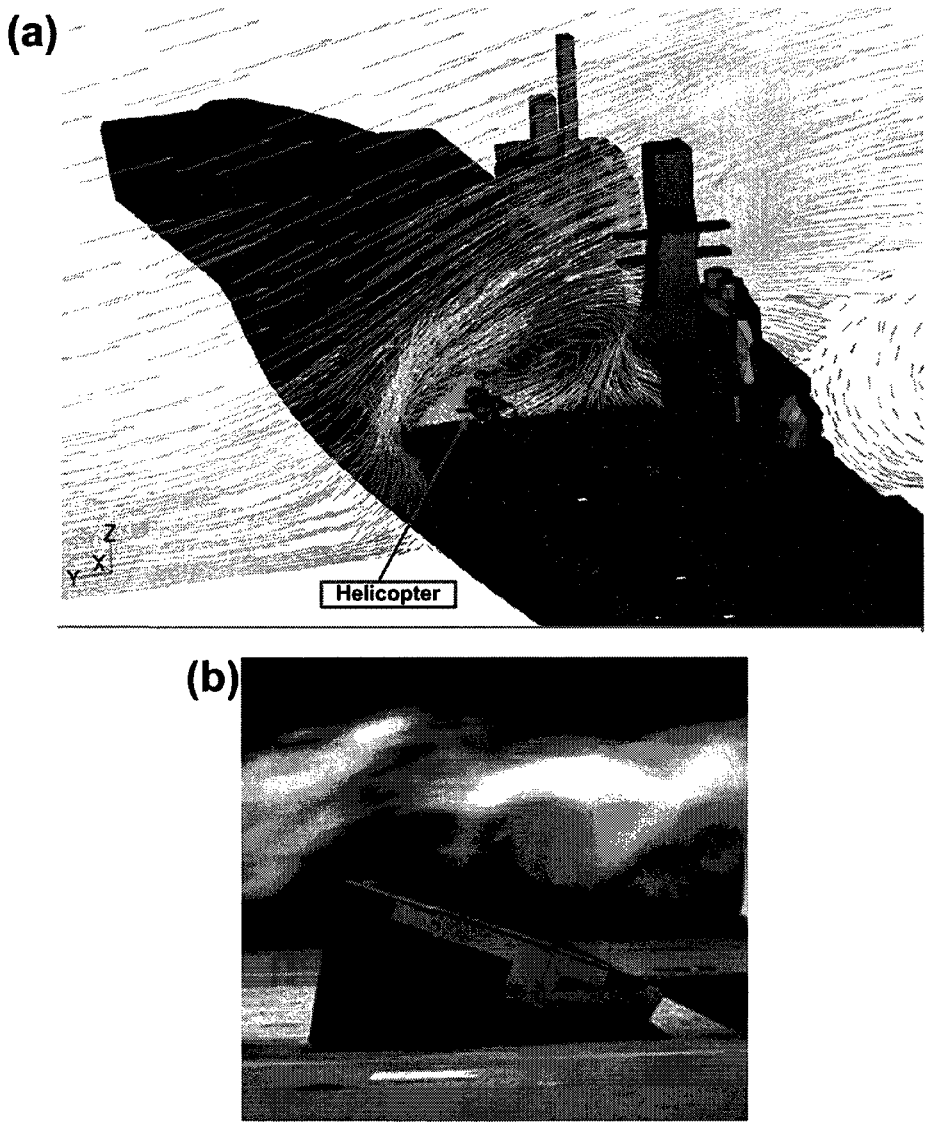

Figure 1.7: (a) Computational airwake using FLUENT 6.1 CFD [2], (b) Experimental airwake visualization over -20° ship deck.

there are reported tunnel strikes even for land operation of some helicopters like the Boeing 107 [14], the land version of the maritime Boeing H-46 helicopter that has experienced many documented cases of tunnel strikes [14, 15, 16].

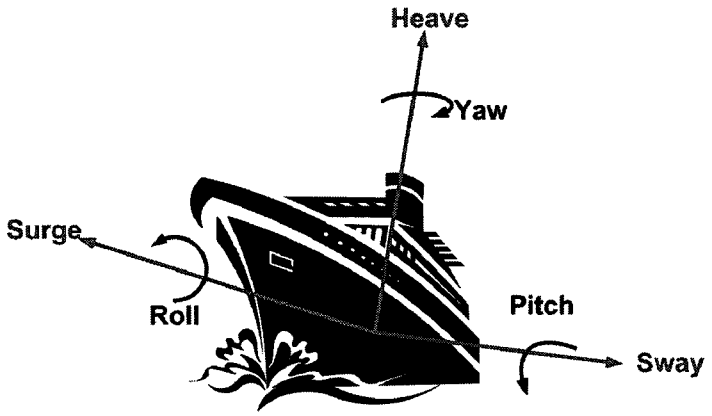

Figure 1.8: Six ship motion degrees of freedom (DOF).

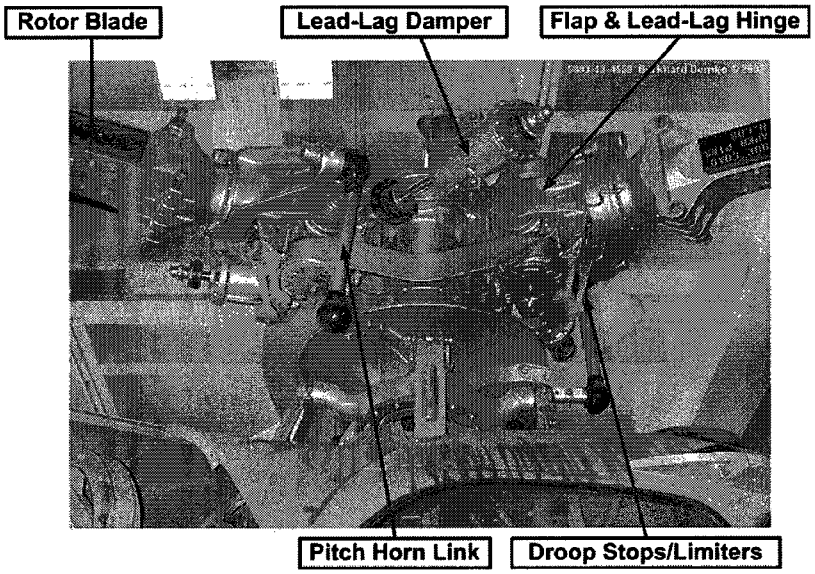

Figure 1.9: Sikorsky H-19 fully articulated rotor head with important components highlighted [Courtesy of Sikorsky/United Technology Company].

1.3 Review of Experimental Investigations and Modelling Techniques of the BSP

Experimental investigations in this review are categorized as those that attempted to study and reproduce the BSP in the laboratory using wind tunnels or in the field. As can be deduced from above, modelling and simulating the BSP depends directly on advances

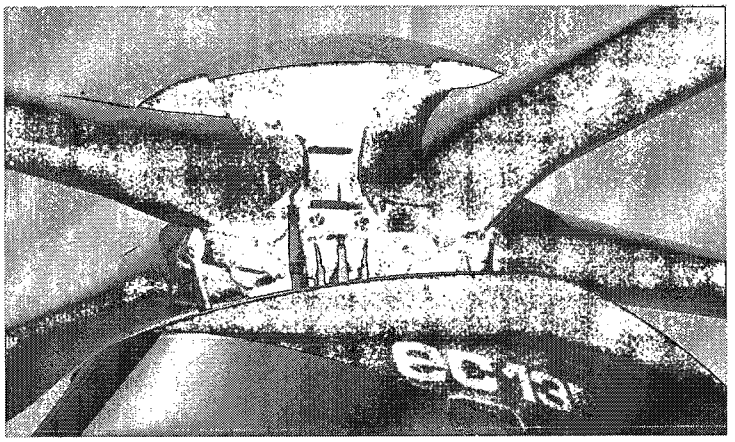

Figure 1.10: Eurocopter 135 hingeless rotor head [Courtesy of Eurocopter].

made in many research areas that can be grouped into three principal categories:

- accurate modelling of the ship airwake and its dependance on the ship superstructures and motion.
- high fidelity modelling of the helicopter rotor system, its aerodynamic loading, and its operating parameters; and
- adopting a representative ship motion during take-off and landing of the helicopter.

Firstly, early investigations into the BSP are discussed. These investigations are typically characterized by over-simplifying assumptions regarding the research categories mentioned above. Therefore, the simulation models utilized in these investigations do not necessarily reflect the state-of-the-art in HSDI. Another characterizing feature of these studies is their emphasis on evaluating the potential for occurrence of the BSP for new maritime helicopters and obtaining the order of magnitude of the HSDI parameters corresponding to when it occurs (if applicable).

Secondly, the more recent investigations into the BSP are reviewed with advances made in the identified research categories enumerated above being highlighted more thoroughly.

Thirdly, experimental investigations of the BSP or any of its aspects are reviewed.

1.3.1 Early Investigations

A thorough review of the early investigations into the BSP was presented by Keller [17] and a brief summary of this review is presented herein. The earliest research into the BSP was conducted for the Westland Whirlwind and the Wasp [18] helicopters. The assumed mode shapes method was used to model the elastic behaviour of the blades that were assumed to be in contact with the droop stops and rotating with constant low angular velocity. Typically, only the first elastic mode of a cantilevered beam was used in the analysis. Simple deterministic wind flows over the rotor disc were used to simulate the ship airwake and no stall or other nonlinear effects were considered in calculating the airloads. The simulations used the three illustrated in Fig. 1.11 simple deterministic models to represent the ship airwake. It was found that the airwake model plays an important role in producing large transverse blade deflections. The investigation demonstrated the susceptibility of articulated rotor blades to the BSP when the more realistic constant and step airwake models are used.

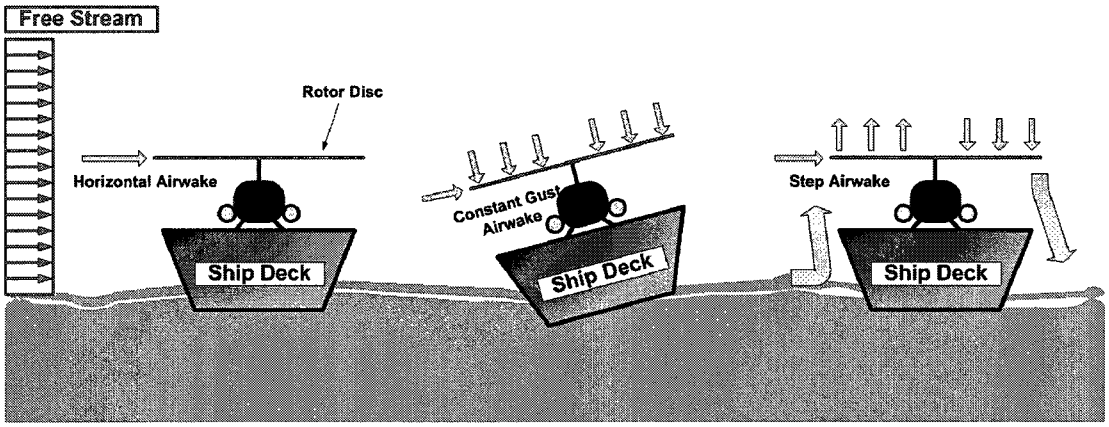

Figure 1.11: Early deterministic models of ship airwake [17].

Subsequently, similar numerical studies were performed for the composite blades of the Sea King and the Lynx helicopters [19, 20] that further confirmed the relevance of the BSP for the articulated and the hingeless rotor systems. The studies also demonstrated

the importance of higher order elastic modes in better predicting and characterizing the BSP. Research into the BSP at the Boeing Company was spurred by the documented H-46 tunnel strike [21] that severely damaged the aircraft, where the BSP was estimated to have occurred in the range of 10% to 20% of maximum RPM of the rotor system. As in earlier investigations, simple analytical tools were employed in the analysis.

Documented analytical investigations of the BSP in Russia were motivated by similar concerns as those in North America and the U.K. Additionally, the danger of blade tip contacts found in coaxial rotor systems, like the one shown in Fig. 1.12, that characterize several Russian-made helicopters [22] presents additional manifestation of the BSP.

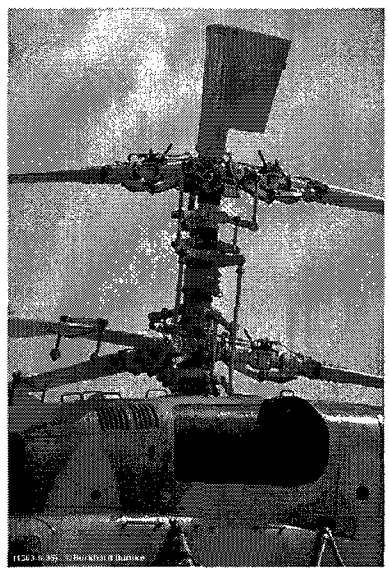

Figure 1.12: Kamov Ka-29TB coaxial rotor head [Courtesy of Kamov Helicopters].

1.3.2 Recent Investigations

Recent investigations into the BSP that started in the early 1990s, like other engineering disciplines that demand high fidelity simulations, utilized the rapid increase in computational power to better predict and characterize the BSP. Moreover, experimental investigation in wind tunnels became indispensable in order to validate simulation tools and

results. An overview of these recent research efforts will be presented focusing on the identified principal research categories.

Ship Airwake

References [23, 24] have presented a comprehensive overview of ship airwake modelling and simulation for helicopter operation and this overview is summarized herein as it pertains to the goals of this research. Advances made in this niche of the BSP research are obviously coupled to those made in computational and experimental fluid dynamics; therefore, only research that directly focuses on the ship airwake will be considered.

The numerous technical challenges in modelling and predicting the ship airwake were alluded to earlier. In summary, accurate representation of the complex ship geometry and its superstructure is required. In addition, the motion of a flight deck due to ship speed and sea state must be taken into consideration. The effect of the atmospheric boundary layer and turbulence must also be taken into account. All of these factors combined result in a low Mach number flow that is 3-D, unsteady, separated, vortical, and turbulent with massive regions of flow separation and shedding of strong turbulent coherent structures. Further complicating the airwake, is the interaction of the flow field with the rotor disc of the helicopter and its fuselage.

Newman conducted early experimental investigations of the ship airwake that gave initial invaluable insight and yielded simple, yet representative, models [25, 26, 27]. The experimental work was unique in terms of measuring the airwake flow field for a full-scale Rover Class Royal Navy ship and its $1/120^{\text{th}}$ model-scale. The experiment was conducted using golf ball and propeller anemometers for wind speeds ranging from 15 to 30 [kn] for the full-scale ship. Measurements of the wind tunnel airwake velocity (in three directions) component were conducted with a laser Doppler anemometer at 75% blade radius. Good correlation was found between the wind tunnel data for the model-scale and the full-scale

ship in terms of the mean velocity flow field. One of the important results yielded by this investigation is the adequacy of simple analytical models of the airwake over the rotor disc for preliminary investigation of the BSP. The most realistic and widely used model is shown in Fig. 1.13

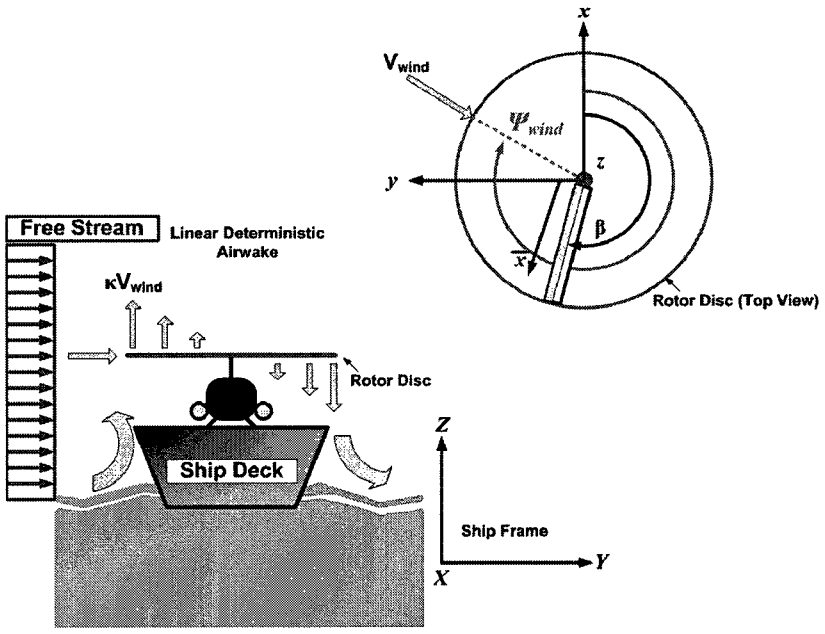

Figure 1.13: Linear deterministic model of the ship airwake.

The governing equations of this semi-empirical model can be summarized as

$$\bar{V}_x = -V_{wind}\ \cos(\psi_{wind}) \tag{1.1}$$

$$\bar{V}_y = V_{wind}\ \sin(\psi_{wind}) \tag{1.2}$$

$$\bar{V}_z = \kappa\ V_{wind}\ \bar{x}\ \sin\left[\beta - (\frac{3\pi}{2} - \psi_{wind})\right] \tag{1.3}$$

where as defined in Fig. 1.13, $\bar{x}$ is the normalized radial direction along the rotor blade; κ is known as the gust factor that determines the fraction of the free stream velocity transferred to the vertical component; β is the blade azimuthal angle (in rad); V_{wind} is the

magnitude of the wind velocity; ψ_{wind} is the wind angle relative to the longitudinal axis of ship deck frame; and $\bar{V}_x$, $\bar{V}_y$, and $\bar{V}_z$ are the three orthogonal airwake velocity components in the ship deck frame.

A three dimensional view of the vertical velocity component due to the linear deterministic model is shown in Fig. 1.14

Figure 1.14: Normalized vertical velocity of the linear deterministic model of a ship airwake over the rotor disk.

Investigators still employ this linear deterministic model of the airwake to draw conclusions about the suitability of certain models to study the BSP [11, 28, 29] or study strategies to attenuate it [17, 30].

Experimental measurements of the ship airwake for various ships have been performed. These investigations included full-scale ship tests [31, 32, 33] and scaled-ship wind tunnel tests [32, 33, 34, 35, 36] with some of these tests focusing on frigates operated by the Canadian Navy [37, 38, 39]. Mostly, the aforementioned studies have focused on characterizing and modelling the steady-state flow topologies; however, experimental ship airwake studies have also focused on measuring the oscillating parts of the flow field [40, 41, 42]. Recently, a mathematical model of the ship airwake that gives the steady-state and the spatially and temporally correlated turbulence component has been developed and validated by a

member of the Applied Dynamics Group at Carleton University (A. S. Wall) based on experimental measurements of the flow field over $1/120^{th}$-scaled ship deck at discrete roll angles ranging from $-20°$ to $20°$ [43]. The model is valid for purely beam winds with no rotor disc effects on the airwake coupled with the assumption that the ship is long enough in the axial direction, which renders the axial flow component to be zero; nevertheless, the model validity, comprehensiveness, and compactness make it versatile enough to accommodate ship motion (mainly due to roll) as shall be demonstrated subsequently. The 2-D flow field contours of the normalized transverse velocity components of the model are shown in Fig. 1.15 for two different deck roll angles.

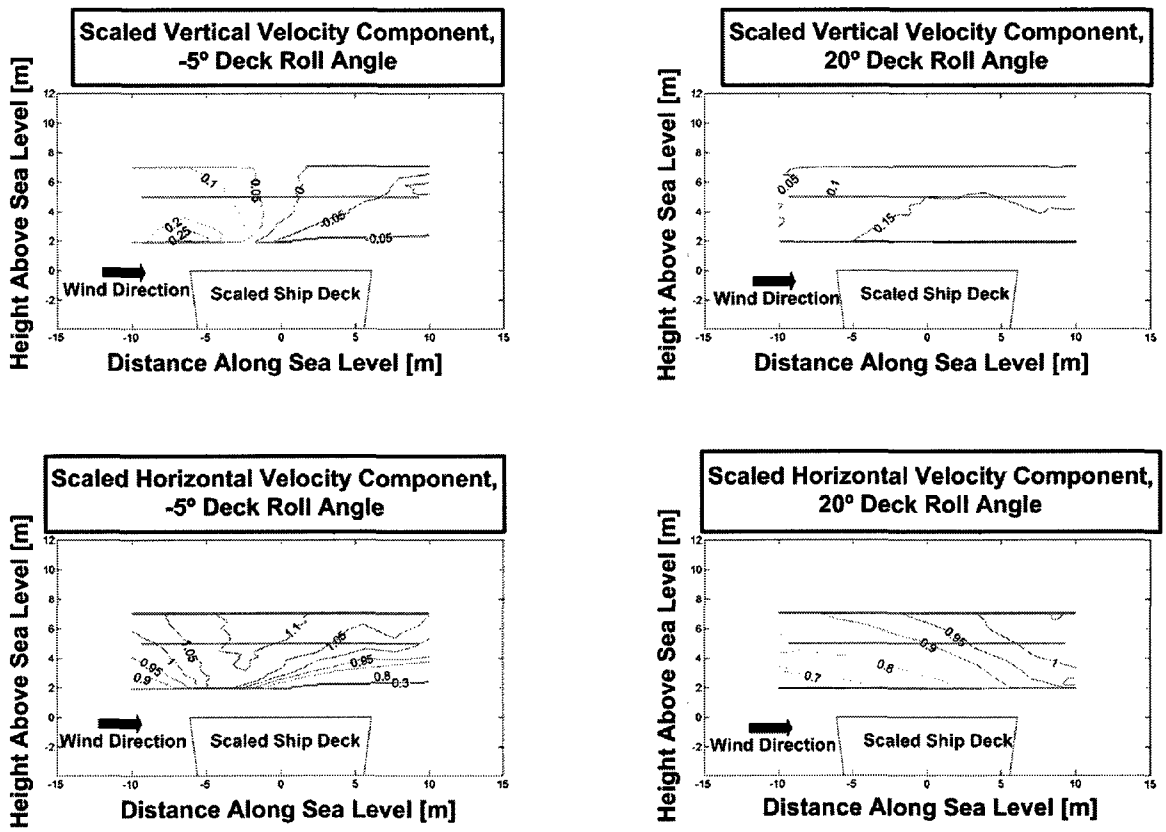

Figure 1.15: Sample $1/120^{th}$ scaled transverse velocity contours of the experimental airwake model at $-5°$ and $20°$ deck roll angle [44].

Experiments have also been conducted to examine the influence of the rotor disc on the

helicopter airwake [45, 46, 47] where the primary purpose of these studies was to examine the effect of the airwake on the produced rotor thrust and hence the pilot workload. Since the BSP occurs at low rotor speeds, the rotor inflow and its influence on the ship airwake has been traditionally assumed to be negligible, which will be the case in this investigation.

Computational airwake investigations using validated CFD tools are becoming more attractive due to increases in computational power and sophistication of current turbulence models. Additionally, CFD simulations can significantly reduce the cost of HSDI analysis by reducing the number of expensive and time-consuming experiments in the field and in wind tunnels. Most recently, the work at Pennsylvania State University [23, 48, 49] and the work at the University of Liverpool [7] have demonstrated the viability of establishing SHOLs using CFD simulations of the ship airwake. Ship airwake from CFD simulations was used in the investigations of References [17, 50], which demonstrated the dependence of the severity of the BSP on the helicopter ship deck location.

Rotor System Modelling and Aerodynamic Loadings

This category of blade sailing investigation, in turn, depends on advances made in three broad mechanical and aerospace engineering fields, which are flexible multibody dynamics, computational elastodynamics, and quasi-steady/unsteady 2-D thin airfoil theory; therefore, the review presented herein is tailored primarily for the BSP research.

As mentioned above, earlier models of the rotor system in BSP research assumed a limited number of cantilevered beam flap modes that physically represent the articulated rotor blades in contact with the droop/flap stops. Newman [26, 25, 51, 11] built upon these earlier investigations by including up to four elastic flap-wise mode shapes in addition to the rigid body mode about the flap hinge. Employing modal analysis for the rotor blades implies linear beam theory that assumes small to moderate geometric deflections, which was argued to introduce an acceptable level of error in the predicted deflections. Further-

more, the first fundamental elastic torsional mode was also included and the droop/flap stops were modelled as high rate linear springs at the blade root. The fourth-order Runge-Kutta time integration scheme was used to generate the time history of the blade response by integrating the modal equations. Further improvements of the model were in terms of the calculation of the blade structural response and the inclusion of more blade stop types [30]. The quasi-steady thin airfoil theory coupled with Kirchoff's trailing edge stall model was used to calculate the aerodynamic loading along the blade lifting lines.

Geyer and Smith used a finite element based modelling approach that built on the work of Newman [52, 28] with eigenvalue analysis to determine the mode shapes and corresponding natural frequencies. Hinged and cantilevered mode shapes were interchanged depending on whether the blade is in contact with the flap limiters or not. As in Newman's work, the fourth-order Runge-Kutta method was used to obtain the transient response of the blade. The torsional elastic mode was found to be of little importance in investigating the BSP. Subsequently, Keller [53, 17] improved on the structural model of the rotor blade used by Geyer by employing the rotating beam theory of Reference [54] and Hermitian polynomials as interpolation functions while retaining the modal swapping technique. High stiffness torsional springs with logical switches were used to simulate blade impact with the blade limiters. Bossak-Newmark time integration was used to integrate the modal space equations and obtain the transient response of the blade. Both studies examined the effect of quasi-steady and unsteady aerodynamic forces on the BSP and concluded that the former is sufficient for reliable analysis and predictions.

Bottasso and Bauchau [29] demonstrated that the capabilities of simulating the BSP do not require the derivation of new equations of motion and the construction of new models that must be validated. Indeed, the problem can be approached from the paradigm of finite element flexible multibody dynamics where a library of carefully validated elements can be used to construct a virtual model of the rotor system. This flexible approach,

which is embodied in the flexible finite element multibody software DYMORE [55], allows for complex system topologies that can be used reliably for engineering analysis. Furthermore, the contact problem between the blade and the flap limiters was carefully and comprehensively analyzed in this investigation. The integration scheme is based on the time-discontinuous Galerkin method that guarantees absolute numerical stability. The aerodynamic loads were calculated based on Peters finite state model for 2-D thin airfoil theory [56].

The investigation by Kang, He, and Carico [50] used FLIGHTLAB, a comprehensive flight analysis code, to simulate shipboard rotor engagement and disengagement. The investigation used nonlinear rotational springs and dampers to model the flap and the lead-lag limiters. More importantly, the landing gear and its interactions with the flight deck were also modelled to examine the effect of the BSP on the helicopter-deck securing, which was shown to have an appreciable effect. The elastic blades were still modelled using the modal approach with rigid body flap and lead-lag modes in addition to three elastic modes for coupled blade flap and lead-lag bending. Blade deformation in torsion and along the blade axis were neglected. The nonlinear transient response analysis is performed using the the Newmark-Beta method extended by the Hilber-Hughes-Taylor (HHT) method. The investigation utilized the extensive capabilities and options of FLIGHTLAB to calculate the airloads on the whole helicopter including the rotor system.

Representative Ship Motion

This contributing factor to the BSP has received less attention than the other factors. Apart from the limited effect of ship roll examined in [25, 52, 28], the only investigation that examined all six degrees of freedom of representative ship motion is reported in Reference [50]. The investigation concluded that ship dynamic motion significantly affects helicopter shipboard engage operations. Ship dynamic motion tends to increase the blade

transient response during engage operations. It also indicated that a fully coupled helicopter/ship model is required for an accurate modelling of the helicopter shipboard engage and disengage operations.

Experimental Investigation

Full-scale experiments were performed to establish the susceptibility of developed rotor systems to the BSP [15, 57]. Model-scale experiments in wind tunnels are limited to those done by Newman [51] using a teetering, semi-rigid, gimballed rotor system and they were used by Newman and other investigators [52, 17] primarily to validate developed simulation tools.

A series of experimental drop tests were performed by Keller and Smith [58] to validate the modelling of the blade-limiters impact problem. Apart from these experiments, no experimental investigations of the BSP have been reported in the engineering literature. The primary reason may be attributed to the costs of these experiments stemming from the required sophistication and wind tunnel time while for full-scale experiments the prohibitive reasons were alluded to above.

1.4 Review of Control and Attenuation Strategies

Research into attenuating and reducing the impact of the BSP on the SHOLs of shipborne helicopters has been limited. This is not surprising considering the complexity of this aeroelastic phenomenon owing to the multitude of factors contributing to it as explained above. Furthermore, any devised control strategy must take into account its nonlinear transient nature. The most notable attempt was performed by Keller [53, 17] where three passive control strategies for the rotor system of the H-46 helicopter were studied. The first strategy examined increasing the collective pitch of the blades during the engage and

disengage operation, in an attempt to transfer some of the high blade lead-lag stiffness to the flap stiffness. However, this increased the aerodynamic loads, which further increased the blade tip deflections in most cases, rendering this approach infeasible. The second strategy considered increasing the flap damper as multiples of the lead-lag damper, but given the small clearance in the flap hinge between the flap and the droop stops (in the order of 2°), the blade total mechanical energy was not sufficiently dissipated to prevent the BSP. The third strategy considered adding deployable leading edge spoilers along the blade to decrease the lift and enhance the drag, hence reducing the blade flapping and consequently alleviating the BSP. The latter strategy was found to be the most successful among the strategies considered in reducing the BSP for all high wind speeds and directions relative to the rotor disc. The drawbacks of this approach revolve around the physical modifications that need to be added to the blade design such as the mechanical controls along-the-spar and the spoilers themselves. Additionally, the large aerodynamic forces experienced by these spoilers would increase the amount of servicing the blades require.

The research in Reference [17] also investigated mechanical control of the swash plate to reduce the BSP for a gimballed rotor. This research yielded significant insight into the required aspects of a feasible controller and the challenges one faces when devising one. Most recently, the work in Reference [30] considered the use of a trailing edge flap like the one shown in Fig. 1.16 for the reduction of the BSP. Results presented show significant reductions in the blade tip deflection and the structural bending moment (for a stiff blade) if the trailing edge flap is operated in opposition to the blade tip deflection velocity. The optimum location of the trailing edge flap was determined to be the farthest outboard possible and with the largest possible flap deflection during the critical phases of the rotor engagement/disengagement (50% of the rotor nominal RPM).

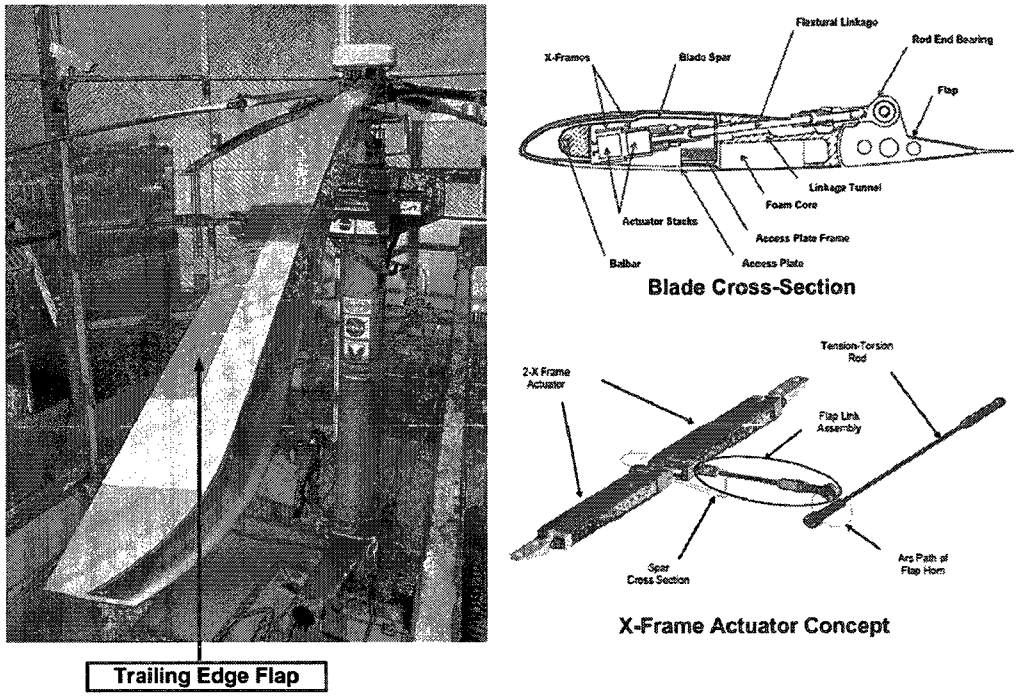

Figure 1.16: Trailing edge concept for vibration and noise reduction [Courtesy of the Boeing Company].

1.5 Overview of Present Research

The existing literature points clearly to the need to devise feasible control strategies to counter the BSP more effectively. This further demands the need to develop reliable simulation tools to conduct a correct assessment of these strategies. Moreover, a gap in the engineering literature regarding further experimental investigation of the BSP is identified along with the need for additional experimental data to validate developed simulation tools of HSO. The present research addresses these important needs and gaps. The presentation of this research is summarized in Fig. 1.17 where three broad research steps are defined:

1. Modelling and Simulation: State-of-the-art simulation tools are developed and individually validated to provide the capabilities to comprehensively model active rotor systems and assess a proposed control strategy to counter/reduce the BSP.

2. Experiment Design and Model Validation: The design evolution of a $1/12^{th}$ Froude-

scale experiment to validate the overall model is presented. Conclusions are also presented regarding the investigation of the BSP in wind tunnels.

3. Feasibility of the Integral Active Twist (IAT) Concept in Countering the BSP: Open-loop control strategies based on the IAT to reduce the BSP are presented and assessed. The investigation attempts to address all factors that contribute to the BSP presented above.

The approach to this investigation follows the trend typically used in rotorcraft analysis where simulation tools are developed to address the problem at hand. However, the lessons learned through the literature review are also applied. As alluded to in [29], the simulation tools developed are versatile and can be easily used to study an aeroelastic problem other than the BSP.

Figure. 1.17 also highlights the purpose of each chapter, where functionality and relevance to each research step is used to group the chapters rather than a specific sequential order. The large horizontal arrows indicate the flow between each research step, where results from the second step were used to correct and modify some simulation tools in the first step. The small arrows indicate the flow of the outputs of the developed simulation tools.

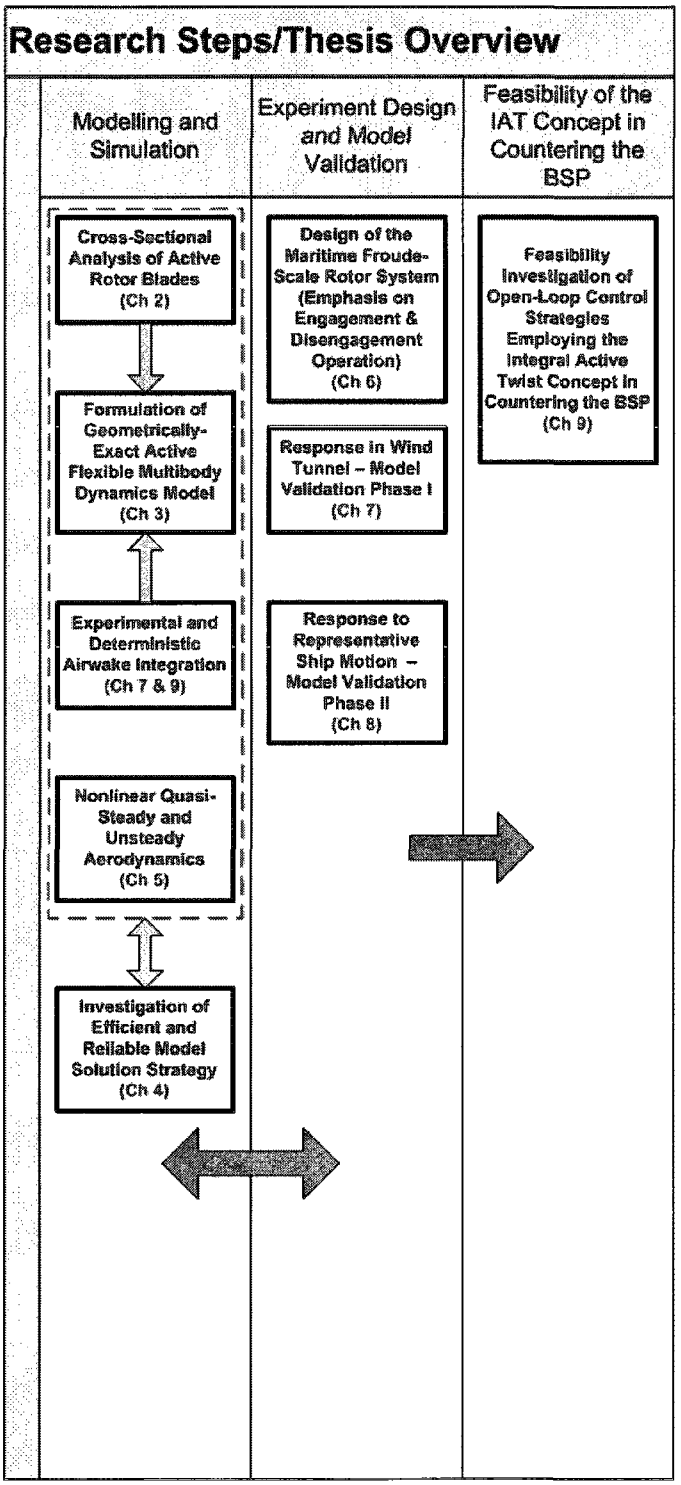

Figure 1.17: Pictorial overview of present research.

Chapter 2

Cross-Sectional Analysis of Active Rotor Blades

2.1 Overview of Chapter 2

In this chapter, an asymptotically-correct linear 2-D cross-sectional theory to analyze active, slender, thin-wall beam-like structures with no initial twist or curvature is developed. The 2-D cross-sectional theory and its implementation are validated against the 2-D finite element software VABS and UM/VABS, which has been validated against experimental, 3-D finite element, and known nonlinear elasticity solutions.

2.2 Motivation

Rotor blades, being primary components of the rotor system, are essential structural components that critically affect rotor performance parameters [59]. Modern rotor blades have advanced significantly in terms of design complexity, manufacturing, and performance relative to their early predecessors. The simple isotropic metallic and wooden rotor blades

have been replaced by composite rotor blades with advanced airfoil geometry and tip design topologies as seen for the Bell 429 helicopter in Fig. 2.1. The aforementioned advances are accompanied by increases in engineering analysis complexity due to the unique features of thin-walled composite structures. It is well known in the engineering community that composite structures offer a high strength-to-weight ratio along with significant improvements in fatigue life and damage tolerance. Additionally, correct laminate design can yield desired enhanced directional strength and elastic couplings that could play a significant role in affecting the operational performance of rotorcraft like dynamic stability of the blades.

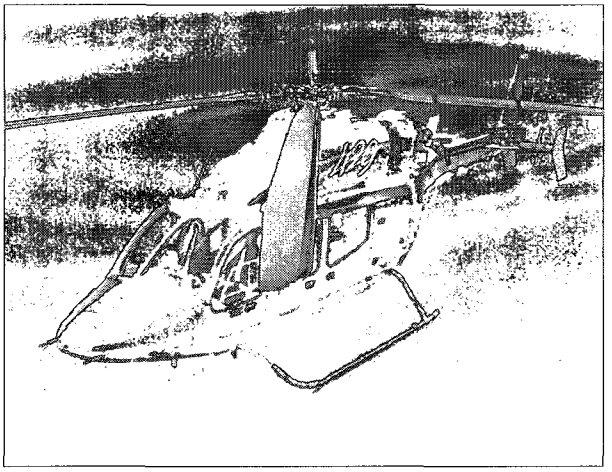

Figure 2.1: Isometric view of Bell 429 rotor system [Courtesy of Bell Helicopters].

Recently, adoption of concepts of smart structures have been proposed for the structural design of next generation of rotor systems with the principal goal of alleviating, if not completely eliminating, noise and vibration associated with helicopter operation [60, 61]. Several approaches to incorporation of engineering concepts from smart structures into the rotor system design have been proposed in the literature. Presenting a comprehensive survey of these is a broad task that is beyond the scope of this work; however, an overview can be found in References [62, 63, 64, 65].

2.3 The Integral Active Twist Concept

Of all concepts proposed in the engineering literature for the incorporation of smart structures in the design of rotor systems, the concept of the Integral Active Twist (IAT) is of interest in this work. The concept is based on replacing the conventional passive twist plies in composite blades with Active Fibre Composites (AFCs) or Macro Fibre Composites (MFCs) plies at ply angles commonly of $\pm 45°$, where other ply angles are also possible in the cross-sectional design. A typical laminate design of a rotor blade with the integral active twist concept is shown in Fig. 2.2, where the most accepted convention of a positive fibre direction in a ply relative to the global frame of the cross-section, which is depicted in Fig. 2.3, is adopted. Additionally, the ply angles and their stacking sequence in each laminate of the cross-section are defined relative to the global coordinate shown in Fig. 2.2 rotated 360° counter clockwise about the x_1 axis.

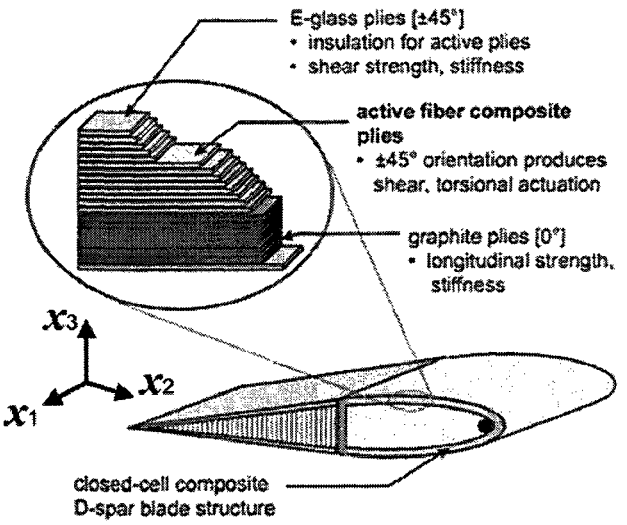

Figure 2.2: Typical laminate design of a rotor blade with the IAT concept [Courtesy of NASA Langley Research Center].

The active fibres are based on the piezoelectric property of certain ceramics like Lead Zirconate Titanate $PbZrTiO_3$ (PZT). When a piezoelectric material is subjected to an

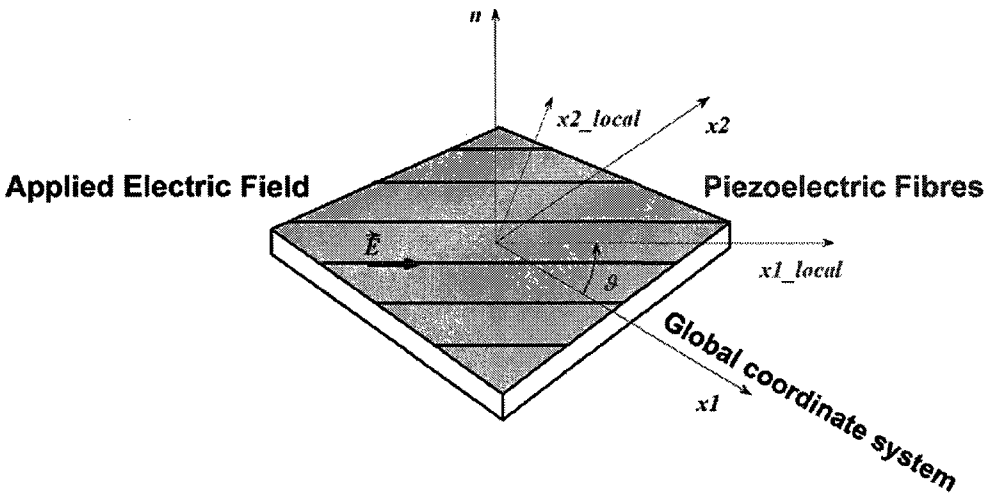

Figure 2.3: Positive fibre orientation convention indicating local and global coordinate systems respectively.

electric signal along a certain crystal (or domain in the case of ceramics) direction, a mechanical deformation is induced in that direction as shown in Fig. 2.3. Conversely, a charge build-up is induced when the piezoelectric material is subjected to a mechanical deformation [66]. A monolithic block of piezoelectric material undergoing mechanical deformation when subjected to an electric field is shown in Fig. 2.4. The largest mechanical strain occurs along the $-x_3$ principal direction, which is assumed to be the crystal polarization direction.

AFCs and MFCs are piezoelectric ceramic fibre-based actuators that are made of polarized unidirectional fibres that are sandwiched between two layers of interdigitated electrodes that are embedded in an epoxy matrix for mechanical protection and electrical insulation. AFCs actuators were first developed at the Massachusetts Institute of Technology (MIT) in the Active Materials and Structure Laboratory (AMSL) [67]. The fibres are cylindrical in shape and they are produced in various diameters via extrusion or spinning where their mechanical properties are highly dependent upon the manufacturing process [68]. A typical section of an AFCs ply is shown in Fig. 2.5, where the polarity of

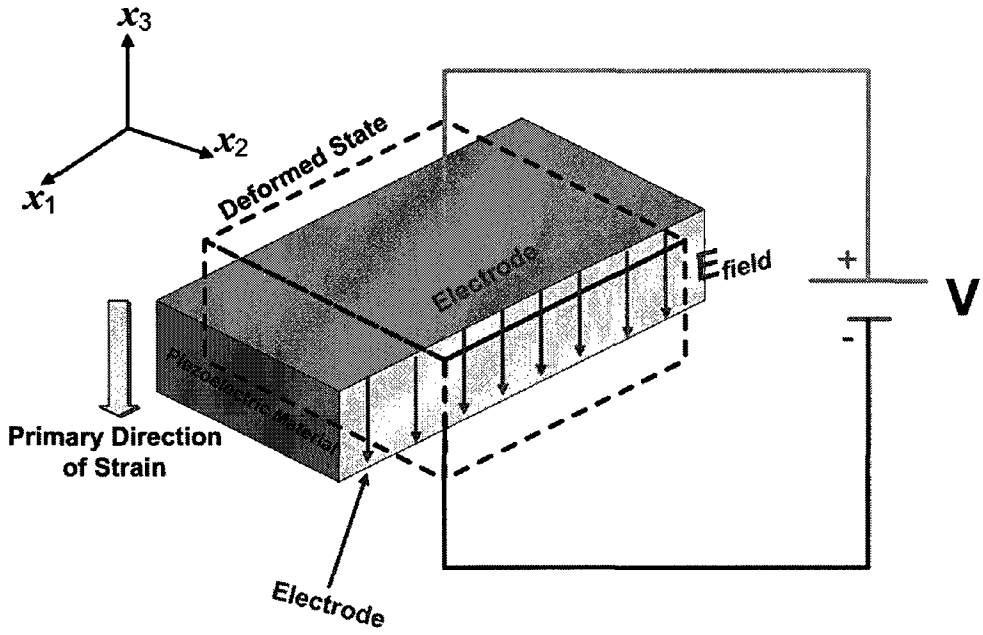

Figure 2.4: A monolithic piezoelectric material block undergoing mechanical deformation due to the application of an electric field.

the interdigitated electrodes relative to the induced axial strain is to be noted.

On the other hand, MFCs are made of rectangular fibres diced from piezoceramic wafers and they were first developed at NASA Langley Research Center [69]. These actuators are the result of efforts to develop a precision manufactured, lower-cost alternative to earlier generation AFCs actuators. They retain all the desired characteristics of AFCs in terms of high strain energy density, directional actuation, conformability, and durability in addition to new features. The most important of these being the use of a low cost fabrication process that yields actuators with uniform and repeatable electromechanical properties. Additionally, all the components needed to manufacture them are commercially available and the procedures are well documented [70]. Furthermore, the electromechanical coupling constants of the MFCs are typically higher than those of the AFCs due primarily to the superior contact between the electrodes and the flat surface of the fibres of the former as compared to the circular one of the latter. A generic MFCs actuator ply is shown in

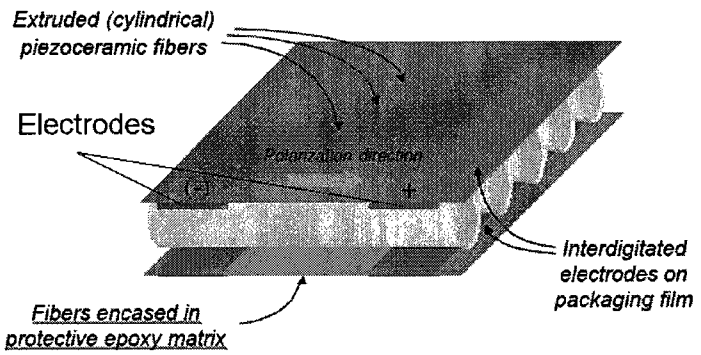

Figure 2.5: Section of an AFCs ply undergoing axial extension due to an applied electric field in the fibre poling direction [Courtesy of NASA Langley Research Center / ARL Vehicle Technology Directorate].

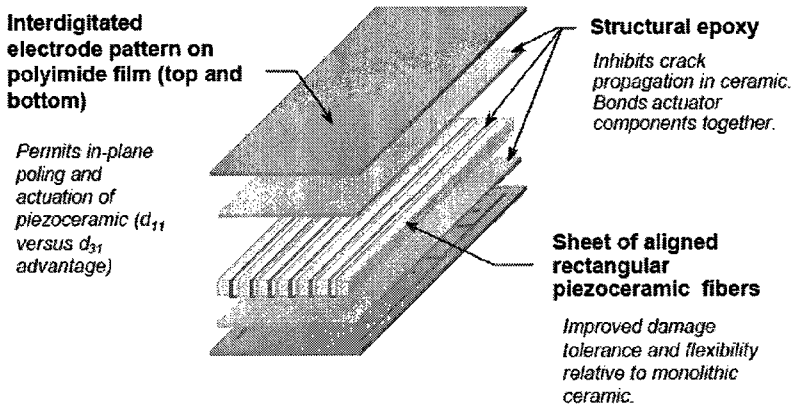

Figure 2.6: Generic MFCs ply design components [Courtesy of NASA Langley Research Center / ARL Vehicle Technology Directorate].

Fig. 2.6 where the operation concept similarity with AFCs is to be noted.

If one assumes that the fibres in a AFCs/MFCs are poled along and opposite to the $\mp 45°$ fibre directions respectively and an electric field $\vec{E}$ is applied along the $-45°$ ply and opposite to the $+45°$, the generic active cross-section shown in Fig. 2.2 will experience a shear strain as to twist the cross-section in a positive sense (out of the page and along the x_1 direction) as shown in Fig 2.7. Conversely, application of the electric field with a reversed polarity will produce a negative twist, although with typically lower twist angles since application of high electric fields opposite to the fibres' poling direction is generally

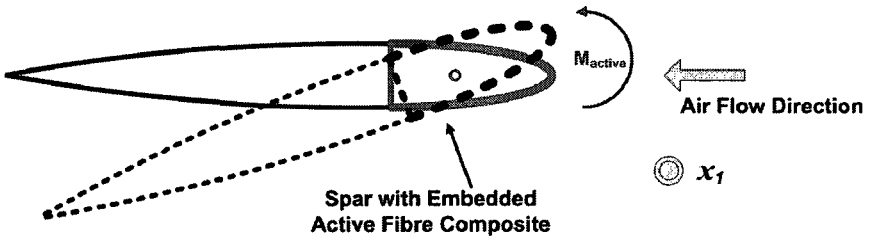

Figure 2.7: Generic IAT concept with an active airfoil undergoing positive active twist due to AFCs/MFCs subjected to an electric field with appropriate polarity.

not a recommended practice [66].

A finished MFCs ply is shown in Fig. 2.8 where its conformity, pliability, and simple design are highlighted. Noise and vibration alleviation are not the only target applications of these actuators, and examples of other envisioned applications in the aerospace field are morphing structures [71] for performance enhancement and space applications like inflatable structures. Many other fields like civil and biomedical engineering are also finding applications for these actuators/sensors [72, 61].

2.4 Overview of Analysis Techniques

Unlike the well established theories that predict the behaviour of passive structures, there are not many engineering theories in the literature that deal with active structures. Theories that can predict the behaviour of active structures are still being developed. Clearly, the predictive capabilities of theories analyzing active structures are highly dependent on advances made in the analysis of passive structures. For active rotor blades with the integral active twist concept, the work of Hagood and duPlessis [73] represents one of the earliest analytical treatments of active thin-wall beams, which is based on the work of Rehfield [74] that invokes a set of restrictive kinematic assumptions regarding the displacement field of the cross-section. The work of Berdichevsky [75] and Badir [76] on passive thin-wall anisotropic single- and two-celled closed cross-section beams, which is based on

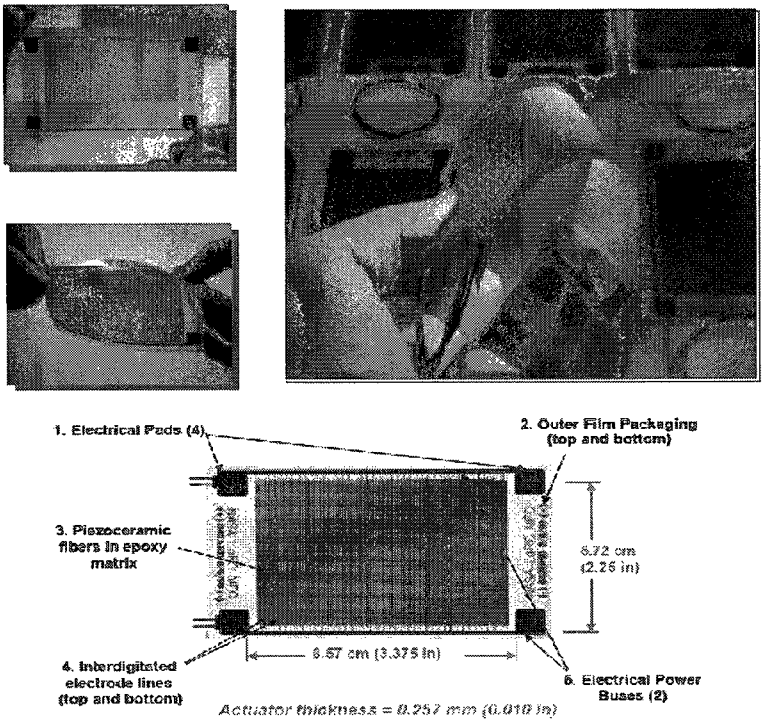

Figure 2.8: Finished MFCs package and its geometric dimensions [Courtesy of NASA Langley Research Center / ARL Vehicle Technology Directorate].

the Variational Asymptotic Method (VAM) developed by Berdichevsky [77], was extended by Cesnik and Shin [78, 79, 80] to include AFCs, where they obtained an asymptotic closed-form solution of the resultants for the actuation stresses. However, the work of [75] has neglected the shell bending strain measures leading to incorrect cross-sectional stiffness constants for certain cross-sections, and would consequently affect the active modelling derived from it. The work of Patil and Johnson [81], still neglected the shell bending strain measures, yet it results in a 6×6 Timoshenko-like flexibility matrix for slender beams and therefore the actuation shear forces are obtained.

All of the previously discussed theories seek to obtain analytical expressions for the resultants of actuation stresses due to AFCs/MFCs at the beam reference line where the 1-D theory is applied. A far more computationally expensive analysis option is to

perform a full 3-D Finite Element Analysis (FEA) using software packages like ANSYS Multiphysics^{TM} and SIMULIA Multiphysics^{TM}. However, even with the present computational capabilities, performing a complete 3-D FEA aeroelastic simulation of the rotorcraft throughout its flight envelope is not feasible from a practical engineering point of view. Additionally, the VAM has also been successfully applied to beams with cross-sections of arbitrary geometry and material anisotropy with initial twist and curvature in the 2-D finite element software package, called Variational Asymptotic Beam Sectional Analysis (VABS) [82, 83, 84]; however, the present VABS only very recently can analyze active beam-like structures. Another variant of the latter engineering tool is the University of Michigan VABS (UM/VABS) [85, 86], which shares the same origin and kernel as VABS but differs in some theoretical aspects like the process of constructing the refined displacement field [87]. Most importantly, UM/VABS has the capability of analyzing slender beam-like structures with embedded AFCs/MFCs.

Considering the engineering tools discussed so far, the need for an analytical theory that quickly yields the correct resultants of the stresses due to embedded AFCs/MFCs without any ad-hoc assumptions in slender structures representative of helicopter rotor blades, airplane wings, and possibly other applications, is highlighted. The characteristics of the sought theory can be summarized as follow:

1. Does not invoke ad hoc kinematic assumptions regarding the deformation of the beam cross-section.

2. Correctly evaluates the in-plane and out-of-plane cross-sectional elastic deformations, known as the warping functions.

3. Correctly and consistently performs a rigorous mathematical reduction of the 3-D electromechanical problem into a 2-D cross-sectional problem and a 1-D problem along the slender structure reference line.

4. Provides the sectional stiffness constants in a form useful for engineering analysis, which provides smooth connection to traditional 1-D beam analysis techniques.

5. Expresses the sectional stiffness matrix in the most compact form possible.

6. Provides mathematical relations between the 1-D strain measures/deformations along the chosen beam reference line and the 3-D strain measures at any point on the cross-section (recovery relations).

7. Tackles arbitrary cross-sectional geometries and material anisotropy.

8. Yields the correct actuation forces/moments due to embedded active materials.

9. Possesses well-grounded mathematical foundations.

While the above characteristics seem like a strict set of conditions, they are required from a structural point of view due to the fact that the classical dimensional reduction (like Euler-Bernoulli with St.Venant field theory) for homogeneous, isotropic, and prismatic beams with its restricted set of assumptions and deformations are not applicable for the problem of modern active composite rotor blades. For the problem at hand, all possible deformations of the three-dimensional structure must be included in the formulation since all elastic couplings are to be anticipated. Additionally, the in-plane and out-of-plane cross-sectional warping deformations are coupled and are expected to significantly affect the sectional stiffness constants and the actuation forces/moments. In this chapter, an analysis tool that possesses the above characteristics will be developed and validated.

2.5 Structural Idealizations of Active Rotor Blades

Since the main focus of this work is helicopter rotor blades, the structural idealization of these members for analysis purposes will be discussed. From an engineering point of

view, rotor blades are treated as slender beam-like structures for the qualitative reasons depicted in Fig. 2.1, which allows for the application of the state-of-the-art beam theories in their analysis as discussed earlier.

Such structural members belong to a class of members identified as reducible structures like shells and plates. Reducible structures are defined as those having a geometric dimension that is dominant over other ones, or at least one geometric aspect ratio that is less than one. The geometric idealization of a generic rotor blade is shown in Fig. 2.9, where the slenderness ratio $\frac{a}{l}$ is clearly defined as the ratio of the characteristic dimension of the cross-section, a, to the span length, l

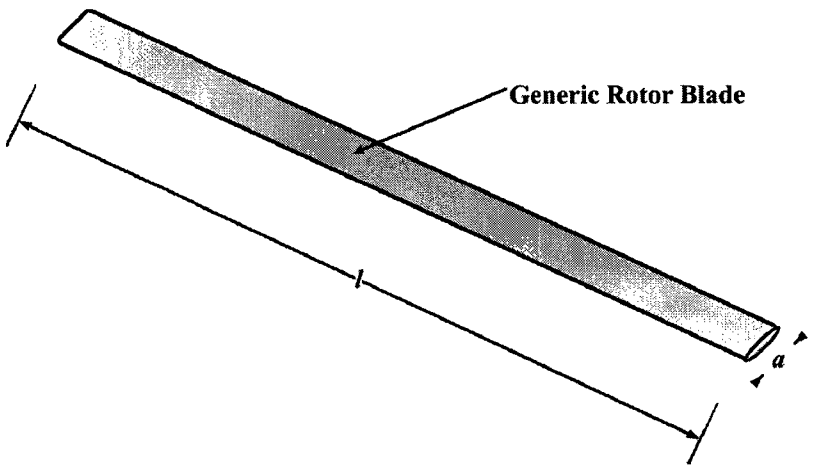

Figure 2.9: Isometric view of a generic helicopter rotor blade.

If one examines the cross-sectional design of the Active Low Vibration Rotor (ALVR) and the generic two-celled rotor blade cross-section in Fig. 2.10, a second aspect ratio $\frac{h}{a}$ is defined as the ratio of the thickness of the wall, h, to the characteristic dimension of the cross-section, a. The latter ratio defines a class of structures that is designated as thin-wall structures, which have a special importance in aerospace applications. Therefore, an active rotor blade has two inherent small parameters that can be defined

$$\frac{a}{l} \ll 1 \tag{2.1}$$

$$\frac{h}{a} \ll 1 \tag{2.2}$$

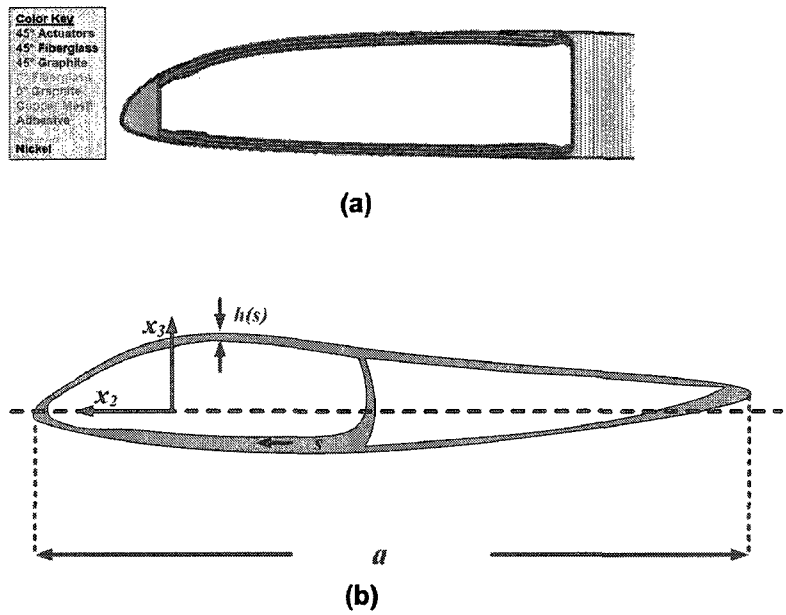

Figure 2.10: (a) Cross-sectional spar design of the Active Low Vibration Rotor (ALVR) [Courtesy of the Boeing Company], (b) Geometric idealization of two-celled rotor blade cross-section.

2.6 The Variational Asymptotic Method (VAM)

As mentioned in Section 2.4, the VAM was originally developed by Berdichevsky and was later expanded and applied to a variety of reducible structures as in the programs VABS and UM/VABS for beam-like structures and the Variational Asymptotic Plate and Shell Analysis (VAPAS) [88, 89] for plates and shells. Therefore, VAM is a very specialized and broad subject and each problem presents a different flavor and details when applying VAM to it. A symbolic/algorithmic description of the method is provided first, followed by its

application to the problem of active thin-wall slender structures.

2.6.1 General Description

A brief symbolic outline of the VAM and its general features are presented first to complement the detailed derivation that follows. The aforementioned slenderness ratio, $\frac{a}{l}$, which is designated as the small parameter ς, is first redefined in terms of the wavelength, ℓ, of the beam elastic deformations along a reference line along the span such as

$$\frac{a}{l} \rightarrow \frac{a}{\ell} \equiv \varsigma \tag{2.3}$$

The redefinition in Eq. 2.3 implies that only elastic deformations with long wavelength, which propagate deep into the beam from its ends, are of importance. These deformations, which are called the global elastic deformations, are the ones of interest here since deformation modes that decay rapidly from the beam ends are localized and are not of interest in this work.

Similar to [90], let the 3-D elastic energy functional of the beam-like structure be symbolically defined as

$$\mathcal{F}(\Gamma, \varsigma) = \mathcal{E}_1(\Upsilon, z_1) + {}^0\mathcal{E}_\varsigma(\Upsilon, z_1, \varsigma) \tag{2.4}$$

$$z_1 = \begin{bmatrix} w_{11} & w_{12} & w_{13} \end{bmatrix} \tag{2.5}$$

where Γ is a 6×1 column matrix that represents a 3×3 symmetric strain field, the vector z_1 represents a perturbation in the classical 3D displacement field, which in reality is the in/out-of-plane warping functions to a first correction, and Υ contains all terms that do not involve the unknown perturbations. The first subscript in the perturbation field denotes the perturbation number while the second one denotes the component. The left superscript

of the second term on the right hand side is used to denote the level of construction of the displacement field, and in this case it is the "zeroth approximation".

The energy functional $\mathcal{F}$ is decomposed into two parts: $\mathcal{E}_1(\Upsilon, z_1)$ which contains all terms of order $\varsigma^0 \equiv 1$ and ${}^0\mathcal{E}_\varsigma(\Upsilon, z_1, \varsigma)$ that contain all terms of order ς^1 and higher with respect to this small parameter. The perturbation in the displacement field, z_1, gives rise to low and high order terms as is apparent from its appearance in both parts of the energy functional. In order to find the first correction to the displacement field, z_1, the high-order component in terms of the small parameter ς in the functional is discarded and then the functional is minimized with respect to z_1. The solution of the Euler-Lagrange minimization problem is not unique and the displacement field is four times redundant. The four rigid body modes: axial translation, two orthogonal transverse translations, and in-plane rotation have to be eliminated from z_1 (the warping field) over the surface area of the cross-section $\mathcal{A}$. Therefore, four constraints $\int_{\mathcal{A}} \bar{\mathcal{C}}_{i=1,2,3,4}()\ \mathrm{d}a$ are imposed on z_1 as such:

$$min_{z_1}\mathcal{F} = min_{z_1}\mathcal{E}_1(\Upsilon, z_1) \tag{2.6}$$

$$\int_A \bar{\mathcal{C}}_1(z_1)\ \mathrm{d}a = 0\ ,\ \int_A \bar{\mathcal{C}}_2(z_1)\ \mathrm{d}a = 0\ ,\ \int_A \bar{\mathcal{C}}_3(z_1)\ \mathrm{d}a = 0\ ,\ \int_A \bar{\mathcal{C}}_4(z_1)\ \mathrm{d}a = 0 \tag{2.7}$$

where $\mathrm{d}a$ is the cross-sectional area differential, and $\bar{\mathcal{C}}_{i=1,2,3,4}()$ represent the constraint functional operators.

When Eqs. 2.6, 2.7 are solved over the cross-section they yield what is called the "zeroth-approximation" or the building block of the solution, z_1. This must not be confused with the order of the components of z_1 itself, which could be of some order of ς, it rather refers to it being obtained by minimizing the part of the energy that has zeroth order of ς (i.e., ς^0). In most cases, there is no closed form solution for z_1, and the problem is

discretized over the cross-section with the constraints leading to a Sturm-Liouville problem followed by finite element calculations, which is the methodology employed in VABS [83, 82]. The order of the components of z_1 in terms of the small parameter is not known a priori but determined throughout the minimization procedure. The solution of Euler-Lagrange equations of the functional and the constraint equations is symbolically written as:

$$z_1 = f_1(\Upsilon, \zeta_2, \zeta_3) \tag{2.8}$$

where ζ_2 and ζ_3 are the coordinate measures along the two perpendicular axes defining the 2D Cartesian plane of the cross section.

To find the next asymptotically-correct approximation of the displacement field, the latter is perturbed again. Let the new perturbation be called z_2 such that:

$$z_2 = z_1 - f_1(\Upsilon, \zeta_2, \zeta_3) \tag{2.9}$$

The new perturbation is substituted back in the energy functional of Eq. 2.4 to obtain:

$$\mathcal{F}(\Gamma, \varsigma) = \mathcal{F}_1(\Upsilon) + \mathcal{E}_2(\Upsilon, z_2) + {}^1\mathcal{E}_\varsigma(\Upsilon, z_2, \varsigma) \tag{2.10}$$

$$z_2 = \begin{bmatrix} w_{21} & w_{22} & w_{23} \end{bmatrix} \tag{2.11}$$

The function $\mathcal{F}_1(\Upsilon)$ represents all the terms that do not contain the new unknown, z_2. It is subscripted with 1 to indicate that it contains contributions from the first correction to the displacement field z_1. The function $\mathcal{E}_2$ contains the lowest-order terms involving z_2, while ${}^1\mathcal{E}_\varsigma$ contains all high-order terms.

Following the same procedure as before, the high order terms (i.e., ${}^1\mathcal{E}_\varsigma$) are discarded

and the functional is minimized with respect to z_2 subject to the same constraints:

$$min_{z_2}\mathcal{F} = \mathcal{F}_1(\Upsilon) + min_{z_2}\mathcal{E}_2(\Upsilon, z_2) \tag{2.12}$$

$$\int_A \bar{C}_1(z_2)\,da = 0\ ,\int_A \bar{C}_2(z_2)\,da = 0\ ,\int_A \bar{C}_3(z_2)\,da = 0\ ,\int_A \bar{C}_4(z_2)\,da = 0 \tag{2.13}$$

Similarly, one obtains,

$$z_2 = f_2(\Upsilon, \zeta_2, \zeta_3) \tag{2.14}$$

The process is repeated until the new perturbation yields no terms in the energy functional of order that is of the highest order yielded by the previous perturbation, and at this point the displacement field is said to have converged. For example, assume that the perturbation z_k produced terms in the energy functional with one being the highest order having an order of $\mathcal{O}(n)$. A further perturbation, z_{k+1}, produces terms that are of order $\mathcal{O}(n+1)$ and higher, then at this stage the iteration is terminated. In fact, one may not have to go as far as this in order to obtain the correct elastic behavior of the beam since ς is a small parameter to start with. Terms of order $\mathcal{O}(\varsigma^0 \equiv 1)$ are the only ones needed to obtain the asymptotically-correct global elastic behaviour of the beam [91].

The energy functional can then be written after the kth perturbation as:

$$\mathcal{F}(\Gamma, \varsigma) = \mathcal{F}_1(\Upsilon) + \mathcal{F}_2(\Upsilon) + \ldots + \mathcal{F}_k(\Upsilon) + \mathcal{E}_{k+1}(\Upsilon, z_{k+1}, \varsigma) + {}^k\mathcal{E}_\varsigma(\Upsilon, z_{k+1}, \varsigma) \tag{2.15}$$

Alternatively, the energy functional is said to have been expanded implicitly as an asymptotic series in the small parameter ς:

$$\mathcal{F}(\Gamma, \varsigma) = \mathcal{O}(\varsigma^0) + \mathcal{O}(\varsigma^1) + \mathcal{O}(\varsigma^2) + \mathcal{O}(\varsigma^3) + \ldots + \mathcal{O}(\varsigma^k) \tag{2.16}$$

The asymptotic expansion in Eq. 2.16 illustrates how the VAM seeks to approximate

the 3-D elastic energy that has been condensed into 1-D along the beam reference line as accurately as possible by accounting for all important terms in that expansion. For instance, if a theory correctly accounts for all the terms up to the order $\mathcal{O}(\varsigma^1)$ in Eq. 2.16, then the theory is said to be asymptotically-correct to that order. The process of dropping high order terms during the minimization or truncating them from the asymptotic expansion of the functional is equivalent to a correct and systematic neglect of insignificant terms in solution methods that rely on the conventional application of the theory of elasticity like the formal asymptotic method. But these conventional methods usually involve a multitude of partial differential equations, rendering the identification of these insignificant terms extremely difficult if not outright impossible.

2.6.2 Application of the VAM to Active Thin-Wall Beams

In this section the VAM outlined above will be applied to the idealized active thin-wall rotor blade discussed in Section 2.5, which will further illustrate its symbolic outline. The geometric idealization of an active helicopter rotor blade as a multi-celled thin-wall beam allows the development to start from 3-D shell theory rather than 3-D elasticity theory. The passive structural theory that represents the basis of this development is the asymptotically-correct theory of multi-cell thin-wall beams of Hodges and Volovoi [92, 93].

Consider the active thin-wall slender anisotropic beam structure depicted in Fig. 2.11. The linear asymptotically-correct cross-sectional theory being sought has the form

$$2\mathcal{U}_{\text{classical-like}} = \bar{\epsilon}^{\mathrm{T}} \bar{S} \bar{\epsilon} + 2\mathcal{U}(\bar{\epsilon})^{(\mathrm{a})}_{\text{classical-like}} \tag{2.17}$$

where $\mathcal{U}_{\text{classical-like}}$ is the strain energy per unit length, $\mathcal{U}(\bar{\epsilon})^{(\mathrm{a})}_{\text{classical-like}}$ is the energy per unit length due to actuation, $\bar{S}$ is a 4×4 cross-sectional stiffness matrix that carries information about the cross-sectional geometry and material design, and $\bar{\epsilon}$ is a vector of the classical

strain measures that corresponds to stretch, twist, and the two orthogonal bending strains arranged as

$$\bar{\epsilon}^{\mathrm{T}} = \begin{bmatrix} u_1' & \theta' & -u_3'' & u_2'' \end{bmatrix} \tag{2.18}$$

where u_1, u_2, u_3, and θ are the mutually orthogonal displacements and rotation of the beam cross-section at the reference line.

The linear electromechanical cross-sectional constitutive relation can be derived from Eq. 2.17 such that

$$\begin{bmatrix} F_1 \\ M_1 \\ M_2 \\ M_3 \end{bmatrix} = \frac{\partial \mathcal{U}_{\text{classical-like}}}{\partial \bar{\epsilon}} \tag{2.19}$$

or

$$\begin{bmatrix} F_1 \\ M_1 \\ M_2 \\ M_3 \end{bmatrix} = \underbrace{\begin{bmatrix} S_{11} & S_{12} & S_{13} & S_{14} \\ S_{12} & S_{22} & S_{23} & S_{24} \\ S_{13} & S_{23} & S_{33} & S_{34} \\ S_{14} & S_{24} & S_{34} & S_{44} \end{bmatrix}}_{\bar{S}} \bar{\epsilon} + \begin{bmatrix} F_1^{(a)} \\ M_1^{(a)} \\ M_2^{(a)} \\ M_3^{(a)} \end{bmatrix} \tag{2.20}$$

where the diagonal terms in $\bar{S}$: S_{11}, S_{22}, S_{33}, and S_{44} correspond to the axial, twist, and two orthogonal bending stiffness respectively; the off-diagonal terms correspond to elastic couplings; the section mechanical force/moments: F_1, M_1, M_2, and M_3 correspond to stretch, twist, and two orthogonal bending with similar correspondence to the section active force/moments: $F_1^{(a)}$, $M_1^{(a)}$, $M_2^{(a)}$, and $M_3^{(a)}$.

Another important small parameter is assumed at this stage, which is the maximum

magnitude of the strain measures, including the prescribed actuation strains, as such

$$\| \bar{\epsilon} \|_{max} \sim \mathcal{O}(\epsilon) \ll 1 \tag{2.21}$$

where large strains imply material nonlinearities which is beyond the scope of this work.

An asymptotically-correct refined theory will have additional degrees of freedom. An example would be a higher axial derivative of the already defined classical 1-D strain measures in Eq. 2.18 relative to the form in Eq. 2.17 such that

$$2\mathcal{U}_{\text{refined}} = \bar{\epsilon}^{\mathrm{T}} \bar{S} \bar{\epsilon} + 2\bar{\epsilon}^{\mathrm{T}} N \bar{\epsilon}' + \bar{\epsilon}' M \bar{\epsilon}' + 2\mathcal{U}(\bar{\epsilon})^{(a)}_{\text{classical-like}} + 2\mathcal{U}(\bar{\epsilon}, \bar{\epsilon}')^{(a)}_{\text{refined}} \tag{2.22}$$

where $(\ )' \equiv \frac{\partial ()}{\partial x_1}$, N is a material and geometry matrix that couples the classical degrees of freedom to the new ones, M is the stiffness matrix of the new degrees of freedom, and $\mathcal{U}(\bar{\epsilon}, \bar{\epsilon}')^{(a)}_{\text{refined}}$ represents the refined actuation stress resultants.

The form of the linear electromechanical cross-sectional constitutive relation derived from Eq. 2.22 will vary depending on the level of refinement. For example, a Timoshenko refinement corresponding to the additional degrees of freedom $-u_3'''$ and u_2''' is symbolically written as

$$\begin{bmatrix} F_1 \\ M_1 \\ M_2 \\ M_3 \\ F_2 \\ F_3 \end{bmatrix} = \frac{\partial \mathcal{U}_{\text{refined-Timoshenko}}}{\partial \bar{\epsilon}} + \frac{\partial \mathcal{U}_{\text{refined-Timoshenko}}}{\partial \bar{\epsilon}'} \tag{2.23}$$

or

$$\begin{bmatrix} F_1 \\ M_1 \\ M_2 \\ M_3 \\ F_2 \\ F_3 \end{bmatrix} = \underbrace{\begin{bmatrix} S_{11} & S_{12} & S_{13} & S_{14} & S_{15} & S_{16} \\ S_{12} & S_{22} & S_{23} & S_{24} & S_{25} & S_{26} \\ S_{13} & S_{23} & S_{33} & S_{34} & S_{35} & S_{36} \\ S_{14} & S_{24} & S_{34} & S_{44} & S_{45} & S_{46} \\ S_{15} & S_{25} & S_{35} & S_{45} & S_{55} & S_{56} \\ S_{16} & S_{26} & S_{36} & S_{46} & S_{56} & S_{66} \end{bmatrix}}_{\bar{S}} \begin{bmatrix} \bar{\epsilon} \\ \gamma_{12} \\ \gamma_{13} \end{bmatrix} + \begin{bmatrix} F_1^{(a)} \\ M_1^{(a)} \\ M_2^{(a)} \\ M_3^{(a)} \\ F_2^{(a)} \\ F_3^{(a)} \end{bmatrix} \tag{2.24}$$

where the stiffness constants are defined as in Eq. 2.20 in addition to the diagonal terms S_{55} and S_{66} that represent the two orthogonal shear rigidities; F_2 and F_3 correspond to the section mechanical shear forces; and $F_2^{(a)}$ and $F_3^{(a)}$ are the section active shear forces.

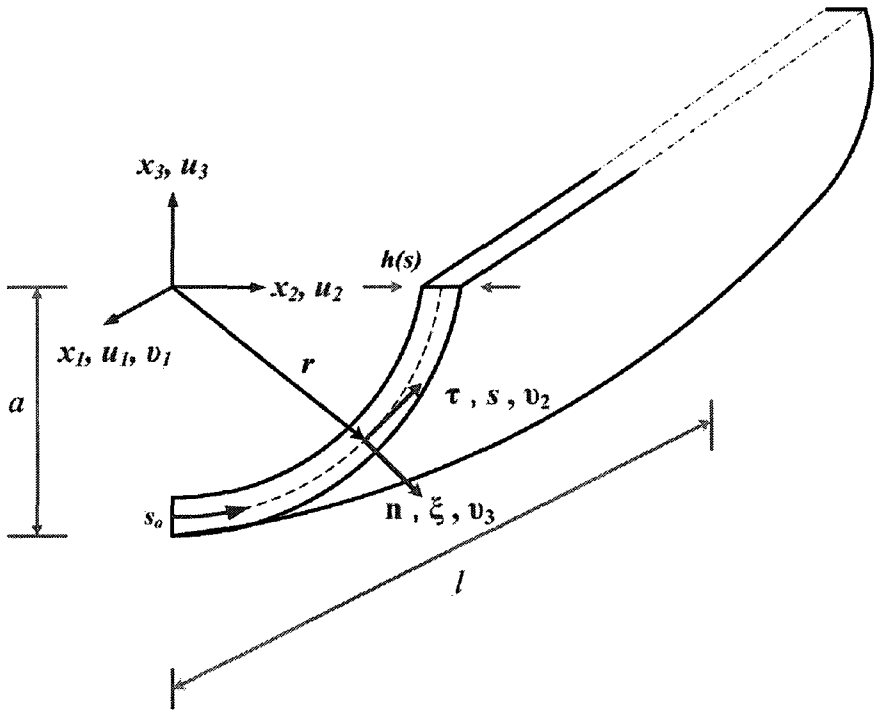

Figure 2.11: Geometry of active thin-wall slender anisotropic beam structure.

In Fig. 2.11, the global cartesian coordinate system is defined by the axes: x_1, x_2, and x_3 and their corresponding displacements: u_1, u_2, and u_3 for each point along the reference

line of the structure. The axes of the curvilinear coordinate system: x_1, s, and ξ and their corresponding displacements: v_1, v_2, and v_3, which is defined for each material point of the cross-section, are also depicted. Adopting the convention $(\ )_{,s} \equiv \frac{\partial()}{\partial s}$, the following quantities based on the geometry of Fig. 2.11 will also be defined

$$\begin{aligned}
\vec{\mathbf{r}} &= x_2\vec{\mathbf{b}}_2 + x_3\vec{\mathbf{b}}_3 \\
\vec{\tau} &= \vec{\mathbf{r}}_{,s} = x_{2,s}\vec{\mathbf{b}}_2 + x_{3,s}\vec{\mathbf{b}}_3 \\
\vec{\mathbf{n}} &= \vec{\tau} \times \vec{\mathbf{b}}_1 = x_{3,s}\vec{\mathbf{b}}_2 - x_{2,s}\vec{\mathbf{b}}_3 \\
r_\tau &= \vec{\tau} \cdot \vec{\mathbf{r}} = x_{2,s}x_2 + x_{3,s}x_3 \\
r_n &= \vec{\mathbf{n}} \cdot \vec{\mathbf{r}} = x_{3,s}x_2 - x_{2,s}x_3 \\
R &= \frac{x_{2,s}}{x_{3,ss}} = -\frac{x_{3,s}}{x_{2,ss}}
\end{aligned} \tag{2.25}$$

where the vectors: $\vec{\mathbf{r}}$, $\vec{\tau}$, and $\vec{\mathbf{n}}$ are defined in Fig. 2.11; and the quantity R being the radius of curvature; r_τ is the component of $\vec{\mathbf{r}}$ along $\vec{\tau}$; r_n is the component of $\vec{\mathbf{r}}$ along $\vec{\mathbf{n}}$; and $\vec{\mathbf{b}}_\mathbf{i}$ are the normal vectors along the x_i axes respectively.

According to the IEEE standard on piezoelectricity [66] the phenomenological law relating the induced piezoelectric strain tensor to the applied electric field in the local frame attached to the active ply in Fig. 2.3 is given by

$$\breve{\varepsilon}_{ij}^{(a)} = d_{kij}E_k \tag{2.26}$$

where d_{kij} is the electromechanical coupling tensor of the material and E_k is the electric field vector.

From a practical point of view, only the component of the electric field along the fibres E_1 is assumed to exist in this two dimensional context.

The elements of the active strain tensor in the global frame of the shell are given by the transformation

$$\begin{bmatrix} \varepsilon_{11}^{(a)} \\ \varepsilon_{22}^{(a)} \\ \varepsilon_{33}^{(a)} \end{bmatrix} = \mathcal{R}(\vartheta) \begin{bmatrix} d_{111}E_1 \\ d_{122}E_1 \\ d_{112}E_1 \end{bmatrix} \tag{2.27}$$

where $\mathcal{R}(\vartheta)$ is given by

$$\mathcal{R}(\vartheta) = \begin{bmatrix} \cos^2(\vartheta) & \sin^2(\vartheta) & -2\cos(\vartheta)\sin(\vartheta) \\ \sin^2(\vartheta) & \cos^2(\vartheta) & 2\cos(\vartheta)\sin(\vartheta) \\ \cos(\vartheta)\sin(\vartheta) & -\cos(\vartheta)\sin(\vartheta) & \cos^2(\vartheta) - \sin^2(\vartheta) \end{bmatrix} \tag{2.28}$$

and ϑ is the orientation of the fibres in the ply relative to the longitudinal axis of the shell x_1.

The mechanical shell strain energy per unit volume is written as

$$2\hat{\mathcal{U}}^{(m)} = D^{\alpha\beta\gamma\delta}(\varepsilon_{\alpha\beta} - \varepsilon_{\alpha\beta}^{(a)})(\varepsilon_{\alpha\beta} - \varepsilon_{\alpha\beta}^{(a)}) \tag{2.29}$$

where $D^{\alpha\beta\gamma\delta}$ are the plane-stress reduced constants that are related to the regular elastic 3-D constants as [92]

$$D^{\alpha\beta\gamma\delta} = E^{\alpha\beta\gamma\delta} - \frac{E^{\alpha\beta 33}E^{\gamma\delta 33}}{E^{3333}} - H_{\mu\lambda}G^{\alpha\beta\mu}G^{\gamma\delta\lambda} \tag{2.30}$$

where

$$\begin{aligned} H_{\mu\lambda}^{-1} &= E^{\mu 3\lambda 3} - \frac{E^{\mu 333}E^{\lambda 333}}{E^{3333}} \\ G^{\alpha\beta\mu} &= E^{\alpha\beta\mu 3} - \frac{E^{\alpha\beta 33}E^{\mu 333}}{E^{3333}} \end{aligned} \tag{2.31}$$

These constants result from the minimization of the 3-D energy with respect to the through-thickness strain component and they are given in terms of the lamina stiffness constants in Appendix A. Furthermore, the elements of the total strain tensor can be expressed in terms of the generalized Koiter and Sanders shell strain measures $\gamma_{\alpha\beta}$ and $\rho_{\alpha\beta}$ [94] as

$$\varepsilon_{\alpha\beta} = \gamma_{\alpha\beta} + \xi\rho_{\alpha\beta} \tag{2.32}$$

where $\gamma_{\alpha\beta}$ and $\rho_{\alpha\beta}$ are the membrane forces and bending moments conjugate strain measures respectively; and ξ is the through-the-shell thickness curvilinear coordinate measure.

Integrating Eq. 2.29 through the thickness and around the closed contour of the shell yields the mechanical strain energy per unit length along the span of the beam

$$2\tilde{\mathcal{U}}^{(m)} = \oint \int_{-\frac{h}{2}}^{\frac{h}{2}} D^{\alpha\beta\gamma\delta}(\gamma_{\alpha\beta} + \xi\rho_{\alpha\beta} - \varepsilon^{(a)}_{\alpha\beta})(\gamma_{\gamma\delta} + \xi\rho_{\gamma\delta} - \varepsilon^{(a)}_{\gamma\delta})\, \mathrm{d}\xi\, \mathrm{d}s \tag{2.33}$$

Grouping the shell strains in a vector format as $\psi^{\mathrm{T}} = \begin{bmatrix} \gamma_{11} & h\rho_{11} & h\rho_{12} \end{bmatrix}$, $\phi^{\mathrm{T}} = \begin{bmatrix} 2\gamma_{12} & \gamma_{22} & h\rho_{22} \end{bmatrix}$ and substituting Eqs. 2.26 and 2.27 into Eq. 2.33 followed by integration through the thickness of the shell yields

$$2\mathcal{U}^{(m)} = \oint \left(\psi^{\mathrm{T}} Q \psi + 2\phi^{\mathrm{T}} S \psi + \phi^{\mathrm{T}} P \phi - 2\psi^{\mathrm{T}} H - 2\phi^{\mathrm{T}} G + \aleph(E_1)\right) \mathrm{d}s \tag{2.34}$$

where the material matrices Q, S, and P; and the electromechanical matrices G and H are given in Appendix A; and the term $\aleph(E_1)$ is a quadratic term of the electric field that is given by

$$\aleph(E_1) = \int_{-\frac{h}{2}}^{\frac{h}{2}} D^{\alpha\beta\gamma\delta} d_{1\alpha\beta} d_{1\gamma\delta} E_1^2\, \mathrm{d}\xi \tag{2.35}$$

The six shell generalized strain measures are expressed in terms of the curvilinear displacements as [76]:

$$\begin{aligned}
\gamma_{11} &= v_{1,1} \\
\rho_{11} &= v_{3,11} \\
2\gamma_{12} &= v_{1,2} + v_{2,1} \\
\rho_{12} &= v_{3,12} + \frac{1}{4R}(v_{1,2} - 3v_{2,1}) \\
\gamma_{22} &= v_{2,2} + \frac{v_3}{R} \\
\rho_{22} &= v_{3,22} - (\frac{v_2}{R})_{,2}
\end{aligned} \tag{2.36}$$

The curvilinear displacements are related to the cartesian displacements of the material point on the shell such as

$$\begin{aligned}
v_1 &= \hat{u}_1 \\
v_2 &= \hat{u}_2 x_{2,s} + \hat{u}_3 x_{3,s} \\
v_3 &= \hat{u}_2 x_{3,s} - \hat{u}_3 x_{2,s}
\end{aligned} \tag{2.37}$$

where cartesian displacements with carat denote those for each material point on the cross-section, while those without denote the global displacements at the beam-like structure reference line.

Closed Cross-Section Active Beams

For the purpose of generality, all the classical strain measures are assumed to be of the same order in the subsequent development, therefore:

$$u_1' \sim \mathcal{O}(\epsilon) \quad a\theta' \sim \mathcal{O}(\epsilon) \quad -au_3'' \sim \mathcal{O}(\epsilon) \quad au_2'' \sim \mathcal{O}(\epsilon) \quad \mathcal{O}(R) \sim \mathcal{O}(a) \tag{2.38}$$

The order of the displacement field warping terms relative to the inherent small parameters of the problem will now be constructed based on the VAM without consideration of the actuation; however, when the warping terms are solved for, the actuation field must be taken into account as shall be demonstrated.

Dropping all terms that involve differentiation with respect to the axial coordinate in Eq. 2.36 since they imply division by the wavelength of the global deformations, the remaining terms are

$$\begin{aligned} 2\gamma_{12} &= v_{1,2} \\ \rho_{12} &= \frac{v_{1,2}}{4R} \\ \gamma_{22} &= v_{2,2} + \frac{v_3}{R} \\ \rho_{22} &= v_{3,22} - (\frac{v_2}{R})_{,2} \end{aligned} \tag{2.39}$$

Substituting in the energy functional in Eq. 2.33, the resulting strain energy functional is positive definite and quadratic in the strain measures

$$2\tilde{\mathcal{U}}^{(m)}(\gamma_{12}^2, \gamma_{12}, \rho_{12}^2, \rho_{12}, \gamma_{22}^2, \gamma_{22}, \rho_{22}^2, \rho_{22}) \geq 0 \tag{2.40}$$

The minimum of this functional is achieved when the strains vanish, which corresponds to the rigid body motion of the cross-section. The solution of the displacement field is obtained from the partial differential equations

$$\begin{aligned} v_{1,2} &= 0 \\ \frac{v_{1,2}}{4R} &= 0 \\ v_{2,2} + \frac{v_3}{R} &= 0 \\ v_{3,22} - (\frac{v_2}{R})_{,2} &= 0 \end{aligned} \tag{2.41}$$

which has the solution

$$\begin{aligned} v_1 &= u_1 \\ v_2 &= u_\alpha x_{\alpha,s} + \theta r_n \\ v_3 &= u_2 x_{3,s} - u_3 x_{2,s} - \theta r_\tau \end{aligned} \tag{2.42}$$

where the resulting displacement field is the rigid body motion of the cross-section at its reference line with u_1, u_2, u_3, and $\theta \equiv v_2/R - v_{3,2}$ as functions of x_1 only as depicted in Fig 2.11.

An equivalent approach for obtaining the above displacement field utilizes the elimination of the so-called "phantom terms" [92] in the energy functional. Developing the displacement field using this approach will serve to illustrate a powerful tool in constructing the warping functions of the cross-section. Substitution of Eqs. 2.37 into Eqs. 2.36 and discarding terms with the axial derivative yields

$$
\begin{aligned}
2\gamma_{12} &= \underbrace{\hat{u}_{1,2}}_{\epsilon\left(\frac{a}{\ell}\right)^{-1}} \\
h\rho_{12} &= \underbrace{\frac{h\hat{u}_{1,2}}{4R}}_{\epsilon\left(\frac{a}{\ell}\right)^{-1}\left(\frac{h}{a}\right)} \\
\gamma_{22} &= \underbrace{\left(\hat{u}_2 x_{2,s} + \hat{u}_3 x_{3,s}\right)_{,2} + \frac{\left(\hat{u}_2 x_{3,s} - \hat{u}_3 x_{2,s}\right)}{R}}_{\epsilon\left(\frac{a}{\ell}\right)^{-2}} \\
h\rho_{22} &= \underbrace{h\left(\hat{u}_2 x_{3,s} - \hat{u}_3 x_{2,s}\right)_{,22} - h\left(\frac{\left(\hat{u}_2 x_{2,s} + \hat{u}_3 x_{3,s}\right)}{R}\right)_{,2}}_{\epsilon\left(\frac{a}{\ell}\right)^{-2}\left(\frac{h}{a}\right)}
\end{aligned}
\tag{2.43}
$$

where the order of the terms relative to the small parameters have been determined based on Eq. 2.38 with the axial and the contour derivatives implying a division by the deformation wavelength ℓ and the characteristic dimension of the cross-section a respectively. An example of determining the order of the term in $2\gamma_{12}$ is shown below

$$
u_1' \sim \mathcal{O}(\epsilon) \;\Rightarrow\; u_1 \sim \mathcal{O}(\ell\epsilon) \;\Rightarrow\; u_{1,2} \sim \mathcal{O}(\frac{\ell}{a}\epsilon) \tag{2.44}
$$

All the terms in Eq. 2.43 are of the order of the inverse of the small parameters, which imply excessively large terms in the energy functional. These terms are labeled "phantom" terms since for the minimization solution to exist, they must vanish and one retrieves Eqs. 2.41, which is the building block of the solution.

Now, the displacement field is perturbed with $z_1 = \begin{bmatrix} \hat{w}_1 & \hat{w}_2 & \hat{w}_3 \end{bmatrix}$ according to the procedure outlined in Subsection 2.6.1 to yield

$$
\begin{aligned}
v_1 &= u_1 + \hat{w}_1 \\
v_2 &= u_\alpha x_{\alpha,s} + \theta r_n + \hat{w}_2 \\
v_3 &= u_2 x_{3,s} - u_3 x_{2,s} - \theta r_\tau + \hat{w}_3
\end{aligned} \tag{2.45}
$$

Substitution of the perturbed displacement field into Eqs. 2.36 yields

$$
\begin{aligned}
\gamma_{11} &= \underbrace{u_1'}_{\epsilon} + \underbrace{\hat{w}_{1,1}}_{?\equiv[\epsilon]} \\
2\gamma_{12} &= \underbrace{x_{2,s}u_2'}_{\epsilon\left(\frac{a}{\ell}\right)^{-1}} + \underbrace{x_{3,s}u_3'}_{\epsilon\left(\frac{a}{\ell}\right)^{-1}} + \underbrace{r_n\theta'}_{\epsilon} + \underbrace{\hat{w}_{1,2}}_{?\equiv\left[\epsilon\left(\frac{a}{\ell}\right)^{-1}\right]} + \underbrace{\hat{w}_{2,1}}_{?\equiv\left[\epsilon\left(\frac{a}{\ell}\right)\left(\frac{a}{h}\right)\right]} \\
\gamma_{22} &= \underbrace{\hat{w}_{2,2}}_{?\equiv\left[\epsilon\left(\frac{a}{h}\right)\right]} + \underbrace{\frac{\hat{w}_3}{R}}_{?\equiv\left[\epsilon\left(\frac{a}{h}\right)\right]} \\
h\rho_{11} &= h\left(\underbrace{x_{3,s}u_2''}_{\epsilon\left(\frac{h}{a}\right)} - \underbrace{x_{2,s}u_3''}_{\epsilon\left(\frac{h}{a}\right)} - \underbrace{r_\tau\theta''}_{\epsilon\left(\frac{h}{a}\right)\left(\frac{a}{\ell}\right)} + \underbrace{\hat{w}_{3,11}}_{?\equiv\left[\epsilon\left(\frac{a}{\ell}\right)^2\right]}\right) \\
h\rho_{12} &= h\left[\frac{1}{4R}\left(\underbrace{x_{\alpha,s}u_\alpha'}_{\epsilon\left(\frac{h}{a}\right)\left(\frac{a}{\ell}\right)^{-1}} + \underbrace{r_n\theta'}_{\epsilon\left(\frac{h}{a}\right)} - \underbrace{\hat{w}_{1,2}}_{?\equiv\left[\epsilon\left(\frac{a}{\ell}\right)^{-1}\left(\frac{h}{a}\right)\right]}\right) - \underbrace{\theta'}_{\epsilon\left(\frac{h}{a}\right)} + \underbrace{\hat{w}_{3,12}}_{?\equiv\left[\epsilon\left(\frac{a}{\ell}\right)\right]} - \underbrace{\frac{3}{4R}\hat{w}_{2,1}}_{?\equiv\left[\epsilon\left(\frac{a}{\ell}\right)\right]}\right] \\
h\rho_{22} &= h\left(\underbrace{\hat{w}_{3,2}}_{?\equiv[\epsilon]} - \underbrace{\frac{\hat{w}_2}{R}}_{?\equiv[\epsilon]}\right)_{,2}
\end{aligned} \tag{2.46}
$$

where the under-braces encompass the term and any multiplying coefficient, and the question mark indicates the order of the term will be determined later.

The order of the perturbations is not assumed a priori as mentioned above, but de-

termined during the minimization procedure using the leading order terms involving the unknown perturbations (with the least amount of differentiation with respect to the axial and then the contour coordinates respectively). Examination of $2\gamma_{12}$ reveals two phantom terms that must be annihilated in the energy functional, and the candidate function is $\hat{w}_{1,2}$, as such:

$$\hat{w}_{1,2} = -u'_\alpha x_{\alpha,s} \;\Rightarrow\; \hat{w}_{1,1} = -u''_\alpha x_\alpha \tag{2.47}$$

where the other candidate function, $\hat{w}_{2,1}$, would generate more phantom terms in the strain field/functional like the term γ_{22} for example, which is impossible. Alternatively, if one drops the terms with the axial derivatives (e.g., $\hat{w}_{2,1}$) one would arrive at the same candidate function in Eq. 2.47, which determined its solution and its order such as

$$\frac{\mathcal{O}(\hat{w}_1)}{a} = \epsilon \left(\frac{a}{\ell}\right)^{-1} \;\Rightarrow\; \mathcal{O}(\hat{w}_1) = \ell\epsilon \tag{2.48}$$

Another phantom term exists with respect to the second small parameter such as

$$\mathcal{O}\left(\gamma_{22}\right) \sim \mathcal{O}\left(\left(\frac{h}{a}\right)^{-1} h\rho_{22}\right) \tag{2.49}$$

All the terms pertaining to $\rho_{\alpha\beta}$ will not enter into the minimization process of the perturbation functions, since all the terms present in these strain measures have their counterparts multiplied by the inverse of the small parameter $\frac{h}{a}$ in the $\gamma_{\alpha\beta}$ strain measures. With the leading order terms of the perturbations having known order in γ_{11} and γ_{12}, the excessively large "phantom terms" in γ_{22} must vanish for the minimization of the functional so that

$$\hat{w}_{2,2} + \frac{\hat{w}_3}{R} = 0 \tag{2.50}$$

With the terms in γ_{22} annihilated, the only surviving terms with leading order are found in ρ_{22}, which are used to determine the order of these perturbations. As mentioned above, the order of these terms is not assumed but determined during the minimization procedure. This is equivalent to reckoning that the leading order terms in the energy functional involving the perturbations must be of the same order. The leading order terms remaining are linear cross terms between the perturbations and a known quantity and quadratic terms of the perturbations. An example of this statement would come from the first term in $h\rho_{22}$ and the third term of $2\gamma_{12}$ such as

$$\mathcal{O}\left[(h\hat{w}_{3,2})^2\right] = \mathcal{O}\left[(h\hat{w}_{3,2} \cdot r_n\theta')\right] \Rightarrow \frac{h^2\mathcal{O}^2(\hat{w}_3)}{a^4} = \frac{h\mathcal{O}(\hat{w}_3)\epsilon}{a^2} \Rightarrow \mathcal{O}(\hat{w}_3) = \frac{a^2}{h}\epsilon \tag{2.51}$$

where a similar order is found for the function $\hat{w}_2$.

This establishes the order of the terms in the strain field of Eq. 2.46 as given in the square brackets beneath the unknown terms. Since the goal is to establish a classical-like theory as in Eq. 2.17, all terms of order $\mathcal{O}(\epsilon)$ in the strain field must be accounted for and further examination of the displacement field is necessary. Therefore, the displacement field is perturbed again with $z_2 = \begin{bmatrix} w_1 & w_2 & w_3 \end{bmatrix}$ to yield

$$\begin{aligned} v_1 &= u_1 + \hat{w}_1 + w_1 \\ v_2 &= u_\alpha x_{\alpha,s} + \theta r_n + \hat{w}_2 + w_2 \\ v_3 &= u_2 x_{3,s} - u_3 x_{2,s} - \theta r_\tau + \hat{w}_3 + w_3 \end{aligned} \tag{2.52}$$

Again, the perturbed field is substituted in Eqs. 2.36 to yield

$$
\begin{aligned}
\gamma_{11} &= \underbrace{u_1'}_{\epsilon} - \underbrace{x_\alpha u_\alpha''}_{\epsilon} + \underbrace{w_{1,1}}_{?\equiv[\epsilon(\frac{a}{\ell})]} \\
2\gamma_{12} &= \underbrace{r_n\theta'}_{\epsilon} + \underbrace{\hat{w}_{2,1}}_{\epsilon(\frac{a}{\ell})(\frac{a}{h})} + \underbrace{w_{1,2}}_{?\equiv[\epsilon]} + \underbrace{w_{2,1}}_{?\equiv[\epsilon(\frac{a}{\ell})]} \\
\gamma_{22} &= \underbrace{w_{2,2}}_{?\equiv[\epsilon]} + \underbrace{\frac{w_3}{R}}_{?\equiv[\epsilon]} \\
h\rho_{11} &= h\left(\underbrace{x_{3,s}u_2''}_{\epsilon(\frac{h}{a})} - \underbrace{x_{2,s}u_3''}_{\epsilon(\frac{h}{a})} - \underbrace{r_\tau\theta''}_{\epsilon(\frac{h}{a})(\frac{a}{\ell})} + \underbrace{\hat{w}_{3,11}}_{\epsilon(\frac{a}{\ell})^2} + \underbrace{w_{3,11}}_{?\equiv[\epsilon(\frac{a}{\ell})^2(\frac{h}{a})]} \right) \\
h\rho_{12} &= h\left[\frac{1}{4R}\left(\underbrace{r_n\theta'}_{\epsilon(\frac{h}{a})} + \underbrace{w_{1,2}}_{?\equiv[\epsilon(\frac{h}{a})]} \right) - \underbrace{\theta'}_{\epsilon(\frac{h}{a})} + \underbrace{\hat{w}_{3,12}}_{\epsilon(\frac{a}{\ell})} + \underbrace{w_{3,12}}_{?\equiv[\epsilon(\frac{h}{a})(\frac{a}{\ell})]} - \frac{3}{4R}\left(\underbrace{\hat{w}_{2,1}}_{\epsilon(\frac{a}{\ell})} + \underbrace{w_{2,1}}_{?\equiv[\epsilon(\frac{h}{a})(\frac{a}{\ell})]} \right) \right] \\
h\rho_{22} &= h\left[\left(\underbrace{\hat{w}_{3,2}}_{\epsilon} + \underbrace{w_{3,2}}_{?\equiv[\epsilon(\frac{h}{a})]} \right) - \frac{1}{R}\left(\underbrace{\hat{w}_2}_{\epsilon} + \underbrace{w_2}_{?\equiv[\epsilon(\frac{h}{a})]} \right) \right]_{,2}
\end{aligned}
\tag{2.53}
$$

As before, the order of the perturbations is determined by reckoning that the leading order terms in the functional are of the same order, which implies

$$
\mathcal{O}(u_1' \cdot w_{i,2}) = \mathcal{O}(w_{i,2}^2) \;\Rightarrow\; \mathcal{O}(w_i) = a\epsilon \tag{2.54}
$$

This is the asymptotically-correct strain field of order $\mathcal{O}(\epsilon)$ arrived at in [92]. One can prove that further perturbation of the displacement field will not yield more significant terms for closed cross-sections as demonstrated in Appendix A and the displacement field is said to have converged. Keeping terms of order $\mathcal{O}(\epsilon)$ in the strain field and denoting the corresponding strains by an over-bar yields

$$
\begin{aligned}
\bar{\gamma}_{11} &= u_1' - x_\alpha u_\alpha'' \\
2\bar{\gamma}_{12} &= r_n \theta' + w_{1,2} \\
\bar{\gamma}_{22} &= w_{2,2} + \frac{w_3}{R} \\
h\bar{\rho}_{11} &= 0 \\
h\bar{\rho}_{12} &= 0 \\
h\bar{\rho}_{22} &= h[(\hat{w}_{3,2} - \frac{\hat{w}_2}{R})_{,2}]
\end{aligned}
\tag{2.55}
$$

where the existence of the unknowns in the components of the vector $\bar{\phi}$: $2\gamma_{12}$, γ_{22}, and $h\rho_{22}$ defined previously is noted.

For a single-cell closed cross-section, the warping field is four times redundant and any set of four independent constraints will render the solution unique. The four constraints are chosen so that the shell bending strain measure $\bar{\rho}_{22}$ and the three orthogonal cartesian displacements of the material points of the shell $\bar{u}_i$ are single valued functions. The constraints are given below along with their mathematical implications on the unknowns in $\bar{\phi}$

$$
\begin{aligned}
\oint h\rho_{22}\, \mathrm{d}s &= 0 \Rightarrow \oint \bar{\phi}_3\, \mathrm{d}s = 0 \\
\oint \bar{u}_{1,2}\, \mathrm{d}s &= 0 \Rightarrow \oint \bar{\phi}_1\, \mathrm{d}s - \oint r_n \theta'\, \mathrm{d}s = 0 \\
\oint \bar{u}_{2,2}\, \mathrm{d}s &= 0 \Rightarrow \oint x_2 \bar{\phi}_3\, \mathrm{d}s = 0 \\
\oint \bar{u}_{2,3}\, \mathrm{d}s &= 0 \Rightarrow \oint x_3 \bar{\phi}_3\, \mathrm{d}s = 0
\end{aligned}
\tag{2.56}
$$

where the mathematical implication of the constraints is further expounded in Appendix A.

The constraints are enforced upon the energy functional using four Lagrange multipliers where Eq. 2.34 in now rewritten as

$$2\mathcal{U}^{(\mathrm{m})} = \oint [\bar{\psi}^{\mathrm{T}} Q \bar{\psi} + 2\bar{\phi}^{\mathrm{T}} S \bar{\psi} + \bar{\phi}^{\mathrm{T}} P \bar{\phi} \tag{2.57}$$

$$+2\bar{\phi}^{\mathrm{T}} \hat{T} \bar{\lambda} + 2\bar{\epsilon}^{\mathrm{T}} E^{\mathrm{T}} \bar{\lambda} - 2\bar{\psi}^{\mathrm{T}} H - 2\bar{\phi}^{\mathrm{T}} G + \aleph(E_1)] \, \mathrm{d}s$$

where $\bar{\epsilon}$ is defined in Eq. 2.18 and the matrices E^{T}, $\hat{T}$, and $\bar{\lambda}$ are given by

$$E^{\mathrm{T}} = \begin{bmatrix} 0 & 0 & 0 & 0 \\ -r_{\mathrm{n}} & 0 & 0 & 0 \\ 0 & 0 & 0 & 0 \\ 0 & 0 & 0 & 0 \end{bmatrix} \quad \hat{T} = \begin{bmatrix} 1 & 0 & 0 & 0 \\ 0 & 0 & 0 & 0 \\ 0 & x_2 & x_3 & 1 \end{bmatrix} \quad \bar{\lambda} = \begin{bmatrix} \lambda_1 \\ \lambda_2 \\ \lambda_3 \\ \lambda_4 \end{bmatrix} \tag{2.58}$$

Minimizing the functional in Eq. 2.57 with respect to the unknown $\bar{\phi}$ yields

$$(2ST\bar{\epsilon} + 2P\bar{\phi} + 2\hat{T}\bar{\lambda} - 2G)\delta\bar{\phi} = 0 \tag{2.59}$$

where the following definition is adopted

$$\bar{\psi} = T\bar{\epsilon} \qquad T = \begin{bmatrix} 1 & 0 & x_3 & -x_2 \\ 0 & 0 & 0 & 0 \\ 0 & 0 & 0 & 0 \end{bmatrix} \tag{2.60}$$

Since $\delta\bar{\phi}$ is arbitrary, the solution for $\bar{\phi}$ is

$$\bar{\phi} = -cT\bar{\epsilon} - P^{-1}\hat{T}\bar{\lambda} + \Pi \tag{2.61}$$

where

$$c = P^{-1}S = \begin{bmatrix} c_1 \\ c_2 \\ c_3 \end{bmatrix} \qquad \Pi = P^{-1}G = \begin{bmatrix} \pi_1 \\ \pi_2 \\ \pi_3 \end{bmatrix} \tag{2.62}$$

To determine the Lagrange multipliers, the solution of $\bar{\phi}$ is substituted in the four constraints in Eq. 2.56 and solving for $\bar{\lambda}$ yields

$$\bar{\lambda} = F^{-1}J\bar{\epsilon} - F^{-1}K \tag{2.63}$$

where F and J are material and geometry matrices given in Appendix A, while K, which shows the explicit dependance of the Lagrange multipliers on the contribution of the AFCs/MFCs, is given by

$$K = \oint \tilde{K}\, \mathrm{d}s = \oint \begin{bmatrix} \pi_1 \\ \pi_3 \\ x_2\pi_3 \\ x_3\pi_3 \end{bmatrix} \mathrm{d}s \tag{2.64}$$

Designating $F^{-1}J = L$ and $F^{-1}K = \Sigma$, and substituting Eq. 2.63 into Eq. 2.61 yields

$$\bar{\phi} = Y(s)\bar{\epsilon} + \Omega(s) \tag{2.65}$$

where

$$Y(s) = -cT - P^{-1}\hat{T}L \qquad \Omega(s) = P^{-1}\hat{T}\Sigma + \Pi \tag{2.66}$$

The contribution of the AFCs/MFCs to the solution of the unknowns can be seen in the last term of Eq. 2.65. Substitution of Eq. 2.65 and Eq. 2.63 into Eq. 2.57 while noting that $ST = -PY(s) - \hat{T}L$ yields

$$2\mathcal{U}^{(\mathrm{m})} = 2\mathcal{U}^{\text{structural}} + 2\mathcal{U}^{(\mathrm{a})} + 2\mathcal{U}^{\text{quadratic E-field}} \tag{2.67}$$

where

$$\begin{aligned} 2\mathcal{U}^{\text{structural}} &= \oint [\bar{\epsilon}^T (T^{\mathrm{T}} Q T - Y^{\mathrm{T}} P Y + 2E^{\mathrm{T}} L)\bar{\epsilon}] \, \mathrm{d}s \\ 2\mathcal{U}^{(\mathrm{a})} &= -\oint [(\Omega^{\mathrm{T}} P Y) + (Y^{\mathrm{T}} \hat{T} \Sigma + Y^{\mathrm{T}} G + 2E^{\mathrm{T}} \Sigma + 2T^{\mathrm{T}} H)^{\mathrm{T}}]\bar{\epsilon} \, \mathrm{d}s \\ 2\mathcal{U}^{\text{quadratic E-field}} &= -\oint [\Omega^{\mathrm{T}} \hat{T} \Sigma + \Omega^{\mathrm{T}} G - \aleph(E_1)] \, \mathrm{d}s \end{aligned} \tag{2.68}$$

The first component of the energy per unit length in Eq. 2.67 yields the asymptotically-correct stiffness matrix obtained by Volovoi and Hodges [92]. The second component is the one yielding the actuation force and moments vector $\mathbb{F}^{(\mathrm{a})\mathrm{T}} = \begin{bmatrix} F_1^{(\mathrm{a})} & M_1^{(\mathrm{a})} & M_2^{(\mathrm{a})} & M_3^{(\mathrm{a})} \end{bmatrix}$ where

$$\mathbb{F}^{(\mathrm{a})} = \frac{\partial \mathcal{U}^{(\mathrm{a})}}{\partial \bar{\epsilon}} \tag{2.69}$$

The last component of the energy per unit length is a quadratic function of the prescribed actuation strains, and does not contribute to the actuation vector.

The linear two-dimensional cross-sectional theory can now be written as

$$\mathbb{F}^{(\mathrm{m})} = \bar{S}\bar{\epsilon} + \mathbb{F}^{(\mathrm{a})} \tag{2.70}$$

where $\bar{S}$ is the 4×4 stiffness matrix, and $\mathbb{F}^{(\mathrm{m})}$ is the mechanical force and moments vector.

The generalization to multi-cell is straightforward. As in [93], for n-celled closed cross-section one needs to impose $4n$ constraints, and consequently $4n$ Lagrange multipliers are to be solved for. Examples of two-cell and three-cell closed cross-section contours with the corresponding outward surface normals are shown in Fig. 2.12, where consistency in terms of the direction of the integration around the contour is to be noted.

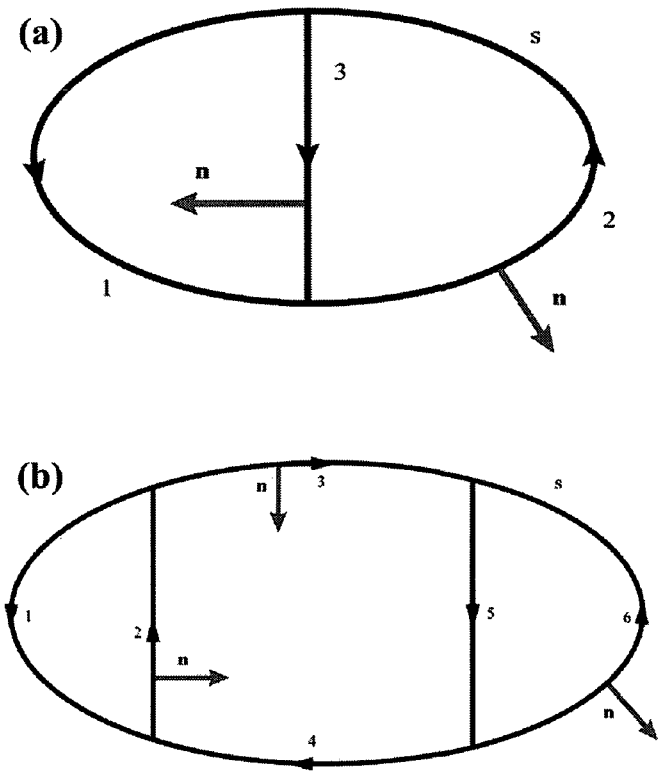

Figure 2.12: (a) Contour of two-cell closed cross-section with surface normals, (b) Contour of three-cell closed cross-section with surface normals

The outward surface normal at any point on the contour is defined as such

$$\vec{n} \times \vec{ds} = \vec{dx_1} \tag{2.71}$$

For the two-cell case, the first cell is made of path 1 and path 2, while the second cell is made of path 2 and path 3. The mechanical strain energy per unit length is written as

$$2\mathcal{U}^{(\mathrm{m})} = \oint_{1+2+3} [\bar{\psi}^{\mathrm{T}} Q \bar{\psi} + 2\bar{\phi}^{\mathrm{T}} S \bar{\psi} + \bar{\phi}^{\mathrm{T}} P \bar{\phi}] \, \mathrm{d}s \tag{2.72}$$

$$+ \oint_{1+2} [2\lambda_1(\bar{\phi}_1 - \theta' r_{\mathrm{n}}) + 2\bar{\phi}_3(\lambda_2 x_2 + \lambda_3 x_3 + \lambda_4)] \, \mathrm{d}s$$

$$+ \oint_{2+3} [2\lambda_5(\bar{\phi}_1 - \theta' r_{\mathrm{n}}) + 2\bar{\phi}_3(\lambda_6 x_2 + \lambda_7 x_3 + \lambda_8)] \, \mathrm{d}s$$

$$+ \oint_{1+2+3} [-2\bar{\psi}^{\mathrm{T}} H - 2\bar{\phi}^{\mathrm{T}} G + \aleph(E_1)] \, \mathrm{d}s$$

The solution for the unknowns has the same form as Eq. 2.61 but with $\hat{T}$ and $\bar{\lambda}$ now having different forms along the closed contour,

For path 1

$$\bar{\lambda}^{\mathrm{T}} = \begin{bmatrix} \lambda_1 & \lambda_2 & \lambda_3 & \lambda_4 \end{bmatrix} \qquad \hat{T} = \begin{bmatrix} 1 & 0 & 0 & 0 \\ 0 & 0 & 0 & 0 \\ 0 & x_2 & x_3 & 1 \end{bmatrix} \tag{2.73}$$

$$E^{\mathrm{T}} = \begin{bmatrix} 0 & 0 & 0 & 0 \\ -r_{\mathrm{n}} & 0 & 0 & 0 \\ 0 & 0 & 0 & 0 \\ 0 & 0 & 0 & 0 \end{bmatrix}$$

For path 2

$$\bar{\lambda}^{\mathrm{T}} = \begin{bmatrix} \lambda_1 & \lambda_2 & \lambda_3 & \lambda_4 & \lambda_5 & \lambda_6 & \lambda_7 & \lambda_8 \end{bmatrix} \tag{2.74}$$

$$\hat{T} = \begin{bmatrix} 1 & 0 & 0 & 0 & 1 & 0 & 0 & 0 \\ 0 & 0 & 0 & 0 & 0 & 0 & 0 & 0 \\ 0 & x_2 & x_3 & 1 & 0 & x_2 & x_3 & 1 \end{bmatrix}$$

$$E^{\mathrm{T}} = \begin{bmatrix} 0 & 0 & 0 & 0 & 0 & 0 & 0 & 0 \\ -r_{\mathrm{n}} & 0 & 0 & 0 & -r_{\mathrm{n}} & 0 & 0 & 0 \\ 0 & 0 & 0 & 0 & 0 & 0 & 0 & 0 \\ 0 & 0 & 0 & 0 & 0 & 0 & 0 & 0 \end{bmatrix}$$

For path 3

$$\bar{\lambda}^{\mathrm{T}} = \begin{bmatrix} \lambda_5 & \lambda_6 & \lambda_7 & \lambda_8 \end{bmatrix} \qquad \hat{T} = \begin{bmatrix} 1 & 0 & 0 & 0 \\ 0 & 0 & 0 & 0 \\ 0 & x_2 & x_3 & 1 \end{bmatrix} \tag{2.75}$$

$$E^{\mathrm{T}} = \begin{bmatrix} 0 & 0 & 0 & 0 \\ -r_{\mathrm{n}} & 0 & 0 & 0 \\ 0 & 0 & 0 & 0 \\ 0 & 0 & 0 & 0 \end{bmatrix}$$

Since path 2 is shared by both cells, it is expected that all eight Lagrange multipliers are to be included when considering this path as can be seen in Eq. 2.74. From the constraints, the solution for the Lagrange multipliers can be obtained as in Eq. 2.63 with F and J having a form given in Appendix A that is different from, yet related to, the case of a single cell, while K has the form

$$K^{\text{two-cells}} = \begin{bmatrix} \oint_{1+2} \tilde{K}\, \mathrm{d}s \\ \oint_{2+3} \tilde{K}\, \mathrm{d}s \end{bmatrix} \tag{2.76}$$

The actuation vector can now be obtained as in Eq. 2.68 and Eq. 2.69 with Y,E,L,$\hat{T}$, and Ω having different forms around the contour as reasoned previously.

A similar approach applies to three-cell cross-sections shown in Fig. 2.12(b), where twelve Lagrange multipliers are needed in this case. The K matrix in this case is given by

$$K^{\text{three-cells}} = \begin{bmatrix} \oint_{1+2} \tilde{K}\, ds \\ \oint_{2+3+4+5} \tilde{K}\, ds \\ \oint_{5+6} \tilde{K}\, ds \end{bmatrix} \tag{2.77}$$

Generalization to an n-cells active cross-section can be extrapolated from [93] and the development presented herein. The presented formulation has the final form of the cross-sectional theory of Eq. 2.17 sought from the outset. Considering Eq. 2.16, the energy functional has essentially been asymptotically expanded into the form

$$\mathcal{F}(\Gamma, \varsigma_1, \varsigma_2) = \underline{\mathcal{O}(\epsilon^2, \varsigma_1^0, \varsigma_2^0)} + \mathcal{O}(\epsilon^2, \varsigma_1^1, \varsigma_2^0) + \mathcal{O}(\epsilon^2, \varsigma_1^0, \varsigma_2^1) + \ldots \tag{2.78}$$

where the underlined term was of interest in the development.

This development of the asymptotically-correct actuation vector is summarized in Reference [95].

Open Cross-Section Active Beams

The development presented above is sufficient to analyze rotor blades since they are classified as closed cross-section beams. However, the development is rigorous and general enough to render it worth investigating active open cross-sections as well given that they receive less attention in the engineering literature compared to their closed counterparts. Moreover, there is the recent interest from the community to use active open cross-sections in morphing structures [96].

The order of the 1-D torsional strain is the differentiating aspect from the outset of

the development where

$$h\theta' \sim \mathcal{O}(\epsilon) \tag{2.79}$$

To avoid repetition, the pivotal changes in the construction of the asymptotically-correct displacement field are highlighted. The "zeroth step", or the rigid body building block of the displacement field is essentially the same. However, the term $r_n\theta'$ in γ_{12} of Eq. 2.46 will have a different order that is

$$2\gamma_{12} = \underbrace{x_{2,s}u_2'}_{\epsilon\left(\frac{a}{\ell}\right)^{-1}} + \underbrace{x_{3,s}u_3'}_{\epsilon\left(\frac{a}{\ell}\right)^{-1}} + \underbrace{r_n\theta'}_{\epsilon\left(\frac{a}{h}\right)} + \underbrace{\hat{w}_{1,2}}_{?\equiv\left[\epsilon\left(\frac{a}{\ell}\right)^{-1}\right]} + \underbrace{\hat{w}_{2,1}}_{?\equiv\left[\epsilon\left(\frac{a}{\ell}\right)\left(\frac{a}{h}\right)\right]} \tag{2.80}$$

where the term is now obviously a phantom one and must be annihilated by the candidate perturbation function as in Eq. 2.47 so that

$$\hat{w}_{1,2} = -u_\alpha' x_{\alpha,s} - r_n\theta' \;\Rightarrow\; \hat{w}_{1,1} = -u_\alpha'' x_\alpha - \eta\theta'' \tag{2.81}$$

where η is known as the sectorial coordinate in thin-wall bars engineering literature [97] and is given by

$$\eta = \int_{s_0}^{s} r_n \, \mathrm{d}s \tag{2.82}$$

with s_0 being the origin of the contour.

The strain field in Eq. 2.53 will now become, for open cross-sections,

$$
\begin{aligned}
\gamma_{11} &= \underbrace{u_1'}_{\epsilon} - \underbrace{x_\alpha u_\alpha''}_{\epsilon} - \underbrace{\eta\theta''}_{\epsilon\left(\frac{a}{\ell}\right)\left(\frac{a}{h}\right)} + \underbrace{w_{1,1}}_{\epsilon\left(\frac{a}{\ell}\right)} \\
2\gamma_{12} &= \underbrace{r_n\theta'}_{\epsilon} + \underbrace{\hat{w}_{2,1}}_{\epsilon\left(\frac{a}{\ell}\right)\left(\frac{a}{h}\right)} + \underbrace{w_{1,2}}_{\epsilon} + \underbrace{w_{2,1}}_{\epsilon\left(\frac{a}{\ell}\right)} \\
\gamma_{22} &= \underbrace{w_{2,2}}_{\epsilon} + \underbrace{\frac{w_3}{R}}_{\epsilon} \\
h\rho_{11} &= h\left(\underbrace{x_{3,s}u_2''}_{\epsilon\left(\frac{h}{a}\right)} - \underbrace{x_{2,s}u_3''}_{\epsilon\left(\frac{h}{a}\right)} - \underbrace{r_\tau\theta''}_{\epsilon\left(\frac{a}{\ell}\right)} + \underbrace{\hat{w}_{3,11}}_{\epsilon\left(\frac{a}{\ell}\right)^2} + \underbrace{w_{3,11}}_{\epsilon\left(\frac{a}{\ell}\right)^2\left(\frac{h}{a}\right)}\right) \\
h\rho_{12} &= h\left[\underbrace{\frac{w_{1,2}}{4R}}_{\epsilon\left(\frac{h}{a}\right)} - \underbrace{\theta'}_{\epsilon} + \underbrace{\hat{w}_{3,12}}_{\epsilon\left(\frac{a}{\ell}\right)} + \underbrace{w_{3,12}}_{\epsilon\left(\frac{h}{a}\right)\left(\frac{a}{\ell}\right)} - \frac{3}{4R}\left(\underbrace{\hat{w}_{2,1}}_{\epsilon\left(\frac{a}{\ell}\right)} + \underbrace{w_{2,1}}_{\epsilon\left(\frac{h}{a}\right)\left(\frac{a}{\ell}\right)}\right)\right] \\
h\rho_{22} &= h\left[\left(\underbrace{\hat{w}_{3,2}}_{\epsilon} + \underbrace{w_{3,2}}_{\epsilon\left(\frac{h}{a}\right)}\right) - \frac{1}{R}\left(\underbrace{\hat{w}_2}_{\epsilon} + \underbrace{w_2}_{\epsilon\left(\frac{h}{a}\right)}\right)\right]_{,2}
\end{aligned}
\tag{2.83}
$$

The term that is of order $\epsilon\left(\frac{a}{\ell}\right)\left(\frac{a}{h}\right)$ in γ_{11} can obviously be quite large, a situation that did not exist for closed cross-sections. This term is responsible for the Vlasov correction [98] for open cross-sections. If, following the second perturbation, the open cross-section displacement field is subjected to a further and third perturbation $z_3 = \begin{bmatrix} \tilde{w}_1 & \tilde{w}_2 & \tilde{w}_3 \end{bmatrix}$, one gets

$$
\begin{aligned}
v_1 &= u_1 + \hat{w}_1 + w_1 + \tilde{w}_1 \\
v_2 &= u_\alpha x_{\alpha,s} + \theta r_n + \hat{w}_2 + w_2 + \tilde{w}_2 \\
v_3 &= u_2 x_{3,s} - u_3 x_{2,s} - \theta r_\tau + \hat{w}_3 + w_3 + \tilde{w}_3
\end{aligned}
\tag{2.84}
$$

Then, the strain field becomes

$$
\begin{aligned}
\gamma_{11} &= \underbrace{u_1'}_{\epsilon} - \underbrace{x_\alpha u_\alpha''}_{\epsilon} - \underbrace{\eta\theta''}_{\epsilon\left(\frac{a}{\ell}\right)\left(\frac{a}{h}\right)} + \underbrace{w_{1,1}}_{\epsilon\left(\frac{a}{\ell}\right)} + \underbrace{\tilde{w}_{1,1}}_{?\equiv\left[\epsilon\left(\frac{a}{\ell}\right)^2\left(\frac{a}{h}\right)\right]} \\
2\gamma_{12} &= \underbrace{r_n\theta'}_{\epsilon} + \underbrace{\hat{w}_{2,1}}_{\epsilon\left(\frac{a}{\ell}\right)\left(\frac{a}{h}\right)} + \underbrace{w_{1,2}}_{\epsilon} + \underbrace{w_{2,1}}_{\epsilon\left(\frac{a}{\ell}\right)} + \underbrace{\tilde{w}_{1,2}}_{?\equiv\left[\epsilon\left(\frac{a}{\ell}\right)\left(\frac{a}{h}\right)\right]} + \underbrace{\tilde{w}_{2,1}}_{?\equiv\left[\epsilon\left(\frac{a}{\ell}\right)^2\left(\frac{a}{h}\right)\right]} \\
\gamma_{22} &= \underbrace{w_{2,2}}_{\epsilon} + \underbrace{\frac{w_3}{R}}_{\epsilon} + \underbrace{\tilde{w}_{2,2}}_{?\equiv\left[\epsilon\left(\frac{a}{\ell}\right)\left(\frac{a}{h}\right)\right]} + \underbrace{\frac{\tilde{w}_3}{R}}_{?\equiv\left[\epsilon\left(\frac{a}{\ell}\right)\left(\frac{a}{h}\right)\right]} \\
h\rho_{11} &= h\left(\underbrace{x_{3,s}u_2''}_{\epsilon\left(\frac{h}{a}\right)} - \underbrace{x_{2,s}u_3''}_{\epsilon\left(\frac{h}{a}\right)} - \underbrace{r_\tau\theta''}_{\epsilon\left(\frac{a}{\ell}\right)} + \underbrace{\hat{w}_{3,11}}_{\epsilon\left(\frac{a}{\ell}\right)^2} + \underbrace{w_{3,11}}_{\epsilon\left(\frac{a}{\ell}\right)^2\left(\frac{h}{a}\right)} + \underbrace{\tilde{w}_{3,11}}_{?\equiv\left[\epsilon\left(\frac{a}{\ell}\right)^3\right]}\right) \\
h\rho_{12} &= h\left[\underbrace{\frac{w_{1,2}}{4R}}_{\epsilon\left(\frac{h}{a}\right)} - \underbrace{\theta'}_{\epsilon} + \underbrace{\hat{w}_{3,12}}_{\epsilon\left(\frac{a}{\ell}\right)} + \underbrace{w_{3,12}}_{\epsilon\left(\frac{h}{a}\right)\left(\frac{a}{\ell}\right)} - \frac{3}{4R}\left(\underbrace{\hat{w}_{2,1}}_{\epsilon\left(\frac{a}{\ell}\right)} + \underbrace{w_{2,1}}_{\epsilon\left(\frac{h}{a}\right)\left(\frac{a}{\ell}\right)}\right)\right] + \\
&\quad h\left[\underbrace{\tilde{w}_{3,12}}_{?\equiv\left[\epsilon\left(\frac{a}{\ell}\right)^2\right]} - \frac{1}{4R}\left(\underbrace{\tilde{w}_{1,2}}_{?\equiv\left[\epsilon\left(\frac{a}{\ell}\right)\right]} - 3\ \underbrace{\tilde{w}_{2,1}}_{?\equiv\left[\epsilon\left(\frac{a}{\ell}\right)^2\right]}\right)\right] \\
h\rho_{22} &= h\left[\left(\underbrace{\hat{w}_{3,2}}_{\epsilon} + \underbrace{w_{3,2}}_{\epsilon\left(\frac{h}{a}\right)} + \underbrace{\tilde{w}_{3,2}}_{?\equiv\left[\epsilon\left(\frac{a}{\ell}\right)\right]}\right) - \frac{1}{R}\left(\underbrace{\hat{w}_2}_{\epsilon} + \underbrace{w_2}_{\epsilon\left(\frac{h}{a}\right)} + \underbrace{\tilde{w}_2}_{?\equiv\left[\epsilon\left(\frac{a}{\ell}\right)\right]}\right)\right]_{,2}
\end{aligned}
\tag{2.85}
$$

where the order of the third set of perturbations is determined by the phantom term in γ_{12}, $\hat{w}_{2,1}$, and the excitation term $\eta\theta''$ coming from γ_{11} so that

$$
\mathcal{O}(\tilde{w}_i) = \frac{a^3}{\ell h}\epsilon \tag{2.86}
$$

Open cross-sections are not subject to any constraints as are closed cross-sections,

which eliminates the need for computing the Lagrange multipliers. To construct a linear cross-sectional theory of the form of Eq. 2.17, terms of order $\mathcal{O}(\epsilon)$ are kept in Eq. 2.83. As the result,

$$2\mathcal{U}^{(\mathrm{m})} = \int_{\Sigma s} \left[\bar{\epsilon}^{\mathrm{T}} T^{\mathrm{T}} Q T \bar{\epsilon} + 2\bar{\phi}^{\mathrm{T}} S T \bar{\epsilon} + \bar{\phi}^{\mathrm{T}} P \bar{\phi} - 2\bar{\epsilon}^{\mathrm{T}} T^{\mathrm{T}} H - 2\bar{\phi}^{\mathrm{T}} G + \aleph(E_1)\right] \, \mathrm{d}s \tag{2.87}$$

where the integral is to be carried out along all the branches of the cross-section, and Eq. 2.60 has been utilized with the following definition of the matrix T

$$T_{\text{open-section}} = \begin{bmatrix} 1 & 0 & x_3 & -x_2 \\ 0 & 0 & 0 & 0 \\ 0 & -h & 0 & 0 \end{bmatrix} \tag{2.88}$$

$$T_{\text{strip}} = \begin{bmatrix} 1 & 0 & 0 & -x_2 \\ 0 & 0 & -h & 0 \\ 0 & -h & 0 & 0 \end{bmatrix} \tag{2.89}$$

The difference between the T matrix for open cross-sections and strips in Eq. 2.88 originates from the constant that multiplies the bending curvature about the x_2 axis to define the order of the strain, where for a strip $-hu_3'' \sim \mathcal{O}(\epsilon)$ while for open cross-sections $-au_3'' \sim \mathcal{O}(\epsilon)$. Minimizing the functional in Eq. 2.87 with respect to the unknown, $\bar{\phi}$, yields the solution

$$\bar{\phi} = -P^{-1} S T \bar{\epsilon} + P^{-1} G \tag{2.90}$$

Substitution of Eq. 2.90 into Eq. 2.87 yields an expression for the strain energy per unit length that is similar to Eq. 2.67 except for the mathematical form of its components,

that is

$$\begin{aligned} 2\mathcal{U}^{\text{structural}}_{\text{open-section}} &= \int_{\Sigma s} \left[\bar{\epsilon}^{\mathrm{T}} T^{\mathrm{T}} \left(Q - S^{\mathrm{T}} P^{-1} S\right) T\bar{\epsilon}\right] \, \mathrm{d}s \\ 2\mathcal{U}^{(\mathrm{a})}_{\text{open-section}} &= \int_{\Sigma s} \left[-2\left(G^{\mathrm{T}} P^{-1} S T\bar{\epsilon}\right)^{\mathrm{T}} + 2\left(H^{\mathrm{T}} T\bar{\epsilon}\right)^{\mathrm{T}}\right] \, \mathrm{d}s \end{aligned} \tag{2.91}$$

where the quadratic E-field component is not given in Eq. 2.91 for brevity.

The first component of Eq. 2.91 yields the 4×4 cross-sectional stiffness matrix and the second component yields the asymptotically-correct actuation vector as in Eq. 2.69. To examine the effect of the Vlasov correction on the actuation problem, terms of order $\mathcal{O}(\epsilon\left(\frac{a}{\ell}\right)\left(\frac{a}{h}\right))$ in Eq. 2.85 are isolated and retained where as before the strain components containing the known quantities are grouped as

$$\tilde{\psi}^{\mathrm{T}} = \begin{bmatrix} \tilde{\gamma}_{11} & h\tilde{\rho}_{11} & h\tilde{\rho}_{12} \end{bmatrix}^{\mathrm{T}} = \begin{bmatrix} -\eta\theta'' & 0 & 0 \end{bmatrix}^{\mathrm{T}} = \left(\tilde{T}\bar{\epsilon}'\right)^{\mathrm{T}} \tag{2.92}$$

where the matrix $\tilde{T}$ is defined as

$$\tilde{T} = \begin{bmatrix} 0 & -\eta & 0 & 0 \\ 0 & 0 & 0 & 0 \\ 0 & 0 & 0 & 0 \end{bmatrix} \tag{2.93}$$

Equation. 2.87 is now rewritten in a refined form such that

$$2\mathcal{U}^{(\mathrm{m})}_{\mathrm{refined}} = \underbrace{2\mathcal{U}^{(\mathrm{m})}}_{\mathcal{O}(\epsilon^2)} + \int_{\Sigma s} \left[\underbrace{\bar{\epsilon}^{\mathrm{T}} T^{\mathrm{T}} Q \tilde{\psi} + \tilde{\psi}^{\mathrm{T}} Q T \bar{\epsilon}}_{\mathcal{O}\left(\epsilon^2 \left(\frac{a}{\ell}\right)\left(\frac{a}{h}\right)\right)} + \underbrace{\tilde{\psi}^{\mathrm{T}} Q \tilde{\psi} + 2\tilde{\phi}^{\mathrm{T}} S \tilde{\psi}}_{\mathcal{O}\left(\epsilon^2 \left(\frac{a}{\ell}\right)^2 \left(\frac{a}{h}\right)^2\right)} \right] \mathrm{d}s + \int_{\Sigma s} \left[\underbrace{\tilde{\phi}^{\mathrm{T}} P \tilde{\phi}}_{\mathcal{O}\left(\epsilon^2 \left(\frac{a}{\ell}\right)^2 \left(\frac{a}{h}\right)^2\right)} - \underbrace{2\tilde{\psi}^{\mathrm{T}} H - 2\tilde{\phi} G}_{\mathcal{O}\left(\epsilon^2 \left(\frac{a}{\ell}\right)^2 \left(\frac{a}{h}\right)^2\right) / \mathcal{O}\left(\epsilon^2 \left(\frac{a}{\ell}\right)\left(\frac{a}{h}\right)\right)} \right] \mathrm{d}s \tag{2.94}$$

where any cross terms between terms of order $\mathcal{O}(\epsilon)$ corresponding to $\bar{\phi}$ and terms of order $\mathcal{O}(\epsilon)\left(\frac{a}{\ell}\right)^2\left(\frac{a}{h}\right)^2$ are non-existent due to the Euler-Lagrange equations for $\bar{\phi}$, which uniquely determined their solution in the previous minimization step.

Minimizing Eq. 2.94 with respect to the unknown $\tilde{\phi}$ will yield a solution similar to Eq. 2.90 except for

$$\tilde{\phi} = -P^{-1} S \tilde{T} \bar{\epsilon}' + P^{-1} G \tag{2.95}$$

Substituting Eq. 2.95 into Eq. 2.94 will yield the Vlasov stiffness constant of the section and the coupling terms with the classical strain measures, and the Vlasov active bi-moment such that

$$\begin{aligned}
\tilde{S}_{\mathrm{Vlasov}} &= \frac{1}{2}\frac{\partial}{\partial \theta''} \int_{\Sigma s} \left[\left(\tilde{\psi}\right)^{\mathrm{T}} Q \tilde{\psi} + 2\left(P^{-1} S \tilde{\psi}\right)^{\mathrm{T}} S \tilde{\psi} + \left(P^{-1} S \tilde{\psi}\right)^{\mathrm{T}} P \left(P^{-1} S \tilde{\psi}\right) \right] \\
\tilde{S}_{\mathrm{Vlasov/Classical}} &= \frac{\partial}{\partial \bar{\epsilon}} \frac{\partial}{\partial \theta''} \int_{\Sigma s} \left[\tilde{\psi}^{\mathrm{T}} Q T \bar{\epsilon} \right] \mathrm{d}s \\
\mathbb{M}^{(\mathrm{a})}_{\omega} &= \frac{\partial}{\partial \theta''} \int_{\Sigma s} \left[\left(-\tilde{\psi}^{\mathrm{T}} H\right) + \left(G^{\mathrm{T}} P^{-1} S \tilde{\psi}\right)^{\mathrm{T}} \right] \mathrm{d}s
\end{aligned} \tag{2.96}$$

The development presented herein for active open cross-sections is summarized in the publication [99], where the nonlinear 1-D deflections due to the integral actuation of exam-

ple active beams have been calculated and compared to 3-D finite element results obtained using ANSYS Multiphysics^{TM}. As in the case of closed cross-sections, the energy functional for open sections has been asymptotically expanded into a similar form but with an additional term corresponding to the Vlasov correction such that

$$\mathcal{F}(\Gamma, \varsigma_1, \varsigma_2) = \underline{\mathcal{O}(\epsilon^2, \varsigma_1^0, \varsigma_2^0)} + \underline{\mathcal{O}(\epsilon^2, \varsigma_1^1, \varsigma_2^{-1})} + \mathcal{O}(\epsilon^2, \varsigma_1^1, \varsigma_2^0) + \mathcal{O}(\epsilon^2, \varsigma_1^0, \varsigma_2^1) + \dots \quad (2.97)$$

The theory is essentially of the refined form given in Eq. 2.22, where the constructed stiffness matrix is 5×5 and the actuation vector is 5×1. With this formulation, the development of an asymptotically-correct theory to obtain the active stress resultants at the reference line of an active thin-wall anisotropic slender beam with no initial twist or curvature is complete.

Numerical Examples and Comparison with Other Theories

Several examples are selected to verify the theory and its implementation against the 2-D finite element software UM/VABS and VABS with more emphasis on the former.

The implementation is first verified against VABS, where as mentioned earlier, at this stage it can only analyze passive cases. The passive three-cell example in Fig. 2.13 is analyzed using the present development, and the resulting sectional stiffness constants are compared to those predicted by VABS in Table. 2.1. The differences, although small, are attributed to the thin-wall assumption in the present development.

Next, consider the active single-cell box beam shown in Fig. 2.14 (a), where the elastic and the electromechanical properties of the composite material AS4/3506-1 and the generic AFCs used to construct the active box beam examples are given in Table. 2.2. Three verification examples that are labeled BB1, BB2t, and the BB2st, which are courtesy of

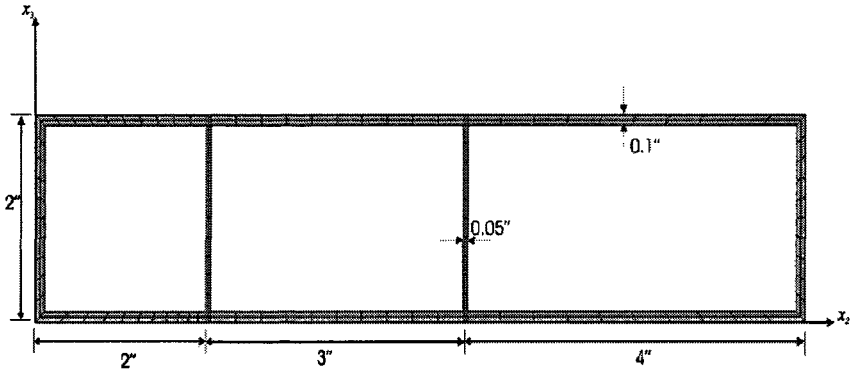

Figure 2.13: Three-cell isotropic box beam [Courtesy of VABS documentation].

Table 2.1: The elements of the stiffness matrix obtained using the thin-wall anisotropic beam theory and VABS for Fig. 2.13.

Stiffness Element	Present	VABS [87]	Difference
S_{11}[lb]	0.0611×10^{13}	0.0608×10^{13}	0.49%
S_{12}[lb · in]	0	0	Exact
S_{13}[lb · in]	0.0611×10^{13}	0.0608×10^{13}	0.49%
S_{14}[lb · in]	-0.2699×10^{13}	-0.2692×10^{13}	0.26%
S_{22}[lb · in^2]	0.0515×10^{13}	0.0540×10^{13}	4.63%
S_{23}[lb · in^2]	0	0	Exact
S_{24}[lb · in^2]	0	0	Exact
S_{33}[lb · in^2]	0.1073×10^{13}	0.1069×10^{13}	0.37%
S_{34}[lb · in^2]	-0.2699×10^{13}	-0.2692×10^{13}	0.26%
S_{44}[lb · in^2]	1.7091×10^{13}	1.7072×10^{13}	0.11%

the Active Aeroelasticity and Structures Research Laboratory (A^{2}SRL) at the University of Michigan. The length of the side is 0.25 [m] for each case, and the laminate designs are given in Table. 2.3, where (**AS**) indicates the **AS4/3506-1** material and (**AF**) indicates the AFCs. The DC actuation voltages of the active plies are given in Table. 2.4.

The electric field is calculated from the electric potential, which in the simple planar case of interdigitated electrodes reduces to

$$E_1 \approx \frac{V}{d} \quad [\text{V/m}] \tag{2.98}$$

where d is the electrode separation distance, which is assumed to be uniform along the

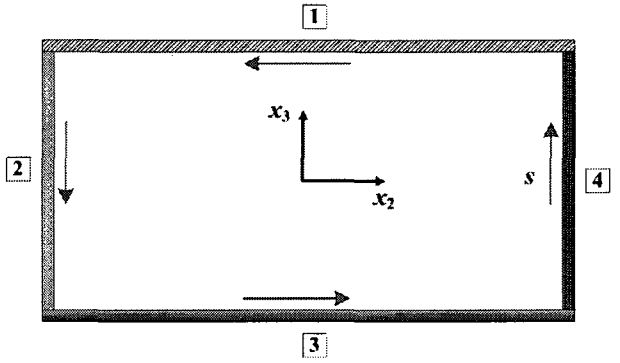

Figure 2.14: Active anisotropic single-cell box beam.

Table 2.2: Elastic parameters of the plies used in the active box beam examples.

	AS4/3506-1	**AFCs**
E_{11}[GPa]	142.000	42.200
E_{22}[GPa]	9.800	17.500
G_{12}[GPa]	6.000	5.500
G_{23}[GPa]	4.800	4.400
ν_{12}	0.300	0.354
ν_{23}	0.420	0.420
ply thickness (t_p)[mm]	0.127	0.127
d_{111}[pm/V]	∅	381.000
d_{122}[pm/V]	∅	-160.000
d_{112}[pm/V]	∅	0
$t_{electrodes}$(mm)	∅	1.143

Table 2.3: Laminate design of the active box beam cases.

	BB1	**BB2t**	**BB2st**
Wall 1	[0°**AS**/±45°**AF**/0°**AS**]	[(45°**AS**)$_2$/(−45°**AS**)$_2$]	[(45°**AS**)$_2$/(−45°**AS**)$_2$]
Wall 3	[0°**AS**/±45°**AF**/0°**AS**]	[(45°**AS**)$_2$/(−45°**AS**)$_2$]	[(45°**AS**)$_2$/(−45°**AS**)$_2$]
Wall 4	[(0°**AS**)$_4$]	[(−45°**AS**/∓45°**AF**/45°**AS**]	[(45°**AS**/±45°**AF**/−45°**AS**]
Wall 2	[(0°**AS**)$_4$]	[(45°**AS**/±45°**AF**/−45°**AS**]	[(45°**AS**/±45°**AF**/−45°**AS**]

AFCs/MFCs packs.

Tables 2.5, 2.6, and 2.7 present a comparison between the predictions of the current theory and those of the UM/VABS. Additionally, Tables 2.6 and 2.7 present the active twist moment as predicted by the asymptotic theory in [78], which neglects the shell bending strain measures. It must be noted that for the case of BB2t and BB2st, the results as

Table 2.4: Actuation DC voltage of active plies.

	BB1	BB2t	BB2st
Wall 1[V]	[ø/-1200/2800/ø]	[ø/ø/ø/ø]	[ø/ø/ø/ø]
Wall 3[V]	[ø/-1200/2800/ø]	[ø/ø/ø/ø]	[ø/ø/ø/ø]
Wall 4[V]	[ø/ø/ø/ø]	[ø/2000/-2000/ø]	[ø/-2000/2000/ø]
Wall 2[V]	[ø/ø/ø/ø]	[ø/-2000/2000/ø]	[ø/-2000/2000/ø]

presented in [100] are the 6×6 Timoshenko-like stiffness matrix and the 6×1 actuating vector. As outlined in [101], a reduction to the 4×4 stiffness matrix was performed for comparison purposes through minimization of the strain energy with respect to the one-dimensional shear strains. The actuation vector was also reduced as was done in [80].

Table 2.5: The nonzero classical stiffness constants and actuation vector elements for the BB1 case.

	Present	UM/VABS	%Difference
S_{11}[N]	5.518×10^6	5.518×10^6	Exact
S_{22}[N·m^2]	5.408×10^1	5.466×10^1	1.061
S_{33}[N·m^2]	4.742×10^2	4.745×10^2	0.063
S_{44}[N·m^2]	6.291×10^2	6.294×10^2	0.048
$F_1^{(a)}$[N]	35.039	35.420	1.067
$M_1^{(a)}$[N·m]	1.684	1.689	0.296

Table 2.6: The nonzero classical stiffness constants and actuation vector elements for the BB2t case.

	Ref [78]	Present	UM/VABS	%Difference
S_{11}[N]	-	9.973×10^5	9.950×10^5	0.231
S_{22}[N·m^2]	-	1.634×10^2	1.634×10^2	Exact
S_{33}[N·m^2]	-	1.017×10^2	1.013×10^2	0.395
S_{44}[N·m^2]	-	9.769×10^1	1.000×10^2	2.32
$M_1^{(a)}$[N·m]	1.834	2.203	2.323	5.16

For the active open cross-section case there are far less examples available in the literature for validation purposes. Therefore, the following examples were generated: passive isotropic C-channel [102] to verify the implementation, which is analyzed using VABS and

Table 2.7: The nonzero classical stiffness constants and actuation vector elements for the BB2st case.

	Ref [78]	**Present**	**UM/VABS**	**%Difference**
S_{11}[N]	-	9.973×10^5	9.971×10^5	0.020
S_{22}[N·m^2]	-	2.182×10^2	2.167×10^2	0.692
S_{33}[N·m^2]	-	1.017×10^2	1.017×10^2	Exact
S_{44}[N·m^2]	-	9.769×10^1	1.000×10^2	2.31
$M_1^{(a)}$[N·m]	1.834	2.709	2.693	0.594

UM/VABS; two active anisotropic I-beams; and an active anisotropic C-channel. The respective cross-sectional geometries are depicted in Fig. 2.15

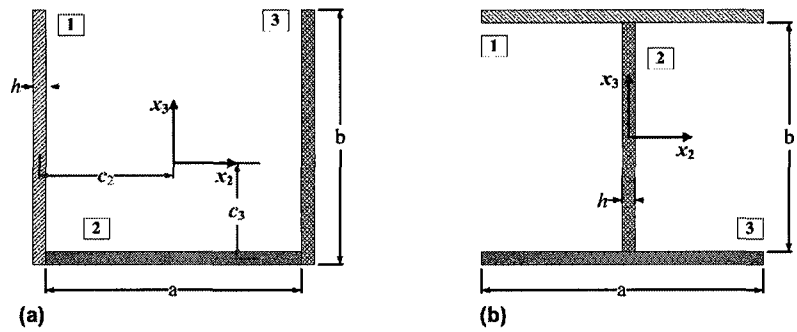

Figure 2.15: Example of open cross-section beams (a) C-channel, (b) I-beam.

The first case analyzed is the isotropic C-channel with the material and the geometric properties given in Table. 2.8

Table 2.8: Material and geometric properties of the passive C-channel.

$E_{11} = E_{22}$	2.6×10^9 [psi]
$G_{12} = G_{23}$	1.0×10^9 [psi]
$\nu_{12} = \nu_{23}$	0.3
a = 18 [in]	b = 20 [in]
h = 2 [in]	c_3 = 6.207 [in]

The significant elements of the 5×5 cross-sectional stiffness matrix are shown in Table 2.9, while the percentage differences are shown in Table 2.10

The second and the third examples are made of the same material as in Table 2.2, where the geometry of the sections is given in Table 2.11

Table 2.9: The elements of the stiffness matrix for the isotropic C-channel.

Stiffness Element	Present	VABS [87]	UM/VABS
S_{11}[lb]	3.016×10^{11}	3.120×10^{11}	3.016×10^{11}
S_{22}[lb · in^2]	1.547×10^{11}	1.591×10^{11}	1.568×10^{11}
S_{33}[lb · in^2]	1.216×10^{13}	1.397×10^{13}	1.220×10^{13}
S_{44}[lb · in^2]	2.769×10^{13}	2.444×10^{13}	2.340×10^{13}
S_{55}[lb · in^4]	6.736×10^{15}	6.561×10^{15}	5.549×10^{15}
S_{45}[lb · in^3]	4.372×10^{14}	3.675×10^{14}	3.299×10^{14}
S_{35}[lb · in^3]	0	-1.031×10^{8}	-1.572×10^{5}

Table 2.10: Percentage difference between the prediction of the present implementation, VABS, and UM/VABS for the isotropic C-channel.

Stiffness Element	%Difference(Present vs VABS)	%Difference(Present vs UM/VABS)
S_{11}	3.33	3.33
S_{22}	2.79	1.44
S_{33}	12.95	12.70
S_{44}	13.32	4.26
S_{55}	2.66	15.43
S_{45}	18.97	32.25

Table 2.11: Geometry of active open cross-sections depicted in Fig. 2.15.

	Active C-Channel	Active I-Beam
a [m]	0.1	0.1
b [m]	0.1	0.1
h [m]	0.7×10^{-2}	0.7×10^{-2}
c_3 [m]	0.035	∅

The laminate design of each wall is given in Table 2.12 and the DC actuation is given in Table 2.13 where the 'L' and 'R' in the third column indicate the left half and the right half of the flange respectively.

Table 2.12: Laminate design of the active open cross-section beam cases.

	Active C-Channel	**Active I-Beam (I) & (II)**
Wall 1	$[(0°\mathbf{AS}/0°\mathbf{AF})_3/0°\mathbf{AS}]$	$[0°\mathbf{AS}/(0°\mathbf{AF})_2/0°\mathbf{AS}/(0°\mathbf{AF})_2/0°\mathbf{AS}]$
Wall 2	$[(45°\mathbf{AS}/0°\mathbf{AS})_3/45°\mathbf{AS}]$	$[(0°\mathbf{AS})_7]$
Wall 3	$[(0°\mathbf{AS}/0°\mathbf{AF})_3/0°\mathbf{AS}]$	$[0°\mathbf{AS}/(0°\mathbf{AF})_2/0°\mathbf{AS}/(0°\mathbf{AF})_2/0°\mathbf{AS}]$

Table 2.13: Laminate actuation of the active open cross-section beam cases.

	Active C-Channel	Active I-Beam (I)	Active I-Beam (II)
Wall 1	[(ø/2000 [V])$_3$/ø]	[ø/(2000 [V])$_2$/ø/(2000 [V])$_2$/ø]	L[ø/(2000 [V])$_2$/ø/(2000 [V])$_2$/ø] , R[ø/(-2000 [V])$_2$/ø/(-2000 [V])$_2$/ø]
Wall 2	[(ø)$_7$]	[(ø)$_7$]	[(ø)$_7$]
Wall 3	[(ø/-2000 [V])$_3$/ø]	[ø/(2000 [V])$_2$/ø/(2000 [V])$_2$/ø]	L[ø/(-2000 [V])$_2$/ø/(-2000 [V])$_2$/ø] , R[ø/(2000 [V])$_2$/ø/(2000 [V])$_2$/ø]

The cross-sections were meshed using GiD 9 Trial Version [103], where the maximum number of four-node quadrilateral elements of 686 was used. The meshed cross-sections were fed into UM/VABS. The significant stiffness constants and the actuation vector are compared to the present development in Tables 2.15 and 2.16 for the active I-beams and the active C-channel respectively.

Table 2.14: The significant elements of the stiffness matrix and the actuation vector of the active I-beam (I).

Stiffness Element	Present	UM/VABS	%Difference
S_{11}[N]	2.183×10^8	2.184×10^8	0.06
S_{22}[N · m^2]	2.017×10^2	2.048×10^2	1.52
S_{33}[N · m^2]	4.233×10^5	4.240×10^5	0.17
S_{44}[N · m^2]	9.912×10^4	9.955×10^4	0.43
S_{55}[N · m^4]	2.879×10^2	2.828×10^2	1.83
$F_1^{(a)}$[N]	2.338×10^4	2.341×10^4	0.15
$M_1^{(a)}$[N · m]	0	0	Exact
$M_2^{(a)}$[N · m]	0	−0.13	-
$M_3^{(a)}$[N · m]	0	0	-
$\mathbb{M}_\omega^{(a)}$[N · m^2]	0	−0.044	-

Table 2.15: The significant elements of the stiffness matrix and the actuation vector of the active I-beam (II).

Stiffness Element	Present	UM/VABS	%Difference
S_{11}[N]	2.183×10^8	2.184×10^8	0.06
S_{22}[N · m^2]	2.017×10^2	2.048×10^2	1.52
S_{33}[N · m^2]	4.233×10^5	4.240×10^5	0.17
S_{44}[N · m^2]	9.912×10^4	9.955×10^4	0.43
S_{55}[N · m^4]	2.879×10^2	2.828×10^2	1.83
$F_1^{(a)}$[N]	0	0	Exact
$M_1^{(a)}$[N · m]	0	0	Exact
$M_2^{(a)}$[N · m]	0	0	Exact
$M_3^{(a)}$[N · m]	0	0	Exact
$\mathbb{M}_\omega^{(a)}$[N · m^2]	31.577	31.115	1.49

Table 2.16: The significant elements of the stiffness matrix and the actuation vector of the active C-channel.

Stiffness Element	Present	UM/VABS	%Difference
S_{11}[N]	1.880×10^8	1.880×10^8	Exact
S_{22}[N · m^2]	2.711×10^2	2.780×10^2	2.42
S_{33}[N · m^2]	2.269×10^5	1.970×10^5	15.47
S_{44}[N · m^2]	4.385×10^5	4.390×10^5	0.17
S_{55}[N · m^4]	2.613×10^3	2.740×10^3	4.78
S_{13}[N · m]	1.962×10^6	6.300×10^5	211.51
S_{45}[N · m^3]	3.173×10^4	3.200×10^4	0.75
$F_1^{(a)}$[N]	0	0	Exact
$M_1^{(a)}$[N · m]	0	0	Exact
$M_2^{(a)}$[N · m]	0	0	Exact
$M_3^{(a)}$[N · m]	-9.377×10^2	-9.380×10^2	0.03
$\mathbb{M}_\omega^{(a)}$[N · m^2]	-7.058×10^1	-7.240×10^1	2.56

2.7 Advantages and Limitations of the Developed Theory

The cross-sectional theory for closed cross-sections presented herein, while having the classical form of the 4×4 stiffness matrix and the 4×1 actuation vector, goes beyond classical beam theories in terms of rigour since all the effects of in-plane and out-of-plane deforma-

tions/warpings are systematically taken into account when deriving the sectional constants. While in-plane shear deformations do not appear explicitly in the cross-sectional theory, their effects on the sectional constants are correctly taken into account in an asymptotic sense. Indeed, as it was demonstrated by Hodges and coworkers in numerous publications [91, 82, 104] for beams that are not weak in shear, if the sectional constants are calculated correctly then all that is needed to capture the global elastic behaviour is the 4×4 stiffness matrix. In this case, the predictions of the classical-like theory will frequently be as good or even better than refined beam theories that include more 1-D degrees of freedom. The correct application of the VAM to anisotropic beam-like structures with arbitrary cross-sectional geometry has invalidated the commonly held misconception that refined beam theories are needed for accurate predictions of elastic beam behaviour. The predictions of the VAM were validated against experimental data, 3-D finite element software packages like ABAQUS and ANSYS, and known solutions of elasticity theory equations in numerous publications [102, 83, 98, 105, 106, 88, 91]. Therefore, the validation of the implementation against VABS or UM/VABS can be considered an indirect validation against other engineering tools/data cited earlier.

Palacios [100] has correctly argued the importance of including the shell bending strain measures when analyzing active thin-wall beams starting from nonlinear shell theory. To the best of the author's knowledge, the present analysis is the first in the literature to include these strain measures when analytically analyzing thin-wall active slender beams with closed cross-section. The verification examples BB2t and BB2st demonstrate this capability, where only the stacking order of the plies in the right wall has been reversed. This causes a significant variation in the stiffness constants and the actuation elements that would not be otherwise captured by theories that neglect the shell bending strains like those of [78] and [81]. Furthermore, the asymptotically-incorrect theory of Reference [78] has failed to predict the correct active twist moment for either case as can be clearly

seen from Tables 2.6 and 2.7. The Mach scaled AMR active rotor blade and its full-scale version [60, 107] being built by the The Boeing Company are based on the concept of controlled active twist using integrated AFCs/MFCs to eliminate vibration and noise. Hodges and Volovoi [92] have demonstrated how neglecting the shell bending strains can lead to an over-prediction of the torsional stiffness for certain cross-sections by almost 100%, which would consequently affect the active twisting moment as was shown by the BB2 examples. Therefore, the current development can be safely used to analyze the AMR or to devise and optimize vibration control strategies during the flight envelope of the rotorcraft.

The present approach is considered to be reliable for most applications involving active slender beam-like structures, where an asymptotically-correct Euler-Bernoulli-like theory of order $\mathcal{O}(\epsilon^2)$ is obtained [86]. But for certain applications like geometrically short/fat beams or beams with high design gradient along their span, the structure can no longer be considered slender and a refined Timoshenko-like theory of order $\mathcal{O}(\epsilon^2(\frac{a}{\ell}))$ or even higher becomes essential. Additionally, Palacios showed that in order to estimate the local active shear loads that are high enough for certain bending actuation in the case of beams that are weak in shear, a Timoshenko-like formulation is necessary to calculate those loads. In these cases, the theory in Reference [81] will have an advantage since it yields the 6×6 stiffness constants and the corresponding 6×1 actuation vector of the active cross-section, but with the absence of the shell bending strains. Furthermore, if high frequency analysis is to be conducted, then the number of nodes required to define the deformation modes along the beam span will increase and the parameter $\left(\frac{a}{\ell}\right)$ would no longer be considered very small and refined theories would be needed. Fortunately, rotor blades are not designed to be weak in shear and they are stiff in bending. Therefore, the classical-like theory can still be used to analyze their behaviour. While the accuracy of predicting the natural frequencies still deteriorates as the mode number increases, the deterioration of the predictive capability will not be as rapid, which can be seen in Fig. 2.16. Also, the blade

sailing phenomenon is characterized as a low frequency one, therefore obtaining accurate predictions of high frequency behaviour is not paramount for this research effort.

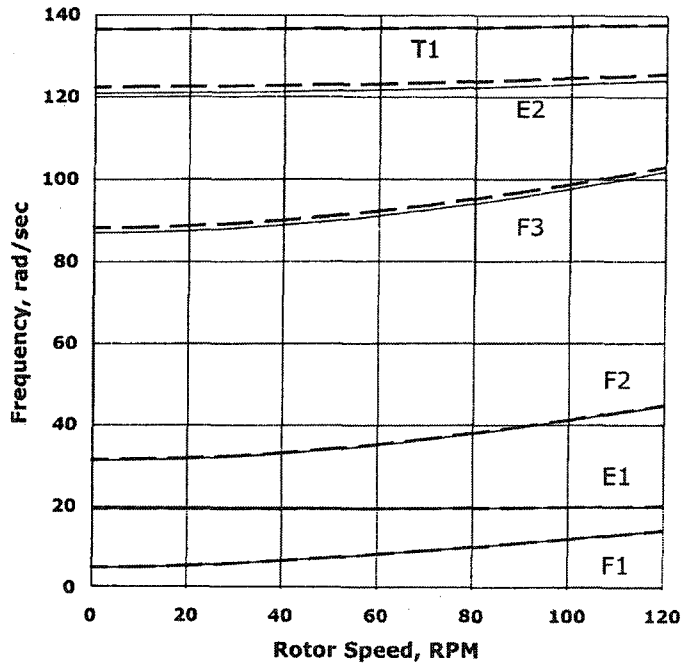

Figure 2.16: Rotating frequencies for an example rotor blade;solid lines with shear flexibility, dashed lines without [108].

For thin-wall open cross-section beams, to the best of the author's knowledge, this is the first time in the literature that an analytical treatment is given for the active Vlasov/bi-moment, which is the conjugate of the additional degree of freedom θ''. The validation examples given, demonstrate that the analytical development is capable of predicting the actuation constants to within excellent engineering accuracy. The theory can serve as a reliable and quick engineering tool for the preliminary design stage of these structures or their incorporation into flexible multibody systems. Additionally, the validation examples have highlighted that for some coupling terms of the stiffness matrix with orders of magnitude less than the primary stiffness terms, the predictions can differ significantly. While for the present development this is primarily attributed to the thin-wall assumption,

this observation is also apparent when comparing the predictions of VABS to UM/VABS, which is documented by other authors in the literature. It must finally be highlighted that although VABS and UM/VABS share the same kernel of the VAM, the implementation, especially for the refined theories like the Vlasov effect, are different [87]. It might seem puzzling that the VAM, which primarily captures the global elastic behaviour of reducible structures, can capture an end effect like the Vlasov one. It is well-established in the literature that asymptotically-correct methods, as in this case, can sometimes produce results beyond their expected range of operation [98].

To reconstruct the displacement field of the cross-section, first the generalized 1-D strains are obtained from the appropriate 1-D beam theory and the constitutive relations. These are used to solve for the unknown perturbations of the displacement field that are functions of the 1-D strain measures, material, and geometry of the cross-section. The strain field is then reconstructed followed by the displacement field. While this step is not required for this research effort, it serves to show that the development still fulfills the requirements of the sought theory outlined in Section 2.4.

The development presented herein provides sufficiently reliable analysis capability for most applications involving the global classical deformation modes of active slender beams. The main advantage being its easy and quick integration into multidisciplinary studies, like the dynamics and control of moving active beams, since it can be used in the preliminary design stages of engineering systems involving such active structures. Additionally, due to its analytical nature, it can be used for parametric and optimization studies without having to deal with the meshing and pre/post-processing steps associated with the finite element approaches, since the design parameters can be easily changed.

2.8 Future Recommendations

The present development did not take into account the effect of initial twist and curvature that are present in most, if not all, modern rotor blades and wind turbines in addition to other advanced design topologies. This will lead to the definition of another small parameter, which is defined in terms of the initial twist and curvature. Clearly, a more realistic modelling of helicopter rotor blades requires the incorporation of these built-in features in the cross-sectional analysis. Recently, the thin-wall beam theory literature is showing a research thrust in that direction to incorporate those features [109, 110], which can be used as a launch pad for incorporating the effects of integral active material.

While it was argued above that for the present research the Timoshenko-like cross-sectional theory is not necessary, future research efforts might focus on high frequency aeroelastic phenomena, which renders employing asymptotically-correct refined cross-sectional theories essential.

Chapter 3

Intrinsic and Geometrically-Exact Modelling of Maritime Active Rotor Systems

3.1 Overview of Chapter 3

This chapter begins with a review of the capabilities, features, and availability of prominent comprehensive codes for analysis of rotorcraft. The review is demonstrated to justify the rationale of developing the unique geometrically-exact (nonlinear) intrinsic model of active rotor systems that is also presented in this research.

The formulation of the geometrically-exact relations between the generalized 1-D strains of beam members and displacements/rotations at the beam reference line is first presented. The governing dynamic equations and associated natural boundary conditions are derived for moving active beams and cast in an intrinsic form. The formulation is completed by deriving additional intrinsic kinematic relations and two intrinsic invariance laws that are essential to assessing proposed solution strategies. The formulation is then augmented by

extending the intrinsic formulation to include additional rigid or flexible members to build a virtual multibody model that is representative of the active rotor system. Finally, an outline is given of the code developed based on the cross-sectional formulation in Chapter 2, the active geometrically-exact intrinsic multibody formulation in this chapter, and the modules that represent the airwake and the evaluation of the aerodynamic loads based on different models.

3.2 Review of Available Rotorcraft Comprehensive Analysis Codes

Rotorcraft Comprehensive Analysis Codes (RCACs) seek to model the aircraft aeroelastic response and the loads acting on it throughout the flight envelope. Therefore, different engineering disciplines, under the mantra of modelling and simulation engineering are combined to develop a comprehensive analysis tool for this complex multidisciplinary problem. Besides their use in assessing vehicle performance, the RCACs have many applications in the design and analysis, fatigue life prediction, and flight control. For these reasons, having a high fidelity RCAC is extremely advantageous and is sought by all rotorcraft designers and manufacturers. While state of the art 3-D finite element modelling has tremendous analysis capability for most aeroelastic problems, one must still consider the tradeoffs between detailed analysis afforded by 3-D finite element modelling and computation time to determine the optimal analysis approach. Performing a complete time-dependent aeroelastic 3-D finite element analysis of the rotor system during a portion of the flight envelope is extremely computationally expensive, requiring millions of degrees of freedom. The complexity of the problem increases exponentially for modern rotor systems, which involve combinations of composite and metallic materials, and advanced design topologies. The systemic rationale behind modelling rotor blades as beams was established in Chapter 2,

and the class of structures to which they belong was identified as reducible structures. RCACs utilize the extensive existence of such structures in the rotorcraft design to significantly reduce the dimensionality of the problem. For example, structural members of the rotor head including the pitch links and the hub shaft can be approximated as flexbeams, while the fuselage can be treated as an assemblage of composite plates and shells. Typically, members that are considered sufficiently stiff, such as the articulation links, the fuselage, and the hub, are treated as rigid bodies.

Early generation RCACs used relatively simple analytical tools, particularly to model the rotor systems and the rotor blades. The predictive capabilities of these tools are very dependent on advances in structural dynamics. The simple differential equation of transverse beam dynamics was replaced by more elaborate theories [54, 111]; nevertheless, these theories still made approximations in terms of truncation of high order terms, small rotations, and ordering schemes. These shortcomings are not suitable for rotor blade applications involving large axial forces and transverse deflections. The comparison of the predictions of these improved theories to the nonlinear experimental beam data, such as the Princeton beam data [112, 113], proved to be less than stellar. Development of geometrically-exact (nonlinear) reducible structure theories has rectified these shortcomings [108]. As a result of these improved capabilities, the use of these RCACs is on the rise in industry and academia.

The most prominent of these modern RCACs are CAMRAD II [114, 115], DYMORE [55, 116, 117, 118], and RCAS [108, 119, 120]. These codes share common capabilities in terms of modelling most aspects of the rotorcraft system. Their governing equations are geometrically-exact and share a common foundation; however, they differ in their formulations. Moreover, their utilization of the finite element method and multibody dynamics techniques allows for modelling complex geometries and material anisotropy; and interconnected bodies respectively. CAMRAD II has extensive multidisciplinary and aerodynamics

modelling capabilities and is the first of these modern RCACs. It was also the first code to be used to study active blades; although, in an approximate sense using applied loads at the tip. DYMORE has advanced structural dynamics capabilities and utilizes a novel time integration scheme based on the discontinuous Galerkin method that guarantees absolute numerical stability. Furthermore, DYMORE was recently extended to analyze active blades [121, 122] and hydraulic components [123]. RCAS is also rapidly gaining a niche in the rotorcraft community and it is being rigorously validated for wind turbine applications [120]. A recently introduced flexible multibody dynamics software package known as MBDyn [124], which is still under development, is also emerging as a competing RCAC and a test bed of novel solution strategies. All of the aforementioned RCACs are under continuous development and validation in addition to being proprietary (with the exception of MBDyn), which makes their acquisition costly if not impossible in some cases.

In this investigation, a unique approach using an intrinsic formulation for flexible multibody dynamics is adopted to model the rotor system and extended to include active rotor blades. The formulation produces compact and weak (in the sense of differentiation) differential equations of motion that can be solved efficiently, accurately, and quickly for the aeroelastic response as shall be demonstrated subsequently.

3.3 Nonlinear Beam Kinematics Preliminaries

Firstly, it is instructive to outline the general procedure that is employed for describing the nonlinear deformation of a beam-like structure and relate the strains at any material point of the cross-section to the generalized/average 1-D strains at the reference line of an initially curved and twisted beam-like structure. This will also illustrate the link between the development presented in Chapter 2 based on nonlinear shell theory and the more general approach implemented in softwares like VABS and UM/VABS. Once the procedure

is illustrated, the generalized 1-D strains will then be used in the last step of the formulation of the model describing the motion of active beams.

As in Danielson [125, 126], consider the arbitrary cross-section of an initially twisted and curved prismatic beam undergoing a deformation as illustrated in Fig. 3.1. The position vector of any material point on the undeformed cross-section is written as

$$\hat{\mathbf{r}}(x_1, x_2, x_3) = \mathbf{r}(x_1) + x_\alpha \mathbf{b}_\alpha \tag{3.1}$$

where as before, Greek indices run from 2 to 3, and Roman indices run from 1 to 3; $\mathbf{r}$ is the position vector of the cross-sectional reference point of the undeformed state; x_α are the measures along their respective axes $\mathbf{b}_\alpha$; with $\mathbf{b}_1$ being tangential to the beam reference line x_1.

The position vector of a material point on the deformed cross-section is written as

$$\hat{\mathbf{R}}(x_1, x_2, x_3) = \mathbf{r}(x_1) + \mathbf{u}(x_1) + x_\alpha \mathbf{B}_\alpha + w_i(x_1, x_2, x_3)\mathbf{B}_i \tag{3.2}$$

where $\mathbf{u}$ is the displacement vector of the beam cross-section at the reference line; w_i are the unknown three dimensional warping functions; $\mathbf{B}_i$ form the triad of the deformed section with $\mathbf{B}_1$ not necessarily tangent to the deformed beam reference line s. The development in Chapter 2 has solved for the warping functions, which can be used to recover the deformed displacement field of the cross-section.

Before the initial twist and curvature of the beam member is considered, slope discontinuities at the reference line that are due to rotor blade tip sweep or anhedral, as shown in Fig. 3.2, must be accounted for. The rotation operator, $\mathcal{C}^{lr}$, is defined to transform a primary vector variable from the broken frame, r, to the unbroken frame, l.

The initial twist and curvature at the beam reference line is written in a column matrix form as

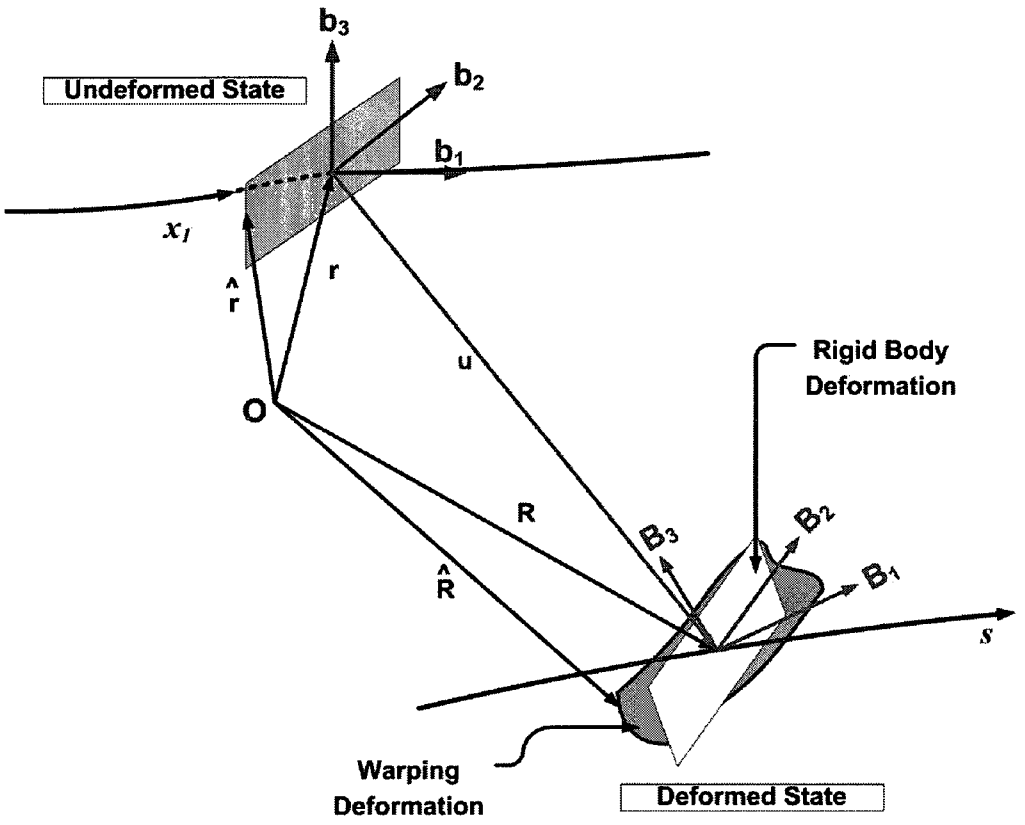

Figure 3.1: Kinematics of general beam deformation.

$$\mathbf{k} = \begin{bmatrix} k_1 \\ k_2 \\ k_3 \end{bmatrix} \tag{3.3}$$

where k_1 is initial twist, and k_2 and k_3 are the initial curvatures of the beam about the 2 and 3 axes of the beam respectively.

According to the Kirchhoff kinetic analogy discussed by Love [127], the initial twist column matrix is related to the operator, $C^{\mathbf{ba}}$, that transforms a vector from the untwisted and uncurved frame, **a**, to the twisted and curved frame, **b**, such that

$$C^{\mathbf{ba}'} = -\tilde{\mathbf{k}} \cdot C^{\mathbf{ba}} \tag{3.4}$$

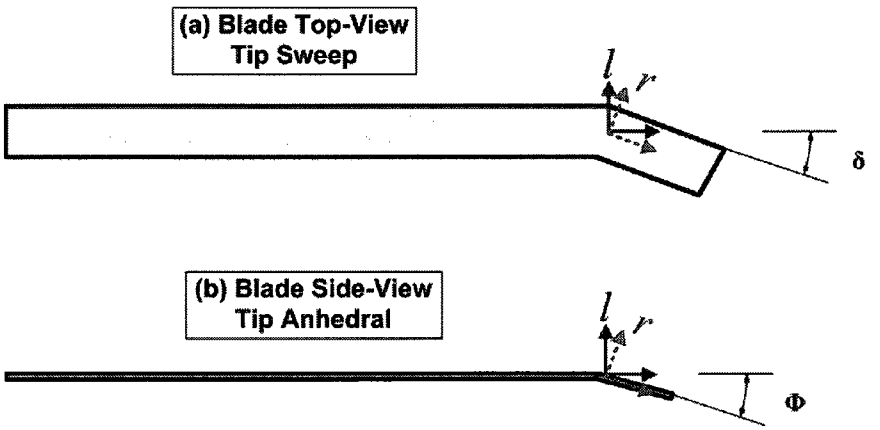

Figure 3.2: Illustration of blade tip (a) sweep and (b) anhedral and associated frames.

where the similarity with the angular velocity operator, $\dot{\mathcal{C}} = -\tilde{\boldsymbol{\omega}} \cdot \mathcal{C}$, is noted when the spatial axial derivative $(\ )'$ along x_1 in Eq. 3.4 is replaced by the time differentiation $(\dot{})$. The skew-symmetric operator $(\tilde{})$ is defined in Appendix B.

In reference to Fig. 3.1, the covariant (natural) base vectors $\mathbf{g}_i$ for any material point on the cross-section of the undeformed beam are defined as being tangent to the position vector $\hat{\mathbf{r}}$, which implies that they are not necessarily orthogonal, such as

$$\mathbf{g}_i(x_1, x_2, x_3) = \frac{\partial \hat{\mathbf{r}}}{\partial x_i} \tag{3.5}$$

The contravariant base vectors are defined based on the covariant ones as [128]

$$\mathbf{g}^i = \frac{1}{\sqrt{g}} \varepsilon_{ijk} \mathbf{g}_j \times \mathbf{g}_k \tag{3.6}$$

where the metric scaling factor, g, is given by

$$g = \det(\mathbf{g}_i \mathbf{g}_j) = (1 - x_2 k_3 + x_3 k_2)^2 \tag{3.7}$$

and the cyclic permutation tensor, ε_{ijk}, is defined as

$$\varepsilon_{ijk} = \begin{cases} 1 & (ijk) \text{ cyclic permutation of } 123 \\ -1 & (ijk) \text{ anticyclic permutation of } 123 \\ 0 & \text{otherwise} \end{cases} \tag{3.8}$$

Similarly, the covariant base vectors, $\mathbf{G}_i$, of the deformed beam are defined as

$$\mathbf{G}_i(x_1, x_2, x_3) = \frac{\partial \hat{\mathbf{R}}}{\partial x_i} \tag{3.9}$$

The global rotation operator, $C^{\mathbf{Bb}}$, that quantifies the rotational deformation of the cross-section at the beam reference line is defined based on the linear combination of the dyads formed from the base vectors as

$$\mathcal{C}^{\mathbf{Bb}} = \mathbf{B}_i \mathbf{b}_i \tag{3.10}$$

where $\mathbf{B}_i$ and $\mathbf{b}_i$ define the deformed and the undeformed frame, respectively as in Fig. 3.1.

Deformation gradients are primitive forms of strain tensors [129] and they quantify the kinematics of deformations in a dyadic form. The deformation gradient, $\mathfrak{A}$, adopted for beam deformation analysis is expressed in terms of the matrix of mixed components as

$$\mathfrak{A}_{ij} = (\mathbf{B}_i \cdot \mathbf{G}_n)(\mathbf{g}^n \cdot \mathbf{b}_j) \tag{3.11}$$

The polar decomposition theorem states that for any non-singular second-order tensor, such as $\mathfrak{A}$, there exist unique positive definite symmetric second-order stretch tensors $\mathfrak{U}$ and $\mathfrak{V}$, and an orthogonal second-order rotation tensor, $\mathcal{R}$, such that [130]

$$\mathfrak{A} = \mathcal{R} \cdot \underbrace{\mathfrak{U}}_{\text{right stretch tensor}} = \underbrace{\mathfrak{V}}_{\text{left stretch tensor}} \cdot \mathcal{R} \tag{3.12}$$

The right stretch tensor convention is adopted herein. It can be shown that the matrix

form of the symmetric Jaumann-Biot-Cauchy strain tensor, $\mathbf{\Gamma}^*$ (3×3 matrix), is defined as [125]

$$\mathbf{\Gamma}^* = \mathfrak{U} - \mathbf{I} = \frac{1}{2}\left(\mathfrak{A} + \mathfrak{A}^{\mathrm{T}}\right) - \mathbf{I} \tag{3.13}$$

where $\mathbf{I}$ is the 3×3 identity matrix.

With the assumption of small strain, the independent components of the strain field can be grouped in a 6×1 column matrix

$$\begin{aligned} \mathbf{\Gamma} &= \begin{bmatrix} \Gamma_{11}^* & 2\Gamma_{12}^* & 2\Gamma_{13}^* & \Gamma_{22}^* & 2\Gamma_{23}^* & \Gamma_{33}^* \end{bmatrix} \\ \mathbf{\Gamma} &= \underline{\frac{1}{h}\mathbf{\Gamma}_h z} + \mathbf{\Gamma}_\epsilon \boldsymbol{\epsilon} + \underline{\mathbf{\Gamma}_R z} + \underline{\mathbf{\Gamma}_\ell z'} \end{aligned} \tag{3.14}$$

The operator matrices $\Gamma_h(6 \times 3)$, $\Gamma_\epsilon(6 \times 4)$, $\Gamma_R(6 \times 3)$ and $\Gamma_\ell(6 \times 3)$ are defined in terms of the nondimensionalized cross-sectional coordinates $\zeta_2 = \frac{x_2}{a}$ and $\zeta_3 = \frac{x_3}{a}$ as:

$$\mathbf{\Gamma}_h = \begin{bmatrix} 0 & 0 & 0 \\ \frac{\partial}{\partial \zeta_2} & 0 & 0 \\ \frac{\partial}{\partial \zeta_3} & 0 & 0 \\ 0 & \frac{\partial}{\partial \zeta_2} & 0 \\ 0 & \frac{\partial}{\partial \zeta_3} & \frac{\partial}{\partial \zeta_2} \\ 0 & 0 & \frac{\partial}{\partial \zeta_3} \end{bmatrix}$$

$$\mathbf{\Gamma}_\epsilon = \frac{1}{\sqrt{g}} \begin{bmatrix} 1 & 0 & -\zeta_3 & \zeta_2 \\ 0 & \zeta_3 & 0 & 0 \\ 0 & -\zeta_2 & 0 & 0 \\ 0 & 0 & 0 & 0 \\ 0 & 0 & 0 & 0 \\ 0 & 0 & 0 & 0 \end{bmatrix}$$

$$\mathbf{\Gamma}_R = \frac{1}{\sqrt{g}} \begin{bmatrix} \tilde{k} + k\mathbf{I}(\zeta_3 \frac{\partial}{\partial \zeta_2} - \zeta_2 \frac{\partial}{\partial \zeta_3}) \\ 0 \end{bmatrix}$$

$$\mathbf{\Gamma}_\ell = \frac{1}{\sqrt{g}} \begin{bmatrix} \mathbf{I} \\ 0 \end{bmatrix} \tag{3.15}$$

where a is the characteristic dimension of the cross-section as before, the column matrix $\boldsymbol{\epsilon}$ represents the generalized/average strains defined at the beam reference line as

$$\boldsymbol{\epsilon} = \begin{bmatrix} \boldsymbol{\gamma} \\ a\boldsymbol{\kappa} \end{bmatrix} \tag{3.16}$$

where $\boldsymbol{\gamma}$ contains the average cross-sectional extensional strain measure defined as

$$\boldsymbol{\gamma} = \mathcal{C}^{\mathbf{B}\mathbf{b}^{\mathrm{T}}} \cdot \mathbf{R}' - \mathbf{r}' \tag{3.17}$$

where $\boldsymbol{\kappa}$ contains the twist/curvature (moment) strain measures.

The Jaumann-Biot-Cauchy stress tensor at a material point is then written as

$$\mathfrak{Z} = \mathbb{D}\mathbf{\Gamma} \tag{3.18}$$

where $\mathbb{D}$ is the symmetric 6×6 material constants.

The strain energy of the beam-like structure per unit length can now be written as

$$\mathcal{U} = \frac{1}{2}\left\langle \mathbf{\Gamma}^{\mathrm{T}} \mathbb{D} \mathbf{\Gamma} \right\rangle \tag{3.19}$$

where the operator $\langle \bullet \rangle$ is defined over the cross-sectional area S as

$$\langle \bullet \rangle = a^2 \int \int_S \bullet \sqrt{g} \mathrm{d}\zeta_2 \zeta_3 \tag{3.20}$$

The underlined terms in Eq. 3.14 contain the unknown warping functions that the VAM solves for asymptotically in terms of the average strains at the beam reference line, the material properties, and the cross-sectional geometry. It is presented here for a general beam-like structure, while the development in Chapter 2 started from nonlinear shell theory. Applying the VAM algorithm to the problem presented in Eq. 3.19 will lead to the kernel of VABS and UM/VABS [90, 86, 82], which is beyond the scope of this research. It is considered illuminating however to highlight these seamless connections between the various developments. The small strain assumption was invoked because a linear 2-D cross-sectional beam theory is sought; however, if a nonlinear elastic effect is to be included, like the trapeze effect, then some terms that couple the warping functions and the generalized strains are to be retained in the strain field of Eq. 3.14 [131, 132].

Similar to Eq. 3.4, the total twist/curvature measure vector, which quantifies the built-in and the deformation induced twist and curvature, is also written in the deformed frame as

$$\mathcal{C}^{\mathbf{Ba'}} = -\tilde{\mathbf{K}} \cdot \mathcal{C}^{\mathbf{Ba}} \tag{3.21}$$

Using the fact that $\mathcal{C}^{\mathbf{Ba}} = \mathcal{C}^{\mathbf{Bb}} \cdot \mathcal{C}^{\mathbf{ba}}$, Eq. 3.21 can be rewritten as

$$\begin{aligned}
\tilde{\mathbf{K}} &= -\left(\mathcal{C}^{\mathbf{Bb}}\mathcal{C}^{\mathbf{ba}}\right)'\mathcal{C}^{\mathbf{ba}^{\mathrm{T}}}\mathcal{C}^{\mathbf{Bb}^{\mathrm{T}}} \\
&= -\left(\mathcal{C}^{\mathbf{Bb}'}\mathcal{C}^{\mathbf{ba}} + \mathcal{C}^{\mathbf{Bb}}\mathcal{C}^{\mathbf{ba}'}\right)\cdot\mathcal{C}^{\mathbf{ba}^{\mathrm{T}}}\mathcal{C}^{\mathbf{Bb}^{\mathrm{T}}} \\
&= -\left(\mathcal{C}^{\mathbf{Bb}'}\mathcal{C}^{\mathbf{ba}}\mathcal{C}^{\mathbf{ab}^{\mathrm{T}}}\mathcal{C}^{\mathbf{Bb}^{\mathrm{T}}} + \mathcal{C}^{\mathbf{Bb}}\mathcal{C}^{\mathbf{ba}'}\mathcal{C}^{\mathbf{ba}^{\mathrm{T}}}\mathcal{C}^{\mathbf{Bb}^{\mathrm{T}}}\right) \\
&= -\left(\mathcal{C}^{\mathbf{Bb}'}\mathcal{C}^{\mathbf{Bb}^{\mathrm{T}}} - \mathcal{C}^{\mathbf{Bb}}\tilde{\mathbf{k}}\mathcal{C}^{\mathbf{Bb}^{\mathrm{T}}}\right)
\end{aligned} \tag{3.22}$$

where the rotation operator fact $\mathcal{C}\cdot\mathcal{C}^{\mathrm{T}} = \mathcal{C}^{\mathrm{T}}\cdot\mathcal{C} = \mathbf{I}$ was invoked.

The moment strain measures defined as $\boldsymbol{\kappa} = \mathbf{K} - \mathbf{k}$ can then be written as

$$\tilde{\boldsymbol{\kappa}} = -\mathcal{C}^{\mathbf{Bb}'}\mathcal{C}^{\mathbf{Bb}^{\mathrm{T}}} + \mathcal{C}^{\mathbf{Bb}}\tilde{\mathbf{k}}\mathcal{C}^{\mathbf{Bb}^{\mathrm{T}}} - \tilde{\mathbf{k}} \tag{3.23}$$

or in an implicit form as

$$\mathcal{C}^{\mathbf{Bb}'} = \mathcal{C}^{\mathbf{Bb}}\tilde{\mathbf{k}} - \tilde{\mathbf{K}}\mathcal{C}^{\mathbf{Bb}} \tag{3.24}$$

The fact that $\mathbf{b}_1$ is tangent to x_1 at every point along the undeformed beam reference line, as illustrated in Fig. 3.1, leads to

$$\frac{\mathrm{d}\mathbf{r}}{\mathrm{d}x_1} = \mathbf{r}'_{\mathbf{b}} + \tilde{\mathbf{k}}\mathbf{r}_{\mathbf{b}} = \mathbf{e}_1 \tag{3.25}$$

where the analogy with the rigid body velocity field is highlighted, the $\mathbf{b}$ subscript indicates the frame in which the differentiation is expressed and

$$\mathbf{e}_1 = \begin{bmatrix} 1 \\ 0 \\ 0 \end{bmatrix} \tag{3.26}$$

Finally, using Eqs. 3.1 and 3.2 to re-express the average extensional strain measure in

Eq. 3.17 as $\boldsymbol{\gamma} = \mathcal{C}^{\mathbf{Bb}}(\mathbf{r}'_{\mathbf{b}} + \widetilde{\mathbf{k}}\mathbf{r}_{\mathbf{b}} + \mathbf{u}'_b + \widetilde{\mathbf{k}}\mathbf{u}_b) - \mathbf{r}'_{\mathbf{b}} + \widetilde{\mathbf{k}}\mathbf{r}_{\mathbf{b}}$ and using Eq. 3.25 to yield the convenient form

$$\boldsymbol{\gamma} = \mathcal{C}^{\mathbf{Bb}}(e_1 + \mathbf{u}'_b + \widetilde{\mathbf{k}}\mathbf{u}_b) - \mathbf{e}_1 \tag{3.27}$$

3.4 Intrinsic Dynamics Equations of Moving Active Beams

As in [133] for a beam of length l, we consider Hamilton's principle that is written as

$$\int_{t_1}^{t_2} \int_0^l \left[\delta\left(\mathcal{T} - \mathcal{U}\right) + \overline{\delta\mathcal{W}}\right] \, \mathrm{d}x_1 \mathrm{d}t = \overline{\delta\mathcal{A}} \tag{3.28}$$

where $\mathcal{T}$ is the kinetic energy per unit length, $\mathcal{U}$ is the elastic energy per unit length, $\overline{\delta\mathcal{W}}$ is the virtual work of applied loads per unit length, and $\overline{\delta\mathcal{A}}$ is the virtual action at the ends of the beam and at the end of the time interval. The over-bar indicates that the terms do not derive from a functional. Since there is no accumulation of electric charges on the surface or the ends of the beam and the applied voltage to the AFCs/MFCs is assumed to be prescribed, the actuation problem does not contribute to the virtual work term.

Given that the strain energy per unit length is a function of $\mathcal{U} = \mathcal{U}(\boldsymbol{\gamma}, \boldsymbol{\kappa})$, its variation is written as

$$\int_0^l \delta\mathcal{U} \, \mathrm{d}x_1 = \int_0^l \left[\delta\boldsymbol{\gamma}^{\mathrm{T}} \left(\frac{\partial\mathcal{U}}{\partial\boldsymbol{\gamma}}\right)^{\mathrm{T}} + \delta\boldsymbol{\kappa}^{\mathrm{T}} \left(\frac{\partial\mathcal{U}}{\partial\boldsymbol{\kappa}}\right)^{\mathrm{T}}\right] \, \mathrm{d}x_1 \tag{3.29}$$

The internal cross-sectional forces and moments that are conjugate to the generalized strains, twist rate, and curvatures are defined in the deformed frame as

$$\left(\frac{\partial \mathcal{U}}{\partial \boldsymbol{\gamma}}\right)^{\mathrm{T}} = \begin{bmatrix} \frac{\partial \mathcal{U}}{\partial \gamma_{11}} \\ \frac{\partial \mathcal{U}}{2\partial \gamma_{12}} \\ \frac{\partial \mathcal{U}}{2\partial \gamma_{13}} \end{bmatrix} = \mathbf{F} = \begin{bmatrix} F_1 \\ F_2 \\ F_3 \end{bmatrix}$$
$$\left(\frac{\partial \mathcal{U}}{\partial \boldsymbol{\kappa}}\right)^{\mathrm{T}} = \begin{bmatrix} \frac{\partial \mathcal{U}}{\partial \kappa_1} \\ \frac{\partial \mathcal{U}}{\partial \kappa_2} \\ \frac{\partial \mathcal{U}}{\partial \kappa_3} \end{bmatrix} = \mathbf{M} = \begin{bmatrix} M_1 \\ M_2 \\ M_3 \end{bmatrix} \tag{3.30}$$

Noting that $\delta \mathbf{k} = 0$ since it is prescribed, the variation of $\boldsymbol{\kappa}$ is obtained from Eq. 3.23 as

$$\delta \boldsymbol{\kappa} = -\delta \mathcal{C}^{\mathbf{Bb}'} \mathcal{C}^{\mathbf{Bb}^{\mathrm{T}}} - \mathcal{C}^{\mathbf{Bb}'} \delta \mathcal{C}^{\mathbf{Bb}^{\mathrm{T}}} + \delta \mathcal{C}^{\mathbf{Bb}} \tilde{\mathbf{k}} \mathcal{C}^{\mathbf{Bb}^{\mathrm{T}}} + \mathcal{C}^{\mathbf{Bb}} \tilde{\mathbf{k}} \delta \mathcal{C}^{\mathbf{Bb}^{\mathrm{T}}} \tag{3.31}$$

The virtual rotations, $\overline{\delta \boldsymbol{\psi}}$, and the virtual displacements, $\overline{\delta \mathbf{q}}$ defined in the deformed frame are given by

$$\widetilde{\overline{\delta \boldsymbol{\psi}}} = -\delta \mathcal{C}^{\mathbf{Bb}} \mathcal{C}^{\mathbf{Bb}^{\mathrm{T}}} \tag{3.32}$$

$$\overline{\delta \mathbf{q}} = \mathcal{C}^{\mathbf{Bb}} \delta \mathbf{u}_{\mathbf{b}} \tag{3.33}$$

where the defined virtual quantities correspond to variation of a set of quasi-coordinates rather than actual physical coordinates unless they are expressed in the undeformed frame.

Differentiating Eq. 3.32 with respect to x_1 yields

$$\widetilde{\overline{\delta \boldsymbol{\psi}}}' = -\delta \mathcal{C}^{\mathbf{Bb}'} \mathcal{C}^{\mathbf{Bb}^{\mathrm{T}}} - \delta \mathcal{C}^{\mathbf{Bb}} \mathcal{C}^{\mathbf{Bb}'^{\mathrm{T}}} \tag{3.34}$$

Using Eq. 3.23, Eq. 3.32, and Eq. 3.34 to simplify Eq. 3.31, as shown in Appendix B,

yields the compact intrinsic (no explicit dependance on physical displacement or finite rotation) form of the variation of the moment strain measures as

$$\delta\boldsymbol{\kappa} = \overline{\delta\psi}' + \tilde{\mathbf{K}}\overline{\delta\psi} \tag{3.35}$$

Similarly, the variation of the generalized extensional/shear strain measures is derived from Eq. 3.27 as

$$\delta\boldsymbol{\gamma} = \delta\mathcal{C}^{\mathbf{Bb}}\left(\mathbf{e}_1 + \mathbf{u}_\mathbf{b}' + \tilde{\mathbf{k}}\mathbf{u}_\mathbf{b}\right) + \mathcal{C}^{\mathbf{Bb}}\left(\delta\mathbf{u}_\mathbf{b}' + \tilde{\mathbf{k}}\delta\mathbf{u}_\mathbf{b}\right) \tag{3.36}$$

Rearranging Eq. 3.27 as shown in Appendix B results in

$$\delta\mathcal{C}^{\mathbf{Bb}}\left(\mathbf{e}_1 + \mathbf{u}_\mathbf{b}' + \tilde{\mathbf{k}}\mathbf{u}_\mathbf{b}\right) = \delta\mathcal{C}^{\mathbf{Bb}}\mathcal{C}^{\mathbf{Bb}^\mathrm{T}}\left(\mathbf{e}_1 + \boldsymbol{\gamma}\right) \tag{3.37}$$

Differentiating Eq. 3.33 with respect to x_1 and then rearranging results in

$$\mathcal{C}^{\mathbf{Bb}}\delta\mathbf{u}_\mathbf{b}' = \overline{\delta\mathbf{q}}' - \mathcal{C}^{\mathbf{Bb}'}\mathcal{C}^{\mathbf{Bb}^\mathrm{T}}\overline{\delta\mathbf{q}} \tag{3.38}$$

Substituting Eqs. 3.38 and 3.37 into Eq. 3.36 yields

$$\delta\boldsymbol{\gamma} = \delta\mathcal{C}^{\mathbf{Bb}}\mathcal{C}^{\mathbf{Bb}^\mathrm{T}}\left(\mathbf{e}_1 + \boldsymbol{\gamma}\right) + \overline{\delta\mathbf{q}}' - \mathcal{C}^{\mathbf{Bb}'}\mathcal{C}^{\mathbf{Bb}^\mathrm{T}}\overline{\delta\mathbf{q}} + \mathcal{C}^{\mathbf{Bb}}\tilde{\mathbf{k}}\delta\mathbf{u}_\mathbf{b} \tag{3.39}$$

Rewriting Eq. 3.32 as, $\delta\mathcal{C}^{\mathbf{Bb}} = -\widetilde{\overline{\delta\psi}}\mathcal{C}^{\mathbf{Bb}}$, and Eq. 3.33 as, $\delta\mathbf{u}_\mathbf{b} = \overline{\delta\mathbf{q}}\mathcal{C}^{\mathbf{Bb}^\mathrm{T}}$, then substituting in Eq. 3.39 yields

$$\delta\boldsymbol{\gamma} = \underline{-\widetilde{\overline{\delta\psi}}\left(\mathbf{e}_1 + \boldsymbol{\gamma}\right)} + \overline{\delta\mathbf{q}}' \underbrace{-\mathcal{C}^{\mathbf{Bb}'}\mathcal{C}^{\mathbf{Bb}^\mathrm{T}}\overline{\delta\mathbf{q}} + \mathcal{C}^{\mathbf{Bb}}\tilde{\mathbf{k}}\mathcal{C}^{\mathbf{Bb}^\mathrm{T}}\overline{\delta\mathbf{q}}}_{} \tag{3.40}$$

Invoking property B.7 in Appendix B of the skew-symmetric operator for the underlined term and Eq. 3.22 for the under-braced term yields the intrinsic form of the variation of

the average extensional strain measure as

$$\delta\boldsymbol{\gamma} = \overline{\delta\mathbf{q}}' + \tilde{\mathbf{K}}\overline{\delta\mathbf{q}} + (\tilde{\mathbf{e}}_1 + \tilde{\boldsymbol{\gamma}})\,\overline{\delta\boldsymbol{\psi}} \tag{3.41}$$

Substituting Eq. 3.30, Eq. 3.35, and Eq. 3.41 into the variation of the strain energy per unit length in Eq. 3.29 yields

$$\delta\mathcal{U} = \left[\overline{\delta\mathbf{q}}'^{\mathrm{T}} - \overline{\delta\mathbf{q}}^{\mathrm{T}}\tilde{\mathbf{K}} - \overline{\delta\boldsymbol{\psi}}^{\mathrm{T}}(\tilde{\mathbf{e}}_1 + \tilde{\boldsymbol{\gamma}})\right]\mathbf{F} + \left[\overline{\delta\boldsymbol{\psi}}'^{\mathrm{T}} - \overline{\delta\boldsymbol{\psi}}^{\mathrm{T}}\tilde{\mathbf{K}}\right]\mathbf{M} \tag{3.42}$$

The variation of the kinetic energy is obtained in a similar fashion. Firstly, the velocity field of the cross-section is derived where the displacement due to elastic warping is neglected. The linear inertial velocity at the reference line of the deformed frame is

$$\mathbf{V} = \mathcal{C}^{\mathbf{Bb}}(\mathbf{v} + \dot{\mathbf{u}}_\mathbf{b} + \tilde{\boldsymbol{\omega}}\mathbf{u}_\mathbf{b}) \tag{3.43}$$

where $\mathbf{v}$ is the total inertial velocity of the undeformed frame, and $\boldsymbol{\omega}$ is the inertial angular velocity of the undeformed frame.

The inertial angular velocity of the deformed cross-section is

$$\tilde{\boldsymbol{\Omega}} = -\dot{\mathcal{C}}^{\mathbf{Bb}}\mathcal{C}^{\mathbf{Bb}^{\mathrm{T}}} + \mathcal{C}^{\mathbf{Bb}}\tilde{\boldsymbol{\omega}}\mathcal{C}^{\mathbf{Bb}^{\mathrm{T}}} \tag{3.44}$$

where the first term stems from the time derivative of the rotation operator $\mathcal{C}^{\mathbf{Bb}}$, and the second term is the angular velocity skew-symmetric operator of the undeformed frame transformed to the deformed frame using a similarity transformation.

The inertial velocity of a material point, $\breve{m}$, on the cross-section in the deformed frame is then

$$\mathbf{V}^{\breve{m}} = \mathbf{V} + \tilde{\boldsymbol{\Omega}}\boldsymbol{\xi} \tag{3.45}$$

where $\boldsymbol{\xi}$ is the position vector of the material point, $\breve{m}$, in the deformed cross-section relative to the reference point such that

$$\boldsymbol{\xi} = \begin{bmatrix} 0 \\ x_2 \\ x_3 \end{bmatrix} \tag{3.46}$$

The kinetic energy per unit length is then

$$\mathcal{T} = \frac{1}{2} \left\langle \mathbf{V}^{\breve{m}\mathrm{T}} \rho(x_2, x_3) \mathbf{V}^{\breve{m}} \right\rangle \tag{3.47}$$

where $\rho(x_2, x_3)$ is the material density.

As demonstrated in Appendix B, the kinetic energy is then written as

$$\mathcal{T} = \frac{1}{2} \left(\bar{m} \mathbf{V}^{\mathrm{T}} \mathbf{V} - 2\boldsymbol{\Omega}^{\mathrm{T}} \tilde{\mathbf{V}} \overline{m\boldsymbol{\xi}} + \boldsymbol{\Omega}^{\mathrm{T}} \bar{i} \boldsymbol{\Omega} \right) \tag{3.48}$$

where the mass per unit length $\bar{m}$, the first mass moment of inertia per unit length $\overline{m\xi}$, and the second mass moment of inertia per unit length $\bar{i}$ are defined as

$$\begin{aligned} \bar{m} &= \langle \rho \rangle \\ \overline{m\xi} &= \langle \xi \rho \rangle \\ \bar{i} &= \left\langle \rho(\xi^{\mathrm{T}} \xi \mathbf{I} - \xi \xi^{\mathrm{T}}) \right\rangle \end{aligned} \tag{3.49}$$

The variation of the kinetic energy can now be written as

$$\int_0^l \delta\mathcal{T} \, \mathrm{d}x_1 = \int_0^l \left[\delta\mathbf{V}^{\mathrm{T}} \left(\frac{\partial \mathcal{T}}{\partial \mathbf{V}} \right)^{\mathrm{T}} + \delta\boldsymbol{\Omega}^{\mathrm{T}} \left(\frac{\partial \mathcal{T}}{\partial \boldsymbol{\Omega}} \right)^{\mathrm{T}} \right] \mathrm{d}x_1 \tag{3.50}$$

where the generalized sectional linear momentum, $\mathbf{P}$, and the generalized sectional angular

momentum, $\mathbf{H}$, that are conjugate to the linear and angular velocity respectively are defined in the deformed frame as

$$\left(\frac{\partial \mathcal{T}}{\partial \mathbf{V}}\right)^{\mathrm{T}} = \begin{bmatrix} \frac{\partial \mathcal{T}}{\partial V_1} \\ \frac{\partial \mathcal{T}}{\partial V_2} \\ \frac{\partial \mathcal{T}}{\partial V_3} \end{bmatrix} = \mathbf{P} = \begin{bmatrix} P_1 \\ P_2 \\ P_3 \end{bmatrix}$$
$$\left(\frac{\partial \mathcal{T}}{\partial \mathbf{\Omega}}\right)^{\mathrm{T}} = \begin{bmatrix} \frac{\partial \mathcal{T}}{\partial \Omega_1} \\ \frac{\partial \mathcal{T}}{\partial \Omega_2} \\ \frac{\partial \mathcal{T}}{\partial \Omega_3} \end{bmatrix} = \mathbf{H} = \begin{bmatrix} H_1 \\ H_2 \\ H_3 \end{bmatrix} \tag{3.51}$$

Taking the variation of Eq. 3.44 yields

$$\delta\tilde{\mathbf{\Omega}} = -\delta\mathcal{C}^{\mathbf{Bb}}\mathcal{C}^{\mathbf{Bb}^{\mathrm{T}}} - \mathcal{C}^{\mathbf{Bb}}\delta\mathcal{C}^{\mathbf{Bb}^{\mathrm{T}}} + \delta\mathcal{C}^{\mathbf{Bb}}\tilde{\boldsymbol{\omega}}\mathcal{C}^{\mathbf{Bb}^{\mathrm{T}}} + \mathcal{C}^{\mathbf{Bb}}\tilde{\boldsymbol{\omega}}\delta\mathcal{C}^{\mathbf{Bb}^{\mathrm{T}}} \tag{3.52}$$

Taking the time derivative of the virtual rotation in Eq. 3.32 leads to an expression that is similar to Eq. 3.34 with the spatial derivative replaced by the time derivative. Also, making use of Eq. 3.44 followed by algebraic manipulations that are quite similar to the ones employed to derive Eq. 3.35, leads to the variation of the generalized angular sectional speed in the simplified form

$$\delta\mathbf{\Omega} = \overline{\dot{\delta\psi}} + \tilde{\mathbf{\Omega}}\overline{\delta\psi} \tag{3.53}$$

In similar fashion, taking the variation of Eq. 3.43 yields

$$\delta\mathbf{V} = \delta\mathcal{C}^{\mathbf{Bb}}(\mathbf{v} + \dot{\mathbf{u}}_{\mathbf{b}} + \tilde{\boldsymbol{\omega}}\mathbf{u}_{\mathbf{b}}) + \mathcal{C}^{\mathbf{Bb}}\left(\delta\dot{\mathbf{u}}_{\mathbf{b}} + \tilde{\boldsymbol{\omega}}\delta\mathbf{u}_{\mathbf{b}}\right) \tag{3.54}$$

Replacing the spatial derivative by the time derivative in Eq. 3.38 leads to the time

derivative of the virtual displacement, which along with Eq. 3.43, can be used to yield the simplified form of the variation of the generalized linear sectional speed as

$$\delta\mathbf{V} = \dot{\overline{\delta\mathbf{q}}} + \tilde{\mathbf{\Omega}}\overline{\delta\mathbf{q}} + \tilde{\mathbf{V}}\overline{\delta\boldsymbol{\psi}} \tag{3.55}$$

Substituting the variations of Eq. 3.53 and Eq. 3.55 into the variation of the kinetic energy per unit length in Eq. 3.50 yields

$$\delta\mathcal{T} = \left(\dot{\overline{\delta\mathbf{q}}}^{\mathrm{T}} - \overline{\delta\mathbf{q}}^{\mathrm{T}}\tilde{\mathbf{\Omega}} - \overline{\delta\boldsymbol{\psi}}^{\mathrm{T}}\tilde{\mathbf{V}}\right)\mathbf{P} + \left(\dot{\overline{\delta\boldsymbol{\psi}}}^{\mathrm{T}} - \overline{\delta\boldsymbol{\psi}}^{\mathrm{T}}\tilde{\mathbf{\Omega}}\right)\mathbf{H} \tag{3.56}$$

The virtual work per unit length of body forces, $\mathbf{f}$, and moments, $\mathbf{m}$, is simply

$$\overline{\delta\mathcal{W}} = \int_0^l \left(\overline{\delta\mathbf{q}}^{\mathrm{T}}\mathbf{f} + \overline{\delta\boldsymbol{\psi}}^{\mathrm{T}}\mathbf{m}\right)\,\mathrm{d}x_1 \tag{3.57}$$

Finally, the action term due to forces and moments applied at the ends of the beam as well as inertial forces and moments is

$$\delta\mathcal{A} = \int_0^l \left(\overline{\delta\mathbf{q}}^{\mathrm{T}}\hat{\mathbf{P}} + \overline{\delta\boldsymbol{\psi}}^{\mathrm{T}}\hat{\mathbf{H}}\right)\,\mathrm{d}x_1\,|_{t_1}^{t_2} - \int_{t_1}^{t_2} \left(\overline{\delta\mathbf{q}}^{\mathrm{T}}\hat{\mathbf{F}} + \overline{\delta\boldsymbol{\psi}}^{\mathrm{T}}\hat{\mathbf{M}}\right)|_0^l\,\mathrm{d}t \tag{3.58}$$

where the hatted symbols refer to boundary terms. Some authors drop the first term in Eq. 3.58 from the derivation at the outset, since it does not contribute to the final result; however, when variational integrators are investigated, the term was found to be essential for numerical stability [134].

Substituting Eq. 3.42, Eq. 3.56, and Eq. 3.58 into Eq. 3.28 yields

$$\begin{aligned}\int_{t_1}^{t_2}\int_0^l \Bigg\{ &\left(\dot{\underline{\overline{\delta\mathbf{q}}}}^{\mathrm{T}} - \overline{\delta\mathbf{q}}^{\mathrm{T}}\tilde{\mathbf{\Omega}} - \overline{\delta\boldsymbol{\psi}}^{\mathrm{T}}\tilde{\mathbf{V}}\right)\mathbf{P} + \left(\dot{\underline{\overline{\delta\boldsymbol{\psi}}}}^{\mathrm{T}} - \overline{\delta\boldsymbol{\psi}}^{\mathrm{T}}\tilde{\mathbf{\Omega}}\right)\mathbf{H} \\ &- \left[\underline{\overline{\delta\mathbf{q}}}'^{\mathrm{T}} - \overline{\delta\mathbf{q}}^{\mathrm{T}}\tilde{\mathbf{K}} - \overline{\delta\boldsymbol{\psi}}^{\mathrm{T}}\left(\tilde{\mathbf{e}}_1 + \tilde{\boldsymbol{\gamma}}\right)\right]\mathbf{F} - \left[\underline{\overline{\delta\boldsymbol{\psi}}}'^{\mathrm{T}} - \overline{\delta\boldsymbol{\psi}}^{\mathrm{T}}\tilde{\mathbf{K}}\right]\mathbf{M}\end{aligned} \tag{3.59}$$

$$+\overline{\delta\mathbf{q}}^{\mathrm{T}}\mathbf{f}+\overline{\delta\boldsymbol{\psi}}^{\mathrm{T}}\mathbf{m}\Big\}\ \mathrm{d}x_1\mathrm{d}t=\int_0^l\left(\overline{\delta\mathbf{q}}^{\mathrm{T}}\hat{\mathbf{P}}+\overline{\delta\boldsymbol{\psi}}^{\mathrm{T}}\hat{\mathbf{H}}\right)|_{t_1}^{t_2}\ \mathrm{d}x_1-\int_{t_1}^{t_2}\left(\overline{\delta\mathbf{q}}^{\mathrm{T}}\hat{\mathbf{F}}+\overline{\delta\boldsymbol{\psi}}^{\mathrm{T}}\hat{\mathbf{M}}\right)|_0^l\ \mathrm{d}t$$

The double underlined terms in Eq. 3.59 are integrated by parts in time while the single underlined terms are integrated by parts in space to yield

$$\int_{t_1}^{t_2}\int_0^l\Big\{\overline{\delta\mathbf{q}}^{\mathrm{T}}\left(\mathbf{F}'+\tilde{\mathbf{K}}\mathbf{F}+\mathbf{f}-\dot{\mathbf{P}}-\tilde{\Omega}\mathbf{P}\right) \tag{3.60}$$

$$+\overline{\delta\boldsymbol{\psi}}^{\mathrm{T}}\left[\mathbf{M}'+\tilde{\mathbf{K}}\mathbf{M}+(\tilde{\mathbf{e}}_1+\tilde{\boldsymbol{\gamma}})\mathbf{F}+\mathbf{m}-\dot{\mathbf{H}}-\tilde{\Omega}\mathbf{H}-\tilde{\mathbf{V}}\mathbf{P}\right]\Big\}\ \mathrm{d}x_1\mathrm{d}t=$$

$$\underbrace{\int_0^l\left[\overline{\delta\mathbf{q}}^{\mathrm{T}}(\hat{\mathbf{P}}-\mathbf{P})+\overline{\delta\boldsymbol{\psi}}^{\mathrm{T}}(\hat{\mathbf{H}}-\mathbf{H})\right]|_{t_1}^{t_2}\ \mathrm{d}x_1}_{0}-\overbrace{\int_{t_1}^{t_2}\left[\overline{\delta\mathbf{q}}^{\mathrm{T}}(\hat{\mathbf{F}}-\mathbf{F})+\overline{\delta\boldsymbol{\psi}}^{\mathrm{T}}(\hat{\mathbf{M}}-\mathbf{M})\right]|_0^l\ \mathrm{d}t}^{0}$$

where the under-braced term is zero since the virtual quantities vanish at the beginning and at the end of the path while in the case of over-braced ones, the quantities $\mathbf{F}$ and $\mathbf{M}$ assume the values of the boundary hatted terms at l and 0.

Since the virtual quantities, $\overline{\delta\mathbf{q}}$ and $\overline{\delta\boldsymbol{\psi}}$, are arbitrary in Eq. 3.60, the intrinsic dynamics equations of a moving beam are then

$$\mathbf{F}'+\tilde{\mathbf{K}}\mathbf{F}+\mathbf{f}\ =\ \dot{\mathbf{P}}+\tilde{\Omega}\mathbf{P} \tag{3.61}$$

$$\mathbf{M}'+\tilde{\mathbf{K}}\mathbf{M}+(\tilde{\mathbf{e}}_1+\tilde{\boldsymbol{\gamma}})\,\mathbf{F}+\mathbf{m}\ =\ \dot{\mathbf{H}}+\tilde{\Omega}\mathbf{H}+\tilde{\mathbf{V}}\mathbf{P} \tag{3.62}$$

To complete the formulation [135], Eq. 3.27 is differentiated with respect to time while Eq. 3.43 is differentiated with respect to x_1 to yield

$$\dot{\boldsymbol{\gamma}}=\dot{\mathcal{C}}^{\mathbf{Bb}}(\mathbf{e}_1+\mathbf{u}_b'+\widetilde{\mathbf{k}}\mathbf{u}_b)+\mathcal{C}^{\mathbf{Bb}}(\dot{\mathbf{u}}_b'+\widetilde{\mathbf{k}}\dot{\mathbf{u}}_b) \tag{3.63}$$

$$\mathbf{V}' = \mathcal{C}^{\mathbf{Bb}'}(\mathbf{v} + \dot{\mathbf{u}}_\mathbf{b} + \tilde{\boldsymbol{\omega}}\mathbf{u}_\mathbf{b}) + \mathcal{C}^{\mathbf{Bb}}(\mathbf{v}' + \dot{\mathbf{u}}'_\mathbf{b} + \tilde{\boldsymbol{\omega}}'\mathbf{u}_\mathbf{b} + \tilde{\boldsymbol{\omega}}\mathbf{u}'_\mathbf{b}) \tag{3.64}$$

Subtracting Eq. 3.63 from Eq. 3.64 yields

$$\begin{aligned}\mathbf{V}' - \dot{\boldsymbol{\gamma}} = \mathcal{C}^{\mathbf{Bb}'}(\mathbf{v} + \dot{\mathbf{u}}_\mathbf{b} + \tilde{\boldsymbol{\omega}}\mathbf{u}_\mathbf{b}) + \mathcal{C}^{\mathbf{Bb}}(\mathbf{v}' + \dot{\mathbf{u}}'_\mathbf{b} + \\ \tilde{\boldsymbol{\omega}}'\mathbf{u}_\mathbf{b} + \tilde{\boldsymbol{\omega}}\mathbf{u}'_\mathbf{b}) - \dot{\mathcal{C}}^{\mathbf{Bb}}(\mathbf{e}_1 + \mathbf{u}'_b + \widetilde{\mathbf{k}}\mathbf{u}_b) - \mathcal{C}^{\mathbf{Bb}}(\dot{\mathbf{u}}'_b + \widetilde{\mathbf{k}}\dot{\mathbf{u}}_b)\end{aligned} \tag{3.65}$$

Performing a series of algebraic manipulations given in Appendix B yields

$$\dot{\boldsymbol{\gamma}} = \mathbf{V}' + \tilde{\mathbf{K}}\mathbf{V} + (\tilde{\boldsymbol{\gamma}} + \tilde{\mathbf{e}}_1) \tag{3.66}$$

Furthermore, differentiating Eq. 3.23 with respect to time while differentiating Eq. 3.44 with respect to x_1 yields

$$\dot{\tilde{\boldsymbol{\kappa}}} = -\dot{\mathcal{C}}^{\mathbf{Bb}'}\mathcal{C}^{\mathbf{Bb}^\mathrm{T}} - \mathcal{C}^{\mathbf{Bb}'}\dot{\mathcal{C}}^{\mathbf{Bb}^\mathrm{T}} + \dot{\mathcal{C}}^{\mathbf{Bb}}\tilde{\mathbf{k}}\mathcal{C}^{\mathbf{Bb}^\mathrm{T}} + \mathcal{C}^{\mathbf{Bb}}\tilde{\mathbf{k}}\dot{\mathcal{C}}^{\mathbf{Bb}^\mathrm{T}} \tag{3.67}$$

$$\tilde{\boldsymbol{\Omega}}' = -\dot{\mathcal{C}}^{\mathbf{Bb}'}\mathcal{C}^{\mathbf{Bb}^\mathrm{T}} - \dot{\mathcal{C}}^{\mathbf{Bb}}\mathcal{C}^{\mathbf{Bb}'^\mathrm{T}} + \mathcal{C}^{\mathbf{Bb}'}\tilde{\boldsymbol{\omega}}\mathcal{C}^{\mathbf{Bb}^\mathrm{T}} + \mathcal{C}^{\mathbf{Bb}}\tilde{\boldsymbol{\omega}}'\mathcal{C}^{\mathbf{Bb}^\mathrm{T}} + \mathcal{C}^{\mathbf{Bb}}\tilde{\boldsymbol{\omega}}\mathcal{C}^{\mathbf{Bb}'^\mathrm{T}} \tag{3.68}$$

Subtracting Eq. 3.67 from Eq. 3.68 and simplifying, as demonstrated in Appendix B, leads to

$$\tilde{\boldsymbol{\Omega}}' - \dot{\tilde{\boldsymbol{\kappa}}} = \tilde{\boldsymbol{\Omega}}\left(\tilde{\boldsymbol{\kappa}} + \tilde{\mathbf{k}}\right) - \left(\tilde{\boldsymbol{\kappa}} + \tilde{\mathbf{k}}\right)\tilde{\boldsymbol{\Omega}} \tag{3.69}$$

Invoking property B.10 in Appendix B of the skew-symmetric operator for the right hand side of Eq. 3.69 yields

$$\dot{\tilde{\boldsymbol{\kappa}}} = -\widetilde{\tilde{\boldsymbol{\Omega}}\mathbf{K}} + \tilde{\boldsymbol{\Omega}}' \tag{3.70}$$

Finally, invoking property B.7 in Appendix B of the skew-symmetric operator yields

$$\dot{\boldsymbol{\kappa}} = \boldsymbol{\Omega}' + \tilde{\mathbf{K}}\boldsymbol{\Omega} \tag{3.71}$$

The set of equations composed of Eqs. 3.61, 3.62, 3.66, and 3.71 represent the intrinsic dynamics equations of initially curved and twisted moving beams.

In this investigation, the secondary variables $\boldsymbol{\gamma}$, $\boldsymbol{\kappa}$, $\mathbf{P}$, and $\mathbf{H}$ are expressed in terms of the primary variables $\mathbf{F}$, $\mathbf{M}$, $\mathbf{V}$, and $\boldsymbol{\Omega}$ using the cross-sectional constitutive relations developed and discussed in Chapter 2, i.e.,

$$\begin{bmatrix} \boldsymbol{\gamma} \\ \boldsymbol{\kappa} \end{bmatrix} = \begin{bmatrix} R & S \\ S^{\mathrm{T}} & T \end{bmatrix} \left\{ \begin{bmatrix} \mathbf{F} \\ \mathbf{M} \end{bmatrix} - \begin{bmatrix} \mathbf{F}^{(a)} \\ \mathbf{M}^{(a)} \end{bmatrix} \right\} \tag{3.72}$$

$$\begin{bmatrix} \mathbf{P} \\ \mathbf{H} \end{bmatrix} = \begin{bmatrix} D & Q \\ -Q & I \end{bmatrix} \begin{bmatrix} \mathbf{V} \\ \boldsymbol{\Omega} \end{bmatrix} \tag{3.73}$$

where the 3×3 submatrices R, S, and T are constructed from the asymptotically-correct Timoshenko-like cross-sectional stiffness matrix or an extended 4×4 classical-like one. The asymptotically-correct 6×1, or the extended 4×1 active traction vector whose entries are denoted by the superscript 'a' is due to any embedded active material in the beam such as MFCs or shape memory alloys. The 3×3 submatrices D, Q, and I represent the mass per unit length, the offset of the cross-sectional mass centre from the beam reference line, and the cross-sectional mass inertia terms respectively.

The conditions under which the extended 4×4 classical-like stiffness matrix and the extended 4×1 actuation vector can be used in place of their corresponding 6×6 and

6×1 counterparts were discussed in Chapter 2. If it is decided to use the 4×4 stiffness matrix, then the elements corresponding to the shear stiffness/flexibility are filled with zero elements in the flexibility matrix and the actuation vector.

An explicit expression of the linear 2-D cross-sectional inertia matrix is given by

$$\begin{bmatrix} D & Q \\ -Q & I \end{bmatrix} = \begin{bmatrix} \bar{m} & 0 & 0 & 0 & \bar{m}\bar{x}_3 & -\bar{m}\bar{x}_2 \\ 0 & \bar{m} & 0 & -\bar{m}\bar{x}_3 & 0 & 0 \\ 0 & 0 & \bar{m} & \bar{m}\bar{x}_2 & 0 & 0 \\ 0 & -\bar{m}\bar{x}_3 & \bar{m}\bar{x}_2 & \bar{I}_1 & 0 & 0 \\ \bar{m}\bar{x}_3 & 0 & 0 & 0 & \bar{I}_2 & \bar{I}_{23} \\ -\bar{m}\bar{x}_2 & 0 & 0 & 0 & \bar{I}_{23} & \bar{I}_3 \end{bmatrix} \tag{3.74}$$

where $\bar{x}_2, \bar{x}_3$ is the location of the mass centre relative to the beam reference line; $\bar{I}_1 = \bar{I}_2 + \bar{I}_3$ is the cross-sectional moment of inertia per unit length about the x_1 axis; $\bar{I}_2$ is the cross-sectional moment of inertia per unit length about the x_2 axis; $\bar{I}_3$ is the cross-sectional moment of inertia per unit length about the x_3 axis; and $\bar{I}_{23}$ is the cross-sectional product of inertia per unit length.

3.4.1 Intrinsic Structural Damping

In order to include structural damping in the geometrically-exact intrinsic beam element formulation, the terms representing the externally applied loads $\mathbf{f}$ and $\mathbf{m}$, which stem from the virtual work of the nonconservative forces, in Eqs. 3.57, 3.61, and 3.62 are separated into the structural damping loads and other external loads, where the damping loads are proportional to the rate of change of strains such that

$$\begin{bmatrix} \mathbf{f}_d \\ \mathbf{m}_d \end{bmatrix} \propto - \begin{bmatrix} \dot{\boldsymbol{\gamma}} \\ \dot{\boldsymbol{\kappa}} \end{bmatrix} \Rightarrow \begin{bmatrix} \mathbf{f}_d \\ \mathbf{m}_d \end{bmatrix} = -\mathbb{C} \begin{bmatrix} \dot{\boldsymbol{\gamma}} \\ \dot{\boldsymbol{\kappa}} \end{bmatrix} \tag{3.75}$$

where $\mathbf{f}_d$ and $\mathbf{m}_d$ are the damping force and moment vectors per unit volume, and $\mathbb{C}$ is the damping matrix.

Assuming Rayleigh structural damping in the beam, the damping proportionality matrix is written in terms of the mass and the stiffness matrix such that

$$\mathbb{C} = \bar{\eta} \begin{bmatrix} D & Q \\ -Q & I \end{bmatrix} + \bar{\delta} \begin{bmatrix} R & S \\ S^{\mathrm{T}} & T \end{bmatrix}^{-1} \tag{3.76}$$

where the parameters $\bar{\eta}$ and $\bar{\delta}$ control the level of damping of the low and high frequency modes respectively [136].

Using Eq. 3.72 to rewrite Eq. 3.75 in terms of the primary variables, Eq. 3.76 is employed to express the structural damping per unit length as:

$$\begin{bmatrix} \mathbf{f}_d \\ \mathbf{m}_d \end{bmatrix} = - \left(\bar{\eta} \begin{bmatrix} D & Q \\ -Q & I \end{bmatrix} \begin{bmatrix} R & S \\ S^{\mathrm{T}} & T \end{bmatrix} + \bar{\delta} \underline{\triangle}_{6\times 6} \right) \begin{bmatrix} \dot{\mathbf{F}} \\ \dot{\mathbf{M}} \end{bmatrix} = \begin{bmatrix} J & N \\ B & W \end{bmatrix} \begin{bmatrix} \dot{\mathbf{F}} \\ \dot{\mathbf{M}} \end{bmatrix} \tag{3.77}$$

where $\underline{\triangle}_{6\times 6}$ is the 6×6 identity matrix.

Substituting Eqs. 3.72, 3.73, and 3.77 into the four intrinsic equations given in Eqs. 3.61, 3.62 , 3.66, and 3.71 yields the intrinsic dynamics equations of a moving active beam with initial twist and curvature in terms of the primary variables as

$$-(D \cdot \dot{\mathbf{V}} + Q \cdot \dot{\boldsymbol{\Omega}}) - J\dot{\mathbf{F}} - N\dot{\mathbf{M}} + \mathbf{F}' + [S^{\mathrm{T}} \cdot (\mathbf{F} - \mathbf{F}^{(a)}) + \widetilde{T \cdot (\mathbf{M} - \mathbf{M}^{(a)})} + \mathbf{k}] \cdot \mathbf{F} \tag{3.78}$$

$$+\mathbf{f} - \widetilde{\boldsymbol{\Omega}} \cdot (D \cdot \mathbf{V} + Q \cdot \boldsymbol{\Omega}) = 0$$

$$-(-Q \cdot \dot{\mathbf{V}} + I \cdot \dot{\boldsymbol{\Omega}}) - B\dot{\mathbf{F}} - W\dot{\mathbf{M}} + \mathbf{M}' + [S^{\mathrm{T}} \cdot (\mathbf{F} - \mathbf{F}^{(a)}) \widetilde{+ T \cdot (\mathbf{M} - \mathbf{M}^{(a)})} + \mathbf{k}] \cdot \mathbf{M} \quad (3.79)$$

$$+[\mathbf{e}_1 + R \cdot (\mathbf{F} - \widetilde{\mathbf{F}^{(a)}) + S \cdot (\mathbf{M} - \mathbf{M}^{(a)})}] \cdot \mathbf{F} + \mathbf{m} - \widetilde{\boldsymbol{\Omega}} \cdot (-Q \cdot \mathbf{V} + I \cdot \boldsymbol{\Omega})$$

$$-\widetilde{V}(D \cdot \mathbf{V} + Q \cdot \boldsymbol{\Omega}) = 0$$

$$-(S^{\mathrm{T}} \cdot \dot{\mathbf{F}} + T \cdot \dot{\mathbf{M}}) + \boldsymbol{\Omega}' + (S^{\mathrm{T}} \cdot \dot{\mathbf{F}}^{(a)} + T \cdot \dot{\mathbf{M}}^{(a)}) \quad (3.80)$$

$$+[S^{\mathrm{T}} \cdot (\mathbf{F} - \mathbf{F}^{(a)}) \widetilde{+ T \cdot} (\mathbf{M} - \mathbf{M}^{(a)}) + \mathbf{k}] \cdot \boldsymbol{\Omega} = 0$$

$$-(R \cdot \dot{\mathbf{F}} + S \cdot \dot{\mathbf{M}}) + \mathbf{V}' + (R \cdot \dot{\mathbf{F}}^{(a)} + S \cdot \dot{\mathbf{M}}^{(a)}) + [S^{\mathrm{T}} \cdot (\mathbf{F} - \mathbf{F}^{(a)}) \widetilde{+ T \cdot} (\mathbf{M} - \mathbf{M}^{(a)}) + \mathbf{k}] \cdot \mathbf{V} \quad (3.81)$$

$$+[\mathbf{e}_1 + R \cdot (\mathbf{F} - \widetilde{\mathbf{F}^{(a)}) + S \cdot (\mathbf{M} - \mathbf{M}^{(a)})}] \cdot \boldsymbol{\Omega} = 0$$

The compactness and the symbolic nature of the above equations is contrasted to conventional nonlinear passive beam equations that usually take several pages to write.

3.4.2 Intrinsic Conservation Laws

Conservation/invariant laws are important in nonlinear elastodynamics in order to assess the feasibility of a proposed time marching scheme and check for potential errors in the solution. Furthermore, they may be used to develop adaptive solution schemes in time. To carry out potential numerical assessments, the passive and undamped problem is usually of interest. As outlined in [135] and expounded herein, the derivation of two intrinsic

conservational laws for moving beams with initial twist and curvature starts from the definition of the kinetic and elastic energy per unit length as

$$\begin{aligned}\mathcal{T} &= \frac{1}{2}\begin{bmatrix}\mathbf{V}\\ \boldsymbol{\Omega}\end{bmatrix}^{\mathrm{T}}\begin{bmatrix}D & Q\\ -Q & I\end{bmatrix}\begin{bmatrix}\mathbf{V}\\ \boldsymbol{\Omega}\end{bmatrix}\\ \mathcal{U} &= \frac{1}{2}\begin{bmatrix}\boldsymbol{\gamma}\\ \boldsymbol{\kappa}\end{bmatrix}^{\mathrm{T}}\begin{bmatrix}R & S\\ S^{\mathrm{T}} & T\end{bmatrix}^{-1}\begin{bmatrix}\boldsymbol{\gamma}\\ \boldsymbol{\kappa}\end{bmatrix}\end{aligned} \tag{3.82}$$

Pre-multiplying Eq. 3.61 by $\mathbf{V}^{\mathrm{T}}$ and Eq. 3.62 by $\boldsymbol{\Omega}^{\mathrm{T}}$, then adding them, and finally integrating them along the beam span and from time t_1 to time t_2 yields

$$\begin{aligned}\int_{t_1}^{t_2}\int_0^l \Big\{\mathbf{V}^{\mathrm{T}}\left(\underline{\mathbf{F}'}+\tilde{\mathbf{K}}\mathbf{F}+\mathbf{f}-\underline{\dot{\mathbf{P}}}-\tilde{\boldsymbol{\Omega}}\mathbf{P}\right)+\boldsymbol{\Omega}^{\mathrm{T}}\Big[\underline{\mathbf{M}'}+\tilde{\mathbf{K}}\mathbf{M}+(\tilde{\mathbf{e}}_1+\tilde{\boldsymbol{\gamma}})\,\mathbf{F}+\mathbf{m}\\ -\underline{\dot{\mathbf{H}}}-\tilde{\boldsymbol{\Omega}}\mathbf{H}-\tilde{\mathbf{V}}\mathbf{P}\Big]\Big\}\,\mathrm{d}x_1\mathrm{d}t=0\end{aligned} \tag{3.83}$$

Expanding and integrating the underlined terms by parts in space and the double underlined ones in time yields

$$\begin{aligned}&\int_{t_1}^{t_2}\int_0^l \left\{-\mathbf{V}'^{\mathrm{T}}\mathbf{F}-\boldsymbol{\Omega}'^{\mathrm{T}}\mathbf{M}+\mathbf{V}^{\mathrm{T}}\left(\tilde{\mathbf{K}}\mathbf{F}+\mathbf{f}\right)+\boldsymbol{\Omega}^{\mathrm{T}}\left[\tilde{\mathbf{K}}\mathbf{M}+(\tilde{\mathbf{e}}_1+\tilde{\boldsymbol{\gamma}})\,\mathbf{F}+\mathbf{m}\right]\right\}\,\mathrm{d}x_1\mathrm{d}t\\ &\qquad+\int_{t_1}^{t_2}\left(\mathbf{V}^{\mathrm{T}}\mathbf{F}+\boldsymbol{\Omega}^{\mathrm{T}}\mathbf{M}\right)\,\mathrm{d}t|_0^l\,\mathrm{d}t\\ &+\int_{t_1}^{t_2}\int_0^l\left\{\dot{\mathbf{V}}^{\mathrm{T}}\mathbf{P}+\dot{\boldsymbol{\Omega}}^{\mathrm{T}}\mathbf{H}-\underline{\mathbf{V}^{\mathrm{T}}\tilde{\boldsymbol{\Omega}}\mathbf{P}}-\underbrace{\underline{\boldsymbol{\Omega}^{\mathrm{T}}\tilde{\boldsymbol{\Omega}}\mathbf{H}}}_{0}-\underline{\boldsymbol{\Omega}^{\mathrm{T}}\tilde{\mathbf{V}}\mathbf{P}}\right\}\,\mathrm{d}x_1\mathrm{d}t\end{aligned} \tag{3.84}$$

$$\underline{\underline{-\int_0^l \left(\mathbf{V}^{\mathrm{T}}\mathbf{P}+\boldsymbol{\Omega}^{\mathrm{T}}\mathbf{H}\right)|_{t_1}^{t_2}\,\mathrm{d}x_1}}=0$$

The underlined terms cancel each other out because of property B.7 in Appendix B of the skew-symmetric operator. Similarly, the under-braced term is zero due to another property, B.6, of the skew-symmetric operator. The double underlined term is rewritten as

$$-\int_0^l \left(\mathbf{V}^{\mathrm{T}}\mathbf{P}+\boldsymbol{\Omega}^{\mathrm{T}}\mathbf{H}\right)|_{t_1}^{t_2}\,\mathrm{d}x_1=-\frac{1}{2}\int_0^l \left(\mathbf{V}^{\mathrm{T}}P+\boldsymbol{\Omega}^{\mathrm{T}}\mathbf{H}\right)|_{t_1}^{t_2}\,\mathrm{d}x_1-\frac{1}{2}\int_0^l\int_{t_1}^{t_2}\left(\mathbf{V}^{\mathrm{T}}\mathbf{P}+\boldsymbol{\Omega}^{\mathrm{T}}\mathbf{H}\right)^{\bullet}\,\mathrm{d}t\,\mathrm{d}x_1 \tag{3.85}$$

where the bullet superscript implies time differentiation of a whole expression.

As demonstrated in Appendix B, the second term of Eq. 3.73 can be written as

$$-\frac{1}{2}\int_0^l\int_{t_1}^{t_2}\left(\mathbf{V}^{\mathrm{T}}\mathbf{P}+\boldsymbol{\Omega}^{\mathrm{T}}\mathbf{H}\right)^{\bullet}\,\mathrm{d}t\mathrm{d}x_1=-\int_{t_1}^{t_2}\int_0^l\left(\dot{\mathbf{V}}^{\mathrm{T}}\mathbf{P}+\dot{\boldsymbol{\Omega}}^{\mathrm{T}}\mathbf{H}\right)\,\mathrm{d}x_1\mathrm{d}t \tag{3.86}$$

Substitution of Eqs. 3.86, and 3.85, and the kinetic energy expression of Eq. 3.82 into Eq. 3.84 yields

$$\int_{t_1}^{t_2}\int_0^l\left\{-\mathbf{V}'^{\mathrm{T}}\mathbf{F}+\mathbf{V}^{\mathrm{T}}\left[\tilde{\mathbf{K}}\mathbf{F}+\mathbf{f}\right]-\boldsymbol{\Omega}'^{\mathrm{T}}\mathbf{M}+\boldsymbol{\Omega}^{\mathrm{T}}\left[\tilde{\mathbf{K}}\mathbf{M}+\left(\tilde{\mathbf{e}}_1+\tilde{\boldsymbol{\gamma}}\right)\mathbf{F}+\mathbf{m}\right]\right\}\,\mathrm{d}x_1\mathrm{d}t \tag{3.87}$$

$$+\int_{t_1}^{t_2}\left(\mathbf{V}^{\mathrm{T}}\mathbf{F}+\boldsymbol{\Omega}^{\mathrm{T}}\mathbf{M}\right)\,\mathrm{d}t|_0^l-\int_0^l\mathcal{T}\,\mathrm{d}x_1=0$$

Using Eqs. 3.66 and 3.71 to eliminate $\mathbf{V}'$ and $\boldsymbol{\Omega}'$ respectively in Eq. 3.87 produces a series of obvious cancelations, rendering Eq. 3.87 to read

$$\int_{t_1}^{t_2}\int_0^l \left\{-\dot{\boldsymbol{\gamma}}^{\mathrm{T}}\mathbf{F} - \dot{\boldsymbol{\kappa}}^{\mathrm{T}}\mathbf{M} + \mathbf{V}^{\mathrm{T}}\mathbf{f} + \boldsymbol{\Omega}^{\mathrm{T}}\mathbf{m}\right\}\, \mathrm{d}x_1\mathrm{d}t \tag{3.88}$$

$$+\int_{t_1}^{t_2}\left(\mathbf{V}^{\mathrm{T}}\mathbf{F} + \boldsymbol{\Omega}^{\mathrm{T}}\mathbf{M}\right)\, \mathrm{d}t|_0^l - \int_0^l \mathcal{T}\, \mathrm{d}x_1 = 0$$

Similar to the derivation of Eq. 3.86 and from the constitutive relation of Eq. 3.73 one can write

$$\int_{t_1}^{t_2}\int_0^l -\dot{\boldsymbol{\gamma}}^{\mathrm{T}}\mathbf{F} - \dot{\boldsymbol{\kappa}}^{\mathrm{T}}\mathbf{M}\, \mathrm{d}x_1\mathrm{d}t = \int_0^l -\mathcal{U}\, \mathrm{d}x_1|_{t_1}^{t_2} \tag{3.89}$$

Substitution of Eq. 3.89 into Eq. 3.88 yields the final sought form of the intrinsic conservation law

$$\int_{t_1}^{t_2}\int_0^l \left\{\mathbf{V}^{\mathrm{T}}\mathbf{f} + \boldsymbol{\Omega}^{\mathrm{T}}\mathbf{m}\right\}\, \mathrm{d}x_1\mathrm{d}t + \int_{t_1}^{t_2}\left(\mathbf{V}^{\mathrm{T}}\mathbf{F} + \boldsymbol{\Omega}^{\mathrm{T}}\mathbf{M}\right)\, \mathrm{d}t|_0^l = \int_0^l (\mathcal{T}+\mathcal{U})\, \mathrm{d}x_1|_{t_1}^{t_2} \tag{3.90}$$

Eq. 3.90 states that for a time interval between t_1 and t_2, the work done by the applied body forces, which is represented by the first term on the left hand side, plus the work done by the forces at both ends of the beam, which is represented by the second term on the left hand side, equals to the change in the total mechanical energy of the system in that time interval.

In a similar fashion, a second intrinsic conservation law, which expectedly reflects the impulse-momentum principle, is derived by pre-multiplying Eq. 3.61 by $(\mathbf{e}_1 + \boldsymbol{\gamma})^{\mathrm{T}}$ and Eq. 3.62 by $\mathbf{K}^{\mathrm{T}}$ then adding them followed by integration along the beam span and from time t_1 to time t_2 to yield

$$\int_{t_1}^{t_2}\int_0^l \left\{(\mathbf{e}_1+\boldsymbol{\gamma})^{\mathrm{T}}\left(\underline{\mathbf{F}'}+\tilde{\mathbf{K}}\mathbf{F}+\mathbf{f}-\underline{\underline{\dot{\mathbf{P}}}}-\tilde{\boldsymbol{\Omega}}\mathbf{P}\right)+\mathbf{K}^{\mathrm{T}}\left[\underline{\mathbf{M}'}+\tilde{\mathbf{K}}\mathbf{M}+(\tilde{\mathbf{e}}_1+\tilde{\boldsymbol{\gamma}})\,\mathbf{F}+\mathbf{m}\right.\right. \tag{3.91}$$

$$\left.\left.-\underline{\underline{\dot{\mathbf{H}}}}-\tilde{\boldsymbol{\Omega}}\mathbf{H}-\tilde{\mathbf{V}}\mathbf{P}\right]\right\}\,\mathrm{d}x_1\mathrm{d}t=0$$

Similar to the derivation of the first conservation law, the underlined terms are integrated by parts while utilizing the constitutive relations in Eq. 3.72 to give

$$\int_{t_1}^{t_2}\int_0^l \left[\dot{\boldsymbol{\gamma}}^{\mathrm{T}}\mathbf{P}+\dot{\boldsymbol{\kappa}}^{\mathrm{T}}\mathbf{H}+(\mathbf{e}_1+\boldsymbol{\gamma})^{\mathrm{T}}\left(\mathbf{f}-\tilde{\boldsymbol{\Omega}}\mathbf{P}\right)\right. \tag{3.92}$$

$$\left.+\mathbf{K}^{\mathrm{T}}\left(\mathbf{m}-\tilde{\boldsymbol{\Omega}}\mathbf{H}-\tilde{\mathbf{V}}\mathbf{P}\right)\right]\,\mathrm{d}x_1\mathrm{d}t+\int_{t_1}^{t_2}\left(\mathbf{e}_1^{\mathrm{T}}\mathbf{F}+\mathbf{k}^{\mathrm{T}}\mathbf{M}+\mathcal{U}\right)\,\mathrm{d}t\Big|_0^l$$

$$-\int_0^l\left[(\mathbf{e}_1+\boldsymbol{\gamma})^{\mathrm{T}}\mathbf{P}+\mathbf{K}^{\mathrm{T}}\mathbf{H}\right]\,\mathrm{d}x_1\Big|_{t_1}^{t_2}=0$$

Using Eq. 3.66 and Eq. 3.71 to eliminate $\dot{\boldsymbol{\gamma}}$ and $\dot{\boldsymbol{\kappa}}$ respectively in Eq. 3.92 yields the desired form of the generalized impulse-momentum conservation law

$$\int_{t_1}^{t_2}\int_0^{\ell}\left[(\mathbf{e}_1+\boldsymbol{\gamma})^{\mathrm{T}}\cdot\mathbf{f}+\boldsymbol{\kappa}^{\mathrm{T}}\cdot\mathbf{m}\right]\,\mathrm{d}x_1\,\mathrm{d}t+\int_{t_1}^{t_2}\left(\mathbf{e}_1^{\mathrm{T}}\cdot\mathbf{F}+\mathcal{U}+\mathcal{T}\right)\,\mathrm{d}t\Big|_0^{\ell}= \tag{3.93}$$

$$\int_0^{\ell}\left[(\mathbf{e}_1+\boldsymbol{\gamma})^{\mathrm{T}}\cdot\mathbf{P}+\boldsymbol{\kappa}^{\mathrm{T}}\cdot\mathbf{H}\right]\,\mathrm{d}x_1\Big|_{t_1}^{t_2}$$

The first term on the left hand side of Eq. 3.93 represents the impulse of the applied body forces and moments while the second one relates to the impulse at the ends of the beam. The term on the right hand side represents the change in generalized momentum over the time interval.

3.5 Intrinsic Multibody Formulation of Active Rotor Systems in a Non-Inertial Frame

The presented intrinsic dynamics equations are sufficient to model hingeless active rotor systems like the one shown in Fig. 3.3. However, in order to be capable of modelling more general rotor blade system configurations, like the fully articulated one shown in Fig. 3.4, the intrinsic model must be augmented with the corresponding dynamics model of the articulation mechanism. Moreover, the operation of the rotor system from the non-inertial frame of the ship as idealized in Fig. 3.5 must be accounted for. If one idealizes that the articulation joints to be simple revolute joints, which is a realistic assumption, then the nonlinear intrinsic dynamics model of the articulation mechanism based on the Newton-Euler formulation expressed in the body frame is

$$\breve{\mathbf{C}}\frac{\partial \mathcal{X}_2}{\partial t} + \mathcal{G}(\mathcal{X}_2, \sum \mathbf{F}_1, \sum \mathbf{M}_1, \sum \mathbf{F}_2, \sum \mathbf{M}_2) = \mathbf{0} \tag{3.94}$$

where the state vector $\mathcal{X}_2$ is composed of the inertial angular and linear velocities at the centre of mass of the articulation rigid flap and lead-lag links in the body frame denoted with the subscripts 1 and 2 respectively such that

$$\mathcal{X}_2 = \begin{bmatrix} \boldsymbol{\Omega}_1 & \mathbf{V}_1 & \boldsymbol{\Omega}_2 & \mathbf{V}_2 \end{bmatrix}^{\mathrm{T}} \tag{3.95}$$

and the 12×12 coefficient matrix $\breve{\mathbf{C}}$ and the vector $\mathcal{G}$ are given by

$$\breve{\mathbf{C}} = \begin{bmatrix} \mathbb{I}_1 & 0_{3\times3} & 0_{3\times3} & 0_{3\times3} \\ 0_{3\times3} & m_1\underline{\triangle}_{3\times3} & 0_{3\times3} & 0_{3\times3} \\ 0_{3\times3} & 0_{3\times3} & \mathbb{I}_2 & 0_{3\times3} \\ 0_{3\times3} & 0_{3\times3} & 0_{3\times3} & m_2\underline{\triangle}_{3\times3} \end{bmatrix} \qquad \mathcal{G} = \begin{bmatrix} \widetilde{\Omega}_1\mathbb{I}_1\Omega_1 - c_{flap}\Omega_1 - \sum \mathbf{M}_1 \\ \widetilde{\Omega}_1 m_1 \mathbf{V}_1 - \sum \mathbf{F}_1 \\ \widetilde{\Omega}_2\mathbb{I}_2\Omega_2 - c_{lead-lag}\Omega_2 - \sum \mathbf{M}_2 \\ \widetilde{\Omega}_2 m_2 \mathbf{V}_2 - \sum \mathbf{F}_2 \end{bmatrix} \tag{3.96}$$

where $\mathbb{I}_1$, m_1, $\mathbb{I}_2$, and m_2 are the mass inertia tensor and the mass of the flap and the lead-lag links respectively, while c_{flap} and $c_{lead-lag}$ are the flap and lead-lag viscous damping coefficients respectively.

Moreover, $\sum \mathbf{M}_1$, $\sum \mathbf{F}_1$, $\sum \mathbf{M}_2$, and $\sum \mathbf{F}_2$ are the resultants of the external forces and moments acting on the flap and lead-lag links resulting from gravitational forces, backlash forces, forces and moments from the flexible blade, and finally the joints' reaction forces and moments.

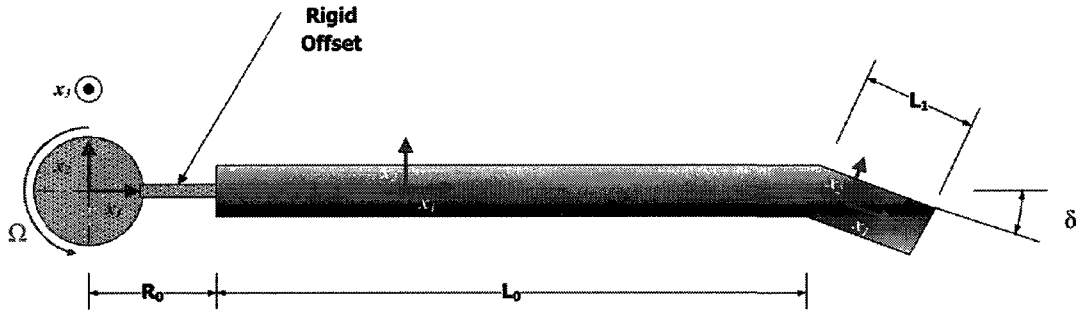

Figure 3.3: Top view of hingeless rotor system.

The state variables in Eq. 3.95, which are the time derivatives of a set of quasi-coordinates, are related to the angular velocities of the joints and the hub through the following driving kinematic constraints

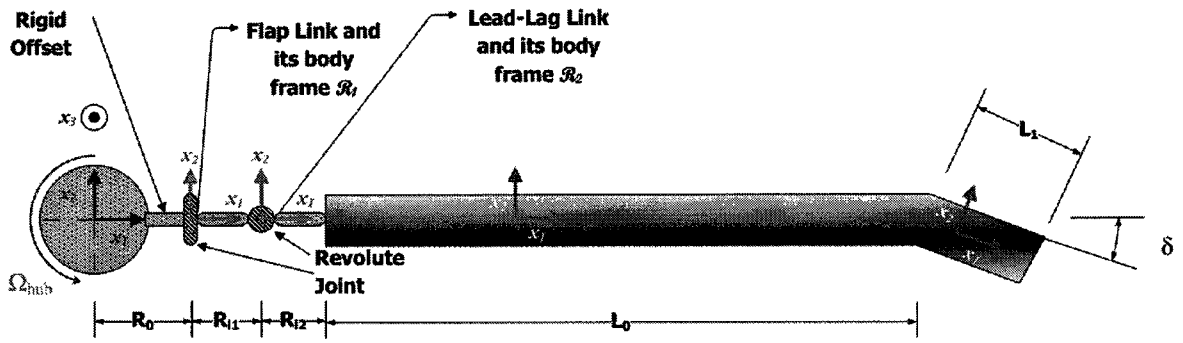

Figure 3.4: Top view of fully articulated rotor system.

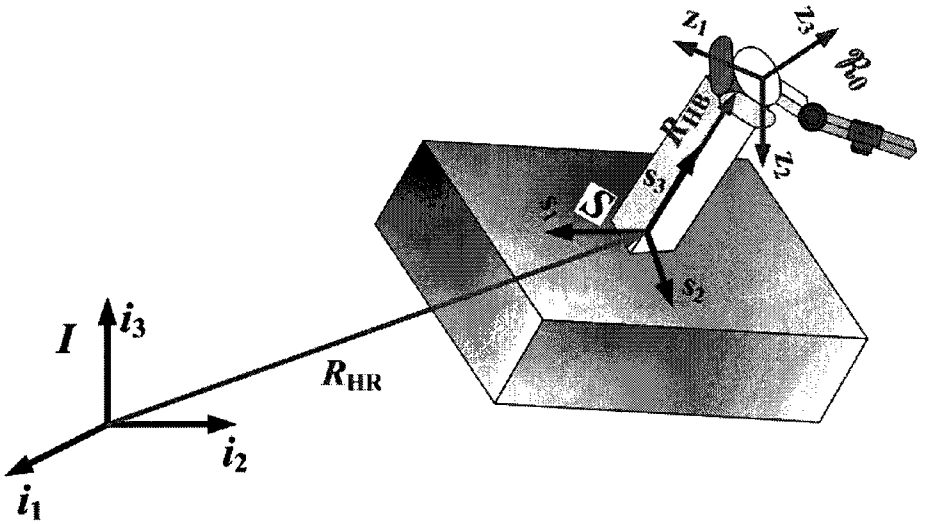

Figure 3.5: Simple and representative multibody dynamics model of the hub system in the non-inertial frame of a moving ship.

$$\boldsymbol{\Omega}_1 = \mathcal{C}^{\mathcal{R}_1\mathcal{R}_0}\mathcal{C}^{\mathcal{R}_0\mathcal{S}}\mathcal{C}^{\mathcal{S}I}\boldsymbol{\Omega}_{ship} + \mathcal{C}^{\mathcal{R}_1\mathcal{R}_0}\boldsymbol{\Omega}_{hub} + \boldsymbol{\Omega}_{flap} \tag{3.97}$$

$$\mathbf{V}_1 = \mathcal{C}^{\mathcal{R}_1\mathcal{R}_0}\mathbf{V}_z + \tilde{\boldsymbol{\Omega}}_1\mathbf{R}_{cm1} \tag{3.98}$$

$$\boldsymbol{\Omega}_2 = \mathcal{C}^{\mathcal{R}_2\mathcal{R}_1}\mathcal{C}^{\mathcal{R}_1\mathcal{R}_0}\mathcal{C}^{\mathcal{R}_0\mathcal{S}}\mathcal{C}^{\mathcal{S}I}\boldsymbol{\Omega}_{ship} + \mathcal{C}^{\mathcal{R}_2\mathcal{R}_1}\mathcal{C}^{\mathcal{R}_1\mathcal{R}_0}\boldsymbol{\Omega}_{hub} + \mathcal{C}^{\mathcal{R}_2\mathcal{R}_1}\boldsymbol{\Omega}_{flap} + \boldsymbol{\Omega}_{lead-lag} \tag{3.99}$$

$$\mathbf{V}_2 = \mathcal{C}^{\mathcal{R}_2\mathcal{R}_1}\left[\mathbf{V}_1 + \tilde{\boldsymbol{\Omega}}_1\left(\mathbf{R}_{l1} - \mathbf{R}_{cm1}\right)\right] + \tilde{\boldsymbol{\Omega}}_2\mathbf{R}_{cm2} \tag{3.100}$$

where $\boldsymbol{\Omega}_{flap}$ is the flap hinge angular velocity, $\boldsymbol{\Omega}_{lead-lag}$ is the lead-lag hinge angular ve-

locity, $\mathbf{\Omega}_{hub}$ is the hub angular velocity, and $\mathbf{\Omega}_{ship}$ is the ship angular velocity in the ocean frame, $\mathbf{R}_0$ is the flap hinge position vector in the hub frame $\mathcal{R}_0$, $\mathbf{R}_{l1}$ is the lead-lag joint position vector in the flap link frame $\mathcal{R}_1$, $\mathbf{R}_{cm1}$ is the centre of mass position vector of the flap link in the $\mathcal{R}_1$ frame, $\mathbf{R}_{l2}$ is the blade root position vector in the lead-lag link frame $\mathcal{R}_2$, $\mathbf{R}_{cm2}$ is the centre of mass position vector of the lead-lag link in the $\mathcal{R}_2$ frame, $\mathcal{C}^{\mathcal{R}_1\mathcal{R}_0}$ is the transformation matrix from the $\mathcal{R}_0$ to the $\mathcal{R}_1$ frame, $\mathcal{C}^{\mathcal{R}_2\mathcal{R}_1}$ is the transformation matrix from the $\mathcal{R}_1$ to the $\mathcal{R}_2$ frame, $\mathcal{C}^{\mathcal{R}_0\mathcal{S}}$ is the transformation matrix from the ship frame S to the hub frame, $\mathcal{C}^{\mathcal{S}I}$ is the transformation matrix from the inertial ocean frame I to the ship frame, and the velocity $\mathbf{V}_z$ is defined as

$$\mathbf{V}_z = \mathcal{C}^{\mathcal{R}_0\mathcal{S}}\mathbf{V}_h + (\mathbf{\Omega}_{hub} + \widetilde{\mathcal{C}^{\mathcal{R}_0\mathcal{S}}\mathcal{C}^{\mathcal{S}I}\mathbf{\Omega}_{ship}})\mathbf{R}_0 \tag{3.101}$$

where $\mathbf{V}_h$ is defined as

$$\mathbf{V}_h = \mathcal{C}^{\mathcal{S}I}\mathbf{V}_{ship} + \widetilde{\mathcal{C}^{\mathcal{S}I}\mathbf{\Omega}_{ship}}\,(\mathbf{R}_{HR} + \mathbf{R}_{HB}) \tag{3.102}$$

where $\mathbf{V}_{ship}$ is ship linear velocity in the ocean frame, and the position vectors $\mathbf{R}_{HR}$ and $\mathbf{R}_{HB}$ being defined in Fig. 3.5.

The root of the flexible blade will then have the following linear and angular velocities that give the necessary time varying essential boundary conditions

$$\mathbf{V}_{N1} = \mathcal{C}^{\mathcal{N}\mathcal{R}_2}\left[\mathbf{V}_2 + \widetilde{\mathbf{\Omega}}_2(\mathbf{R}_{l2} - \mathbf{R}_{cm2})\right] + \widetilde{\mathcal{C}^{\mathcal{N}\mathcal{R}_2}\mathbf{\Omega}_2}\mathbf{R}_{N1} \tag{3.103}$$

$$\mathbf{\Omega}_{N1} = \mathcal{C}^{\mathcal{N}\mathcal{R}_2}\mathbf{\Omega}_2 \tag{3.104}$$

where $\mathbf{R}_{N1}$ is the position vector of the beam reference line relative to the point of attachment of the articulation mechanism, and $\mathcal{C}^{\mathcal{N}\mathcal{R}_2}$ is the transformation matrix from the $\mathcal{R}_2$

frame to the blade root frame $\mathcal{N}$, which normally varies as the blade pitch angle setting changes, as shown in Fig. 3.6.

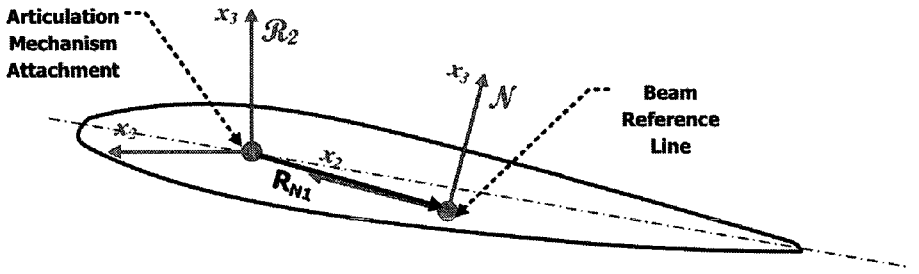

Figure 3.6: Articulation point of attachment relative to the beam reference line.

The constraints of Eqs. 3.97-3.100 can be added to the set of equations used to solve the dynamics model of the articulated rotor system, which is known as the augmented formulation in the multibody dynamics literature, or used to eliminate the dependent angular and linear accelerations in Eq. 3.94, which precedes the embedding technique. The latter is adopted in this formulation to rewrite Eq. 3.94 in terms of the independent angular velocities $\mathbf{\Omega}_{flap}$ and $\mathbf{\Omega}_{lead-lag}$, although it is not widely used in multibody dynamics [137]. In this formulation, the joint reaction forces and moments of the links that are embedded in the $\mathcal{G}$ vector in Eq. 3.96 are unknowns and have to be calculated along with the other unknowns that are grouped as such

$$\chi = \begin{bmatrix} \mathbf{F}_{R1} & \mathbf{M}_{R1} & \mathbf{\Omega}_{flap} & \mathbf{F}_{R2} & \mathbf{M}_{R2} & \mathbf{\Omega}_{lead\_lag} \end{bmatrix} \tag{3.105}$$

where $\mathbf{F}_{R1}$, $\mathbf{M}_{R1}$, $\mathbf{F}_{R2}$, and $\mathbf{M}_{R2}$ are the joint reaction forces and moments of the flap and the lead-lag links respectively.

Furthermore, the simple revolute joints chosen to model the articulated rotor blade system impose the following additional joint constraints on the unknowns

$$\begin{bmatrix} \mathbf{e}_0^T & \mathbf{e}_2^T & \mathbf{e}_0^T & \mathbf{e}_0^T & \mathbf{e}_0^T & \mathbf{e}_0^T \\ \mathbf{e}_0^T & \mathbf{e}_0^T & \mathbf{e}_1^T & \mathbf{e}_0^T & \mathbf{e}_0^T & \mathbf{e}_0^T \\ \mathbf{e}_0^T & \mathbf{e}_0^T & \mathbf{e}_3^T & \mathbf{e}_0^T & \mathbf{e}_0^T & \mathbf{e}_0^T \\ \mathbf{e}_0^T & \mathbf{e}_0^T & \mathbf{e}_0^T & \mathbf{e}_0^T & \mathbf{e}_3^T & \mathbf{e}_0^T \\ \mathbf{e}_0^T & \mathbf{e}_0^T & \mathbf{e}_0^T & \mathbf{e}_0^T & \mathbf{e}_0^T & \mathbf{e}_1^T \\ \mathbf{e}_0^T & \mathbf{e}_0^T & \mathbf{e}_0^T & \mathbf{e}_0^T & \mathbf{e}_0^T & \mathbf{e}_2^T \end{bmatrix} \chi = \mathbf{0} \tag{3.106}$$

where $\mathbf{e}_2 = [\ 0 \quad 1 \quad 0\ ]^T$, $\mathbf{e}_3 = [\ 0 \quad 0 \quad 1\ ]^T$, and $\mathbf{e}_0 = [\ 0 \quad 0 \quad 0\ ]^T$.

This provides a set of nonlinear intrinsic equations that can be used to model the articulated rotor blade system presented. The symbolic nature of the above presented development is noted at this point. Other configurations of blade articulation can be easily incorporated with the above development. For example, a universal joint articulation is simply represented by one link attached to the hub with a state vector of

$$\chi = \begin{bmatrix} \mathbf{F}_{R1} & \mathbf{M}_{R1} & \mathbf{\Omega}_{flap/lead-lag} \end{bmatrix} \tag{3.107}$$

with the joint constraints being

$$\begin{bmatrix} \mathbf{e}_0^T & \mathbf{e}_0^T & \mathbf{e}_1^T \\ \mathbf{e}_0^T & \mathbf{e}_2^T & \mathbf{e}_0^T \\ \mathbf{e}_0^T & \mathbf{e}_3^T & \mathbf{e}_0^T \end{bmatrix} \chi = \mathbf{0} \tag{3.108}$$

Similarly, for a flap-articulated rotor the joint constraints are

$$\begin{bmatrix} \mathbf{e}_0^T & \mathbf{e}_0^T & \mathbf{e}_1^T \\ \mathbf{e}_0^T & \mathbf{e}_0^T & \mathbf{e}_3^T \\ \mathbf{e}_0^T & \mathbf{e}_2^T & \mathbf{e}_0^T \end{bmatrix} \chi = \mathbf{0} \tag{3.109}$$

3.5.1 Backlash Modelling

To prevent excessive blade drooping at low hub rotational speeds due to lack of centripetal stiffening, stops are added to hold the flap hinge from drooping or flapping beyond certain angle settings as indicated in Fig 3.7. Various approaches have been used by different researchers to calculate the impact forces of the backlash during contact of the flap hinge with the flap/droop stops. An early investigation was done by Newman [11], where the stops were modelled as a spring with high stiffness. Keller and Smith [58] performed further theoretical analysis, where the forces of the droop stop impact were modelled using a torsional spring and damper combination that is activated under certain conditions. Additionally, experimental validation was performed to establish a benchmark for validating the theoretical analysis. Bottasso and Bauchau [29] also tackled the problem of backlash in articulated rotor systems more thoroughly and the results of their analysis were successfully validated against the experiments of Keller and Smith to further add to the validation of DYMORE.

In this work, the Voigt-Kelvin viscoelastic model is used to calculate the backlash elastic and dissipative forces during impact due to its simplicity, despite its limited physical validity in terms of representing the actual behavior of the contact forces during impact [138]. According to Fig. 3.7, the phenomenological forces during impact are

$$\mathbf{F}_{impact} = \underbrace{(k \cdot a \cdot \mathbf{e}_{\S})}_{elastic\ component} + \underbrace{(-c \cdot \dot{a} \cdot \mathbf{e}_{\S})}_{dissipative\ component} \tag{3.110}$$

where the symbol § runs from 1 to 2, a is the penetration distance due to impact, k is the linear spring stiffness, and c is the viscous damper damping coefficient. The latter two quantities are assumed to be given.

Based on the geometry in Fig. 3.7, the penetration distance a is calculated based on the assumption of small penetration angle as

$$a = D_{\S} \mid \phi_{flap/droop} - \Theta_{flap\ hinge} \mid \tag{3.111}$$

where $\Theta_{flap\ hinge}$ is the post-processed flap hinge angle during an impact event.

The rate of change of the penetration distance is approximated using a suitable finite difference scheme. Naturally, the flap and the lead-lag links are subjected to these backlash forces where similar model is used for the lead-lag link.

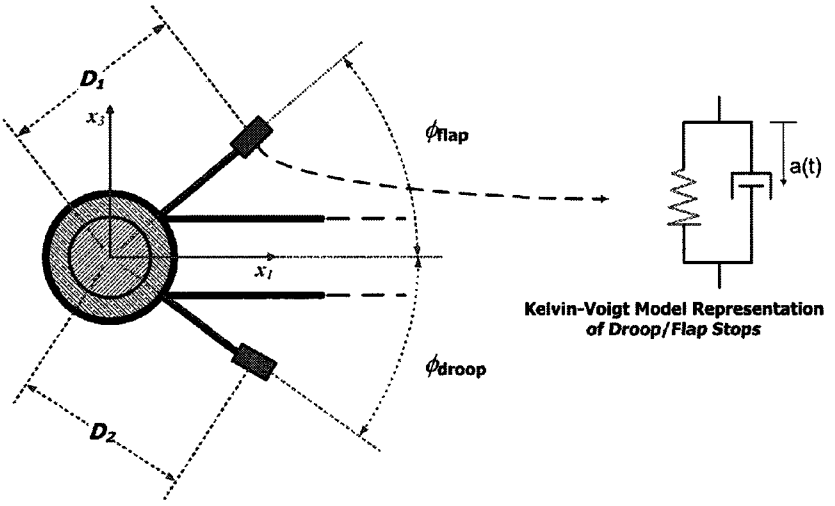

Figure 3.7: Droop/flap stops mechanism attached to the flap link, and the stops viscoelastic model used to evaluate impact forces.

3.6 Implementation

The cross-sectional theory of active rotor blades developed in Chapter 2 and the intrinsic geometrically exact flexible multibody model of active rotor systems outlined in this chapter were implemented using the MATLAB® scientific programming language. The imported experimental ship airwake module was written in FORTRAN90 and had to be interfaced with the developed MATLAB code through gateway functions. The implementation of the code is pictorially detailed in Fig. 3.8. A time adaptive strategy is implemented, where the time step is refined when the implemented solution strategy fails

to converge or when an impact with the blade limiters/stops is anticipated. The latter is needed due to the high frequency modes associated with impact problems. The software is then compiled into a stand-alone executable.

3.7 Future Recommendations

Further investigations are still needed before the geometrically exact flexible multibody model is generalized for larger models that are not necessarily rotor systems. The techniques and algorithms that are being continuously developed to model multibody systems can still be applied to the intrinsic model herein to reduce computational costs and provide more efficient and compact mathematical formulations. Additionally, other reducible structural members like shells and plates are still to be incorporated to provide more complete modelling capabilities of maritime helicopters. However, intrinsic formulations tend to shield the physics of the problem that reveal interesting features and special relations between the state variables. Finally, some investigators argue that the fixed pole formulation is more suitable for multibody systems modelling than the body fixed frames approach presented herein [139] and the debate is not yet resolved.

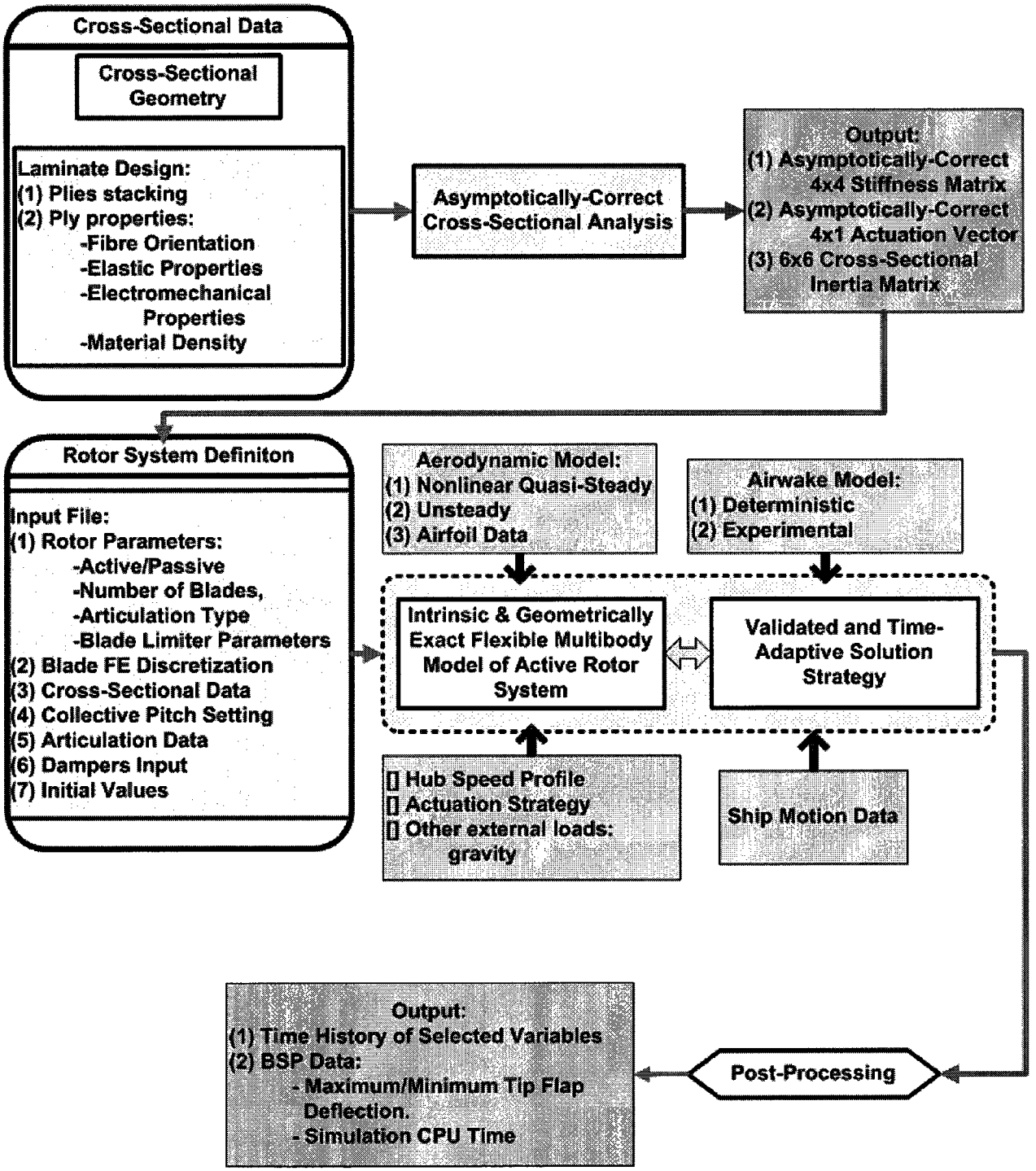

Figure 3.8: Detailed block diagram of the implementation of developed models to simulate active rotor systems.

Chapter 4

Solution of the Intrinsic and Geometrically-Exact Model of Active Rotor Systems

4.1 Overview of Chapter 4

In this chapter, a solution strategy to solve the models developed in the preceding chapters in the time domain, and consequently the frequency domain through Fourier transform, is proposed. The solution strategy is shown to retain all of its desirable characteristics displayed in the linear regime of unconditional stability, numerical consistency and accuracy, and high frequency algorithmic dissipation. The results reinforce the established notion that the form of the nonlinear elastodynamics model plays a critical role in determining the suitability of a time integration scheme for the problem at hand.

4.2 Overview of Numerical Solution of Nonlinear Elastodynamics Models of Multibody Systems

The models developed in Chapters 2 and 3 led to a set of nonlinear partial differential equations in space and time. Given the appropriate boundary conditions and initial values, a solution in time, and consequently the frequency domain, is required. However, any proposed solution strategy must be capable of handling the challenges posed by the nonlinear problem in addition to demonstrating accuracy and numerical consistency. As briefly noted previously, intrinsic formulations of multibody systems have the advantage of expressing the model equations without the explicit appearance of rotational or displacement variables, and Newton-Euler equations of motion are examples of the intrinsic form of the equations of motion of rigid bodies. This offers a compact and weak set of partial differential equations that can be solved for the selected state variables using a suitably designed integration scheme, while obtaining the rotational and displacement variables in a post-processing step. Consequently, the order of nonlinearities is reduced in intrinsic formulations, which eases some stringent requirements on the solution methodology. In contrast, mixed formulations have the rotational and the displacement variables and their derivatives appearing explicitly in the equations of motion in addition to other state variables. Generally, investigation into robust and efficient numerical solutions of geometrically exact intrinsic formulations is still lacking as is their integration into multibody dynamics software.

Nonlinearities in the equations of motion have been recognized as being responsible for exciting the high frequency modes with the attentive interchange of energy with the lower modes. In addition to the inaccuracies introduced in the solution in terms of artificially adding energy into the system, these high frequency modes hinder the convergence process. Energy decaying schemes have been proposed to solve the nonlinear finite element

problems encountered in flexible multibody dynamics due to their attractive characteristic of attenuating high frequency components in the solution and imposing an algorithmic bound on the total energy of the system in the absence of external loads. Therefore, the unconditional stability of the scheme in the nonlinear regime can be established. However, recently a review of the advantages and drawbacks of these specifically tailored schemes reported and highlighted the critical importance of the form of the governing equations in determining the suitability of an energy decaying scheme for certain nonlinear problems [140].

Gobat and Grosenbaugh [141, 142] proposed a first order generalized-α scheme based on the second order one developed by Chung and Hulbert [143]. Their target application was solving the mixed nonlinear dynamics formulation of cables and chains with emphasis on ocean mooring applications. Apparently, the development of the first order method was also done in parallel by Jansen et al. [144] to solve the Navier-Stokes equations with spatial finite element discretization. The derived first order method was also a one parameter family (the spectral radius at infinity ρ_∞) that controls the high frequency content within the resolution level (for linear problems). This was achieved by imposing certain constraints on the eigenvalues of the amplification matrix (of the linear problem) to achieve second order accuracy and to prevent bifurcation. Both of these studies have been successful in showing that the salient features of the method demonstrated for linear problems are inherited in their respective nonlinear problems.

Rotor blade systems have traditionally been a numerical challenge in structural dynamics and represented a test platform for numerical space-time integration methods of nonlinear elastodynamics models. This is mainly due to the nonlinearities, gyroscopic terms, structural coupling, and the attentive numerical stiffness encountered. Some of these problems are further amplified in advanced composite blades with advanced design topologies. Within the community of flexible multibody dynamics, the generalized-α

method is sometimes viewed as a classical approach in structural dynamics that loses its desirable algorithmic characteristics demonstrated in the linear regime when applied to the nonlinear one, especially since it is generally tailored and does not take into account the details of the equations of motion [140]. This may be the case when the method is applied to, for instance, a mixed formulation of an elastodynamics model where the nonlinearities are more complex as discussed earlier. However, an appropriate reformulation of the equations of motion into a suitable intrinsic form may render a scheme that was deemed unsuitable before the reformulation suitable henceforth. The purpose of this chapter is to demonstrate the suitability of the first order generalized-α method, which has the typical features of an energy decaying scheme, to solve the geometrically-exact model of rotor systems in its intrinsic form in an almost symbolic sense.

4.3 Setting up the Problem

Starting from a problem that has an apparent mathematical structure similar to the one at hand, the mixed nonlinear dynamics model of a two-dimensional, inextensible, perfectly flexible cable is given by [141]:

$$\breve{\mathbf{M}}\frac{\partial \mathbf{Y}}{\partial t} + \breve{\mathbf{K}}\frac{\partial \mathbf{Y}}{\partial s} + \mathcal{F}(\mathbf{Y}, s, t) = 0 \tag{4.1}$$

where s is the Lagrangian measure of length along the unstretched cable, t is the time, and the state vector $\mathbf{Y}$ is composed of the four state variables of the model that are tangential and normal velocity, u and v, tension T, and inclination from the vertical ϕ such that

$$\mathbf{Y} = \begin{bmatrix} T & u & v & \phi \end{bmatrix}^{\mathrm{T}} \tag{4.2}$$

and the matrices $\breve{\mathbf{M}}$, $\breve{\mathbf{K}}$, and $\mathcal{F}$ are given by

$$\breve{\mathbf{M}} = \begin{bmatrix} 0 & m & 0 & -mv \\ 0 & 0 & m & mu \\ 0 & 0 & 0 & 0 \\ 0 & 0 & 0 & -1 \end{bmatrix} \quad \breve{\mathbf{K}} = \begin{bmatrix} -1 & 0 & 0 & 0 \\ 0 & 0 & 0 & -T \\ 0 & 1 & 0 & -v \\ 0 & 0 & 1 & u \end{bmatrix} \quad \mathcal{F} = \begin{bmatrix} mg\cos\phi \\ -mg\sin\phi \\ 0 \\ 0 \end{bmatrix} \tag{4.3}$$

where g is the acceleration due to gravity, and m is the mass per unit length.

It is duly noted at this stage that the coefficient matrices $\breve{\mathbf{M}}$ and $\breve{\mathbf{K}}$ are dependent on the state variables of the model. The geometrically exact intrinsic model of initially twisted and curved moving beams in Eqs. 3.78, 3.79, 3.80, 3.81 can be rewritten in a matrix form as

$$\mathbb{A}\frac{\partial \mathcal{X}_1}{\partial t} + \mathbb{B}\frac{\partial \mathcal{X}_1}{\partial x_1} + \mathcal{Z}(\mathcal{X}_1, \mathbf{f}, \mathbf{m}, \mathbf{F}^{(a)}, \mathbf{M}^{(a)}, \dot{\mathbf{F}}^{(a)}, \dot{\mathbf{M}}^{(a)}) = \mathbf{0} \tag{4.4}$$

where the state vector $\mathcal{X}_1$ is composed of

$$\mathcal{X}_1 = \begin{bmatrix} \mathbf{F} & \mathbf{M} & \mathbf{V} & \mathbf{\Omega} \end{bmatrix}^{\mathrm{T}} \tag{4.5}$$

if the 3×3 zero and the identity submatrices are denoted by $0_{3\times3}$ and $\underline{\triangle}_{3\times3}$ respectively, the 12×12 matrices $\mathbb{A}$ and $\mathbb{B}$ are simply

$$\mathbb{A} = -\begin{bmatrix} J & N & D & Q \\ B & W & -Q & I \\ S^{\mathrm{T}} & T & 0_{3\times3} & 0_{3\times3} \\ R & S & 0_{3\times3} & 0_{3\times3} \end{bmatrix} \quad \mathbb{B} = \begin{bmatrix} \underline{\triangle}_{3\times3} & 0_{3\times3} & 0_{3\times3} & 0_{3\times3} \\ 0_{3\times3} & \underline{\triangle}_{3\times3} & 0_{3\times3} & 0_{3\times3} \\ 0_{3\times3} & 0_{3\times3} & 0_{3\times3} & \underline{\triangle}_{3\times3} \\ 0_{3\times3} & 0_{3\times3} & \underline{\triangle}_{3\times3} & 0_{3\times3} \end{bmatrix} \tag{4.6}$$

and the 12×1 vector $\mathcal{Z}$ contains the rest of the terms in Eq. 3.78 through Eq. 3.81 and is

not shown here for brevity. The actuation vector components and their time derivatives are assumed to be prescribed at all times.

When the intrinsic beam dynamics model in the form of Eq. 4.4 is compared to the mixed dynamics model of chains and cables in Eq. 4.1, the apparent mathematical structures are similar; however, the similarity ends at this point. Most importantly, unlike the coefficient matrices of the cables/chains mixed dynamics model, the coefficient matrices of the intrinsic beam model shown in Eq. 4.6 do not depend on the state variables in Eq. 4.5, and in fact they are constant in time. This will have an implication on the integration scheme and its stability as shall be discussed subsequently.

The model that is compactly written in Eq. 4.4 is coupled with the models of other members of the multibody system succinctly contained in Eq. 3.94.

4.4 Problem Discretization (Shape Functions)

The weak form of the beam intrinsic dynamics model in Eq. 4.4 makes it possible to choose simple spatial shape functions to interpolate the state variables within a beam element. Patil and Hodges [145] used C^0 shape functions within the element that is related to the nodal values through the midpoint rule as shown in Fig. 4.1 where

$$\overline{\mathbf{X}}_k^j = \frac{\mathbf{X}_i^j + \mathcal{C}_k^{lr}\mathbf{X}_{i+1}^j}{2} \tag{4.7}$$

where overbarred quantities are used to denote quantities at the midpoint of the beam element, the superscript is used to denote the temporal index, and the subscript is used to denote the spatial/element index.

Furthermore, the spatial derivative of the k^{th} element is given by

$$\overline{\mathbf{X}}_k'^j = \frac{\mathcal{C}_k^{lr}\mathbf{X}_{i+1}^j - \mathbf{X}_i^j}{\Delta x_k} \tag{4.8}$$

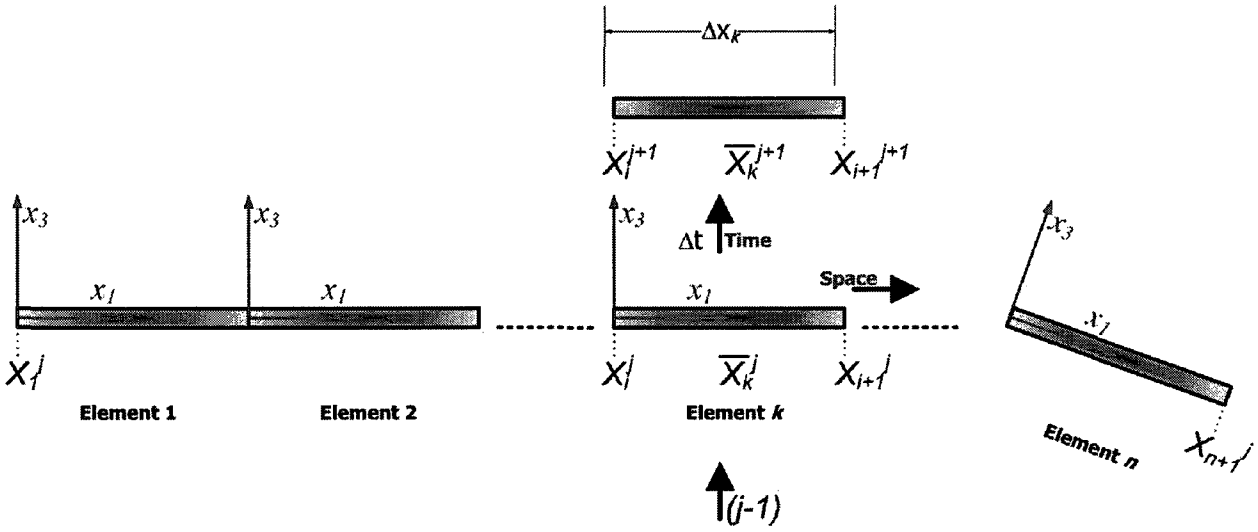

Figure 4.1: Space-time discretization of the blade into n beam elements.

where $\mathcal{C}_k^{lr}$ is the transformation matrix from the right node frame to the left node frame of the beam element for beams with broken reference lines defined in Chapter 3, and Δx_k is the length of the k^{th} element.

Shape functions similar to the aforementioned interpolating functions are adopted for this work. Choosing higher order shape functions would increase the resolution of the solution but this can be compensated for by increasing the number of elements using simpler shape functions.

The spatial derivative of the k^{th} element in Eq. 4.8 can be expressed in terms of the midpoint values of the other elements and the right or left boundary conditions respectively through the sums

$$\frac{\mathbf{X}_{i+1}^j - \mathbf{X}_i^j}{\Delta x_k} = \frac{-2\overline{\mathbf{X}}_k + \mathcal{C}_{k+1}^{lr:k+1\to k} 4\overline{\mathbf{X}}_{k+1} - \mathcal{C}_{k+2}^{lr:k+2\to k} 4\overline{\mathbf{X}}_{k+2} \cdots + \mathcal{C}_n^{lr:n\to k}(-1)^{m-1} 4\overline{\mathbf{X}}_n + \mathcal{C}_n^{lr:n\to k}(-1)^m 2\mathbf{X}_{n+1}}{\Delta x_k} \tag{4.9}$$

$$m = n - k + 1$$

$$\frac{\mathbf{X}_{i+1}^{j}-\mathbf{X}_{i}^{j}}{\Delta x_k} = \frac{2\overline{\mathbf{X}}_k - \mathcal{C}_{k-1}^{rl:k-1\to k}4\overline{\mathbf{X}}_{k-1} + \mathcal{C}_{k-2}^{rl:k-2\to k}4\overline{\mathbf{X}}_{k-2} \cdots + \mathcal{C}_{2}^{rl:2\to k}(-1)^{m-1}4\overline{\mathbf{X}}_2 + \mathcal{C}_{1}^{rl:1\to k}(-1)^{m}2\mathbf{X}_1}{\Delta x_k} \tag{4.10}$$

$$m = k+1$$

where $\mathbf{X}_{n+1}$ and $\mathbf{X}_1$ are the right and left boundary conditions of the beam respectively, $\mathcal{C}_n^{lr:n\to k}$ is the transformation matrix from the right node frame of the n^{th} element to the left node frame of the k^{th} element, and $\mathcal{C}_1^{rl:1\to k}$ is the transformation matrix from the left node frame of the first element to the right node frame of the k^{th} element.

The expressions in Eq. 4.9 and Eq. 4.10 can be used to eliminate the nodal quantities from the resulting discrete ordinary differential equations or to write the boundary values in terms of the midpoint values.

Based on the discretization discussed above and illustrated in Fig. 4.1, and using the rectangular and the trapezoidal quadrature to approximate the spatial and temporal integrals respectively, the discretized form of the first conservation law is

$$\begin{aligned}&\frac{\sum_{q=1}^{n}\left[\left(\overline{\mathbf{V}}_q^{\mathrm{T}j}\cdot\overline{\mathbf{f}}_q^{(j-1)}+\overline{\mathbf{\Omega}}_q^{\mathrm{T}j}\cdot\overline{\mathbf{m}}_q^{(j-1)}\right)+\left(\overline{\mathbf{V}}_q^{\mathrm{T}(j-1)}\cdot\overline{\mathbf{f}}_q^{(j-1)}+\overline{\mathbf{\Omega}}_q^{\mathrm{T}(j-1)}\cdot\overline{\mathbf{m}}_q^{(j-1)}\right)\right]\Delta x_q}{2}\Delta t+\\ &\frac{\left(\overline{\mathbf{V}}_v^{\mathrm{T}j}\cdot\overline{\mathbf{F}}_v^{j}+\overline{\mathbf{\Omega}}_v^{\mathrm{T}j}\cdot\overline{\mathbf{M}}_v^{j}\right)+\left(\overline{\mathbf{V}}_v^{\mathrm{T}(j-1)}\cdot\overline{\mathbf{F}}_v^{(j-1)}+\overline{\mathbf{\Omega}}_v^{\mathrm{T}(j-1)}\cdot\overline{\mathbf{M}}_v^{(j-1)}\right)}{2}\Delta t\Big|_{v=1}^{v=n}=\\ &\sum_{z=1}^{n}\left(\overline{T}_z^v+\overline{U}_z^v\right)\Delta x_z\Big|_{v=j-1}^{v=j}\end{aligned} \tag{4.11}$$

Similarly the discretized and rearranged form of the second conservation law is

$$\sum_{q=1}^{n} \left\{ \left[\left(\mathbf{e}_1 + \overline{\boldsymbol{\gamma}}_q^j \right)^{\mathrm{T}} \cdot \overline{\mathbf{f}}_q^{(j-1)} + \overline{\boldsymbol{\kappa}}_q^{\mathrm{T}j} \cdot \overline{\mathbf{m}}_q^{(j-1)} \right] + \left[\left(\mathbf{e}_1 + \overline{\boldsymbol{\gamma}}_q^{(j-1)} \right)^{\mathrm{T}} \cdot \overline{\mathbf{f}}_q^{(j-1)} + \overline{\boldsymbol{\kappa}}_q^{\mathrm{T}(j-1)} \cdot \overline{\mathbf{m}}_q^{(j-1)} \right] \right\} \Delta x_q \frac{\Delta t}{2}$$

$$+ \frac{\left(\mathbf{e}_1^{\mathrm{T}} \overline{\mathbf{F}}_v^j + \overline{\mathcal{U}}_v^j + \overline{\mathcal{T}}_v^j \right) + \left(\mathbf{e}_1^{\mathrm{T}} \overline{\mathbf{F}}_v^{(j-1)} + \overline{\mathcal{U}}_v^{(j-1)} + \overline{\mathcal{T}}_v^{(j-1)} \right)}{2} \Delta t \Big|_{v=1}^{v=n} \tag{4.12}$$

$$- \sum_{z=1}^{n} \left[\left(\mathbf{e}_1 + \overline{\boldsymbol{\gamma}}_z^v \right)^{\mathrm{T}} \overline{\mathbf{P}}_z^v + \overline{\boldsymbol{\kappa}}_z^{\mathrm{T}v} \overline{\mathbf{H}}_z^v \right] \Delta x_z \Big|_{v=j-1}^{v=j} = 0$$

Satisfying these laws during the nonlinear transient simulation of beam dynamics is a necessary, but not sufficient, condition in establishing the accuracy of the solution [135]. In the absence of externally applied loads, an energy preserving/decaying integration scheme would imply that

$$\sum_{z=1}^{n} \left(\overline{\mathcal{T}}_z^v + \overline{\mathcal{U}}_z^v \right) \Delta x_z \Big|_{v=j-1}^{v=j} = c_E \qquad \begin{cases} c_E = 0 & \text{energy preserving} \\ c_E < 0 & \text{energy decaying} \end{cases} \tag{4.13}$$

The above mathematical statement, if satisfied, is a sufficient proof of the unconditional stability of an integration scheme for nonlinear problems. Depending on the form of the proposed integration scheme and the form of the equations, Eq. 4.13 can be shown to be satisfied analytically by simply substituting the scheme into the equation, or numerically by running various test cases. Recently developed energy decaying schemes are specifically tailored to analytically demonstrate the algorithmic energy bound of Eq. 4.13 as demonstrated in [146].

4.5 The Proposed First Order Generalized-α Scheme

Similar to [141, 144], the following time marching scheme is proposed for the intrinsic geometrically exact beam model of Eq. 4.4

$$(1-\alpha_m)\mathbb{A}\dot{\overline{\mathcal{X}}}^{j}_{1k} + \alpha_m\mathbb{A}\dot{\overline{\mathcal{X}}}^{(j-1)}_{1k} + (1-\alpha_k)\mathbb{B}\overline{\mathcal{X}}'^{j}_{1k} + \alpha_k\mathbb{B}\overline{\mathcal{X}}'^{(j-1)}_{1k} + \tag{4.14}$$

$$(1-\alpha_k)\overline{\mathcal{Z}}^{j}_{k}(\overline{\mathcal{X}}^{j}_{1k}, \overline{\mathbf{f}}^{j}_{k}, \overline{\mathbf{m}}^{j}_{k}, \mathbf{F}^{(a)j}, \mathbf{M}^{(a)j}, \dot{\mathbf{F}}^{(a)j}, \dot{\mathbf{M}}^{(a)j}) +$$

$$\alpha_k\overline{\mathcal{Z}}^{j}_{k}(\overline{\mathcal{X}}^{(j-1)}_{1k}, \overline{\mathbf{f}}^{(j-1)}_{k}, \overline{\mathbf{m}}^{(j-1)}_{k}, \mathbf{F}^{(a)(j-1)}, \mathbf{M}^{(a)(j-1)}, \dot{\mathbf{F}}^{(a)(j-1)}, \dot{\mathbf{M}}^{(a)(j-1)}) = 0$$

where

$$\dot{\overline{\mathcal{X}}}^{j}_{1k} = \frac{\overline{\mathcal{X}}^{j}_{1k} - \overline{\mathcal{X}}^{(j-1)}_{1k}}{\gamma\Delta t} - \frac{(1-\gamma)}{\gamma}\dot{\overline{\mathcal{X}}}^{(j-1)}_{1k} \tag{4.15}$$

and the second-order accurate one-parameter family is defined in terms of the amplification matrix Eigenvalue Value at Infinity (EVI) λ^∞ as

$$\begin{aligned} \alpha_m - \alpha_k + \gamma &= \frac{1}{2} \\ \alpha_m &= \frac{3\lambda^\infty + 1}{2\lambda^\infty - 2} \\ \alpha_k &= \frac{\lambda^\infty}{\lambda^\infty - 1} \end{aligned} \tag{4.16}$$

where for stability (in the linear problem)

$$\lambda^\infty \in [-1, 0] \;\Rightarrow\; \alpha_k \leq \tfrac{1}{2} \quad \alpha_m \leq \tfrac{1}{2} \quad \gamma \geq \tfrac{1}{2} \tag{4.17}$$

The asymptotic annihilation of the scheme is achieved for $\lambda^\infty = 0$, while an energy preserving scheme is recovered for $\lambda^\infty = -1$, which is a variant of the midpoint rule as ex-

pected. The Spectral Radius at Infinity (SRI) is defined in terms of the EVI as $\rho_\infty = |\lambda^\infty|$.

Similar disctretization is performed for the intrinsic model of the rigid bodies that represent the articulation mechanism for rotor systems with full articulation, which is coupled to the intrinsic model in Eq. 4.14. The only difference would be the absence of the spatial derivative in the rigid body model.

It is further highlighted at this stage that in the geometrically exact intrinsic dynamics model of the system, none of the coefficient matrices of the spatial or the temporal derivatives are time dependent. In essence, the averaging of matrices technique that is usually applied to circumvent the conditional stability that arises when transferring an integration scheme from linear to nonlinear problems [141] is not required here due to the intrinsic form of the formulation.

Eq. 4.14 results in a set of nonlinear algebraic equations that is to be solved for every time step. Standard techniques like the Newton-Raphson method and its variants can be employed to obtain a solution; however, a good initial predictor or a small time step is usually required to obtain a solution. The latter approach is not recommended, since the algorithmic damping of high frequency modes is proportional to the size of the time step, and varying it without care may cause spurious peaks in the solution as shall be demonstrated.

4.6 Validation and Numerical Investigation

The first set of examples to be investigated is based on the experimental aluminum blades with various tip sweeps, whose natural frequencies have been reported by Epps and Chandra [147]. The blade sectional stiffness, mass-inertia constants, and length are given in Table C.1 in Appendix C. The blades are initially cantilevered in a zero gravitational field, then they are suddenly subjected to the earth gravitational field and allowed to oscillate

about their static/dynamic equilibrium. Twenty five beam elements are used to uniformly discretize the beams. Three cases are examined: case 1(a) is a tip sweep angle of $\delta = 0°$, rotational velocity of $\Omega = 750$ revolution per minute (RPM), time step size of $\Delta t = 10^{-3}$ sec, EVI of $\lambda^{\infty} = -0.50$; case 1(b) is $\delta = 30°$, $\Omega = 0$ RPM, $\Delta t = 10^{-3}$ sec, $\lambda^{\infty} = -0.15$; and case 1(c) $\delta = 45°$, $\Omega = 0$ RPM, $\Delta t = 10^{-3}$ sec, $\lambda^{\infty} = -0.15$.

The flap displacement u_3 of the tenth element was analyzed using the Fast Fourier Transform (FFT) to obtain the first flap frequency. The displacement field and the rotations parameters are obtained as a post-processing step as shown in Appendix C. Case (a) was run for a period of 10 sec and a rectangular window of 2 sec to 10 sec was used for the FFT analysis, while for the other two cases no windowing was used. The latter is due to the fact that the blade was jump started at the given RPM from the start, and given the modest algorithmic dissipation provided, some time should be given for the high frequency contents to be dissipated. The predicted natural frequencies versus the experimentally reported ones are presented in Table. 4.1.

Table 4.1: Predicted first mode natural frequencies versus the experimental ones for examined hingeless aluminum blade cases.

Case	Predicted Frequency(Hz)	Experimental Frequency(Hz)
1(a)	13.61	14.70
1(b)	1.50	1.80
1(c)	1.50	1.85

The success in terms of predicting the first flap natural frequency of the aluminum beam configurations demonstrated in Table 4.1 adds to the validity of the implementation, but it should not be surprising. Hodges et al. [148] used the mixed formulation in [133] to successfully predict the natural frequencies of the cantilevered aluminum and composite beam configurations reported in [147]. Nevertheless, the natural frequencies seem to be a standard benchmark test for most proposed elastodynamics models as seen in the literature. Any beam response after the external loading has ceased could be used to obtain the

beam natural frequencies as demonstrated in subsequent examples, where more than the first mode are clearly present; however, the first set of examples demonstrate that even with $\lambda^{\infty} = -0.50$ for a beam suddenly starting with a high RPM but with no tip sweep, the high frequency content is quickly annihilated. Beams with tip sweep present more numerical challenge due to the presence of inherited geometric and gyroscopic couplings that tend to excite the high frequency modes. Therefore, a lower value EVI of -0.15 was used for the latter, and although this value is still away from the asymptotic annihilation of the scheme, the high frequency content is quickly annihilated as demonstrated by the absence of any windowing in the FFT analysis.

The second set of examples is geared towards examining the performance of the scheme in terms of its energy decaying characteristic and satisfaction of the intrinsic conservational law of Eq. 4.12 for the hingeless blade configuration. Considering the Epps and Chandra aluminum blades uniformly discretized with twenty five beam elements again, three cases are examined: case 2(a) is $\delta = 0°$ that is initially at rest, the tip is a subjected to a flap force follower symmetric triangular pulse with a duration of 10 sec peaking at 5 sec with a value of 10 psi·in^2, $\Delta t = 10^{-3}$ sec, $\lambda^{\infty} = -0.15$; case 2(b) is $\delta = 45°$ that is initially at rest, the tip is a subjected to a flap delta function force of 400 psi·in^2 at t = 0, $\Delta t = 10^{-2}$ sec, $\lambda^{\infty} = -0.19$; case 2(c) is identical to case 2(b) except for $\lambda^{\infty} = -0.01$; case 2(d) is identical to case 2(b) except for $\lambda^{\infty} = 0$, which is at the asymptotic annihilation of the scheme.

For case 2(a), the total mechanical energy of the blade along with its difference in time normalized by the total mechanical energy after the loading is ceased are shown in Fig. 4.2(I). The second intrinsic conservation law is shown in Fig. 4.2(II). The axial and the flap shear forces of the 25$^{\text{th}}$ beam element are also shown in Fig. 4.3(I) and 4.3(II) respectively. The total mechanical energy of cases 2(b), (c), and (d) normalized by the total mechanical energy after the loading is ceased are shown for the initial and final phases of the simulation

for visual illustration purposes in Fig. 4.4(I) and 4.4(II) respectively. The second intrinsic conservation law for the aforementioned cases is shown in Fig. 4.5.

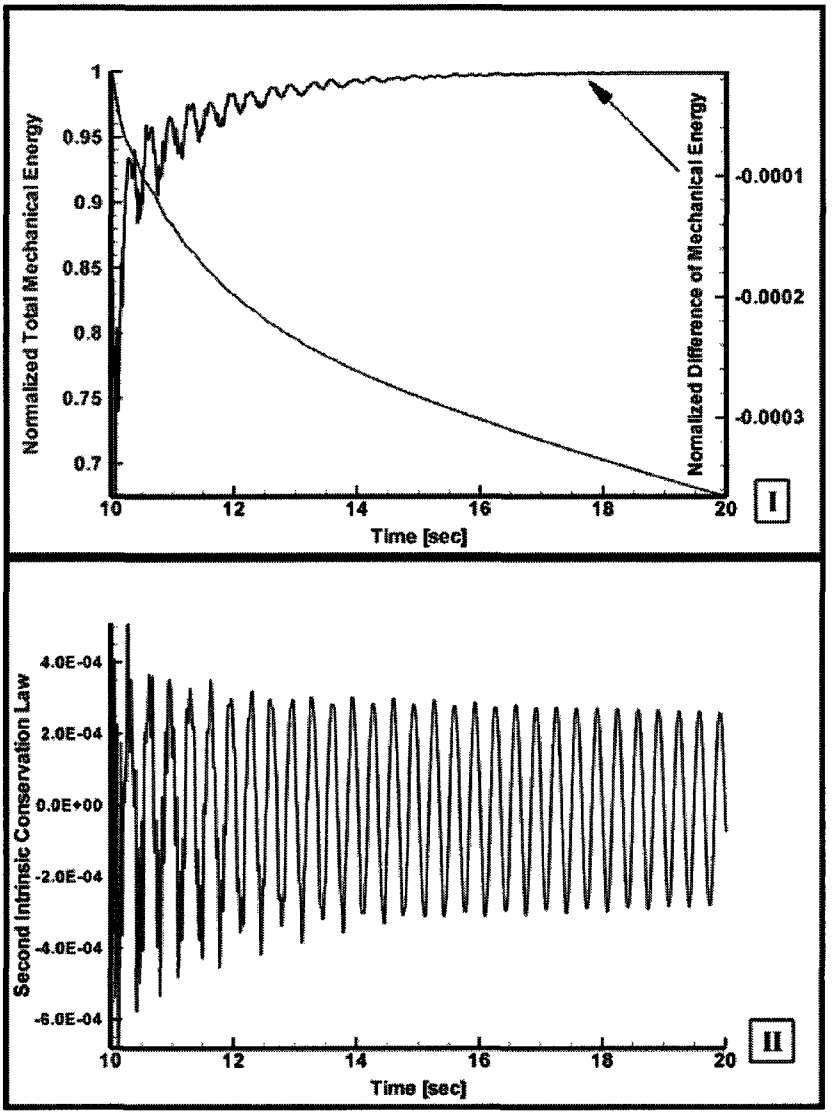

Figure 4.2: Time history of: (I) The blade normalized total mechanical energy and its difference after the loading is ceased, (II) The second intrinsic conservation law of the blade after the loading is ceased of case 2(a).

In the second set of examples, the two intrinsic invariants of energy and impulse-momentum are examined and the numerical dissipation dependance on the EVI is clearly observed. As discussed earlier, a high frequency dissipating characteristic is recognized as essential for most nonlinear elastodynamics integration schemes. The results of case 2(a)

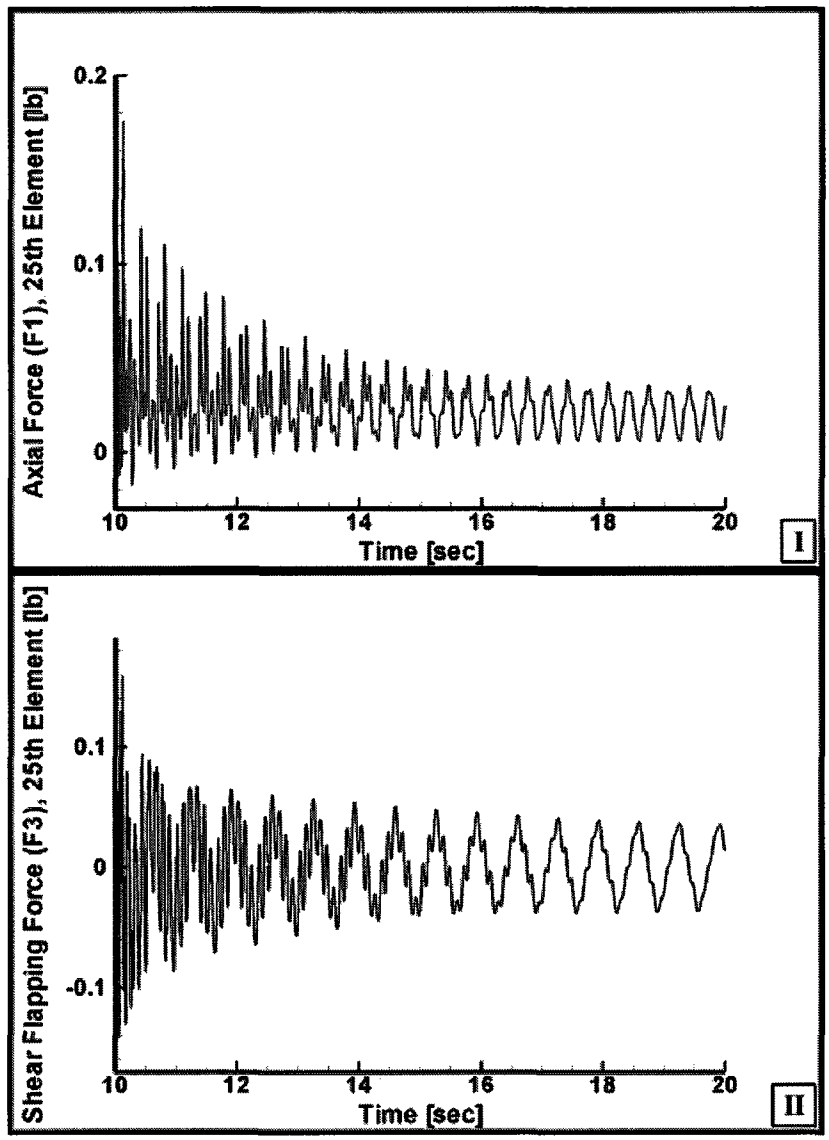

Figure 4.3: Time history of: (I) The axial force F_1, (II) The flapping shear force of the blade F_3 of the 25^{th} beam element after the loading is ceased of case 2(a).

clearly demonstrate these characteristics for the proposed scheme even for the given value of the EVI. Most of the energy dissipation occurs immediately after the loading has ceased as seen in Fig. 4.2(I), which is expected. Additionally, the second intrinsic conservation law is satisfied to within the accuracy limit as shown in Fig. 4.2. The time history of the internal forces in Fig. 4.3 demonstrates that the dynamics of the problem that are of interest (within the resolution level) are well represented. Cases 2(b), 2(c) , and 2(d) are

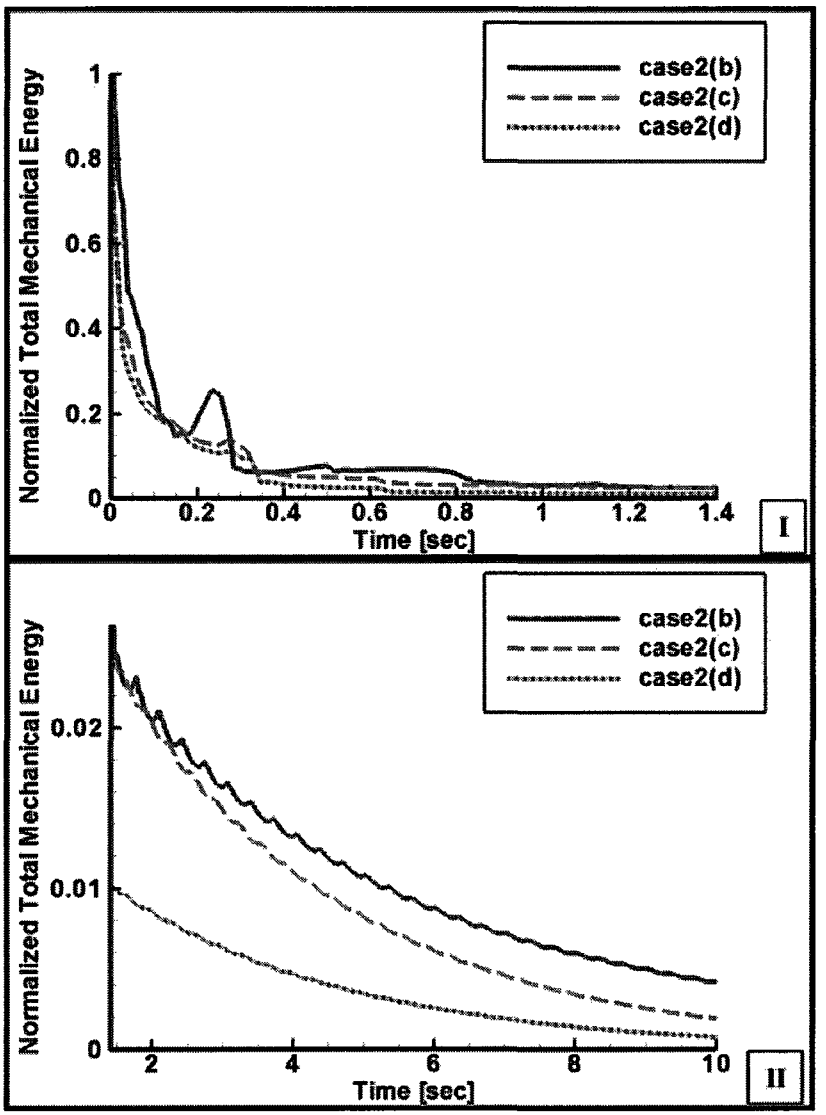

Figure 4.4: Time history of: (I) The normalized total mechanical energy of the blade during the initial steps of the simulation, (II) The normalized total mechanical energy of the blade during the final steps of the simulation of cases 2(b), (c), and (d).

more challenging for the reasons discussed earlier. Furthermore, the intentionally-chosen high number of discretizing beam elements gives rise to the potential of exciting very high frequency modes. This is demonstrated by applying a delta function flap force at the tip, which excites all the modes. The chosen EVI in case 2(b) is not sufficiently low in magnitude to dissipate the high frequency modes that are above the spectral radius fast enough, which results in the spurious energy peaks seen in Fig. 4.4(I),(II) in the early and

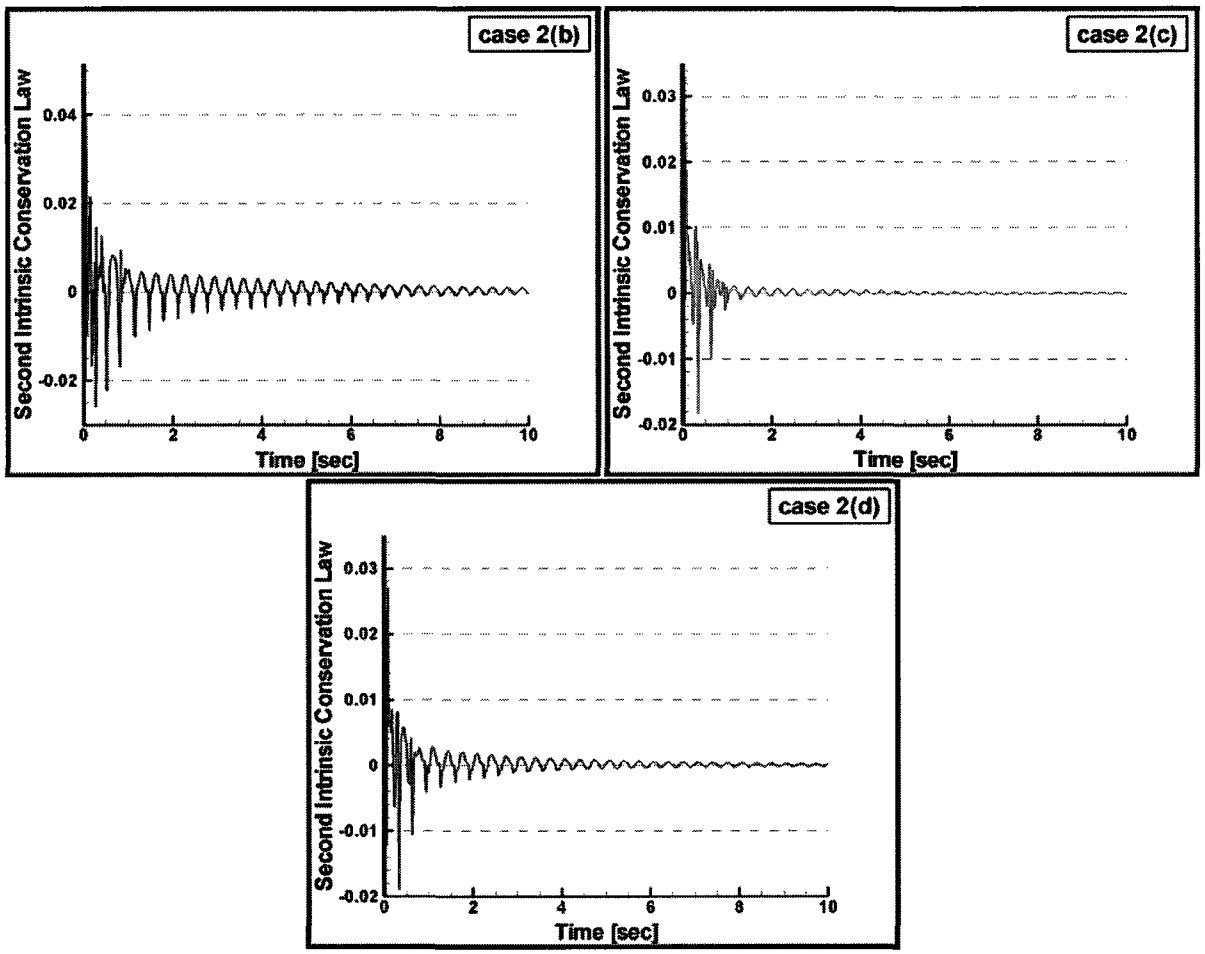

Figure 4.5: Time history of the second intrinsic conservation law of the blade after the loading is ceased of cases 2(b), (c), and (d).

later stages of the simulation. Despite the spuriously added energy to the system, the solution does not go unstable because the high frequency contents are eventually dissipated as observed, which reinforces the notion of the unconditional stability of the scheme. Furthermore, Fig. 4.4 which presents cases similar to case 2(b) but with lower magnitude of EVI, the spurious energy peaks are observed to be reduced, but not completely eliminated, for case 2(c). However, as the value of the EVI approaches the asymptotic annihilation, the more reduced the problem becomes and the spurious energy peaks are seen to be eliminated as demonstrated in case 2(d). Furthermore, the $\Delta t = 10^{-2}$ sec chosen for the simulation was not strictly enforced for case 2(c) and the solver was allowed to reduce the

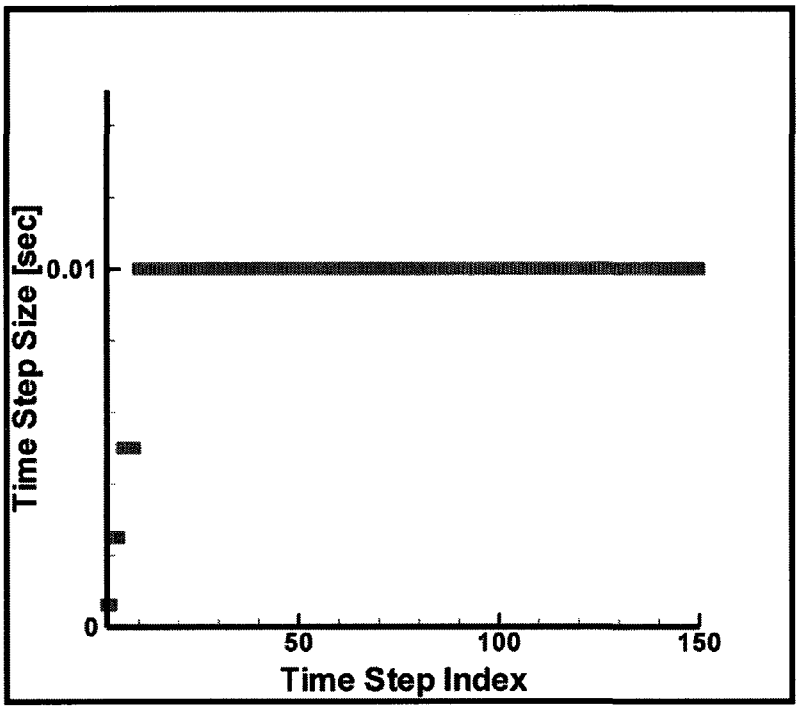

Figure 4.6: Size of the time step used by the solver during the initial stages of the simulation of case 2(c).

time step by half each time until it could converge to a solution. This will negatively affect the performance of the scheme, since the algorithmic damping is reduced and additional high frequency modes may appear. A sample of the initial time steps taken by the solver for this particular case are shown in Fig. 4.6, where it is clear that during the initial phase of the simulation that corresponds to the spurious energy peaks, the reduced time steps are occurring. Integration schemes like the one in [146] would not have this problem, since it is always set at the asymptotic annihilation of the scheme. This can be considered a drawback of the proposed scheme, but not one without a solution. One can appropriately reduce the magnitude of the EVI until the problem is eliminated as demonstrated earlier. Figure 4.5 demonstrates that the second intrinsic conservation law is also satisfied to within the accuracy level; however, the effect of the high frequency contents that are outside the resolution level is seen more profoundly immediately after the delta function load

has ceased which explains the observed amplitude of the oscillations. This seems to be supported by the reduction of those amplitudes as the scheme approaches its asymptotic annihilation. The increase in amplitudes seen in case 2(d) compared to 2(c) might be related to the fact that most implicit time marching schemes focus on parametric control of the total mechanical energy of the system rather than satisfying the impulse-momentum invariant.

The third example examines the proposed scheme when applied to fully articulated systems represented by the simple multibody model depicted in Fig. 3.4 where the only damping present in the system is algorithmic damping. Case 3 is similar to case 2(a) in terms of the analyzed elastic blade, however the rigid links are taken as uniform and cylindrical in shape with length of 1.25 in, radii of 0.25 in, mass of 0.1 lb, the tip is subjected to a flap-wise symmetric triangular follower pulse force with a duration of 0.2 sec peaking at 0.1 sec with a magnitude of 5 psi·in^2, $\Delta t = 10^{-2}$ sec, $\lambda^{\infty} = -0.50$. As a virtual model, the objects of the model are allowed to penetrate each other to allow examination of the motion for extended periods of time. The only limitation one might face in this case is the possibility of a lock up (singular configurations) of the motion, which is carefully monitored. The total mechanical energy of the elastic blade and the articulation mechanism are presented in Fig. 4.7. The flapping shear force in the 25^{th} element, the flap tip displacement u_3, and the flap hinge angle for case 3 are shown in Fig. 4.8(I),(II), and (III) respectively.

The third example demonstrates the energy decaying characteristic of the scheme for the simple multibody system considered when the mechanical energy of the elastic and the rigid bodies are combined as observed in Fig. 4.7. The significant elastic displacement of the beam tip in Fig. 4.8(II) is also noted, while sub-figures (I) and (III) demonstrate again that the dynamic response of the system that is of interest is well represented.

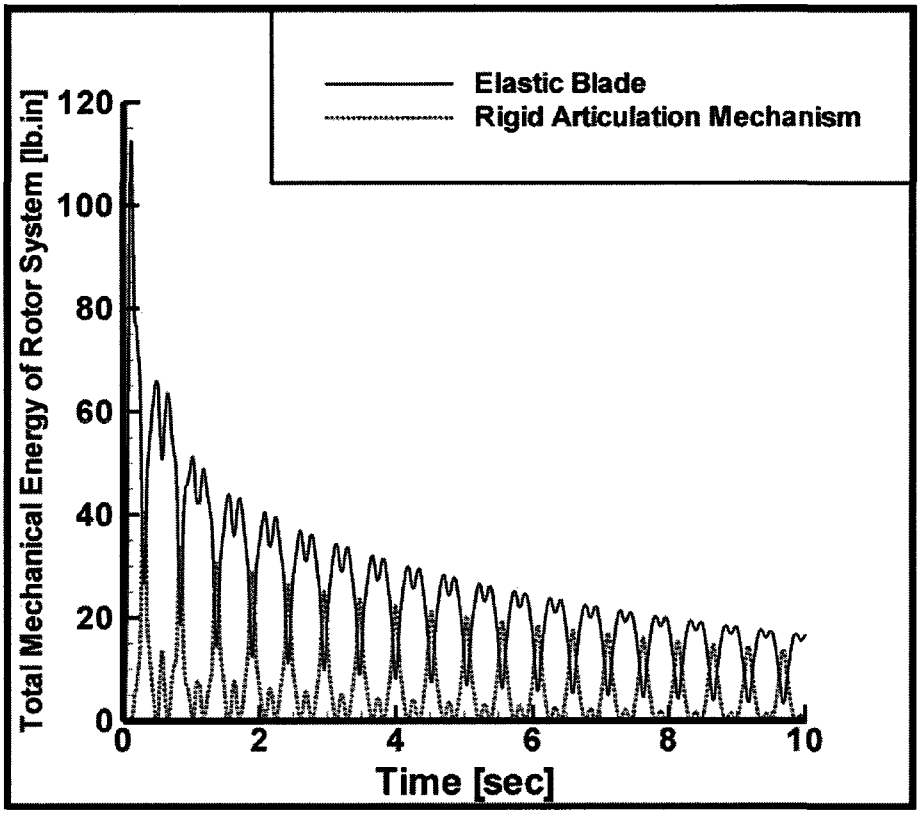

Figure 4.7: Time history of the total mechanical energy of the fully articulated rotor system of case 3.

The fourth set of examples is used to assess the numerical accuracy and consistency of the scheme. Similar to the system configuration of case 3 above, the tip is subjected to a flap-wise symmetric triangular follower pulse force with a duration of 0.1 sec peaking at 0.05 sec with a magnitude of 0.5 psi·in^2, the simulation duration is 0.75 sec, with $\lambda^{\infty} = 0$. The system was solved using 100, 200, 400, 800, 1600, 3200, 6400, and 12800 time steps. Since the problem does not have an analytical solution, the simulation run with 12800 steps is taken as the reference solution. The error was calculated for the linear flap velocity V_3, the tip displacement u_3, and the flapping shear force F_3 of the 25^{th} element in addition to the second intrinsic conservation law using the Root Mean Square (RMS) of the signal normalized by the reference solution. The normalized errors are plotted versus the time step size in Fig. 4.9.

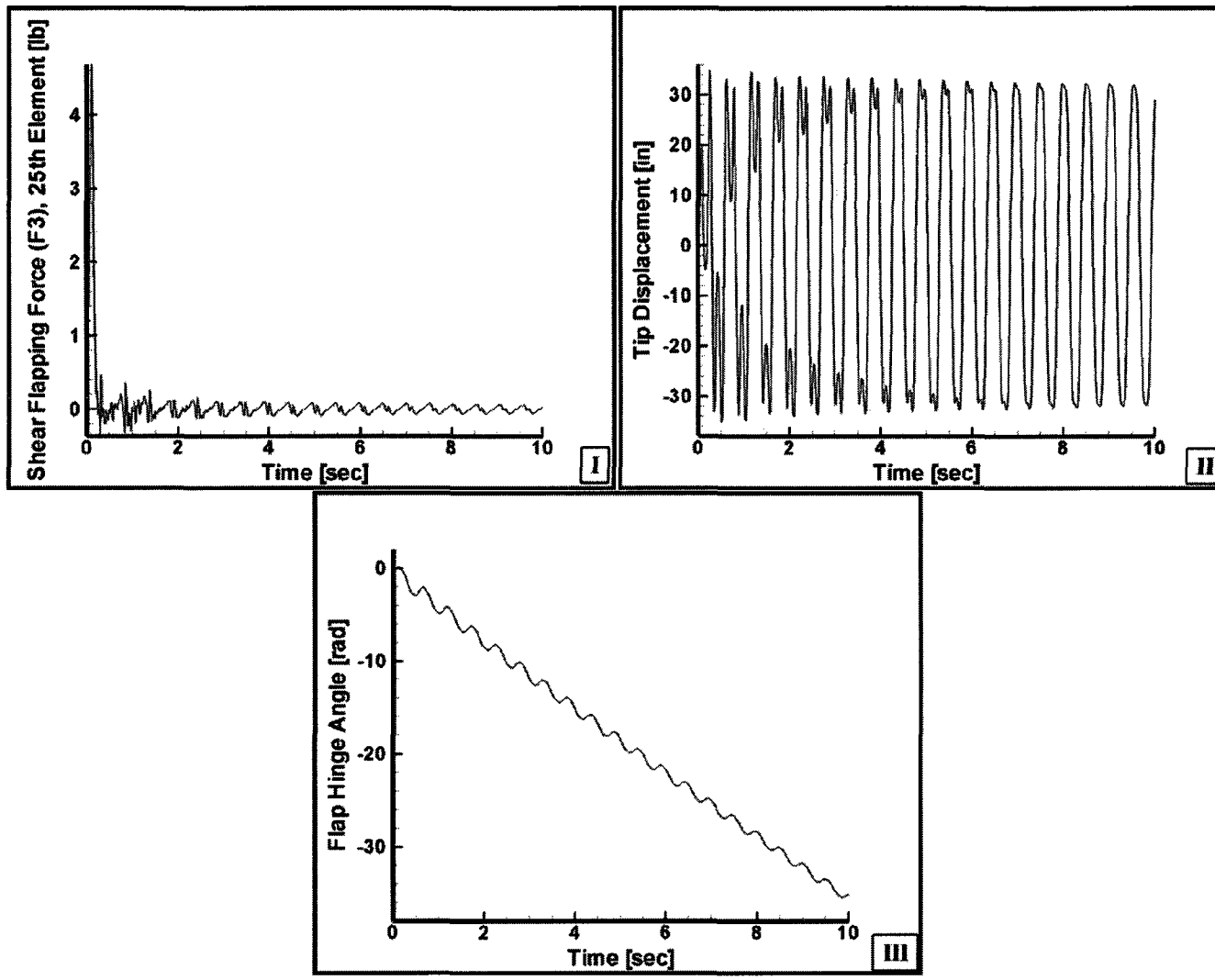

Figure 4.8: Time history of: (I) The flapping shear force F_3, (II) The tip flap displacement u_3, (III) the flap hinge angle ϕ_{flap} of case 3.

Figure. 4.9 proves the numerical consistency of the scheme in addition to its retained second order accuracy as required by Eq. 4.16 in the linear domain. Sub-figure (II) demonstrates that the second intrinsic conservation law can be used to gauge the accuracy of a given solution and forms a basis for a time step adaptive scheme.

The fifth set of examples is used to examine the dependance of the algorithmic damping on the size of the time step. Considering the Epps and Chandra aluminum blade with the flap-only articulation configuration and a tip sweep of $\delta = 30°$, the tip is subjected to

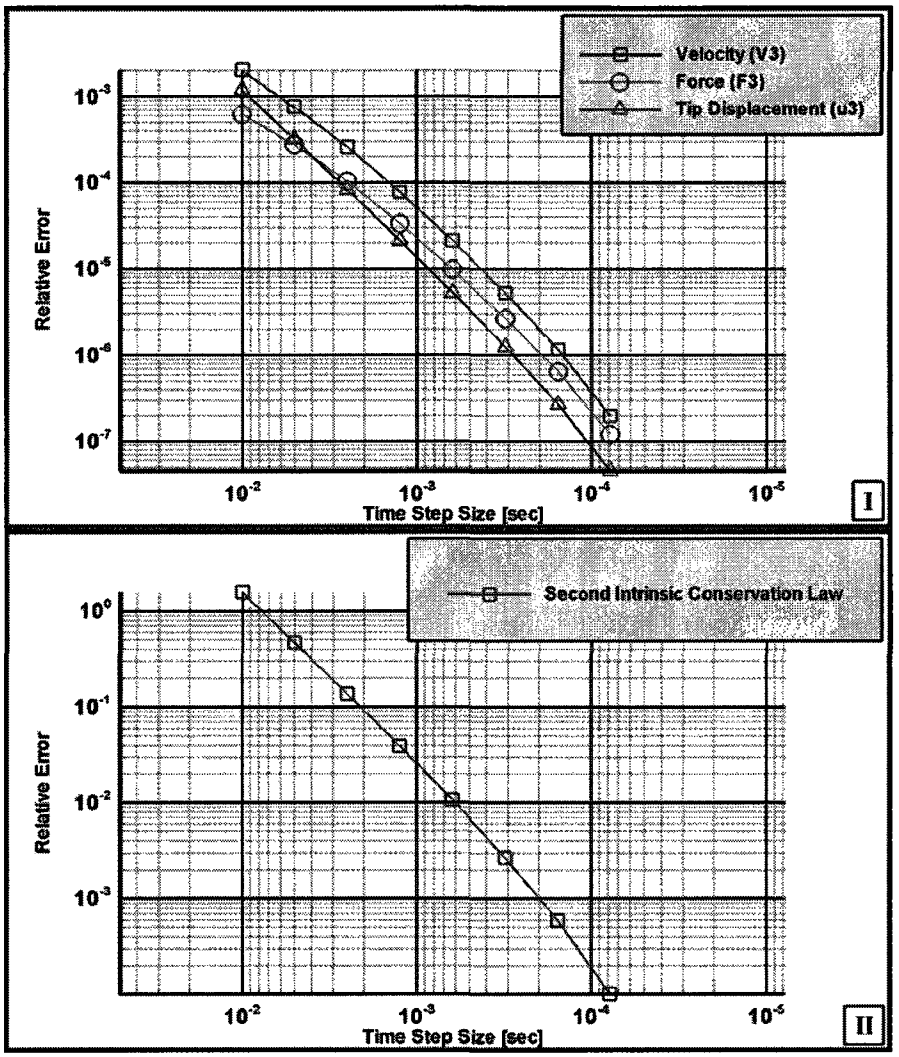

Figure 4.9: Normalized relative error based on the signal RMS of: (I) Cases 4 using the linear flap velocity V_3, the tip displacement u_3, and the shear flapping force F_3 of the 25^{th} beam element, (II) The second intrinsic conservation law.

symmetric triangular follower pulse forces in the flap and the lead-lag directions each with a duration of 0.1 sec peaking at 0.05 sec with a magnitude of 0.5 psi·in^2, and a simulation duration of 7 sec with $\lambda^{\infty} = 0$. Cases 5(a), 5(b), and 5(c) were solved using a time step size of $\Delta t = 10^{-2}$ sec, $\Delta t = 2.5 \times 10^{-3}$ sec, and $\Delta t = 6.25 \times 10^{-4}$ sec respectively. The FFT of the tip displacement after the external loading is ceased normalized by the maximum spectral intensity of each respective case is shown in Fig. 4.10(I), while the twisting

moment of the second beam element from the root of the blade of cases 5(a) and (c) is shown in Fig. 4.10(II).

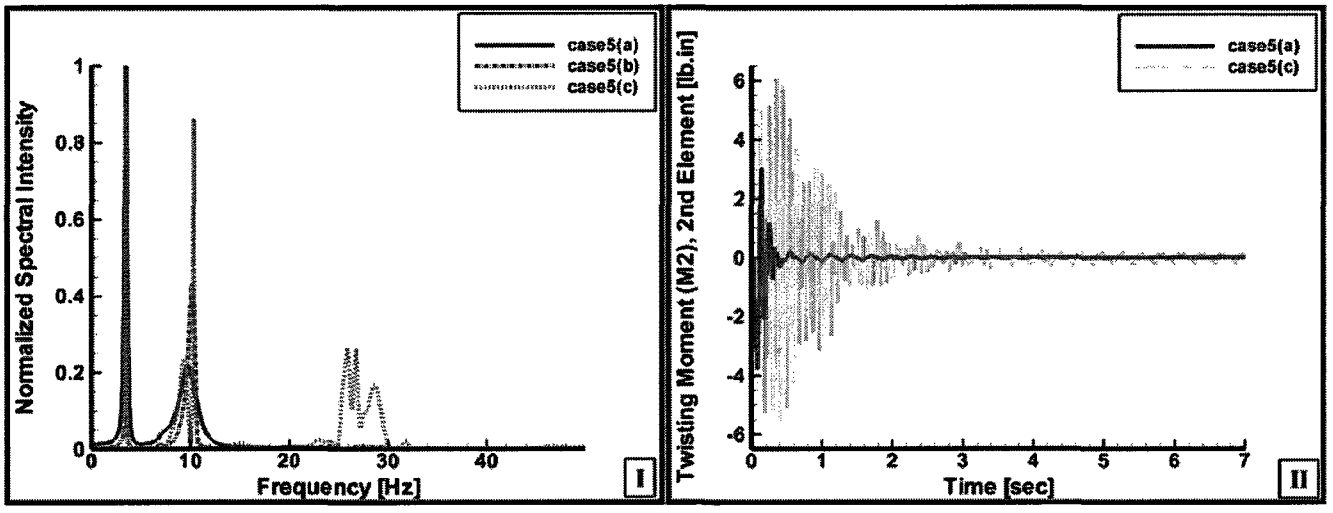

Figure 4.10: (I) Normalized FFT of the tip displacement u_3 of cases 5(a), (b) and (c), (II) Time history of the twisting moment of the second beam element of cases 5(a) and (c).

The effect of the time step size on the high frequency numerical damping is demonstrated in Fig. 4.10(I), where the size of the secondary peaks compared to the primary one corresponding to the first fundamental, qualitatively shows the consistent decrease of the algorithmic damping with decreasing time step size as would be expected from a conventional analysis of the scheme in the linear domain [149]. Decreasing the size of the time step to a point where the high frequency dissipation is very low will negatively affect the predicted response of the system since the high frequency contents will hinder the convergence process and may add spurious energy to the system as demonstrated earlier and sub-figure (II) displays the onset of this process for case 5(c).

The last set of examples examine a real engineering problem and compares the numerical predictions to the results of the experiment under consideration. A series of experimental blade drop tests were reported in [150], and the one of interest here is the one where the blade was dropped from a 9.7° flap hinge angle to impact the droop stops

set at an angle of $\phi_{droop} = 0°$. The flap hinge angle, the strains at 40% of blade length station, and the blade tip deflection were recorded in addition to other measurements. The reader is referred to the aforementioned reference for more details. The properties of the blade are presented in Table. C.2 in Appendix. C. Ten beam elements were used to spatially discretize the blade. The blade static configuration at an angle of 9.7° relative to the gravitational field was first determined using the present scheme, then the system was released from that static configuration to impact the droop stops that were modelled using the simple model discussed in Section 3.5.1. Since the information regarding the material that the droop stop is made of is presently unavailable, arbitrarily high stiffness was given to the spring without any dissipative viscoelastic damping. The time history of the flap hinge angle and the strain at the 40% of blade length station are predicted using the proposed scheme with $\lambda^{\infty} = -0.30$ and $\Delta t = 10^{-4}$ sec. Three cases labelled Drop Test (a), (b), and (c) are examined where no external damping aside from the algorithmic damping is used in (a) while a structural damping of $\bar{\sigma}[\text{s/m}] = \bar{\xi}[\text{m/s}] = 0.004$ is included in (b), and a 10% reduction in the flap-wise stiffness of the blade in addition to the latter structural damping is included in (c). The predicted flap hinge angle and the strain at 40% of blade length station are compared against the experimental data in Fig. 4.11(I) and Fig. 4.11(II) respectively.

The last set of examples clearly shows the suitability of the proposed scheme to tackle real engineering problems. In Fig. 4.11 the prediction of the model clearly matches the experimental trend and data. While the trend of drop test (a) matches the experimental one well throughout the duration of the experiment, the difference between the experimental data and the numerical predictions after the flap hinge loses contact with the droop stops is tackled in drop tests (b) and (c) based on Reference [150]. Drop test (b) demonstrates the improvement in the predicted bounce of the blade flap hinge after impacting the droop stops for a slight addition of structural damping which is based on fine tuning of Rayleigh

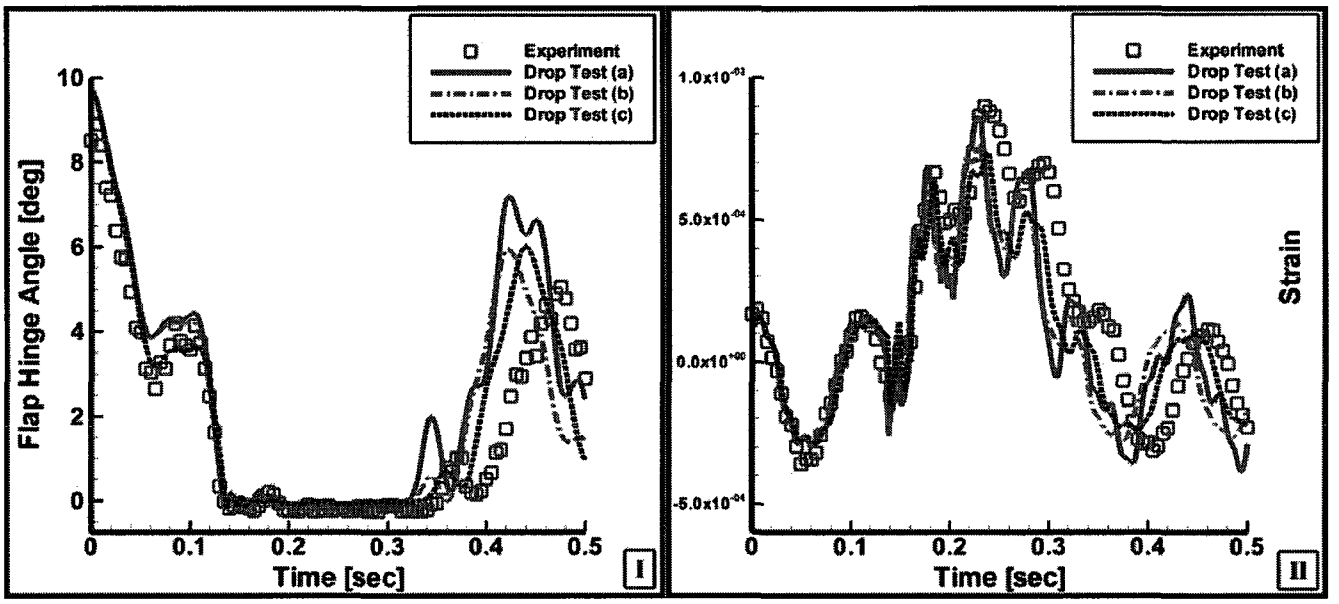

Figure 4.11: Time histories of: (I) The experimental/theoretical flap hinge angle, (II) The Experimental/Theoretical strain at 40% blade length station of the drop test/droop stop impact from 9.7°.

damping parameters. Drop test (c) includes the reduction in the structural flap stiffness of the blade as recommended in the aforementioned reference to decrease the phase lag between the numerical and the experimental signals. The results of this last set of simulations should be considered a success for the model and the scheme proposed, while noting that the EVI chosen for this simulation is -0.30. The model in its present intrinsic form has to be adjusted accordingly if one encounters a mechanical joint or constraint that has a displacement/rotation dependent stiffness. Two options are suggested: introduce the essential new degree of freedom only into the model augmented with the associated constraint equations; or evaluate its dynamic effect in a post-processing step after the system is solved for one time step. The latter approach was used to update the contact forces between the blade hinge and the droop stops in the simulated drop tests discussed above.

It becomes apparent that choosing the magnitude of the EVI and the resolution level for the scheme clearly depends on a proper qualitative assessment of the problem at hand. This includes the number of beam elements used in the simulation, the geometric and

the structural couplings present, the type of loading to be expected, and other factors as well. Despite the likelihood of the present scheme being not the most optimum for the geometrically exact intrinsic dynamics model of beams, it clearly demonstrates that certain reformulations of a given model allow for the successful application of schemes that were deemed unsuitable previously. This fact has also been alluded to in [140] for energy decaying schemes that are tailored to analytically prove an algorithmic bound on the energy of the system. While it would be ideal to analytically prove this bound for the present scheme at its asymptotic annihilation, complex nonlinear algebraic terms were faced and rendered this effort challenging. This was also reported by Hodges in [135] for the midpoint energy preserving scheme that was proposed in that work.

Finally, the features that are required for a nonlinear elastodynamics solver: accuracy, numerical consistency, stability, and high frequency numerical dissipation, were all demonstrated by the proposed scheme. Therefore, it will be utilized in the rest of this investigation to solve for the time history of selected state variables. The results of this investigation are summarized in [151].

4.6.1 Active Beam Element Validation

To validate the active beam element implementation, an example that was recently analyzed using ANSYS Multiphysics and DYMORE is adopted [121]. The cross-sectional elastic properties and the actuation vector is given in Table C.3 in Appendix C. The predicted static deformations due to embedded active material are compared to those predicted by ANSYS, DYMORE, and a linear beam theory in Table 4.2. Once again, the agreement is excellent and this validates the present implementation of geometrically exact intrinsic active beam elements.

Table 4.2: Tip deformation due to embedded active material. Active beam element implementation validation example.

Displacement	ANSYS	DYMORE	Present	Linear	Error(Present vs ANSYS)
u_1[mm]	-0.0271	-0.0271	-0.0272	-0.0254	0.4%
u_3[mm]	0.7157	0.6969	0.71430	0.7321	0.1%

4.7 Future Recommendations

Variational integrators that derive from the geometric structure of the equations of motion seem to hold promise in terms of efficiency, invariance preservation, and accuracy [152]. It is definitely worth investigating these integrators for engineering applications like the one presented in this research.

Chapter 5

Nonlinear Quasi-Steady and Unsteady Aerodynamics Modelling

5.1 Overview of Chapter 5

In this chapter, the quasi-steady aerodynamic coefficients of the NACA0012 and NACA64A010 airfoils is given. Additionally, the unsteady aerodynamic theory of 2-D thin-airfoils based on the AMT is outlined and its implementation validated. The semi-empirical L-B dynamic stall model that represents a natural extension of the attached flow unsteady theory is also outlined and validated.

5.2 Nonlinear Quasi-Steady Model of NACA0012 with Stall Effects

The quasi-steady behaviour of an airfoil refers to its aerodynamic coefficients [59] when the airfoil motion relative to the incoming flow is not changing rapidly according to a predefined quantitative criterion. This criterion is called the reduced frequency and it is

defined as

$$\bar{\mathcal{K}} = \frac{c\omega}{2V} \tag{5.1}$$

where c is the airfoil chord length measured from the leading edge to the trailing edge of the airfoil as shown in Fig. 5.1, ω is the frequency of the airfoil varying phenomenon like its pitch angle, and V is the incoming free-stream velocity relative to the airfoil.

A value of $\bar{\mathcal{K}} > 0.06$ [153] is generally indicative of the importance of the unsteady effects. Other rapid variations in the aerodynamic environment typically found in rotary flight can be envisioned, including variations in the Mach number or encountered gusts and vortices. These considerations would significantly complicate the analysis [154, 155] and they will not be considered in this investigation as the current focus is on the detailed modelling of the rotor aeroelastic response during engagement/disengagement phase of operation.

The NACA 0012 airfoil, shown in Fig. 5.1, is extensively used to conduct aeroelasticity research. The primary reasons for this are the extensive availability of aerodynamic data and constants, the airfoil symmetry and hence ease of manufacturing, and its linear behaviour for small angles of attack at moderate and high Mach numbers. Its nonlinear quasi-steady behaviour over the full range of angle of attack with stall effects and Mach number dependance is well documented in the engineering literature [156, 17]. The aerodynamic lift, drag, and twisting moment coefficients are determined experimentally and so is their dependance on the free-stream Mach number. For the whole range of the angle of attack, denoted as α [deg], and a flow Mach number of M, the semi-empirical nonlinear quasi-steady coefficients are given in Eqs. 5.2 through 5.6 [156]

$$
\begin{aligned}
a &= \frac{0.1}{\sqrt{1-M^2}} - 0.01M \\
\alpha_l &= 15 - 16M \\
K_1 &= 0.0233 + 0.342M^{7.15} \\
K_2 &= 2.05 - 0.95M
\end{aligned} \tag{5.2}
$$

$$
\begin{aligned}
C_l &= a\alpha && ,0 \leq \alpha \leq \alpha_l \\
C_l &= a\alpha - K_1\left(\alpha - \alpha_l\right)^{K_2} && ,\alpha_l \leq \alpha \leq 20 \\
C_l &= 1.15\sin(2\alpha) && ,20 \leq \alpha \leq 161 \\
C_l &= -0.7 && ,161 \leq \alpha \leq 173 \\
C_l &= 0.1\left(\alpha - 180\right) && ,173 \leq \alpha \leq 187 \\
C_l &= 0.7 && ,187 \leq \alpha \leq 201 \\
C_l &= 1.15\sin(2\alpha) && ,201 \leq \alpha \leq 340 \\
C_l &= -a|\alpha - 360| - K_1\left(|\alpha - 360| - \alpha_l\right)^{K_2} && ,340 \leq \alpha \leq 360 - \alpha_l \\
C_l &= -a|\alpha - 360| && ,360 - \alpha_l \leq \alpha \leq 360
\end{aligned} \tag{5.3}
$$

$$
\begin{aligned}
C_{d0} &= 0 \\
\alpha_d &= 17 - 23.4M \\
K_3 &= 0.00066 \\
K_4 &= 2.54 \\
C_{1di} &= C_{d0} + (65.8\alpha^2 - 0.226\alpha^4 + 0.0046\alpha^6) \times 10^{-6} \\
C_{2di} &= C_{d0} + (65.8(\alpha - 360)^2 - 0.226(\alpha - 360)^4 + 0.0046(\alpha - 360)^6) \times 10^{-6}
\end{aligned} \tag{5.4}
$$

$$
\begin{aligned}
C_d &= C_{1di} && ,0 \leq \alpha \leq \alpha_d \\
C_d &= C_{1di} + K_3(\alpha - \alpha_d)^{K_4} && ,\alpha_d \leq \alpha \leq 20 \\
C_d &= 1.03 - 1.02\cos(2\alpha) && ,20 \leq \alpha \leq 340 \\
C_d &= C_{2di} + K_3(\mid \alpha - 360 \mid -\alpha_d)^{K_4} && ,340 \leq \alpha \leq 360 - \alpha_d \\
C_d &= C_{2di} && ,360 - \alpha_d \leq \alpha \leq 360
\end{aligned} \tag{5.5}
$$

$$
\begin{aligned}
C_m &= 0 && ,0 \leq \alpha \leq 12 \\
C_m &= 4.69 \times 10^{-5} \times \alpha^2 - 1.17 \times 10^{-2} \times \alpha^2 + 0.133 && ,12 \leq \alpha \leq 120 \\
C_m &= -4.23 \times 10^{-7}\alpha^4 + 2.36 \times 10^{-4}\alpha^3 - 4.98 \times 10^{-2}\alpha^2 + 4.52\alpha - 155.46 && ,120 \leq \alpha \leq 172 \\
C_m &= 0.05(\alpha - 180) && ,172 \leq \alpha \leq 188 \\
C_m &= 2.16 \times 10^{-7}\alpha^4 - 1.96 \times 10^{-4}\alpha^3 + 6.64 \times 10^{-2}\alpha^2 - 9.96\alpha + 556.78 && ,188 \leq \alpha \leq 240 \\
C_m &= -4.69 \times 10^{-5}\alpha^2 + 2.20 \times 10^{-2}\alpha - 1.98 && ,240 \leq \alpha \leq 348 \\
C_m &= 0 && ,348 \leq \alpha \leq 360
\end{aligned} \tag{5.6}
$$

where C_l, C_d, and C_m are the quasi-steady lift, drag, and moment aerodynamic coefficients respectively. A plot of these coefficients at a Mach number of 0.3 is shown in Fig. 5.2. Additionally, the approximate corresponding constants for the NACA64A010 airfoil nonlinear quasi-steady coefficients are provided in Appendix D due to its importance for subsequent analysis in this research.

If the quasi-steady aerodynamic coefficients were evaluated based on the angle of attack seen at the three-quarter chord point shown in Fig. 5.1 then the approximate apparent wind velocity as seen by the airfoil is

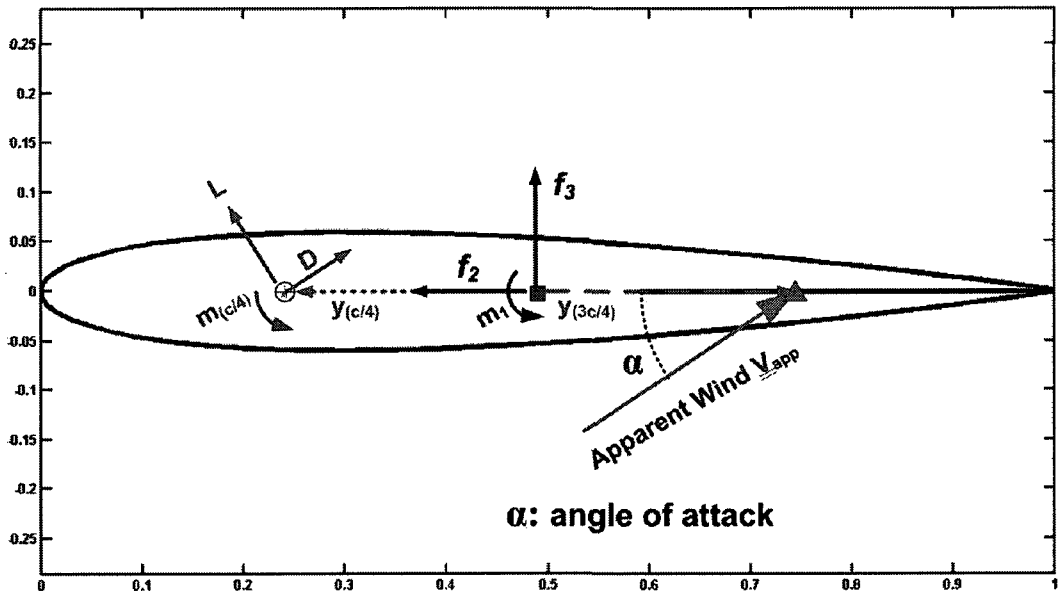

$y_{(c/4)}$: quarter chord point measured from reference line

$y_{(3c/4)}$: three-quarter chord point measured from reference line

quarter chord point
beam reference line point
three quarter chord point

Figure 5.1: NACA0012 airfoil with the relevant aerodynamic frames and points.

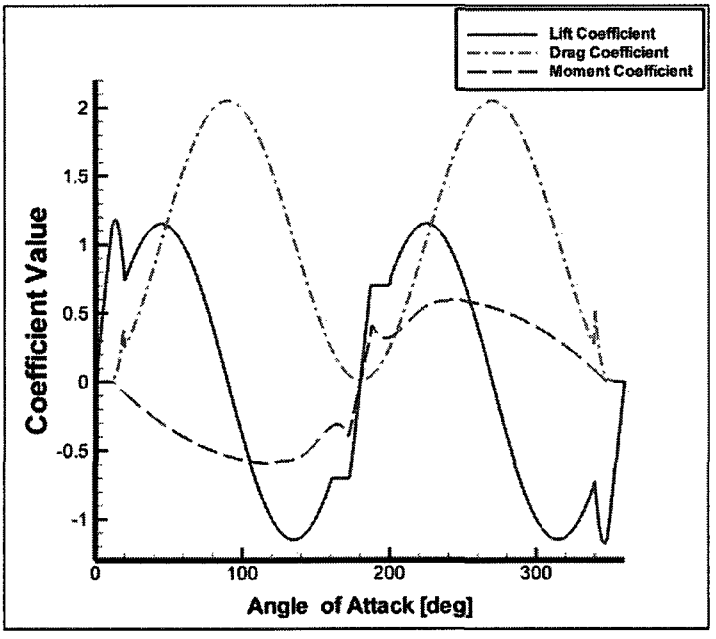

Figure 5.2: Nonlinear quasi-steady aerodynamic coefficients of NACA0012 at a Mach number of 0.3.

$$V_{\text{app}} = V_{\text{wind}} - (\overline{V} + \widetilde{\overline{\Omega}} y_{3c/4}) \tag{5.7}$$

$$\alpha = \pi - \arctan(\frac{e_3^{\text{T}} V_{\text{app}}}{e_2^{\text{T}} V_{\text{app}}}) \tag{5.8}$$

where $\overline{V}$ is the linear inertial velocity of the section in its deformed frame, $\overline{\Omega}$ is the inertial angular velocity of the section in its deformed frame, and e_2 and e_3 are the Cartesian unit vectors defined in Chapter 3.

Subsequently, if the resulting aerodynamic coefficients are applied at the quarter-chord point, then the quasi-steady theory is a good approximation of the unsteady one [153] such that

$$\left\{ \begin{array}{c} C_l \\ C_d \\ C_{m_{3c/4}} \end{array} \right\}_{\text{unsteady}} \approx \left\{ \begin{array}{c} C_l(\alpha, M) \\ C_d(\alpha, M) \\ C_{m_{c/4}}(\alpha, M) \end{array} \right\}_{\text{quasi-steady}\,\frac{3c}{4}} \tag{5.9}$$

The cross-section circulatory aerodynamic forces per-unit-length expressed in the wind frame as seen in Fig. 5.1 are then

$$\begin{aligned} L &= \frac{1}{2}\rho \parallel V_{\text{app}} \parallel^2 cC_l \\ D &= \frac{1}{2}\rho \parallel V_{\text{app}} \parallel^2 cC_d \\ m_{c/4} &= \frac{1}{2}\rho \parallel V_{\text{app}} \parallel^2 c^2 C_m \end{aligned} \tag{5.10}$$

where ρ is the flow medium density, L is the normal aerodynamic force per-unit-length, D is the drag aerodynamic force per-unit-length, and $m_{c/4}$ is the aerodynamic twisting moment per-unit-length.

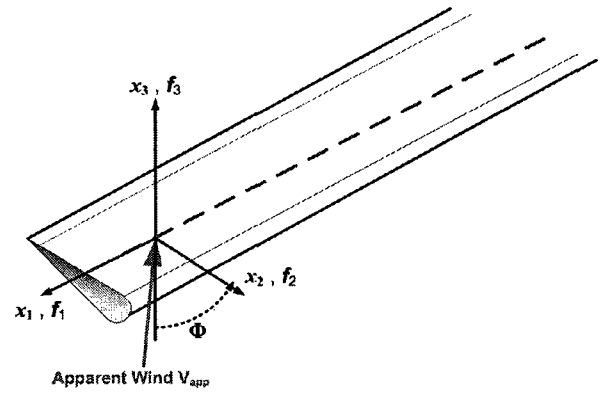

Figure 5.3: Blade frame view and incoming wind.

The skew angle of the wind relative to the blade in the $x_1 - x_2$ plane, shown in Fig. 5.3, is also taken into account and the aerodynamic forces per-unit-length are transferred to the beam reference line and transformed to the airfoil deformed frame so that

$$\begin{aligned} f_1 &= -D\sin(\Phi) \\ f_2 &= L\sin(\alpha) - D\cos(\Phi)\cos(\alpha) \\ f_3 &= L\cos(\alpha) + D\cos(\Phi)\sin(\alpha) \\ m_1 &= m_{c/4} + \widetilde{y}_{c/4} f_3 \end{aligned} \tag{5.11}$$

5.3 The Arbitrary Motion Theorem (Dynamic Wake Modelling)

The quasi-steady aerodynamic theorem presented above gave the aerodynamic loads based on the instantaneous angle of attack. As mentioned earlier, this form of analysis is valid if the airfoil motion or the oncoming wind velocity is varying slowly with time. If the variations are deemed to be rapid based on the reduced frequency criterion, then unsteady

aerodynamic theory becomes necessary. In the unsteady analysis, the effects of the shed wake are taken into account, which is reflected in the finite time it takes for the circulatory aerodynamic lift to build up as the angle of attack changes.

Historically, rotorcraft unsteady aerodynamics borrows heavily from the mature fixed-wing theory with appropriate modifications that are suitable for the unique environment of rotary flight. A historical presentation of the evolution of the unsteady aerodynamic theory for rotary wing is presented in many references [153, 157, 158] and it will not be reproduced here. Rotary unsteady aerodynamic theories can be categorized as those in the frequency domain and those in the time domain. Obviously, the interest here is in the latter knowing that theories in the two domains are related in most cases through the Fourier transform pair. The two suitable time domain theories are the Arbitrary Motion Theorem (AMT) [159] that is based on indicial functions derived from frequency domain theories and linear system principles, and the finite-state model of Peters and He [56] that is developed from both vorticity and acceleration potential models based on modal reduction via closed-form eigenfunctions. The former has the advantages of being intuitive and its ease of derivation while the latter is hierarchial and can be easily integrated into state-space models. The equivalence of the two theorems has been demonstrated in the engineering literature [158]. As was done in Keller [17], the former approach is adopted in this investigation. The primary reason for including the unsteady effects in this research is to further assess their role in the BSP, which were theoretically shown to be of low importance at low speeds [17, 11, 28].

5.3.1 Unsteady Circulatory Aerodynamic Loads

Circulatory aerodynamic forces are those that derive from attached circulating flow over the airfoil, which can be obtained from potential flow theory. According to the AMT, the circulatory lift at the three-quarter chord point is written in terms of the Duhamel integral

such that

$$L = \frac{C_l}{2}\rho V_{flow}(t)c \underbrace{\left[w_{3/4}(0)\phi(s) + \int_0^s \frac{\mathrm{d}w_{3/4}(\sigma)}{\mathrm{d}\sigma}\phi(s-\sigma)\ \mathrm{d}\sigma\right]}_{w_{3/4,eff}} \tag{5.12}$$

where C_l is the attached flow linear quasi-steady lift coefficient; c is the airfoil chord length; $V_{flow}(t)$ is the free stream velocity; σ is a dummy integration variable; s is the aerodynamic time variable defined as

$$s \equiv \frac{2}{c}\int_0^t V_{flow}(t)\ \mathrm{d}t \tag{5.13}$$

and $w_{3/4}(t)$ is the airfoil vertical velocity defined as

$$w_{3/4}(t) = V_{flow}(t)\sin(\alpha(t)) + \frac{c}{2}\left(\frac{1-2a}{2}\right)\dot{\alpha}(t) \tag{5.14}$$

where the over-dot represents time differentiation, a is a measure of the distance between the beam reference line and the geometric centre of the airfoil in terms of half the chord length, and $\phi(s)$ is the indicial function that is derived from the airfoil response to a step change in the angle of attack such that

$$\phi(s) = \frac{1}{2\pi}\int_{-\infty}^{+\infty}\frac{C(k)}{ik}e^{iks}\ \mathrm{d}k \tag{5.15}$$

where $C(k)$ is the well known Theodorsen function defined in the frequency domain [160].

The explicit dependance on time in Eqs. 5.12 to 5.14 is duly noted, which implies time varying values of relevant parameters. The effective vertical velocity, $w_{3/4,eff}$, highlighted in Eq. 5.12 contains the history of the changes in the apparent flow encountered by the airfoil. Using an asymptotic expansion of the Duhamel integral and a good approximation of the indicial function in Eq. 5.15 to obtain compact recursive relations that minimize the computational cost of calculating the unsteady effects is one of the principal premises of

the AMT. Adopting a general two-term exponential indicial function in the aerodynamic time domain, the effective vertical velocity is written as

$$\begin{aligned} \phi(s) &= 1 - A_1 e^{-b_1 s} - A_2 e^{-b_2 s} \\ w_{3/4,eff} &= w_{3/4}(0)\left[1 - A_1 e^{-b_1 s} - A_2 e^{-b_2 s}\right] + \\ &\int_0^s \frac{\mathrm{d}w_{3/4}(\sigma)}{\mathrm{d}\sigma}\left[1 - A_1 e^{-b_1(s-\sigma)} - A_2 e^{-b_2(s-\sigma)}\right]\,\mathrm{d}\sigma \end{aligned} \tag{5.16}$$

where the coefficients A_1, A_2, b_1, and b_2 are given by the Jones approximation [153]

$$\begin{aligned} A_1 &= 0.165 \quad b_1 = 0.0455 \\ A_2 &= 0.335 \quad b_2 = 0.3 \end{aligned} \tag{5.17}$$

Rewriting $w_{3/4,eff}$ as

$$w_{3/4,eff} = w_{3/4}(0) \underbrace{-A_1 w_{3/4}(0)\exp(-b_1 s) - A_2 w_{3/4}(0)\exp(-b_2 s)}_{\ll w_{3/4}(0) \text{ as } s\to\infty} + \underbrace{\int_0^s \mathrm{d}w_{3/4}(\sigma)}_{w_{3/4}(s)-w_{3/4}(0)} - X(s) - Y(s) \tag{5.18}$$

one obtains $X(s)$ and $Y(s)$, known as the deficiency functions that contain the time history of the motion and are given as

$$\begin{aligned} X(s) &= A_1 \int_0^s \frac{\mathrm{d}w_{3/4}(\sigma)}{\mathrm{d}\sigma} e^{-b_1(s-\sigma)}\,\mathrm{d}\sigma \\ Y(s) &= A_2 \int_0^s \frac{\mathrm{d}w_{3/4}(\sigma)}{\mathrm{d}\sigma} e^{-b_2(s-\sigma)}\,\mathrm{d}\sigma \end{aligned} \tag{5.19}$$

To write the deficiency functions in a useful form, the aerodynamic time is advanced

incrementally by Δs to time index j while the integration and the differentiation are approximated by Simpson's rule and the backward difference respectively to arrive at [157]

$$\begin{aligned} X^j &= X^{j-1}e^{-b_1\Delta s} + \frac{A_1}{6}\Delta w^j_{3/4}\left[1 + 4e^{-b_1\frac{\Delta s}{2}} + e^{-b_1\Delta s}\right] \\ Y^j &= Y^{j-1}e^{-b_2\Delta s} + \frac{A_2}{6}\Delta w^j_{3/4}\left[1 + 4e^{-b_2\frac{\Delta s}{2}} + e^{-b_2\Delta s}\right] \end{aligned} \tag{5.20}$$

where X^{j-1} and Y^{j-1} are the deficiency functions at the previous aerodynamic step; and $\Delta w^j_{3/4}$ is the finite difference of the vertical velocity that can be derived from Eq. 5.14 as

$$\Delta w^j_{3/4} = \left[V^j_{flow} - V^{j-1}_{flow}\right]\sin(\alpha^j) + V^j_{flow}\cos(\alpha^j)\left[\alpha^j - \alpha^{j-1}\right] + \frac{c}{2}\left(\frac{1-2a}{2}\right)\left[\dot{\alpha}^j - \dot{\alpha}^{j-1}\right] \tag{5.21}$$

The aerodynamic time step Δs is approximated based on Eq. 5.13 and trapezoidal quadrature, while backward difference is used to approximate the time derivatives in Eq. 5.21. The effective vertical velocity is therefore written compactly as

$$w_{3/4,eff} = w_{3/4}(s) - X(s) - Y(s) \tag{5.22}$$

The effective angle of attack α_{eff} is defined as

$$\alpha_{eff} = \arcsin\left(\frac{w_{3/4,eff}}{V_{flow}}\right) \tag{5.23}$$

Eq. 5.23 allows for the unsteady circulatory lift coefficient to be defined based on Eq. 5.12 as

$$C^c_l = C_l\alpha_{eff} \tag{5.24}$$

One can simply replace the lift coefficient in Eq. 5.10 with the one in Eq. 5.24 to calculate the lift force per-unit-length. This force is normal to the flow onto the airfoil at the effective angle of attack where it is then resolved to a normal lift force coefficient C_n^c and a chord-wise coefficient C_c^c that represents the drag such that

$$C_n^c = C_l^c \cos(\alpha_{eff}) \tag{5.25}$$

$$C_c^c = C_l^c \sin(\alpha_{eff}) \tag{5.26}$$

The validation of the implemented theory was performed for a NACA0012 airfoil that is pitching with a functional form of $\alpha = 2.1° + 8.2° \sin(wt)$ at a reduced frequency of $\bar{\mathcal{K}} = 0.074$ in a constant free stream with a Mach number of 0.383. The relevant unsteady circulatory coefficients are shown in Fig. 5.4, which have remarkable resemblance in terms of magnitude and form to the reported experimental data under the same conditions in Reference [161].

Another form of unsteady aerodynamic load arises from the inertial interactions between the air inertial mass and the airfoil and this form is known as the non-circulatory aerodynamic loads. The derivation of these loads can be found in many references [157, 160] and it will not be shown here. Denoting these aerodynamic loads with superscript nc and using the backward difference scheme to approximate time derivatives, they are given at the quarter-chord point in a discretized form by

$$\begin{aligned} L_n^{nc,\,j} &= \frac{\pi\rho c^2}{4}\left[\frac{V_j - V_{j-1}}{\Delta t}\sin(\alpha_j) + V_j\frac{\alpha_j - \alpha_{j-1}}{\Delta t}\cos(\alpha_j) + \frac{c}{4}\frac{\dot{\alpha}_j - \dot{\alpha}_{j-1}}{\Delta t}\right] \\ m_m^{nc,\,j} &= \frac{\pi\rho c^3}{8}\left[\frac{-(V_j - V_{j-1})}{2\Delta t}\sin(\alpha_j) - V_j\frac{\alpha_j - \alpha_{j-1}}{\Delta t}\cos(\alpha_j) - \frac{3c}{16}\frac{\dot{\alpha}_j - \dot{\alpha}_{j-1}}{\Delta t}\right] \end{aligned} \tag{5.27}$$

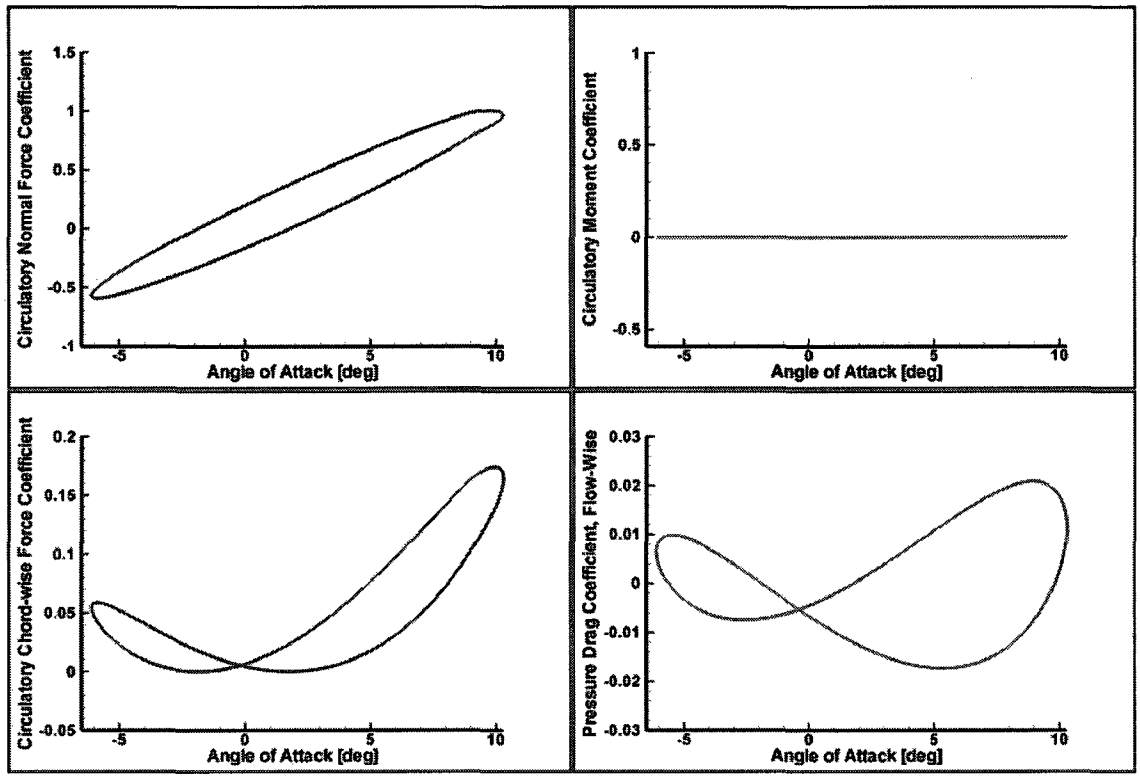

Figure 5.4: Unsteady circulatory aerodynamic coefficient of an airfoil pitching with a functional form of $\alpha = 2.1° + 8.2° \sin(wt)$, $\bar{K} = 0.074$, $M = 0.383$.

The non-circulatory aerodynamic coefficients, that can be defined from Eq. 5.27, are added to the circulatory ones in Eq. 5.26 to give the total unsteady aerodynamic loads.

5.4 Leishman and Beddoes Dynamic Stall Model

The airfoil stalls when the flow is no longer attached to the airfoil surface, which signals the onset of unsteady and complex flow regions over the airfoil. The phenomenon is highly nonlinear and is known to cause rotor stability problems known as stall flutter. The effect of the stall was modelled in the quasi-steady theory under section 5.2 along with its Mach number dependance, where the effect of the stall can be seen in Fig. 5.2 around 15° angle of attack as a steep drop in the lift coefficient. When unsteady effects are present, the stall becomes time dependent and the ability to predict the unsteady aerodynamic loads

presented earlier is critical to the prediction of dynamic stall. When the dynamic stall is fully developed and flow separation is complete, the quasi-steady model is used to predict the aerodynamic loads until the flow reattaches; therefore, dynamic stall is a buffer zone with its unique characteristics that separates the unsteady regime from the quasi-steady one in this research. The research in dynamic stall is still ongoing and some of its aspects are yet to be understood and modelled. In this research, the semi-empirical Leishman and Beddoes (L-B) dynamic stall model [161, 162] is adopted. The model is a natural extension of the unsteady AMT presented above, it is simple to implement despite the high complexity of the phenomenon it seeks to model, and it has demonstrated relatively good success when compared to experimental data [162]. Furthermore, the L-B model is used in many rotorcraft comprehensive analysis codes [163]. A pictorial illustration of the dynamic stall and relevant quantities, which will be defined subsequently, is shown in Fig. 5.5.

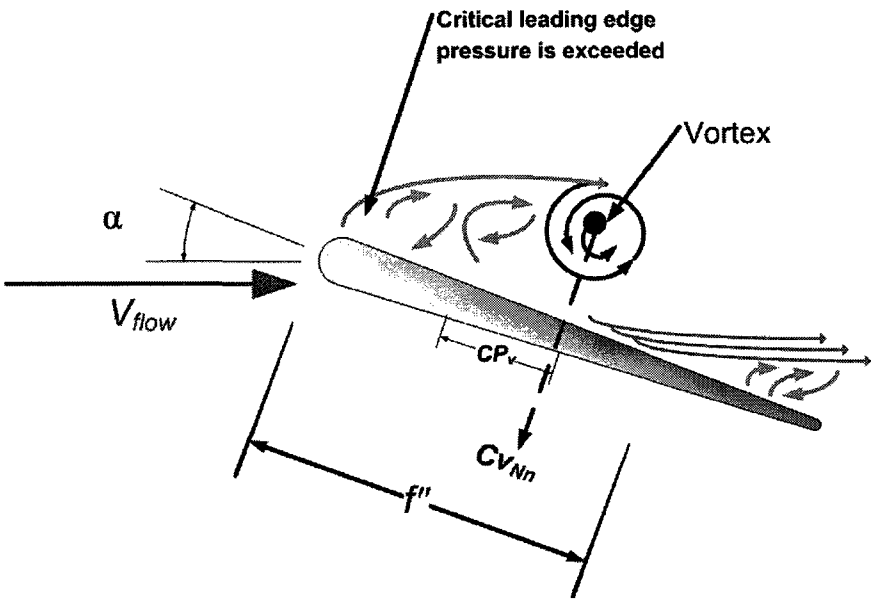

Figure 5.5: Illustration of dynamic stall and relevant physical quantities.

The criterion of airfoil flow leading edge separation is critical to predicting dynamic stall, which is represented in the L-B model as a critical leading edge pressure and its

gradient. This is equivalent to defining a corrected quasi-steady normal coefficient, C'_{n_j} at time index j such as

$$C'_{\mathrm{n}_j} = C_{\mathrm{n}_j} - D^{\mathrm{p}}_{\mathrm{n}_j} \tag{5.28}$$

where the deficiency function $D^{\mathrm{p}}_{\mathrm{n}_j}$ is defined as

$$D^{\mathrm{p}}_{\mathrm{n}_j} = D^{\mathrm{p}}_{\mathrm{n}_{j-1}} e^{\frac{\Delta s_j}{T_p}} - \left(C_{\mathrm{n}_j} - C_{\mathrm{n}_{j-1}}\right) e^{\frac{\Delta s_j}{2T_p}} \tag{5.29}$$

The attainment of $C'_{\mathrm{n}} \geq C_{\mathrm{quasi-stall}}$ causes leading edge flow separation, which is equivalent to the phenomenon observed in the quasi-steady model but time delayed due to the unsteady effects. The delay in reaching dynamic stall causes a slight enhancement of the normal lift coefficient. The constant T_p is determined experimentally and it is almost independent of airfoil shape. Appendix D contains the values of the airfoil constants used throughout this section. Conversely, the condition $C'_{\mathrm{n}} < C_{\mathrm{quasi-stall}}$ can be used to check leading edge reattachment.

Trailing edge separation must also be monitored since it is the aspect of dynamic stall that causes loss of recirculation and introduces the nonlinear effects in the aerodynamic loads. The criterion in this case is the location of the trailing edge separation point measured from the airfoil leading edge. This point is defined by:

$$f'_j = \begin{cases} 1 - 0.3e^{\frac{|\alpha_f| - \alpha'_1}{S_1}} & |\,\alpha_f\,| \leq \alpha'_1 \\ 0.04 + 0.66e^{\frac{\alpha'_1 - |\alpha_f|}{S_2}} & |\,\alpha_f\,| > \alpha'_1 \end{cases} \tag{5.30}$$

where f'_j is the uncorrected trailing edge separation point, S_1 and S_2 are empirical airfoil constants, α'_1 is an angle of attack that is particular to the airfoil, and α_f is defined as

$$\alpha_f = \frac{C'_{\mathrm{n}}}{C_{\mathrm{quasi-stall}}} \tag{5.31}$$

The unsteady effects will introduce a lag in the development of the trailing edge separation point and this is taken into account as

$$f''_j = f'_j - D_{f'_j} \tag{5.32}$$

where the deficiency function $D_{f'_j}$ is defined as

$$D_{f'_j} = D_{f'_{j-1}} e^{\frac{-\Delta s_j}{T_f}} + \left(f'_j - f'_{j-1}\right) e^{\frac{-\Delta s_j}{2T_f}} \tag{5.33}$$

where the time constant T_f is unique for each airfoil.

When the trailing edge separation point is at 70% of the chord length from the leading edge ($f'' > 0.7$), trailing edge separation is considered significant. The nonlinear normal force coefficient due to the trailing edge separation is then

$$C^f_{\mathrm{n}_j} = C_{\mathrm{quasi-n}}(\alpha) \left(\frac{1 + \sqrt{f''_j}}{2}\right) \alpha_{eff} \tag{5.34}$$

Similarly, the moment coefficient is

$$C^f_{\mathrm{m}_j} = \left[K_0 + K_1\left(1 - f''_j\right) + K_2 \sin(\pi(f''_j))^m\right] C_{\mathrm{n}_j} \tag{5.35}$$

where K_0, K_1, K_2, and m are constants that are determined experimentally for the airfoil.

The chord force is calculated from Kirchhoff's theory as

$$C^f_{\mathrm{c}_j} = \eta C_{\mathrm{quasi-n}} \alpha^2_{eff} \sqrt{f''_j} \tag{5.36}$$

where η is an airfoil constant.

Another phenomenon that accompanies dynamic stall is vortex shedding. A vortex is generated at the leading edge of the airfoil during the early stages of the dynamic stall and subsequently travels along the airfoil to be shed with the flow. This physical process gives

rise to aerodynamic force and moment with their coefficients modelled semi-empirically. The coefficient for lift force

$$C^v_{\mathrm{n}_j} = C_{\mathrm{n}}(1 - K_{\mathrm{n}_j}) \tag{5.37}$$

where K_{n_j} is given by

$$K_{\mathrm{n}_j} = (1 + \sqrt{f''_j})/4 \tag{5.38}$$

Delay in vortex shedding is also introduced due to unsteady effects and a deficiency function is used to express the total accumulated lift force coefficient as

$$C^v_{N_{\mathrm{n}_j}} = C^v_{N_{\mathrm{n}_{j-1}}} e^{\frac{-\Delta s_j}{T_v}} + \left(C^v_{\mathrm{n}_j} - C^v_{\mathrm{n}_{j-1}}\right) e^{\frac{-\Delta s_j}{2T_v}} \tag{5.39}$$

where T_v is an experimentally determined constant.

The centre of pressure of the vortex causes a twisting moment to occur as it traverses the airfoil surface to be shed. The empirical location of the centre of pressure (aft of the quarter-chord point) is empirically modelled as

$$CP_{v_j} = 0.2\left[1 - \cos\left(\frac{\pi\tau_{v_j}}{T_{vl}}\right)\right] \tag{5.40}$$

where T_{vl} is a constant determined from experimental results, and τ_v is a non-dimensional vortex time defined as

$$\tau_{v_j} = \frac{c}{V_j} \tag{5.41}$$

The vortex moment coefficient about the quarter-chord point is then

$$C^v_{N_{\mathrm{m}_j}} = -CP_{v_j} * C^v_{N_{\mathrm{n}_j}} \tag{5.42}$$

When the vortex is completely shed, dynamic stall is considered complete and the flow is fully separated with the quasi-steady model being used to calculate the aerodynamic loads. The phenomenon of multiple vortex shedding is not considered in this investigation due to its less frequent occurrence despite its importance in some cases.

The total normal aerodynamic force coefficient due to trailing edge separation and vortex shedding is then

$$C_{\mathrm{n}}^{\mathrm{dynamic-stall}} = C_{\mathrm{n}}^{f} + C_{N_{\mathrm{n}}}^{v} \tag{5.43}$$

Similarly, the total moment coefficient at the quarter-chord point is

$$C_{\mathrm{m}}^{\mathrm{dynamic-stall}} = C_{\mathrm{m}}^{f} + C_{N_{\mathrm{m}}}^{v} \tag{5.44}$$

Resolving the coefficients in the airfoil frame and considering the drag in Eq. 5.36 yields

$$\begin{aligned} \breve{C}_{\mathrm{n}}^{\mathrm{dynamic-stall}} &= C_{\mathrm{n}}^{\mathrm{dynamic-stall}} \cos(\alpha) + C_{\mathrm{c}}^{f} \sin(\alpha) \\ \breve{C}_{\mathrm{d}}^{\mathrm{dynamic-stall}} &= C_{\mathrm{n}}^{\mathrm{dynamic-stall}} \sin(\alpha) - C_{\mathrm{c}}^{f} \cos(\alpha) \end{aligned} \tag{5.45}$$

The coefficients in Eq. 5.44 and Eq. 5.45 can be used with Eq. 5.10 to calculate the cross-section aerodynamic forces per-unit-length. The L-B dynamic stall model has been implemented in collaboration with another member of the Applied Dynamics Group [44] and integrated with the unsteady aerodynamics model. Results of applying the model to a NACA0012 airfoil pitching with $\alpha = 10.3° + 8.1° \sin(wt)$ at a reduced frequency of $\bar{\mathcal{K}} = 0.075$ in a free-stream with a Mach number of $M = 0.379$ are shown in Fig. 5.6. The dynamic stall phenomenon can be clearly seen in the normal lift coefficient along with the vortex shedding effect on the moment coefficient. The results are remarkably similar to

the reported experimental data for the same airfoil flight conditions in Reference [161].

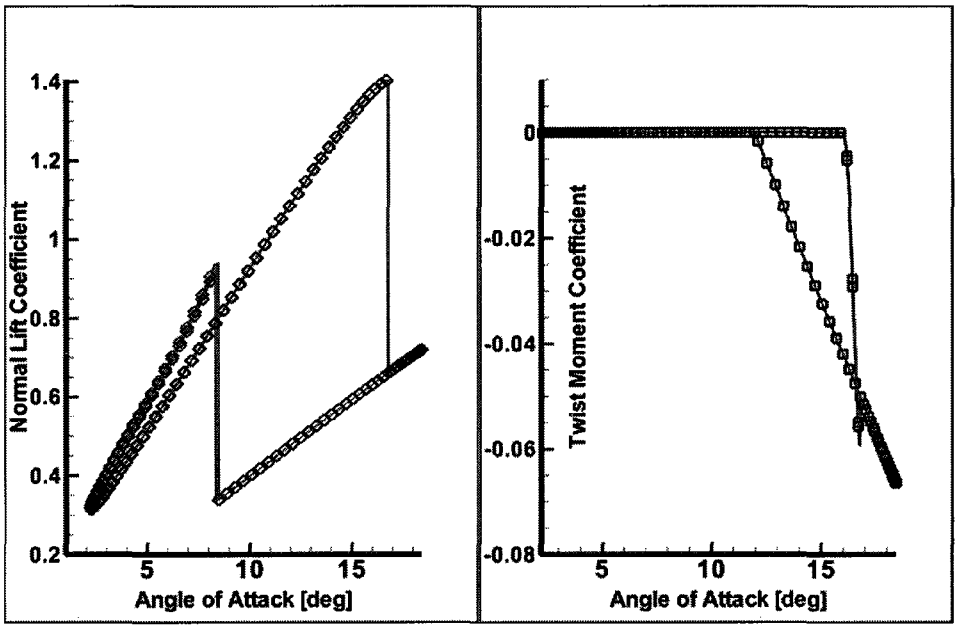

Figure 5.6: Normal lift and moment coefficients of a NACA0012 airfoil pitching with $\alpha = 10.3° + 8.1° \sin(wt)$, $\bar{K} = 0.075$, and $M = 0.379$.

The main components of the L-B dynamic stall model and their interaction are shown in Fig. 5.7.

5.5 Future Recommendations

The improvements to the overall model as presented in this chapter are numerous since they are directly tied to the still evolving and challenging fields of unsteady aerodynamics and dynamic stall. It is important to mention that the AMT is valid for moderate rigid body motion of the airfoil, which is obviously not always the case during the BSP, and alternative theories might be more suitable for future research. The recently developed theory of unsteady aerodynamics of flexible airfoils in Reference [158], which builds upon the successful finite-state model of Peters and He [56], seems to be a suitable improvement. Furthermore, there are strong indications that for low Mach numbers ($M < 0.3$), the L-B

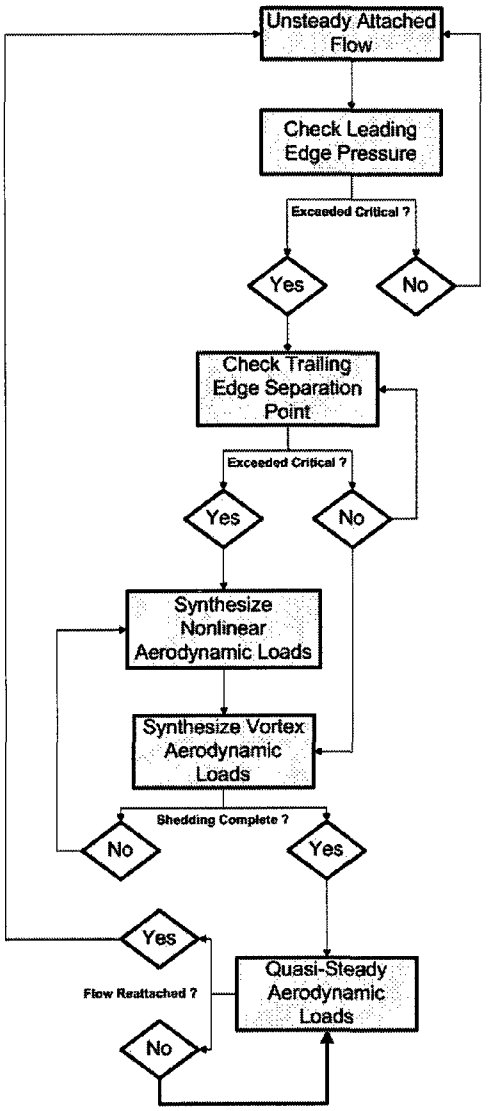

Figure 5.7: Flow chart illustration of the L-B dynamic stall algorithm.

dynamic stall model does not perform as well as it does for high ones. Recently, this problem has been tackled and resulted in an improved L-B model that works well for a wide range of low and high Mach numbers [163] and it is certainly more suitable for the low speed blade sailing research.

Chapter 6

Design and Manufacture of a $1/12^{\text{th}}$ Froude-Scaled Flap-articulated Rotor System

6.1 Overview of Chapter 6

An overview of the design and construction of a $\mathbf{1/12^{th}}$ Froude-scale rotor system is presented. Experimental challenges that were identified during and after the experimental phase and their impact are also discussed. The rotor system will be used to validate the overall simulation model developed in previous chapters and draw some experimental observations regarding the BSP.

6.2 Experiment Motivation and Goals

Each module of the simulation package that was introduced in Chapter 1 has been validated individually using experimental or computational data that were available in the engineering literature. The need to validate the overall simulation package, and consequently further validate the individual modules, and to establish its utility as a computational tool to study attenuation strategies of the BSP is highlighted. There is also a certain gap in the existing literature that was identified in terms of available experimental data for rotor dynamics operation in general and on ship decks in particular. Furthermore, while some experimental work related to the BSP by other researchers was cited in Chapter 1, the need for further quantitative and qualitative experimental characterization is still present.

The goals of the experiment described in this chapter were identified early in the research project in order to focus the scope of the design space and identify the necessary components and instrumentation. The design goals are enumerated as follow:

1. Record the time history of the flexible blade flap deflection profile during all phases of the rotor operation.

2. Induce large blade deflections in order to verify the geometrically-exact dynamic flexible beam model.

3. Construct a scaled rotor engagement and disengagement on a ship deck with representative ship motion process to assess the effect of deck motion on the rotor response.

4. Establish a baseline setup and design of a scaled rotor system for future experimental work involving more advanced blade designs including active/smart blades.

Since it is difficult to produce representative scaled ship motion in wind tunnels, it was decided to conduct the experiment in two phases, one addressing the effect of unsteady

flight deck aerodynamics; and the second addresses the effect of deck motion:

Phase 1: A principal goal of this phase is examining the effects of the airwake, in terms of wind speed and deck roll angle, on the rotor response during its engage/disengage operation. Additionally, the role played by the engagement/disengagement profile parameters like duration and acceleration is examined. It was decided to conduct this phase of the experiment in the 2[m]×3[m] wind tunnel facility at the National Research Council of Canada, Institute for Aerospace Research (NRC-IAR).

Phase 2: This phase examines the effects of scaled representative ship motion on the rotor response during its engage/disengage operation. It was decided to conduct this phase of the experiment using the six degrees of freedom MOOG 6DOF2000E motion platform available in the Applied Dynamics Laboratory at Carleton University.

It is acknowledged that the airwake effects are coupled to those of the ship motion in a nonlinear fashion and therefore, the separate experimental phases provided above will not give a fully representative reproduction of the conditions under which the BSP occurs. However, the experiment still presents the essential aspects of those conditions and it represents a further step in the experimental study of the BSP in the literature in terms of examining the effect of ship motion. Using the two experiments, it is possible to experimentally validate essential features of the computational models; these models can then be used to investigate the fully-coupled BSP.

In this chapter, the firmware and the experimental setup of a $1/12^{\text{th}}$ Froude-scaled rotor system that resulted from the above motivation and meets the enumerated goals will be described.

6.3 Design Evolution of the Hardware

6.3.1 Froude Scaling

To design and construct a properly scaled rotor system, five invariants that relate to aerodynamic, elastic, inertial, and gravitational interactions should be observed when comparing to the full-scale model [164, 153, 165] and these are:

$$\text{Frequency scaling}: \quad \lambda_f = \frac{E}{\rho(\Omega R)^2} \tag{6.1}$$

$$\text{Lock number}: \quad \gamma_l = \frac{\rho a c R^2}{I_b} \tag{6.2}$$

$$\text{Advance ratio}: \quad \mu = \frac{V}{\Omega R} \tag{6.3}$$

$$\text{Froude number}: \quad F_r = \frac{\Omega^2 R}{g} \tag{6.4}$$

$$\text{Mach number}: \quad M_{ch} = \frac{\Omega R}{a_\infty} \tag{6.5}$$

where E is the elastic modulus; ρ is the blade density; Ω is the maximum angular velocity of the rotor; R is the blade radius; a is the slope of the lift curve; c is the chord length; I_b is the transverse bending mass moment of inertia about the blade reference line (about the x_2 axis); V is the tip tangential velocity; g is the gravitational acceleration; and a_∞ is the far field flow velocity.

Of the five scaling considerations, at most four can be satisfied [165] since only four are considered independent at any time. In order to achieve absolute similarity, one has to actually build the full-scale model. Two scaling paradigms are used for scaled rotor tests: Froude and Mach scaling. Froude scaling is selected for this experiment since it represents the ratio between inertial forces and gravitational forces and is traditionally used for aeroelastic stability and control studies in hover. Additionally, the similarity of

the turbulence reduced frequency in terms of the rotor rotational speed and the frequency of the incoming turbulent vortices is preserved for Froude scaling where the turbulence reduced frequency is defined as

$$f^*_{\text{turb}} = \frac{f_{\text{turb}} R}{V} \tag{6.6}$$

where f_{turb} is the characteristic frequency of the turbulence.

However, the elastic frequency invariant in Eq. 6.1 was deliberately violated to amplify the flap-wise deflections in order to validate the geometrically-exact model of the flexible beam. The lock number γ_l is an important non-dimensional scaling coefficient, giving the ratio of aerodynamic to inertia forces acting on a rotor blade. For this experiment, the Lock number is set to be unity, which determined the blade mass scaling factor. Table. 6.1 lists the Froude-scaling of the fundamental physical quantities in terms of the scaling factor n_{Fr} that is defined as

$$n_{Fr} = \frac{\text{characteristic length of scaled model}}{\text{characteristic length of full} - \text{scale model}} \tag{6.7}$$

Additionally, Table 6.2 lists the values of the relevant Froude-scaled parameters and their associated relaxed values to meet the requirements outlined above, where a typical maritime helicopter, the AH101, was selected to represent the full-scale model. The scaling factor n_{Fr} was chosen to be $\frac{1}{12}$ according to the dimensions of the available test space.

Table 6.1: Scaling laws for Froude aeroelastic scaling.

Parameter	Froude-Scaling Factor	Parameter	Froude-Scaling Factor
Velocity	$\sqrt{n_{Fr}}$	Young's Modulus	n_{Fr}
Angular velocity	$\frac{1}{\sqrt{n_{Fr}}}$	Frequency	$\frac{1}{\sqrt{n_{Fr}}}$
Bending stiffness	n^5_{Fr}	Linear Acceleration	1
Torsional stiffness	n^5_{Fr}	Force	n^3_{Fr}
Mass per unit length	n^2_{Fr}	Reynolds number	$n^{3/2}_{Fr}$

From Table 6.2, the effect of reducing the bending stiffness, in order to induce large

Table 6.2: Relevant $1/12^{th}$ Froude-scaled parameters of the experimental rotor system.

Parameter	Full-Scale	Froude-Scale	Relaxed Froude-Scale
Blade length [m]	9.30	0.78	0.82
Ship deck width [m]	12.25	1.02	1.00
Rotor height [m]	5	0.42	0.44
Chord length [m]	0.6	0.05	0.05
Wind speed [m/s]	15	4.3	4.3
Ship deck angle [deg]	0/-20	0/-20	0/-20
Blade mass [kg]	250	0.145	0.137
Static tip deflection [m]	0.3	0.025	0.12
Droop stop angle [deg]	2	2	8
Flap stop angle [deg]	2	2	6.3
First flap frequency [Hz]	1.13	3.91	1.04

deflections, on the first flap frequency is observed. Also, the angular range of the blade rigid body rotation about its flap hinge is amplified to allow for large rigid body motion in addition to the large elastic flexibility of the blade. For this reason, the experimental results are not meant as a study of blade sailing conditions of the AH101 helicopter in themselves, but more of a validation of the simulation tools developed.

6.3.2 Rotor Blades

The rotor system is designed to be two-bladed where Fig. 6.1 shows the blades with and without the airfoil segments. As shown in the figure, each blade is instrumented with five full-wheatstone bridge strain gauges to measure the bending strain only. The airfoil axial profile has been segmented as to eliminate its contribution to the stiffness of the blade. Therefore, the cross-sectional stiffness constants are derived from the aluminum spine only. The airfoil segments were machined from RenShape [166], a polyurethane foam, in two halves and glued together over the aluminum spine.

The aerodynamic profile of the airfoil was chosen based on its performance for low Reynolds numbers encountered during the stages of the engagement/disengagement where

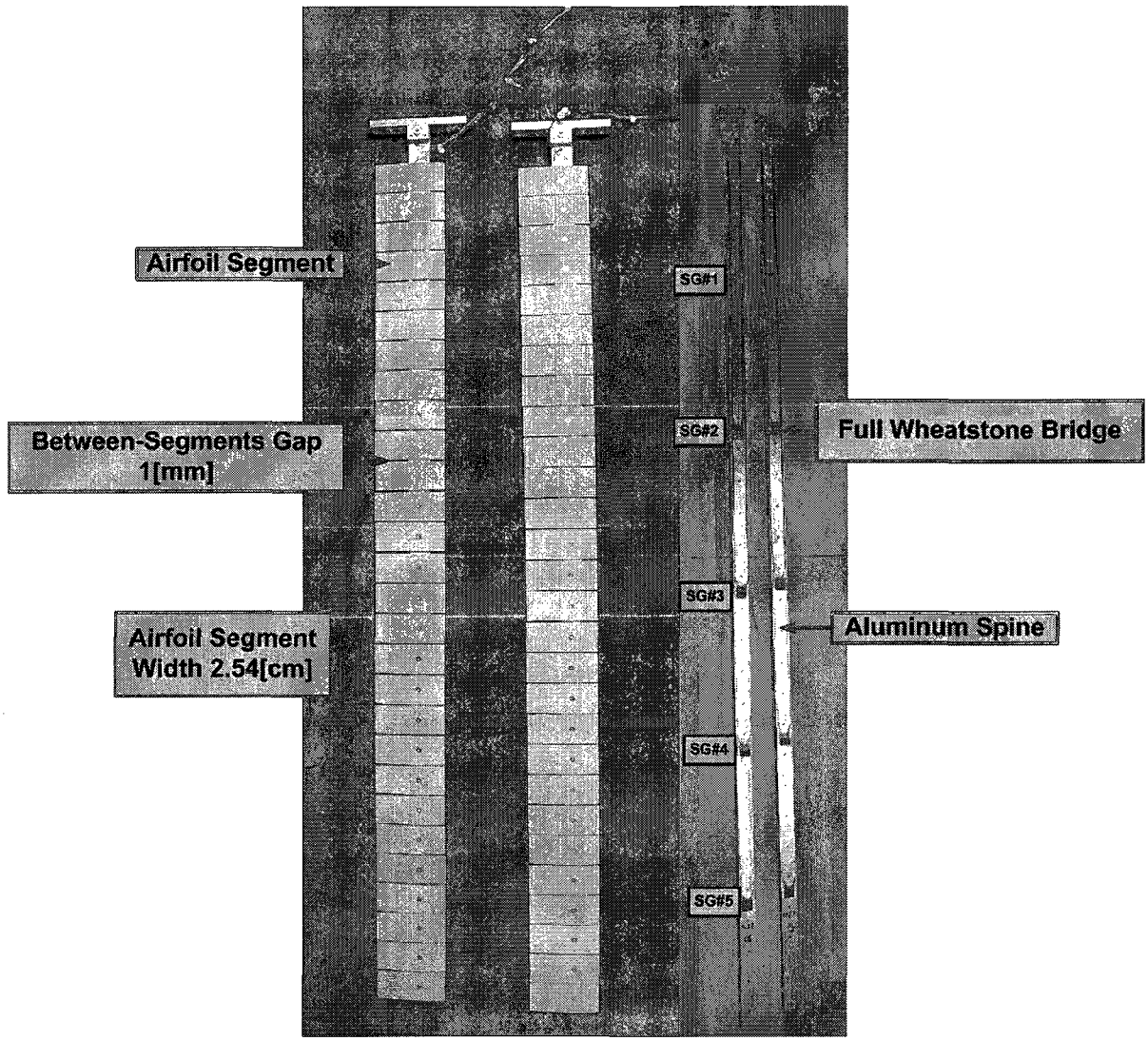

Figure 6.1: Top view of the blades with and without the airfoil segments.

the BSP occurs. Table. 6.3 presents the expected aerodynamic parameters of the full-scale and the Froude-scale blades at 33% of full RPM. The experimental airfoil Reynolds numbers are expected to be below 100 000; in this range, the NACA 0012 behaves in a non-linear manner. The airfoil NACA 64A010 was selected since it is known to give relatively consistent attached flow lifting characteristics in the Reynolds number range of 30 000 to 100 000 [167]. A typical lift-curve for the selected airfoil at the extremes of this range is shown in Appendix E. The lift-curve is not strictly linear and it has some lift

deficiency near the 0° angle of attack point. However, the roughness of the airfoil may contribute to smoothing the nonlinearity, which further justifies a linear approximation of the lift curve.

Table 6.3: Rotor system operation parameters at 33% full rotor speed.

Parameter	Full-Scale	Froude-Scale
Rotor Speed [rad/s]	7	22
Tip Speed [m/s]		
Advancing Blade	80	22.3
Retreating Blade	50	13.7
Tip Reynolds Number		
Advancing Blade	3.2×10^6	7.4×10^4
Retreating Blade	2×10^6	4.6×10^4
Tip Mach Number		
Advancing Blade	0.23	0.07
Retreating Blade	0.15	0.04
Unsteady Aerodynamic Reduced Frequency	0.24	0.01

6.3.3 Rotor Hub

The mechanical components of the rotor hub are illustrated in Fig. 6.2. The main features to be highlighted are its ease of assembly and disassembly and the collective pitch settings that are possible using the mounting hole patterns. The only drawback is the requirement of having to stop the rotor completely in order to manually change the collective pitch setting. The neoprene bumpers were selected to act as flap stops/limiters that are set at the fixed angles given in Table 6.2

6.3.4 Instrumentation

The Ametes 360ASMF2-01 Hall-effect sensor shown in Fig. 6.2, which has a range of 0-30° and accuracy of ±0.1°, in addition to a Nickel-plated square magnet were used to measure the flap-hinge angle. These sensors were selected for their small size, large linear output over a small angular range, and excellent accuracy. In addition, the sensor is non-contact

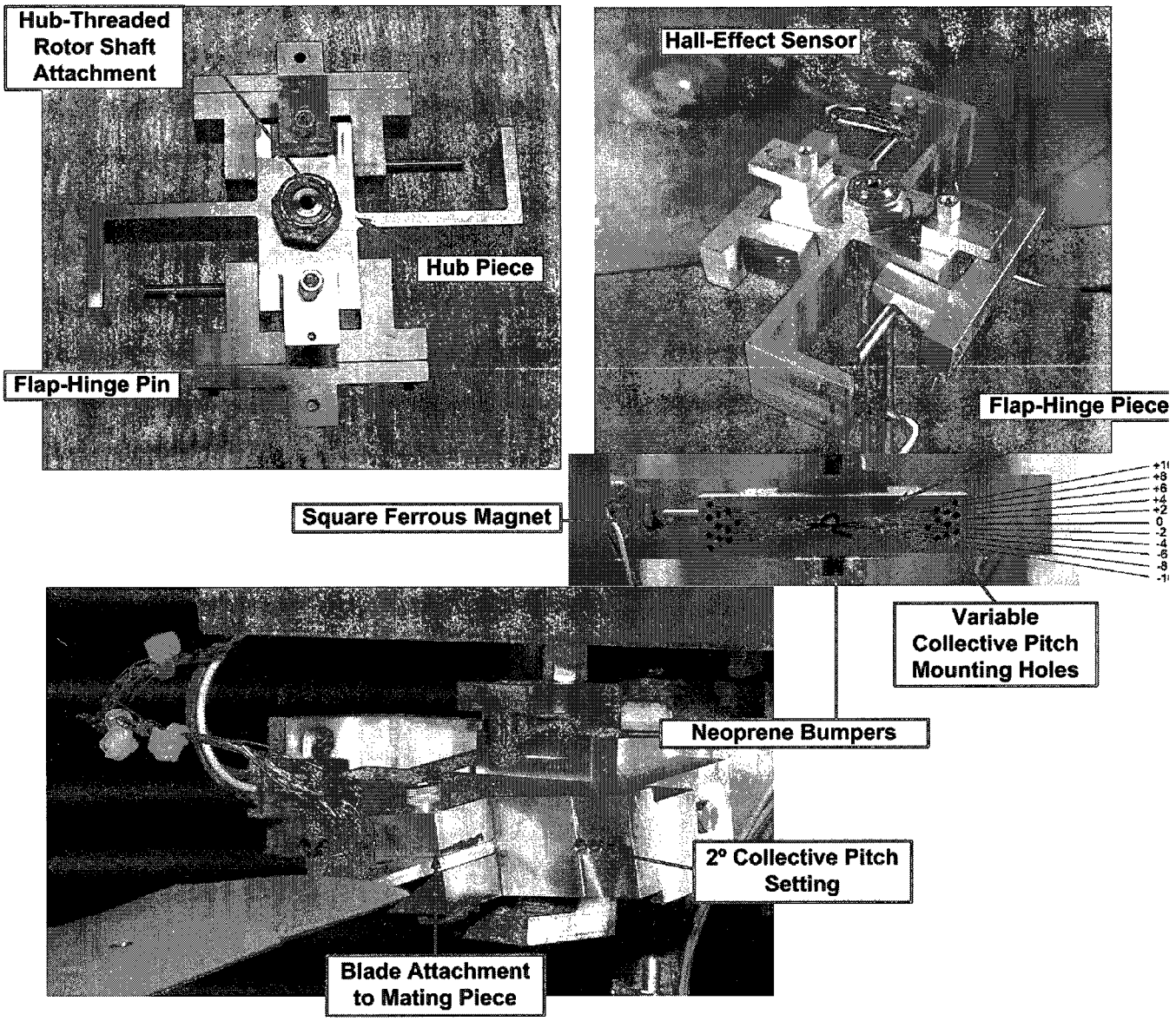

Figure 6.2: Rotor hub components of the Froude-scaled rotor system.

and therefore does not cause any resistance to the hinge motion. The sensors exhibit up to an 11 ms time lag between measurement and output. At the highest rotational speed projected for this experiment, this lag corresponds to a hub rotation of 14 degrees. Since the hinge angle is expected to vary at the rotational frequency of the hub, this offset was considered acceptable for capturing the hinge behaviour.The magnet was glued to the pin of the flap hinge, which allows it to rotate with blade, and the sensor was rigidly attached

to the rotor hub.

The strain gauge bridges shown in Fig. 6.1 consist of dual parallel strain gauges from OMEGA ENGINEERING, INC. with a nominal resistance of 1000Ω. Effectively, the arrangement of the strain gauges on the top and the bottom of the aluminum spine allows for continuous reading of the bending strain only at five blade stations. The strain gauges are wired using coated thin wires as shown in Fig. 6.3 that pass through special gaps beneath the airfoil segments.

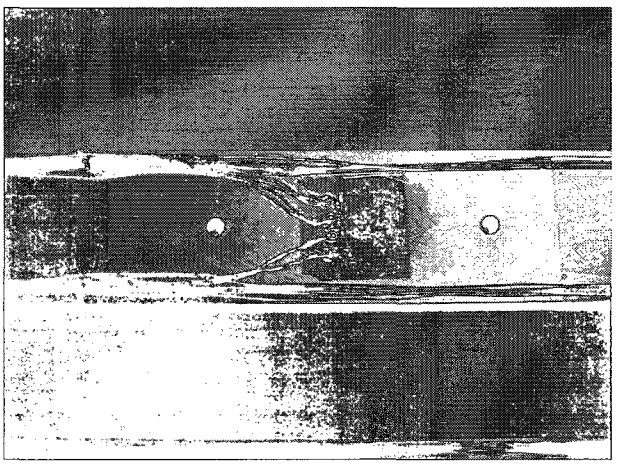

Figure 6.3: Wired strain gauge.

The collection of data was performed using the two wireless voltage nodes, V-Link from Microstrain®, shown in Fig. 6.4, where each blade is assigned a node. Each node has seven analog input voltage channels. Four of these channels are differential ones, with internal amplification and filtering. The first four strain gauges were read through these differential channels. Further, the four differential channels were custom calibrated to read the strain gauge signals using the commercial software Agilelink v 1.3.7 supplied with the voltage nodes. The optical encoder shown in Fig. 6.5 that consists of a 1000 counts-per-revolution ring and a reader is used to measure the azimuthal angle of the rotating shaft. The counter signal of the optical encoder is reset with the index pulse. The in-house custom designed circuit board performs functions that include preconditioning the signals

into the remaining three channels, which can be summarized as:

- Distribution of the +5[V] DC power supply to all functioning components of the DAQ system.
- Amplification of the fifth strain gauge signal before it is fed into the voltage node.
- Performing voltage division of the Hall-effect signal from +5[V] to +3[V].
- Counting of the encoder pulses, converting them to an analog signal using a D/A converter, and resetting the signal when the index pulse is encountered.

The casing of the rotor base shown in Fig. 6.5 contains the servo motor and a 3-to-1 gear box. The slip ring shown in the latter figure as well, supplies the +5[V] DC power to the system from an external regulated source.

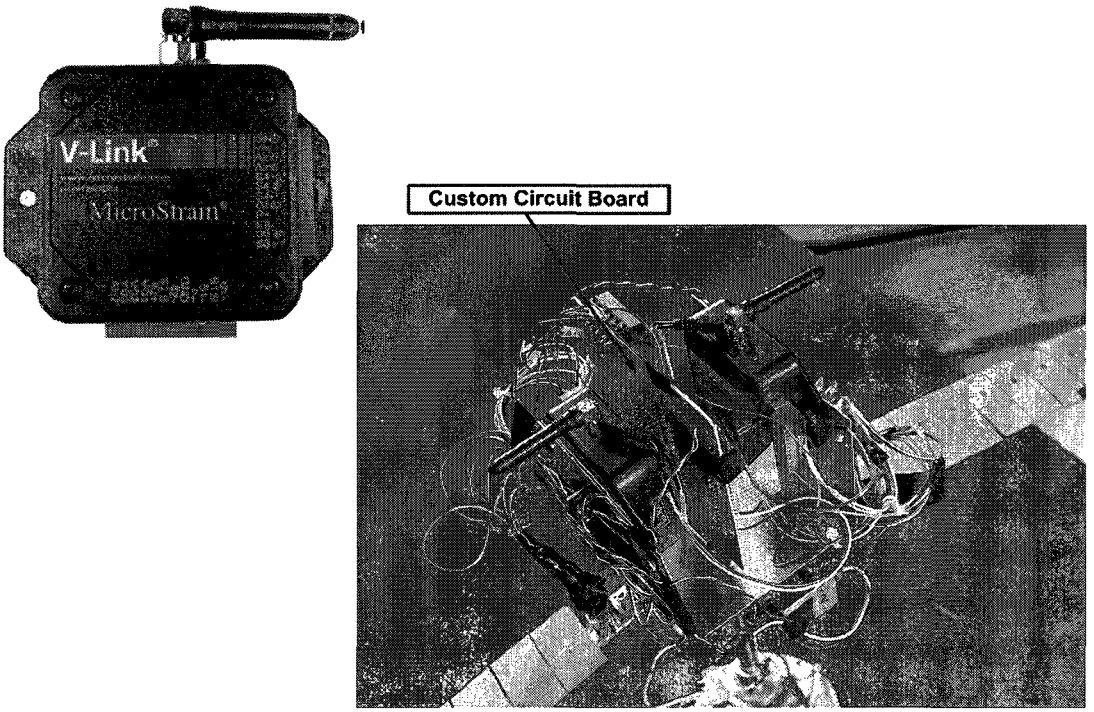

Figure 6.4: Voltage node V-Link and top view of the DAQ.

The rotor model was designed to be easily assembled and disassembled. It was also designed to withstand rotational speeds beyond those of the test specification.

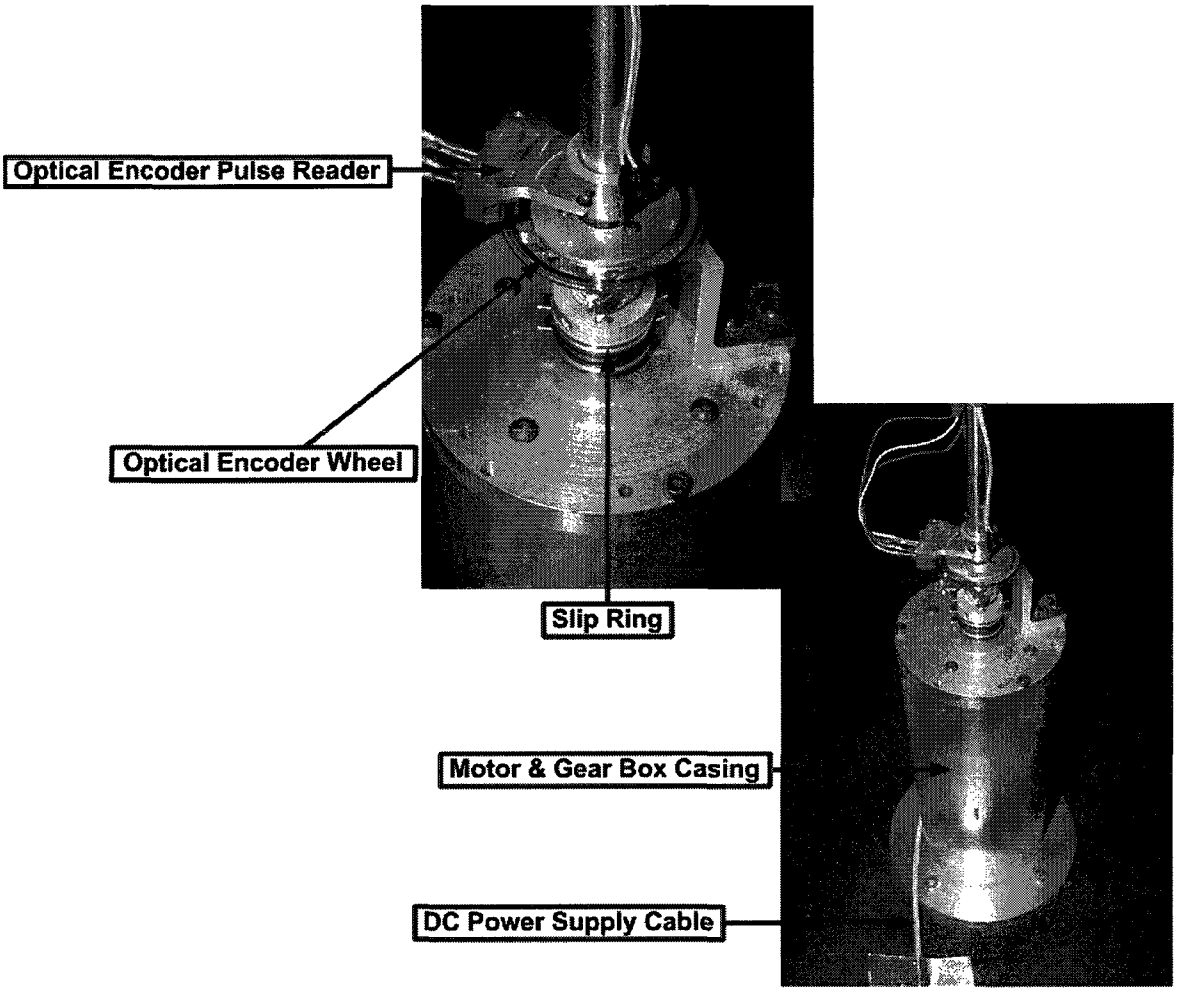

Figure 6.5: Rotor hub shaft and base casing.

6.3.5 Identified Challenges and Limitations

During set-up, the two outboard gauges on one blade were damaged. Data was collected from the working gauges on both blades for all experiments. Blade 2, having five working gauges, was sampled at 452 [Hz]. Blade 1, having 3 working gauges, was sampled at 520 [Hz]. The supporting circuitry was identified later to be missing adequate voltage regulation, which affects the consistency of the voltage supplied to the instrumentation. The impact on the collected data varies. The wireless devices have their own voltage regulators, and so the four differential strain gauges were not affected. The encoder analog

signal was directly affected by variations in supply voltage. While the exact azimuthal position at a given time is therefore uncertain, the reset angle is available, and so the rotor azimuthal profile can still be obtained. Since the supply voltage to the onboard circuitry was not recorded, the variation in the encoder reset voltage gives some insight into the magnitude of the supply voltage variation. The reset voltage varies by an amount in the order of 0.27 [V]. The Hall Effect sensor information is most affected by the varying supply voltage. The magnitude of sensor output is affected by the magnitude of voltage input at a rate of $\Delta V_{\text{out}} = 0.35\Delta V_{\text{in}}$. Therefore the hinge angle uncertainty due to slip ring voltage supply is in the order of 0.095 [V], which corresponds to at most 1.2 degrees.

An additional limitation was identified with the neoprene bumpers that exhibited a nonlinear second order force-displacement behaviour that derives from a cubic elastic potential as shown in Fig. 6.6. To further examine the behaviour of the bumpers, their response to an applied load of 6.5 [N] was recorded using a stop watch and a dial gauge to assess the time constant of the elastic deformation decay. Throughout the analysis of the experiment the bumpers were treated as linear springs with a constant that best fits the experimental data in Fig. 6.6

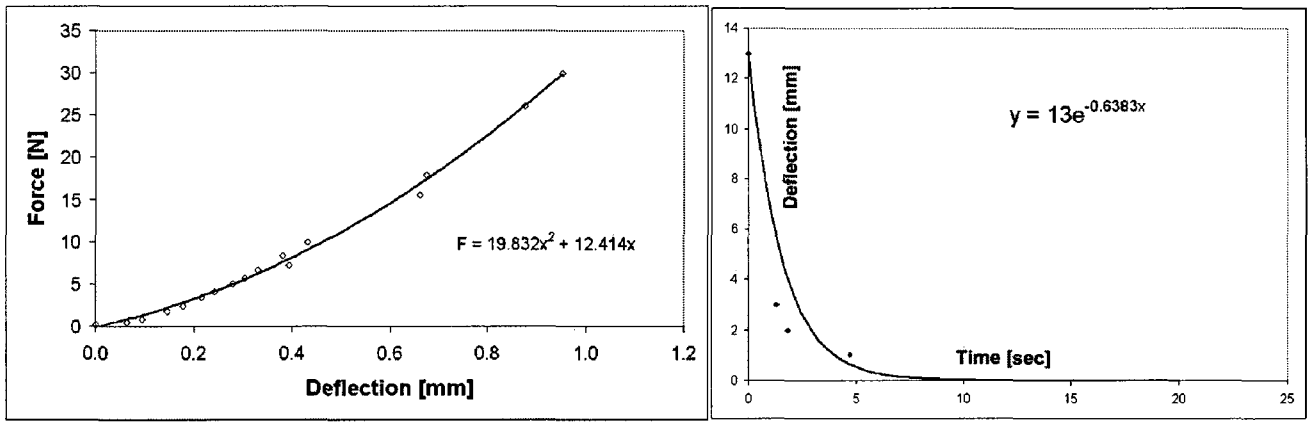

Figure 6.6: Neoprene bumper behaviour characterization.

Finally, in Phase [I] of the experiment the collected data by the DAQ was transmitted

wirelessly in real-time, which was reasoned to cause some data packets to drop; however, in Phase [II] the data was logged in the nodes and downloaded after the end of each experimental run to overcome the aforementioned limitation.

6.4 Design Evolution of the Software

The rotor motion was controlled to a pre-defined engage/disengage profile of angular velocity that follows a sinusoidal rotational acceleration during engage and a linear rotational deceleration during disengage as shown in Appendix E. The rotor was engaged over the specified engagement period to the hold speed, which was most often 33% full rotor speed, held for 30 seconds, and disengaged over the same period as the engagement time. The motion control system consisted of a National Instruments© universal motion interface card, National Instruments© motion control card, and a current adjustable amplifier all connected to a single CPU. The LabView Virtual Instruments (VIs) provided with the motion control card were used to develop a motor control Graphical User Interface, which allowed easy modification of the engage/disengagement profile parameters. A PID controller was set up with user defined inputs for position and velocity control. The controller was tuned for velocity control primarily due to the importance of accurately tracing the specified rotor angular velocity profile. The position control was occasionally employed to orient the rotor system followed by a manual azimuth position tuning. The motion control CPU and the software are shown in Fig. 6.7

6.4.1 Identified Challenges and Limitations

The earlier version of the motion control software relied on an internal loop timer in the software to generate the time advance for the rotor angular speed profile. As a result, a cumulative phase lag was generated between the internal time of the software application

and real time. This effect was identified after Phase [I] of the experiment was completed; however, due to the nature of this software error, only the later stages of the rotor operation were affected and this is mainly the disengagement part. Figure. 6.8, which shows a comparison between the experimental and the simulation azimuthal angle signal illustrates this point, where the rotor takes longer to stop as compared to the ideal hub angular velocity profile. This effect was eliminated in Phase [II] of the experiment by relying on the CPU clock to generate the hub angular velocity profile.

6.5 Calibration and Data Reduction

The strain gauges were initially zeroed by setting the blade on their edges so that the gravitational effect is nullified and initiating a reset command of the four differential channels. The offsets of all five strain gauges were recorded. Additionally, the following static and dynamic tests of the strain gauges were conducted:

- Blade static deflections due to gravity were measured and recorded as seen in Fig. 6.9.
- The damping profile of the blade was measured by conducting a drop test of the blade from a fixed hinge angle onto the droop neoprene bumper.
- Further drop tests were conducted to validate the dynamic response of the strain gauges and the DAQ.

The voltage response of the Hall Effect sensors at known hinge angles was recorded and the linearity of the sensors across the hinge angle range was verified. The sensitivity of the Hall Effect sensors to variations in the input voltage was measured, and found to vary between the sensors and with hinge angle. The accuracy of the wireless transmitted single-ended channels was documented to be within 15 mV.

With respect to the wind tunnel in Phase [I] of the experiment, the boundary layer

profile, including turbulence, resulting from the upstream grid was measured using a three-hole Cobra probe. Due to the large wind tunnel blockage resulting from the boundary layer grid and the ship decks, the wind tunnel velocity at the hub location was calibrated for the 0 and -20 degree ship deck roll angles at rotor height using a vane anemometer. These measurements were used to compute the corresponding freestream flow velocity at rotor height for use as input into the airwake model.

As mentioned above, the four differential channels of the V-links were transmitted as strain signals in units of μ-strain. The fifth channel was digitally filtered and converted to strain according to the conversion

$$\epsilon_{\text{Gauge5}} = \alpha_{\text{Gauge5}}(V_{\text{r}} - V_{\text{offset}}) \tag{6.8}$$

where α_{Gauge5} is a proportionality factor that depends on the bridge gain, the bridge factor, the voltage divider ratio, and the bridge driving voltage.

Similarly, the Hall Effect sensor signal was digitally filtered and converted to angular measurements in degrees using

$$\Theta_{\text{Hinge}} = \alpha_{\text{He}}(\Delta V_{\text{He}}) + \beta_{\text{He}} \tag{6.9}$$

where $\alpha_{\text{He}}[^\circ/\text{V}]$ is the proportionality factor of the device; ΔV_{He} is the measured voltage difference of the device; and β_{He} is offset of the angular measurement at 0 [V].

The blade flap deflection was obtained by processing the strain gauge readings at every time sample. If small strain is assumed with no coupling between the elastic modes, then the bending strain for a cantilevered beam can be written as

$$\epsilon(x) = \frac{v\frac{d^2z}{dx^2}}{\left[1 + \left(\frac{dz}{dx}\right)^2\right]^{\frac{3}{2}}} \qquad z(0) = 0\ ,\ \frac{dz}{dx}(0) = 0 \tag{6.10}$$

where $\epsilon(x)$ is the axial strain measure profile due to bending, which is obtained by curve fitting the strain readings; v is the distance from the beam reference line to its top surface (half the thickness); z is the sought flap elastic displacement measured from the beam reference line; and x is the axial measure along the undeformed beam reference line.

The problem in Eq. 6.10 was transformed to a first order one and solved as an initial value-like problem using Butcher's Runge-Kutta method for the slope of the flap displacement $\frac{dz}{dx}$. Finally, a numerical quadrature was used to obtain the flap displacement at the respective stations of the blade.

6.6 Future Recommendations

In addition to the improvements that can be identified from the limitations and challenges discussed above, future experiments that build upon this experiment may benefit from the following recommendations:

- Design and build the blade as a single-cell composite blade to examine the effect of coupled elastic modes.
- Incorporate active materials in the blade design to impart adaptive capabilities to conduct and validate control studies.
- Automate the process of changing the collective pitch.
- Consider investigating the hingeless blade concept to measure the transmitted hub moment during the engagement/disengagement given that modern helicopters are moving in that direction in terms of hub design.

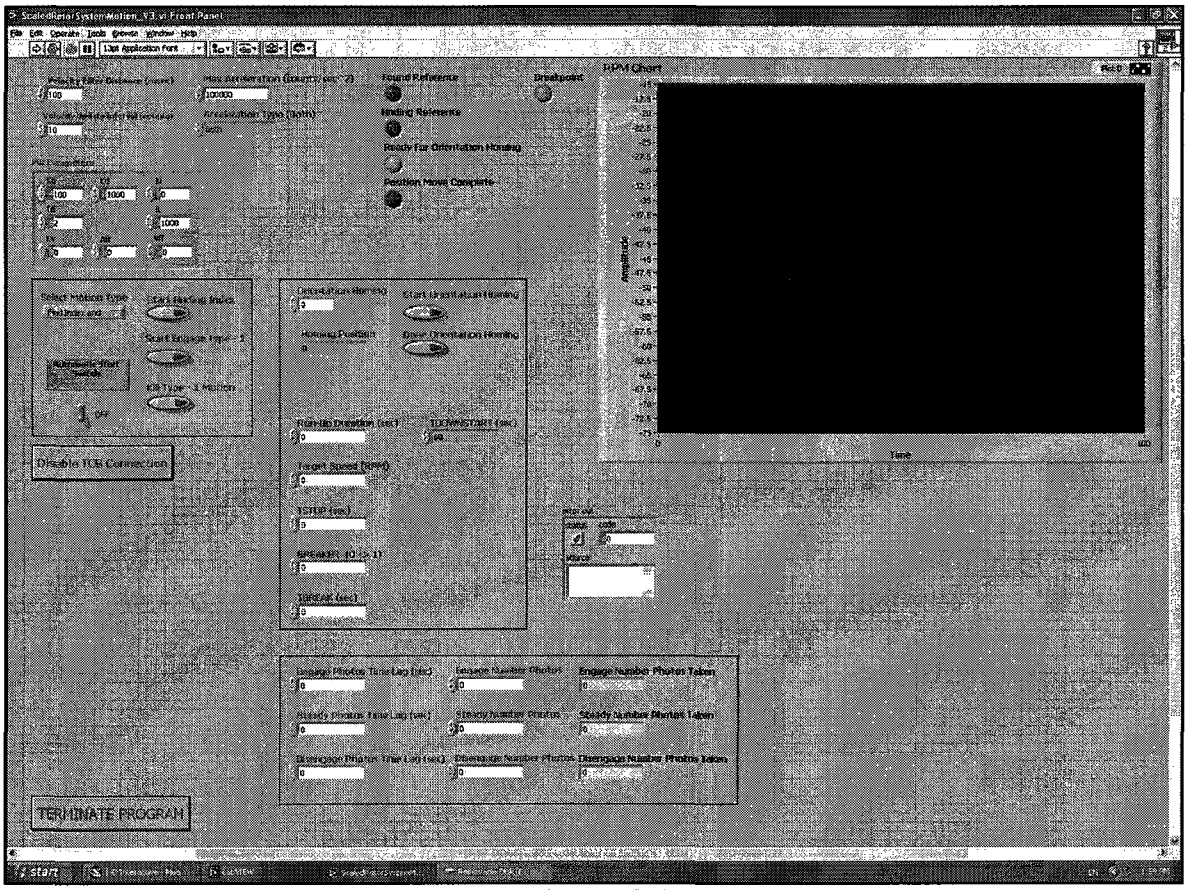

Motion Control Software

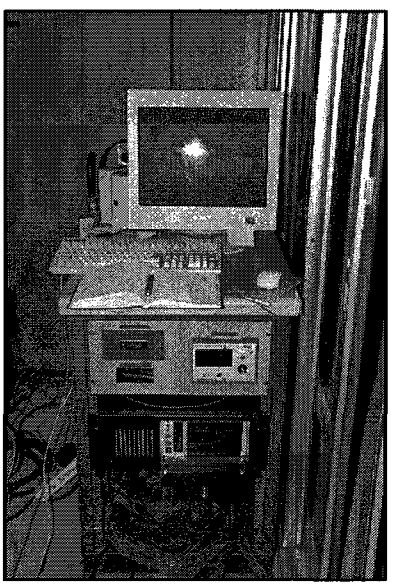

Motion Control Hardware

Figure 6.7: Motion control software and hardware.

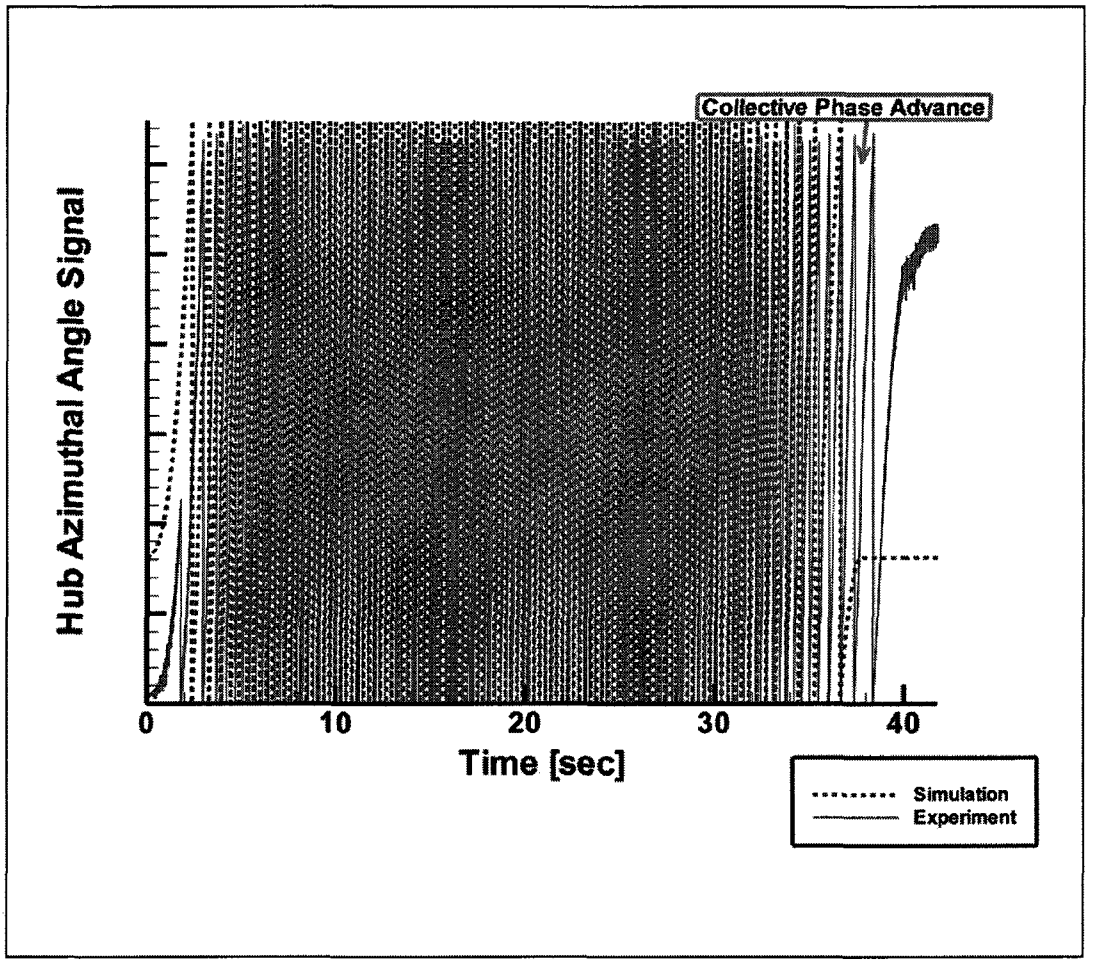

Figure 6.8: Experimental and theoretical optical encoder signal.

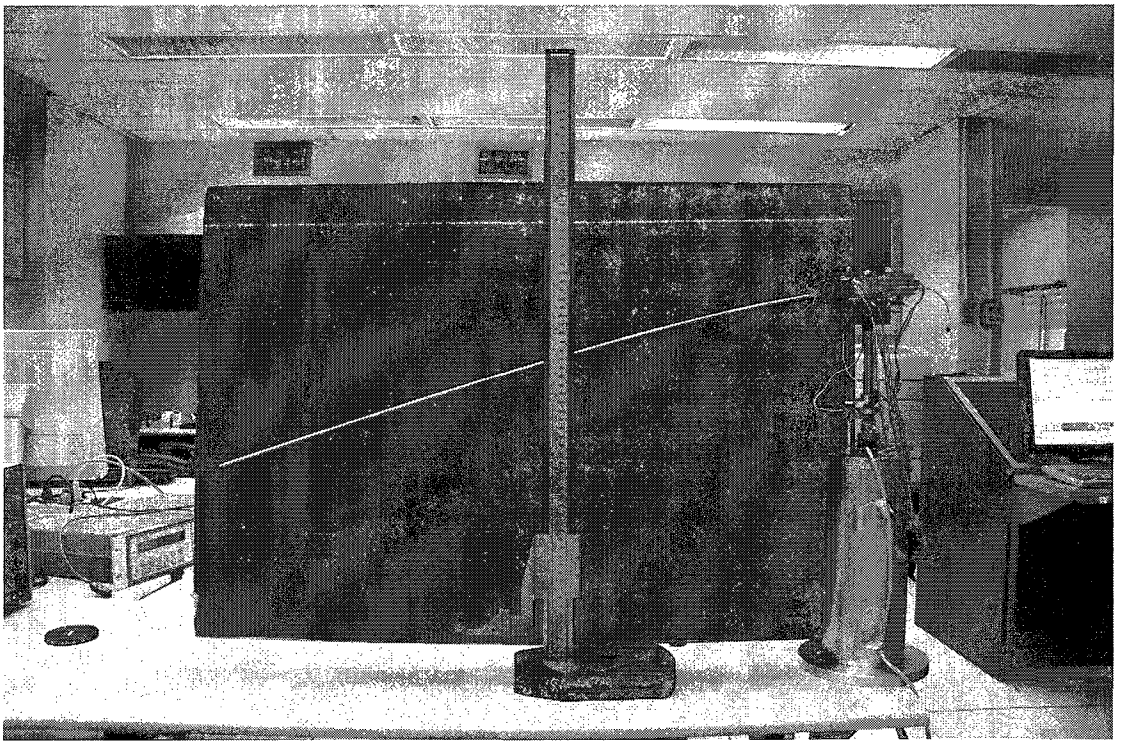

Figure 6.9: Blade static deflection under gravitational loading.

Chapter 7

Aeroelastic Response of the $1/12^{th}$ Froude-scaled Flap Articulated Rotor System in the NRC-IAR 2×3 Meter Wind Tunnel

7.1 Summary of Chapter 7

In this chapter, Phase [I] of the $1/12^{th}$ Froude-scaled flap articulated rotor system is outlined and the experimental results analyzed as they pertain to the BSP. The effects of the engagement/disengagement profile, the collective pitch setting, and two ship roll angles on the blade maximum flap response are examined using experimental and simulation data. The aeroelastic modelling of rotor systems outlined in this research without ship motion is validated against experimental data.

7.2 Overview of Experimental Setup and Runs

In Phase [I] of the experimental work, the Froude-scaled rotor system was placed in the 2×3[m] wind tunnel facility at the NRC-IAR. The ship deck of a typical Canadian Navy frigate was represented using two 1:35-scaled 2×1[m] wooden decks, where the first one is at a roll angle of 0° while the second one is at -20°. The deck configurations constructed allow for two ship airwake types to be considered for the same wind speed. The rotor system was placed at the centre point of the deck and the motor control cables extended through a circular gap in the deck beneath the hub to the external motor control system. The downstream view of the rotor system on each of the two decks along with the scaled turbulence generation grid is shown in Fig. 7.1 inside the wind tunnel. As indicated previously, the steady airwake for this particular ship deck was experimentally measured and subsequently modelled by a member of the Applied Dynamics Group as shown in Fig. 7.2. These steady airwake models are used throughout the rest of this chapter. The increased upward gust (the cliff-edge effect) is noted for the vertical component of the $-20°$ deck when compared to the 0° deck. The ship airwake velocity field is normalized by the far field free stream velocity at the ship deck level.

A schematic of the system components and their interactions for this phase of experimental work is shown in Fig. 7.3. From the diagram it is clear that the process was automated as much as possible, where an experimental run was triggered from the wind tunnel control panel.

The motor controller was designed to automatically reset the azimuthal orientation of the rotor to the reference position when commanded; however, it was proven difficult to accurately control the position and the velocity of the motor simultaneously using the available instrumentation. Instead, the motor was manually reset to the reference azimuthal orientation shown in Fig. 7.4 before each experimental run. The numbering of

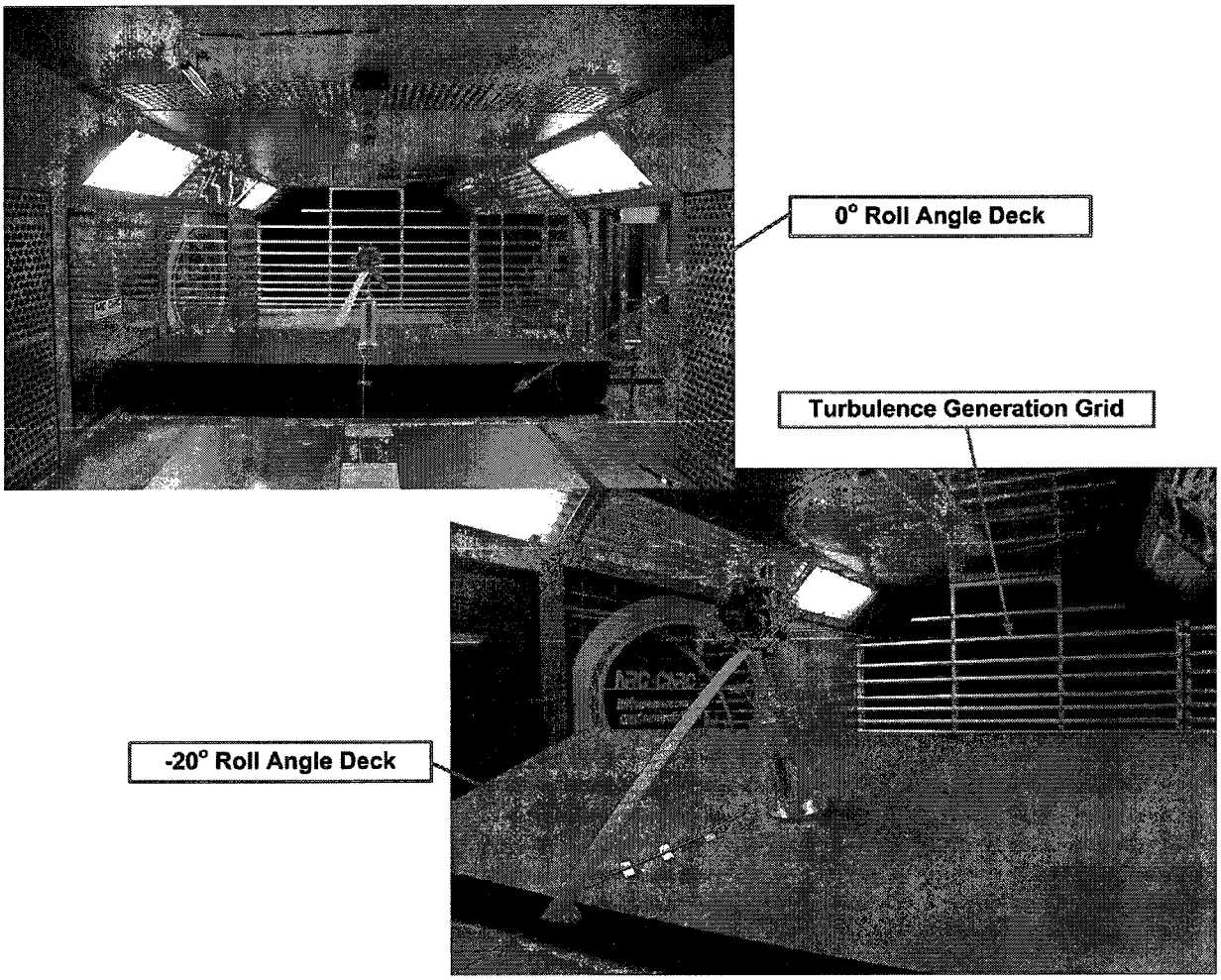

Figure 7.1: Downstream view of the rotor system on the two ship decks considered inside the 2×3[m] wind tunnel.

the blades shown in the figure was according to the numbering scheme of the respective data acquisition V-Link assigned to each blade. Early in the experimental study, two strain gauges on blade 706 stopped functioning properly; therefore, the entire emphasis of the analysis is focused on blade 705 without any loss of generality. The failure of the strain gauges was attributed to abrasion of the bridges or their wiring when the airfoil segments were being attached to the blade.

A drop test of blade 705 on the droop stop was conducted to test the wireless data acquisition system, to tune the Rayleigh damping parameters in the intrinsic model, and

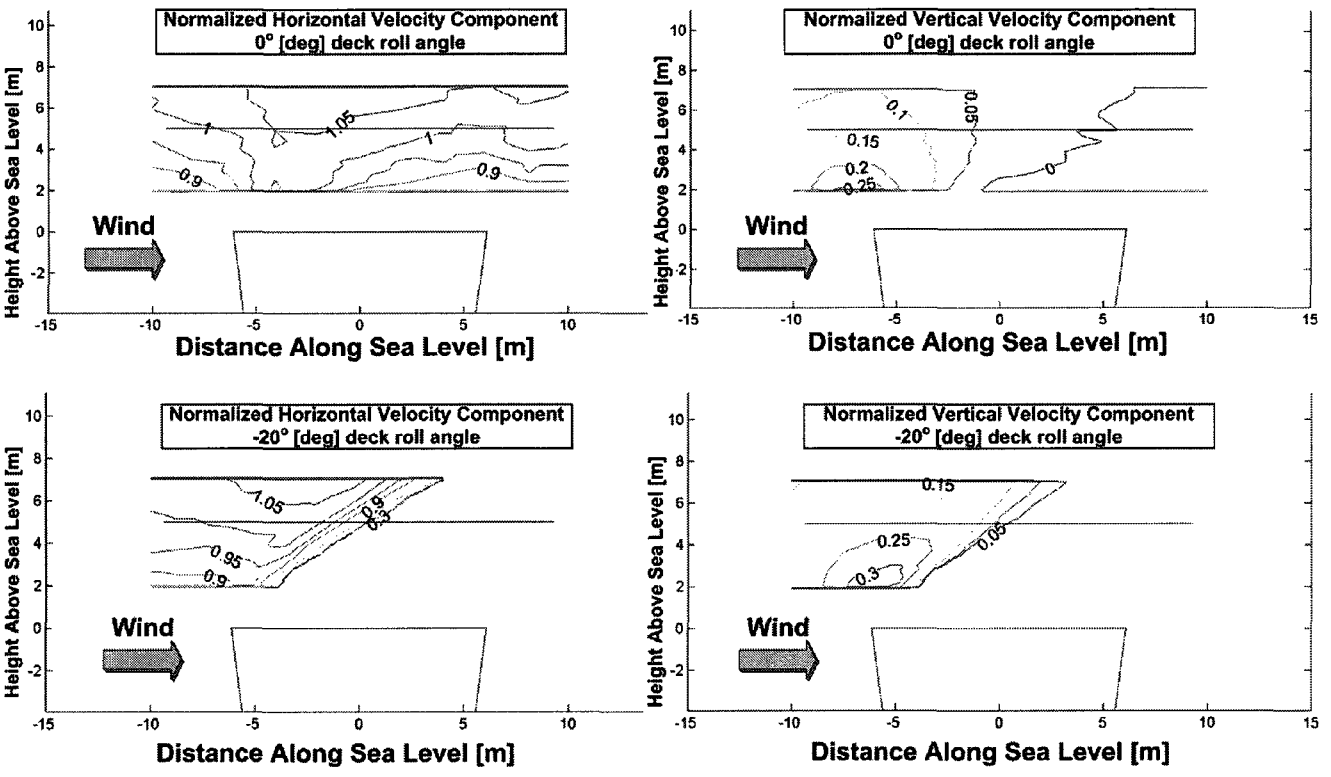

Figure 7.2: The steady airwakes of the 0° and −20° decks.

to obtain an initial test of the predictive capability of the model. The blade was dropped from the angular setting of the flap stop by manually holding it up at the rigid flap hinge. Several simulations were performed with and without aerodynamic loadings and with various values of the Rayleigh damping parameters where the optimal values were found to be: $\bar{\eta}[\mathrm{m/s}] = \bar{\delta}[\mathrm{s/m}] = 0.018$. The simulations without aerodynamic loadings were performed in vacuum in the presence of the gravitational field. The experimental and the simulated drop test are compared in Fig. 7.5 with and without aerodynamic loadings. The results demonstrate the importance of aerodynamic forces even for this drop test without airwake flow. Additionally, the remarkable agreement with experimental data validate the linear approximation of the blade-neoprene contact problem.

The experimental runs conducted were permutations of the rotor system settings and wind tunnel conditions shown in Table 7.1. The wind tunnel speeds in the table are the

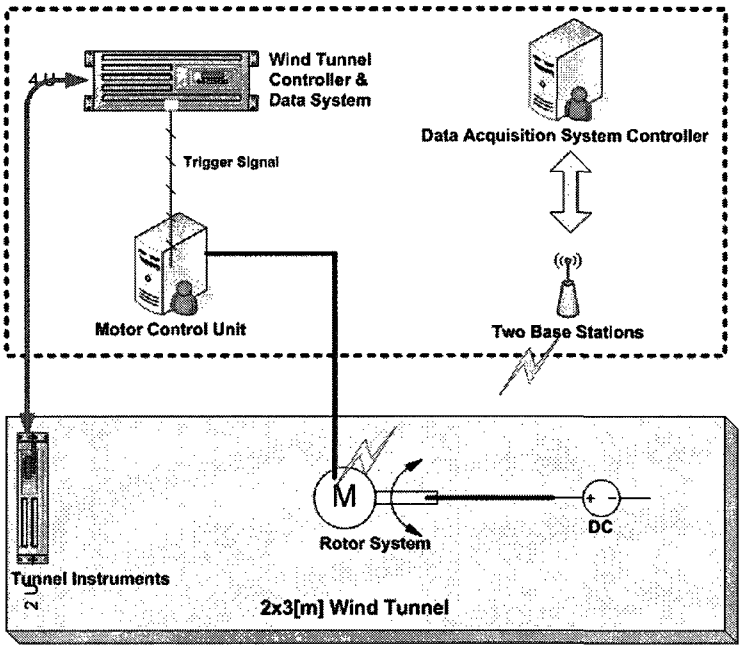

Figure 7.3: System components and their interaction in the 2×3[m] wind tunnel.

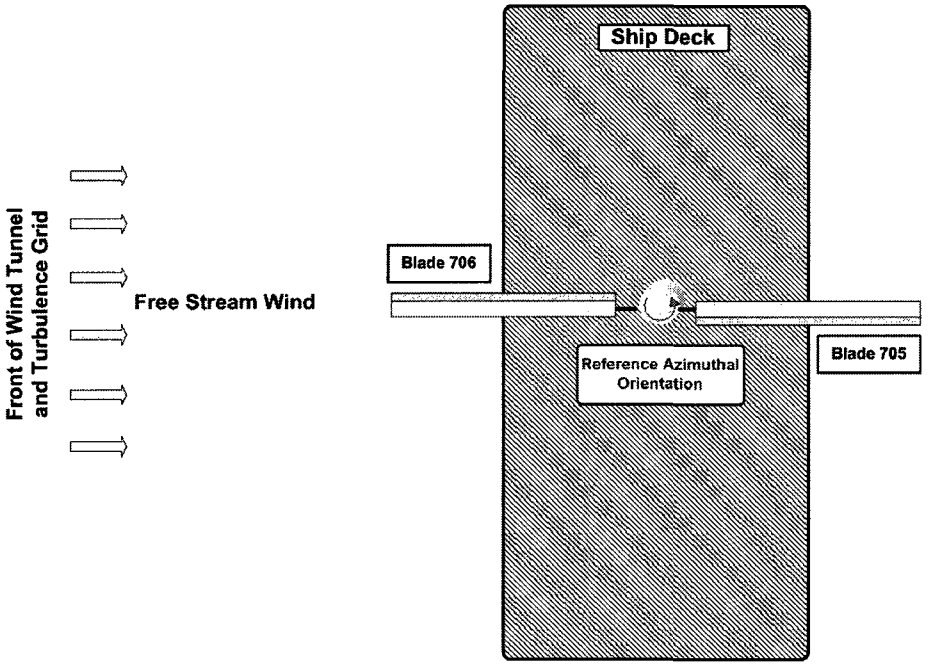

Figure 7.4: Reference/Initial azimuthal orientation of the rotor system in the wind tunnel.

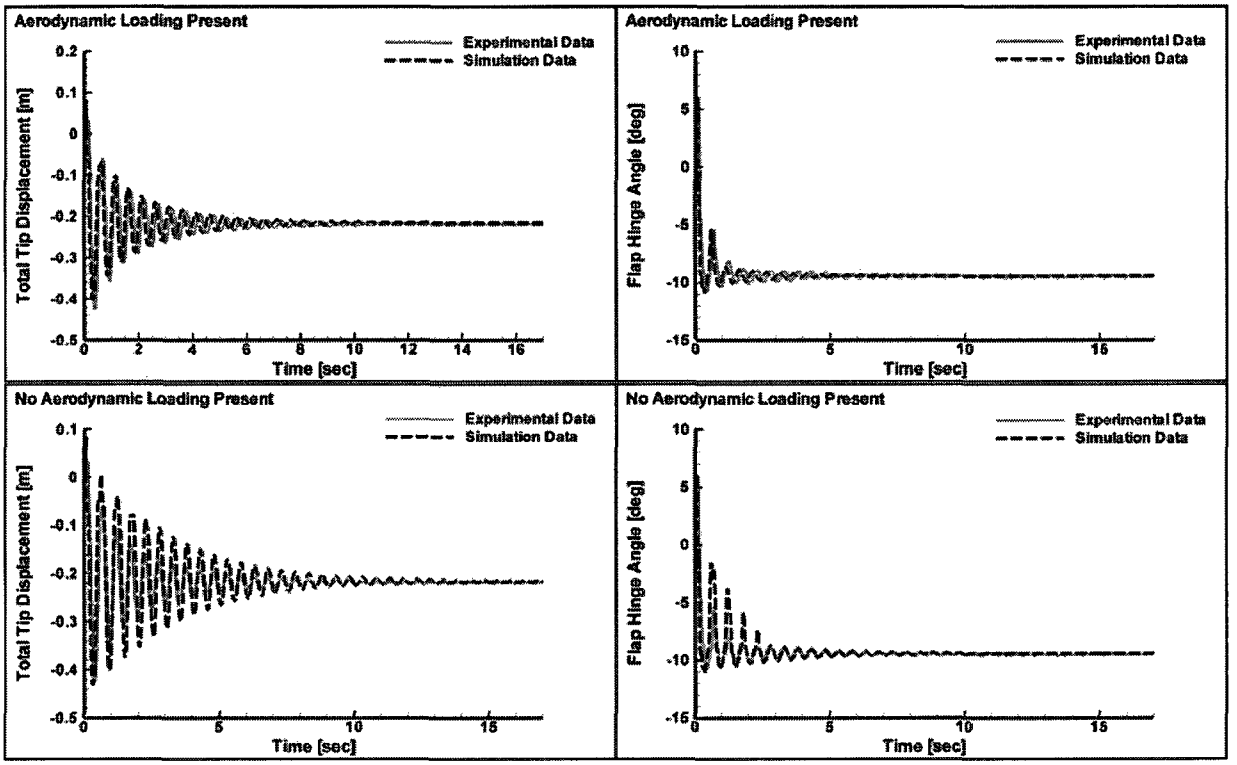

Figure 7.5: Experimental and simulated drop test of the blade on the neoprene stops with and without aerodynamic forces

ideal ones and the speeds achieved through manual control in the tunnel are always within $\pm 10\%$ of these speeds but never exactly at the commanded speed. This variation was taken into account in the simulations although the ideal values of the wind speed are used to denote the experimental runs. Effectively, the experimental results will address the following questions regarding the BSP:

- The effect of the engagement/disengagement profile on the BSP in terms of the maximum tip displacements registered.
- The effect of positive/negative collective pitch setting of the blade illustrated in Fig. 7.6.
- The effect of two ship roll angles in a steady sense.

Table 7.1: Experiment parameters of Phase[I].

Parameter	Settings
Wind Speed [m/s]	4 6 8
Max Rotor Speed [rad/s]	22
Collective Pitch Setting [deg]	-8 -4 0 4 6 8
Ship Deck Roll Angle [deg]	-20 0
Engage/Disengage Time [sec]	2 4 8 12 15

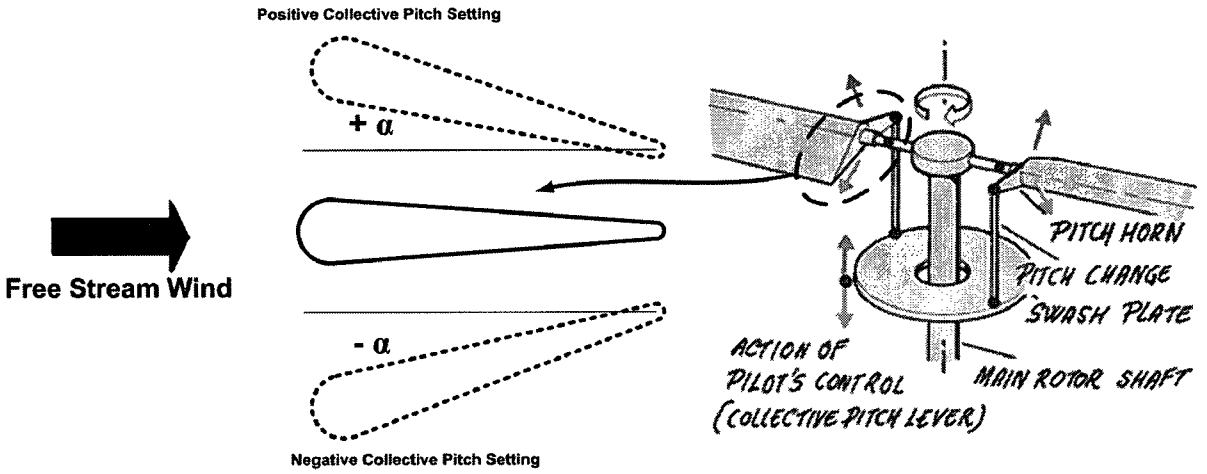

Figure 7.6: Illustration of positive and negative collective pitch setting.

The time history of the unprocessed and the unfiltered signals received from blade 705 during the experimental run of deck roll angle of $-20°$, wind speed 7.66 [m/s], collective pitch setting of -4°, and engage/disengage time of 8 [sec] is shown in Fig. 7.7. The signals of the four strain gauges being fed to the four differential inputs on the V-link are contrasted to the analog signal coming from the fifth gauge.

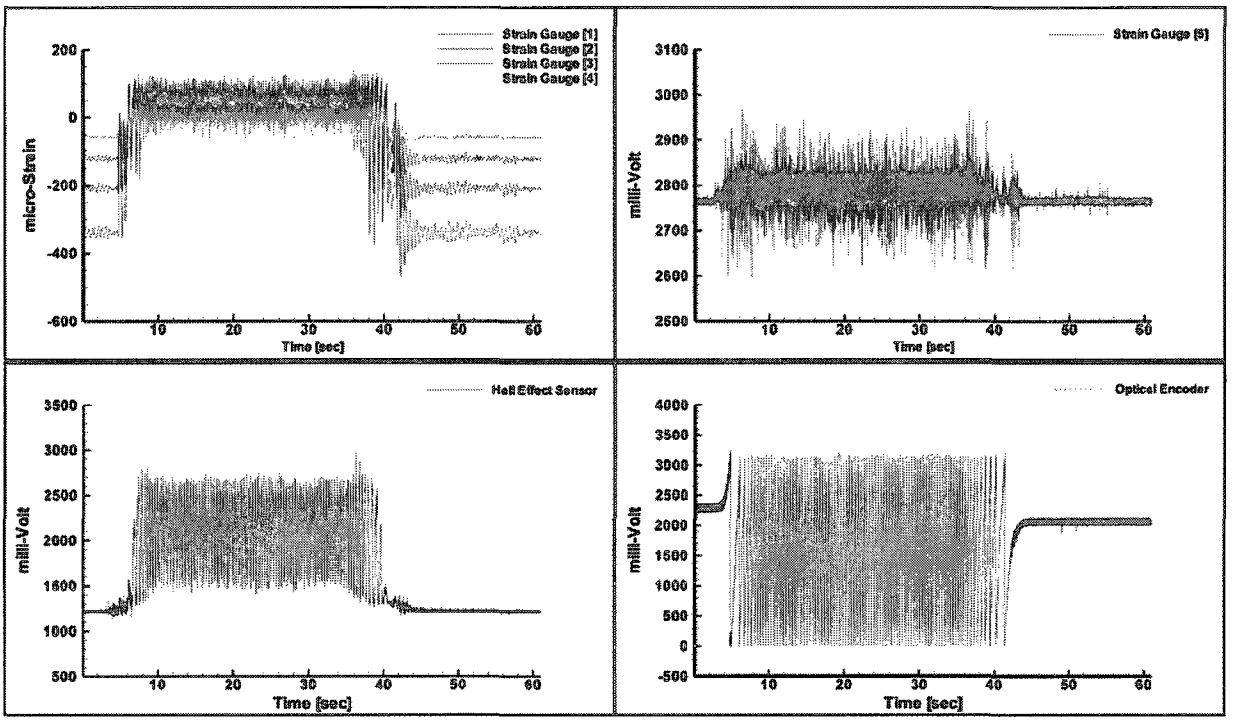

Figure 7.7: Raw signals received blade 705 for the experimental run of deck roll angle of $-20°$, wind speed 7.66 [m/s], collective pitch setting of -4°, engage/disengage time of 8 [sec].

7.3 Experimental and Simulated Aeroelastic Response

7.3.1 Analysis of Experimental Results

The maximum and minimum tip displacements relative to the datum line shown in Fig. 7.8, which corresponds to zero gravitational field in vacuum, registered during the experimental runs are of interest. The registered downward extremum of the tip of blade 705 for the 0° deck roll angle as a function of the engagement/disengagement time for the wind speeds in Table 7.1 considered in sequence and the collective pitch settings of: (I) 0°, (II) 4°, (III) 6°, (IV) 8°, (V) $-4°$, and (VI) $-8°$ are shown in Fig. 7.9. For the same case, the registered upward extremum is shown in Fig. 7.10.

Careful examination of Fig. 7.9 and Fig. 7.10 yields the following conclusions:

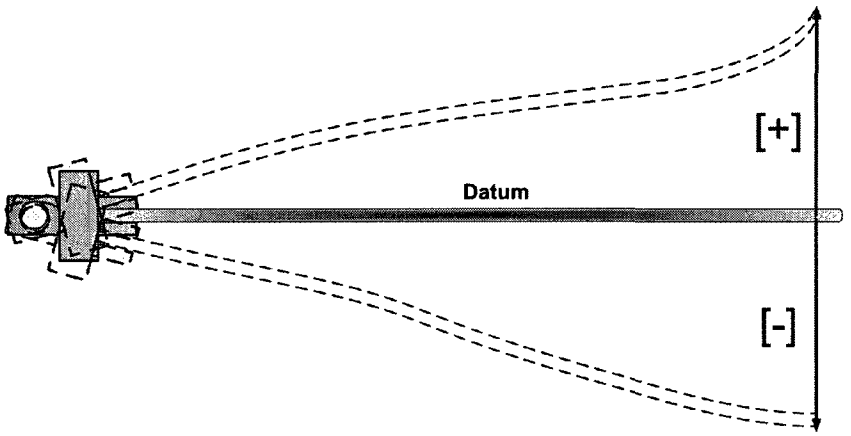

Figure 7.8: Datum of the tip displacement and sign convention used.

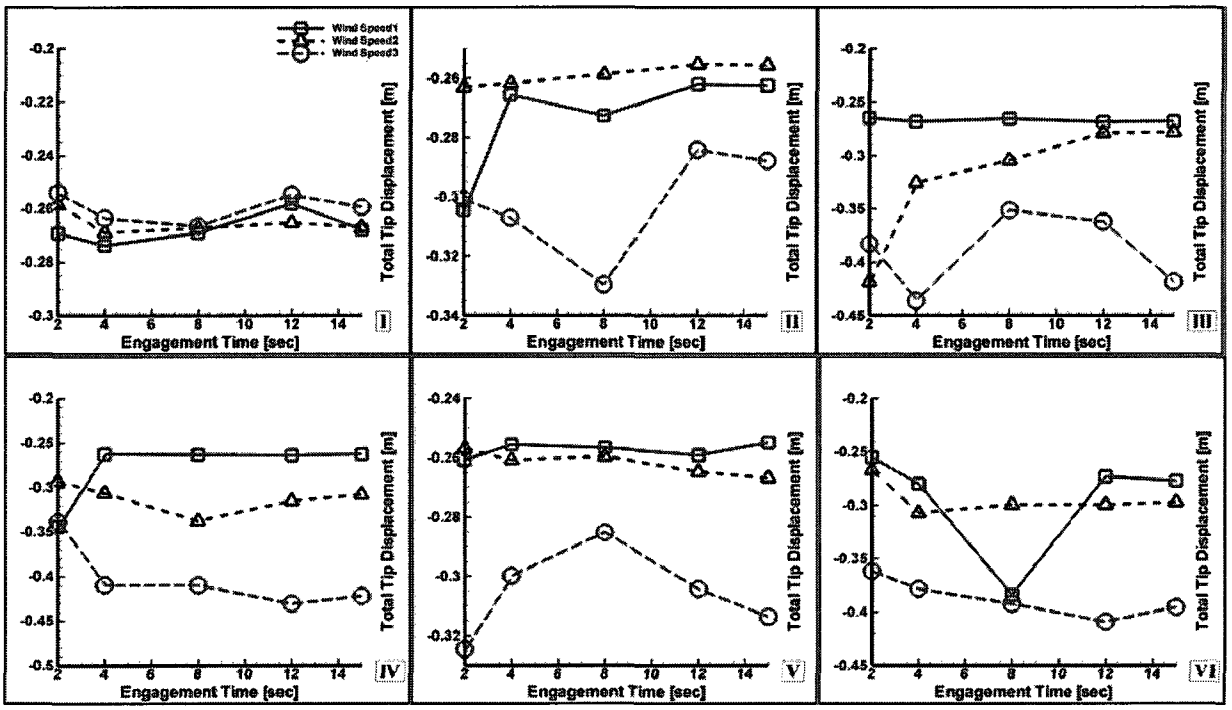

Figure 7.9: Registered downward extremum of blade 705 as a function of engage/disengage time for 0° deck roll angle; wind speeds of:(1) 4, (2) 6, and (3) 8 [m/s]; collective pitch setting of: (I) 0°, (II) 4°, (III) 6°, (IV) 8°, (V) −4°, (VI) −8°.

1. Increasing the wind speed negatively impacts the BSP by increasing the maximum of both downward and upward tip deflections. It seems that the maximum downward deflection is weakly dependent upon the wind speed at 0° collective pitch setting for

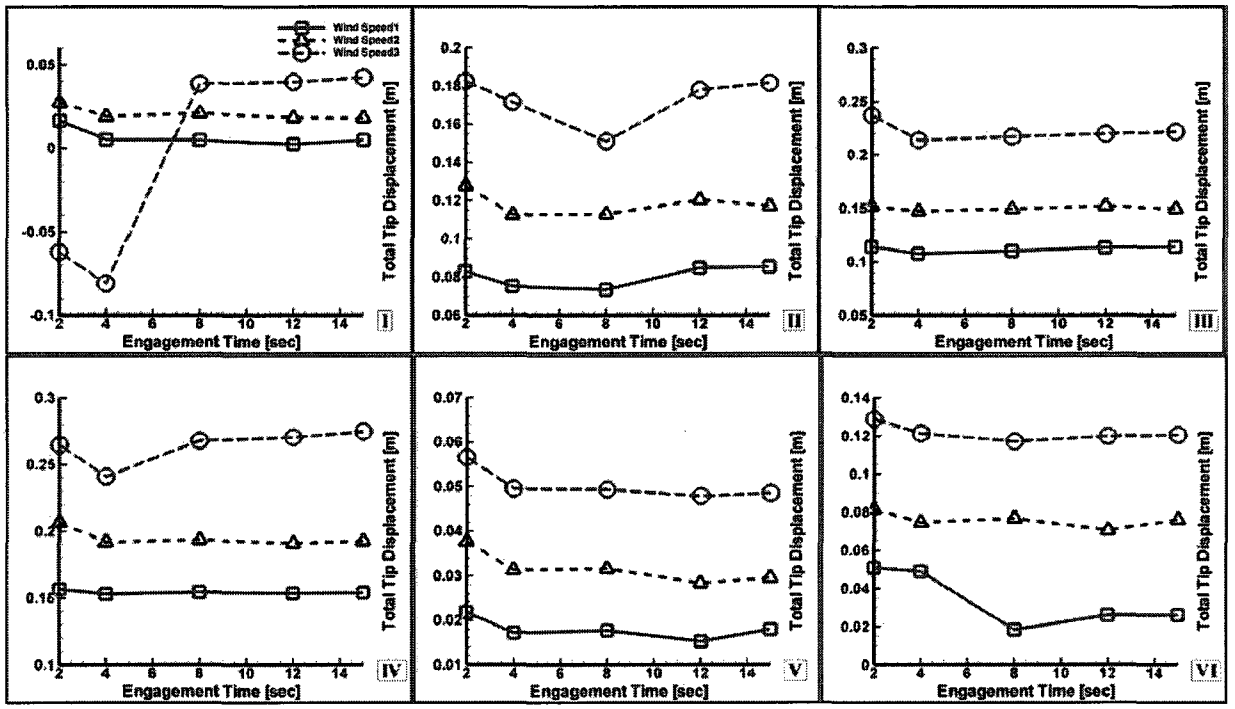

Figure 7.10: Registered upward extremum of blade 705 as a function of engage/disengage time for 0° deck roll angle; wind speeds of:(1) 4, (2) 6, and (3) 8[m/s]; collective pitch setting of: (I) 0°, (II) 4°, (III) 6°, (IV) 8°, (V) −4°, (VI) −8°.

the 0° deck. This is expected given that the only source of transverse aerodynamic perturbation is the upward gust of the airwake, which explains the increase in the maximum upward deflection with wind speed for the same case.

2. Increasing the magnitude of the positive or the negative collective pitch setting increases the magnitude of deflections with the latter having a greater effect. This confirms the conclusions of previous theoretical studies [17] that attempted to reduce the BSP by increasing the collective pitch.

3. The duration of the rotor engagement/disengagement operation has minimal effect on the magnitude of maximum deflections observed with a negative low rate of change in the observed magnitudes as the duration increases. This suggests that modifying the engagement/disengagement profile alone to reduce the BSP may not be a feasible

strategy.

4. The magnitude of the downward deflections are greater than those of the upward ones despite the existence of the upward gust.

The exception to the above observations seems to be the 2 [sec] engagement/disengagement duration; however, this is due to the difficulties encountered by the motor controller in reaching the acceleration levels demanded by the velocity profile. The motor was observed to undergo some erratic behaviour, which caused significant deviations from the commanded velocity profile. The case of the $-20°$ deck is shown in Fig. 7.11 and Fig. 7.12 for the same conditions in Table 7.1; however, with a smaller number of experimental runs. The case of 2 [sec] enagegement/disengagement duration is not included and the collective pitch settings of: (I) 0°, (II) 4°, (III) 6° are the only ones shown. The conclusions reached regarding the 0° deck seem to be still applicable except that increasing the collective pitch setting seems to have a lesser impact on the observed downward deflections. The upward deflections are significantly increased however, and they are larger in magnitude than the downward ones. These deviations are explained by the increased upward gust of the airwake in this case. This further illustrates the size of the large space of parameters that contribute to the BSP.

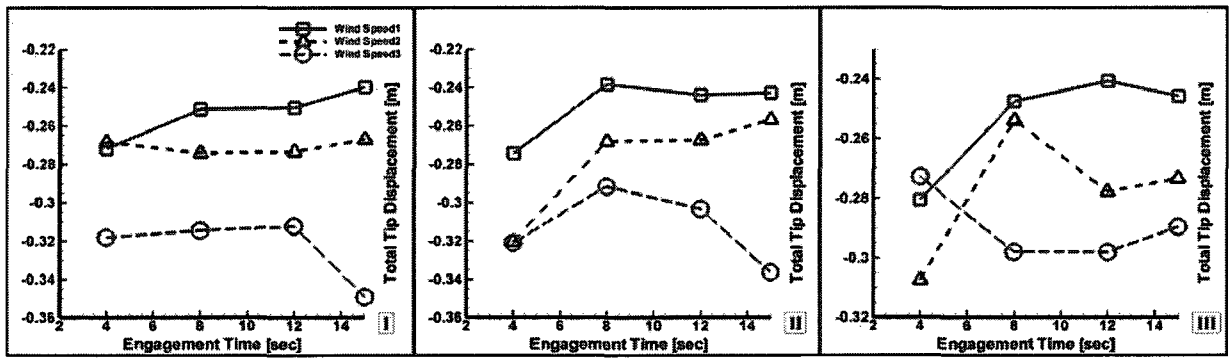

Figure 7.11: Registered downward extremum of blade 705 as a function of engage/disengage time for $-20°$ deck roll angle; wind speeds of:(1) 4, (2) 6, and (3) 8[m/s]; collective pitch setting of: (I) 0°, (II) 4°, (III) 6°.

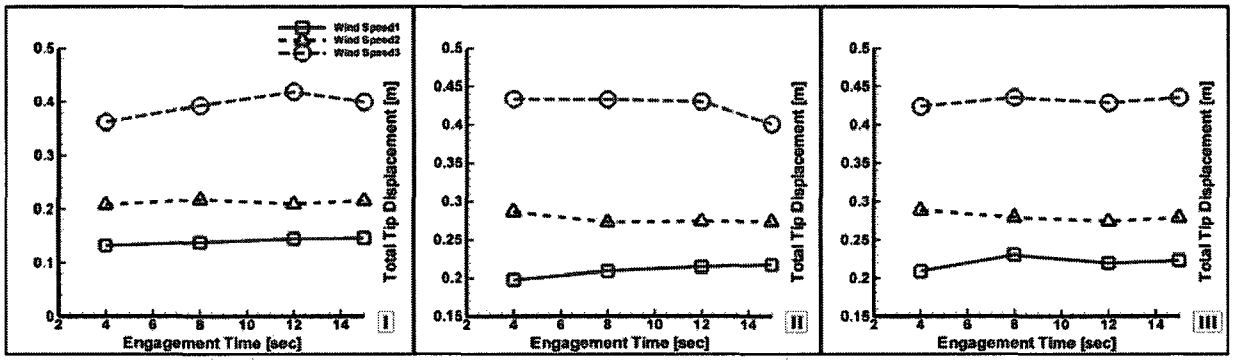

Figure 7.12: Registered upward extremum of blade 705 as a function of engage/disengage time for $-20°$ deck roll angle; wind speeds of:(1) 4, (2) 6, and (3) 8 [m/s]; collective pitch setting of: (I) 0°, (II) 4°, (III) 6°.

7.3.2 Simulation of Experimental Runs

An intrinsic multibody system was set up based on the rotor system properties given in Chapter 6 and Appendix D. The system was solved to its initial values in vacuum under the influence of the gravitational field. The system was then immersed in the airwake model and given 6 [sec] to reach its corrected initial values prior to commencing the engagement/disengagement profile. The experimental runs simulated were the ones with 8 [sec] engagement/disengagement duration of the experiment matrix generated from Table 7.1. The goals of the simulation study were:

1. Further validation of the intrinsic multibody model, code, and the solution scheme.

2. Validation of the overall model in a ship airwake environment.

3. Comparison of the quasi-steady, unsteady with noncirculatory loads, and unsteady without noncirculatory loads.

The cases selected to examine the effect of the aerodynamic model are given in Table 7.2, where each case was examined using: the nonlinear quasi-steady model that depends on the instantaneous angle of attack and the Mach number; the unsteady model with Leishman-Beddoes dynamic stall model that takes into account the time history of

the flow over the airfoil; and the latter augmented with the noncirculatory (air inertia) airloads. The naming convention of the experimental runs is based on the NRC-IAR wind tunnel operation, where a Run indicates resetting of the wind tunnel data system and a Point indicates an element of the test matrix generated by Table 7.1.

Table 7.2: Experimental runs examined using the three different aerodynamic models.

	Deck Roll [deg]	Collective Pitch [deg]	Wind Speed [m/s]
Run12,P3	0	0	4
Run12,P10	0	0	6
Run13,P3	0	4	4
Run16,P16	0	6	8
Run17,P10	0	8	6
Run19,P3	0	-4	4

Predictions of the maximum downward tip deflection by the three models compared to the experimental results are shown in Fig. 7.13 to Fig. 7.18.

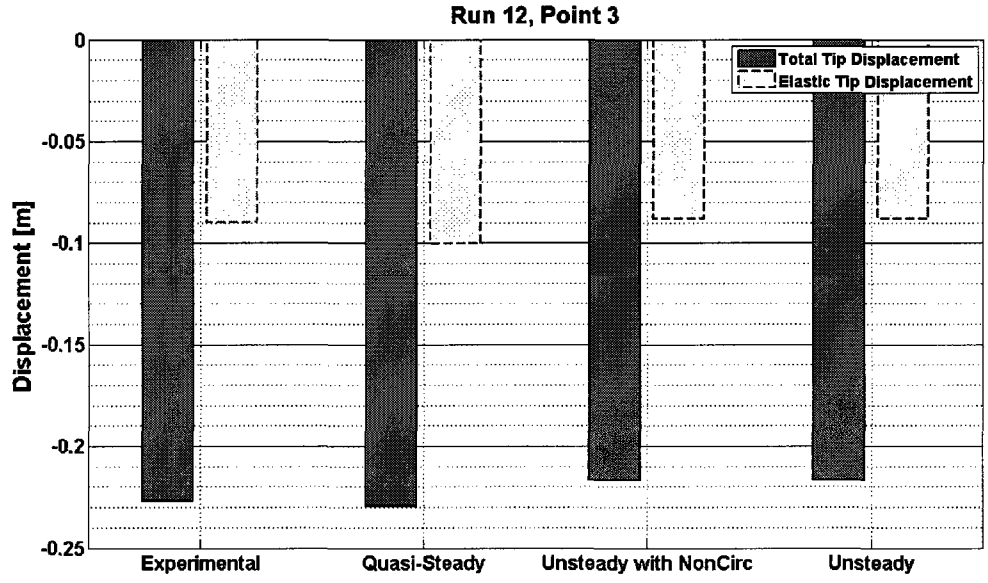

Figure 7.13: The maximum downward tip displacement predicted by the three aerodynamic models considered in this investigation versus experimental data, Run12, P3 (Deck Angle: 0°, Collective Pitch Setting: 0°, Wind Speed: 4[m/s]).

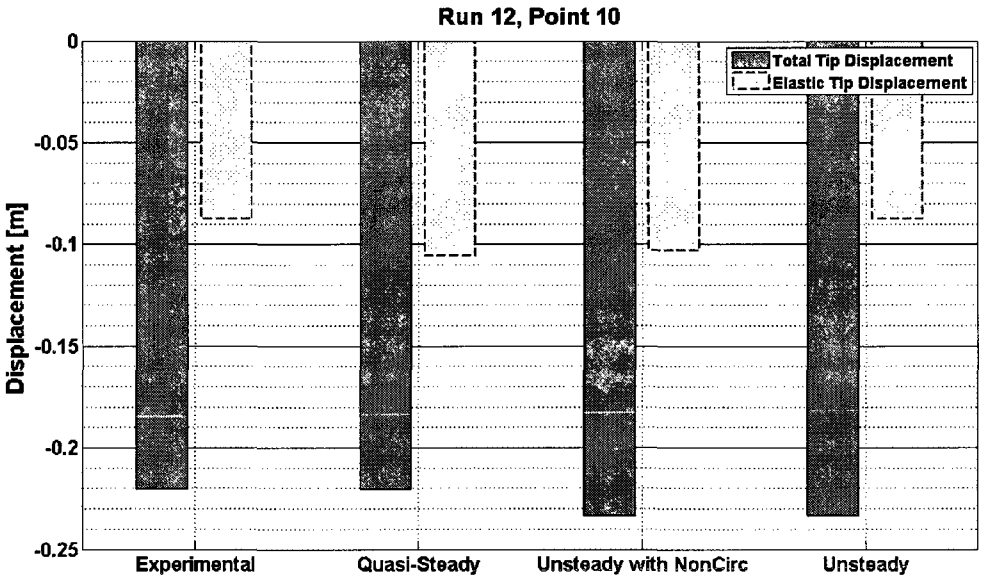

Figure 7.14: The maximum downward tip displacement predicted by the three aerodynamic models considered in this investigation versus experimental data, Run12, P10 (Deck Angle: 0°, Collective Pitch Setting: 0°, Wind Speed: 6[m/s]).

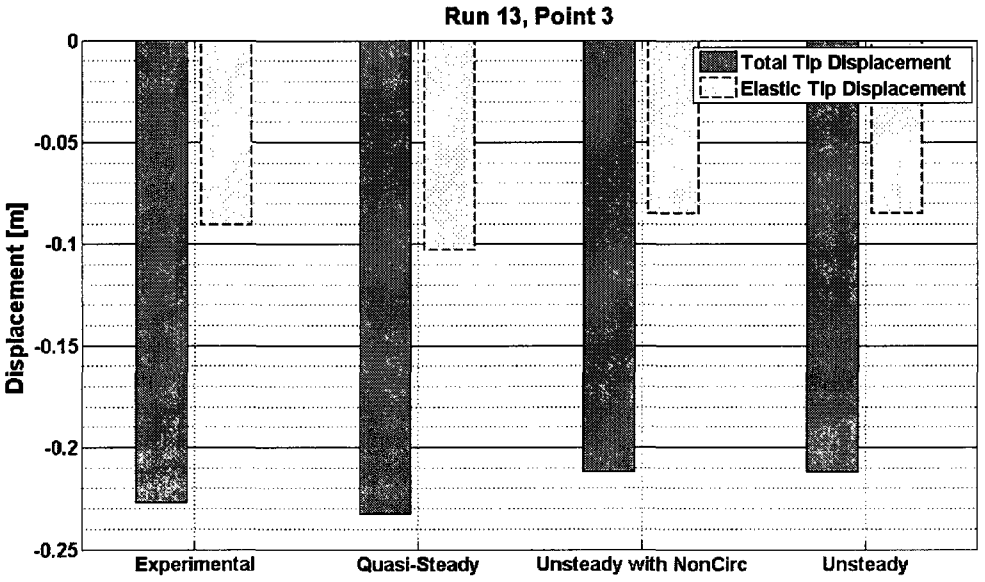

Figure 7.15: The maximum downward tip displacement predicted by the three aerodynamic models considered in this investigation versus experimental data, Run13, P3 (Deck Angle: 0°, Collective Pitch Setting: 4°, Wind Speed: 4[m/s]).

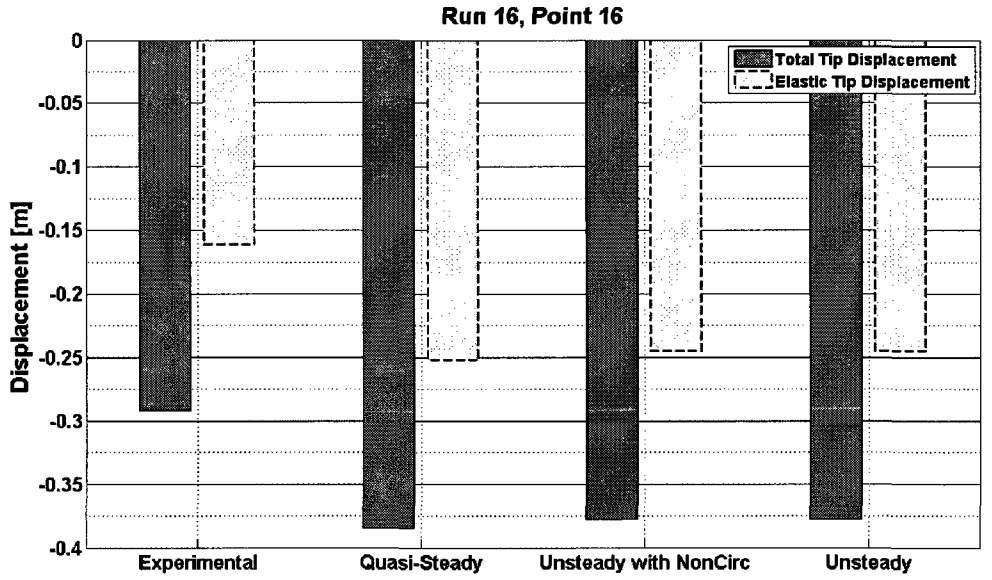

Figure 7.16: The maximum downward tip displacement predicted by the three aerodynamic models considered in this investigation versus experimental data, Run16, P16 (Deck Angle: 0°, Collective Pitch Setting: 6°, Wind Speed: 8[m/s]).

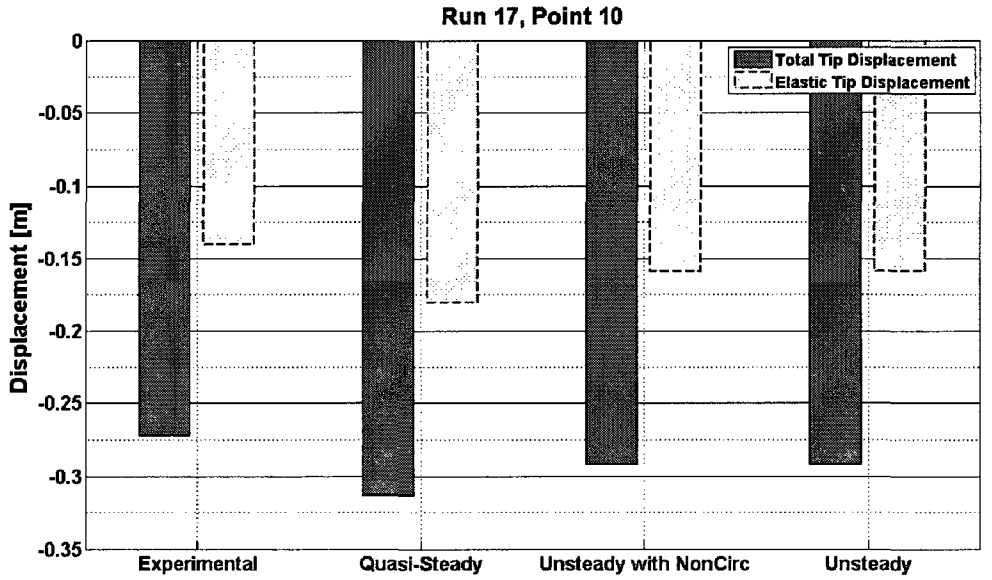

Figure 7.17: The maximum downward tip displacement predicted by the three aerodynamic models considered in this investigation versus experimental data, Run17, P10 (Deck Angle: 0°, Collective Pitch Setting: 8°, Wind Speed: 6[m/s]).

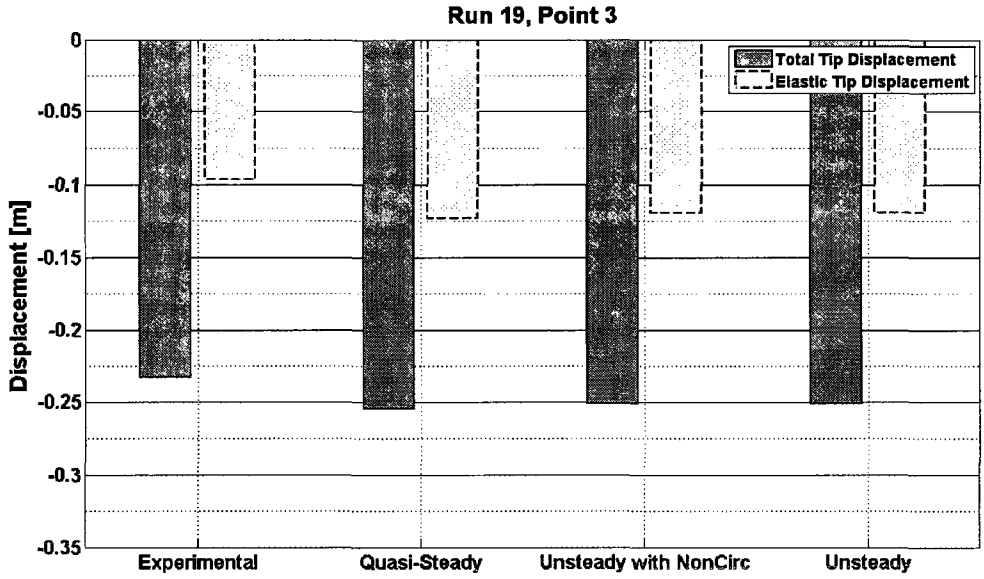

Figure 7.18: The maximum downward tip displacement predicted by the three aerodynamic models considered in this investigation versus experimental data, Run19, P3 (Deck Angle: 0°, Collective Pitch Setting: −4°, Wind Speed: 4[m/s]).

It is clear that the quasi-steady model is sufficient to capture the main characteristics of the BSP, which confirms the theoretical conclusions reached by previous investigators [11, 28]. However, in general, the quasi-steady model tends to slightly over-predict the airloads (and hence the displacement) when compared to the unsteady model, especially when the elastic displacement is examined which excludes the contribution of the hinge. This tendency seems to increase with increasing wind velocity, which also makes it attractive for the BSP reduction studies [17, 30] since it represents a worst case scenario. The noncirculatory aerodynamic loads seem to play a minimal role in this problem and neglecting them is easily justified in blade sailing research. This is supported by the physical fact that the air density is orders of magnitude less than the average density of the blade, especially in this problem where blade plunging is the dominant mode of motion. However, for other phases of the helicopter flight envelope the inclusion of some of their terms is essential as they play significant role in damping certain blade limit-cycle diver-

gence phenomena [153]. The case of Run 16, Point 16 in Fig. 7.16 shows that when one of the aerodynamic models displays poor predictive capabilities in terms of the maximum deflection, the rest of the models will similarly display poor predictions. This is attributed to the approximations involved in modelling the aerodynamic profile of the NACA64A010 and not to the aerodynamic models of the airloads. In summary, the unsteady model is better suited to reproduce the experimental data and it is used for the rest of the investigation. The time histories produced by the quasi-steady and the unsteady model are compared with the experimental data in Fig. 7.19 for the case of Run 12,P 3, and one can see that, on average, the features of the engagement are well captured by both models.

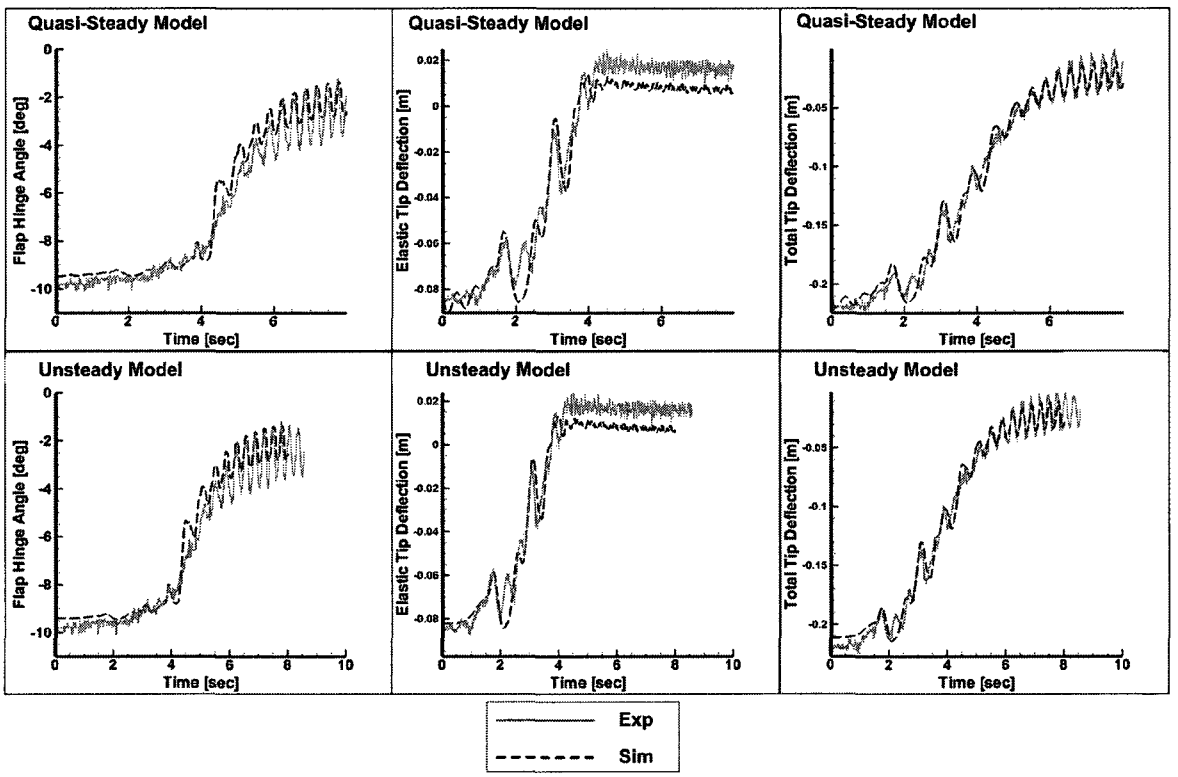

Figure 7.19: Time histories of the engagement for Run 12,P 3 produced by the quasi-steady and the unsteady model.

The maximum downward total and elastic tip deflections, and the upward elastic deflection and hinge angle for the simulated runs of the 0° deck case are shown in Fig. 7.20

and Fig. 7.21 respectively. Table 7.3 gives a summary of these simulated runs. In most cases, the maximum downward hinge angle corresponds to the blade resting on the neoprene stops and that is why they are not included in Figs. 7.20 and 7.21. The data are based on the engagement part of the rotor operation only due to the phase lag between the ideal profile and the commanded profile introduced by the software clock that was discussed in Chapter. 6.

Table 7.3: Simulated experimental runs of the 0° deck case[C:collective pitch setting,W:wind speed].

	C [°]	W [m/s]		C [°]	W [m/s]
Run12,P3	0	4	**Run12,P10**	0	6
Run12,P18	0	8	**Run13,P3**	4	4
Run15,P8	4	6	**Run15,P18**	4	8
Run16,P4	6	4	**Run16,P10**	6	6
Run16,P16	6	8	**Run17,P3**	8	4
Run17,P10	8	6	**Run17,P15**	8	8
Run19,P3	-4	4	**Run19,P9**	-4	6
Run19,P17	-4	8	**Run20,P5**	-8	4
Run22,P3	-8	6	**Run22,P10**	-8	8

The data in Figs. 7.20 and 7.21 is grouped according to the collective pitch setting of: 0°, 4°, 6°, 8°, -4°, and -8° respectively. As expected, increasing the magnitude of the collective pitch setting, whether positive or negative, increases the maximum downward deflection while the upward deflections are increased for positive pitch and decreased for the negative one. The experimental trends are well captured in the simulations as seen in the plots. The differences between the experimental and the simulation data that are occasionally observed could be attributed to the following factors:

- Uncertainties in the elastic and inertial properties of the system.
- Uncertainties in the flap hinge and the strain gauge signals and the phase lag in their response.
- Approximations in the aerodynamic profile of the airfoil.

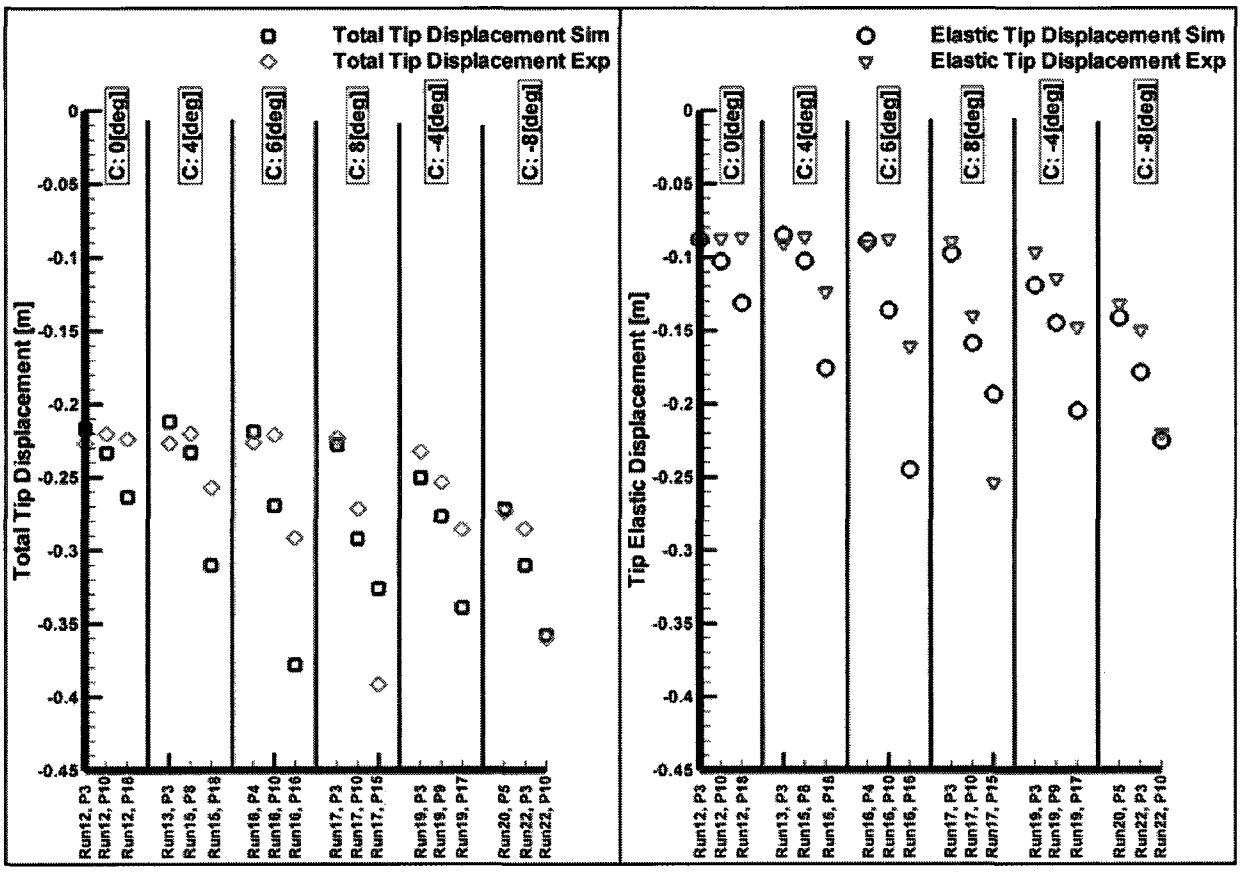

Figure 7.20: Simulated versus experimental maximum downward total and elastic tip displacement, 0° deck roll angle case.

- The small gaps between segments modifying the flow over the rotor blade in addition to irregularities in the manufactured airfoil profile.
- The lack of turbulence in the airwake modelling used in this investigation.
- The drift in the commanded motor velocity profile alluded to in previous discussion.
- A power surge in the Hall Effect sensor due to the lack of voltage regulation.

It is also clear that the upward deflections are better predicted by the simulations than the downward ones. This could be attributed to the nonlinear response of the droop neoprene bumpers not being adequately modelled in the simulations, especially for repetitive

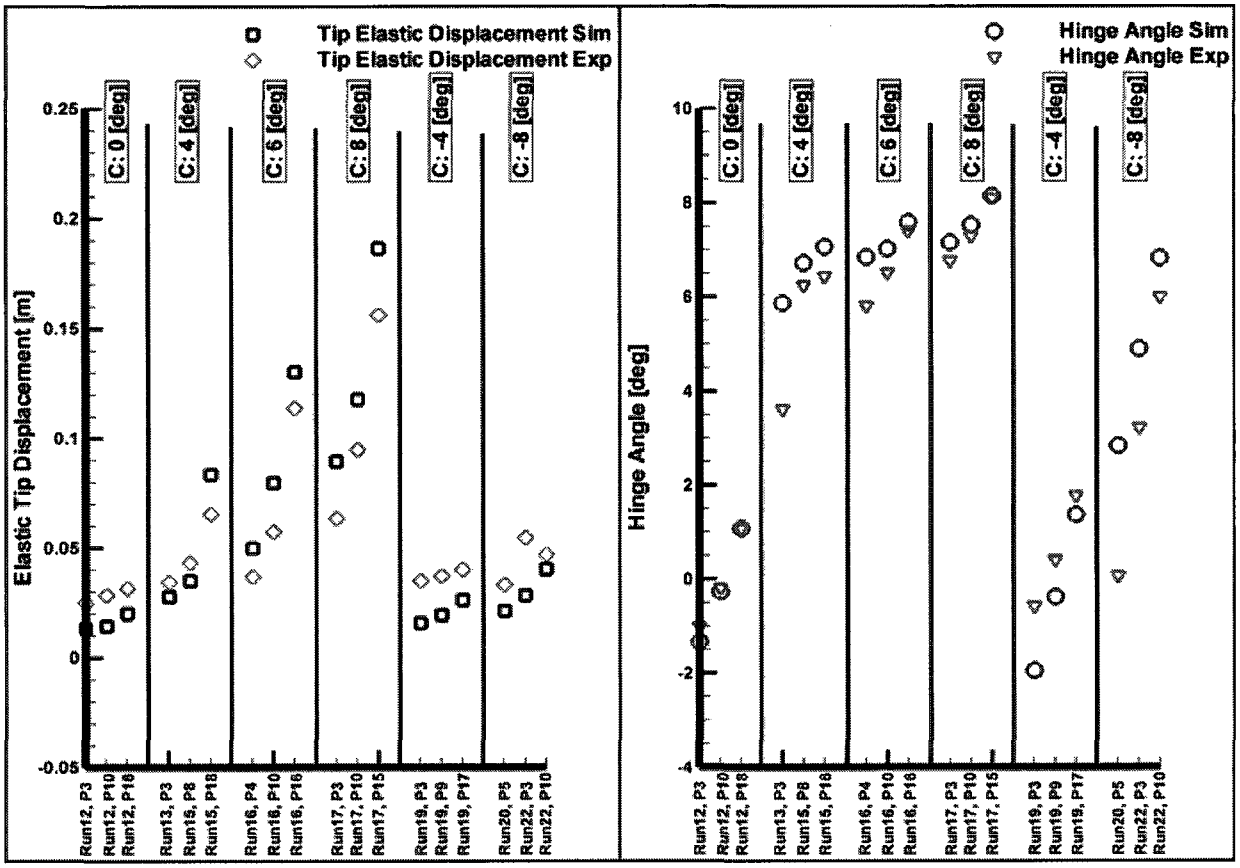

Figure 7.21: Simulated versus experimental maximum upward elastic tip displacement and hinge angle, 0° deck roll angle case.

impacts with a short time interval in between. Given that the time constant of the neoprene bumper recovery after impact is on the order of 1.5 [sec], as seen in Fig. 6.6, two consecutive impacts within that time interval will certainly lead to maximum downward deflections that are off from the ones predicted by the simulations.

Similar to the 0° deck case, the experimental runs of the $-20°$ deck case tabulated in Table. 7.4 were also simulated. The maximum downward total and elastic tip deflections, and the upward elastic deflection and hinge angle are shown in Figs. 7.22 and 7.23 respectively. The data is grouped according to the collective pitch settings of: -8°, -4°, 0°, 2°, 4°, 6°, and 8°. While the trends are captured, the simulation results are not as favorable as those seen for the 0° deck case. This is attributed to the uniqueness of the airwake for the

$-20°$ deck case including the separation bubble seen in Fig. 7.2 and sections of the blade that are expected to stall more often as it traverses the airwake. The dynamic stall model implemented, while sufficient as a first order approximation of the phenomenon, is deficient at low Mach numbers as discussed previously since it was designed mainly for hovering and forward moving rotors. Therefore, the nonlinear aerodynamic forces predicted are not entirely accurate for this problem. Certainly, this modelling deficiency contributed to the deviations seen in the $0°$ deck case and more so in the $-20°$ case.

Table 7.4: Simulated experimental runs of the $-20°$ deck case[C:collective pitch setting,W:wind speed].

	C [°]	W [m/s]		C [°]	W [m/s]
Run25,P9	-8	4	**Run25,P15**	-8	6
Run26,P3	-4	4	**Run26,P9**	-4	6
Run26,P15	-4	8	**Run27,P4**	0	4
Run27,P10	0	6	**Run27,P17**	0	8
Run28,P3	2	4	**Run28,P9**	2	6
Run28,P14	2	8	**Run30,P4**	4	4
Run30,P22	4	8	**Run31,P6**	6	4
Run31,P12	6	6	**Run31,P22**	6	8
Run33,P5	8	4	**Run33,P17**	8	8

Sample engagement time histories of the total tip displacement, elastic tip displacement, and the flap hinge angle are compared to the experimental data of Run (19, P9); Run (20, P5); and Run (27, P4) in Figs. 7.24 through 7.32. The rest of the cases are compiled in Appendix F. The effect of the drift in the experimental rotor velocity profile is clearly visible in all plots once steady state is reached.

The motor velocity profile drift causes the predicted disengagement to be different from the experimental one as in Fig. 7.33. However, this can be corrected by measuring and correcting this phase difference as was done in Figs. 7.34 through 7.39. Several aspects of the close agreements between the simulation and the experimental data are worth highlighting at this stage. Firstly, the experimental features of the early and late engagement transient are well captured by the simulations as seen for example in Fig. 7.27 and Fig. 7.32. This

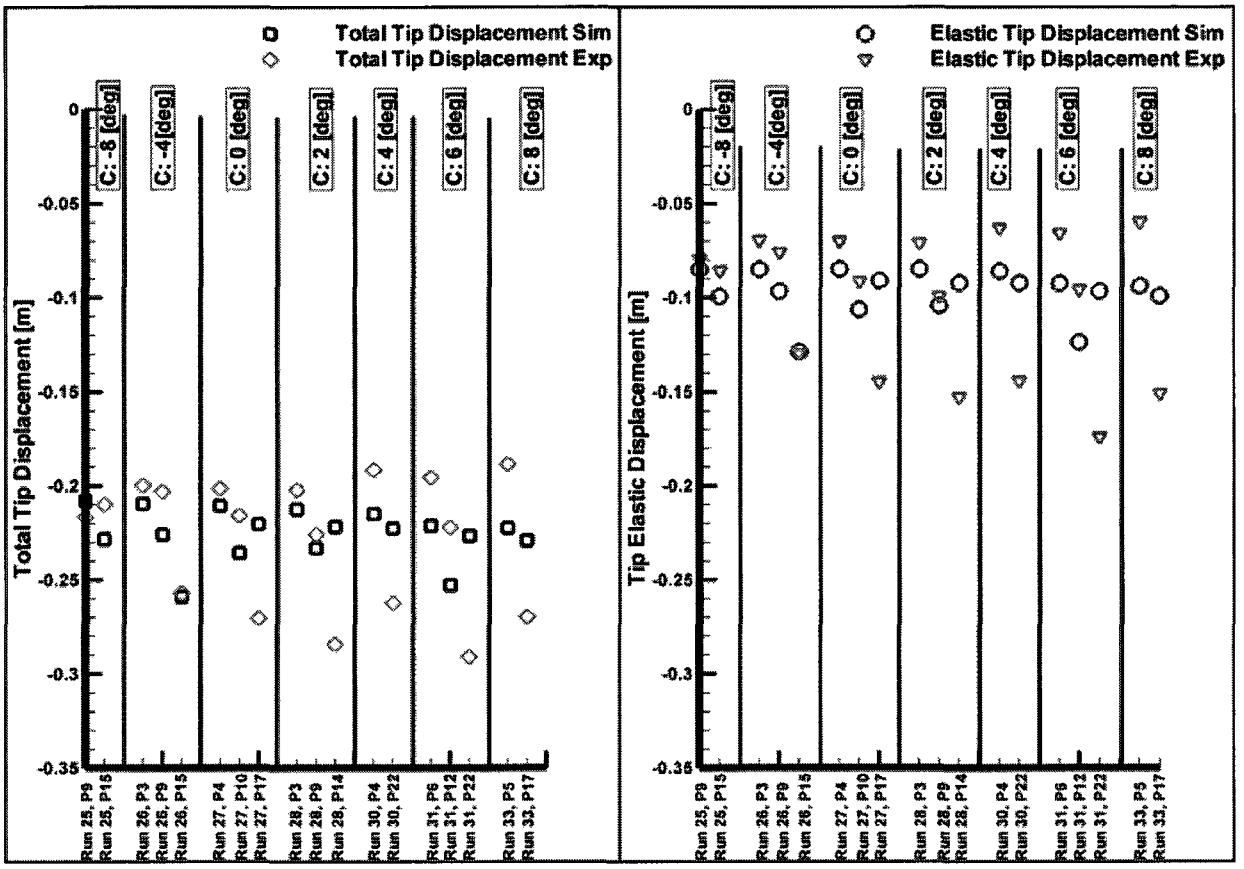

Figure 7.22: Simulated versus experimental maximum downward total and elastic tip displacement, $-20°$ deck roll angle case.

can also be said about the disengagement phase as seen for in Fig. 7.37 and Fig. 7.34. Secondly, the important experimental rigid and elastic modes (frequencies) are all present in the simulations as can be qualitatively observed. Thirdly, the amplitudes of the modes are also well represented in the simulations as is in the case of Fig. 7.28 and Fig. 7.30. This observation extends to the dips/bumps in the very early stages of engagement as in Fig. 7.32 or the very late stages of disengagement as in Fig. 7.34. Finally, the results clearly validate the developed simulation tools to study and reduce the impact of the BSP.

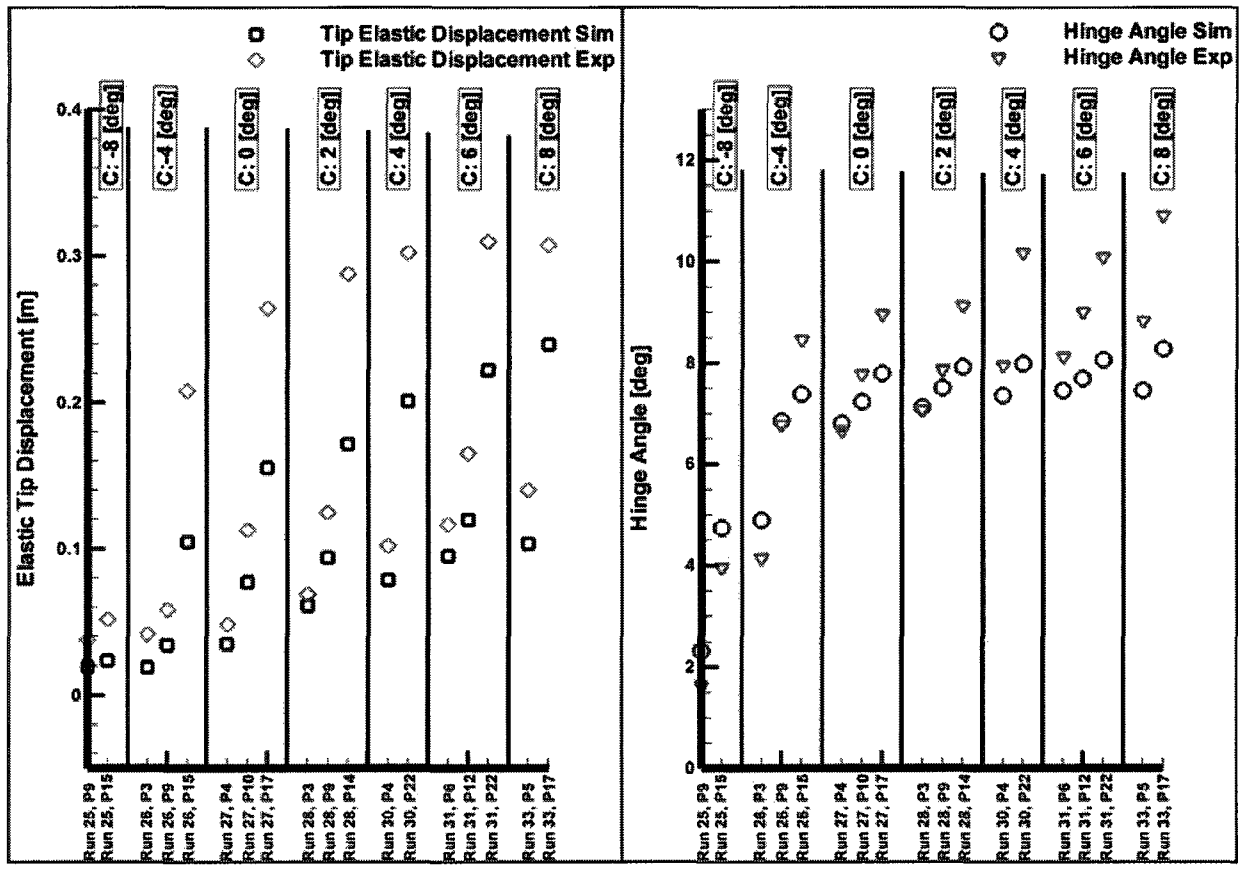

Figure 7.23: Simulated versus experimental maximum upward elastic tip displacement and hinge angle, $-20°$ deck roll angle case.

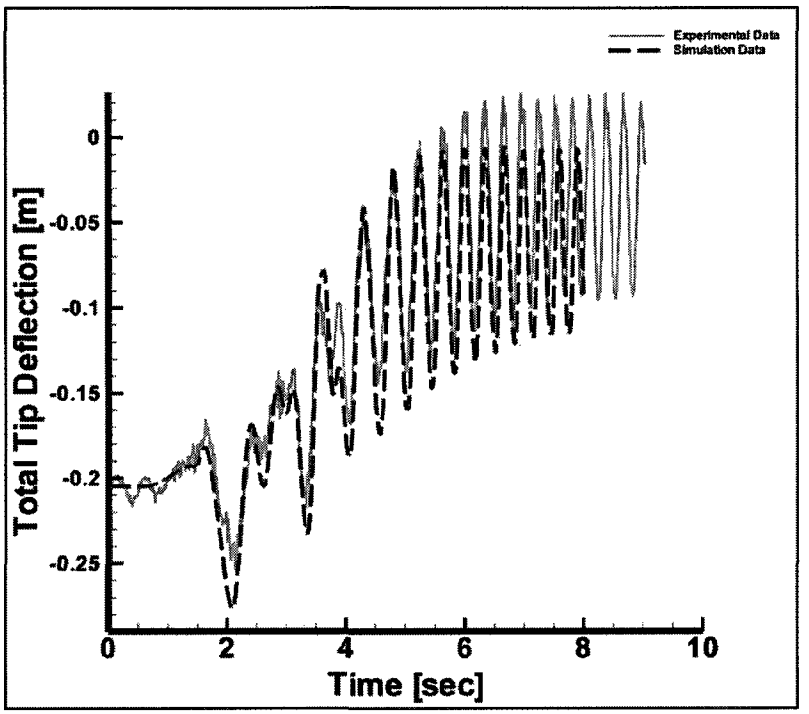

Figure 7.24: Engagement of Run (19, P9); total tip displacement.

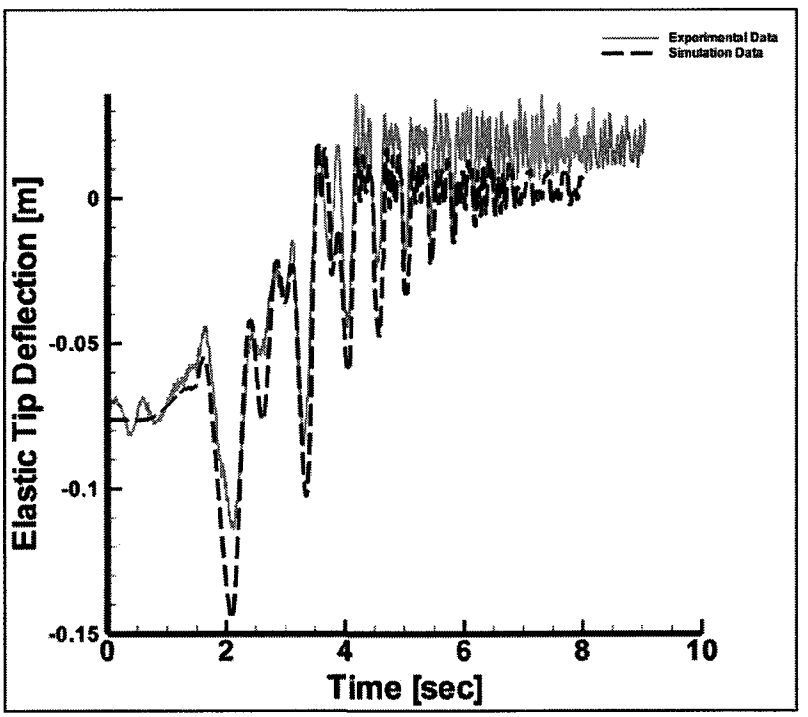

Figure 7.25: Engagement of Run (19, P9); tip elastic displacement.

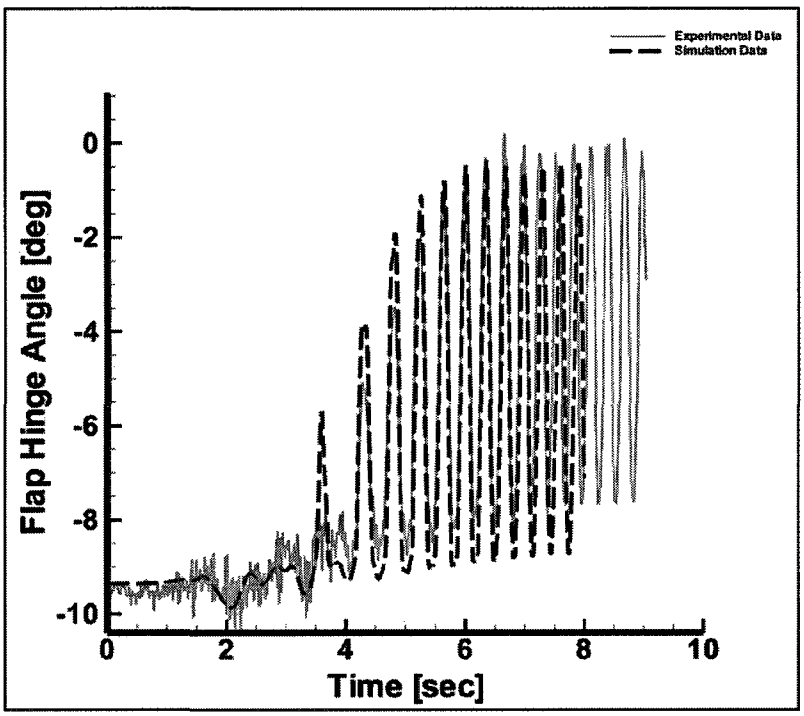

Figure 7.26: Engagement of Run (19, P9); hinge angle.

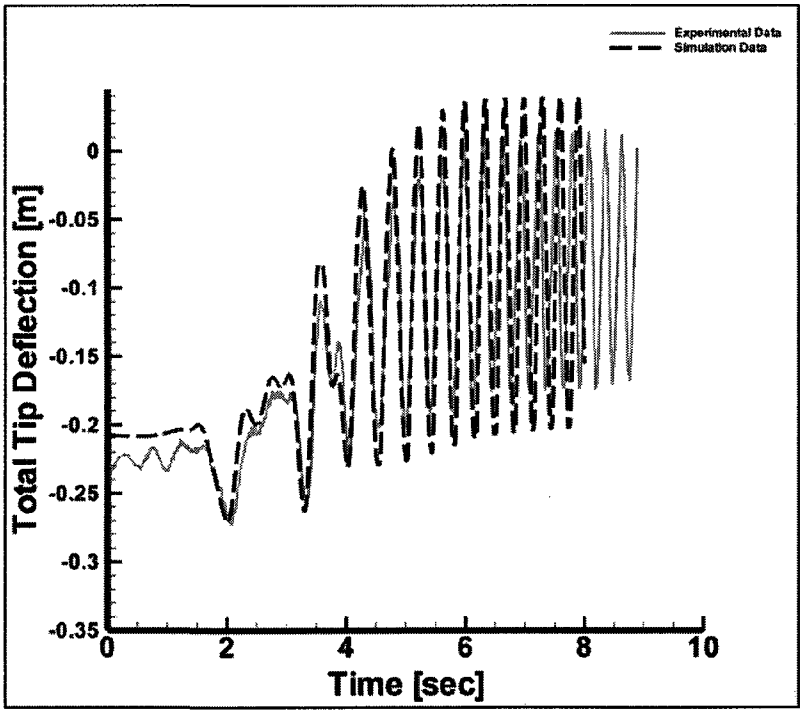

Figure 7.27: Engagement of Run (20, P5); total tip displacement.

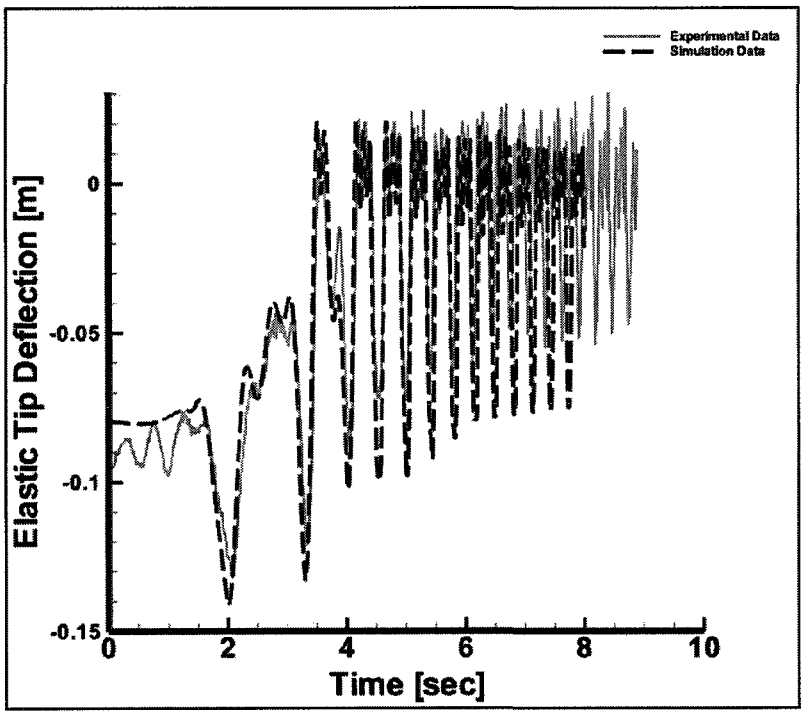

Figure 7.28: Engagement of Run (20, P5); tip elastic displacement.

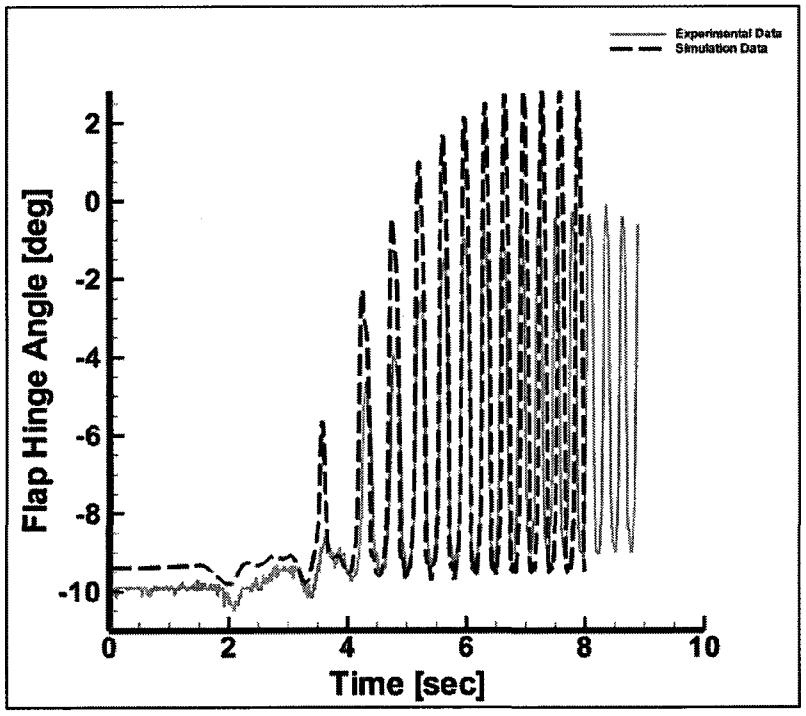

Figure 7.29: Engagement of Run (20, P5); hinge angle.

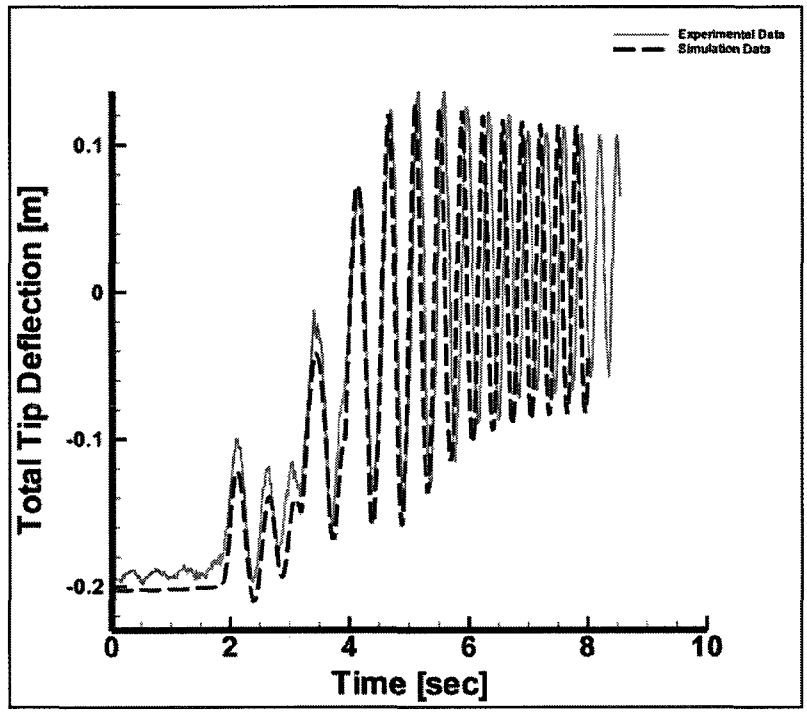

Figure 7.30: Engagement of Run (27, P4); total tip displacement.

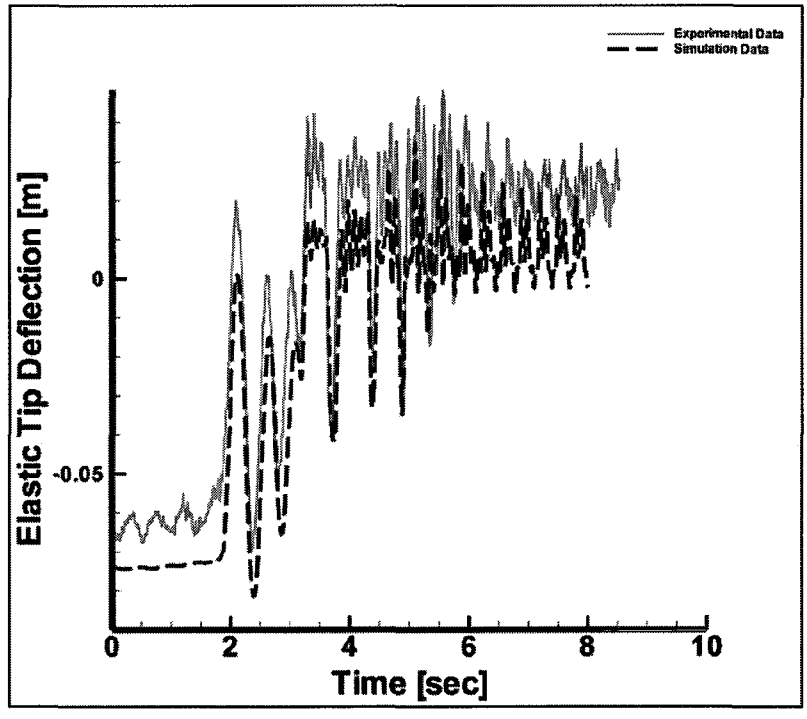

Figure 7.31: Engagement of Run (27, P4); tip elastic displacement.

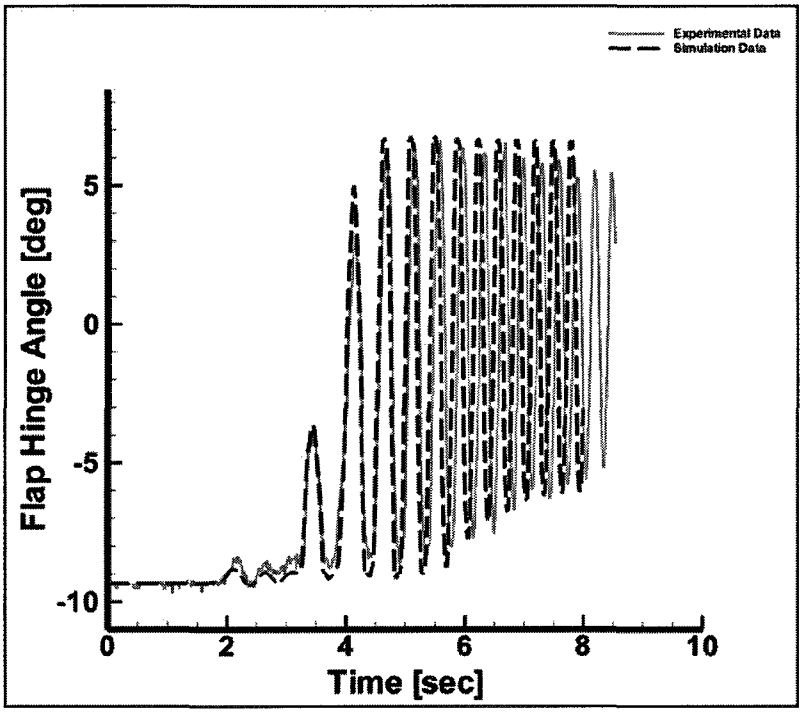

Figure 7.32: Engagement of Run (27, P4); hinge angle.

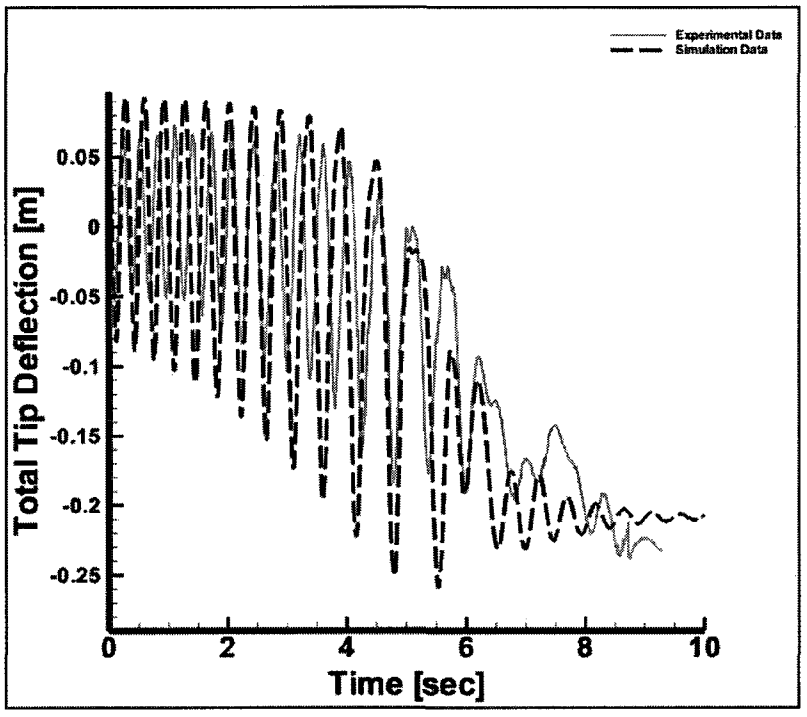

Figure 7.33: Disengagement of Run (13, P3); total tip displacement [Uncorrected].

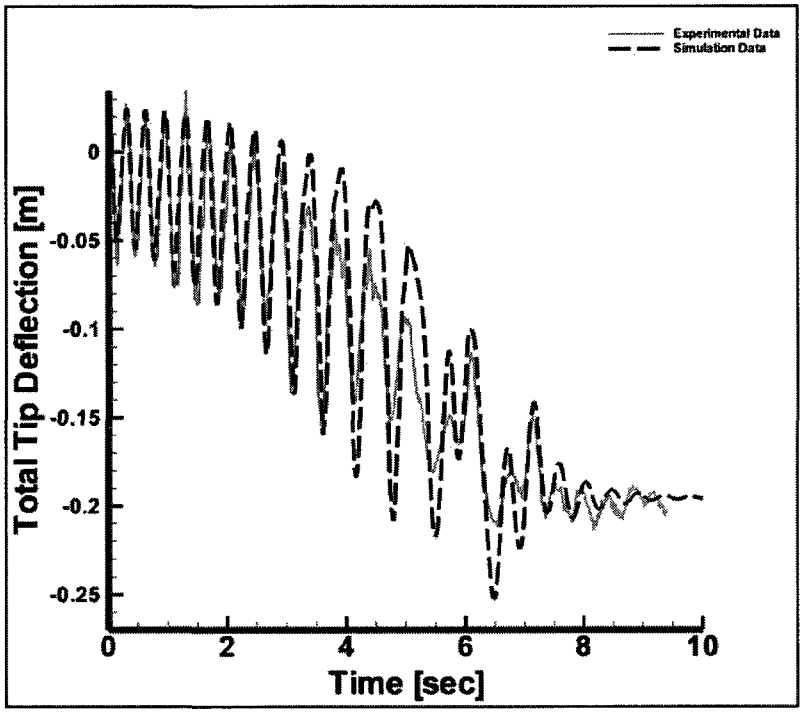

Figure 7.34: Disengagement of Run (12, P18); total tip displacement.

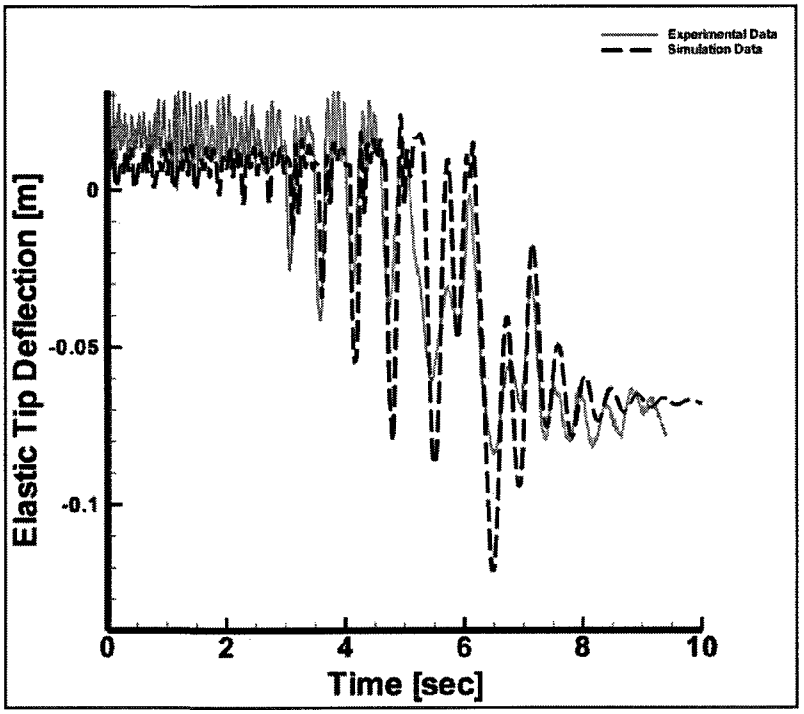

Figure 7.35: Disengagement of Run (12, P18); tip elastic displacement.

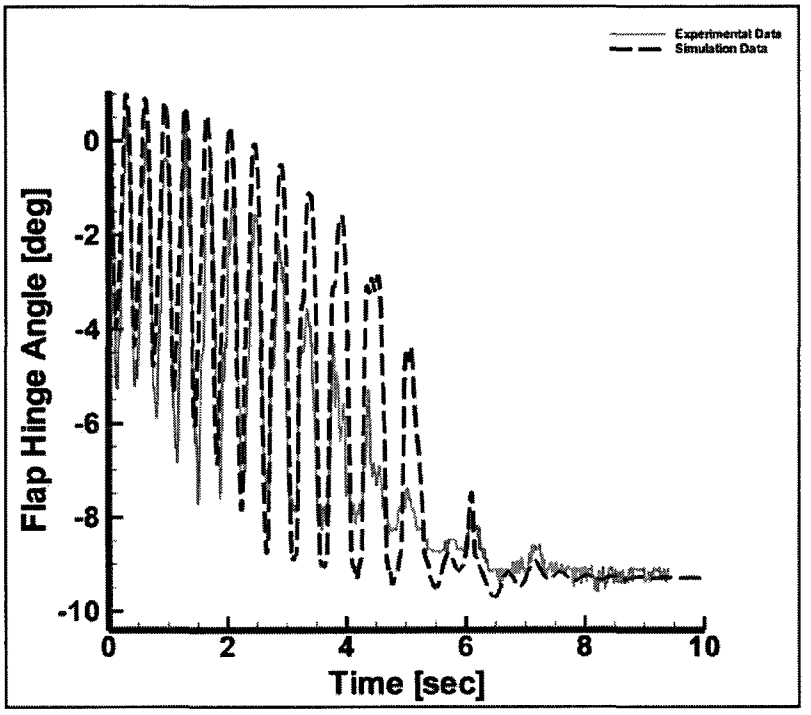

Figure 7.36: Disengagement of Run (12, P18); hinge angle.

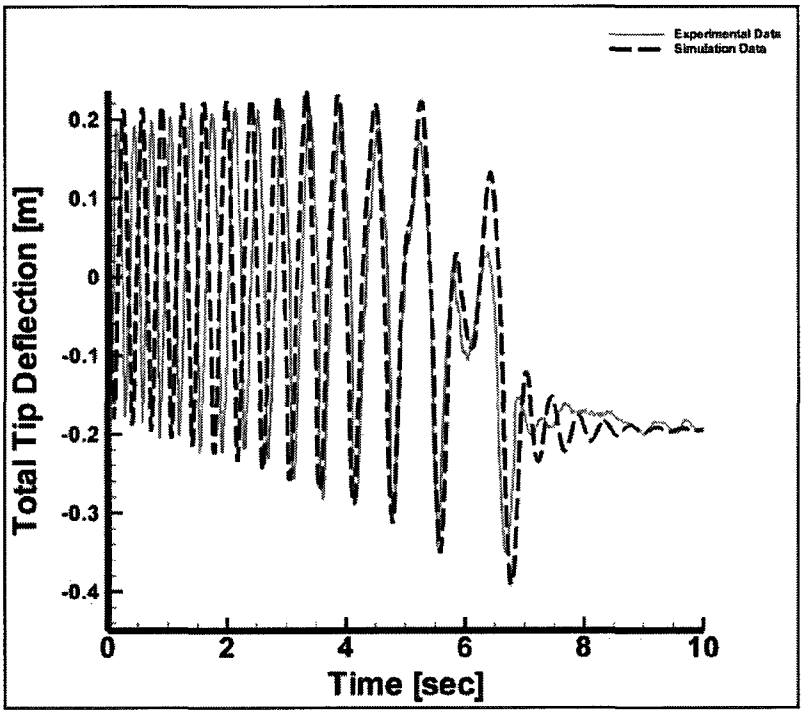

Figure 7.37: Disengagement of Run (16, P16); total tip displacement.

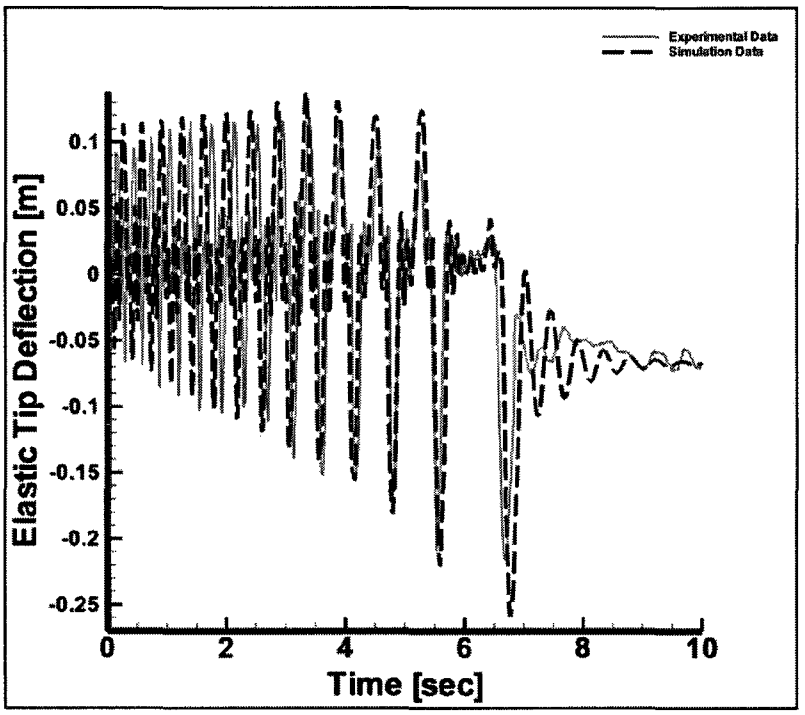

Figure 7.38: Disengagement of Run (16, P16); tip elastic displacement.

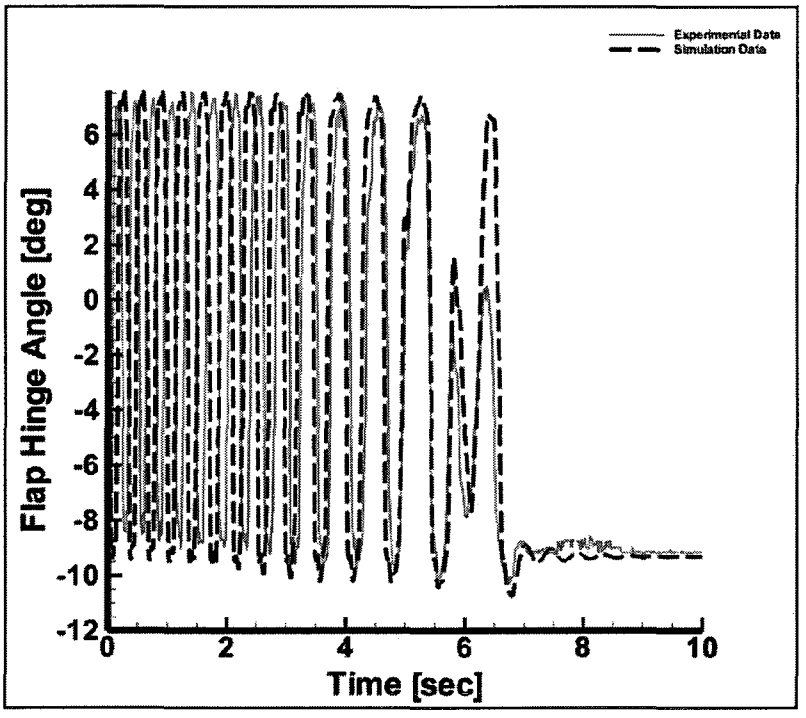

Figure 7.39: Disengagement of Run (16, P16); hinge angle.

Chapter 8

Dynamic response of the $1/12^{\text{th}}$ Froude-scaled Flap Articulated Rotor System to Representative Scaled Ship Motion

8.1 Overview of Chapter 8

In this chapter, the experimental investigation of the $1/12^{\text{th}}$ Froude-scaled rotor system engagement/disengagement on a moving ship is outlined and analyzed. The effect of scaled roll/pitch motion frequency and hub angular speed, in isolation from the ship airwake, on the maximum tip deflection is examined. Additionally, the geometrically-exact intrinsic model of active rotor systems on a moving ship is validated against the experimental time history of the rotor system tip position or deflection during the engage/disengage operation on a moving ship.

8.2 Overview of Experimental Setup and Runs

In Phase [II] of the experimental work, the Froude-scaled rotor system was placed on a flat wooden deck that was attached to a 6 degrees of freedom (6DOF) Stewart motion platform (MOOG model 6DOF2000E) in the Applied Dynamics Laboratory at Carleton University. An isometric schematic of the motion platform along with its reference frame and degrees of freedom is shown in Fig. 8.1. The rotor system attached to the motion platform while stationary and moving is shown in Fig. 8.2.

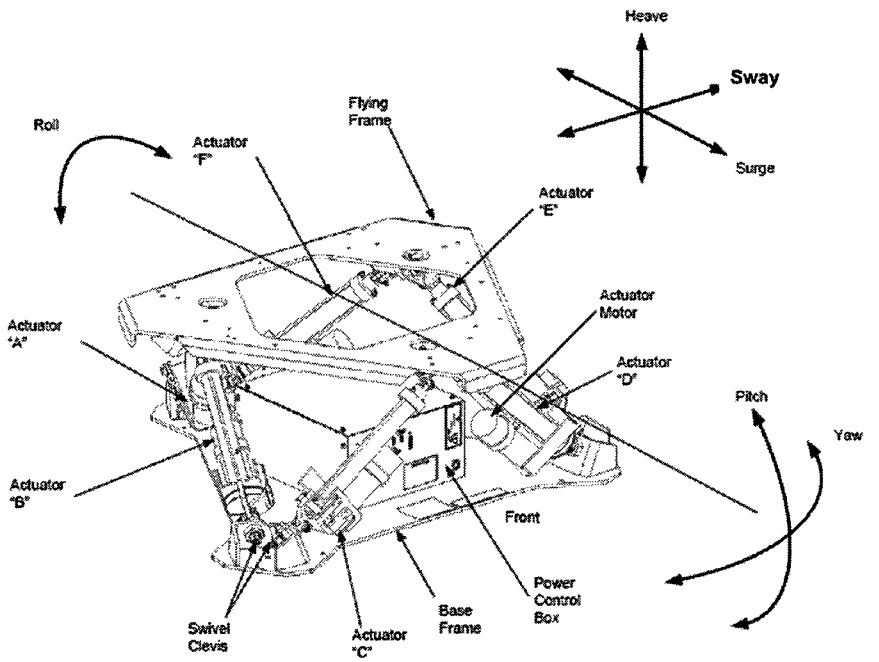

Figure 8.1: Isometric schematic of the MOOG 6DOF2000E motion platform [Courtesy of MOOG MOTION SYSTEMS DIVISION].

This experimental phase was divided into the following three sub-phases:

Sub-phase (I) The rotor system, operating at a constant angular velocity, was subjected to a uniform and constant harmonic roll motion at selected roll frequencies that were scaled and selected to span representative ship roll and pitch frequencies. The range

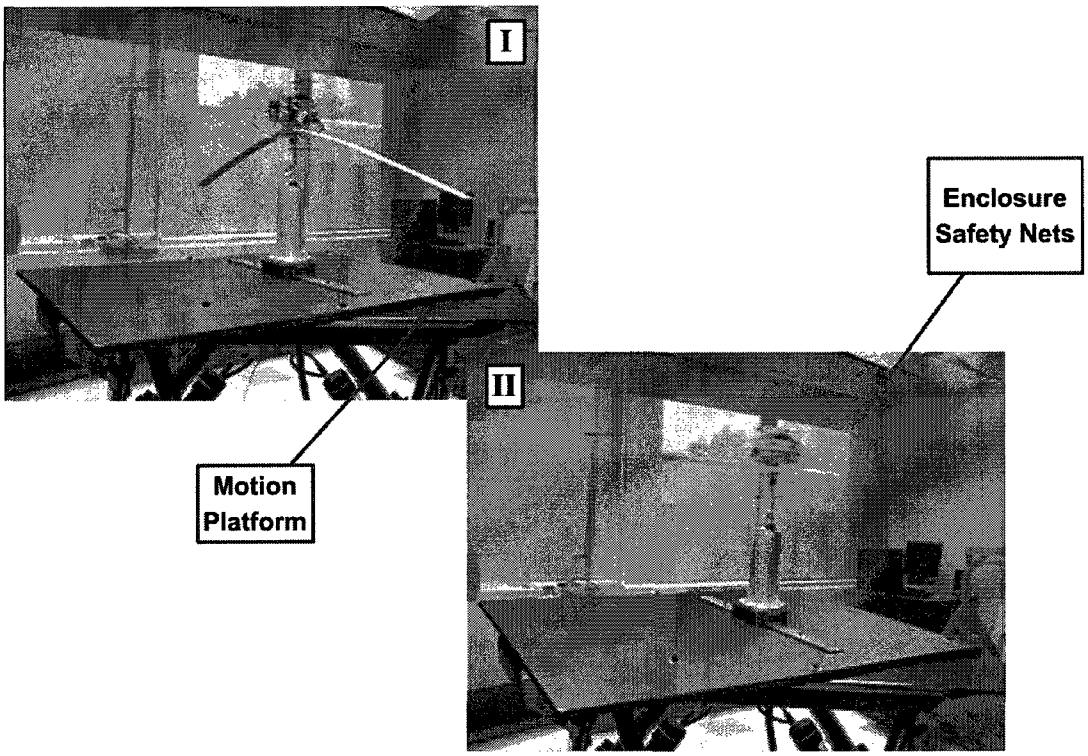

Figure 8.2: Froude-scaled rotor system attached to the motion platform while: (I) being stationary (II) moving with the platform and engaged.

of the selected rotor angular velocity was selected to span up to 33% of the Froude-scaled full rotor speed.

Sub-phase (II) The rotor system went through a complete engagement/disengagement profile while being subjected to Froude-scaled and representative ship motion in mild and severe sea states.

Sub-phase (III) The rotor system, operating at a constant angular velocity, was subjected to Froude-scaled and representative ship motion in mild and severe sea states. The rotor angular velocity was selected to be 5.5% of the Froude-scaled full rotor speed.

The representative ship motions used in Sub-phases II and III are tabulated in Ta-

ble 8.1, where the convention of quoting the significant[1] wave height followed by the ship heading relative to the principal wave direction and then ship speed is used to denote the ship motion conditions. The ship motions are produced based on measured amplitudes, frequencies, and phases for each of the 6 DOFs of a typical Canadian frigate at the origin of its reference frame. A time series is then generated for each degree of freedom, its velocity and its acceleration such that

$$D(t) = \sum_{i=1}^{N} A_i \sin(2\pi f_i t + \phi_i) \tag{8.1}$$

$$\dot{D}(t) = \sum_{i=1}^{N} 2\pi f_i A_i \cos(2\pi f_i t + \phi_i) \tag{8.2}$$

$$\ddot{D}(t) = -\sum_{i=1}^{N} (2\pi f_i)^2 A_i \sin(2\pi f_i t + \phi_i) \tag{8.3}$$

where D is the degree of freedom, N is the number of frequency components in the measured spectrum, A_i is the i^{th} amplitude, f_i is the i^{th} frequency, ϕ_i is the i^{th} phase, and t is the time in seconds.

The ship degrees of freedom correspond to surge, sway, heave, roll, pitch, and yaw. The ship motion kinematics is transferred to the helicopter flight deck then the rotor hub where the Cardan/Bryant sequence of rotations is used to form the rotation matrix from the ocean frame to the ship frame such as

$$\mathcal{C}^{sI} = \mathcal{C}(\varphi_3, e_3)\,\mathcal{C}(\varphi_2, e_2)\,\mathcal{C}(\varphi_1, e_1) \tag{8.4}$$

where $\mathcal{C}(\varphi_i, e_i)$ represents the rotation about the i^{th} unit vector with an amplitude of φ_i.

The elements of the test matrix for each of the sub-phases are given in Table 8.2 through

[1] *Significant wave height* is the average of the one third highest wave heights. It is commonly expected that the maximum wave height in a seaway will reach twice the significant value.

Table 8.4 respectively.

Table 8.1: Ship motion files used in the test matrices of Phase [II].

Ship Motion	Significant Wave Height [m]	Ship Heading Relative to Waves [deg]	Ship Speed [kn]
1	4	0	10
2	4	0	25
3	4	45	10
4	4	45	25
5	4	90	10
6	4	90	25

Table 8.2: Elements of the test matrix of sub-phase (I).

Roll Frequency [Hz]	0	0.25	0.35	0.45	0.55	0.65	0.75	0.85	0.95
Hub Frequency/Speed [Hz]	0	0.56	1.11	1.67	2.22	2.78	3.33		
Collective Pitch Setting [deg]	0	4	8	-4	-8				
Roll Amplitude [deg]	5								

Table 8.3: Elements of the test matrix of sub-phase (II).

Ship Motion	1	2	3	4	5	6
Engage/Disengage Time [sec]	4	8				
Collective Pitch Setting [deg]	0	4	8	-4	-8	

Table 8.4: Elements of the test matrix of sub-phase (III).

Ship Motion	1	2	3	4	5	6
Collective Pitch Setting [deg]	0	-4	8			
Hub Frequency [Hz]	0.56					

The first sub-phase is designed to examine the effect of the ship roll/pitch frequency and rotor speed on the maximum tip deflections. The second phase is geared towards validating the response of the simulation model to representative ship motions and examining the capability of the motion platform to produce those motions. The third sub-phase was intended to examine the rotor response at a heuristically selected constant low rotor speed to representative ship motion. The latter sub-phase is considered secondary relative to the first two and it will not be treated in this investigation. For all investigations, the rotor is started from the reference orientation depicted in Fig. 8.3.

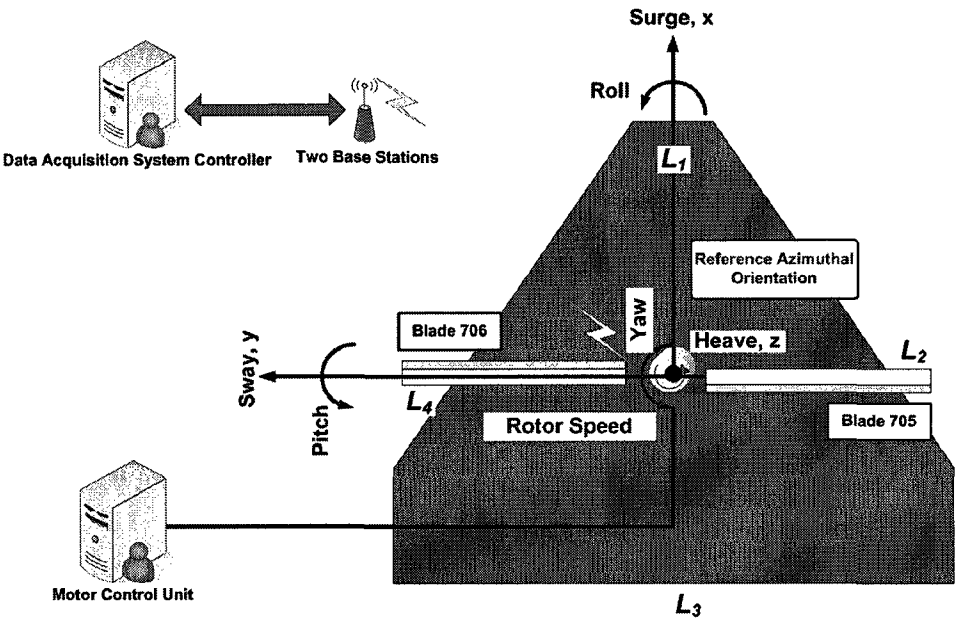

Figure 8.3: Rotor system reference orientation for Phase (II) of the experimental work.

8.3 Experimental and Simulated Dynamics Response

8.3.1 Sub-phase(I)

The experimental runs conducted in this sub-phase are all permutations of the parameter values listed in Table 8.2. The maximum downward and upward blade tip deflections are registered during each run. The data is presented as a family of curves for each collective pitch setting, where each curve represents the maximum tip displacement registered as a function of the roll frequency at a fixed hub frequency. The results for all collective pitch settings are shown in Fig. 8.4 to Fig. 8.8 due to their importance to the conclusions subsequently drawn. The hub frequencies shown in the figures are numbered according to how they sequentially appear in Table 8.2.

Expectedly, as the hub frequency (hub angular velocity) increases, the magnitude of the maximum downward deflection decreases while that of the upward one increases. This

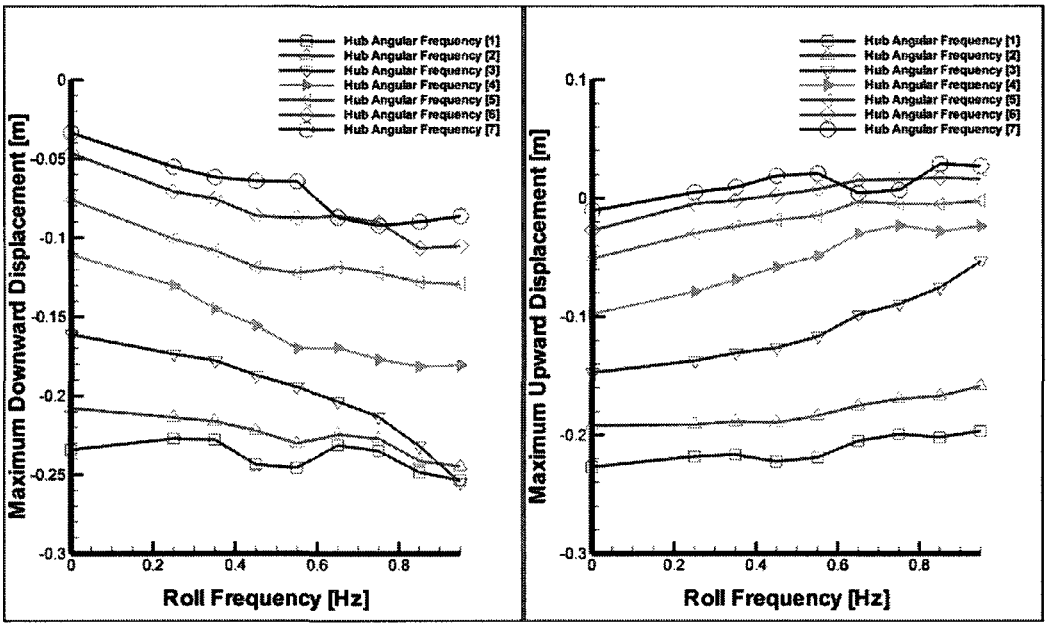

Figure 8.4: Maximum downward and upward tip deflection as a function of ship roll frequency and hub angular velocity [0° collective pitch setting], sub-phase(I).

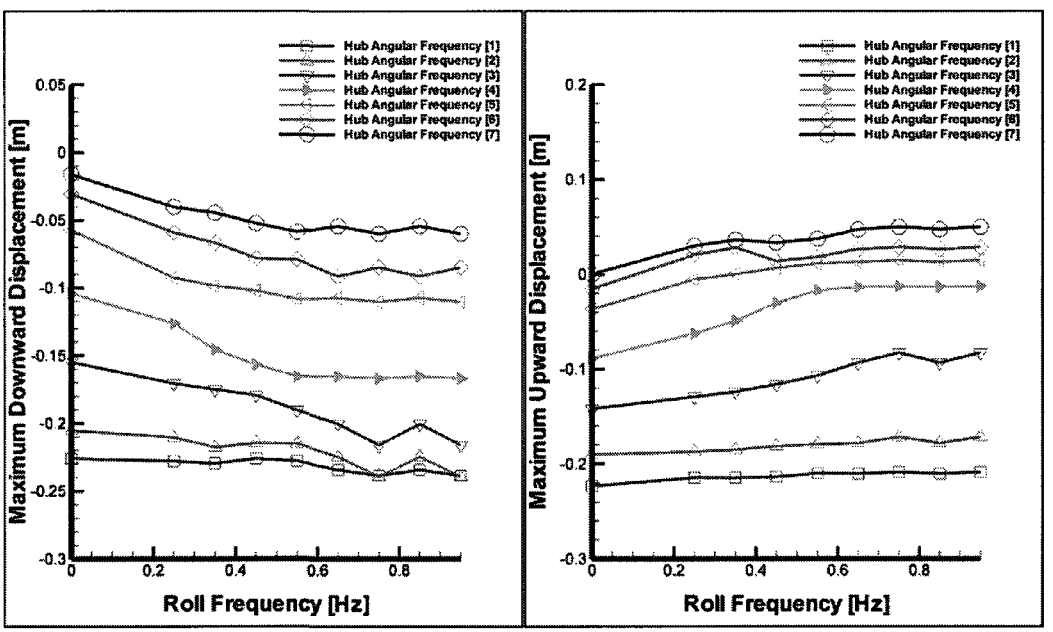

Figure 8.5: Maximum downward and upward tip deflection as a function of ship roll frequency and hub angular velocity [4° collective pitch setting], sub-phase(I).

is attributed to the increased centripetal acceleration that is proportional to the square of the hub angular velocity. With the exception of the hub third angular velocity in Figs. 8.4

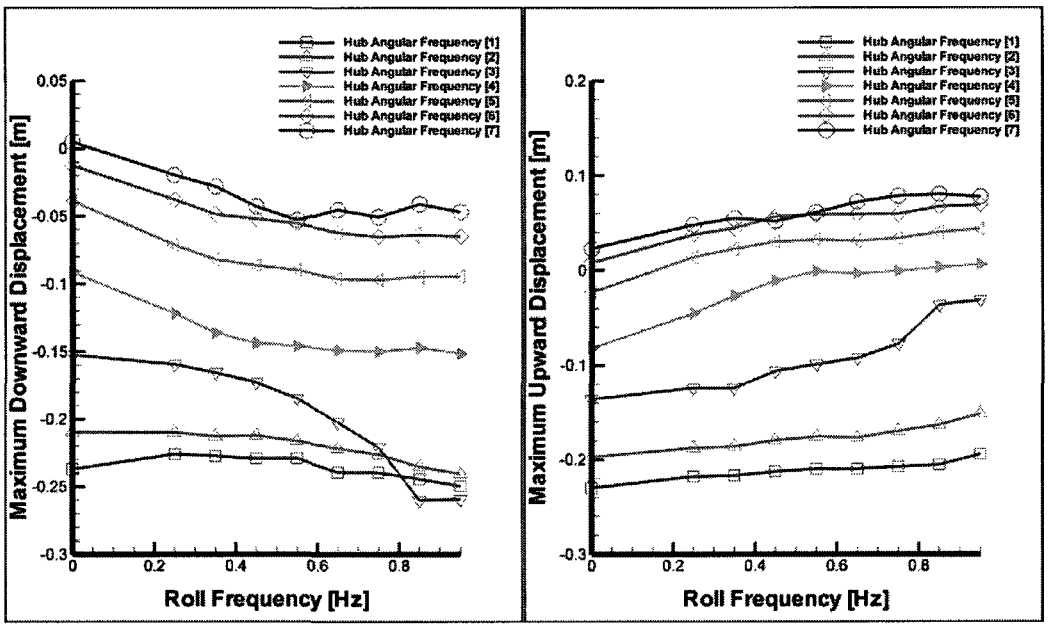

Figure 8.6: Maximum downward and upward tip deflection as a function of ship roll frequency and hub angular velocity [8° collective pitch setting], sub-phase(I).

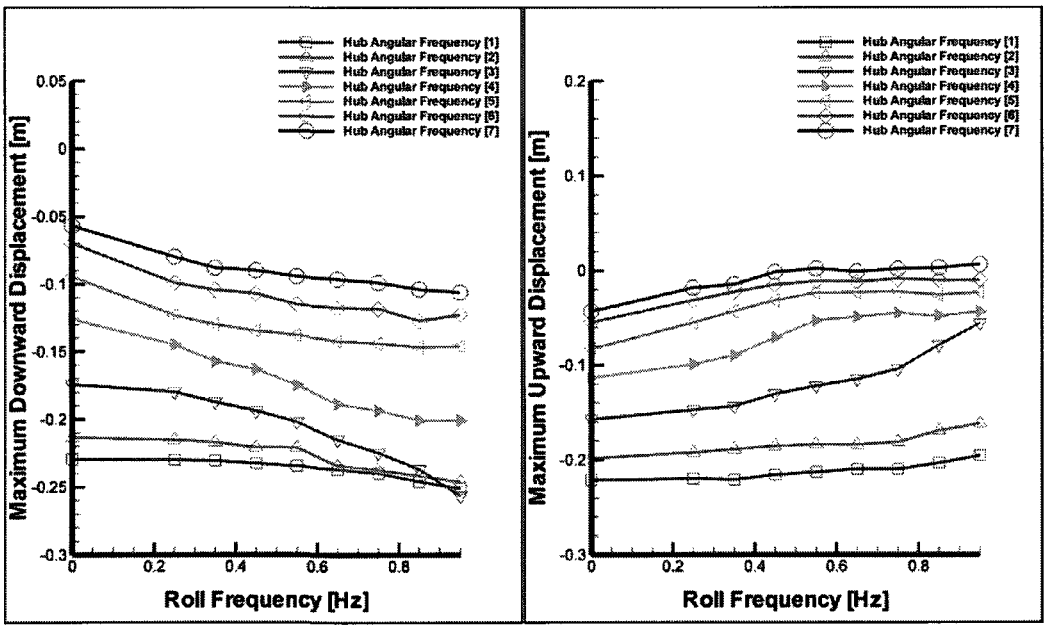

Figure 8.7: Maximum downward and upward tip deflection as a function of ship roll frequency and hub angular velocity [−4° collective pitch setting], sub-phase(I).

through 8.8, a downward inflection is observed in the mid-range of the roll frequencies examined. This phenomenon shifts towards higher roll frequencies as the hub angular

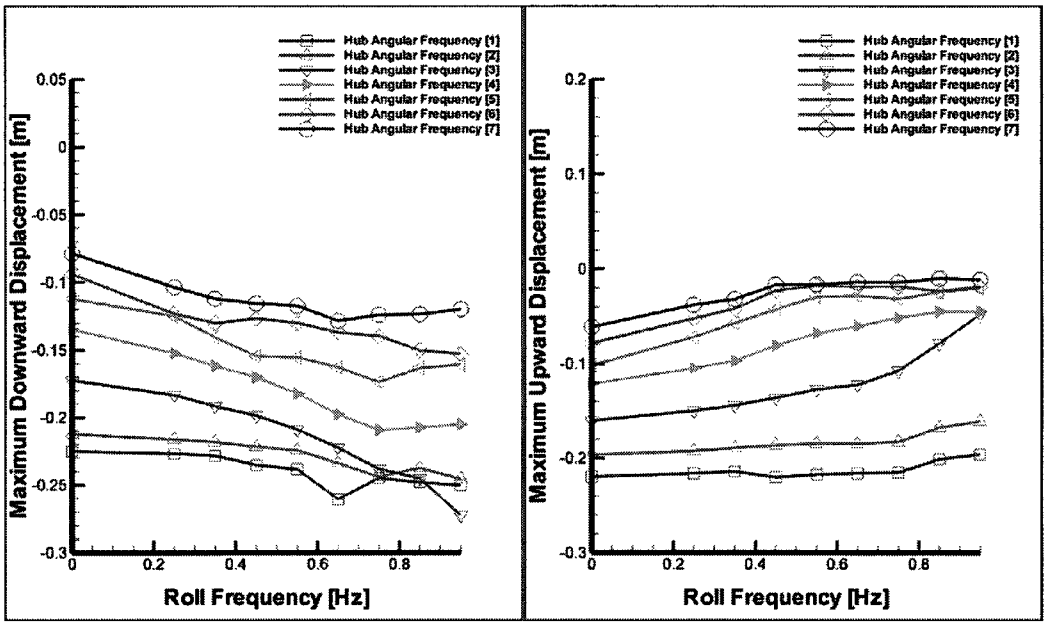

Figure 8.8: Maximum downward and upward tip deflection as a function of ship roll frequency and hub angular velocity [$-8°$ collective pitch setting], sub-phase(I).

velocity increases. Additionally, it is more pronounced for the $0°$ collective pitch setting where the aerodynamic interference is expected to be minimal. The aerodynamic loads seems to smear this phenomenon for the other collective pitch settings; however, its effect is still observed. This is a resonance-like phenomenon that is attributed to other components of the rotor/motion platform system, and only more detailed flexible multibody dynamics modelling and experimental investigation can identify its source with certainty.

In general, as the roll frequency increases, so do the magnitudes of the upward and downward deflections. This is expected given that the inertial forces experienced by the tips at locations L_2 and L_4 in Fig. 8.3 increase with the roll frequency. Furthermore, the magnitude of the rate of change of the maximum tip displacement with respect to the hub angular velocity at a fixed roll frequency is significant around the hub third angular speed to start decreasing again for higher and lower speeds. Therefore, the families of curves are clustered in a lower band and an upper one corresponding to the lower and higher angular speeds respectively. This is more pronounced at low roll frequencies.

The third hub speed presents an interesting case that merits more analysis. It is observed that the maximum tip displacement is more sensitive to changes in the roll frequency at higher values than the other hub speeds. Also, the changes in the maximum displacement with roll frequency is more uniform. More importantly, at high roll frequencies, the registered maximum downward deflections for this hub speed can exceed those registered at lower hub speeds. These observations are generally valid for all collective pitch settings including the 0° case where aerodynamic loading plays a minimal role. This clearly demonstrates that even in the absence of the ship airwake there exists a hub speed and ship motion that are detrimental to maritime helicopter engagement/disengagement. Moreover, the contribution of inertial forces due to ship motion to the severity of the BSP is said to be experimentally established. This observation can be explained by examining the form of the centripetal stiffening force and the gyroscopic force that are proportional to

$$\vec{F}_{\text{centripetal}} \propto \tilde{\vec{\omega}}\tilde{\vec{\omega}}\vec{R} \qquad \vec{F}_{\text{gyroscopic}} \propto 2 * \tilde{\vec{\omega}}_{\text{roll}}(\tilde{\vec{\omega}}\vec{R}) \tag{8.5}$$

where $\vec{\omega}$ is the hub angular frequency, $\vec{\omega}_{\text{roll}}$ is the roll/pitch frequency, and $\vec{R}$ is a generic position vector from the hub centre to a blade station.

The gyroscopic force peaks at locations L_1 and L_3 and vanishes at locations L_2 and L_4 in Fig. 8.3 while the centripetal force is independent of the azimuthal location. For certain combinations of hub and roll frequencies, the magnitude of the gyroscopic force is sufficient to overcome the centripetal stiffening of the blade and cause the excessive downward, or upward, deflections registered. These characteristics are observed to a lesser extent for the hub fourth angular speed as well.

Table 8.5: Simulated experimental runs of sub-phase (II).

Run Number	Ship Motion	Collective Pitch Setting [deg]
1	4_000_10	0
2	4_000_25	0
3	4_045_10	0
4	4_045_25	0
5	4_090_10	0
6	4_090_25	0

8.3.2 Sub-phase(II)

The experimental runs conducted in this sub-phase are all permutations of the parameter values listed in Table 8.3. To validate the response of the geometrically-exact intrinsic model of active maritime rotor systems, the experimental runs tabulated in Table 8.5 are simulated. Runs 1 through 6 were selected to minimize the aerodynamic influence, which is represented by their 0° collective pitch setting. The rotor system was modelled using the same properties of flexible members and rigid bodies given in Appendix E.

The nonlinear quasi-steady model was used in all simulations to calculate the aerodynamic loads. The time histories of the tip displacement of Runs 1 through 6 are shown in Figs. 8.9 through 8.14 respectively.

Comparing the experimental to the simulation time histories demonstrates that the features in the rotor aeroelastic response due to the ship motion are all captured in the simulations. From the time histories, it seems that most of the experimental frequencies are captured by the simulations. This is confirmed when the steady-state periods of the rotor system operation for Runs 1 through 6 are windowed and analyzed in the frequency domain in Figs. 8.15 through 8.20 using the FFT.

Differences between the simulation results and experimental data can be attributed to deficiencies in the aerodynamic modelling of the NACA 64A010 airfoil and lack of modelling of other moving parts of the motion platform. Also, the original test matrices in sub-phase (I) and sub-phase(II) were intended to include additional experimental

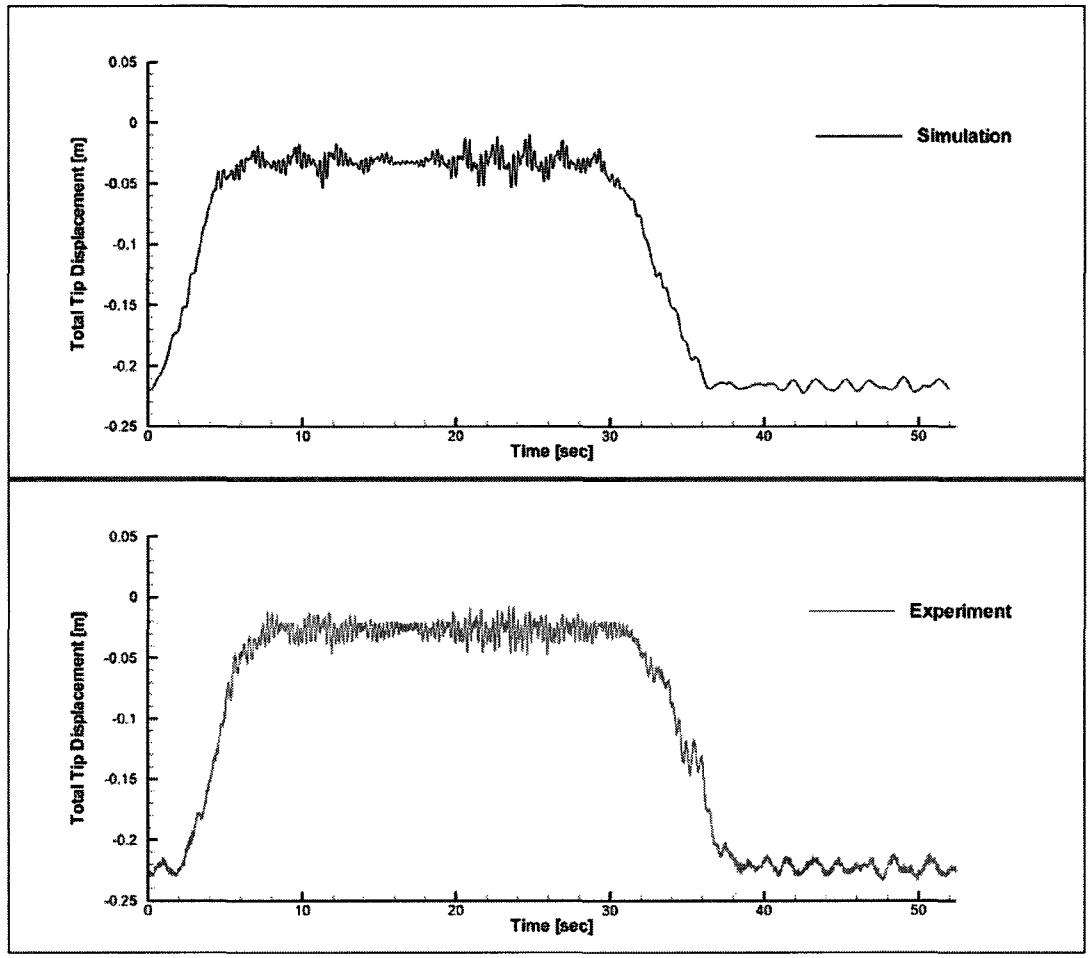

Figure 8.9: Time history of the tip displacement of Run 1 of sub-phase(II).

runs that were found to exceed the motion platform operation limits. These limits were position/orientation and linear/angular velocity. The proposed experimental runs were reexamined and reduced as a result of these motion limitations. Since these limits were based on the assumption of one degree of freedom motion, simultaneous motion along all six degrees of freedom may pose more stringent limits on accelerations for instance. It was observed that when one of the limits is exceeded the motion platform tends to clip the motion, which might be another source of error. Sample ship motion degrees of freedom and their time rate of change are provided in Appendix G.

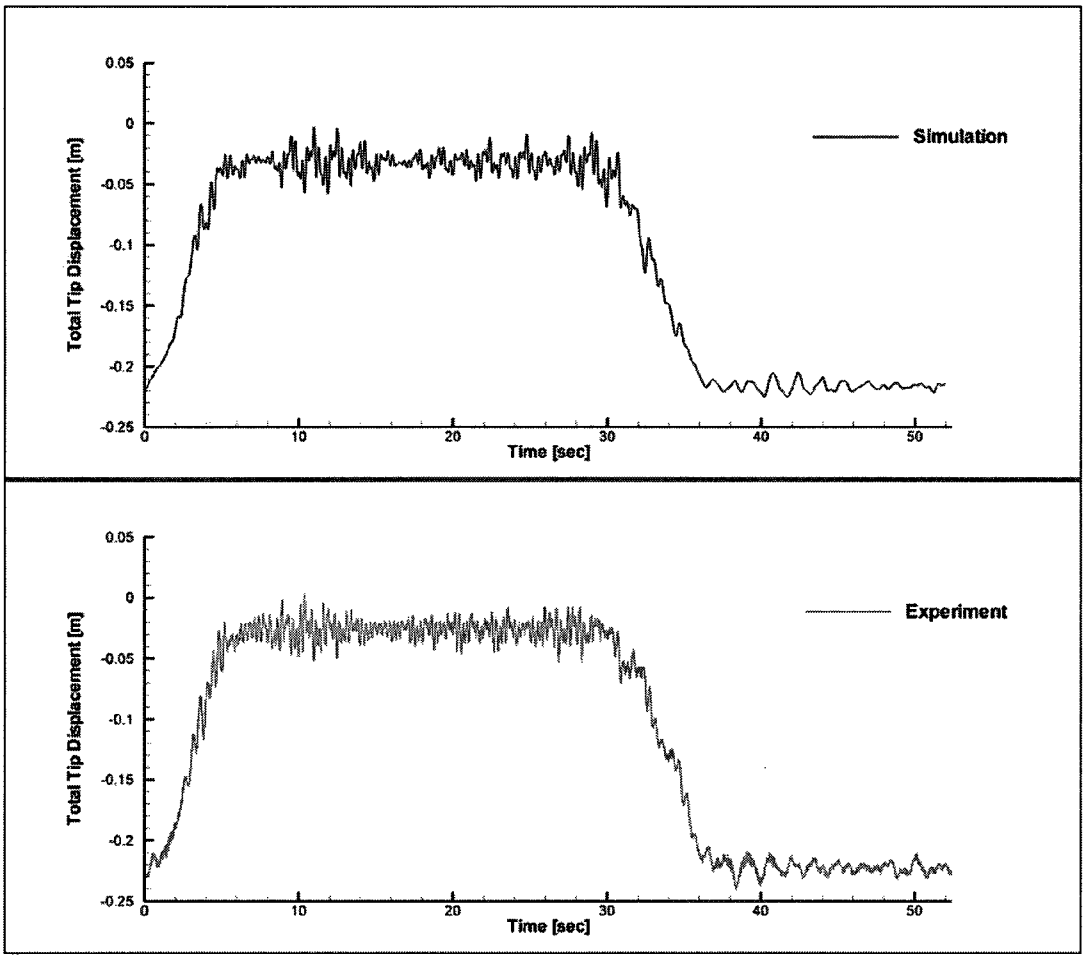

Figure 8.10: Time history of the tip displacement of Run 2 of sub-phase(II).

8.4 Future Recommendations

Examining the effect of ship motion in the presence of ship airwake is the next experimental step beyond this investigation.

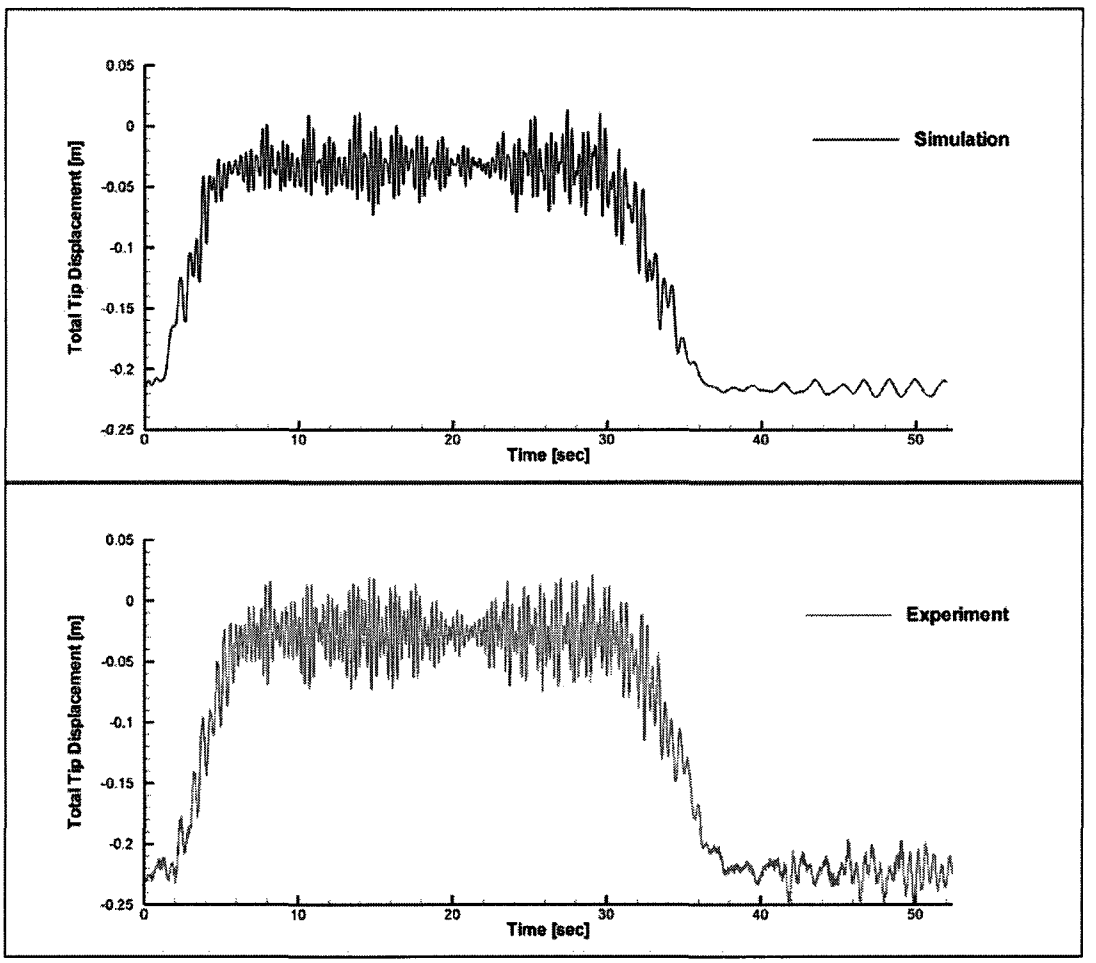

Figure 8.11: Time history of the tip displacement of Run 3 of sub-phase(II).

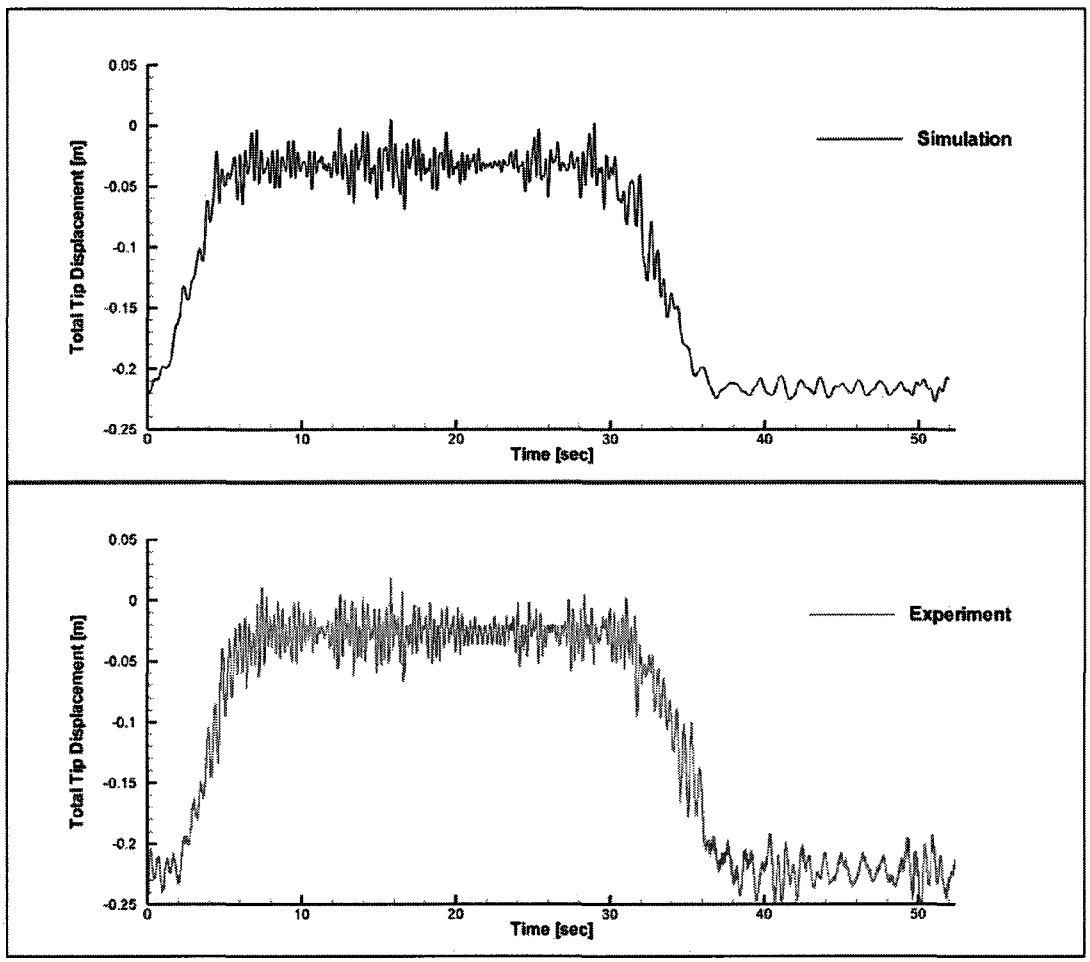

Figure 8.12: Time history of the tip displacement of Run 4 of sub-phase(II).

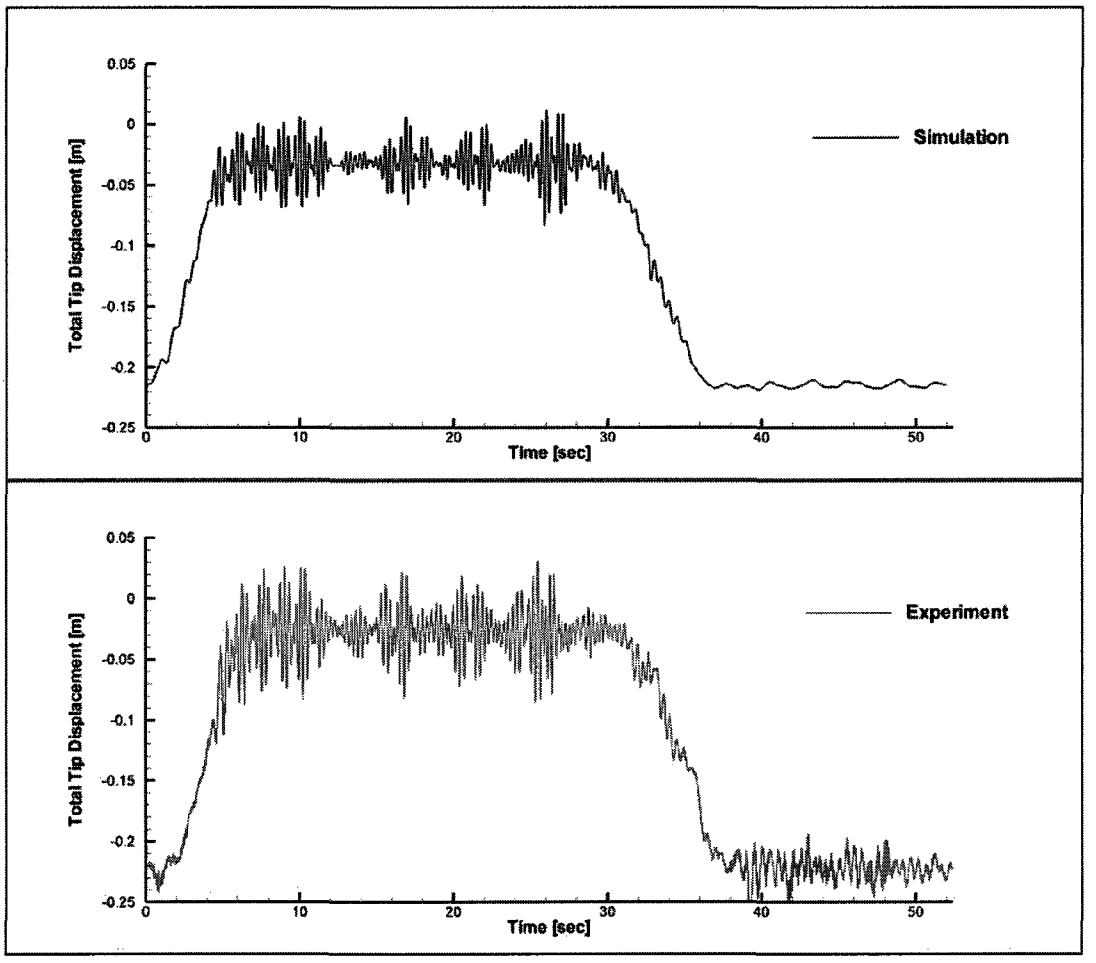

Figure 8.13: Time history of the tip displacement of Run 5 of sub-phase(II).

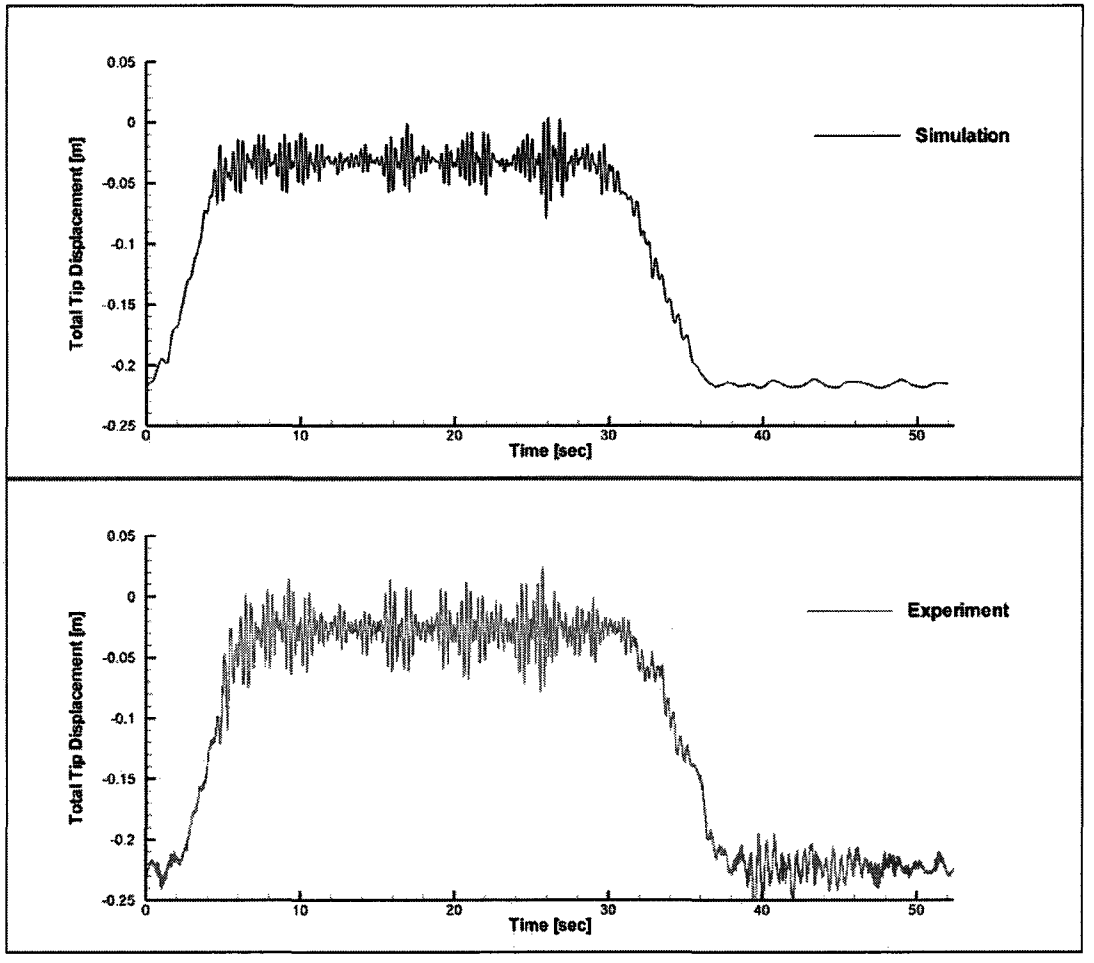

Figure 8.14: Time history of the tip displacement of Run 6 of sub-phase(II).

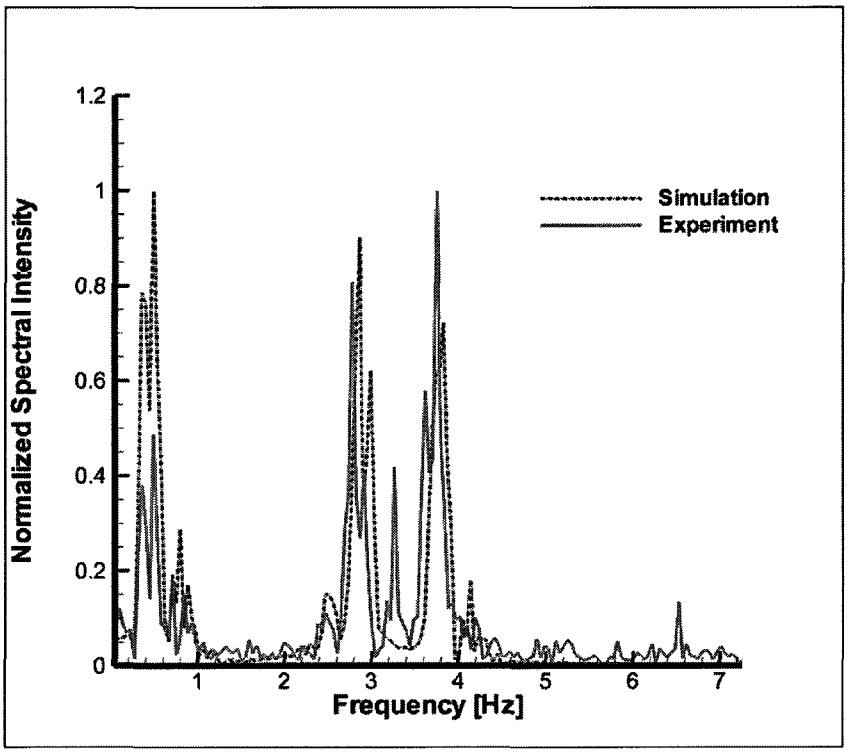

Figure 8.15: Spectrum of the tip displacement during steady-state for Run 1 of sub-phase(II).

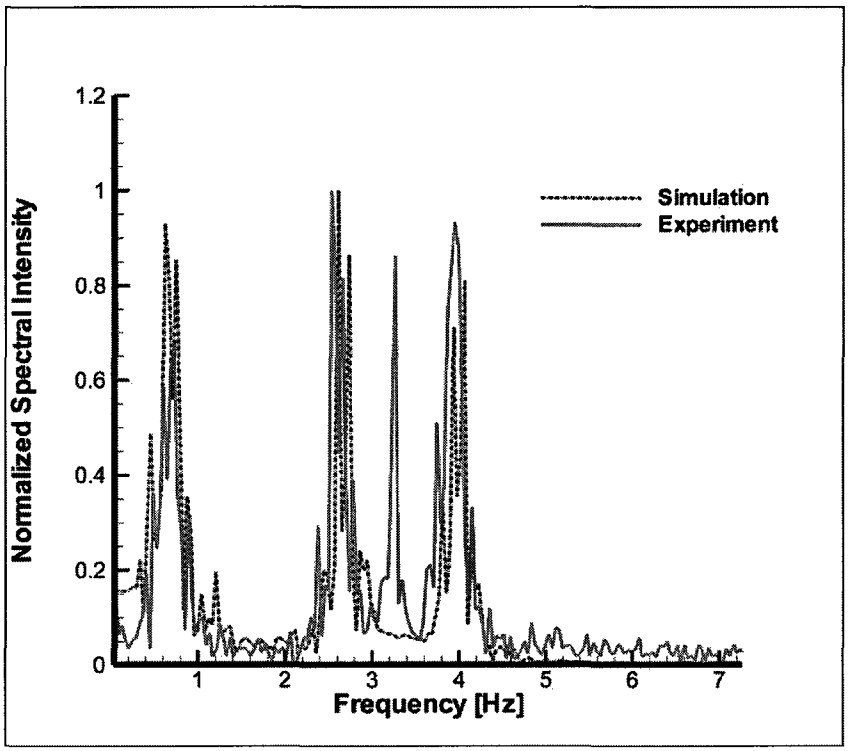

Figure 8.16: Spectrum of the tip displacement during steady-state for Run 2 of sub-phase(II).

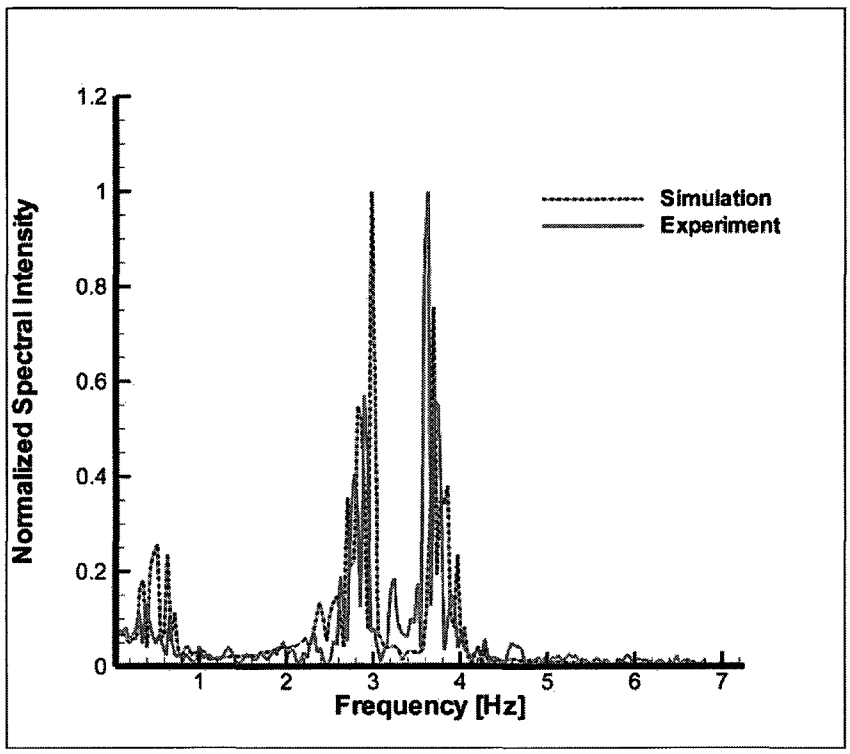

Figure 8.17: Spectrum of the tip displacement during steady-state for Run 3 of sub-phase(II).

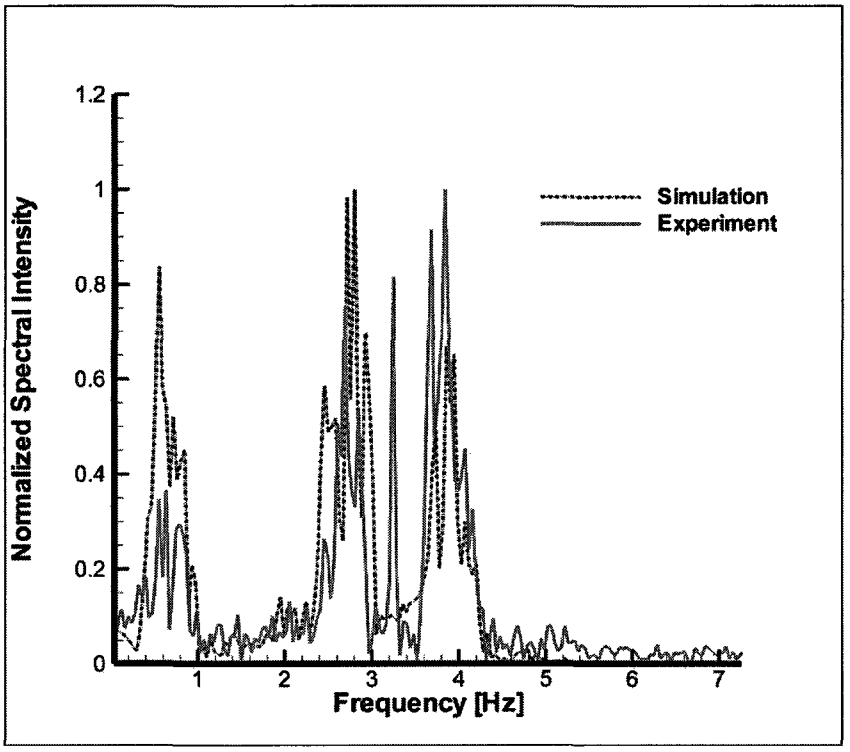

Figure 8.18: Spectrum of the tip displacement during steady-state for Run 4 of sub-phase(II).

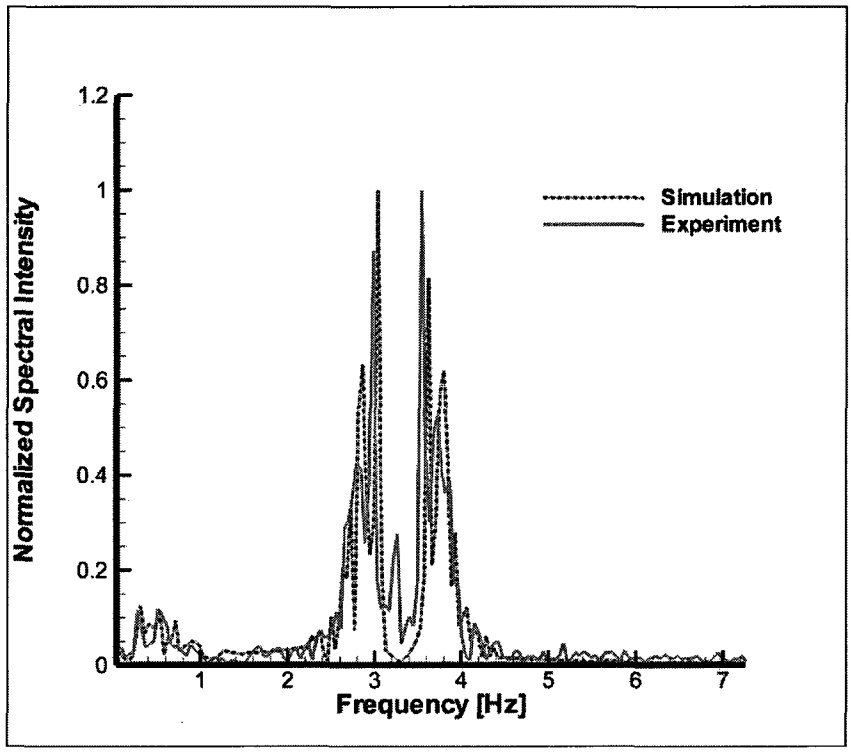

Figure 8.19: Spectrum of the tip displacement during steady-state for Run 5 of sub-phase(II).

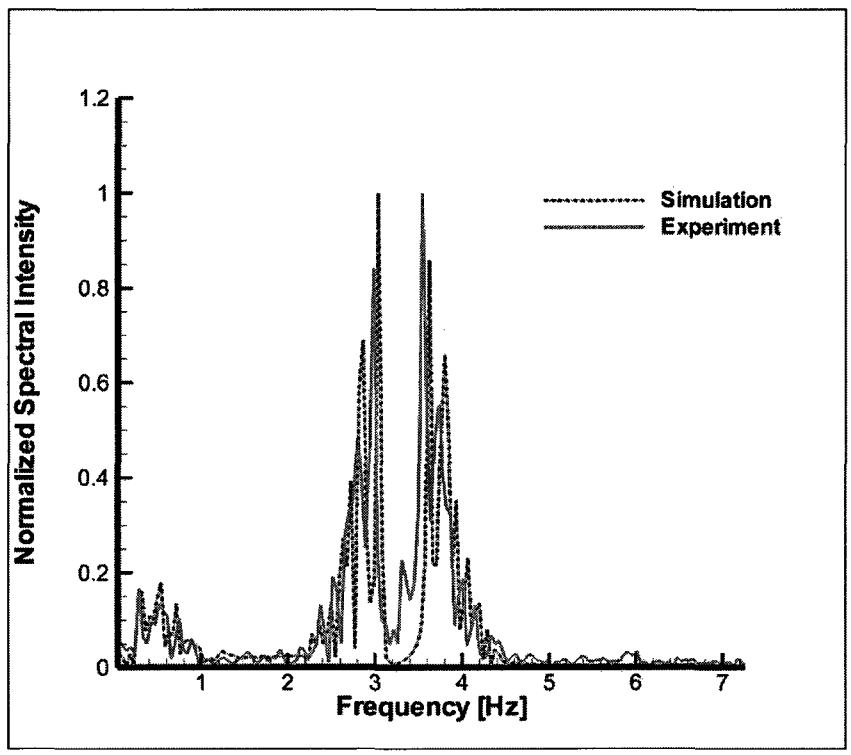

Figure 8.20: Spectrum of the tip displacement during steady-state for Run 6 of sub-phase(II).

Chapter 9

Feasibility Study of Open-Loop Integral Active Twist Actuation Strategies for Countering the Blade Sailing Phenomenon

9.1 Overview of Chapter 9

A $1/6^{th}$ Mach-scaled integral active twist rotor is adopted, modified, and modelled to examine the potential of the IAT concept in eliminating/reducing the negative impact of the BSP. The susceptibility of the rotor system to the BSP is first established followed by investigation of a static active twist strategy that is shown to reduce downward deflections while increasing the upward ones. A more advanced dynamic actuation strategy based on the structure of the ship airwake and the hub angular velocity profile is proposed and shown to remarkably reduce the downward and the upward tip deflections. The validity of the proposed strategy is also proven when representative ship motion coupled with

appropriately modified experimental and deterministic airwake models is present. Finally, the validity of the proposed strategy is proven when the perfectly-correlated turbulence model, a worst case scenario, is imposed on the steady airwake for various deck roll angles.

9.2 The $1/6^{th}$ Mach-scaled Integral Active Twist CH-47D Rotor

The BSP is well documented for the H-46 rotor system, particularly its susceptibility to tunnel strikes [28] as mentioned in Chapter 1. The H-46 uses a fully articulated rotor system as seen in Fig. 9.1. For the purpose of considering practical active rotor control, it is essential to adopt a representative rotor system with the IAT concept already taken into account in its design.

Figure 9.1: Close up of H-46 Sea King on USS Midway.

The Integral Active Twist Rotor (IATR) shown in Fig. 9.2 fulfills this role. The IATR active blade is a $1/6^{th}$ Mach-scaled CH-47D helicopter rotor system used by the air force, which is similar to the H-46 system used by the marines, that was an early joint research effort between the Boeing Company and the Massachusetts Institute of Technology (MIT) that was built and tested in a wind tunnel to investigate noise and vibration reduction in hover flight [168, 169]. More specifically, the purpose of the latter investigation was to

prove the concept of Individual Blade Control (IBC) to reduce the N/rev, $(N-1)$/rev, and $(N+1)$/rev harmonics of the rotor system where N is the number of blades. The IATR rotor system is adopted in this work to examine the feasibility of IBC to reduce the BSP, which contrasts markedly with the original purpose of the system which was reducing noise and vibration.

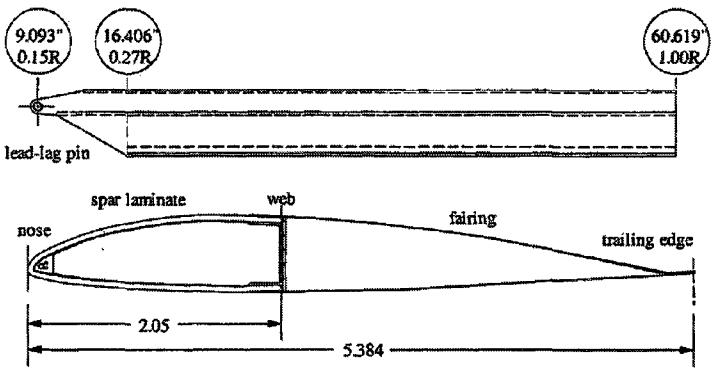

Figure 9.2: Cross-section and top view of the IATR [all dimensions are in inches].

The second reason for adopting this early generation of integral active twist blade is the relative availability of design data when compared to modern active rotor blades that are being built or still in their design phase like the Active Low Vibration Rotor (ALVR) [107], the Advanced Active Twist Rotor (AATR) [170], or the Active Twist Blade (ATB) [171], where most of the design specifications are considered classified and/or proprietary. Finally, it was demonstrated by Friedmann [165] that while rotary-wing aeroelastic scaling requirements can be partially satisfied by either Mach-scaled or Froude-scaled rotors, Mach-scaled rotors have to be used to obtain correct actuation requirements for actively controlled blades. Based on this, it is qualitatively apparent that the IATR is an ideal design candidate to be adopted for this research.

9.2.1 Design Parameters

The design parameters of the IATR that are relevant to the modelling required for this research are highlighted and discussed in the following.

The laminate design of the cross-section is given in Table 9.1 along with the cross-sectional geometry in metric units. The following abbreviations are used in the table: E indicates E-glass fabric, S indicates S-glass tape, I indicates IM7 carbon-fibres tape, and AF indicates PZT5A AFCs (or MFCs). The elastic and the electromechanical properties of the plies are given in Table 9.2.

Table 9.1: Laminate design and cross-sectional geometry of the IATR from Reference [168].

	Laminate Design	**Length [m]**
spar region	[0°I/45°E/45°AF/-45°E/-45°AF/0°S/45°AF/45°E]	0.0521
fairing region	[45°E]	0.1369
web	$[(45°E)_3]$	

Table 9.2: Elastic and electromechanical properties of the IATR plies.

	E-glass	**S-glass**	**Graphite IM7**	**AFCs PZT5A**	**MFCs** [172]
$\mathbf{E_{11}}$[GPa]	19.300	43.400	165.000	30.180	30.180
$\mathbf{E_{22}}$[GPa]	19.300	12.000	8.300	14.910	14.910
$\mathbf{G_{12}}$[GPa]	4.100	3.600	4.900	5.130	5.130
$\mathbf{G_{23}}$[GPa]	3.280	3.600	4.900	4.050	4.050
ν_{12}	0.148	0.280	0.340	0.454	0.454
ν_{23}	0.148	0.280	0.340	0.408	0.408
thickness[m]	0.118E-3	0.225E-3	0.138E-3	0.165E-3	0.165E-3
$\mathbf{d_{111}}$[m/V]	∅	∅	∅	350E-12	460E-12
$\mathbf{d_{112}}$[m/V]	∅	∅	∅	0	0
$\mathbf{d_{122}}$[m/V]	∅	∅	∅	-150E-12	-210E-12
$\mathbf{t_{electrodes}}$[m]	∅	∅	∅	1.140E-3	1.140E-3
ρ [kg/m^3]	1700	1850	1550	4060	4060

The IATR is a fully-articulated rotor system with separate flap and lead-lag rigid links that extend from the 0.15R point shown in Fig. 9.3 to the the centre of the hub. The links are assumed to be cylindrical in shape, uniform, and similar. Their inertial properties are

deduced based on the $1/6^{th}$ Mach-scaled data of the actual H-46 helicopter rotor blade [173] and they are summarized in Table 9.3.

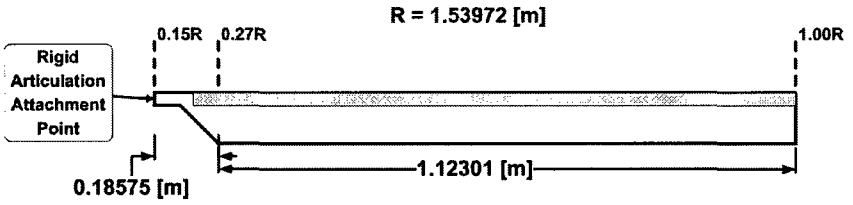

Figure 9.3: Top view of the elastic portion of the adopted IATR blade.

Table 9.3: Inertial and geometric properties of the articulation links of the IATR.

	Flap Link	**Lead-Lag Link**
Length[m]	0.1155	0.1155
Radius[m]	0.0231	0.0231
Mass[kg]	0.4584	0.4584

The lead-lag damper of the H-46 blade is 3500 [ft·lb·s], which was Mach-scaled below for illustration purposes

$$3500[\text{lb}\cdot\text{ft}\cdot\text{s}] \underbrace{\rightarrow}_{\frac{1}{6}\times\frac{1}{6}\times\frac{1}{6}} 16[\text{lb}\cdot\text{ft}\cdot\text{s}] \equiv 22[\text{N}\cdot\text{m}\cdot\text{s}] \tag{9.1}$$

The Mach-scaled engagement/disengagement parameters based on the operation parameters of the H-46 helicopter [173] are given in Table 9.4.

9.2.2 Design Modifications

Some design modifications to the IATR were adopted in order to update its design relative to advanced active blades or due to the unavailability of the data in the literature. In essence, the rotor system used in this analysis is not exactly the $1/6^{th}$ Mach-scaled rotor. However, its parameters are not likely significantly different. These design modification are summarized below:

Table 9.4: $1/6^{th}$ Mach-scaled operation parameters of the adopted IATR.

Parameter	Value
Blade Droop/Flap Stops Setting [deg]/[rad]	$\mp 1/0.0175$
Blade Lead/Lag Stops Setting [deg]/[rad]	$\pm 12/0.2094$
Linear Stiffness of the Blade Limiters [N/m]	10^7
Lead-Lag/Flap Hinge Damper [N·m·s]	50
Maximum Angular Speed of Rotor Hub(Ω_{max}) [rev/s]	28.650
Engagement Profile	$\frac{1}{2}\{\cos[\frac{3\pi}{10}(t - t_{engage}) + \pi] + 1\}$
Disengagement Profile	$\frac{1}{2}\{\cos[\frac{3\pi}{10}(t - t_{disengage})] + 1\}$
Engagement/Disengagement Time($t_{engage/disengage}$) [s]	10/3
Blade Limiters Disengage Condition	$\Omega(t) \geq 0.5\Omega_{max}$
Flow Medium Density [kg/m^3]	$\rho_{air} \times 1.28$
Standard Collective Pitch Setting [deg]	3

1. The first major design modification is the shape of the airfoil, where for the original IATR it is the Boeing VR-7, while in this work the NACA0012 is adopted. This is standard for academic purposes, but the main reason is the extensive availability of aerodynamic data and constants for the latter.

2. The effective linear initial twist of the blade is within the limits reported for the H-46, which is $-8.50°$, whilst for the IATR it is $-12°$. In this work it is taken to be $-10°$, which is similar to the AATR. Fig 9.4 depicts the linear initial twist of the elastic portion of the blade.

3. The lead-lag dampers of modern rotor blades are more powerful, therefore a lead-lag damper of 50 [N·m·s] is adopted, which is roughly double that of the H-46 helicopter damper in 1977.

4. In some instances, elastic material properties that were used to manufacture the rotor blade had to be estimated based on the best sources in the engineering literature.

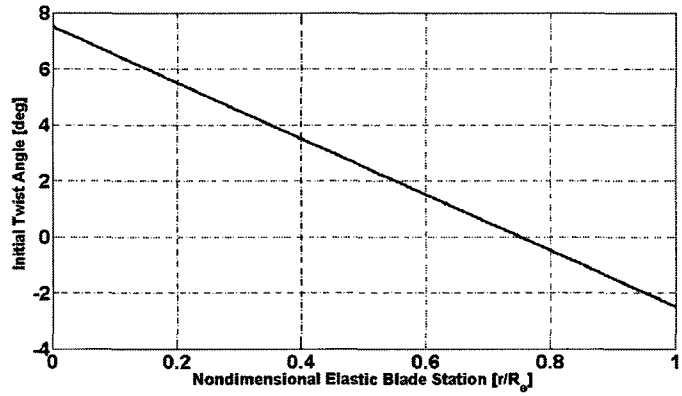

Figure 9.4: Linear initial twist of the IATR.

9.2.3 Cross-Sectional Analysis

Performing a cross-sectional analysis of the adopted IATR with the design modifications listed above as shown in Fig. 9.5, yielded the 4×4 stiffness matrix, the cross-sectional inertial properties, and the actuation vectors for AFCs and MFCs actuation with an applied voltage of ±2000 [V] for the ∓45° active plies such that

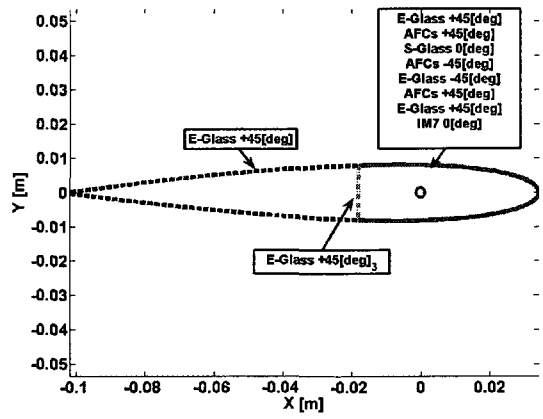

Figure 9.5: Cross-section of the modified IATR.

$$\bar{S} = \begin{bmatrix} 5.1734 \times 10^6[\mathrm{N}] & -31.0039[\mathrm{N}\cdot\mathrm{m}] & -0.2288[\mathrm{N}\cdot\mathrm{m}] & -0.2841 \times 10^5[\mathrm{N}\cdot\mathrm{m}] \\ -31.0039 & 21.0032[\mathrm{N}\cdot\mathrm{m}^2] & 0[\mathrm{N}\cdot\mathrm{m}^2] & 0.2802[\mathrm{N}\cdot\mathrm{m}^2] \\ -0.2288 & 0 & 245.17193[\mathrm{N}\cdot\mathrm{m}^2] & 0.0017[\mathrm{N}\cdot\mathrm{m}^2] \\ -0.0284 \times 10^6 & 0.2802 & 0.0017 & 0.2593 \times 10^4[\mathrm{N}\cdot\mathrm{m}^2] \end{bmatrix} \tag{9.2}$$

$$\mathbb{F}^{(\mathrm{a})}_{\mathrm{AFCs}} = \begin{bmatrix} 71.2349[\mathrm{N}] \\ -0.3700[\mathrm{N}\cdot\mathrm{m}] \\ -0.0002[\mathrm{N}\cdot\mathrm{m}] \\ -0.6242[\mathrm{N}\cdot\mathrm{m}] \end{bmatrix} \qquad \mathbb{F}^{(\mathrm{a})}_{\mathrm{MFCs}} = \begin{bmatrix} 81.1139[\mathrm{N}] \\ -0.4905[\mathrm{N}\cdot\mathrm{m}] \\ -0.0019[\mathrm{N}\cdot\mathrm{m}] \\ -0.7093[\mathrm{N}\cdot\mathrm{m}] \end{bmatrix} \tag{9.3}$$

$$\mathcal{I} = \begin{bmatrix} i_2 + i_3[\mathrm{kg}\cdot\mathrm{m}] & 0 & 0 \\ 0 & i_2[\mathrm{kg}\cdot\mathrm{m}] & i_{23}[\mathrm{kg}\cdot\mathrm{m}] \\ 0 & i_{32}[\mathrm{kg}\cdot\mathrm{m}] & i_3[\mathrm{kg}\cdot\mathrm{m}] \end{bmatrix} = \begin{bmatrix} 0.2769 & 0 & 0 \\ 0 & 0.0184 & 0 \\ 0 & 0 & 0.2585 \end{bmatrix} \times 10^{-3} \tag{9.4}$$

$$m[\mathrm{kg/m}] = 0.3969 \tag{9.5}$$

$$\bar{m}_c = \begin{bmatrix} \bar{m}_{c_x}[m] & \bar{m}_{c_y}[m] \end{bmatrix} = \begin{bmatrix} 0.0025 & 0 \end{bmatrix} \tag{9.6}$$

where $\mathcal{I}$ is the cross-sectional inertia tensor , m is the sectional mass per unit length, and $\bar{m}_c$ is the location of the mass centre relative to the beam reference line, which is taken to be the quarter chord point.

The sectional constants are within the expected range of values established based on the experimentally-reported ones [168]. Differences can be attributed to the cross-sectional

geometry, the selected beam reference line, and the incapability of the present analysis to include further cross-sectional details like the metallic nose cap and the metallic honeycomb/foam core filling, which add additional features to the rotor blade such as resistance to lightning strikes.

9.2.4 Simulation Model Setup

The active flexible multibody system is set up with the design parameters given above, and it is shown is Fig. 9.6.

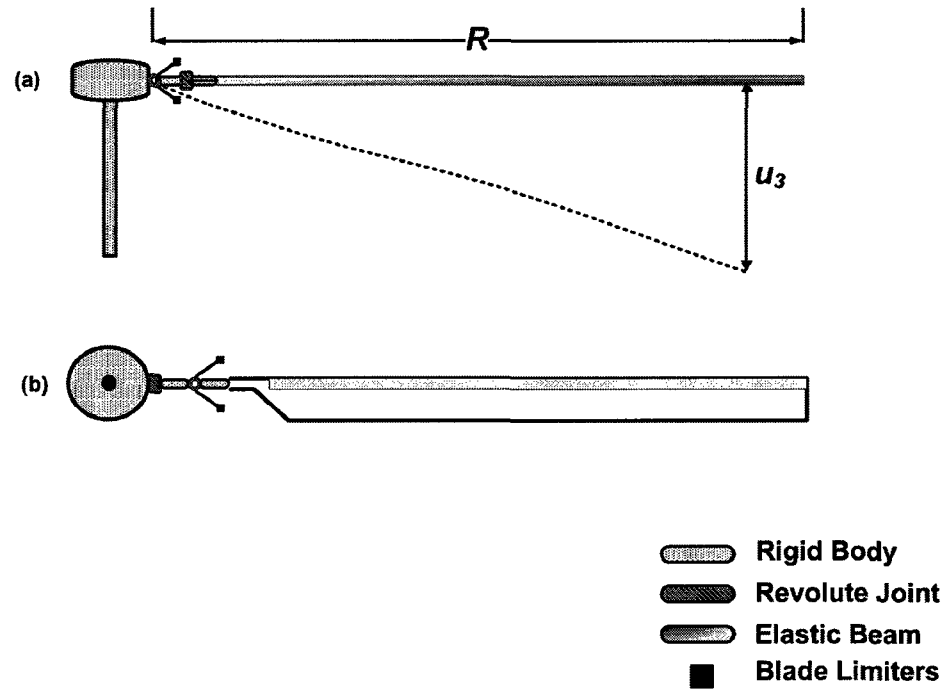

Figure 9.6: (a) Side view of the generic IATR system, (b) Top view of the generic IATR system.

The cutoff region in Fig. 9.3 that is between 0.27R and 0.15R is assigned one and a half times the stiffness and the inertial properties of the elastic blade, which is approximately in agreement with the H-46 blade reference data [173]. A convergence study is performed to determine a suitable number of beam elements to discretize the elastic blade. The cutoff region is always modelled as one beam element while a variable number of elements is

used for the rest of the blade. The blade is cantilevered and the tip transverse deflection is obtained through simulations under the assumption of a gravitational field in vacuum. Since the problem has no analytical solution, the solution with 41 beam elements is taken as the reference solution and the percentage change versus the number of beam elements is shown in Fig. 9.7

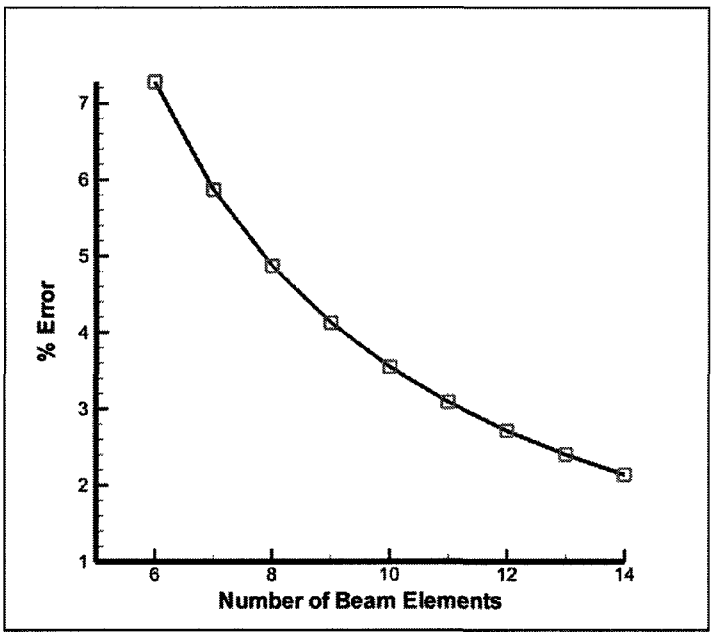

Figure 9.7: Percentage error of the tip deflection relative to the reference solution of the cantilevered generic IATR in the gravitational field versus number of beam elements.

Based on Fig. 9.7 and computational speed considerations, eleven beam elements were determined to be suitable for the simulation of the engagement and the disengagement of the generic IATR. Also, the simulation CPU time of the IATR engagement/disengagement depends on the size of the time step used. The Intel Core 2 Duo Processor CPU time for the engagement/disengagement of the IATR using the number of beam elements selected above is shown in Fig. 9.8 for three different time stepping techniques. The adaptive technique, which refines the time step when impact with the blade stops/limiters is anticipated, is used in subsequent investigations.

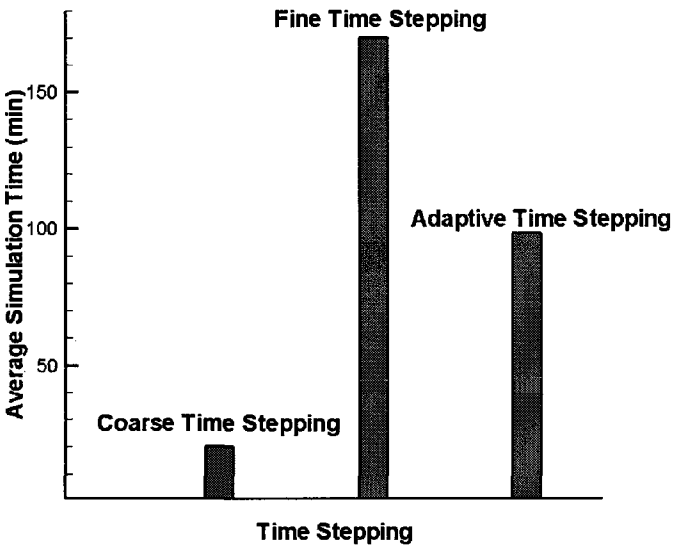

Figure 9.8: Comparison of simulation CPU time using three different time stepping strategies.

9.2.5 Relevant Dynamic Active Twist Study

In anticipation of applying the IAT concept for a certain range of frequencies at a varying rotor speed to counter the BSP, a limited system identification study was conducted for the rotor system at the hub rotational speeds shown in Table 9.5, where the frequency of the first fundamental flap mode is shown as well. As mentioned previously, the BSP has been known to be most severe in the neighborhood of $20\%\Omega_{max}$.

Table 9.5: Selected rotor speeds for system identification study and the first flap fundamental.

Rotor Speed $\%\Omega_{max}$	Hub Frequency [Hz]	First Flap Frequency [Hz]
0	0	8.898
10	2.865	9.398
20	5.730	10.900

The rotor dynamic actuation response is examined for the regimes of interest in this research. The rotor with MFCs actuator packs is subjected to the following actuation voltage signal

$$V(t) = \frac{2000}{N}\left(\sum_{i=0}^{N}\sin(2\pi f_i t)\right) \quad [\text{V}] \quad \text{where} \quad N = 10, \{f_i = [0 \rightarrow 10] \mid f_i \in \mathbb{I}\} \qquad (9.7)$$

where N is the number of discrete frequencies comprising the signal, and f_i is the i^{th} frequency of the signal.

The time-domain tip twist response at the first hub frequency in Table 9.5 is shown in Fig. 9.9 and the frequency-domain response is shown in Fig. 9.10. Similarly, the frequency-domain system responses at the two remaining frequencies in Table 9.5 are shown in Fig. 9.11 and Fig. 9.12 respectively.

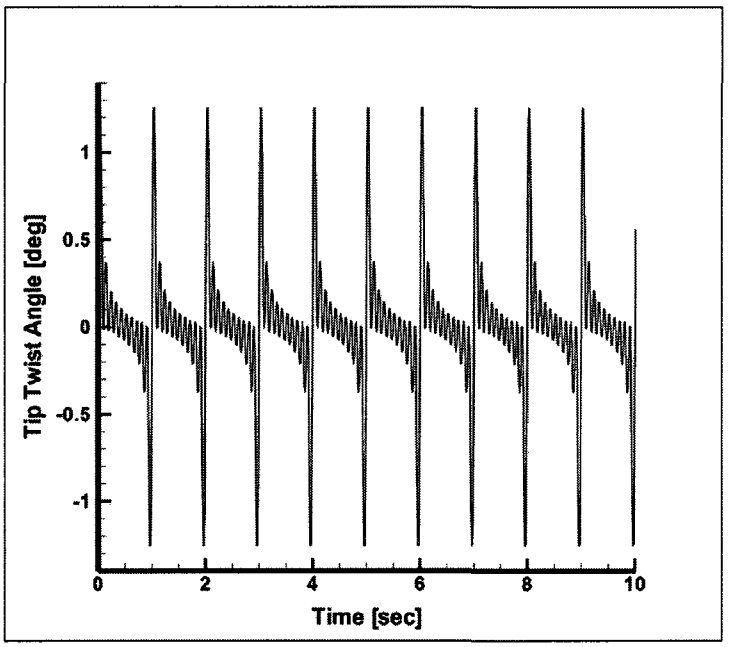

Figure 9.9: Time-domain tip twist response of the active rotor blade subjected to the signal in Eq. 9.7 at 0[Hz] hub frequency.

The time-domain and the frequency domain responses are in accordance with the more extensive theoretical and experimental dynamic actuation system identification studies conducted for other active rotor systems [174, 170] where it was concluded that:

1. The system behaves linearly at a fixed hub frequency (about nonlinear dynamic

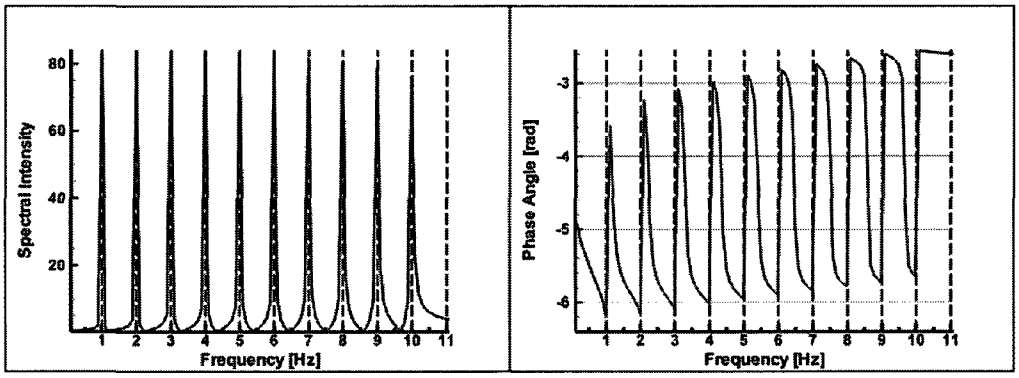

Figure 9.10: Frequency-domain tip twist response of the active rotor blade subjected to the signal in Eq. 9.7 at 0[Hz] hub frequency.

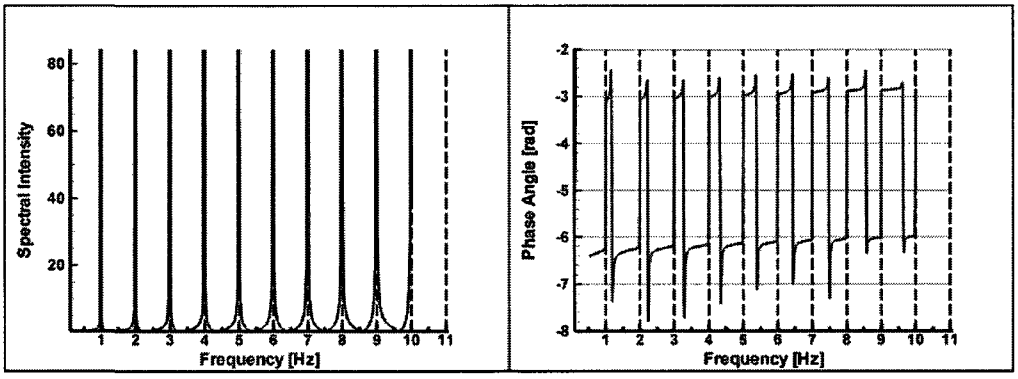

Figure 9.11: Frequency-domain tip twist response of the active rotor blade subjected to the signal in Eq. 9.7 at 2.865[Hz] hub frequency.

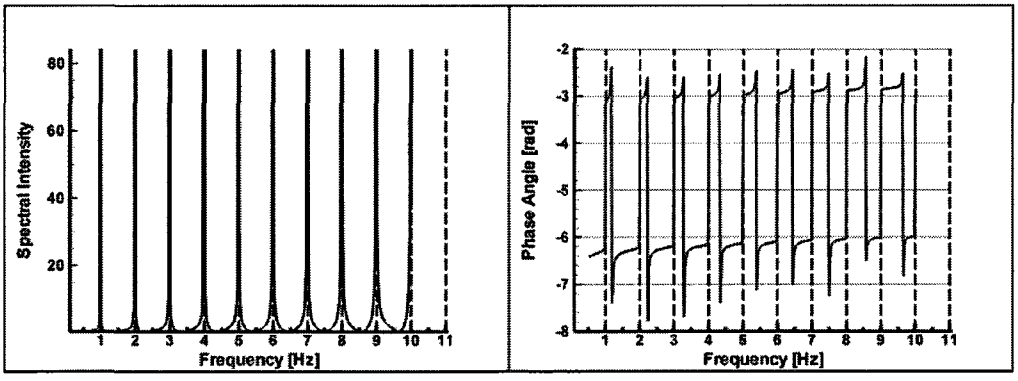

Figure 9.12: Frequency-domain tip twist response of the active rotor blade subjected to the signal in Eq. 9.7 at 5.730[Hz] hub frequency.

equilibrium point).

2. The phase lag between the command signal and tip twist response generally increases with increasing signal frequency.

3. The response is almost independent of the medium density and the collective pitch setting.

4. The response is independent of the initial twist/curvature of the blade.

5. The response is strongly dependent on the blade tip geometry (sweep, taper, and anhedral) [175].

For the targeted application of this research, the dynamic response of the active system is concluded to be acceptable.

9.3 Aeroelastic Response of the IATR During Engagement and Disengagement Operation Using the Linear Deterministic Airwake Model

For the purpose of this investigation, the IATR is engaged and disengaged in the following wind conditions: 35[kn], 45[kn], 55[kn] and 60[kn] for Wind Over the Deck (WOD) at relative angles of 0° to 360° in 15° increments, where the WOD is pictorially defined in Fig. 9.13

The system is first solved to its initial conditions in the gravitational field in the vacuum where it would be resting on the droop stops for the engage state and running at full RPM for the disengage one. The system is then immersed in the airwake modelled using the linear deterministic model discussed previously with a 0.25 gust factor for a period of 3 [sec] before the commencement of the engagement/disegagement operation. The nonlinear quasi-steady aerodynamic model with stall effects corresponding to the

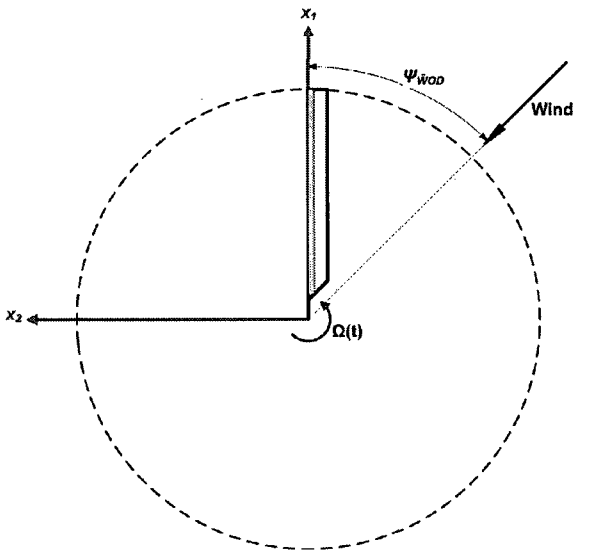

Figure 9.13: Definition of Wind Over the Deck (WOD) angle, ψ_{WOD}.

NACA0012 airfoil is used to calculate the aerodynamic loads. It is highlighted at this stage that the performance of a proposed control loop algorithm is assessed based on the percentage amount of upward and downward blade tip deflections normalized by the total blade length, which is depicted in Fig. 9.6(a) and evaluated as

$$\text{Tip Deflection}_{\text{downward/upward}}[\%R] = \frac{|u_3|}{R} \times 100 \tag{9.8}$$

A time history of the tip displacement, flap hinge angle, lead-lag hinge angle, and the flap link transverse force for the engagement and the disengagement under the wind conditions of 60[kn], 270°WOD; and 45[kn], 60°WOD are shown in Fig. 9.14 and Fig. 9.15 respectively. More time histories for different WODs and wind speeds are shown in Appendix H.

A more comprehensive examination of the engagement and the disengagement of the IATR is presented for the wind speeds of 35[kn], 45[kn], 55[kn], and 60[kn] in 15° WOD increments in Fig. 9.16 and Fig. 9.17 respectively in (Ship-Helicopter-Operation-Limits) SHOLs format.

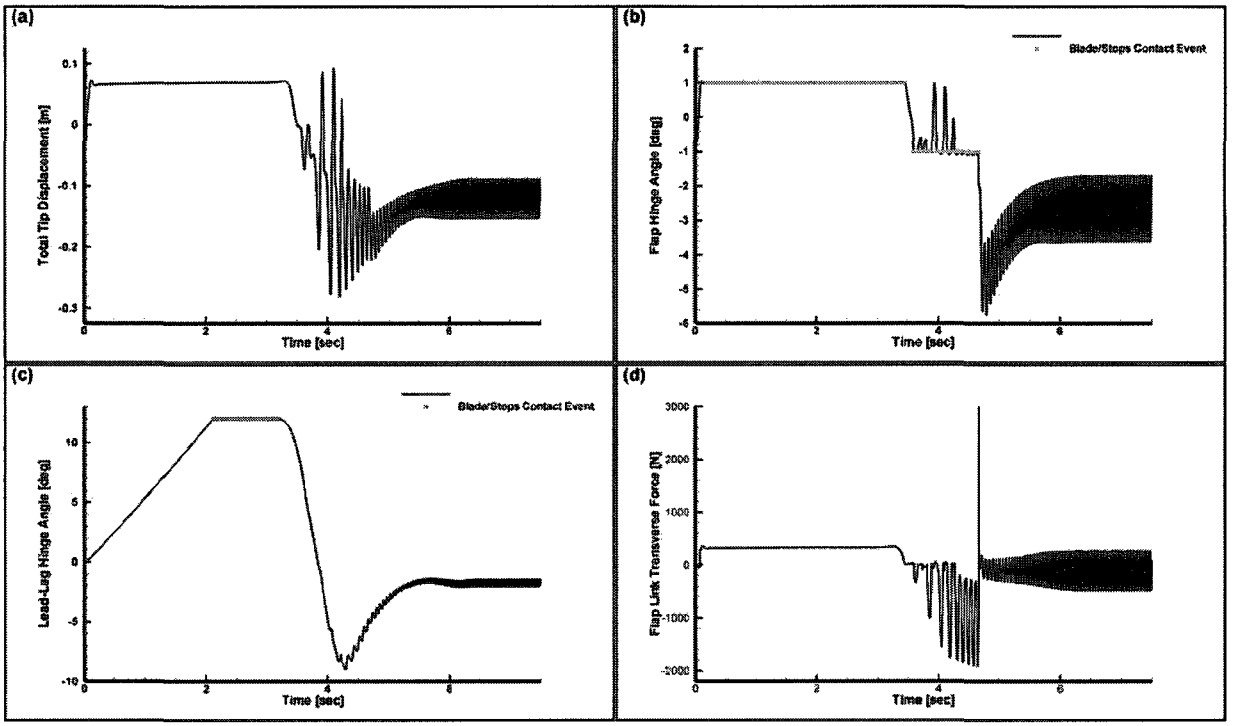

Figure 9.14: Time history of the adopted IATR engagement under the wind conditions of 60[kn], 270°WOD for:(a) Total tip displacement, (b) Flap hinge angle, (c) Lead-lag hinge angle, (d) Flap-link transverse force.

Examination of the tip displacement time history in Fig. 9.14(a) demonstrates the BSP during the early stages of the engagement, where significant downward tip deflections are registered. After approximately 3 seconds from the start of the engagement, the centripetal stiffening of the blade is sufficiently high to prevent any excessive downward tip deflection. The flap link starts the engagement in contact with the flap stop as seen in Fig. 9.14(b) and subsequent droop stop strikes are observed that are associated with the BSP before the stops are retracted at 50% Ω_{max}. The effect of the BSP on the forces transmitted to the hub components are observed in Fig. 9.14(d) where significant forces are observed in the flap link during the early stages of the engagement that later subside when the rotor steady state angular speed is reached. The transverse force delta function-like behaviour seen around 5 seconds on the time axis is due to the sudden retraction of the blade limiters, which is modelled in the simulation using a logical switch. In reality, the retraction

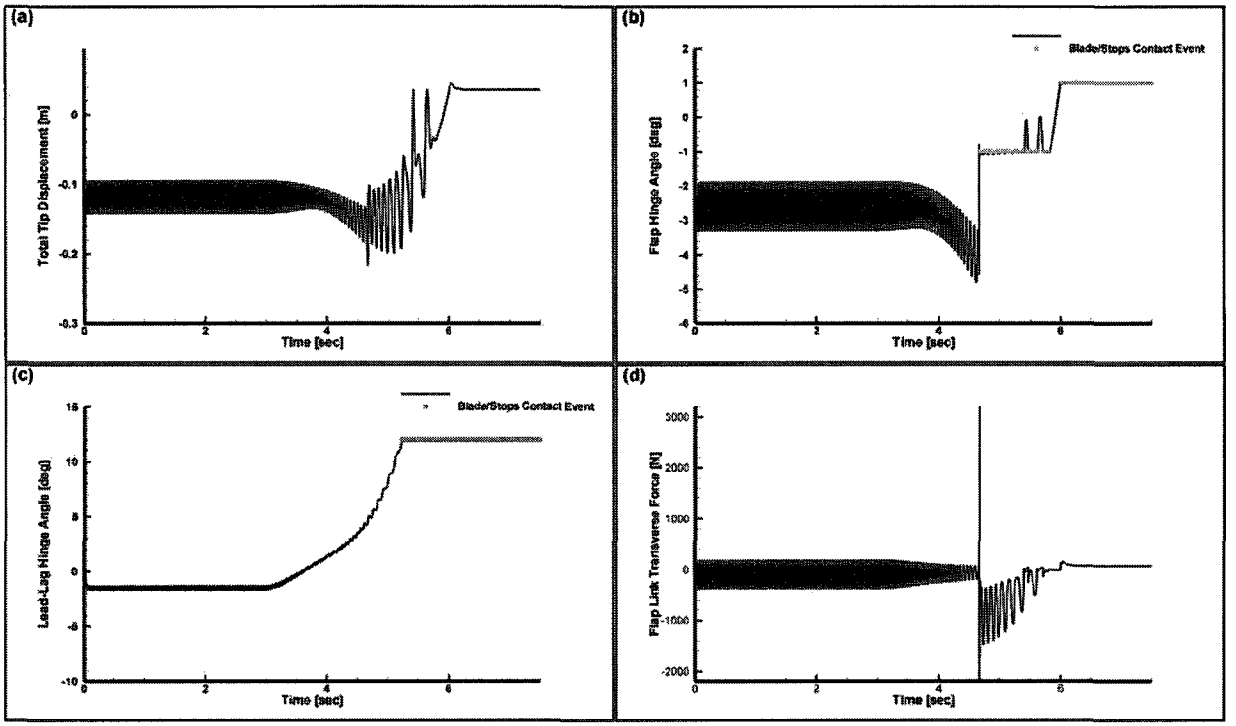

Figure 9.15: Time history of the adopted IATR disengagement under the wind conditions of 45[kn], 60°WOD for:(a) Total tip displacement, (b) Flap hinge angle, (c) Lead-lag hinge angle, (d) Flap-link transverse force.

is gradual and the spike observed in the simulation would not occur or would not be as severe. Similar conclusions are reached regarding the time histories of the rotor system parameters during disengagement in Fig. 9.15.

The more comprehensive examination of the blade downward/upward tip deflection during rotor engagement as a function of wind speed and WOD in Fig. 9.16, which is presented in SHOLs format, reveals the potential danger of the BSP where H-46 tunnel strikes, which is the tip of the blade striking the fuselage of the helicopter, are precariously approached for the 55[kn] wind speed and certainly do occur for the 60[kn] wind speed case for a band of WOD between 240° and 320° even without ship motion or wind turbulence. It must be noted that Keller [17] appears to be the first to use this convention to illustrate the BSP. The upward tip deflections, while not being as severe as the downward deflections, are also to be reduced in the ideal case to lessen their contribution to the downward ones.

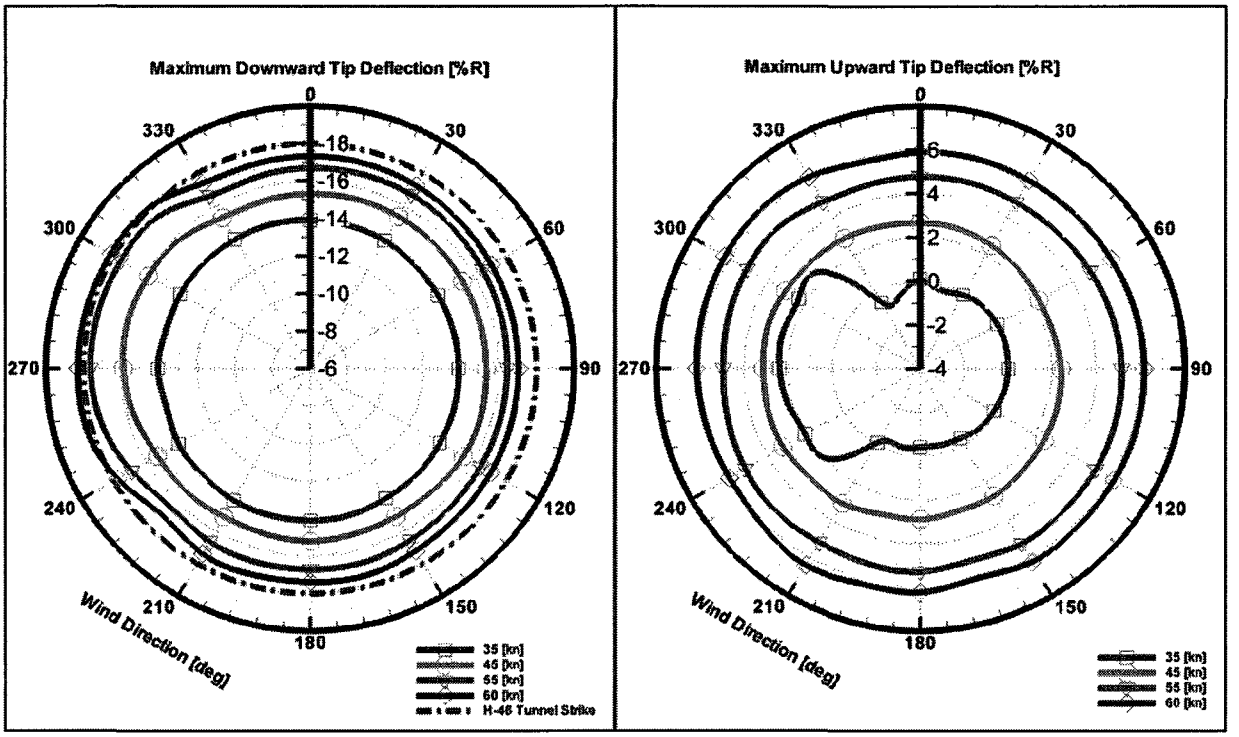

Figure 9.16: Maximum downward and upward tip deflection of the engagement of the adopted IATR.

This difference between the upward and the downward tip deflections was also observed in the rotor system engagement/disengagement study conducted in [29] using DYMORE which contrasts with the significant upward tip deflections reported in [17, 28]. This observation was attributed in [29] to the difference in aerodynamic modelling.

Finally, while the disengagement of the rotor system still exhibits the characteristics of the BSP, the downward tip deflections are not as severe as those observed in the engagement due to the higher angular momentum possessed by the disengaging rotor relative to the engaging one in the neighborhood of the same point on the angular velocity temporal profile.

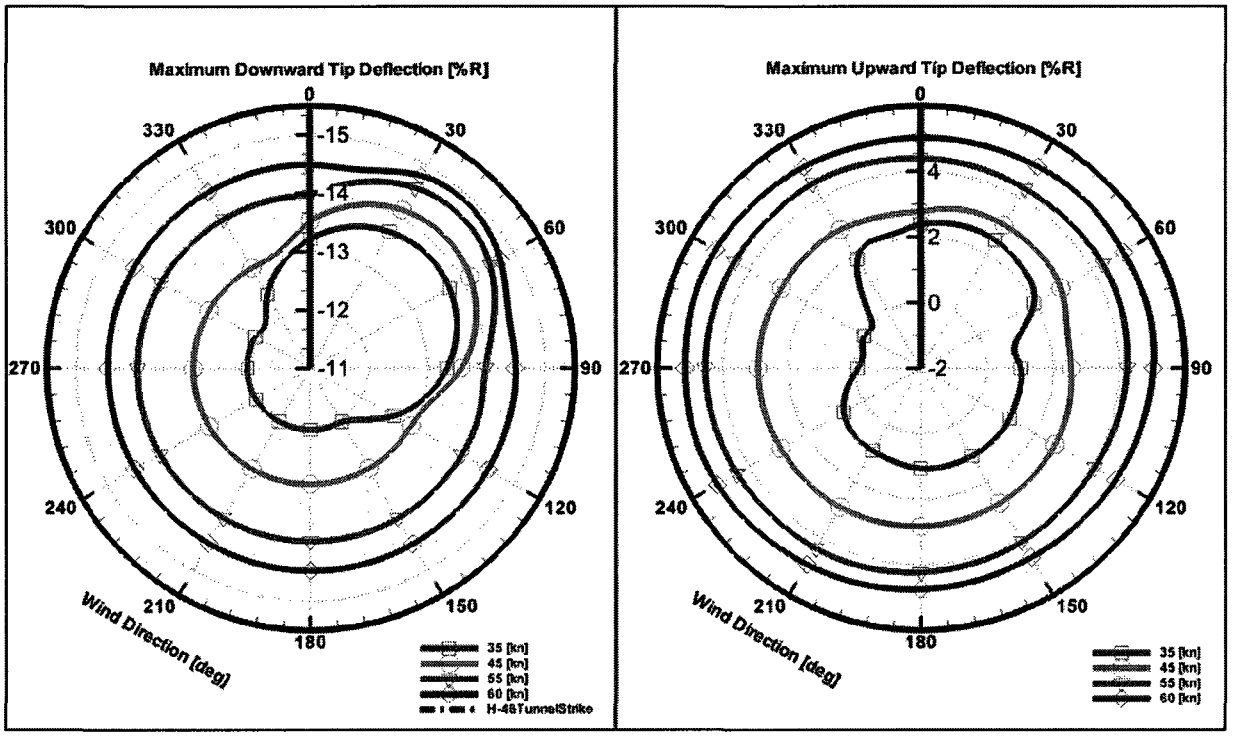

Figure 9.17: Maximum downward and upward tip deflection of the disengagement of the adopted IATR.

9.3.1 Investigation of Two Open-Loop Control Strategies

Static Actuation

The first actuation strategy to be investigated is to twist the blade in a positive sense as to induce enough lift at the outboard stations of the blade (where the induced twist matters the most) to prevent the excessive tip downward deflections. The actuating constant voltage is set for a magnitude of 2000[V], which corresponds to moderate early-generation operational voltages for the IAT concept, and it is activated when the rotor starts the engagement or the disengagement phase. The examination of this strategy was performed for both AFCs and MFCs and the resulting downward and upward tip deflections for the 45[kn] and 60[kn] wind speeds are shown in Fig. 9.18 through Fig. 9.21 for the engagement and the disengagement phase. The results that include additional wind speeds are given

in Appendix H.

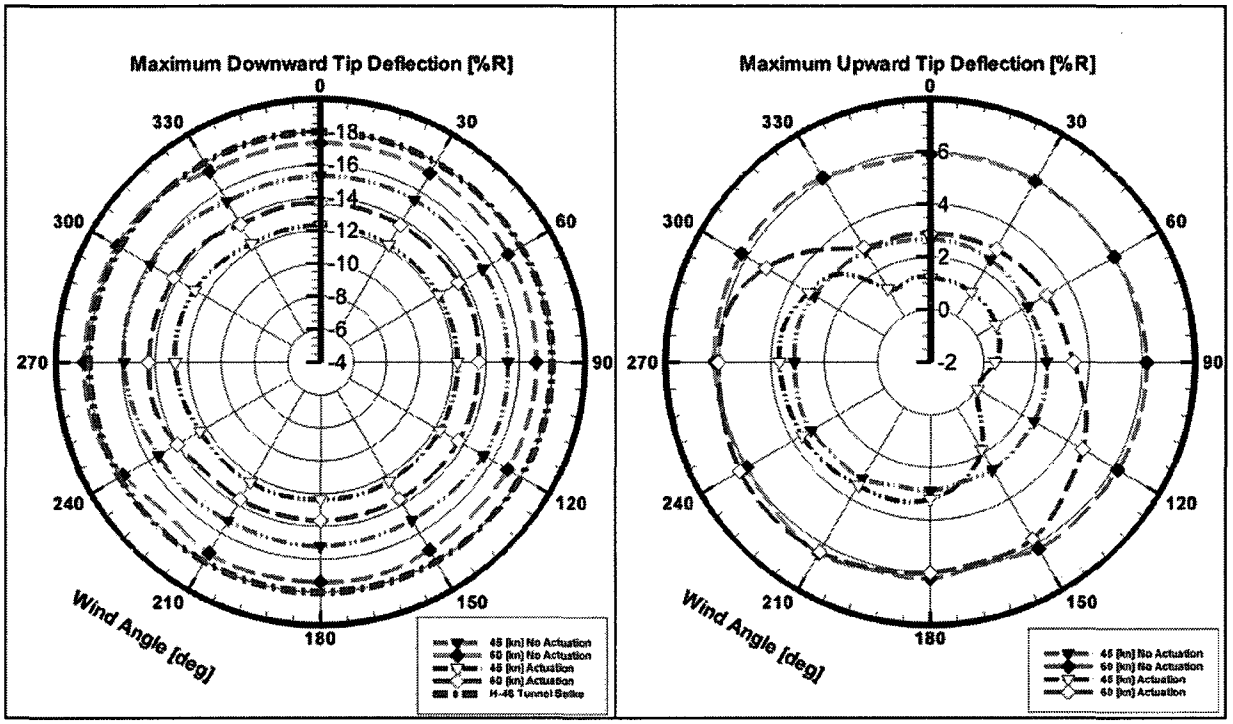

Figure 9.18: Maximum downward and upward tip deflection of the engagement of the adopted IATR with DC actuation of the integrated AFCs.

Investigating the SHOLs in Fig. 9.20 and Fig. 9.21 demonstrates that the proposed strategy reduces the maximum downward tip deflections, where tunnel strikes during engagement are completely avoided even for the moderate operational voltage of the early generation AFCs as can be seen in Figs. 9.18 and 9.19. The downward deflections are reduced by employing MFCs by as much as 28%. While the upward tip deflections are reduced due to the reduction of the downward deflections for some range of WOD angles, they start to appreciably increase for the MFCs actuation between WOD angles of 120° through 300°. This is attributed to the increased lift during the early stages of the engagement, which can be seen in Fig. 9.22 that depicts the time histories of the engagement for the same wind conditions as those in Fig. 9.14 with MFCs static DC actuation.

Similar behaviour is observed for the disengagement where the upward tip deflections

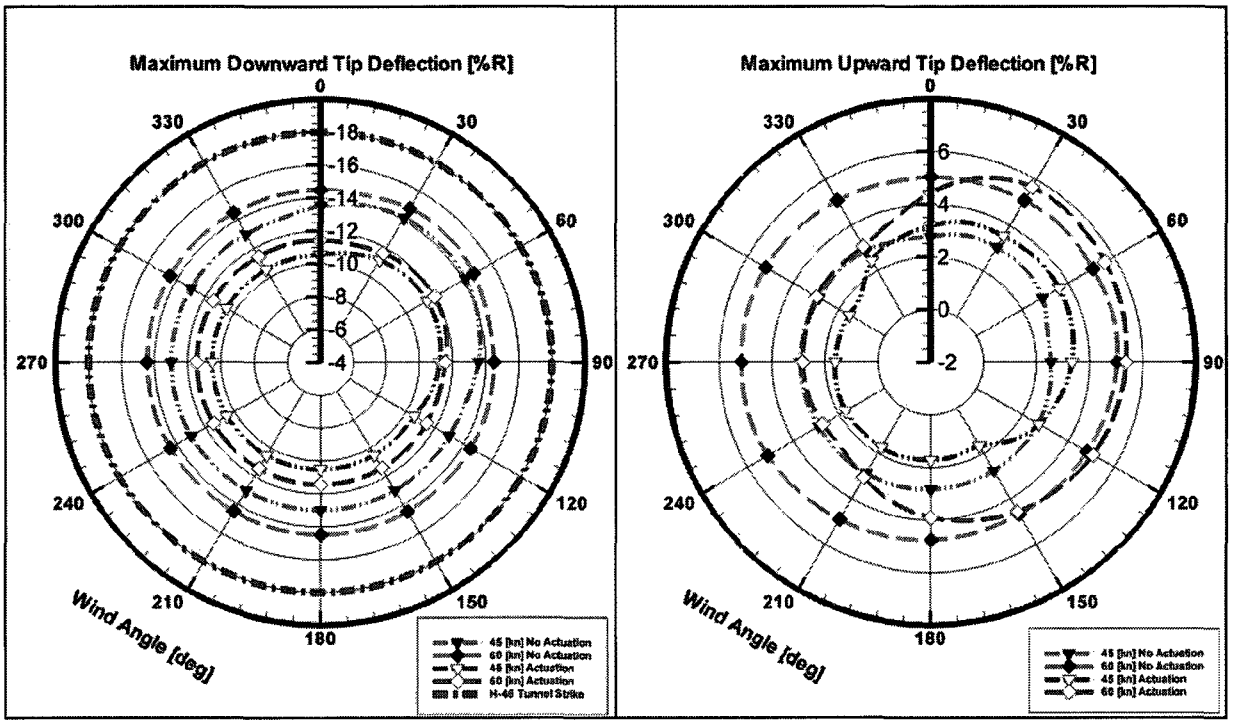

Figure 9.19: Maximum downward and upward tip deflection of the disengagement of the adopted IATR with DC actuation of the integrated AFCs.

are increased between WOD angles of 30° through 120°. This is also attributed to the increased lift in the late stages of the disengagement as well, which is observed in Fig. 9.23 that depicts the time histories of the disengagement for the same wind conditions as those in Fig. 9.15 with MFCs static DC actuation. The reduction in the amplitude of the transverse force transmitted to the flap link is also observed, which reduces the impact of another negative aspect of the BSP in terms of the fatigue of hub components.

Dynamic Actuation

Inducing blade twist according to a predesigned actuation strategy that seeks to vary the amplitude and the polarity of the actuation according to a set of criteria represents the next improvement over the simple static strategy proposed above. Additionally, a dynamic/variable actuation strategy will likely result in reduction of power requirements

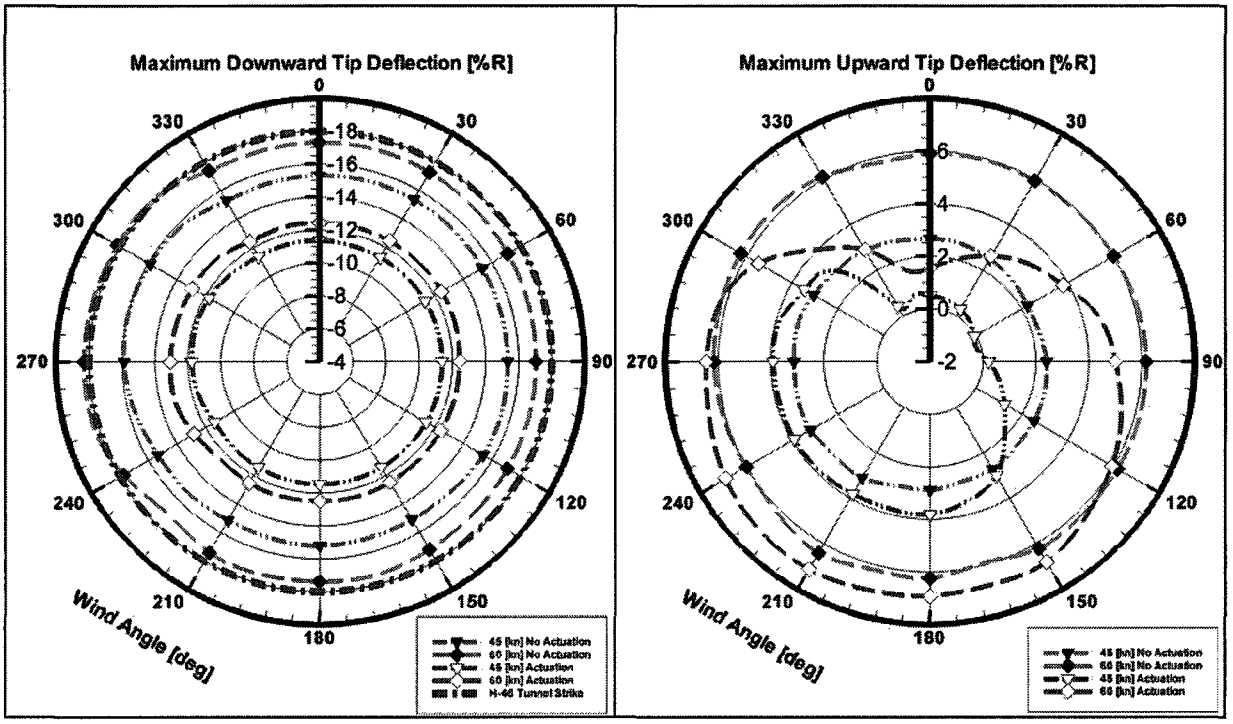

Figure 9.20: Maximum downward and upward tip deflection of the engagement of the adopted IATR with DC actuation of the integrated MFCs.

when compared to the previous strategy. The open-loop control strategy presented herein will be established based on the evolution of the blade angular speed according to the engagement/disengagement profile and its azimuthal orientation relative to the WOD.

Consider Fig. 9.24 that depicts a top view of the rotating blade immersed in the linear deterministic model airwake. According to the form of the linear deterministic model, location (a) will have the maximum upward gust while location (c) will have the maximum downward one. The variable actuation strategy is proposed such that the blade is twisted in a positive sense to increase the aerodynamic lift when the blade root azimuthal orientation is at (c) while the mirror orientation (a) will experience a negative twist as to induce aerodynamic drag. The modified aerodynamic forces at the outboard stations of the blade are of importance due to their high tangential velocity as the blade rotates. The blade integral twist will vanish at (b) and (d) and will vary smoothly between all four orientations. Fur-

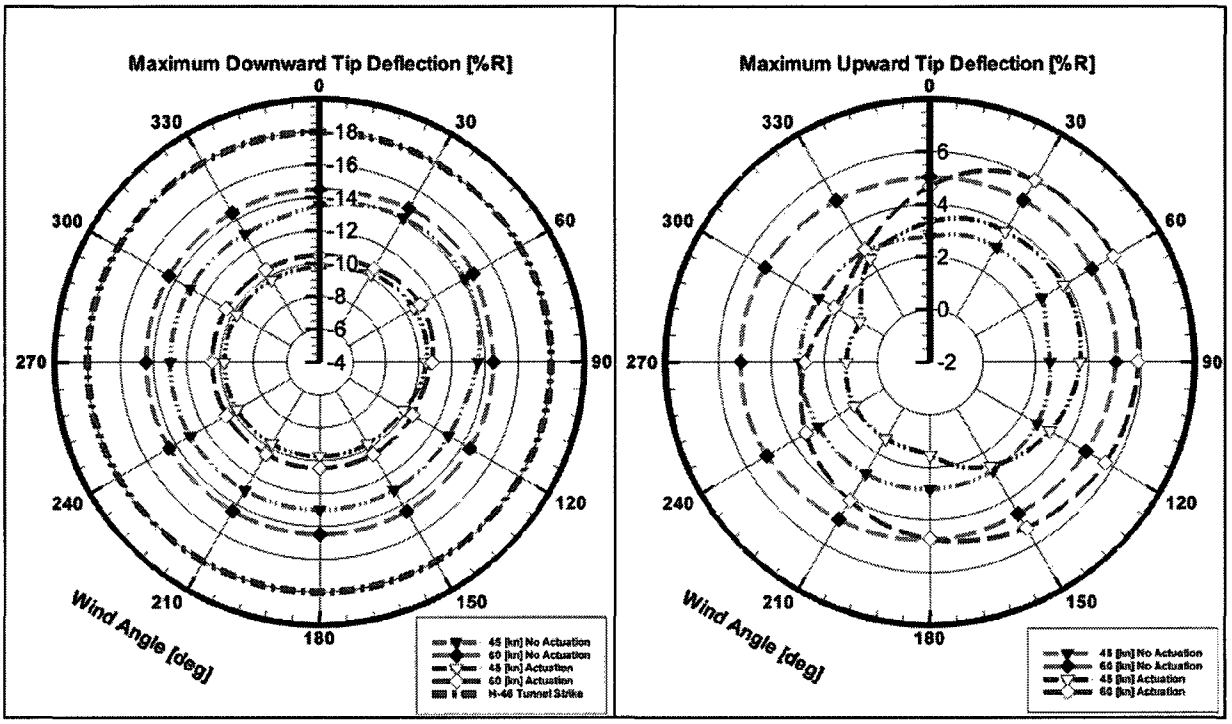

Figure 9.21: Maximum downward and upward tip deflection of the disengagement of the adopted IATR with DC actuation of the integrated MFCs.

thermore, it is reasoned that at some temporal point during engagement/disengagement, the blade will have gained enough angular momentum that twisting the blade according to the latter strategy will have a negative impact on the downward/upward deflection due to the downward/upward component of the aerodynamic drag force. At this temporal point, a switch from the proposed strategy to a steadily vanishing voltage signal is proposed that reaches zero integral twist when steady state is reached. It is difficult to determine this, up-to-now qualitative, temporal point for the flexible multibody system that represents the rotor given the number of parameters and variables involved. At best, a quantitative analysis of this point can be carried out under some set of assumptions in order to simplify the problem. If it is stipulated that this temporal point is reached when the root moment due to aerodynamic lift is sufficient to counter the root moment due to weight of the blade in addition to the compressive aerodynamic load at the (c) orientation in Fig. 9.24, then

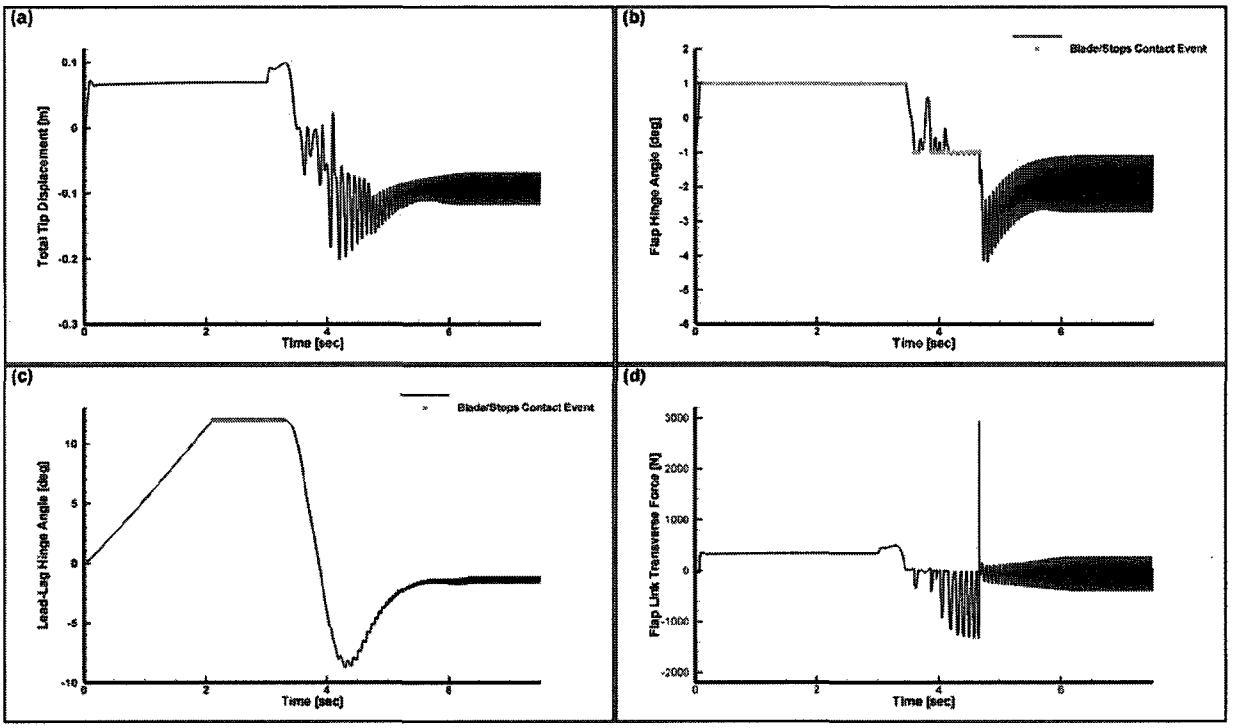

Figure 9.22: Time history of the adopted IATR engagement with MFCs static DC actuation under the wind conditions of 60[kn], 270°WOD for:(a) Total tip displacement, (b) Flap hinge angle, (c) Lead-lag hinge angle, (d) Flap-link transverse force.

a critical rotor speed can be found from the solution of the nonlinear equation

$$\sum_{i=1}^{N} f_{\mathrm{l}}^{i}(\Omega_{\mathrm{critical}}, \alpha(x^i), M^i, \ldots) + \sum_{i=1}^{N} f_{\mathrm{c}}^{i}(\Omega_{\mathrm{critical}}, \alpha(x^i), M^i, \mu, V_{\mathrm{wind}}, \ldots) + \sum_{i=1}^{N} f_{\mathrm{g}}^{i} = 0 \quad (9.9)$$

where f_{l}^{i} represents the functional form of the moment at the blade root due to the aerodynamic lift force per beam element i; f_{c}^{i} is the functional form of the moment due to the aerodynamic downward compression per beam element i; f_{g}^{i} is the functional form of the moment at the root due to the gravitational force per beam element i; $\Omega_{\mathrm{critical}}$ is the sought angular speed of the rotor; $\alpha(x^i)$ is the angle of attack of the beam element; M^i is the local Mach-number of the beam element; μ is the gust factor; V_{wind} is the wind speed; and ... includes other relevant parameters like the medium density and the functional

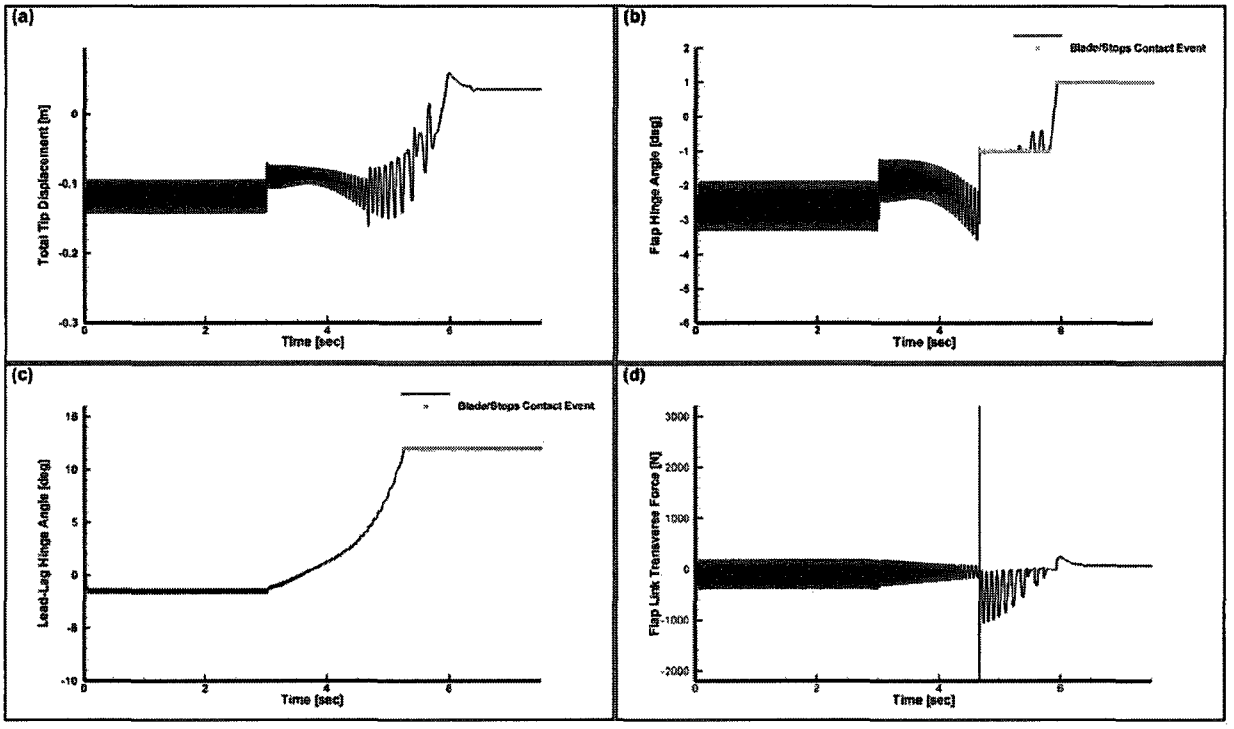

Figure 9.23: Time history of the adopted IATR disengagement with MFCs static DC actuation under the wind conditions of 45[kn], 60°WOD for:(a) Total tip displacement, (b) Flap hinge angle, (c) Lead-lag hinge angle, (d) Flap-link transverse force.

form of the lift/drag curve slope.

As mentioned above, determining Ω_{critical} from Eq. 9.9 for each possible scenario is difficult. However, if one imposes the following assumptions, then a value for Ω_{critical} can be found numerically for any wind speed:

1. The IATR is in a cantilevered configuration and it is assumed to be rigid.

2. The incoming in-plane flow as seen by the blade is purely due to its angular momentum, which is equivalent to considering the blade to be in the azimuthal orientation (c) in Fig. 9.24.

3. The compressive aerodynamic loads are purely due to the gust loading, which is linearly dependent on the gust factor μ.

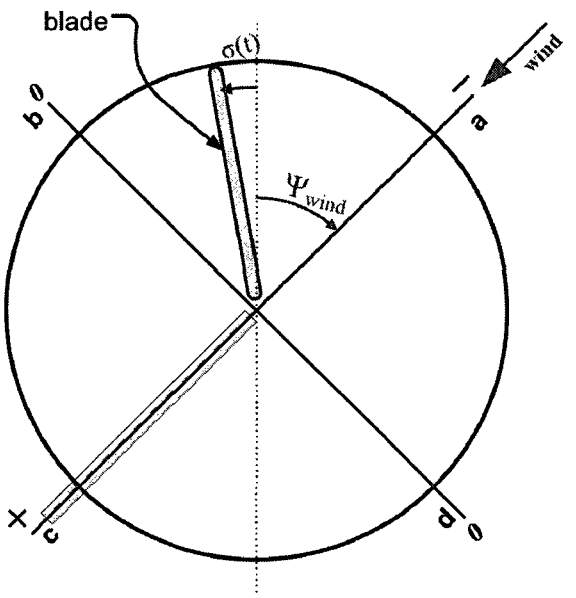

Figure 9.24: Top view of a proposed variable actuation strategy with the proposed twist polarity indicated.

4. The angle of attack of each beam element is determined by the built-in initial twist and the standard collective pitch setting.

5. The Mach number of the flow is set to be 0.3

Based on the above assumptions, Eq. 9.9 is solved for t_{critical}, which is based on three seconds initialization and the engagement profile in Table. 9.4, in Table. 9.6. The wind speeds considered are also listed in Table 9.6 with a gust factor of 0.25.

Table 9.6: Ω_{critical} and t_{critical} for a set of wind speeds and a gust factor of 0.25.

Wind Speed [kn]	Ω_{critical} **[rad/s]**	% of Ω_{max}	t_{critical} [s]
35	18.64	10.35	3.695
45	21.64	12.02	3.751
55	24.96	13.87	3.810
60	26.64	14.80	3.838

Similarly, the disengagement temporal point where the actuation is switched between quasi-steady and variable is also based on Table 9.4 such that

$$t_{\mathrm{d/critical}} = \frac{28}{3} - t_{\mathrm{critical}} \tag{9.10}$$

where t_{critical} and $t_{\mathrm{d/critical}}$ are both measured from the start of the simulation run.

Since $\Omega_{\mathrm{critical}}$ in Table 9.4 is based on several simplifying assumptions, it is necessary to investigate other temporal points before and after this point to establish its validity. Considering temporal points in increments of 0.25 starting from $0.5\Omega_{\mathrm{critical}}$ up to $2\Omega_{\mathrm{critical}}$, the actuation strategy is examined for each one of those points. The value of these temporal points for the 0.5, 1.25, and 2 cases are given in Table 9.7 through Table 9.9, while the values of the rest of these temporal points are given in Appendix H. As before, they are based on the engagement/disengagement profile given in Table 9.4 where all of the tabulated values are for the IATR engagement with the disengagement temporal point given by Eq. 9.10.

Table 9.7: $0.5\Omega_{\mathrm{critical}}$ and t_{critical} for a set of wind speeds and a gust factor of 0.25.

Wind Speed [kn]	$0.5\Omega_{\mathrm{critical}}$ **[rad/s]**	% of Ω_{max}	t_{critical} **[s]**
35	9.32	5.18	3.487
45	10.82	6.01	3.526
55	12.48	6.93	3.565
60	13.32	7.40	3.585

Table 9.8: $1.25\Omega_{\mathrm{critical}}$ and t_{critical} for a set of wind speeds and a gust factor of 0.25.

Wind Speed [kn]	$1.25\Omega_{\mathrm{critical}}$ **[rad/s]**	% of Ω_{max}	t_{critical} **[s]**
35	23.30	12.94	3.781
45	27.05	15.03	3.845
55	31.20	17.33	3.911
60	33.30	18.50	3.944

Subsequent to the determined temporal point in the simulations, the quasi-steady or the low frequency actuation is activated. The voltage of the latter signal is maximum at the temporal point and smoothly reaches zero when steady state is reached for the engagement. Conversely, the signal is zero when the disengagement starts and reaches its

Table 9.9: $2\Omega_{\text{critical}}$ and t_{critical} for a set of wind speeds and a gust factor of 0.25.

Wind Speed [kn]	$2\Omega_{\text{critical}}$ [rad/s]	% of $\Omega_{\max}$	t_{critical} [s]
35	37.28	20.71	4.003
45	43.28	24.04	4.088
55	49.92	27.73	4.177
60	53.28	29.60	4.221

maximum at the temporal point. The functional form of the resulting actuation vector that satisfies the above criteria is

$$\mathcal{F}^{(a)}_{\text{engagement}}(t) = \begin{cases} \mathcal{F}^{(a)}_{1200} + \mathcal{F}^{(a)}_{2000} \cos\left[\int_{t_0}^{t} \Omega(t)\, \mathrm{d}t + \sigma(t_0) + \Psi_{\text{wind}} + \pi\right] & : \ 0 < \Omega(t) < \Omega_{\text{critical}} \\ \mathcal{F}^{(a)}_{1200} + \mathcal{F}^{(a)}_{2000} \cos\left[\frac{\pi}{2\left(\frac{19}{3} - t_{\text{critical}}\right)}\left(t - t_{\text{critical}}\right)\right] & : \ \Omega_{\text{critical}} \leq \Omega(t) < \Omega_{\max} \\ 0 & : \ \Omega(t) = 0, \Omega_{\max} \end{cases} \tag{9.11}$$

$$\mathcal{F}^{(a)}_{\text{disengagement}}(t) = \begin{cases} \mathcal{F}^{(a)}_{1200} + \mathcal{F}^{(a)}_{2000} \cos\left[\int_{t_0}^{t} \Omega(t)\, \mathrm{d}t + \sigma(t_0) + \Psi_{\text{wind}} + \pi\right] & : \ 0 < \Omega(t) < \Omega_{\text{critical}} \\ \mathcal{F}^{(a)}_{1200} + \mathcal{F}^{(a)}_{2000} \cos\left[\frac{\pi}{2\left(t_{\text{d/critical}} - 3\right)}\left(t - t_{\text{d/critical}}\right)\right] & : \ \Omega_{\text{critical}} \leq \Omega(t) < \Omega_{\max} \\ 0 & : \ \Omega(t) = 0, \Omega_{\max} \end{cases} \tag{9.12}$$

where $\sigma(t_0)$ is the initial azimuthal angle of the rotor blade, and $\mathcal{F}^{(a)}_{2000}$ and $\mathcal{F}^{(a)}_{1200}$ are the amplitudes of the actuation vector at 2000[V] and 1200[V] respectively. The voltage amplitudes are similar to the extended operation cycle that was envisioned for the ATR blade based on CAMRAD II and PETRA simulations [174], where a DC offset is added to improve the performance of the piezoelectric fibres.

A point worth mentioning at this stage is the advantages gained by adding a DC offset to the applied signal. In addition to the obvious added advantage of larger positive twist in this investigation, a positive DC bias offers the following enumerated advantages [176] that prompt engineers to apply it for most piezoelectric fibre applications:

1. Prevents the depoling of the PZT material when applying large driving AC fields.
2. Stabilizes the domain structure and inhibits deaging and depoling in the PZT material at high AC fields.
3. Suppresses the nonlinearity in the piezoelectric response under large AC fields.
4. Stabilizes the domain walls and the alignment of the polarization.
5. Domain clamping is introduced without adding much to the polarization of the PZT material, which stabilizes the electromechanical coupling tensor d_{ijk} for low frequency applications.

The scaled functional shape of the first component of the voltage signal for 270° WOD and wind speed of 60 [kn] for $2\Omega_{\text{critical}}$ is shown in Fig. 9.25, where the changing frequency of the signal with time as required by this application is apparent. The scaled functional shape of the second component (without the DC bias) is shown for the same wind conditions in Fig. 9.26. Additionally, the application of the overall proposed actuation strategy for a rotor engagement under the same wind conditions is further illustrated in the time domain in Fig. 9.27. The spatial trace of the twist command of the first component is shown in Fig 9.28 for some given wind conditions.

The results of applying the actuation strategy of Eq. 9.11 and Eq. 9.12 to the 45[kn] and 60[kn] wind speeds examined at Ω_{critical} are displayed in Figs. 9.29 and 9.30 for MFCs actuation. A more comprehensive examination in terms of wind speed for both MFCs and AFCs is given in Appendix H

The improvement in terms of reduction of the downward deflections is clear. However, the upward deflections are not increased despite the higher generated lift that would be anticipated for a higher integral positive twist, a phenomenon that was observed for the static DC actuation above. In fact, the upward deflections are reduced when comparing

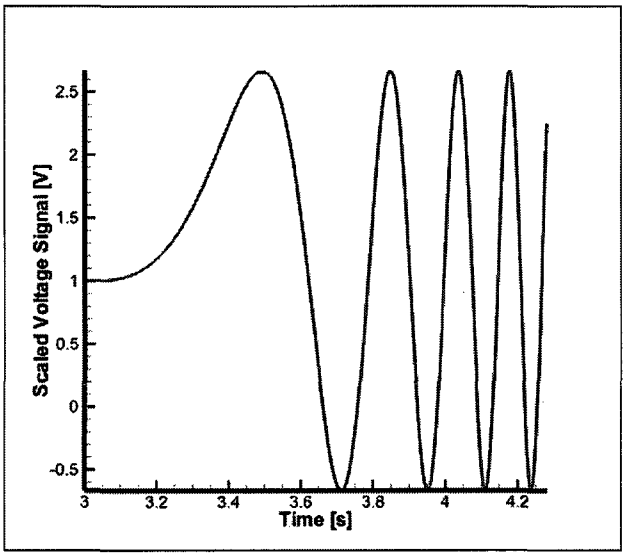

Figure 9.25: Scaled first component of voltage signal of the proposed dynamic actuation strategy for $2\Omega_{\text{critical}}$, WOD of 270°, and 60 [kn] wind speed.

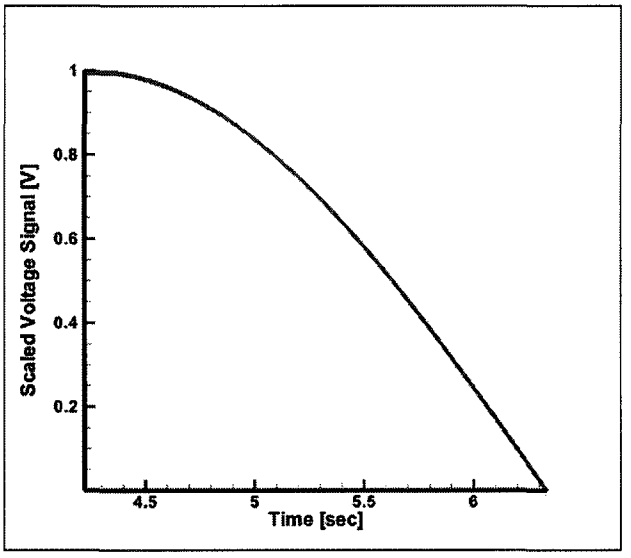

Figure 9.26: Scaled second component of voltage signal of the proposed dynamic actuation strategy for $2\Omega_{\text{critical}}$, WOD of 270°, and 60 [kn] wind speed.

Fig. 9.29 and Fig. 9.30 to Fig. 9.20 and Fig. 9.21 for the engagement and the disengagement respectively. To further establish the validity of this actuation strategy, the above transitional temporal points of $\Lambda\Omega_{\text{critical}}$, where $\Lambda \in [0.5, 0.75, 1.25, 1.5, 1.75, 2]$, are also investigated. The results are displayed in Fig. 9.31 through Fig. 9.33 for the 0.5, 1.25,

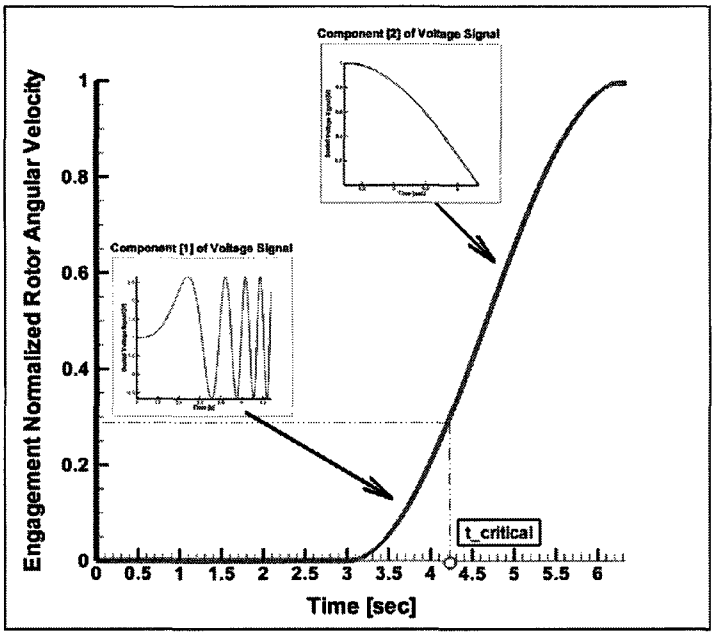

Figure 9.27: Application of the proposed actuation strategy for $2\Omega_{\text{critical}}$, WOD of 270°, and 60 [kn] wind speed for the engagement phase.

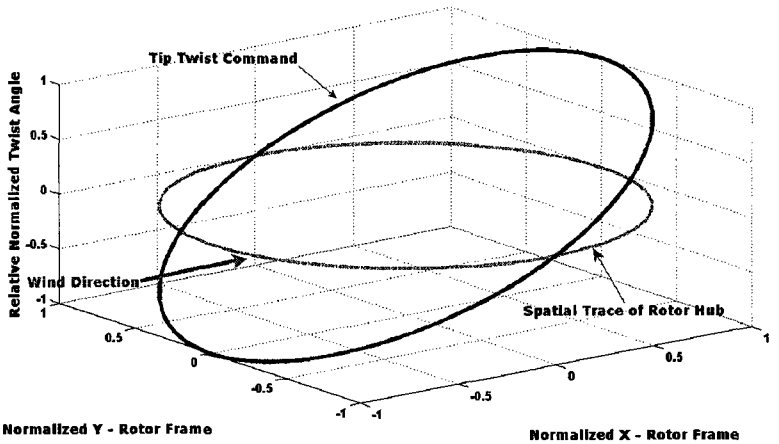

Figure 9.28: Twist command of the first component of the actuation voltage signal as a function of the rotor azimuthal angle.

and 2 points only at wind speeds of 45[kn] and 60[kn] for the engagement phase knowing that similar conclusions can be drawn regarding the disengagement. The results of examining all of the transitional temporal points at all considered wind speeds are presented in Appendix H.

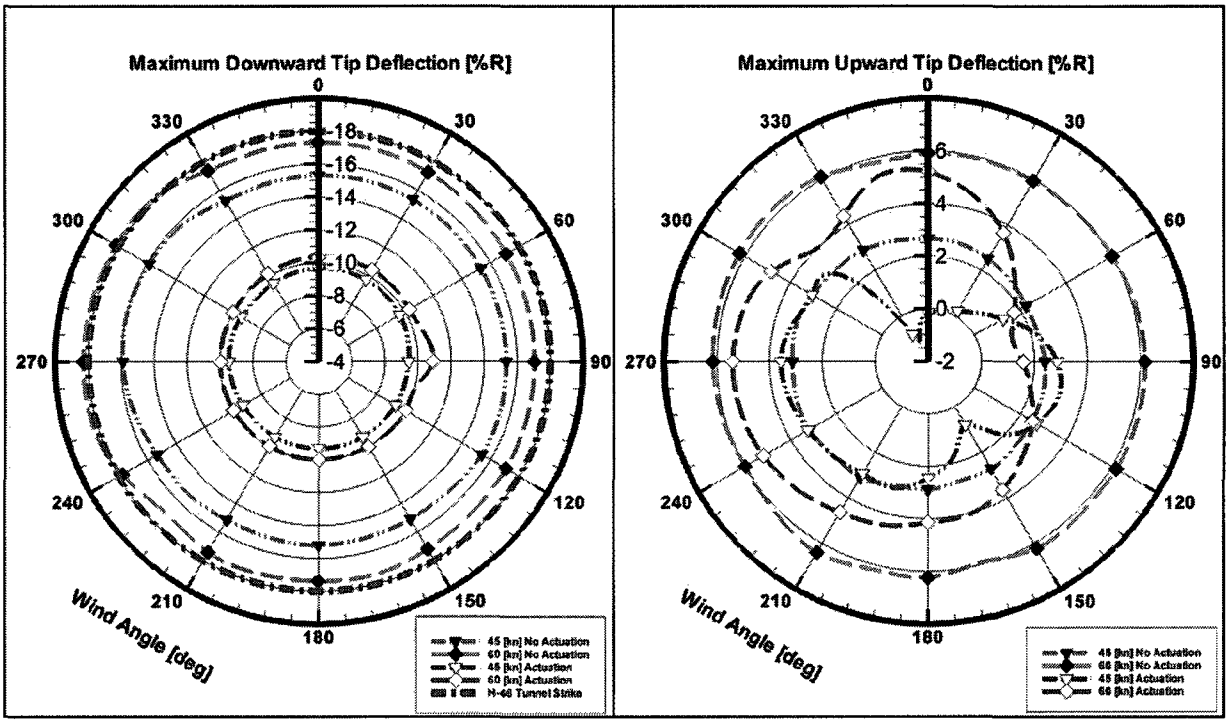

Figure 9.29: Maximum downward and upward tip deflection of the engagement of the adopted IATR with dynamic actuation of the integrated MFCs for $\Omega_{critical}$.

Examination of Fig. 9.31 to Fig. 9.33 demonstrates that reaching $\Omega_{critical}$ indeed represents a temporal point where it is advantageous to switch the actuation from the variable frequency mode to the single low frequency one. For instance, comparing the upward tip deflection in Fig. 9.31 to the one in Fig. 9.29 demonstrates that $\Omega_{critical}$ offers better performance than $0.5\Omega_{critical}$. The case of $0.75\Omega_{critical}$ in Appendix H appears to be very close in performance to $\Omega_{critical}$ with the former demonstrating a slightly improved and more uniform performance. This is qualitatively expected given that $0.75\Omega_{critical}$ is in the vicinity of $\Omega_{critical}$. From Table 9.6 and the engagement/disengagement phase duration in Table 9.4, it is evaluated that the first part of the actuation strategy takes approximately 20% of that duration, which is the region shown by other investigators to have the maximum deflections during the BSP.

The deteriorating performance of the actuation strategy that is markedly seen even for

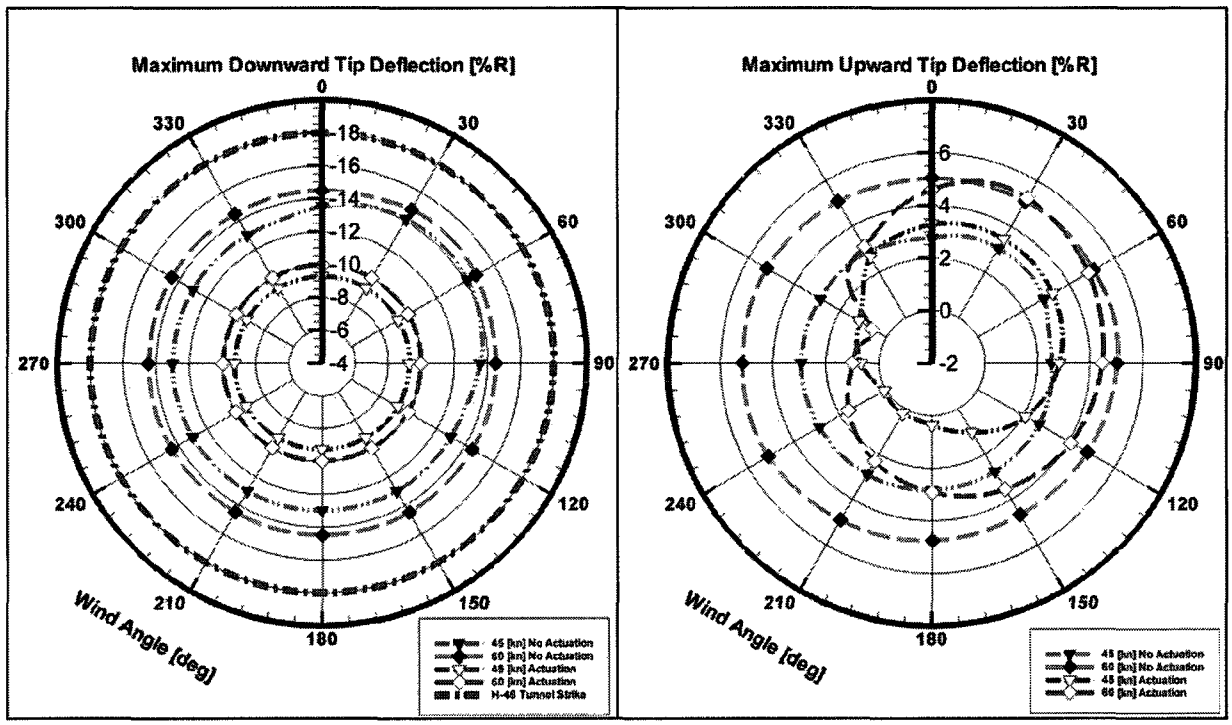

Figure 9.30: Maximum downward and upward tip deflection of the disengagement of the adopted IATR with dynamic actuation of the integrated MFCs for $\Omega_{critical}$.

the $1.25\Omega_{critical}$ case in Fig. 9.32 adds more to the validity of the analysis and the reasoning presented above. The progressive and rapid nature of this deterioration culminates with the $2\Omega_{critical}$ case in Fig. 9.33 that closely resembles the unactuated case in functional shape and magnitude.

The time histories of the engagement for wind conditions of 60[kn] and 270° WOD with dynamic actuation at $\Omega_{critical}$ are shown in Fig. 9.34 while those of the disengagement for 60[kn] and 270° WOD wind conditions are shown in Fig. 9.35. The tip twist angle time history of the former is shown in Fig. 9.36, where the effect of the two components of the actuation strategy is clear in addition to the effects of aerodynamic loading and turning-off/on the DC bias signal. It is interesting to note that the maximum downward deflections registered in Fig. 9.35 are during the steady-state phase before the disengagement commences, which explains the uniform patterns seen in Fig. 9.30 that were not seen

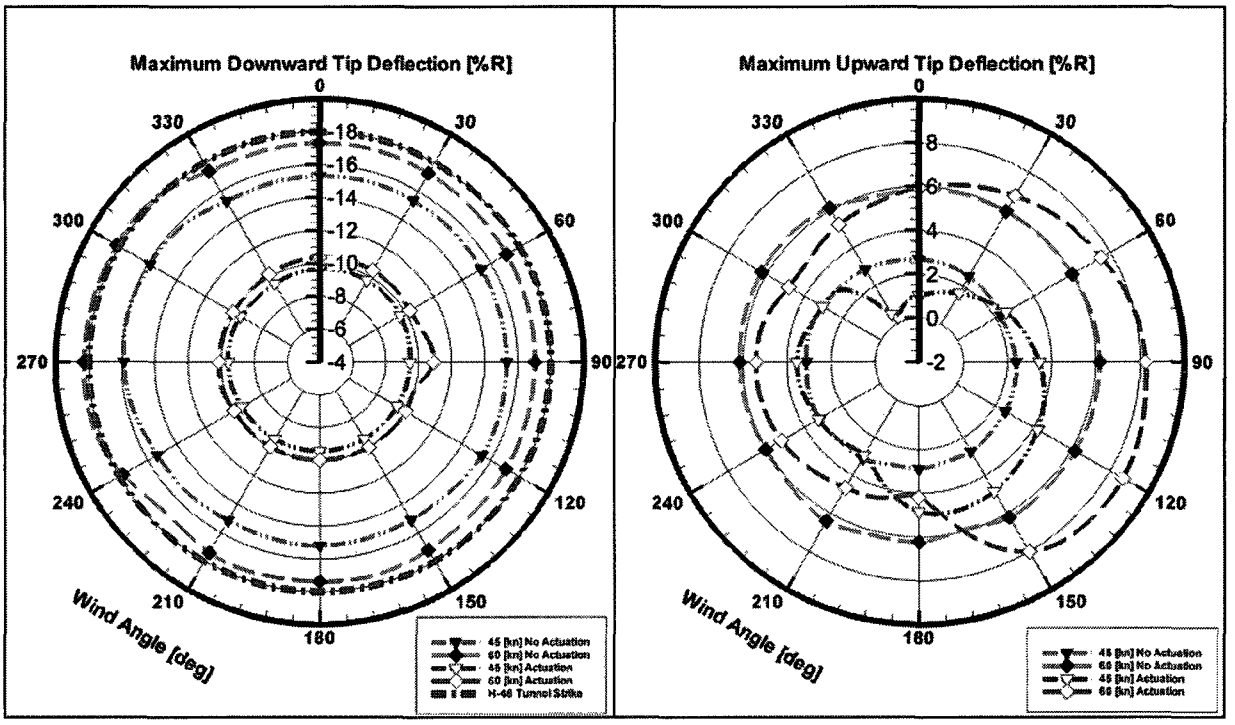

Figure 9.31: Maximum downward and upward tip deflection of the engagement of the adopted IATR with dynamic actuation of the integrated MFCs for $0.5\Omega_{\text{critical}}$.

in Figs. 9.21 and 9.17. This demonstrates that any excessive downward deflections during the disengagement phase have been effectively reduced.

9.3.2 Effect of Ship Motion and Turbulence

The important effects of ship motion in addition to turbulence are investigated separately in order to assess the impact of each effect on the actuation strategy proposed above. The same actuation strategy will be applied in addition to some slight modifications that are necessary in the case of the presence of ship motion. The effect of ship motion is examined first followed by the effect of turbulence.

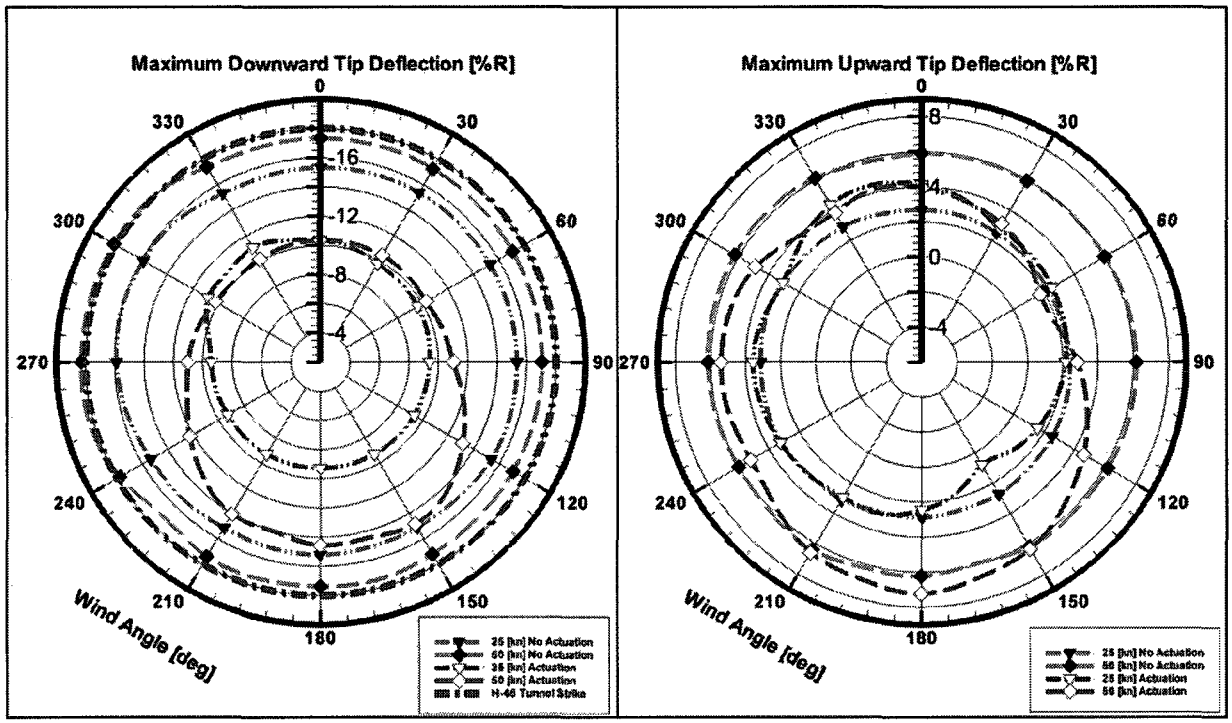

Figure 9.32: Maximum downward and upward tip deflection of the engagement of the adopted IATR with dynamic actuation of the integrated MFCs for $1.25\Omega_{\text{critical}}$.

Ship Motion Effect

The effect of ship motion in terms of the inertial forces experienced by the active rotor system is easily accommodated using the development outlined in Chapter 3 and implemented and validated in Chapter 8 where the multibody system is modelled in the non-inertial frame of the ship relative to the inertial frame represented by that of the ocean. The difficulty lies primarily in the effect of ship motion on the airwake, which is difficult enough to model even without ship motion as discussed previously. Therefore, any effect of ship motion on the airwake that is adopted in this study is acknowledged to be approximate and will likely not exhibit all of the important features seen for a true dynamic airwake that is affected by ship motion.

The experimental airwake model developed by a member of the Applied Dynamics Group and described in Chapter 1 [44] and the linear deterministic model are modified

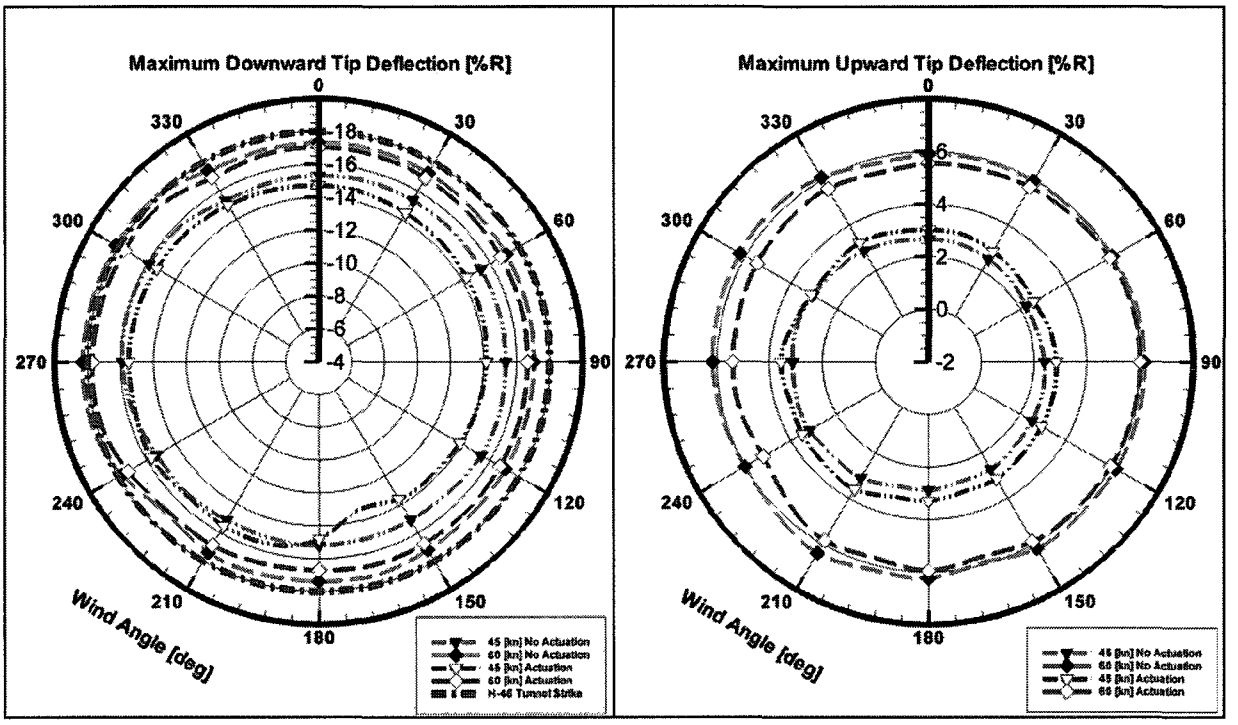

Figure 9.33: Maximum downward and upward tip deflection of the engagement of the adopted IATR with dynamic actuation of the integrated MFCs for $2\Omega_{\text{critical}}$.

to handle the effect of ship motion. Considering Fig. 9.37, where a top and back view of a ship are shown in sub-figures (a) and (b) respectively, the free stream wind is first transformed from the inertial frame of the ocean to the ship frame according to

$$\begin{bmatrix} V_{\text{wind\_x}} \\ \underline{V_{\text{wind\_y}}} \\ \underline{V_{\text{wind\_z}}} \end{bmatrix} = \mathcal{C}^{SI} \begin{bmatrix} -V_{\text{wind}} \cos(\Psi_{\text{wod}}) \\ V_{\text{wind}} \sin(\Psi_{\text{wod}}) \\ 0 \end{bmatrix} \tag{9.13}$$

where $\mathcal{C}^{SI}$ is the transformation operator from the inertial ocean frame to the ship frame; $V_{\text{wind\_x}}$, $\underline{V_{\text{wind\_y}}}$, and $\underline{V_{\text{wind\_z}}}$ are the components of the free stream velocity expressed in the ship frame.

The velocity component $V_{\text{wind\_x}}$ in addition to the ship heading speed, shown in Fig. 9.37(a), is used as the axial component of the experimental airwake flow field since the actual

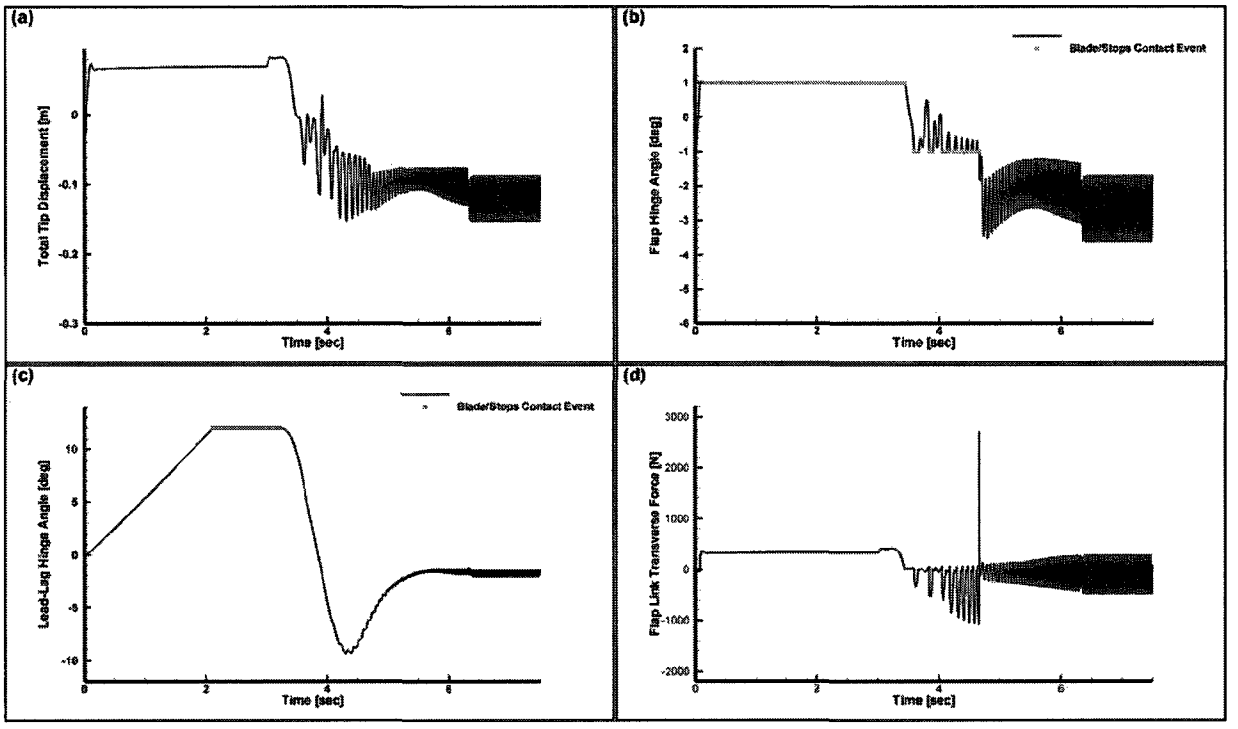

Figure 9.34: Time history of the adopted IATR engagement with MFCs dynamic actuation under the wind conditions of 60[kn], 270°WOD for:(a) Total tip displacement, (b) Flap hinge angle, (c) Lead-lag hinge angle, (d) Flap-link transverse force.

model lacks one, while the underlined components $\underline{V_{\text{wind\_y}}}$ and $\underline{V_{\text{wind\_z}}}$ are discarded. The free stream component $V_{\text{wind\_Y}}$, expressed in the ocean frame and shown in Fig. 9.37(b), is obtained as

$$V_{\text{wind\_Y}} = V_{\text{wind}} \sin(\Psi_{\text{wod}} + \Psi_{\text{yaw}}) \tag{9.14}$$

The speed component $V_{\text{wind\_Y}}$ is used as the beam wind input into the experimental model in addition to the ship roll angle Φ_{roll} to obtain the airwake flow field components $V_{\text{wind\_y}}$ and $V_{\text{wind\_z}}$ depicted in Fig. 9.37(b). It is obvious that the following assumptions are embedded in this development:

- No ship pitch effect on the airwake lateral flow components is included in this analysis. For instance, if the ship encounters bow or stern winds then the flow field seen by

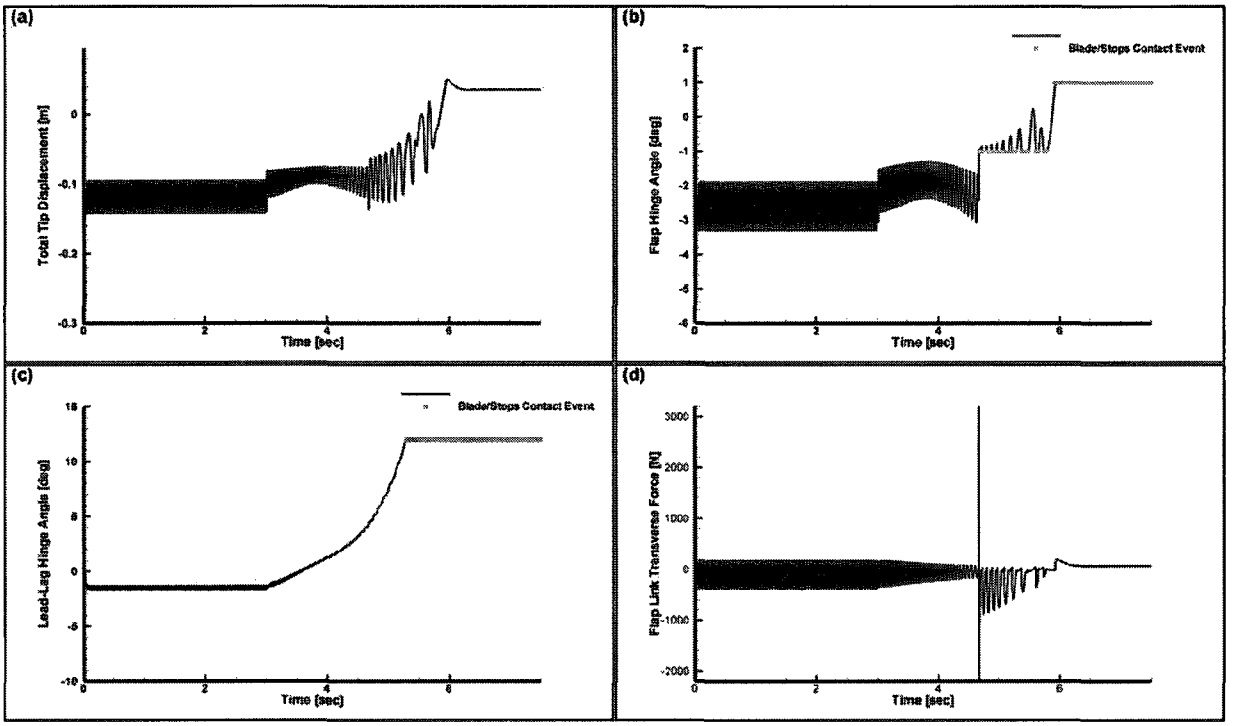

Figure 9.35: Time history of the adopted IATR disengagement with MFCs dynamic actuation under the wind conditions of 45[kn], 60°WOD for:(a) Total tip displacement, (b) Flap hinge angle, (c) Lead-lag hinge angle, (d) Flap-link transverse force.

the rotor is equivalent to the horizontal deterministic airwake explained in Chapter 1

- The inertial beam wind speed component depends on the ship yaw angle only with the effect of the other rotational degrees of freedom and the Cardan/Bryant sequence of finite rotations being neglected as seen in Eq. 9.14.

- Dynamic effects on the airwake due to ship motion are neglected and the airwake is assumed to vary in a quasi-steady sense according to the ship roll angle and the magnitude of the wind beam velocity component.

- The helicopter is assumed to be taking-off from a location on the ship that is similar to the one highlighted in Fig. 9.38, which justifies the assumption of a laminar axial flow on the ship deck for stern or bow wind.

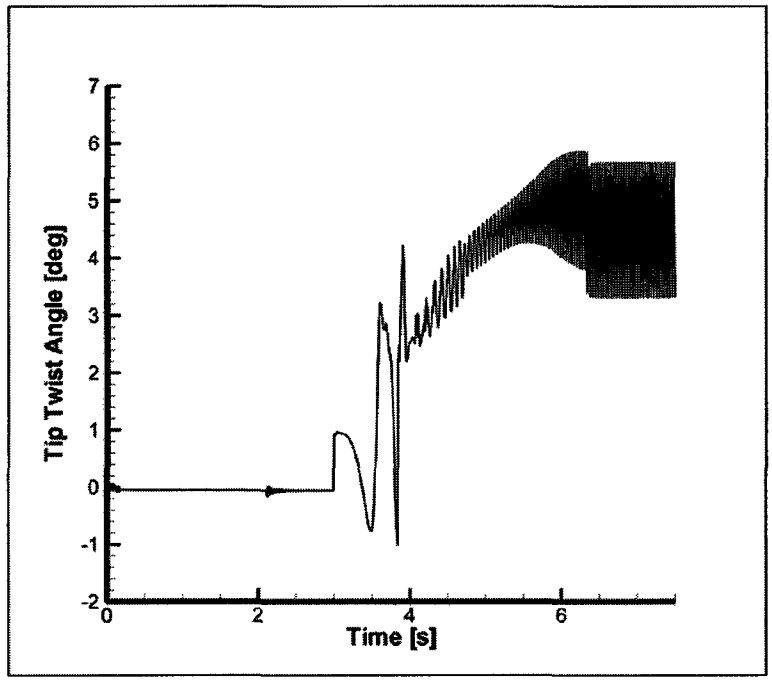

Figure 9.36: Time history of the tip twist angle of the adopted IATR engagement with MFCs dynamic actuation under the wind conditions of 60[kn], 270°WOD.

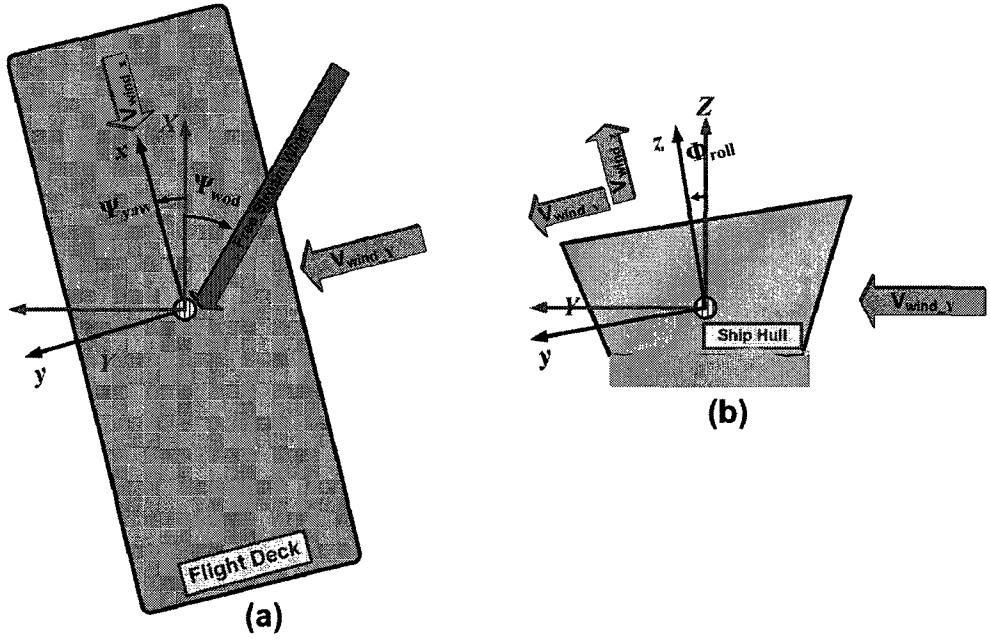

Figure 9.37: Analysis of ship motion effect on the experimental airwake model (a) top view, (b) back view.

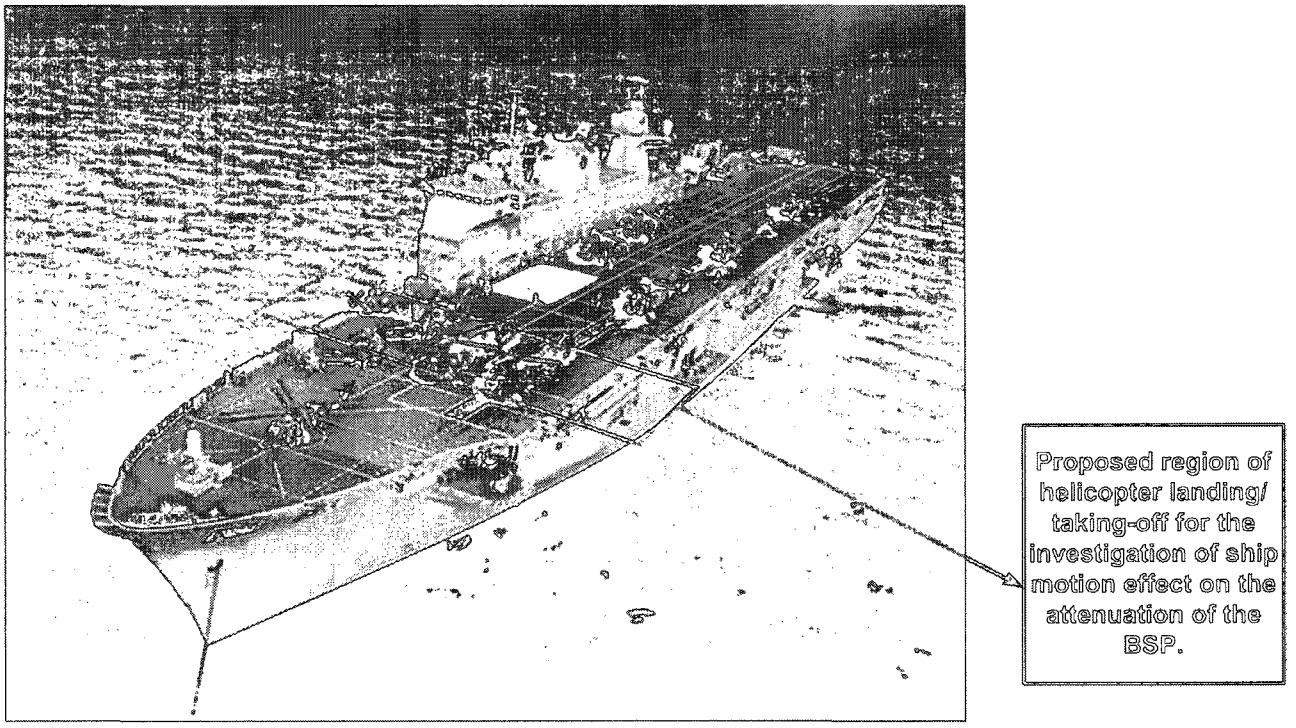

Figure 9.38: Flight deck of the aircraft carrier HMSOcean [Courtesy of the Royal Navy].

Similarly, the linear deterministic model is modified to include the effect of ship motion on the airwake. Considering the transformation in Eq. 9.13 and the illustrations in Fig. 9.37, the local wind over the deck angle α is defined as

$$\alpha = 2\pi - \arctan(\frac{V_{\text{wind\_y}}}{V_{\text{wind\_x}}}) \quad , \quad 0 \leq \alpha \leq 2\pi \tag{9.15}$$

where $V_{\text{wind\_y}}$ and $V_{\text{wind\_x}}$ are the free-stream velocity components resulting from Eq. 9.13.

The rotor disc lateral velocity loading becomes

$$\bar{V}_z = \left[\kappa\sqrt{V_{\text{x}}^2 + V_{\text{y}}^2}x\sin((\sigma+\varphi) - (\frac{3\pi}{2} - \alpha))\right]\sin(\alpha) + V_{\text{z}} \tag{9.16}$$

where similar to the conventional definition of the linear deterministic model, σ is the azimuthal angle of the rotor hub; φ is the lead-lag hinge angle; and V_{z} is an additional

lateral velocity component given by Eq. 9.13; and the trigonometric term $\sin(\alpha)$ ensures that the cliff-edge effect of the airwake vanishes for stern/bow winds and is maximum for the beam ones.

The rotor engagement/disengagement studies were performed with $1/6^{th}$ Mach-scaled representative ship motion typical of a Canadian frigate for the sea states shown in Table 9.10. The time history of the ship motion was examined and a quiescent period that fulfills a certain criteria for roll angle, and heave acceleration was selected to perform the engagement/disengagement, which is a standard procedure for (Helicopter-Ship-Dynamic-Interface) HSDI.

Table 9.10: Sea states selected to examine the effect of ship motion on the proposed strategy to counter the BSP.

	Deterministic Airwake	**Experimental Airwake**
Significant Wave Height [m]	4	4
Ship Heading [deg]	0, 30, 60, 90	0, 30, 60, 90
Ship Speed [kn]	10	10
Wind Speed [kn]	25, 50	25, 50
Wind Direction [deg]	$0° \rightarrow^{15°} 360°$	$0° \rightarrow^{15°} 360°$

The resulting maximum deflection response for the rotor engagement and disengagement for the 4_000_10 and 4_060_10 sea states coupled with the experimental airwake model is shown in Fig. 9.39 through 9.42 along with the effect of the dynamic actuation strategy developed in section 9.3.1. Similarly, the rotor response coupled with the modified linear deterministic airwake model is shown in Fig. 9.43 through 9.46 for the same sea states. The results for the rest of the sea states enumerated in Table 9.10 are given in Appendix H

Examination of the SHOLs-like minimum/maximum tip deflections in Fig. 9.39 through Fig. 9.46 yields the following observations regarding the differences between the two airwake models with ship motion present:

I. For both airwake models, the ship motion affects the BSP in generally a negative way as expected.

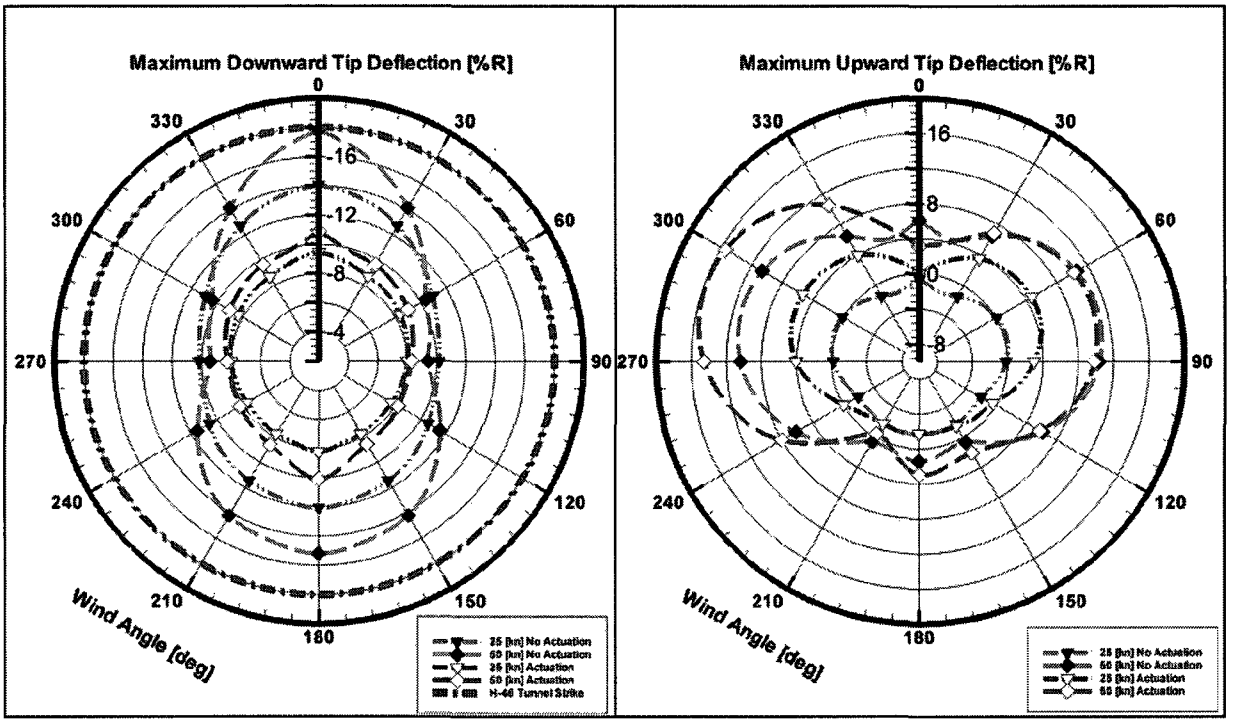

Figure 9.39: Maximum downward and upward tip deflection of the engagement of the adopted IATR, sea state 4_000_10, experimental airwake.

II. In the case of the experimental airwake model, the only tunnel strike is predicted when the angle between the ship heading and the waves is zero. This is primarily attributed to the implementation of the experimental airwake with ship motion where the axial wind is highest for the aforementioned ship motion at 0° WOD. Another contributing factor is the high forward heave velocity and acceleration of the ship.

III. In the case of the experimental airwake, the downward tip deflections increase with increasing angle of the ship heading relative to the incoming waves for the WOD angle between 210° and 330° and to a lesser extent between 30° and 150°. A similar conclusion can be drawn regarding the upward tip deflections for the WOD angle between 210° and 330° with the exception of the 30° ship heading.

IV. In the case of the experimental airwake model (as with the linear deterministic one), the BSP is more severe for engagement compared to disengagement.

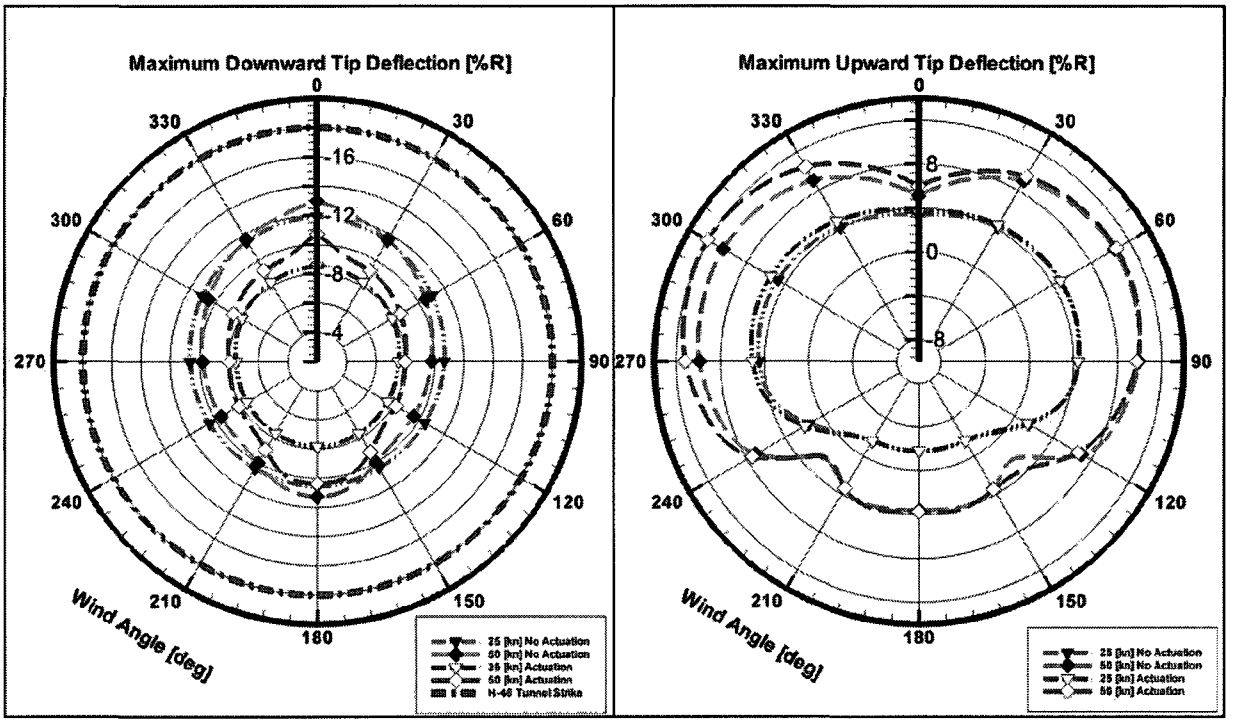

Figure 9.40: Maximum downward and upward tip deflection of the disengagement of the adopted IATR, sea state 4_000_10, experimental airwake.

V. In the case of the linear deterministic model, even the disengagement is registering tunnel strikes, which was not observed without ship motion.

VI. In the case of the linear deterministic model, the downward tip deflections are more severe than those of the experimental model while for the upward deflections the contrary is true. This is attributed to the main difference between the two models, which is the absence of the downward compressive portion in the experimental airwake. This is neither a contradiction nor a deficiency with either model, but a reflection of different ship deck structural environments for which the models are applicable.

In regard to the effectiveness of the actuation strategy when ship motion is present, one can also draw the following conclusions:

I. Despite the actuation strategy being developed using the linear deterministic model,

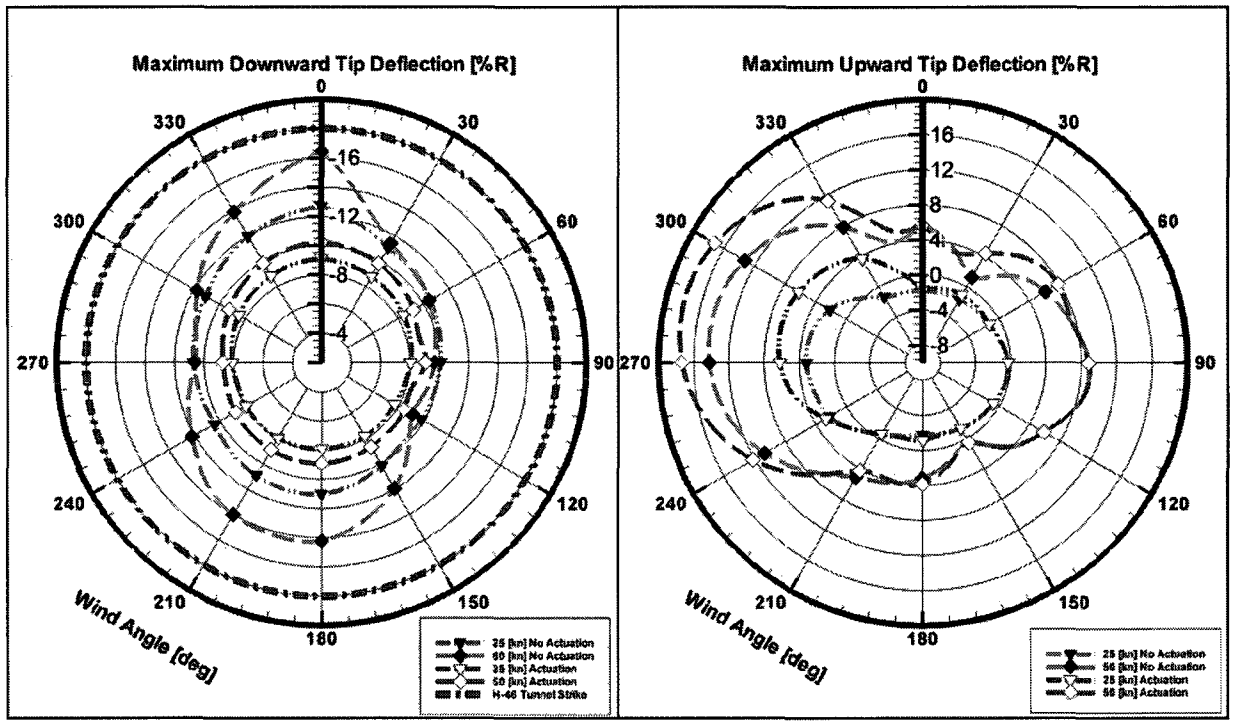

Figure 9.41: Maximum downward and upward tip deflection of the engagement of the adopted IATR, sea state 4_060_10, experimental airwake.

it is overall still successful, but not as effective, in reducing the BSP to safe levels for the experimental airwake model. For both airwake models, the proposed actuation strategy managed to reduce the downward tip deflection.

II. The actuation strategy increases the upward tip deflection in the case of the experimental airwake model for WOD of 210° to 330° for all sea states and it is more pronounced for the higher wind speed.

III. In the case of the deterministic airwake model, the strategy gradually loses its effectiveness as the ship heading, WOD angle, and wind speed increase, which is expected since the ship rolling motion induced at those sea states directly impacts the lateral component of the airwake model. For instance, the tunnel strikes are completely eliminated for the 4_000_10 sea state for both wind speeds considered while tunnel strikes are still present for the 50[kn] wind speed in the 4_060_10 sea state. Nev-

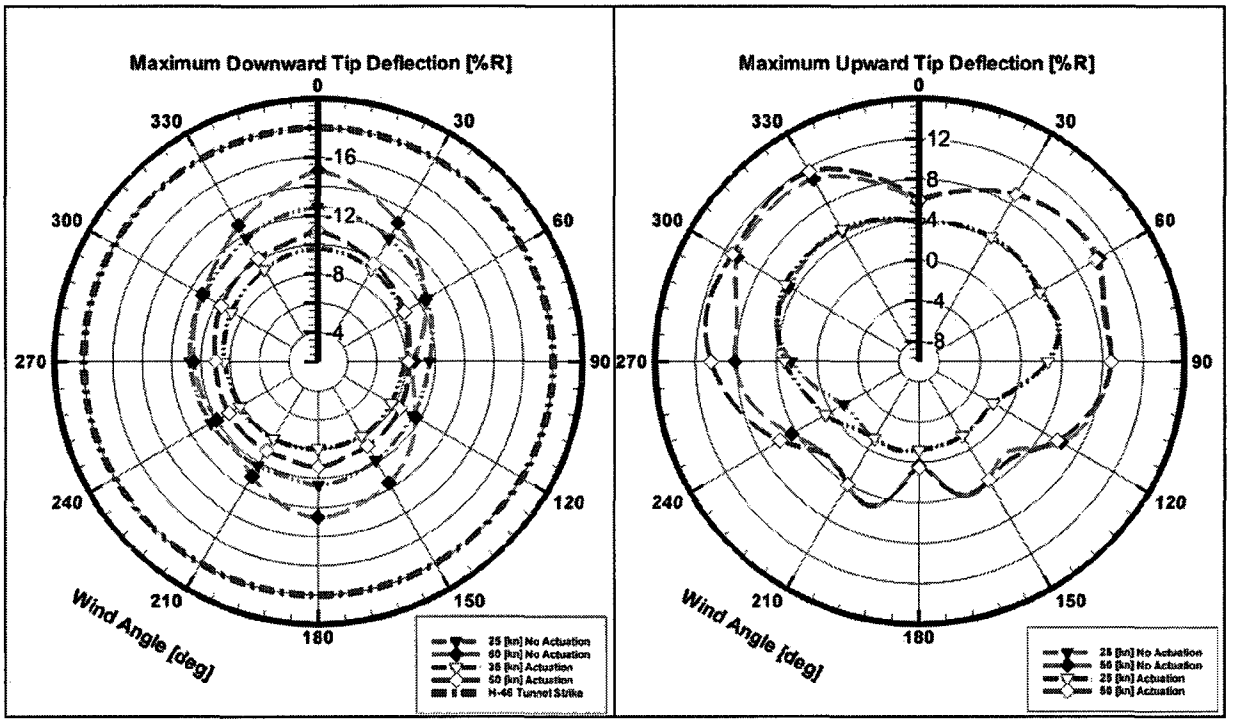

Figure 9.42: Maximum downward and upward tip deflection of the disengagement of the adopted IATR, sea state 4_060_10, experimental airwake.

ertheless, the actuation strategy created zones in the SHOLs where the helicopter would not normally be able to operate such as the one defined by 150° $\leq$ WOD $\leq$ 210°. Furthermore, for the 4_060_10 sea state, the 25[kn] wind speed has been rendered completely safe for engagement and disengagement and the safe zone is greatly enlarged for disengagement at the 50[kn] wind speed.

IV. The 4_030_10 sea state is observed to be between the 4_000_10 and the 4_060_10 while the 4_090_10 is more challenging than the 4_060_10 in terms of the effectiveness of the actuation strategy.

V. The upward deflection is not significantly increased for the deterministic model as in the experimental one. However, when it increases, it is generally within the same range of WOD identified earlier and it is also more pronounced for the higher wind speed.

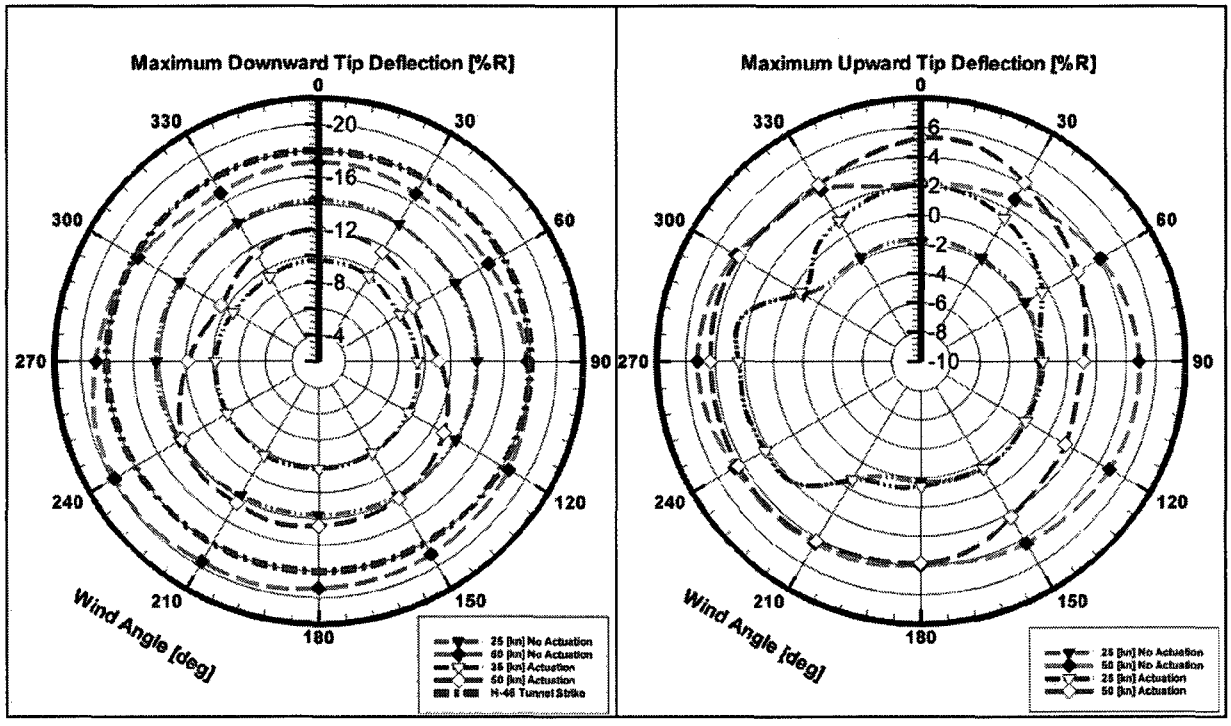

Figure 9.43: Maximum downward and upward tip deflection of the engagement of the adopted IATR, sea state 4_000_10, deterministic airwake.

In summary, it seems that even with ship motion the actuation strategy proposed is still capable of reducing the BSP to safe levels considering that the sea states chosen for this study are not mild and the 50[kn] wind speed in addition to 10[kn] ship cruise speed could create very high speed ship airwake. For illustrative purposes, time histories of the engagement of the IATR using both airwake models with and without the actuation strategy for selected ship motions are shown in Fig. 9.47 through Fig. 9.50, which further reveals the additional complexity of the problem when ship motion is present. Additional disengagement time histories are given in Appendix H

Turbulence Effect

A semi-empirical modelling of the turbulence present in the ship airwake, which complements the steady experimental one, has also been developed by a member of the Applied

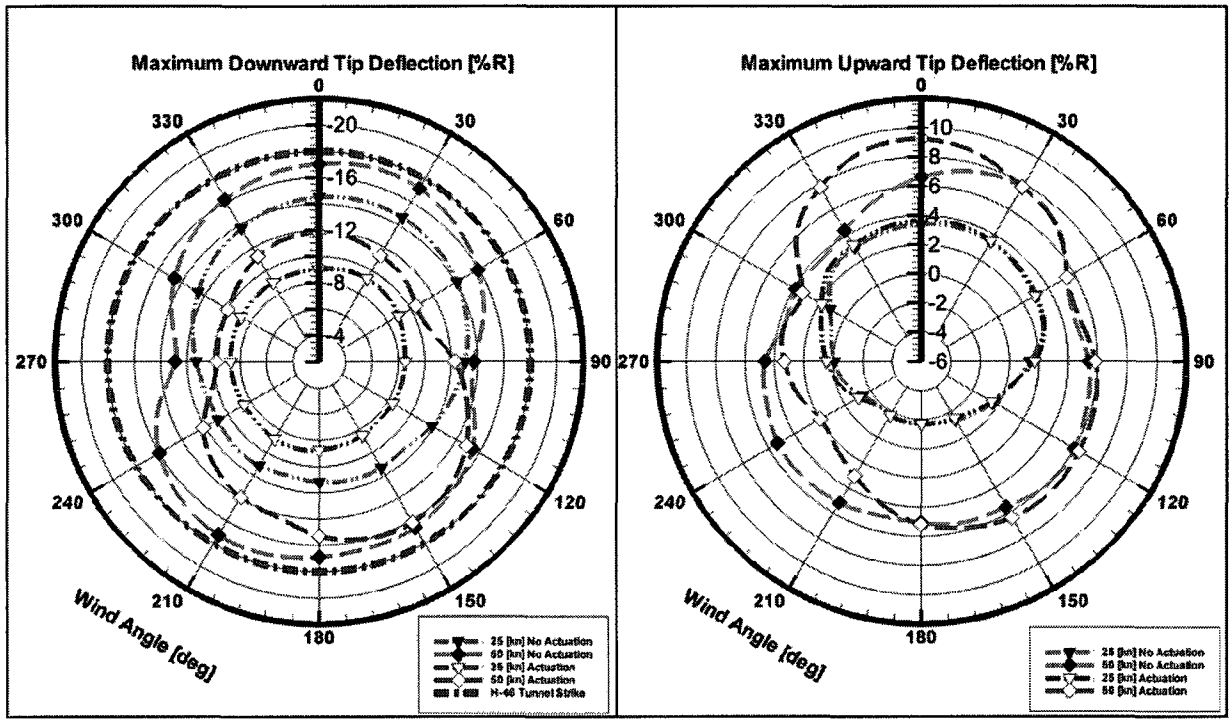

Figure 9.44: Maximum downward and upward tip deflection of the disengagement of the adopted IATR, sea state 4_000_10, deterministic airwake.

Dynamics Group [44]. The basis of this modelling invokes some simplifying assumptions to render the problem tractable. Turbulent fluctuations in atmospheric flows are often represented using the Von Karman equations for turbulence auto-spectra and coherence. Using a Von Karman turbulence spectrum from constants as determined by experiment, a representative time history of velocity fluctuation is calculated using a Fourier Series. The perfectly-correlated turbulence model involves the assumption that this representative time history is applied at every point in the flow field. The magnitudes are adjusted to reflect a local representative RMS value and these turbulent fluctuations are superimposed on representative mean flow velocities such as

$$\vec{V}(x,y,z,t) = \bar{\vec{V}}(x,y,z) + \breve{\vec{V}}(t) \tag{9.17}$$

where $\vec{V}(x,y,z,t)$ represents the airwake velocity field, $\bar{\vec{V}}(x,y,z)$ is the steady component

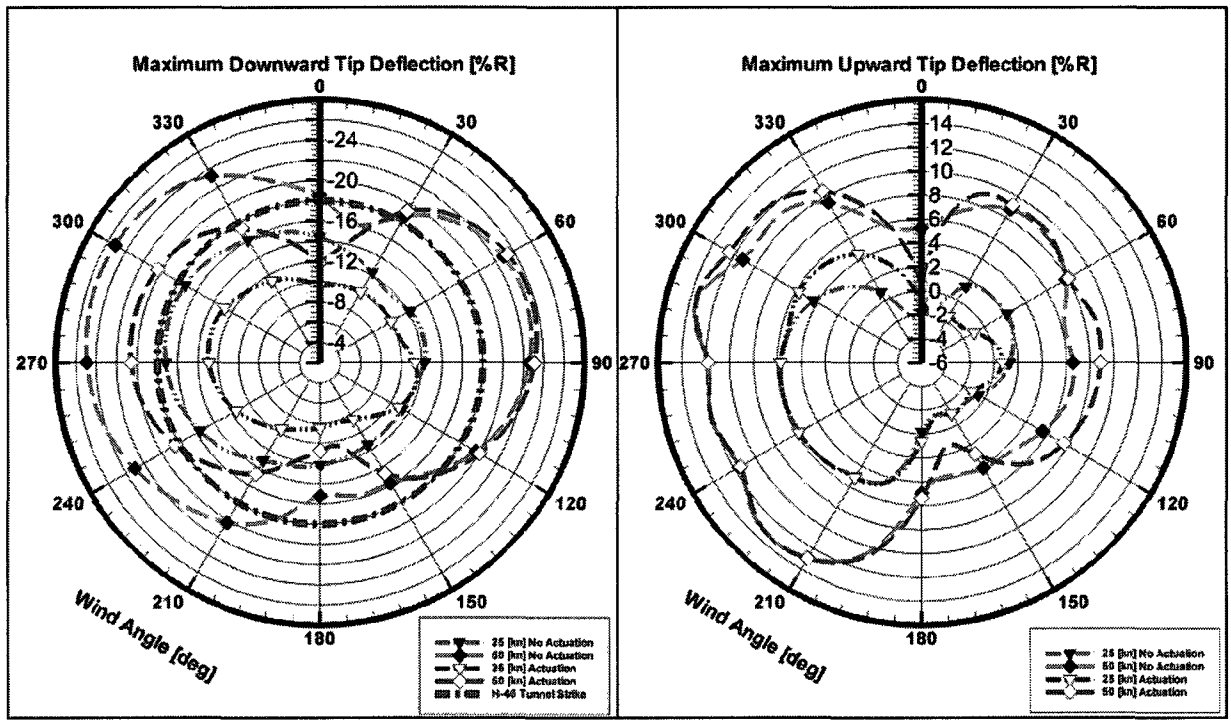

Figure 9.45: Maximum downward and upward tip deflection of the engagement of the adopted IATR, sea state 4_060_10, deterministic airwake.

of the airwake velocity field, and $\breve{V}(t)$ is the perfectly correlated velocity turbulence component where its spatial independence is duly noted.

The model also includes a correction for the Taylor hypothesis, which assumes that turbulent eddies are convected with the mean flow velocity. This means that an appropriate phase shift is applied to the base time history signal to compensate for the fact that some points are further downstream than others. The perfectly correlated assumption results in an over-estimation of the effect of turbulence on the velocity flow field.

The effect of the perfectly correlated turbulence model is first examined for the wind speeds and the ship deck roll angles given in Table 9.11, where only beam winds are considered. Throughout this investigation, only the engagement phase is considered knowing that it is more severe in terms of the BSP compared to the disengagement phase.

The resulting maximum downward and upward tip deflections for the 45[kn] case are

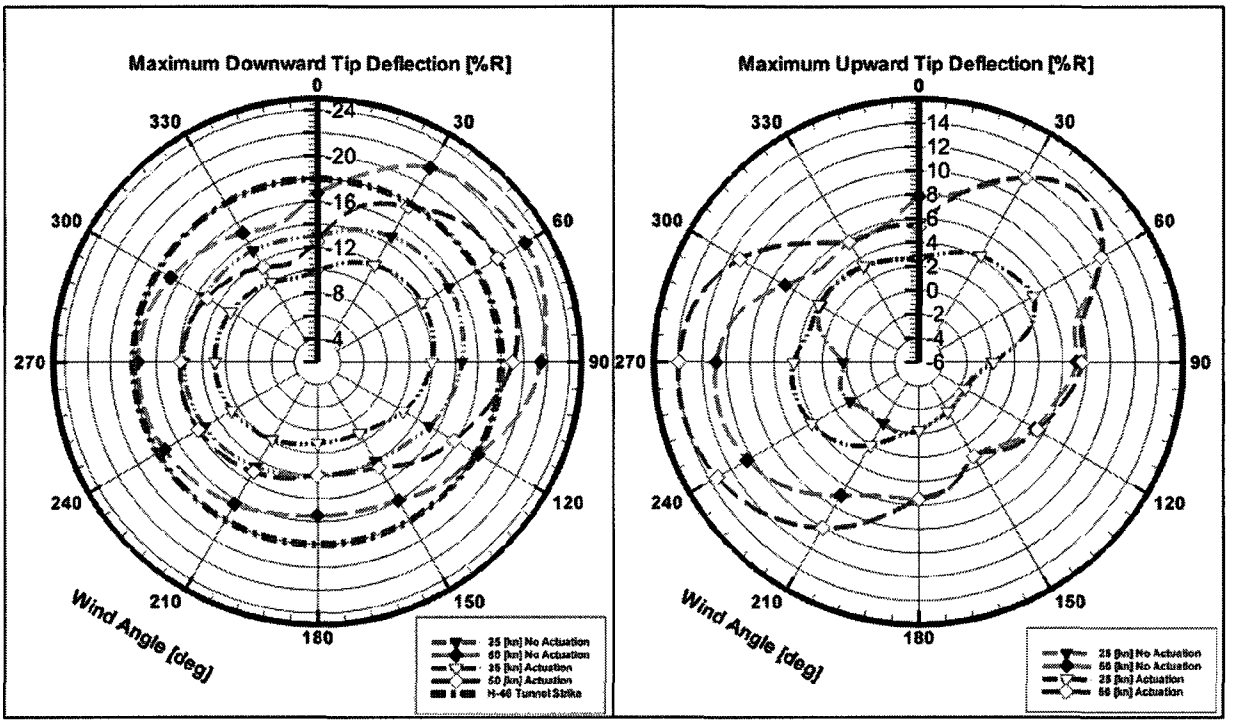

Figure 9.46: Maximum downward and upward tip deflection of the disengagement of the adopted IATR, sea state 4_060_10, deterministic airwake.

Table 9.11: Experimental airwake conditions selected to examine the effect of the perfectly correlated turbulence.

	45/60[kn] Wind Speed
Ship Deck Roll Angle [deg]	-10, -5, 0, 5, 10

shown in Fig. 9.51 and Fig. 9.52 and compared to those predicted when turbulence is neglected. The 60[kn] wind speed case is given in Appendix H.

The turbulence appreciably increases the downward tip deflection and its influence becomes sufficiently pronounced for positive roll angles as to cause tunnel strikes. The upward deflection decreases for negative roll angles while it increases for positive ones. The increase in downward deflection is not unexpected and it is attributed to the structure of the steady airwake model discussed previously and the additional energy in the flow introduced by the fluctuating components. The temporal random phase angle of the fluctuating component certainly plays a role in determining the change in magnitude of

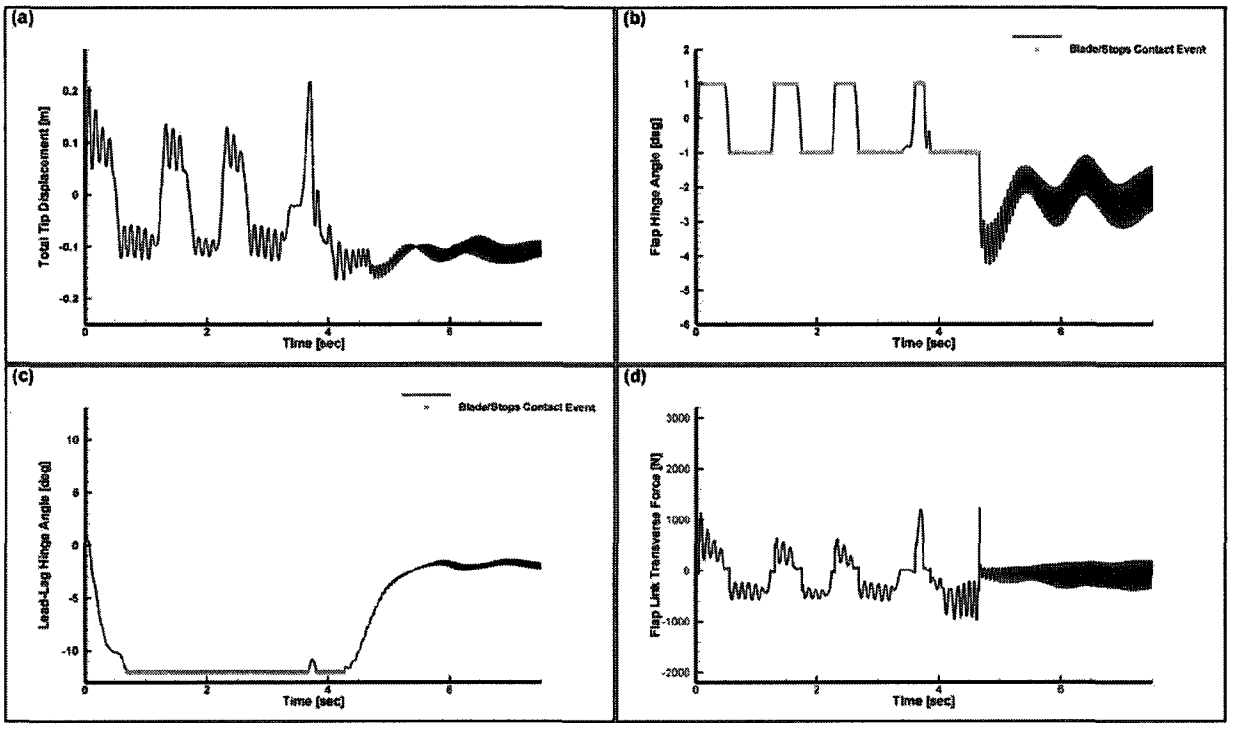

Figure 9.47: Time history of the adopted IATR engagement under the wind conditions of 50[kn], 270° WOD with 4_060_10 sea state using the experimental airwake model for:(a) Total tip displacement, (b) Flap hinge angle, (c) Lead-lag hinge angle, (d) Flap-link transverse force.

the steady component, which explains the peculiar behaviour sometimes encountered when turbulence is present.

Since the turbulence model represents a worst-case scenario, the effectiveness of the actuation strategy is assessed based on the percentage change it is capable of inducing in the maximum tip deflections. Fig. 9.53 and Fig. 9.54 show that with the exception of small increases in the upward deflection for negative deck roll angles, the maximum downward and upward deflections are remarkably reduced. The positive deck roll angles are expected to be the most challenging given that the whole rotor disc is subjected to a persistent compressive gust. The scenario in this investigation resembles an engagement of the IATR from an off-shore platform rather than a ship deck given that the roll angle is fixed. Finally, it is highlighted that the actuation strategy seems to gradually lose

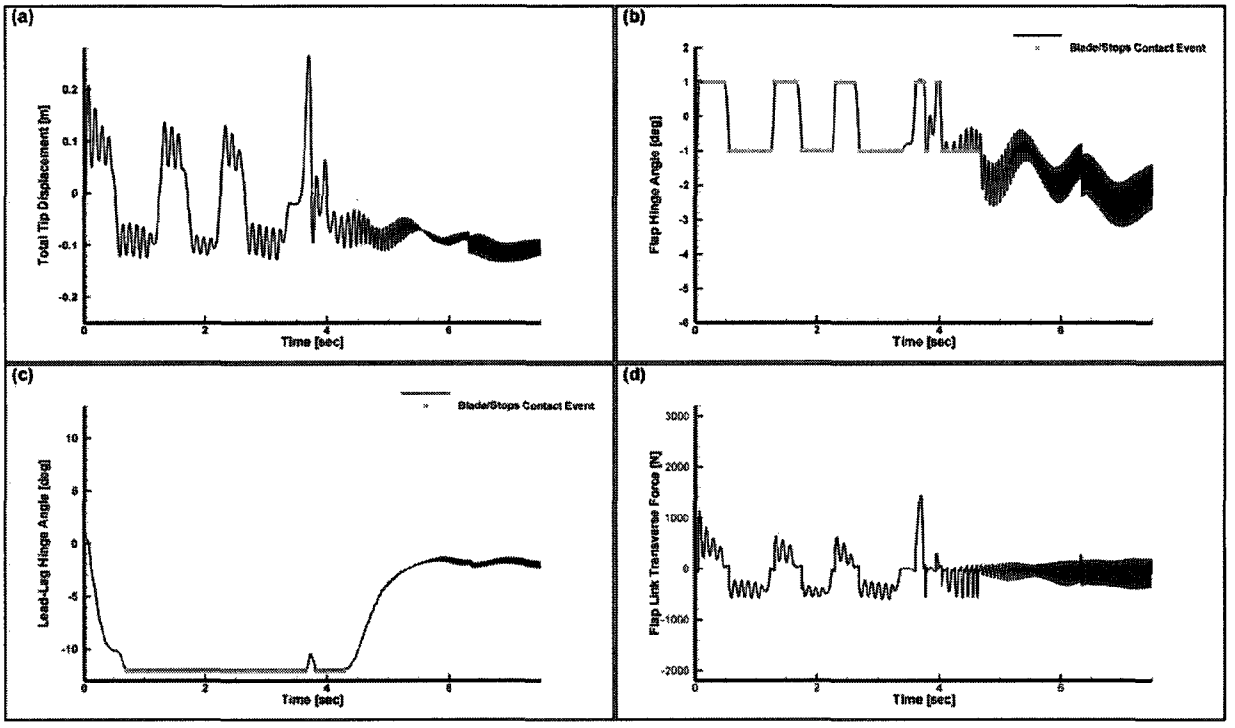

Figure 9.48: Time history of the adopted IATR engagement with the actuation strategy employed under the wind conditions of 50[kn], 270° WOD with 4_060_10 sea state using the experimental airwake model for:(a) Total tip displacement, (b) Flap hinge angle, (c) Lead-lag hinge angle, (d) Flap-link transverse force.

its effectiveness as the wind speed and the platform roll angle increase. This is seen in Fig. H.29 in Appendix H where an increase in the downward deflection is registered for even the -10° case. Again, the perfectly-correlated turbulence coupled with the fixed roll angle and the high wind speed are reasoned to be responsible for this one-time failure of the actuation strategy. Time histories of the rotor response that show the effect of turbulence are shown in Appendix H

9.4 Future Recommendations

The study presented herein is proof of a concept and is meant to be a feasibility investigation, albeit with state-of-the-art modelling tools, to justify the need for further

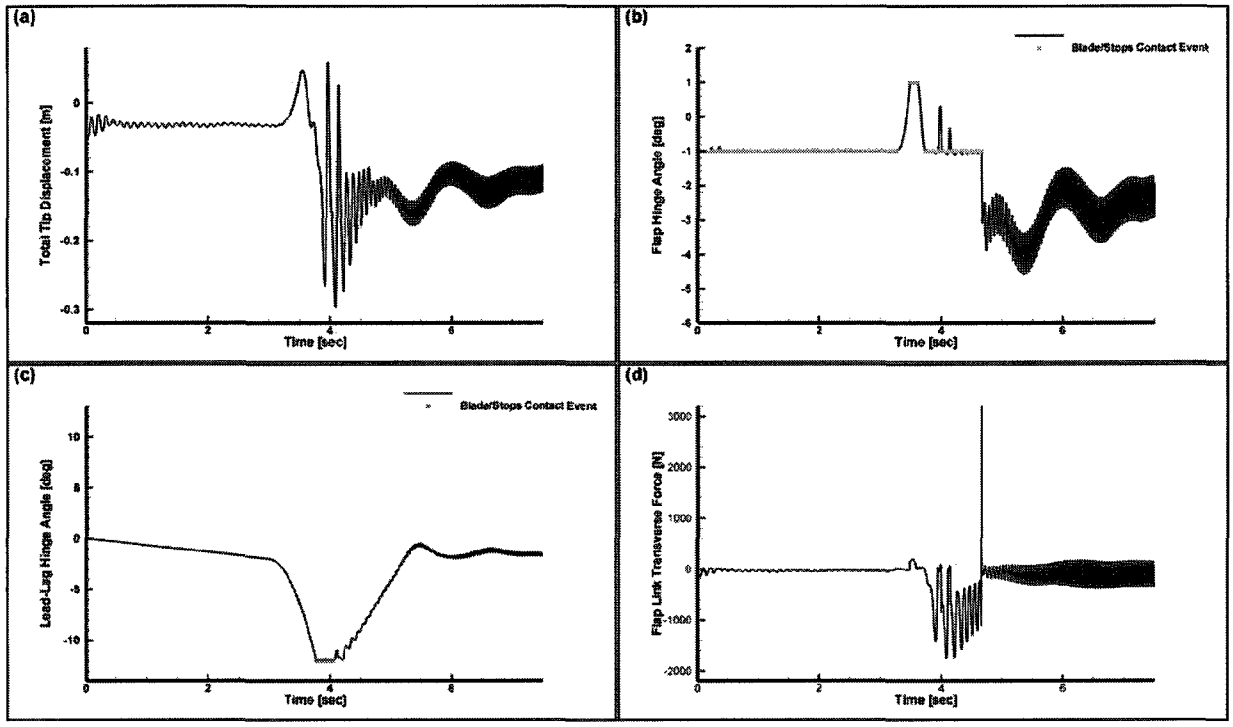

Figure 9.49: Time history of the adopted IATR engagement under the wind conditions of 50[kn], 180° WOD with 4_000_10 sea state using the linear deterministic airwake model for:(a) Total tip displacement, (b) Flap hinge angle, (c) Lead-lag hinge angle, (d) Flap-link transverse force.

investigation. It definitely shows that the IAT concept is capable of countering the BSP for the Mach-scaled environment considered. Obviously, more advanced modelling tools will add further refinement to the results presented and these modelling advancements have been enumerated in previous chapters and they will not be repeated here.

The first most important follow-up to this investigation is the experimental study of the proposed strategies in wind tunnels. This entails the construction of scaled active rotor system as discussed previously. In addition to validating the promise of the concept demonstrated in this investigation, it will add further insight into its engineering practicality in terms of cost and ease of implementation.

The second follow-up would be adopting more advanced and full-scale rotor systems that employ designs that optimize the tip twist for the least amount of MFCs plies and

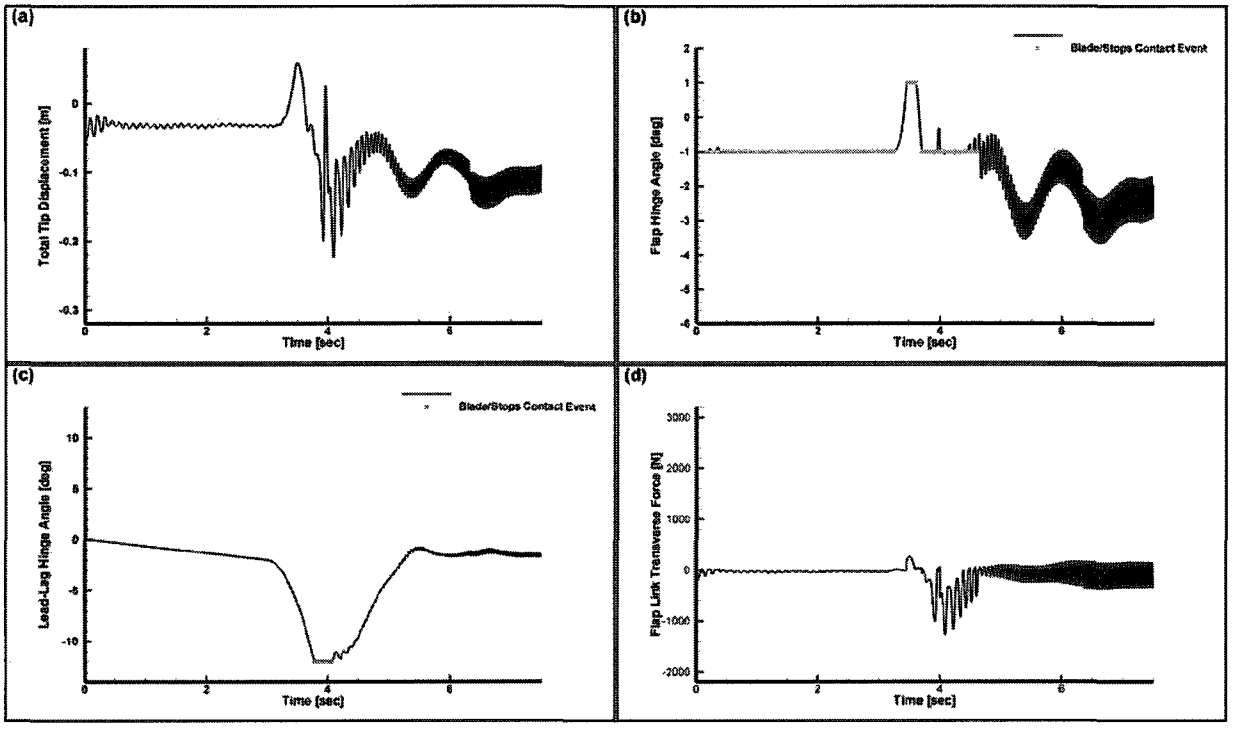

Figure 9.50: Time history of the adopted IATR engagement with the actuation strategy employed under the wind conditions of 50[kn], 180° WOD with 4_000_10 sea state using the linear deterministic airwake model for:(a) Total tip displacement, (b) Flap hinge angle, (c) Lead-lag hinge angle, (d) Flap-link transverse force.

power consumption. Obviously, having larger amplitudes for the tip twist angle is advantageous in addition to establishing the validity of the actuation strategy for a full-scale system. Confirmation of the aforementioned outcome cannot be overemphasized if the proposed strategy is to merit additional investigations and if it is to find its way to actual application in maritime helicopter operation.

Thirdly, investigating closed-loop control strategies with the attentive nonlinear system identification is a natural progression beyond this study and it will likely overcome the hurdles faced by an open-loop system more easily including the inadvertent increase in upward deflection or the sensitivity to the ship airwake model and structure. This task may be complicated by the nonlinear and the highly transient nature of the problem. Nevertheless, classical control schemes that rely on certain approximations of the problem

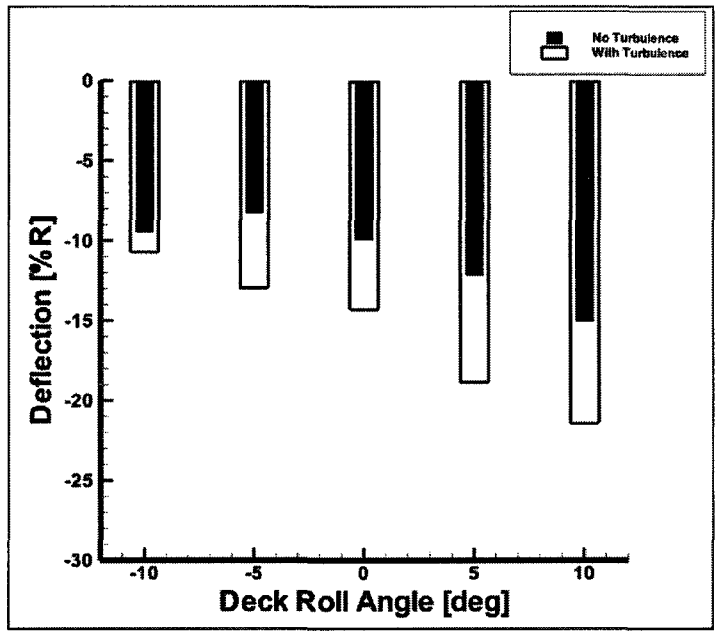

Figure 9.51: Maximum downward tip deflections for various deck roll angles when the perfectly correlated turbulence is considered.

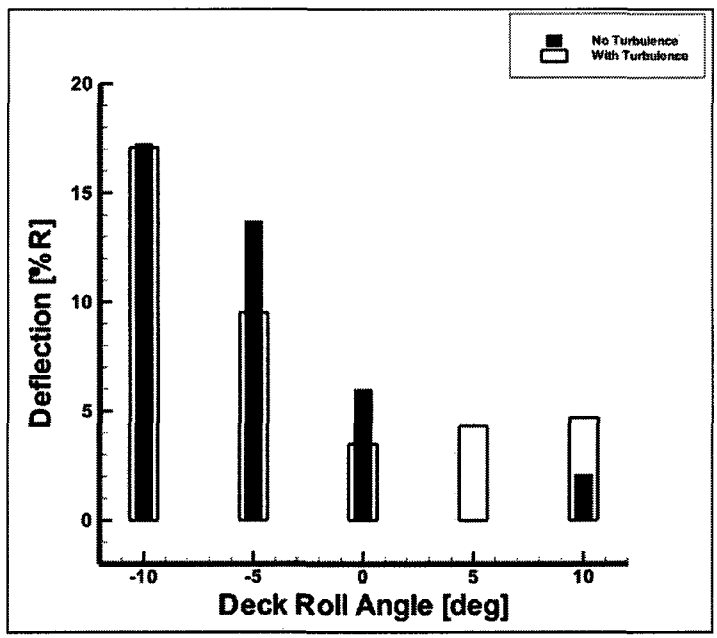

Figure 9.52: Maximum upward tip deflections for various deck roll angles when the perfectly correlated turbulence is considered.

may prove to be effective, such as gain scheduling, where the rotor system is approximated by a series of transfer functions with each function being approximately valid for a certain

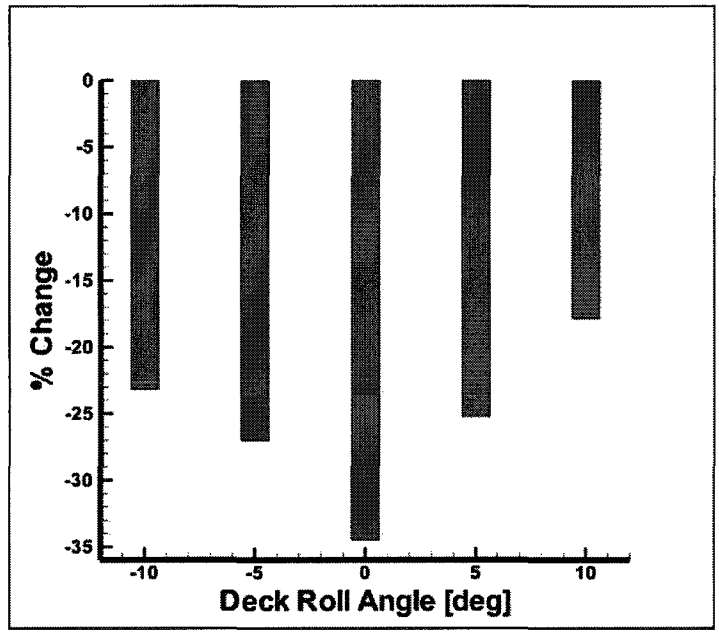

Figure 9.53: Percent change in the maximum downward tip deflections for various deck roll angles with the perfectly correlated turbulence model and the actuation strategy.

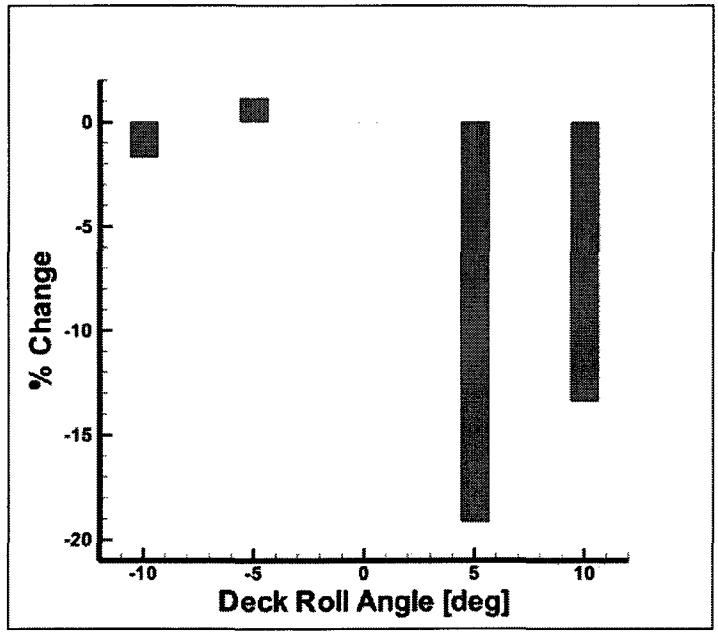

Figure 9.54: Percent change in the maximum upward tip deflections for various deck roll angles with the perfectly correlated turbulence model and the actuation strategy.

range of hub angular speed. Strain sensors, or the piezoelectric fibres themselves, could act as feedback sensors for the control law.

Chapter 10

Conclusions

In this research an aeroelastic phenomenon encountered during maritime operation of helicopters, known as the blade sailing phenomenon, was identified as being a limiting factor in some elevated sea conditions in which it would otherwise be possible and desirable to launch and recover maritime helicopters. The multidisciplinary engineering nature of the problem in addition to associated hazards and complexity, owing to the number of factors contributing to its occurrence, was shown to render it very difficult to investigate in the field. As other investigators have concluded, it was demonstrated that advanced and validated simulation tools are best suited to investigate this phenomenon. Most importantly, a research gap was identified in terms of practical engineering solutions to alleviate, if not eliminate, the impact of this phenomenon on the tactical flexibility of maritime helicopters.

In order to model the BSP and investigate the feasibility of a proposed strategy to counter it, advancements and gaps in modelling of rotor systems that employ the integral active twist concept were identified and tackled. A cross-sectional theory that consistently reduces the 3-D elastic energy of thin-walled composite beams/blades with arbitrary geometry and material anisotropy to a linear 2-D theory over the cross-section without invoking

any ad hoc assumptions was extended to include embedded active macro fibre composites. The resulting electromechanical theory was validated against general active beam cross-sectional finite element analysis codes that were in turn validated against nonlinear multiphysics 3-D elasticity finite element calculations and experimental data. The theory also corrected previously published developments for active thin-walled beams. Its analytical nature allows for efficient implementation and provides an ideal tool for optimization studies during the design stages of thin-walled active rotor blades. Furthermore, the applicability of the theory to low frequency phenomena renders it ideal for blade sailing analysis, which is characterized by low frequency components. Finally, a refined theory for active thin-walled open cross-section beams, which incorporates the Vlasov effect, was developed and validated. The latter theory has the same advantages as its closed cross-section counterpart and can be used to analyze variant concepts of active rotor blades or other slender structural members.

A geometrically exact intrinsic theory of moving beams, which allows for large deformations under the condition of small strain, was extended to model more realistic active rotor blades. The theory is deemed essential for the investigation due to the large deflections that characterize the BSP. The geometrically exact beam theory was integrated into an intrinsic formulation of active flexible multibody systems in a non-inertial frame that is representative of rotors operating on ship decks. The intrinsic formulation was shown to be advantageous in terms of being symbolic; reducing the level of nonlinearity; and being weak in the sense of derivatives, which allows for simple shape functions to be used. Furthermore, it was demonstrated that the intrinsic formulation allows for the salient features of the first order generalized-α method demonstrated in the linear domain to be retained when applied to the nonlinear domain. This has reinforced the notion that the formulation of the nonlinear elastodynamic equations plays a significant role in determining the success of a proposed integration scheme.

A Froude-scale experimental rotor was designed and built to validate the simulation tools and investigate some aspects of the BSP. The validity and the efficiency of the rotor system modelling was successfully established in two phases. The first phase was conducted in a wind tunnel and the second one was conducted in a laboratory using a 6DOF motion platform, to reproduce the aeroelastic response to a representative airwake and ship motion respectively. It is concluded that the parameters of the engagement/disengagement profile play a minimal role in the occurrence of the BSP. Increasing or decreasing the collective pitch setting along with increasing the wind speed and ship deck roll angle was found to amplify the BSP. Additionally, it was further verified that the nonlinear quasi-steady aerodynamic model with Mach number effects on the stall point is sufficient for blade sailing research when compared to the unsteady aerodynamic model; however, the latter was shown to be more accurate, particularly at higher wind speeds. The second phase consisted of securing the rotor system to a motion platform and planning the experimental runs to achieve the following three goals: Sub-phase (I) examined the blade aeroelastic response to scaled and representative frequencies of harmonic ship pitch/roll motion at constant selected rotor hub speeds; Sub-phase (II) examined the aeroelastic response of the rotor during the whole engagement/steady-state/disengagement operation profile to scaled and representative ship motion of a Canadian frigate; and Sub-phase (III), which is considered secondary relative to the other goals, subjected the rotor spinning at a constant hub speed to a scaled and representative ship motion. It was experimentally shown that in the absence of a ship airwake, there exists a rotor speed at which moderate to high roll/pitch frequency will have a detrimental impact on the blade response in terms of amplifying the BSP. Various collective pitch settings were shown to demonstrate the same observation. This observation was argued to be theoretically expected given the interaction between the inertial forces on the rotor system while operating on ship decks. Furthermore, additional observations are noted regarding the impact of increased hub speed and collective pitch

setting on the maximum blade tip deflection. The validity of the geometrically exact intrinsic flexible multibody dynamics model to investigate the aeroelastic response of rotors operating from ships was also established based on Goal (II).

The integral active twist concept was demonstrated to reduce the BSP to very safe levels in Mach-scaled rotor system operation. Static and dynamic open-loop actuation strategies were proposed. The successful performance of the latter was demonstrated through numerical simulations using the validated modelling tools and comparison with variant strategies. In addition to being tested in a deterministic (analytical) ship airwake representation, the strategy displayed the same success when an experimental ship airwake was used. Also, the strategy's performance was successful when tested with representative ship motion coupled with the corresponding simplified airwake modifications. Furthermore, when an experimental fully-correlated turbulence model was added to the ship airwake, the proposed strategy was successful once more. The success of the open-loop control strategy is attributed to the modification of the aerodynamic loads at the outboard blade stations where it matters the most; the minimal phase lag of the response of the active twist at the frequencies of interest; and its design and validation.

Finally, despite the success of the developed simulation tools and the open-loop control strategy in modelling and reducing the BSP to safe levels respectively, recommended future improvements and investigations were outlined in each chapter to propel this research to the next level. It is concluded that the research was successful in advancing the efficient, yet comprehensive, modelling of active rotor systems operating from ship decks and in demonstrating the feasibility of the integral active twist approach for countering the BSP.

Bibliography

[1] M. LaRosa, J. Ma, and H. Z. Zheng. Fatigue analysis of helicopter landing probe by helicopter/ship dynamic interface simulation. In *63rd Annual Forum Proceedings - American Helicopter Society*, volume 2, pages 1068–1076. American Helicopter Society, 2007.

[2] T. Neville. Dynamic and aerodynamic clearance of the apache ah mk1 attack helicopter for embarked operations. *Proceedings of the Institution of Mechanical Engineers, Part G (Journal of Aerospace Engineering)*, 219(G5):459–469, 2005.

[3] R. Bradley, C.A. Macdonald, and T.W. Buggy. Quantification and prediction of pilot workload in the helicopter/ship dynamic interface. *Proceedings of the Institution of Mechanical Engineers, Part G (Journal of Aerospace Engineering)*, 219(G5):429–443, 2005.

[4] D. Carico and B. Ferrier. Evaluating landing aids to support helicopter/ship testing and operations. In *2006 IEEE Aerospace Conference*. IEEE, 2006.

[5] J. Hommel, G. C. S.; Van Der Vorst. ROtorcraft Ship Dynamic Interface Simulation (ROSDIS). In *National Aerospace Laboratory NLR - 32nd European Rotorcraft Forum, ERF 2006*, volume 3, pages 1252–1264, 2007.

[6] S.J Tate. A dynamic challenge: helicopter/ship interface simulation-development, integration and application. In *Flight Simulation - Where are the Challenges?*, pages 10/1–16, 1996.

[7] J. S. Forrest, S. J. Hodge, I. Owen, and G. D. Padfield. Towards fully simulated ship-helicopter operating limits: The importance of ship airwake fidelity. In *64th Annual Forum Proceedings - American Helicopter Society*, volume 1, pages 339–351. American Helicopter Society, 2008.

[8] D.M. Roper, I. Owen, G.D. Padfield, and S.J. Hodge. Integrating CFD and piloted simulation to quantify ship-helicopter operating limits. *Aeronautical Journal*, 110(1109):419–428, 2006.

[9] D. Howe, R. Toffoletto, and J. Blackwell. Helicopter-ship on deck simulation - recent advances and future directions. In *American Helicopter Society International - 6th Australian Pacific Vertiflite Conference on Helicopter Technology and International Helicopter Safety Team South Pacific Regional Conference 2007*, pages 33–39, 2007.

[10] S. J. Newman. The safety of shipborne helicopter operation. *Aircraft Engineering and Aerospace Technology*, 76(5):487–501, 2004.

[11] S. J. Newman. The phenomenon of helicopter blade sailing. *Proceedings of the Institution of Mechanical Engineers*, 213G:347–363, 1999.

[12] S. J. Newman. *An Investigation into the Phenomenon of Helicopter Blade Sailing.* PhD thesis, Department of Aeronautics and Astronautics, University of Southampton, 1995.

[13] T. C. Porteous. Commerical Chinook - first year of operations. In *Proceedings of the 26th Symposium of the Society of Experimental Test Pilots*, 1982.

[14] Anonymous. 107/H-46 tunnel strike. Technical report, Boeing Vertol Company, Interoffice Memorandum #8-7930-0-366, April 1983.

[15] L. L. Trick. H-46/cv engage/disengage DI test. Technical report, NAVAIRTESTCEN Project Test Plan, Naval Air Test Center, Patuxent River, MD, August 1983.

[16] W. W. Scheffler. H-46 tunnel strike mishap data. Technical report, Naval Air Safety Report#3750, April 1994.

[17] J. A. Keller. *Analysis and control of the transient aeroelastic response of rotors during shipboard engagement and disengagement operations.* PhD thesis, The Pennsylvannia State University, 2001.

[18] M. A. P. Willmer. The motion of helicopter blades at low rotor speeds in high winds. Technical Report No. Naval 181, RAE TM, 1963.

[19] K. W. Burton. Blade Sailing. Technical Report GEN/DYN/146N, Westland Helicopters Dynamics Department, 1978.

[20] S. P. King. An Analaytical Investigation of Blade Sailing. Technical Report GEN/DYN/214N, Westland Helicopters Dynamics Department, 1981.

[21] P.F. Leone. Analytic correlation with mishap report of a CH-46D aft rotor blade tunnel strike induced by a wind flow up through the aft rotor disk during a startup operation while shipboard at sea. Interoffice Memo 8-7450-PFL-06, Boeing Vertol Company, 1982.

[22] V. A. Pavlov, S. A. Mikhaliov, and E. I. Nikolaev. Approach of coaxial main rotor blades during startup on a ship deck. *Soviet Aeronautics*, 32(1):30–34, 1989.

[23] N. Sezor-Uzol, A. Sharma, and L. N. Long. Computational fluid dynamics simulations of ship airwake. *Proceedings of the Institution of Mechanical Engineers, Part G (Journal of Aerospace Engineering)*, 219(G5):369–392, 2005.

[24] C. H. Wilkinson, S. J. Zan, N. E. Gilbert, and J. D. Funk. Modelling and simulation of ship airwakes for helicopter operations - a collaborative venture. In *Fluid Dynamics Problems of Vehicles Operating Near or in the Air-Sea Interface*, Amesterdam, The Netherlands, October 5-8 1998. NATO RTO Applied Vehicle Technology Panel (AVT).

[25] S. J. Newman. A theoretical model for predicting the blade sailing behaviour of a semi-rigid rotor helicopter. *Vertica*, 14(4):531–544, 1990.

[26] D.W. Hurst and S. J. Newman. Wind tunnel measurements of ship induced turbulence and the predictions of helicopter rotor blade response. *Vertica*, 12(3):267–278, 1988.

[27] D.W. Hurst and S. J. Newman. Wind tunnel measurements of ship induced turbulence and the predictions of helicopter rotor blade response. In *Proceedings of the 11th European Rotorcraft Forum*, number 99, 1985.

[28] W. P. Jr. Geyer, E. C. Smith, and J. A. Keller. Aeroelastic analysis of transient blade dynamics during shipboard engage/disengage operations. *Jounral of Aircraft*, 35(3):445–453, 1998.

[29] C.L. Bottasso and O.A. Bauchau. Multibody modeling of engage and disengage operations of helicopter rotors. *Journal of the American Helicopter Society*, 46(4), 2001.

[30] M. P. Jones and S. J. Newman. A method of reducing blade sailing through the use of trailing edge flaps. In *63rd Annual Forum Proceedings - American Helicopter Society*, volume 1, pages 411–422. American Helicopter Society, 2007.

[31] C. H. Wilkinson, M. F. Roscoe, and G. M. VanderVliet. Determining fidelity standards for the shipboard launch and recorevy task. In *AIAA Modelling and Simulation Technologies Conference and Exhibit*, Montreal, Canada, 6-9 August 2001. AIAA.

[32] S. A. Polsky and Bruner C. W. S. Time-accurate computational simulations of an lha ship airwake. In *18th AIAA Applied Aerodynamics Conference*, Denver, CO, 14-17 August 2000. AIAA.

[33] S. A. Polsky. A computational study of unsteady ship airwake. In *40th AIAA Aerospace Sciences Meeting and Exhibit*, Reno, Nevada, 14-17 January 2002. AIAA.

[34] W. H. Daley. Flow visualization of the airwake around a model of a tarawa class lha in a simulated atmospheric boundary layer. Master's thesis, Naval Postgraduate School, 1988.

[35] M. K. Johns. Flow visualization of the airwake around a model of a dd-963 class destroyer in a simulated atmospheric boundary layer. Master's thesis, Naval Postgraduate School, 1988.

[36] J. V. Healey. Establishing a database for flight in the wakes of structures. *Journal of Aircraft*, 29(4):559–564, 1992.

[37] S. J. Zan and E. A. Garry. Wind tunnel measurements of the airwake behind a model of a generic frigate. Technical Report LTR-AA-13, NRC-CNRC (IAR), 1994.

[38] S. J. Zan, G. F. Syms, and B. T. Cheney. Analysis of patrol frigate air wakes. In *NATO RTO Symposium on Fluid Dynamics Problems of Vehicles Operating near or in the Air-Sea Interface*, Amesterdam, The Netherlands, 1998.

[39] S. J. Zan. Surface flow topology for a simple frigate shape. *Canadian Aeronautics and Space Journal*, 47(1):33–43, 2001.

[40] M. J. Guillot and M. A. Walker. Unsteady analysis of the air wake over the lpd-17. In *18th AIAA Applied Aerodynamics Conference*, Denver, CO, 14-17 August 2000. AIAA.

[41] A. Taghizad, C. Verbeke, and A. Desopper. Aerodynamic perturbations encountered by a helicopter landing on a ship - effects on the helicopter flight dynamics. In *Symposium on Fluid Dynamics Problems of Vehicles Operating near or in the Air-Sea Interface*, Amesterdam, The Netherlands, October 5-8 1998. NATO RTO Applied Vehicle Technology Panel (AVT).

[42] Valuev N. D. Maslov, L. A. and A. V. Zharinov. The experience of aerodynamic disturbances research behind an aircraft-carrier ship with elements for safe operation of ship-based aircraft. In *Symposium on Fluid Dynamics Problems of Vehicles Operating near or in the Air-Sea Interface*, Amesterdam, The Netherlands, October 5-8 1998. NATO RTO Applied Vehicle Technology Panel (AVT).

[43] A. S. Wall, S. J. Zan, R. G. Langlois, and F. F. Afagh. A numerical model for studying helicopter blade sailing in an unsteady airwake. In *RTO AVT Symposium on "Flow-Induced Unsteady Loads and the Impact on Military Applications*, 2005.

[44] A. S. Wall. *A Discrete Approach to Modelling Helicopter Blade Sailing.* PhD thesis, Carleton University, Department of Mechanical and Aerospace Engineering, 2008.

[45] J. C. Ball and W. R. White. H-46 dynamic interface tests aboard USS GUAM (LPH-9). NAVAIRTESTCEN Technical report. Technical Report RW-28R-83, NAVAIR, 1984.

[46] S. J. Zan. Experimental determination of rotor thrust in a ship airwake. *Journal of American Helicopter Society*, 47(2):100–114, 2002.

[47] R. G. Lee and S. J. Zan. Unsteady aerodynamic loading on a helicopter fuselage in a ship airwake. *Journal of American Helicopter Society*, 49(2):149–159, 2004.

[48] L. N. Long, J. Liu, and A. Modi. Higher order accurate solutions of ship airwake flow fields using parallel computers. In *Symposium on Fluid Dynamics Problems of Vehicles Operating near or in the Air-Sea Interface*, Amesterdam, The Netherlands, October 5-8 1998. NATO RTO Applied Vehicle Technology Panel (AVT).

[49] J. Liu and L. N. Long. Higher order accurate ship airwake predictions for the helicopter-ship interface problem. In *54$^{\text{th}}$ Annual Forum Proceedings - American Helicopter Society*, volume 1, pages 58–70. American Helicopter Society, 1998.

[50] K. Hao, H. Chengjian, and D. Carico. Modeling and simulation of rotor engagement and disengagement during shipboard operations. In *60th Annual Forum Proceedings - American Helicopter Society*, pages 315–324. American Helicopter Society, Jun 7-10 2004.

[51] S. J. Newman. The verification of a theoretical helicopter rotor blade sailing method by means of windtunnel testing. *Aeronautical Journal*, 99:41–51, 1995.

[52] W. P. Jr. Geyer, E. C. Smith, and J. Keller. Validation and application of a transient aeroelastic analysis for shipboard engage/disengage operations. In *55$^{\text{th}}$ Annual Forum Proceedings - American Helicopter Society*, pages 152–167. American Helicopter Society, Jun 4-6 1996.

[53] J.A. Keller and E.C. Smith. Analysis and control of the transient shipboard engagement behavior of rotor systems. In *55th Annual Forum Proceedings - American Helicopter Society*, pages 1064–1079. American Helicopter Society, May 25-27 1999.

[54] D.H. Hodges and E.H. Dowell. Nonlinear equations of motion for the elastic bending and torsion of twisted nonuniform rotor blades. Technical note, Ames Research Center, NASA and U.S. Army Air Mobility R&D Laboratory, National Aeronautics and Space Administration, Washington, D.C. 20546, December 1974.

[55] O. A. Bauchau. *DYMORE User's and Theory Manual.* Georgia Institute of Technology.

[56] D. A. Peters and W. M. Cao. Finite state induced flow models part i: two-dimensional thin airfoil. *Journal of Aircraft*, 32(2):313–322, 1995.

[57] G. E. Hurley, C. W. Pittman, and L. L. Trick. HH-46E/CV-64 rotor engage/disengage test report of test results. Technical Report RW-55R-84, NAVAIRTESTCEN, 1984.

[58] J. A. Keller and E. C. Smith. Experimental and theoretical correlation of helicopter rotor blade-droop stops impacts. *Journal of Aircraft*, 36(2):443–450, 1999.

[59] J. SEDDON and S. Newman. *BASIC HELICOPTER AERODYNAMICS.* AIAA Education Series. AIAA, second edition, 2001.

[60] R. Derham, D. Weems, M. B. Mathew, and R. Bussom. The design evolution of an active materials rotor. In *AHS 57th Annual Forum.* The Vertical Flight Society, The American Helicopter Society, 9-11 May 2001.

[61] H. S. Tzou, H. J. Lee, and S. M. Arnold. Smart materials, precision sensors/actuators, smart structures, and structronic. *Mechanics of Advanced Materials and Structures*, 11(4-5):367–393, 2004.

[62] Y. Chen, V. Wickramasinghe, and D. G. Zimick. Development of smart structure systems for helicopter vibration and noise control. *Transactions of the Canadian Society for Mechanical Engineering*, 31(1):39–56, 2007.

[63] E. W. Aiken, R. A. Ormiston, and L. A. Young. Future Directions in Rotorcraft Technology at Ames Research Center. Technical Report 20000119051, NASA Ames Research Center, 2000.

[64] A.-M.R. McGowan, W.K. Wilkie, R.W. Moses, R.C. Lake, J. Pinkerton Florance, C.D. Weiseman, M.C. Reaves, B.K. Taleghani, P.H. Mirick, and M.L. Wilbur. Aeroservoelastic and structural dynamics research on smart structures conducted at NASA Langley Research Center. In *Proceedings of the SPIE - The International Society for Optical Engineering*, volume 3326, pages 188–201, 1998.

[65] V. Giurgiutiu. Review of smart-materials actuation solutions for aeroelastic and vibration control. *Journal of Intelligent Material Systems and Structures*, 11(7):525–544, 2000.

[66] Ferroelectrics Standards Committe of the IEEE Ultrasonics and Frequency Control Society. IEEE standard on piezoelectricity-ANSI/IEEE Standard 176-1987. In *KEY PAPERS IN PHYSICS - PIEZOELECTRICITY*. The American Institute of Physics, 1992.

[67] A.A. Bent and N.W. Hagood. Piezoelectric fiber composites with interdigitated electrodes. *Journal of Intelligent Material Systems and Structures*, 8(11):903–919, 1997.

[68] X. Kornmann and C. Huber. Microstructure and mechanical properties of pzt fibres. *Journal of the European Ceramic Society*, 24(7):1987–1991, 2004.

[69] W.K. Wilkie, R.G. Bryant, J.W. High, R.L. Fox, R.F. Hellbaum, Jr. Jalink, A., B.D. Little, and P.H. Mirick. Low-cost piezocomposite actuator for structural control applications. In *Proceedings of the SPIE - The International Society for Optical Engineering, Smart Structures and Materials 2000: Industrial and Commercial Applications of Smart Structures Technologies*, volume 3991, pages 323–334. SPIE-Int. Soc. Opt. Eng, 2000.

[70] J. W. High and W. K. Wilkie. Method of Fabricating NASA-Standard Macro-Fibre Composite Piezoelectric Actuators. Technical Report NASA/TM-2003-212427, ARL-TR-2833, NASA Langley Research Center and the U.S Army Research Laboratory, 2003.

[71] C. E. S. Cesnik, H. R. Last, and C. A. Martin. A framework for morphing capability assessment. In *Proceedings of the* 45^{th} *AIAA/ASME/ASCHE/ASC structures, structural dynamics and materials conference*, pages 1582–1592, Palm Springs, CA, 19-22 April 2004. AIAA.

[72] H. Janocha, editor. *Adaptronics and Smart Structures, Basics, Materials, Design, and Applications.* Springer-Verlag, first edition, 1999.

[73] A.J. duPlessis and N. W. Hagood. Modeling and experimental testing of twist actuated single cell composite beams for helicopter rotor blade control. AMSL 96-1, Massachusetts Institute of Technology, 1996.

[74] L. W. Rehfield. Design analysis methodology for composite rotor blades. In *Proceedings of the Seventh DoD/NASA Conference on Fibrous Composites in Structural Design*, pages 17–20, Denver, Colorado, 1985.

[75] V. Berdichevsky, E. Armanios, and A. Badir. Theory of anisotropic thin-walled closed-cross-section beams. *Composites Engineering*, 2:411–432, Nov 1992.

[76] Ashraf. M. Badir. *Analysis of advanced thin-walled composite structures.* PhD thesis, Georgia Institute of Technology, 1992.

[77] V.L. Berdichevsky. On the energy of an elastic rod. *PMM*, 45:518–529, 1982.

[78] C.E.S. Cesnik and S. Shin. On the modeling of integrally actuated helicopter blades. *International Jounral of Solids and Structures*, 38:1765–1789, 2001.

[79] C.E.S. Cesnik and S. Shin. On the twist performance of a multiple-cell active helicopter blade. *Smart Materials and Structures*, 10:53–61, 2001.

[80] C.E.S. Cesnik and S. Shin. Structural analysis for designing rotor blades with integral actuators. In *Proc. 39th AIAA Conf. on structures, structural dynamics and materials*, number 2107, Long Beach, CA, 20-23 April 1998. AIAA.

[81] M. J. Patil and E. R. Johnson. Cross-sectional analysis of anisotropic, thin-walled, closed-section beams with embedded strain actuation. In *Proceedings of 46th AIAA/ASME/ASCE/AHS/ASC structures, structural dynamics and materials conference*, Austin, Texas, April 2005. AIAA.

[82] C.E.S. Cesnik and D.H. Hodges. VABS: a new concept for composite rotor blade cross-sectional modeling. *Journal of the American Helicopter Society*, 42(1):27–38, January 1997.

[83] C.E.S. Cesnik, V.G. Sutyrin, and D.H. Hodges. A refined composite beam theory based on the variational-asymptotic method. In *Proceedings of the 34th Structures, Structural Dynamics, and Materials Conference*, number 93-1616, pages 2710 – 2720, La Jolla, California, April 1993. AIAA.

[84] B. Popescu and D. H. Hodges. On asymptotically correct Timoshenko-like anisotropic beam theory. *International Journal of Solids and Structures*, 37:535–558, 2000.

[85] C. E. S. Cesnik and M. Ortega-Morales. Active beam cross-sectional modeling. *Journal of Intelligent Material Systems and Structures*, 12(7):483–496, 2001.

[86] C. E. S. Cesnik and R. Palacios. Modeling piezocomposite actuators embedded in slender structures. In *Proceedings of the* 44^{th} *AIAA/ASME/ASCHE/AHS structures, structural dynamics and materials conference*, Norfolk, Virginia, 7-10 April 2003.

[87] W. Yu. *VABS Homepage.* Utah State University.

[88] W. Yu, D. H. Hodges, and V. V. Volovoi. Asymptotic construction of reissner-like composite plate theory with accurate strain recovery. *International Journal of Solids and Structures*, 39(20):5185–5203, 2002.

[89] W. Yu and D. H. Hodges. Mathematical construction of an engineering thermopiezoelastic model for smart composite shells. *Smart Materials and Structures*, 14(1):43–55, 2005.

[90] Carlos. Eduardo. Stolf. Cesnik. *Cross-sectional analysis of initially twisted and curved composite beams.* Ph.d., Georgia Institute of Technology, 1994.

[91] V.V. Volovoi, D.H. Hodges, C.E.S. Cesnik, and B. Popescu. Assessment of beam modeling methods for rotor blade application. *Mathematical and Computer Modelling*, 33:1099–1112, 2001.

[92] D.H. Hodges and V.V. Volovoi. Theory of anisotropic thin-walled beams. *Journal of Applied Mechanics*, 67:453–459, September 2000.

[93] D.H. Hodges and V.V. Volovoi. Single- and multi-celled composite thin-walled beams. *AIAA Journal*, 40(5):960–965, May 2002.

[94] A. N. Palazotto and S. T. Dennis. *Nonlinear Analysis of Shell Structures.* AIAA, 1992.

[95] F. Khouli, R. G. Langlois, and F. F. Afagh. Analysis of active closed-cross section slender beams based on asymptotically correct thin-wall beam theory. *Smart Materials and Structures*, 16(1):221–229, 2007.

[96] M. Mistry, F. Gandhi, and R. Chandra. Twist control of an I-beam through Vlasov bimoment actuation. In *Proceedings of the* 49^{th} *AIAA/ASME/ASCHE/AHS/ASC structures, structural dynamics and materials conference*, Schaumburg, IL, April 2008. AIAA.

[97] Gjelsvik A. *The Theory of Thin Walled Bars.* JOHN WILEY & SONS, first edition, 1981.

[98] V.V. Volovoi, D.H. Hodges, V.L. Berdichevsky, and V.G. Sutyrin. Asymptotic theory for static behavior of elastic anisotropic I-beams. *International Journal of Solids and Structures*, 36:1017–1043, 1999.

[99] F. Khouli, J. Griffiths, R. G. Langlois, and F. F. Afagh. Actuation of slender thin-wall anisotropic open cross-section beams based on asymptotically-correct Vlasov. *Submiited to the Journal of Intelligent Material Systems and Structures*, 2008.

[100] Rafael Palacios. *Asymptotic models for integrally-strained slender structures for high-fidelity nonlinear aeroelastic analysis.* PhD thesis, University of Michigan, April 2005.

[101] D. H. Hodges, Atilgan A. R., C. E. S. Cesnik, and M. V. Fulton. On a simplified strain energy function for geometrically nonlinear behaviour of anisotropic beams. *Composites Engineering*, 2(5-7):513–526, 1992.

[102] W. Yu, .V.V. Volovoi, D.H. Hodges, and X. Hong. Validation of the variational asymptotic beam sectional analysis (VABS). *AIAA Journal*, 40(10):2105–2113, 2002.

[103] CIMNE. *GiD The personal pre and post processor.* International Center for Numerical Methods in Engineering.

[104] D. H. Hodges, V. V. Volovoi, V. L. Berdichevsky, and V. G. Sutyrin. Dynamic dispersion curves for non-homogeneous, anisotropic beams with cross-sections of arbitrary geometry. *Journal of Sound and Vibration*, 215(5):1101–1120, 1998.

[105] W.1 Yu, D.H. Hodges, V.V. Volovoi, and E.D. Fuchs. A generalized vlasov theory for composite beams. *Thin-Walled Structures*, 43(9):1493–1511, 2005.

[106] W. Yu and D. H. Hodges. Elasticity solutions versus asymptotic sectional analysis of homogeneous, isotropic, prismatic beams. *Journal of Applied Mechanics*, 71(1):15–23, 2004.

[107] D. B. Weems, D. M. Anderson, Mathew. M. B., and R. C. Bussom. A large-scale active-twist rotor. In *60$^{\text{th}}$ Annual Forum Proceedings - American Helicopter Society*, volume 1, pages 579–590. American Helicopter Society, 2004.

[108] D. H. Hodges, S. Hossein, and R. A. Ormiston. Development of nonlinear beam elements for rotorcraft comprehensive analyses. *Journal of the American Helicopter Society*, 52(1):36–48, 2007.

[109] W. Yu, Liao L., D. H. Hodges, and V.V. Volovoi. Theory of initially twisted, composite, thin-walled beams. *Thin-Walled Structures*, 48(8):1296–1311, 2005.

[110] R. Sitikantha. *A Variational Asymptotic Methodology of Smart Slender Structure Modelling.* PhD thesis, Utah State University, 2007.

[111] D.H. Hodges and R.A. Ormiston. Stability of elastic bending and torsion of uniform cantilever rotor blades in hover with variable structural coupling. Technical note, Ames Research Center, NASA and U.S. Army Air Mobility R&D Laboratory, National Aeronautics and Space Administration, Washington, D.C. 20546, April 1976.

[112] D.H. Hodges and M.J. Patil. Correlation of geometrically-exact beam theory with the Princeton data. *Journal of the American Helicopter Society*, 49(3):357–360, July 2005.

[113] E. H. Dowell, J. Traybar, and D. H. Hodges. An experimental-theoretical correlation study of non-linear bending and torsion deformations of a cantilever beam. *Journal of Sound and Vibration*, 50(4):533–544, 1977.

[114] W. Johnson. Rotorcraft aerodynamics models for a comprehensive analysis. In *Proceedings of the 54th Annual Forum of American Helicopter Society*, volume 1, pages 71–93, 1998.

[115] W. Johnson. Rotorcraft dynamics models for a comprehensive analysis. In *Proceedings of the 54th Annual Forum of American Helicopter Society*, volume 1, pages 452–471, 1998.

[116] O.A. Bauchau, C.L. Bottasso, and Y.G. Nikishkov. Modeling rotorcraft dynamics with finite element multibody procedures. *Mathematical and Computer Modelling*, 33(10-11):1113–1137, 2001.

[117] O. A. Bauchau and D. H. Hodges. Analysis of nonlinear multibody systems with elastic couplings. *Multibody System Dynamics*, 3(2):163–188, 1999.

[118] S. Ozbay, O. Bauchau, D. S. Dancila, and E. A. Armanios. Extension-twist coupling optimization in composite rotor blades. In *Proceedings of the* 46^{th} *AIAA/ASME/ASCE/AHS/ASC structures, structural dynamics and materials conference*, Austin, Texas, 18 - 21 April 2005.

[119] A. S. Hopkins and R. A. Ormitson. An examination of selected problems in rotor blade structural mechanics and dynamics. In *Proceedings of the* 59^{th} *American Helicopter Society Anuual Forum*, Phoenix,AZ, MAY 2003. American Helicopter Society(AHS).

[120] G.S. Bir. Structural dynamics verification of rotorcraft comprehensive analysis system(RCAS). Technical report, National Renewable Energy Laboratory, 1817 Cole Boulevard, Golden, Colorado, 80401-3393, Febraury 2005.

[121] D. Han, W. Yu, and R. Sitikantha. A geometrically exact active beam theory for multibody dynamics simulation. *Smart Materials and Structures*, 16(4):1136–1147, 2007.

[122] S-J. Shin and C. E. S. Cesnik. Forward flight response of the active twist rotor for helicopter vibration reduction. In *Proceedings of the* 42^{th} *AIAA/ASME/ASCHE/AHS structures, structural dynamics and materials conference*, Seattle, WA, April 2001. AIAA.

[123] O. A. Bauchau and H. Liu. On the modeling of hydraulic components in rotorcraft systems. *Journal of the American Helicopter Society*, 51(2):175–184, 2006.

[124] Dipartimento di Ingegneria Aerospaziale. *MBDyn - MultiBody Dynamics Software.* Politecnico di Milano.

[125] D.A. Danielson and D.H. Hodges. Nonlinear beam kinematics by decomposition of the rotation tensor. *Journal of Applied Mechanics*, 54:258–262, 1987.

[126] D.A. Danielson and D.H. Hodges. A beam theory for large global rotation, moderate local rotation. *Journal of Applied Mechanics*, 55:179–184, 1988.

[127] A. E. H. Love. *A Treatise of the Mathematical Theory of Elasticity.* Dover Publications, 1944.

[128] J. G. Simmonds. *A Brief on Tensor Analysis.* New York : Springer-Verlag, 2 edition, 1994.

[129] Y. M. Haddad. *Mechanical Behaviour of Engineering Materials, Volume 1.* Kluwer Academic Publishers, 2001.

[130] R. W. Ogden. *Non-Linear Elastic Deformations.* E. Horwood, Halsted Press, 1984.

[131] C. E. S. Cesnik, D. H. Hodges, and V. G. Sutyrin. Cross-sectional analysis of composite beams including large initial twist and curvature effects. *AIAA Journal*, 34(9):1913–1920, 1996.

[132] B. Popescu and D. H. Hodges. Asymptotic treatment of the trapeze effect in finite element cross-sectional analysis of composite beams. *International Journal of Non-Linear Mechanics*, 34(4):709–721, 1999.

[133] D. H. Hodges. A mixed variational formulation based on exact intrinsic equations for dynamics of moving beams. *Internataional Journal of Solids and Structures*, 26(11):1253–1273, 1990.

[134] D. A. Peters and A. P. Izadpanah. hp-version finite elements for the space-time domain. *Computational Mechanics*, 3:73–88, 1988.

[135] D. H. Hodges. Geometrically exact, intrinsic theory for dynamics of curved and twisted anisotropic beams. *AIAA Journal*, 41(6):1131–1137, 2003.

[136] M. Paz and W. Leigh. *Structural dynamics : theory and computation.* Kluwer Academic Publishers, 2004.

[137] A. A. Shabana. *Computational Dynamics.* Wiley-Interscience, 2001.

[138] C.L. Bottasso. *Notes on unilateral contact modeling in multibody dynamics.* Politecnico di Milano.

[139] O. A. Bauchau and N. K. Kang. A multibody formulation for helicopter structural dynamic analysis. *Journal of American Helicopter Society*, 38(2):3–14, 1993.

[140] C. L. Bottasso and L. Trainelli. An attempt at the classification of energy decaying schemes for structural and multibody dynamics. *Multibody System Dynamics*, 12(2):173185, 2004.

[141] J. I. Gobat and M. A. Grosenbaugh. Application of the generalized-α method to the time integration of the cable dynamics equations. *Computer Methods in Applied Mechanics and Engineering*, 190(37-38):4817–4829, 2001.

[142] J. I. Gobat, M. A. Grosenbaugh, and Triantofyllou. Generalized-α time integration solutions for hanging chain dynamics. Technical report, Woods Hole Oceanographic Institution, Woods Hole, MA 02543, 2002.

[143] J. Chung and G. M. Hulbert. Time integration algorithm for structural dynamics with improved numerical dissipation: the generalized-α method. *Journal of Applied Mechanics*, 60(2):371–375, 1993.

[144] K. E. Jansen, C. H. Whiting, and G. M. Hulbert. A genralized-α method for integrating the filtered Navier-Stokes equations with a stabilized finite element method. *Computer Methods in Applied Mechanics and Engineering*, 190(3-4):305–319, 2000.

[145] M. J. Patil and D. H. Hodges. Flight dynamics of highly flexible flying wings. *Journal of Aircraft*, 43(6), 2006.

[146] O.A. Bauchau and N.J. Theron. Energy decaying scheme for non-linear beam models. *Computer Methods in Applied Mechanics and Engineering*, 134(1-2):37–56, 1996.

[147] J. J. Epps and R. Chandra. Natural frequencies of rotating composite beams with tip sweep. *Journal of the American Helicopter Society*, 41(1):29–36, 1996.

[148] D. H. Hodges, X. Shang, and C. E. S Cesnik. Finite element solution of nonlinear intrinsic equations for curved composite beams. *Journal of the American Helicopter Society*, 41(4):313–321, 1996.

[149] T. J. R. Hughes. *The finite element method: linear static and dynamic finite element analysis.* Prentice-Hall, 1987.

[150] J. A. Keller and E. C. Smith. Experimental and theoretical correlation of helicopter rotor blade-droop stop impacts. *Journal of Aircraft*, 36(2), 1999.

[151] F. Khouli, F. F. Afagh, and R. G. Langlois. Application of the first order generalized-α method to the solution of an intrinsic geometrically exact model of rotor blade system. *Journal of Computational and Nonlinear Dynamics*, 4(1):011006(1)–011006(12), 2008.

[152] S. Leyendecker, J.E. Marsden, and M. Ortiz. Variational integrators for constrained dynamical systems. *Zeitschrift fur Angewandte Mathematik und Mechanik*, 88(9):677–708, 2008.

[153] R. L. Bielawa. *Rotary wing structural dynamic and aeroelasticity.* AIAA, 1992.

[154] A.I. Jose, J.G. Leishman, and J.D. Baeder. Unsteady aerodynamic modeling with time-varying free-stream mach numbers. *Journal of the American Helicopter Society*, 51(4):299–318, 2006.

[155] J. G. Leishman. Unsteady aerodynamics of airfoils encountering traveling gusts and vortices. *Journal of Aircraft*, 34(6):719–729, 1997.

[156] C. C. Critzos, H. H. Heyson, and R. W. Boswinkle. Aerodynamic characteristics of NACA0012 airfoil section at angles of attack from 0° to 180°. Technical Report NACA TN-3361, National Advisory Committee for Aeronautics, 1955.

[157] J. G. Leishman. *Principles of Helicopter Aerodynamics*. Cambridge University Press, 2002.

[158] D.A. Peters, M.-c.A Hsieh, and A. Torrero. A state-space airloads theory for flexible airfoils. *Journal of the American Helicopter Society*, 52(4):329–342, 2007.

[159] B. G. van der Wall and J. G. Leishman. On the influence of time-varying flow velocity on unsteady aerodynamics. *Journal of the American Helicopter Society*, 39(4):25–36, 1994.

[160] T. Theodorsen. General theory of aerodynamic instability and the mechanism of flutter. Technical Report NACA 496, Langley Memorial Aeronautical Laboratory, National Advisory Committee for Aeronautics, 1934.

[161] J. G. Leishman and T. S. Beddoes. A semi-empirical model for dynamic stall. *Journal of the American Helicopter Society*, pages 3–17, 1989.

[162] S. Gupta and J. G. Leishman. Dynamic stall modelling of the S809 aerofoil and comparison with experiments. *WIND ENERGY*, 9:521547, 2006.

[163] W. Sheng, R.A.McD. Galbraith, and F.N. Coton. A modified dynamic stall model for low mach numbers. In *Proceedings of the* 45^{th} *AIAA Aerospace Sciences Meeting and Exhibit*, Reno, Nevada, 8 - 11 January 2007. AIAA.

[164] G. K. Hunt. Similarity requirements for aeroelastic models of helicopter rotors. Technical Report CP 1245, Aeronautical Research Council, 1973.

[165] P.P. Friedmann. Aeroelastic scaling for rotary-wing aircraft with applications. *Journal of Fluids and Structures*, 19(5):635–650, 2004.

[166] Freeman Manufacturing & Supply Company. *RenShape 5045®*. http://www.freemansupply.com/RenShape5045Polyur.htm.

[167] M.S. Selig, J.J. Guglielmo, A.P. Broeren, and P. Giguere. *Summary of Low-Speed Airfoil Data*, volume 1. SoarTech Publications, Virginia Beach, Virginia, USA, 1995.

[168] J. P. Rodgers. *Development of an integral twist-actuated rotor blade for individual blade control.* PhD thesis, Massachusetts Institute of Technology (MIT), 1999.

[169] J.P. Rodgers and N.W. Hagood. Design, manufacture and testing of an integral twist-actuated rotor blade. In *Proceedings of the Eighth International Conference on Adaptive Structures Technology*, pages 63–72, 1998.

[170] M. L. Wilbur and M. K. Sekula. The effect of tip geometry on active-twist rotor response. In 31^{st} *European Rotorcraft Forum*, pages 126.1–126.12, 2005.

[171] P. Masarati, Morandini M., J. Riemenschneider, and P. Wierach. Optimal design of an active twist 1:2.5 scale rotor blade. In *Proceedings of the* 31^{st} *European Rotorcraft Forum*, pages 37.1–37.14, 2005.

[172] Smart Material, Advanced Piezo Composites. *MFCs, Engineering Properties.*

[173] B. Gardner. Theoretical physical properties of the A02R1702 composite rotor blade. Technical Report A02-SS-027-1, Boeing Vertol Company, 1977.

[174] C.E.S. Cesnik, S. Shin, and M.L. Wilbur. Dynamic response of active twist rotor blades. *Smart Materials and Structures*, 10(1):62–76, 2001.

[175] F. Khouli, A.S. Wall, F. F. Afagh, R. G. Langlois, and S. J. Zan. Investigation of the active-twist rotor response of various rotor system configurations during shipboard engagement and disengagement operations. In *Proceedings of the 18th International Conference of Adaptive Structures and Technologies*, Ottawa, ON, October 3-5 2007.

[176] A. J. Masys, w. Ren, G. Yang, and B. K. Mukherjee. Piezoelectric strain in lead zirconate titante ceramics as a function of electric field, frequency, and dc bias. *Journal of Applied Physics*, 94(2):1155–1162, 2003.

[177] I. M. Daniel and O. Ishai. *Engineering mechanics of composite materials.* Oxford University Press, 1994.

[178] J. P. Traugott, M. J. Patil, and F. Holzapfel. Nonlinear dynamics and control of integrally actuated helicopter blades. In *Proceedings of the 46th AIAA/ASME/ASCHE/AHS structures, structural dynamics and materials conference*, Austin, TX, April 2005. AIAA.

[179] J. B. Kuipers. *Quaternions and Rotation Sequences.* Princeton University Press, 1998.

Appendix A

A.1 The Plane-Stress Reduced Constants $D^{\alpha\beta\gamma\delta}$

The lamina stiffness matrix $\breve{Q}$ can be found in any introductory composite engineering book like Reference [177] along with its transformation to the global frame

$$\bar{Q} = \mathcal{R}^{\mathrm{T}}(\vartheta)\,\breve{Q}\mathcal{R}(\vartheta) \tag{A.1}$$

where $\mathcal{R}(\vartheta)$ is defined in Eq. 2.28

The reduced 2-D material constants $D^{\alpha\beta\gamma\delta}$ can be written as

$$[D] = [Q^1] - 2[Q^2][Q^3]^{-1}[Q^4] + [Q^4]^{\mathrm{T}}[Q^3]^{-1}[Q^4] \tag{A.2}$$

where

$$
\begin{aligned}
[D] &= \begin{bmatrix} D^{1111} & D^{1122} & D^{1112} \\ D^{1122} & D^{2222} & D^{1222} \\ D^{1112} & D^{1222} & D^{1212} \end{bmatrix} \\
[Q^1] &= \begin{bmatrix} \bar{Q}_{11} & \bar{Q}_{12} & \bar{Q}_{16} \\ \bar{Q}_{12} & \bar{Q}_{22} & \bar{Q}_{26} \\ \bar{Q}_{16} & \bar{Q}_{26} & \bar{Q}_{66} \end{bmatrix} \\
[Q^2] &= \begin{bmatrix} \bar{Q}_{13} & \bar{Q}_{15} & \bar{Q}_{14} \\ \bar{Q}_{23} & \bar{Q}_{25} & \bar{Q}_{24} \\ \bar{Q}_{36} & \bar{Q}_{56} & \bar{Q}_{46} \end{bmatrix} \qquad \text{(A.3)} \\
[Q^3] &= \begin{bmatrix} \bar{Q}_{33} & \bar{Q}_{35} & \bar{Q}_{36} \\ \bar{Q}_{35} & \bar{Q}_{55} & \bar{Q}_{45} \\ \bar{Q}_{36} & \bar{Q}_{45} & \bar{Q}_{44} \end{bmatrix} \\
[Q^4] &= \begin{bmatrix} \bar{Q}_{13} & \bar{Q}_{23} & \bar{Q}_{36} \\ \bar{Q}_{15} & \bar{Q}_{25} & \bar{Q}_{56} \\ \bar{Q}_{14} & \bar{Q}_{24} & \bar{Q}_{46} \end{bmatrix} \qquad \text{(A.4)}
\end{aligned}
$$

A.2 The Shell Energy Per Unit Length Material and Electromechanical Matrices

The material matrices Q, S, and P in Eq. 2.34 are defined in terms of the 2-D material constants corresponding to membrane, bending, and coupling between these two modes $E_e^{\alpha\beta\gamma\delta}$, $E_b^{\alpha\beta\gamma\delta}$, and $E_{eb}^{\alpha\beta\gamma\delta}$ such that [92]

$$
\left\{E_e^{\alpha\beta\gamma\delta}, E_{eb}^{\alpha\beta\gamma\delta}, E_b^{\alpha\beta\gamma\delta}\right\} = \frac{1}{h}\int_{-\frac{h}{2}}^{\frac{h}{2}} D^{\alpha\beta\gamma\delta}\left\{1, \frac{\xi}{h}, \left(\frac{\xi}{h}\right)^2\right\}\, \mathrm{d}\xi \qquad \text{(A.5)}
$$

$$
\begin{aligned}
Q &= \begin{bmatrix} E_e^{1111} & hE_{eb}^{1111} & 2hE_{eb}^{1112} \\ hE_{eb}^{1111} & h^2E_b^{1111} & 2h^2E_b^{1112} \\ 2hE_{eb}^{1112} & 2h^2E_b^{1112} & 4h^2E_b^{1212} \end{bmatrix} \\
S &= h\begin{bmatrix} E_e^{1112} & hE_{eb}^{1112} & 2hE_{eb}^{1212} \\ E_e^{1122} & hE_{eb}^{1122} & 2hE_{eb}^{1222} \\ hE_{eb}^{1122} & h^2E_b^{1122} & 2h^2E_b^{1222} \end{bmatrix} \\
P &= h\begin{bmatrix} E_e^{1212} & E_e^{1222} & hE_{eb}^{1222} \\ E_e^{1222} & E_e^{2222} & hE_{eb}^{2222} \\ hE_{eb}^{1222} & hE_{Eb}^{2222} & h^2E_b^{2222} \end{bmatrix}
\end{aligned} \tag{A.6}
$$

The electromechanical matrices H and G represent the coupling between the piezoelectric strains and the mechanical strains such that

$$
H = \begin{bmatrix} Z_1^a \\ Z_1^a/h \\ W_2^a/h \end{bmatrix} \quad G = \begin{bmatrix} Z_2^a/2 \\ Z_3^a \\ W_3^a/h \end{bmatrix} \tag{A.7}
$$

where

$$
\begin{aligned}
Z_1^a &= \int_{-\frac{h}{2}}^{\frac{h}{2}} [D^{1111}\grave{d}_{111} + 2D^{1112}\grave{d}_{112} + D^{1122}\grave{d}_{122}]E_1 \, \mathrm{d}\xi \\
Z_2^a &= \int_{-\frac{h}{2}}^{\frac{h}{2}} [2D^{1112}\grave{d}_{111} + 4D^{1212}\grave{d}_{112} + 2D^{1222}\grave{d}_{122}]E_1 \, \mathrm{d}\xi \\
Z_3^a &= \int_{-\frac{h}{2}}^{\frac{h}{2}} [D^{1122}\grave{d}_{111} + D^{2222}\grave{d}_{112} + 2D^{1222}\grave{d}_{122}]E_1 \, \mathrm{d}\xi\xi
\end{aligned} \tag{A.8}
$$

$$W_1^a = \int_{-\frac{h}{2}}^{\frac{h}{2}} [D^{1111}\grave{d}_{111} + 2D^{1112}\grave{d}_{112} + D^{1122}\grave{d}_{122}]E_1\xi \, \mathrm{d}\xi$$
$$W_2^a = \int_{-\frac{h}{2}}^{\frac{h}{2}} [2D^{1112}\grave{d}_{111} + 4D^{1212}\grave{d}_{112} + 2D^{1222}\grave{d}_{122}]E_1\xi \, \mathrm{d}\xi$$
$$W_3^a = \int_{-\frac{h}{2}}^{\frac{h}{2}} [D^{1122}\grave{d}_{111} + D^{2222}\grave{d}_{112} + 2D^{1222}\grave{d}_{122}]E_1\xi \, \mathrm{d}\xi \tag{A.9}$$

and

$$\begin{bmatrix} \grave{d}_{111} \\ \grave{d}_{122} \\ \grave{d}_{112} \end{bmatrix} = \mathcal{R}(\vartheta) \begin{bmatrix} d_{111} \\ d_{122} \\ d_{112} \end{bmatrix} \tag{A.10}$$

A.3 Convergence of the Displacement Field of Closed Cross-Sections

As the result of a third perturbation of the displacement field in Eq. 2.84, the resulting strain field becomes

$$
\begin{aligned}
\gamma_{11} &= \underbrace{u_1'}_{\epsilon} - \underbrace{x_\alpha u_\alpha''}_{\epsilon} + \underbrace{w_{1,1}}_{\epsilon\left(\frac{a}{\ell}\right)} + \underbrace{\tilde{w}_{1,1}}_{?\equiv\left[\epsilon\left(\frac{a}{\ell}\right)^2\left(\frac{a}{h}\right)\right]} \\
2\gamma_{12} &= \underbrace{r_n\theta'}_{\epsilon} + \underbrace{\hat{w}_{2,1}}_{\epsilon\left(\frac{a}{\ell}\right)\left(\frac{a}{h}\right)} + \underbrace{w_{1,2}}_{\epsilon} + \underbrace{w_{2,1}}_{\epsilon\left(\frac{a}{\ell}\right)} + \underbrace{\tilde{w}_{1,2}}_{?\equiv\left[\epsilon\left(\frac{a}{\ell}\right)\left(\frac{a}{h}\right)\right]} + \underbrace{\tilde{w}_{2,1}}_{?\equiv\left[\epsilon\left(\frac{a}{\ell}\right)^2\right]} \\
\gamma_{22} &= \underbrace{w_{2,2}}_{\epsilon} + \underbrace{\frac{w_3}{R}}_{\epsilon} + \underbrace{\tilde{w}_{2,2}}_{?\equiv\left[\epsilon\left(\frac{a}{\ell}\right)\right]} + \underbrace{\frac{\tilde{w}_3}{R}}_{?\equiv\left[\epsilon\left(\frac{a}{\ell}\right)\right]} \\
h\rho_{11} &= h\left(\underbrace{x_{3,s}u_2''}_{\epsilon\left(\frac{h}{a}\right)} - \underbrace{x_{2,s}u_3''}_{\epsilon\left(\frac{h}{a}\right)} - \underbrace{r_\tau\theta''}_{\epsilon\left(\frac{h}{a}\right)\left(\frac{a}{\ell}\right)} + \underbrace{\hat{w}_{3,11}}_{\epsilon\left(\frac{a}{\ell}\right)^2} + \underbrace{w_{3,11}}_{\epsilon\left(\frac{a}{\ell}\right)^2\left(\frac{h}{a}\right)} + \underbrace{\tilde{w}_{3,11}}_{?\equiv\left[\epsilon\left(\frac{a}{\ell}\right)^3\left(\frac{h}{a}\right)\right]}\right) \\
h\rho_{12} &= h\left[\frac{1}{4R}\left(\underbrace{r_n\theta'}_{\epsilon\left(\frac{h}{a}\right)} + \underbrace{w_{1,2}}_{\epsilon\left(\frac{h}{a}\right)} + \underbrace{\tilde{w}_{1,2}}_{?\equiv\left[\epsilon\left(\frac{a}{\ell}\right)\right]}\right) - \underbrace{\theta'}_{\epsilon\left(\frac{h}{a}\right)} + \underbrace{\hat{w}_{3,12}}_{\epsilon\left(\frac{a}{\ell}\right)} + \underbrace{w_{3,12}}_{\epsilon\left(\frac{h}{a}\right)\left(\frac{a}{\ell}\right)} + \underbrace{\tilde{w}_{3,12}}_{?\equiv\left[\epsilon\left(\frac{h}{a}\right)\left(\frac{a}{\ell}\right)^2\right]}\right] - \\
&\quad h\left[\frac{3}{4R}\left(\underbrace{\hat{w}_{2,1}}_{\epsilon\left(\frac{a}{\ell}\right)} + \underbrace{w_{2,1}}_{\epsilon\left(\frac{h}{a}\right)\left(\frac{a}{\ell}\right)} + \underbrace{\tilde{w}_{2,1}}_{?\equiv\left[\epsilon\left(\frac{h}{a}\right)\left(\frac{a}{\ell}\right)^2\right]}\right)\right] \\
h\rho_{22} &= h\left[\left(\underbrace{\hat{w}_{3,2}}_{\epsilon} + \underbrace{w_{3,2}}_{\epsilon\left(\frac{h}{a}\right)} + \underbrace{\tilde{w}_{3,2}}_{?\equiv\left[\epsilon\left(\frac{h}{a}\right)\left(\frac{a}{\ell}\right)\right]}\right) - \frac{1}{R}\left(\underbrace{\hat{w}_2}_{\epsilon} + \underbrace{w_2}_{\epsilon\left(\frac{h}{a}\right)} + \underbrace{\tilde{w}_2}_{?\equiv\left[\epsilon\left(\frac{h}{a}\right)\left(\frac{a}{\ell}\right)\right]}\right)\right]_{,2}
\end{aligned}
\tag{A.11}
$$

As reasoned previously, the order of $\tilde{w}_1$ can be determined by requiring that the phantom term in $2\gamma_{12}$ be annihilated. The candidate function is $\tilde{w}_{1,2}$ which implies

$$
\mathcal{O}\left(\tilde{w}_1\right) = \frac{a^3}{\ell h}\epsilon \tag{A.12}
$$

The only leading order terms that are not of order $\mathcal{O}\left(\epsilon\right)$ are those of order $\mathcal{O}\left(\epsilon\frac{a}{\ell}\right)$, which determine the order of the remaining perturbations $\tilde{w}_\alpha$ such as

$$\frac{\mathcal{O}\left(\tilde{w}_\alpha^2\right)}{a^2} = \frac{a\epsilon}{\ell}\frac{\mathcal{O}\left(\tilde{w}_\alpha\right)}{a} \Rightarrow \mathcal{O}(\tilde{w}_\alpha) = \frac{a^2}{\ell}\epsilon \tag{A.13}$$

where cross-terms between the new perturbations and terms of order $\mathcal{O}(\epsilon)$ vanish due to the Euler-Lagrange equations of the latter in the previous cycle.

Examining Eq. A.11 demonstrates that no terms of order $\mathcal{O}\left(\epsilon\right)$ are generated and the displacement field is said to have converged to that order.

A.4 Mathematical Implications of the Constraints on the Displacement Field of Closed Cross-Sections

The first equation of Eq. 2.56 is straight forward since

$$\bar{\rho}_{22} \equiv \bar{\phi}_3 \tag{A.14}$$

which physically implies that the shell bending strain measure is single valued around the contour.

The second constraint follows from realizing that the total elastic displacement v_1 is single valued, so that

$$\oint v_{1,2}\, \mathrm{d}s = \oint \bar{u}_{1,2}\, \mathrm{d}s + \oint w_{1,2}\, \mathrm{d}s = 0 \tag{A.15}$$

with $\oint \bar{u}_{1,2} = 0$, which implies that the axial translation of the rigid body is eliminated from the warping function such as

$$\oint w_{1,2}\, \mathrm{d}s = 0 \tag{A.16}$$

Therefore

$$\oint \bar{\phi}_1 \, \mathrm{d}s = \oint 2\bar{\gamma}_{12} \, \mathrm{d}s = \overbrace{\oint w_{1,2} \, \mathrm{d}s}^{0} + \oint r_n \theta' \, \mathrm{d}s \tag{A.17}$$

The last two constraints are derived from representing the elastic displacements by the warping functions, that is

$$\begin{aligned} v_2 &= \bar{u}_2 x_{2,s} + \bar{u}_3 x_{3,s} \Rightarrow \hat{w}_2 = \bar{u}_2 x_{2,s} + \bar{u}_3 x_{3,s} \\ v_3 &= \bar{u}_2 x_{3,s} - \bar{u}_3 x_{2,s} \Rightarrow \hat{w}_3 = \bar{u}_2 x_{3,s} - \bar{u}_3 x_{2,s} \end{aligned} \tag{A.18}$$

Multiplying the first equation by $\dot{x}_2$ and the second one by $\dot{x}_3$ one can solve for $\bar{u}_2$ and $\bar{u}_3$ to yield

$$\begin{aligned} \bar{u}_2 &= \hat{w}_2 x_{2,s} + \hat{w}_3 x_{3,s} \\ \bar{u}_3 &= \hat{w}_2 x_{3,s} + \hat{w}_3 x_{2,s} \end{aligned} \tag{A.19}$$

where the relation $\left(\frac{\partial x_2}{\partial s}\right)^2 + \left(\frac{\partial x_3}{\partial s}\right)^2 = 1$ has been utilized in deriving Eq. A.19

Differentiating Eq. A.19 with respect to s and integrating around the contour yields

$$\oint \left[\hat{w}_{2,2} x_{2,s} + \hat{w}_2 x_{2,ss} + \hat{w}_{3,2} x_{3,s} + \hat{w}_3 x_{3,ss}\right] \mathrm{d}s = 0 \tag{A.20}$$

$$\oint \left[\hat{w}_{2,2} x_{3,s} + \hat{w}_2 x_{3,ss} - \hat{w}_{3,2} x_{2,s} - \hat{w}_3 x_{2,ss}\right] \mathrm{d}s = 0 \tag{A.21}$$

utilize the last of Eq. 2.25 to rewrite Eq. A.21 as

$$\oint \left[x_{2,s} \left(\hat{w}_{2,2} + \frac{\hat{w}_3}{R} \right) + x_{3,s} \left(\hat{w}_{3,2} - \frac{\hat{w}_2}{R} \right) \right] \mathrm{d}s = 0 \tag{A.22}$$

$$\oint \left[x_{3,s} \left(\hat{w}_{2,2} + \frac{\hat{w}_3}{R} \right) + x_{2,s} \left(\hat{w}_{3,2} - \frac{\hat{w}_2}{R} \right) \right] \mathrm{d}s = 0 \tag{A.23}$$

Recalling Eq. 2.50 followed by integration by parts to yield

$$\oint x_{\alpha,s} \bar{\phi}_{3,2} \, \mathrm{d}s = 0 \Rightarrow \oint x_\alpha \bar{\phi}_3 \, \mathrm{d}s = 0 \tag{A.24}$$

A.5 Material and Geometry Matrices of Single- and Two-Cell Cross-Section

The matrices F and J for a single-cell are given by

$$F = \oint \tilde{F}(s) \, \mathrm{d}s \qquad J = \oint \tilde{J}(s) \, \mathrm{d}s \tag{A.25}$$

where

$$\tilde{F}(s) = -\begin{bmatrix} P_{11}^{-1} & x_2 P_{13}^{-1} & x_3 P_{13}^{-1} & P_{13}^{-1} \\ x_2 P_{13}^{-1} & x_2^2 P_{33}^{-1} & x_2 x_3 P_{33}^{-1} & x_2 P_{33}^{-1} \\ x_3 P_{13}^{-1} & x_2 x_3 P_{33}^{-1} & x_3^2 P_{33}^{-1} & x_3 P_{33}^{-1} \\ P_{13}^{-1} & x_2 P_{33}^{-1} & x_3 P_{33}^{-1} & P_{33}^{-1} \end{bmatrix}$$

$$\tilde{J}(s) = \begin{bmatrix} c_1 & r_n & x_3 c_1 & -x_2 c_1 \\ x_2 c_3 & 0 & x_2 x_3 c_3 & -x_2^2 c_3 \\ x_3 c_3 & 0 & x_3^2 c_3 & -x_2 x_3 c_3 \\ c_3 & 0 & x_3 c_3 & -x_2 c_3 \end{bmatrix} \tag{A.26}$$

For the two-cell case the matrices F and J have the form

$$F^{\text{two-cells}} = \begin{bmatrix} \oint_{1+2} \tilde{F}\, ds & \int_2 \tilde{F}\, ds \\ \int_2 \tilde{F}\, ds & \oint_{2+3} \tilde{F}\, ds \end{bmatrix}$$

$$J^{\text{two-cells}} = \begin{bmatrix} \oint_{1+2} \tilde{J}\, ds \\ \oint_{2+3} \tilde{J}\, ds \end{bmatrix} \tag{A.27}$$

For the three-cell case the matrices F and J have the form

$$
\begin{aligned}
F^{\text{three-cells}} &= \begin{bmatrix} \oint_{1+2} \tilde{F}\, \mathrm{d}s & \int_{2} \tilde{F}\, \mathrm{d}s & \mathbf{0}_{3\times 3} \\ \int_{2} \tilde{F}\, \mathrm{d}s & \oint_{2+3+4+5} \tilde{F}\, \mathrm{d}s & \int_{5} \tilde{F}\, \mathrm{d}s \\ \mathbf{0}_{3\times 3} & \int_{5} \tilde{F}\, \mathrm{d}s & \oint_{5+6} \tilde{F}\, \mathrm{d}s \end{bmatrix} \\
J^{\text{three-cells}} &= \begin{bmatrix} \oint_{1+2} \tilde{J}\, \mathrm{d}s \\ \oint_{2+3+4+5} \tilde{J}\, \mathrm{d}s \\ \oint_{5+6} \tilde{J}\, \mathrm{d}s \end{bmatrix}
\end{aligned}
\tag{A.28}
$$

Appendix B

B.1 Properties of the Skew-Symmetric Operator

Consider the 3×1 vector $\mathbf{Z}$ expressed as

$$\mathbf{Z} = \begin{bmatrix} Z_1 \\ Z_2 \\ Z_3 \end{bmatrix} \tag{B.1}$$

The skew-symmetric (cross product) operator of the vector $\mathbf{Z}$ denoted as $\tilde{\mathbf{Z}}$ is defined in a dyadic form as

$$\tilde{\mathbf{Z}} = \mathbf{Z} \times \underline{\Delta}_{3\times 3} \tag{B.2}$$

where $\underline{\Delta}_{3\times 3}$ is the 3×3 identity dyadic.

The matrix form of the skew-symmetric tensor of Eq. B.2 is

$$\tilde{\mathbf{Z}} = \begin{bmatrix} 0 & -Z_3 & Z_2 \\ Z_3 & 0 & -Z_1 \\ -Z_2 & Z_1 & 0 \end{bmatrix} \tag{B.3}$$

If $\mathbf{B}$ is also a 3×1 vector, then the following properties of the skew-symmetric operator,

which can be proven using term by term expansion, are given as

$$\widetilde{(\mathbf{Z}+\mathbf{B})} = \tilde{\mathbf{Z}}+\tilde{\mathbf{B}} \tag{B.4}$$

$$\tilde{\mathbf{Z}}^{\mathrm{T}} = -\tilde{\mathbf{Z}} \tag{B.5}$$

$$\tilde{\mathbf{Z}}\mathbf{Z} = \mathbf{0} \tag{B.6}$$

$$\tilde{\mathbf{B}}\mathbf{Z} = -\tilde{\mathbf{Z}}\mathbf{B} \tag{B.7}$$

$$\mathbf{B}^{\mathrm{T}}\tilde{\mathbf{Z}} = -\mathbf{Z}^{\mathrm{T}}\tilde{\mathbf{B}} \tag{B.8}$$

$$\tilde{\mathbf{B}}\tilde{\mathbf{Z}} = \mathbf{Z}\mathbf{B}^{\mathrm{T}} - \underline{\Delta}_{3\times 3}\mathbf{B}^{\mathrm{T}}\mathbf{Z} \tag{B.9}$$

$$\tilde{\mathbf{B}}\tilde{\mathbf{Z}} = \tilde{\mathbf{Z}}\tilde{\mathbf{B}} + \widetilde{\tilde{\mathbf{B}}\mathbf{Z}} \tag{B.10}$$

B.2 Intrinsic Beam Dynamic Relations

To prove Eq. 3.35, the relation in Eq. 3.34 is first rewritten as

$$\delta\mathcal{C}^{\mathbf{Bb}'} = -\widetilde{\delta\psi}'\mathcal{C}^{\mathbf{Bb}} - \widetilde{\delta\psi}\mathcal{C}^{\mathbf{Bb}'} \tag{B.11}$$

Taking the variation of Eq. 3.24 gives

$$\delta\mathcal{C}^{\mathbf{Bb}'} = \delta\mathcal{C}^{\mathbf{Bb}}\tilde{\mathbf{k}} - \widetilde{\delta\mathbf{K}}\mathcal{C}^{\mathbf{Bb}} - \tilde{\mathbf{K}}\delta\mathcal{C}^{\mathbf{Bb}} \tag{B.12}$$

Equating Eq. B.11 and Eq. B.12 gives

$$-\widetilde{\delta\psi}'\mathcal{C}^{\mathbf{Bb}} - \widetilde{\delta\psi}\mathcal{C}^{\mathbf{Bb}'} = \delta\mathcal{C}^{\mathbf{Bb}}\tilde{\mathbf{k}} - \widetilde{\delta\mathbf{K}}\mathcal{C}^{\mathbf{Bb}} - \tilde{\mathbf{K}}\delta\mathcal{C}^{\mathbf{Bb}} \tag{B.13}$$

Using Eq. 3.32 to eliminate $\delta\mathcal{C}^{\mathbf{Bb}}$, and Eq. 3.22 to eliminate $\mathcal{C}^{\mathbf{Bb}'}$, Eq. B.13 is rewritten as

$$-\widetilde{\delta\psi}'\mathcal{C}^{\mathbf{Bb}} - \widetilde{\delta\psi}\mathcal{C}^{\mathbf{Bb}}\tilde{\mathbf{k}} + \widetilde{\delta\psi}\tilde{\mathbf{K}}\mathcal{C}^{\mathbf{Bb}} = -\widetilde{\delta\psi}\mathcal{C}^{\mathbf{Bb}}\tilde{\mathbf{k}} - \widetilde{\delta\mathbf{K}}\mathcal{C}^{\mathbf{Bb}} + \tilde{\mathbf{K}}\widetilde{\delta\psi}\mathcal{C}^{\mathbf{Bb}} \tag{B.14}$$

Eliminating opposite terms in Eq. B.14 and isolating the term $\widetilde{\delta\mathbf{K}}\mathcal{C}^{\mathbf{Bb}}$ on left hand side after rewriting it as $\widetilde{\delta\boldsymbol{\kappa}}\mathcal{C}^{\mathbf{Bb}}$ since $\widetilde{\delta\mathbf{K}} = \widetilde{\delta\boldsymbol{\kappa}}$ yields

$$\widetilde{\delta\boldsymbol{\kappa}}\mathcal{C}^{\mathbf{Bb}} = \tilde{\mathbf{K}}\widetilde{\delta\psi}\mathcal{C}^{\mathbf{Bb}} + \widetilde{\delta\psi}'\mathcal{C}^{\mathbf{Bb}} - \widetilde{\delta\psi}\tilde{\mathbf{K}}\mathcal{C}^{\mathbf{Bb}} \tag{B.15}$$

Pre-multiplying both sides of Eq. B.15 by $\mathcal{C}^{\mathbf{Bb}^{\mathrm{T}}}$ gives

$$\widetilde{\delta\boldsymbol{\kappa}} = \widetilde{\delta\psi}' + \underbrace{\tilde{\mathbf{K}}\widetilde{\delta\psi} - \widetilde{\delta\psi}\tilde{\mathbf{K}}} \tag{B.16}$$

Invoking the last property of the skew-symmetric operator, Eq. B.10, for the under-braced terms yields Eq. 3.35.

To derive Eq. 3.37, Eq. 3.27 is first written as

$$\boldsymbol{\gamma} + \mathbf{e}_1 = \mathcal{C}^{\mathbf{Bb}}(\mathbf{e}_1 + \mathbf{u}_b' + \tilde{\mathbf{k}}\mathbf{u}_b) \tag{B.17}$$

Post-multiplying Eq. B.17 by $\delta\mathcal{C}^{\mathbf{Bb}}\mathcal{C}^{\mathbf{Bb}^{\mathrm{T}}}$ yields Eq. 3.37.

To derive the kinetic energy expression in Eq. 3.48, Eq. 3.47 is written as

$$\mathcal{K} = \frac{1}{2}\int\int_S \rho\left(\mathbf{V} + \tilde{\boldsymbol{\Omega}}\boldsymbol{\xi}\right)^{\mathrm{T}}\left(\mathbf{V} + \tilde{\boldsymbol{\Omega}}\boldsymbol{\xi}\right)\sqrt{g}\,\mathrm{d}x_2\mathrm{d}x_3 \tag{B.18}$$

$$\mathcal{K} = \frac{1}{2}\int\int_S \rho\left(\mathbf{V}^{\mathrm{T}}\mathbf{V} + \underline{\underline{\mathbf{V}^{\mathrm{T}}\tilde{\boldsymbol{\Omega}}\boldsymbol{\xi} + \boldsymbol{\xi}^{\mathrm{T}}\tilde{\boldsymbol{\Omega}}^{\mathrm{T}}\mathbf{V}}} + \underline{\boldsymbol{\xi}^{\mathrm{T}}\tilde{\boldsymbol{\Omega}}^{\mathrm{T}}\tilde{\boldsymbol{\Omega}}\boldsymbol{\xi}}\right)\sqrt{g}\,\mathrm{d}x_2\mathrm{d}x_3 \tag{B.19}$$

Applying properties B.7 and B.8 twice to the double underlined terms while applying property B.9 to the single underlined term yields

$$\mathcal{K} = \frac{1}{2}\int\int_S \rho\left[\mathbf{V}^{\mathrm{T}}\mathbf{V} - \boldsymbol{\Omega}^{\mathrm{T}}\tilde{\mathbf{V}}\boldsymbol{\xi} - \boldsymbol{\Omega}^{\mathrm{T}}\tilde{\mathbf{V}}\boldsymbol{\xi} - \boldsymbol{\xi}^{\mathrm{T}}\left(\boldsymbol{\Omega}\boldsymbol{\Omega}^{\mathrm{T}} - \underline{\Delta}_{3\times 3}\boldsymbol{\Omega}^{\mathrm{T}}\boldsymbol{\Omega}\right)\boldsymbol{\xi}\right]\sqrt{g}\,\mathrm{d}x_2\mathrm{d}x_3 \quad \text{(B.20)}$$

Upon rearranging Eq. B.20 and invoking the definitions in Eq. 3.49, Eq. 3.48 is retrieved.

To derive Eq. 3.66, a procedure that is similar to the one outlined in Reference [178] is employed where the following inverted relations are first written

$$\mathbf{u}_{\mathbf{b}}' = \mathcal{C}^{\mathbf{Bb}^{\mathrm{T}}}(\boldsymbol{\gamma} + \mathbf{e}_1) - \mathbf{e}_1 - \tilde{\mathbf{k}}\mathbf{u}_{\mathbf{b}} \quad \text{(B.21)}$$

$$\dot{\mathbf{u}} = \mathcal{C}^{\mathbf{Bb}^{\mathrm{T}}}\mathbf{V} - \tilde{\boldsymbol{\omega}}\mathbf{u}_{\mathbf{b}} - \mathbf{v} \quad \text{(B.22)}$$

$$\mathcal{C}^{\mathbf{Bb}'} = -\tilde{\boldsymbol{\kappa}}\mathcal{C}^{\mathbf{Bb}} + \mathcal{C}^{\mathbf{Bb}}\tilde{\mathbf{k}} - \tilde{\mathbf{k}}\mathcal{C}^{\mathbf{Bb}} \quad \text{(B.23)}$$

$$\dot{\mathcal{C}}^{\mathbf{Bb}} = -\tilde{\boldsymbol{\Omega}}\mathcal{C}^{\mathbf{Bb}} + \mathcal{C}^{\mathbf{Bb}}\tilde{\boldsymbol{\omega}} \quad \text{(B.24)}$$

$$\boldsymbol{\omega}' = -\tilde{\mathbf{k}}\boldsymbol{\omega} \quad \text{(B.25)}$$

$$\mathbf{v}' = -\tilde{\mathbf{k}}\mathbf{v} \quad \text{(B.26)}$$

Substituting Eqs. B.21 through B.26 into Eq. 3.65 yields

$$V' - \dot{\boldsymbol{\gamma}} = \left(-\tilde{\boldsymbol{\kappa}}\mathcal{C}^{\mathbf{Bb}} + \mathcal{C}^{\mathbf{Bb}}\tilde{\mathbf{k}} - \tilde{\mathbf{k}}\mathcal{C}^{\mathbf{Bb}}\right)\left[\mathbf{v} + \tilde{\boldsymbol{\omega}}\mathbf{u}_{\mathbf{b}} + \left(\mathcal{C}^{\mathbf{Bb}^{\mathrm{T}}}\mathbf{V} - \tilde{\boldsymbol{\omega}}\mathbf{u}_{\mathbf{b}} - \mathbf{v}\right)\right] \quad \text{(B.27)}$$

$$+\mathcal{C}^{\mathbf{Bb}}\left[-\tilde{\mathbf{k}}\mathbf{v} + \tilde{\boldsymbol{\omega}}\left[\mathcal{C}^{\mathbf{Bb}^{\mathrm{T}}}(\boldsymbol{\gamma} + \mathbf{e}_1) - \mathbf{e}_1 - \tilde{\mathbf{k}}\mathbf{u}\right] - \widetilde{\tilde{\mathbf{k}}\boldsymbol{\omega}}\mathbf{u}_{\mathbf{b}}\right]$$

$$-\left(-\tilde{\boldsymbol{\Omega}}\mathcal{C}^{\mathbf{Bb}} + \mathcal{C}^{\mathbf{Bb}}\tilde{\boldsymbol{\omega}}\right)\left[\mathbf{e}_1 + \mathcal{C}^{\mathbf{Bb}^{\mathrm{T}}}(\boldsymbol{\gamma} + \mathbf{e}_1) - \mathbf{e}_1 - \tilde{\mathbf{k}}\mathbf{u}_{\mathbf{b}} + \tilde{\mathbf{k}}\mathbf{u}_{\mathbf{b}}\right] - \mathcal{C}^{\mathbf{Bb}}\tilde{\mathbf{k}}\left[\mathcal{C}^{\mathbf{Bb}^{\mathrm{T}}}\mathbf{V} - \tilde{\boldsymbol{\omega}}\mathbf{u} - \mathbf{v}\right]$$

After a series of obvious cancelations in Eq. B.27 and using property B.10 such as $-\tilde{\boldsymbol{\omega}}\tilde{\mathbf{k}} - \widetilde{\tilde{\mathbf{k}}\boldsymbol{\omega}} + \tilde{\mathbf{k}}\tilde{\boldsymbol{\omega}} = 0$ one retrieves Eq. 3.66.

Subtracting Eq. 3.67 from Eq. 3.68 yields

$$\tilde{\Omega}' - \dot{\tilde{\kappa}} = -\dot{C}^{\mathrm{Bb}'} C^{\mathrm{Bb}^{\mathrm{T}}} - \dot{C}^{\mathrm{Bb}} C^{\mathrm{Bb}'^{\mathrm{T}}} + C^{\mathrm{Bb}'} \tilde{\omega} C^{\mathrm{Bb}^{\mathrm{T}}} + C^{\mathrm{Bb}} \tilde{\omega}' C^{\mathrm{Bb}^{\mathrm{T}}} + \tag{B.28}$$

$$C^{\mathrm{Bb}} \tilde{\omega} C^{\mathrm{Bb}'^{\mathrm{T}}} + \dot{C}^{\mathrm{Bb}'} C^{\mathrm{Bb}^{\mathrm{T}}} + C^{\mathrm{Bb}'} \dot{C}^{\mathrm{Bb}^{\mathrm{T}}} - \dot{C}^{\mathrm{Bb}} \tilde{\mathbf{k}} C^{\mathrm{Bb}^{\mathrm{T}}} - C^{\mathrm{Bb}} \tilde{\mathbf{k}} \dot{C}^{\mathrm{Bb}^{\mathrm{T}}}$$

As before, using Eqs. B.23 through B.25 in Eq. B.28 yields

$$\begin{aligned}
\tilde{\Omega}' - \dot{\tilde{\kappa}} = & -\left(-\tilde{\Omega} C^{\mathrm{Bb}} + C^{\mathrm{Bb}} \tilde{\omega}\right) \left(-\tilde{\kappa} C^{\mathrm{Bb}} + C^{\mathrm{Bb}} \tilde{\mathbf{k}} - \tilde{\mathbf{k}} C^{\mathrm{Bb}}\right)^{\mathrm{T}} \\
& + \left(-\tilde{\kappa} C^{\mathrm{Bb}} + C^{\mathrm{Bb}} \tilde{\mathbf{k}} - \tilde{\mathbf{k}} C^{\mathrm{Bb}}\right) \tilde{\omega} C^{\mathrm{Bb}^{\mathrm{T}}} \\
& - C^{\mathrm{Bb}} \widetilde{\tilde{\mathbf{k}} \omega} C^{\mathrm{Bb}^{\mathrm{T}}} + C^{\mathrm{Bb}} \tilde{\omega} \left(-\tilde{\kappa} C^{\mathrm{Bb}} + C^{\mathrm{Bb}} \tilde{\mathbf{k}} - \tilde{\mathbf{k}} C^{\mathrm{Bb}}\right)^{\mathrm{T}} \\
& + \left(-\tilde{\kappa} C^{\mathrm{Bb}} + C^{\mathrm{Bb}} \tilde{\mathbf{k}} - \tilde{\mathbf{k}} C^{\mathrm{Bb}}\right) \left(-\tilde{\Omega} C^{\mathrm{Bb}} + C^{\mathrm{Bb}} \tilde{\omega}\right)^{\mathrm{T}} \\
& - \left(-\tilde{\Omega} C^{\mathrm{Bb}} + C^{\mathrm{Bb}} \tilde{\omega}\right) \tilde{\mathbf{k}} C^{\mathrm{Bb}^{\mathrm{T}}} - C^{\mathrm{Bb}} \tilde{\mathbf{k}} \left(-\tilde{\Omega} C^{\mathrm{Bb}} + C^{\mathrm{Bb}} \tilde{\omega}\right)^{\mathrm{T}}
\end{aligned} \tag{B.29}$$

After a series of obvious cancelations Eq. 3.69 is retrieved.

B.3 Intrinsic Conservation Laws Relations

To prove Eq. 3.86, the time differentiation of the quantity inside the integral on the left hand side is carried out to yield

$$\left(\mathbf{V}^{\mathrm{T}} \mathbf{P} + \boldsymbol{\Omega}^{\mathrm{T}} \mathbf{H}\right)^{\bullet} = \dot{\mathbf{V}}^{\mathrm{T}} \mathbf{P} + \mathbf{V}^{\mathrm{T}} \dot{\mathbf{P}} + \dot{\boldsymbol{\Omega}}^{\mathrm{T}} \mathbf{H} + \boldsymbol{\Omega}^{\mathrm{T}} \mathbf{H} \tag{B.30}$$

Using the constitutive relation of Eq. 3.73 to eliminate $\mathbf{P}$ and $\mathbf{H}$ leads to

$$\left(\mathbf{V}^{\mathrm{T}}\mathbf{P}+\boldsymbol{\Omega}^{\mathrm{T}}\mathbf{H}\right)^{\bullet}=\dot{\mathbf{V}}^{\mathrm{T}}\left(D\mathbf{V}+Q\boldsymbol{\Omega}\right)+\mathbf{V}^{\mathrm{T}}\left(D\dot{\mathbf{V}}+Q\dot{\boldsymbol{\Omega}}\right)+\dot{\boldsymbol{\Omega}}^{\mathrm{T}}\left(-Q\mathbf{V}+I\boldsymbol{\Omega}\right)+\boldsymbol{\Omega}^{\mathrm{T}}\left(-Q\dot{\mathbf{V}}+I\dot{\boldsymbol{\Omega}}\right) \tag{B.31}$$

The quantities in Eq. B.31 are scalars and recalling that the matrices D and I are symmetric while the matrix Q is anti-symmetric allows one to write

$$\begin{aligned}\left(\mathbf{V}^{\mathrm{T}}D\dot{\mathbf{V}}\right)^{\mathrm{T}} &= \mathbf{V}^{\mathrm{T}}D\dot{\mathbf{V}}=\dot{\mathbf{V}}^{\mathrm{T}}D^{\mathrm{T}}\mathbf{V}=\dot{\mathbf{V}}^{\mathrm{T}}D\mathbf{V}\\ \left(\boldsymbol{\Omega}^{\mathrm{T}}I\dot{\boldsymbol{\Omega}}\right)^{\mathrm{T}} &= \boldsymbol{\Omega}^{\mathrm{T}}I\dot{\boldsymbol{\Omega}}=\dot{\boldsymbol{\Omega}}^{\mathrm{T}}I^{\mathrm{T}}\boldsymbol{\Omega}=\dot{\boldsymbol{\Omega}}^{\mathrm{T}}I\boldsymbol{\Omega}\end{aligned} \tag{B.32}$$

and

$$\left(-\boldsymbol{\Omega}^{\mathrm{T}}Q\dot{\mathbf{V}}\right)^{\mathrm{T}}=-\boldsymbol{\Omega}^{\mathrm{T}}Q\dot{\mathbf{V}}=\dot{\mathbf{V}}^{\mathrm{T}}Q\boldsymbol{\Omega} \tag{B.33}$$

Substitution of Eqs. B.33 through B.32 into Eq. B.31 and re-invoking the constitutive relation of Eq. 3.73 leads to

$$\left(\mathbf{V}^{\mathrm{T}}\mathbf{P}+\boldsymbol{\Omega}^{\mathrm{T}}\mathbf{H}\right)^{\bullet}=2\left(\dot{\mathbf{V}}^{\mathrm{T}}\mathbf{P}+\dot{\boldsymbol{\Omega}}^{\mathrm{T}}\mathbf{H}\right) \tag{B.34}$$

Appendix C

C.1 Cross-Sectional Properties Used in Numerical Examples

The elastic and inertial properties of the examples used in Chapter 4 are given in Tables C.1 through C.3.

Table C.1: Sectional stiffness constants, sectional mass/inertia constants, and beam length of the Aluminum blade in [147].

$\mathbf{EA}$(psi·in^2)	6.678×10^5	$\mathbf{EI_{flap}}$(psi·in^4)	220.875
$\mathbf{GJ}$(psi·in^4)	333.396	$\mathbf{EI_{lead-lag}}$(psi·in^4)	556.486×10^2
$\mathbf{m_{per-length}}$($\mathrm{lb_m}$/in)	1.581×10^{-5}	$\mathbf{I_{axial}}$($\mathrm{lb_m}$·in^2)	1.323×10^{-6}
$\mathbf{I_{flap}}$($\mathrm{lb_m}$·in^2)	5.230×10^{-9}	$\mathbf{I_{lead-lag}}$($\mathrm{lb_m}$·in^2)	1.318×10^{-6}
$\mathbf{L_0}$(in)	31.5	$\mathbf{L_1}$(in)	6

Table C.2: Sectional stiffness constants, sectional mass/inertia constants, and beam length of the Aluminum blade in [150].

$\mathbf{EA}$(N)	6.359×10^6	$\mathbf{EI_{flap}}$(N·m^2)	7.379
$\mathbf{GJ}$(N·m^2)	11.096	$\mathbf{EI_{lead-lag}}$(N·m^2)	1.206×10^5
$\mathbf{m_{per-length}}$(kg/m)	0.25	$\mathbf{I_{axial}}$(kg·m^2)	1.079×10^{-3}
$\mathbf{I_{flap}}$(kg·m^2)	6.601×10^{-8}	$\mathbf{I_{lead-lag}}$(kg·m^2)	1.079×10^{-3}
$\mathbf{L_0}$(m)	1	$\mathbf{L_1}$(m)	-

Table C.3: Sectional stiffness and actuation constants. Active beam element implementation validation example [121].

Parameter	Value
S_{11}[N]	1.502594×10^7
S_{22}[N]	4.845361×10^6
S_{33}[N]	4.198040×10^6
S_{15}[N.m]	3.062168×10^3
S_{24}[N.m]	-4.248526×10^2
S_{44}[N.m^2]	1.301767×10^2
S_{55}[N.m^2]	1.277672×10^2
S_{66}[N.m^2]	5.008097×10^2
$F_1^{(a)}$[N]	-2.024539×10^3
$M_2^{(a)}$[N.m]	-4.843369

C.2 Post-Processing to Obtain Rotation and Displacement Parameters

To obtain the deformation rotational matrix $\mathcal{C}^{\mathbf{Bb}}$ at every blade station, the discretization in Fig. 4.1 is considered first. Once again, considering linear interpolation functions within the beam element, the midpoint twist/moments strain measures is defined as

$$\bar{\boldsymbol{\kappa}} = \frac{\boldsymbol{\kappa}_{n+1} + \boldsymbol{\kappa}_n}{2} \tag{C.1}$$

where the strain measures were obtained from the constitutive relation of Eq. 3.72 once the primary variables $\mathbf{F}$ and $\mathbf{M}$ were solved for.

Eq. 3.21 can be then written in a discretized form as

$$\frac{\mathcal{C}^{\mathbf{Ba}_{n+1}} - \mathcal{C}^{\mathbf{Ba}_n}}{\Delta x_n} = -\left(\tilde{\bar{\boldsymbol{\kappa}}} + \tilde{\mathbf{k}}\right)\left(\frac{\mathcal{C}^{\mathbf{Ba}_{n+1}} + \mathcal{C}^{\mathbf{Ba}_n}}{2}\right) \tag{C.2}$$

where the rotation matrix operator $\mathcal{C}^{\mathbf{Ba}}$, which transforms a vector from the unbroken and undeformed frame to the deformed one, is expressed in the broken frame of the element using the similarity transformation $\mathcal{C}^{\mathbf{Ba}} \mapsto \mathcal{C}^{rl}\mathcal{C}^{\mathbf{Ba}}\mathcal{C}^{rl^{\mathrm{T}}}$

Rearranging Eq. C.2 yields

$$\mathcal{C}^{\mathbf{B}\mathbf{a}_{n+1}} = \left(\frac{\underline{\Delta}_{3\times3}}{\Delta x_n} + \frac{\tilde{\tilde{\boldsymbol{\kappa}}} + \tilde{\mathbf{k}}}{2}\right)^{-1} \left(\frac{\underline{\Delta}_{3\times3}}{\Delta x_n} - \frac{\tilde{\tilde{\boldsymbol{\kappa}}} + \tilde{\mathbf{k}}}{2}\right) \mathcal{C}^{\mathbf{B}\mathbf{a}_n} \tag{C.3}$$

where knowing the boundary condition represented by $\mathcal{C}^{\mathbf{B}\mathbf{a}_0}$ will render the solution to Eq. C.3 established.

Similarly, Eq. 3.4 can be written in a discretized form as

$$\mathcal{C}^{\mathbf{b}\mathbf{a}_{n+1}} = \left(\frac{\underline{\Delta}_{3\times3}}{\Delta x_n} + \frac{\tilde{\mathbf{k}}}{2}\right)^{-1} \left(\frac{\underline{\Delta}_{3\times3}}{\Delta x_n} - \frac{\tilde{\mathbf{k}}}{2}\right) \mathcal{C}^{\mathbf{B}\mathbf{a}_n} \tag{C.4}$$

Using the fact that $\mathcal{C}^{\mathbf{B}\mathbf{a}_{n+1}} = \mathcal{C}^{\mathbf{B}\mathbf{b}_{n+1}} \cdot \mathcal{C}^{\mathbf{b}\mathbf{a}_{n+1}}$ one obtains the rotation matrix $\mathcal{C}^{\mathbf{B}\mathbf{b}_{n+1}}$ that is due purely to elastic deformations.

To obtain the tip twist angle θ due to aeroelastic loads or active actuation, the following factorization of the rotation operator is considered

$$\mathcal{C}^{\mathbf{B}\mathbf{b}} = \mathcal{C}_{\mathbf{b}_{1\mathsf{T}}} \mathcal{C}_{\mathsf{T}} \tag{C.5}$$

where $\mathcal{C}_{\mathsf{T}}$ is known as the tracking matrix [179] that represents a rotation about the $\mathbf{b}_3$ axis followed by a rotation about the intermediate translational axis $\mathbf{b}_{2\mathsf{T}}$.

It is clear that any rotation matrix operator can be factored according to Eq. C.5 and the sequence in known as the aerospace sequence $Z \rightarrow Y \rightarrow X$. The principal axis factor is obviously the $\mathcal{C}_{\mathbf{b}_{1\mathsf{T}}}$ operator, which represents the tip twist of interest, and is given by

$$\mathcal{C}_{\mathbf{b}_{1\mathsf{T}}} = \begin{bmatrix} 1 & 0 & 0 \\ 0 & \cos(\theta) & \sin(\theta) \\ 0 & -\sin(\theta) & \cos(\theta) \end{bmatrix} \tag{C.6}$$

The matrix $\mathcal{C}_{\mathsf{T}}$ has an explicit form where $\mathcal{C}_{\mathsf{T}}(2,3) = 0$, which from Eq. C.5 implies that

$$\theta = \arctan\left(\frac{\mathcal{C}^{\mathbf{Bb}}(2,3)}{\mathcal{C}^{\mathbf{Bb}}(3,3)}\right) \tag{C.7}$$

where θ is the deformation tip twist angle in radians.

Similar procedure can be used to obtain the elastic displacement $\mathbf{u}$ in the undeformed, untwisted/uncurved, and unbroken frame. Considering the interpolating functions again and Eq. 3.27, one can write

$$\mathbf{u}_{n+1} = \mathbf{u}_n + \left(\mathcal{C}^{lr}\mathcal{C}^{\mathbf{Ba}}\right)^{\mathrm{T}}(\bar{\gamma} + \mathbf{e}_1)\Delta x_n - \left(\mathcal{C}^{lr}\mathcal{C}^{\mathbf{ba}}\right)^{\mathrm{T}} e_1 \Delta x_n \tag{C.8}$$

where knowing the boundary condition represented by $\mathbf{u}_0$ will render the solution to Eq. C.8 established.

Appendix D

D.1 Quasi-steady Constants of the NACA64A010

Some of the constants used to calculate the quasi-steady coefficients in Eqs. 5.2 through 5.6 are modified to suit the NACA64A010 according to data available in the engineering literature

$$\begin{aligned} a &= 4.8701 * \frac{\pi}{180} \\ \alpha_l &= 0.1745 * \frac{\pi}{180} \end{aligned} \tag{D.1}$$

$$
\begin{aligned}
C_l &= a\alpha && ,0 \leq \alpha \leq \alpha_l \\
C_l &= 1.15\ \sin(2\alpha) && ,\alpha_l \leq \alpha \leq 161 \\
C_l &= -0.7 && ,161 \leq \alpha \leq 173 \\
C_l &= 0.10(\alpha - 180) && ,173 \leq \alpha \leq 187 \\
C_l &= 0.7 && ,187 \leq \alpha \leq 201 \\
C_l &= 1.15\ \sin(2\alpha) && ,201 \leq \alpha \leq (360 - \alpha_l) \\
C_l &= -a \mid \alpha - 360 \mid && ,(360 - \alpha_l) \leq \alpha \leq 360
\end{aligned}
\tag{D.2}
$$

The drag and the moment coefficients are taken to be the same as those of NACA0012.

D.2 Leishman and Beddoes Dynamic Stall Model Constants

The Leishman and Beddoes dynamic stall model constants are given for the NACA0012 and NACA64A010 airfoils in Table D.1. These constants are mildly Mach number dependent. Therefore, a nominal Mach number of $M = 0.3$ is selected for these constants throughout this investigation. The identical constants for the two airfoils again reflects the extensive availability of data for the NACA0012, which can be used to approximate those of airfoils in the same family.

The angle α_1' in Eq. 5.30 that is used to calculate the uncorrected trailing edge separation point must account for an experimentally observed hysteresis effect through

$$\alpha_1' = \alpha_1 - \Delta\alpha_1' \tag{D.3}$$

where

Table D.1: L-B dynamic stall model constants at $M = 0.3$.

Parameter	NACA0012	NACA64A010
T_p	1.7	1.7
S_1	0.0524	0.0524
S_2	0.0401	0.0401
α_1[rad]	0.2356	0.1745
α_2[rad]	0.1222	0.1222
$\Delta\alpha_1$[rad]	0.0367	0.0367
T_f	3	3
K_0	0.0025	0.0025
K_1	-0.135	-0.135
K_2	0.04	0.04
m	2	2
T_v	6	6
η	0.95	0.95

$$\Delta\alpha_1' = \begin{cases} \Delta\alpha_1 (1-f)^{\frac{1}{4}} & K_\alpha < 0 \\ 0 & K_\alpha \geq 0 \end{cases} \tag{D.4}$$

where K_α is given by

$$K_\alpha = \frac{\Delta\alpha}{\Delta t} \tag{D.5}$$

and the point f is defined similar to f' in Eq. 5.30 such that

$$f = \begin{cases} 1 - 0.3e^{\frac{|\alpha|-\alpha_1}{S_1}} & |\alpha| \leq \alpha_1 \\ 0.04 + 0.66e^{\frac{\alpha_1-|\alpha|}{S_2}} & |\alpha| > \alpha_1 \end{cases} \tag{D.6}$$

In this investigation, the L-B dynamic stall model has been implemented to handle reverse flow over the airfoil ($160° \leq \alpha \leq 200°$) where the constant α_2 is used instead of α_1 along with the appropriate quasi-steady coefficients obtained from Eq. 5.2. The same conditions used to monitor the occurrence of dynamic stall are also used to monitor for flow reattachment along with the sign of the airfoil pitch rate and flow direction.

Appendix E

E.1 Basic Properties of NACA 64A010 Blade Cross-Section

The profile of the NACA 64A010 is illustrated in Fig. E.1 along with basic dimensions of the blade cross-section. Typical lift-curves for the airfoil at the boundaries of the Reynolds number regime of interest are shown in Fig. E.2.

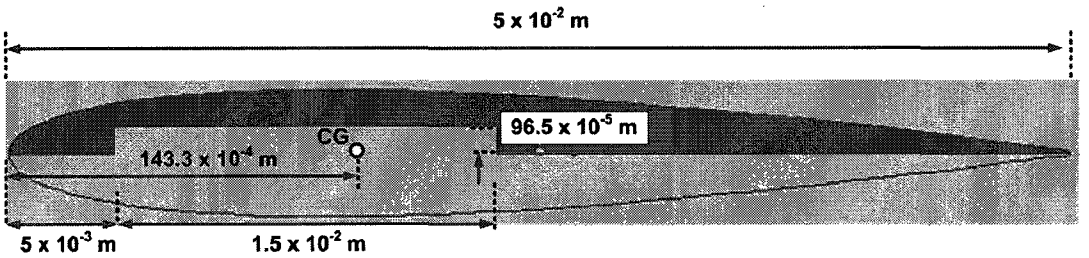

Figure E.1: Cross-section of the $1/12^{th}$ Froude-scale rotor based on NACA64A010.

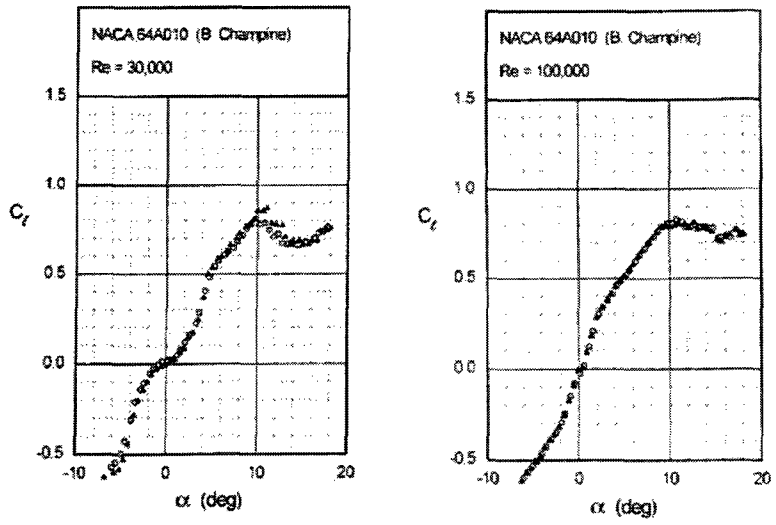

Figure E.2: Lift-curves for the NACA 64A010 at two Reynolds numbers of interest [167].

E.2 Elastic and Inertial Properties of the $1/12^{\text{th}}$ Froude-Scale Rotor Blade

The elastic and the inertial properties of the inertial section of the blade are shown in Fig. E.3 and Fig E.4 respectively. These properties and and the number of elements shown are used in setting up the intrinsic flexible multibody dynamics model of the rotor system. The number of the beam elements selected were based on balancing accuracy and computational speed.

The flap link has the following inertial properties

$$m = 7.15 \times 10^{-2} \text{ [Kg]} \quad \mathcal{I} = \begin{bmatrix} 2.76 \times 10^{-5} & 0 & 0 \\ 0 & 1.05 \times 10^{-5} & 0 \\ 0 & 0 & 3.49 \times 10^{-5} \end{bmatrix} \text{ [Kg.m]}$$

$$\ell = 4.34 \times 10^{-2} \text{ [m]} \qquad R_{\text{cm}} = \begin{bmatrix} 1.93 \times 10^{-2} & 0 & 0 \end{bmatrix} \text{ [m]} \tag{E.1}$$

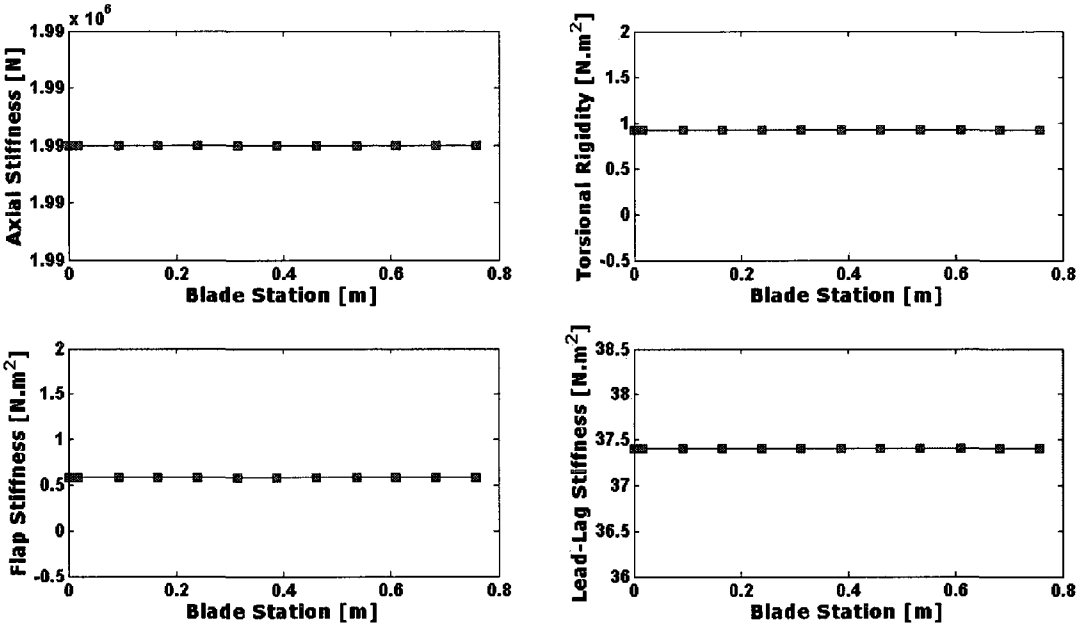

Figure E.3: Elastic properties of the $1/12^{\text{th}}$ Froude-Scale Rotor Blade.

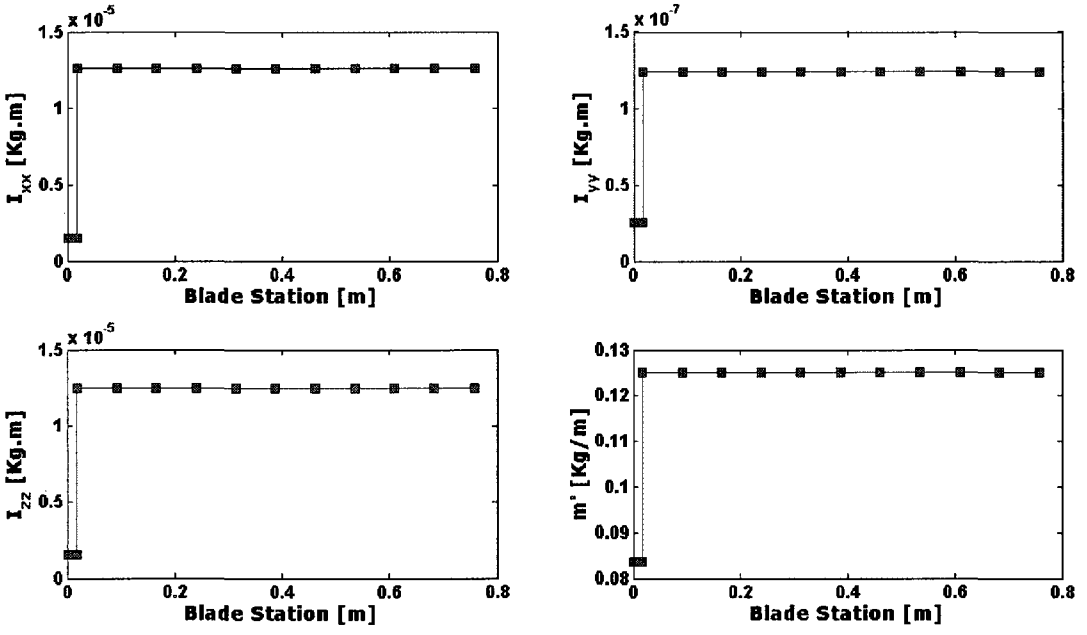

Figure E.4: Inertial properties of the $1/12^{\text{th}}$ Froude-Scale Rotor Blade.

The neoprene stops were modelled as linear springs with the following elastic constant and location vector relative to the centre of the hub

$$K_{\text{neoprene}} = 8 \times 10^4 \text{ [N/m]} \quad R_{\text{flap-stops}} = \begin{bmatrix} 2 \times 10^{-2} & 0 & 0 \end{bmatrix} \text{ [m]} \tag{E.2}$$

E.3 Engagement and Disengagement Profile of the 1/12$^{\text{th}}$ Froude-Scale Rotor Blade

$$\Omega_{\text{Engagement}}(t) = \frac{\breve{\Omega}_{\text{hub}} * 2\pi}{60}\left[-0.5\cos\left(\frac{\pi}{t_{\text{engage}}}t\right) + 0.5\right] \tag{E.3}$$

$$\Omega_{\text{Disengagement}}(t) = \frac{-\breve{\Omega}_{\text{hub}} * 2\pi}{60 * t_{\text{disengage}}}t + \frac{\mathcal{R}_{\text{hub}} * 2\pi}{60 * t_{\text{disengage}}} \tag{E.4}$$

where $\breve{\Omega}_{\text{hub}}$ is the maximum hub revolution per minute, t_{engage} is the duration of the engagement in seconds, and $t_{\text{disengage}}$ is the duration of the disengagement in seconds.

Appendix F

F.1 Predicted Time Histories of Total Tip Displacement, Elastic Tip Displacement, and Flap Hinge Angle of Experimental Runs of Phase (I)

The compiled time histories herein are of the simulated experimental runs in Table 7.3 and Table 7.4 where the already displayed cases in Chapter 7 are not repeated here. Fig. F.28 displays a motor free-wheeling phenomenon at the end of the run that was observed in the $-20°$ deck roll angle case. The phenomenon is caused by the motor shaft being unlocked at the end of the run, which causes the aerodynamic and gravitational loads to influence the hub by rotating it towards a dynamic equilibrium point. However, in the simulations, the rotor hub disengages where commanded and remains at its final azimuthal orientation.

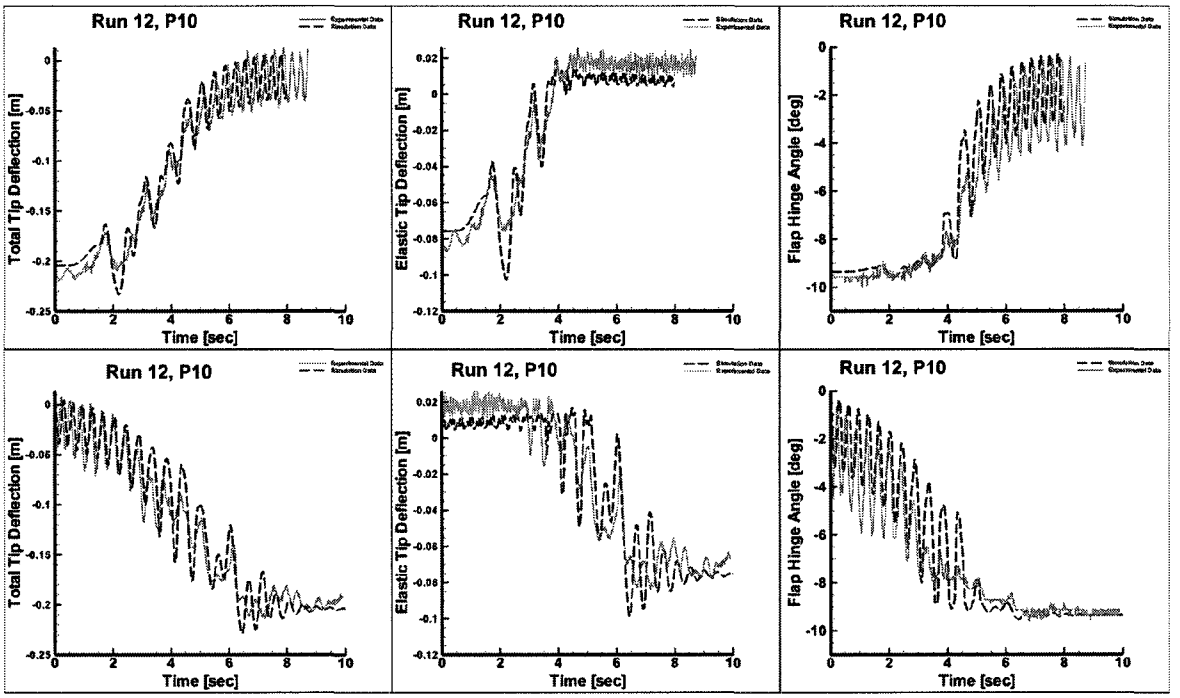

Figure F.1: Time histories of Run 12, P10 [Simulation: dashed line, Experiment: solid line].

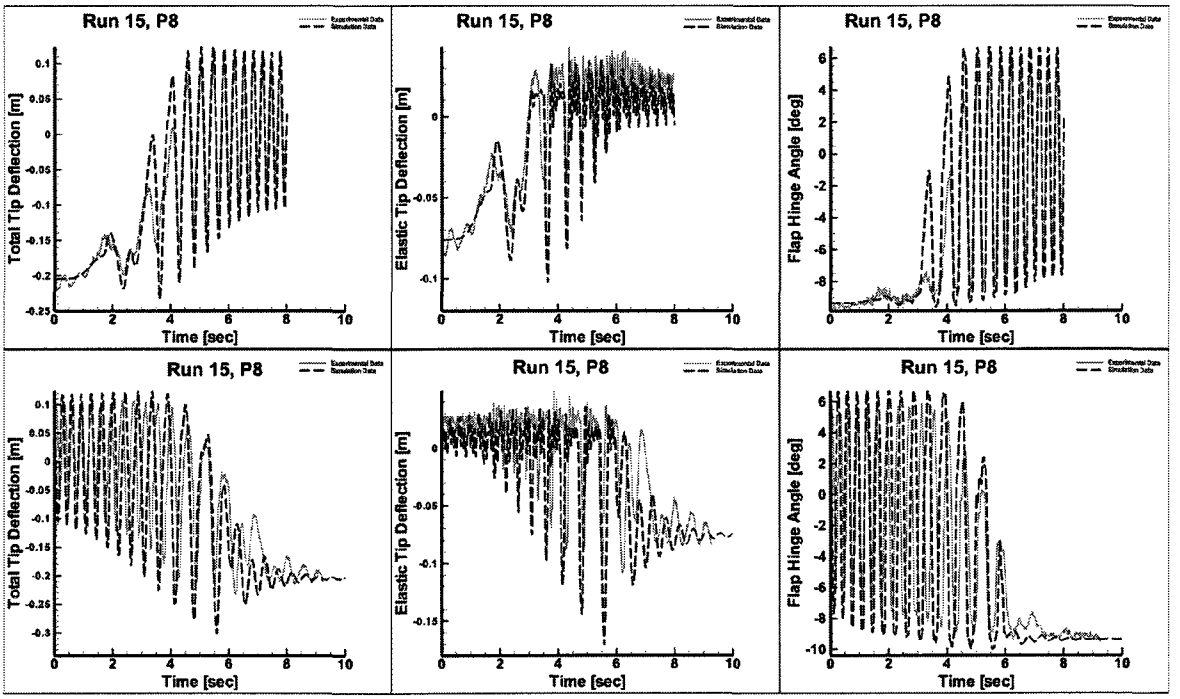

Figure F.2: Time histories of Run 15, P8 [Simulation: dashed line, Experiment: solid line].

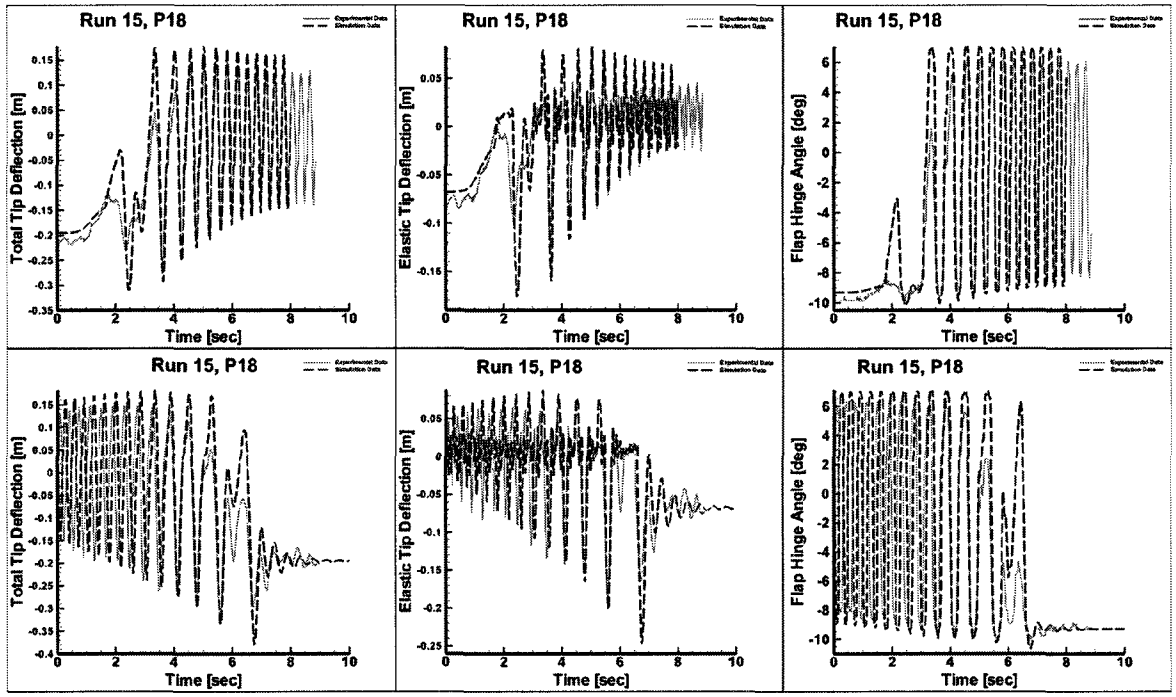

Figure F.3: Time histories of Run 15, P18 [Simulation: dashed line, Experiment: solid line].

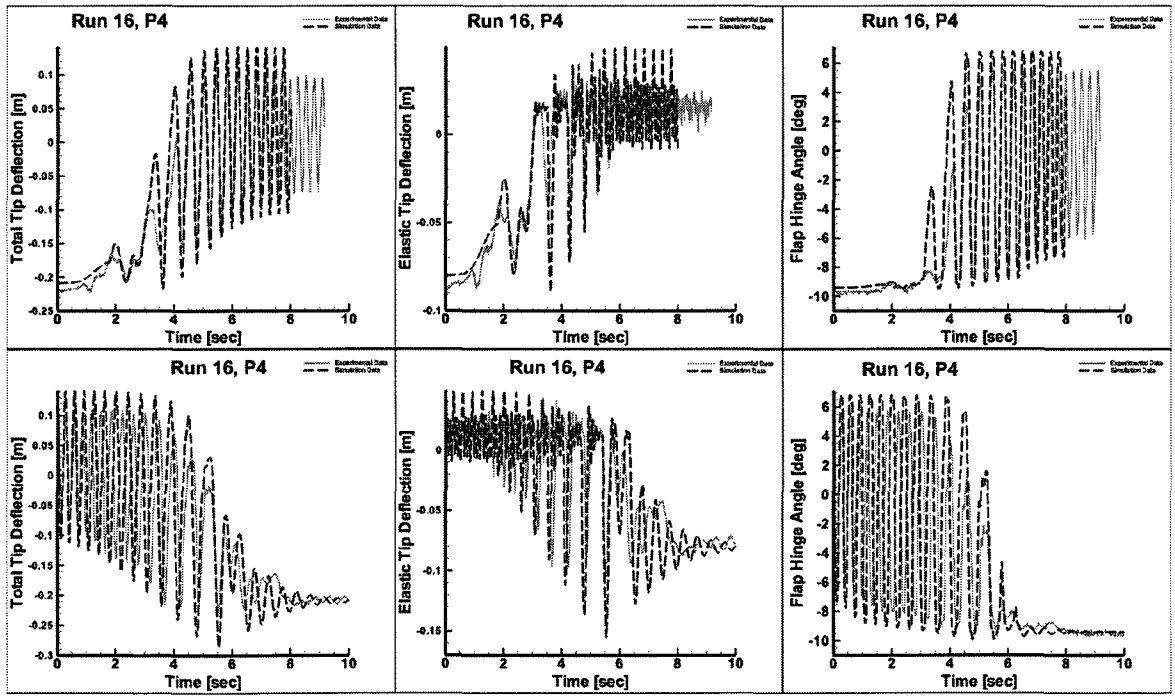

Figure F.4: Time histories of Run 16, P4 [Simulation: dashed line, Experiment: solid line].

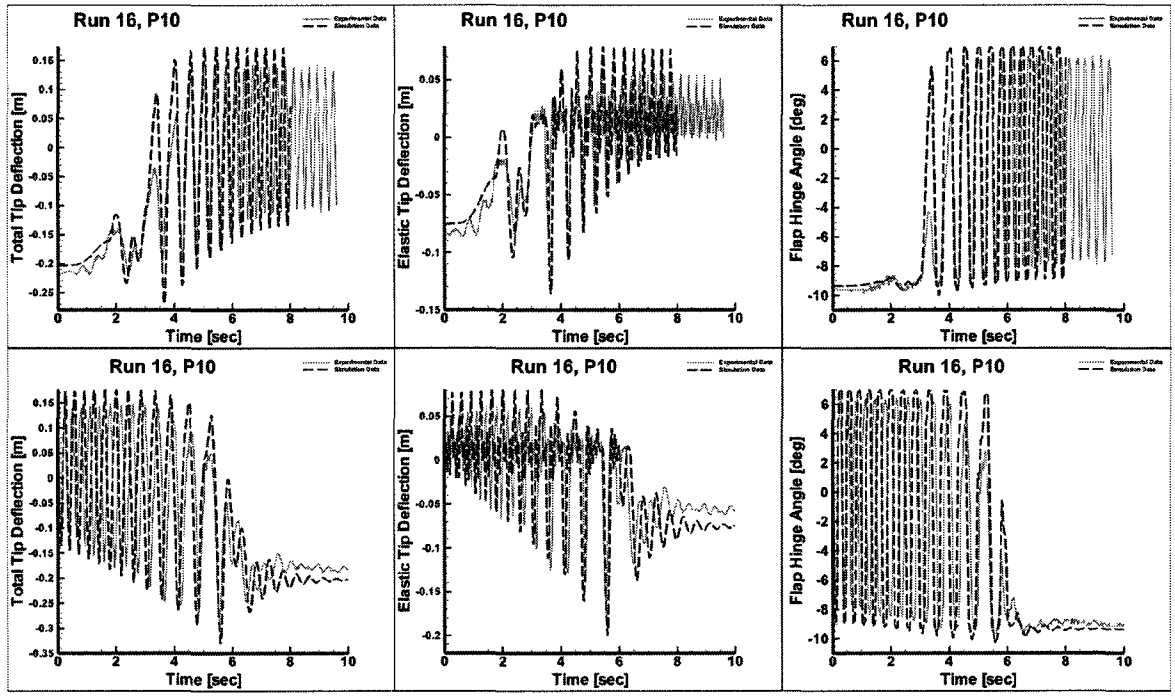

Figure F.5: Time histories of Run 16, P10 [Simulation: dashed line, Experiment: solid line].

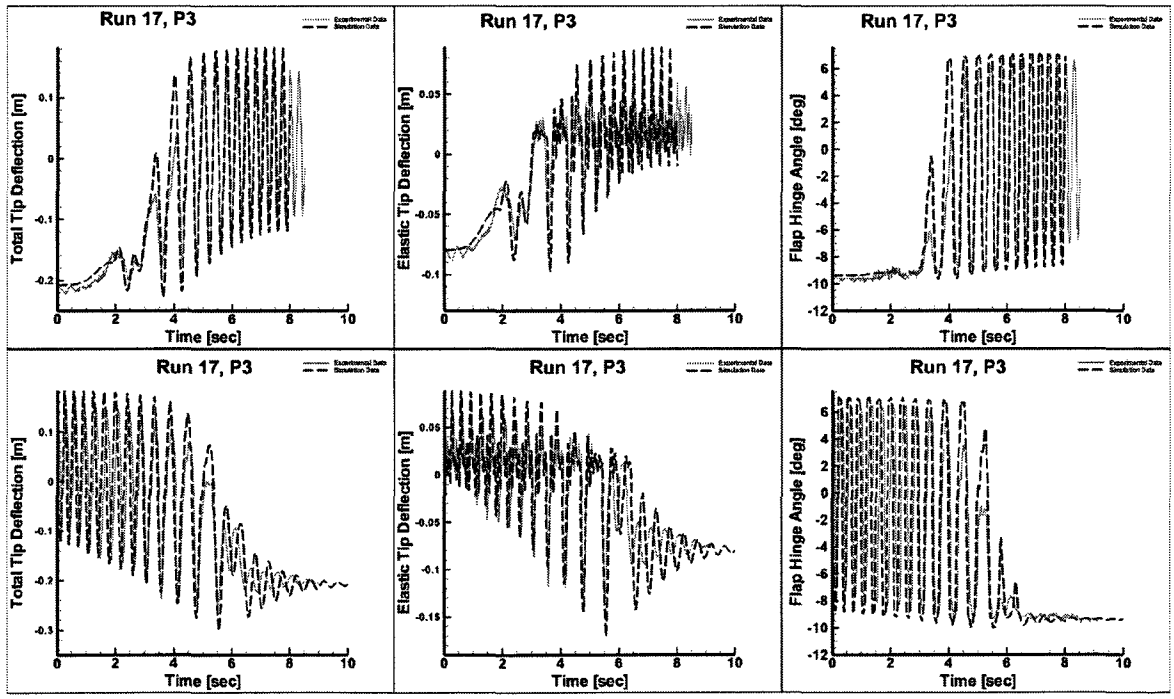

Figure F.6: Time histories of Run 17, P3 [Simulation: dashed line, Experiment: solid line].

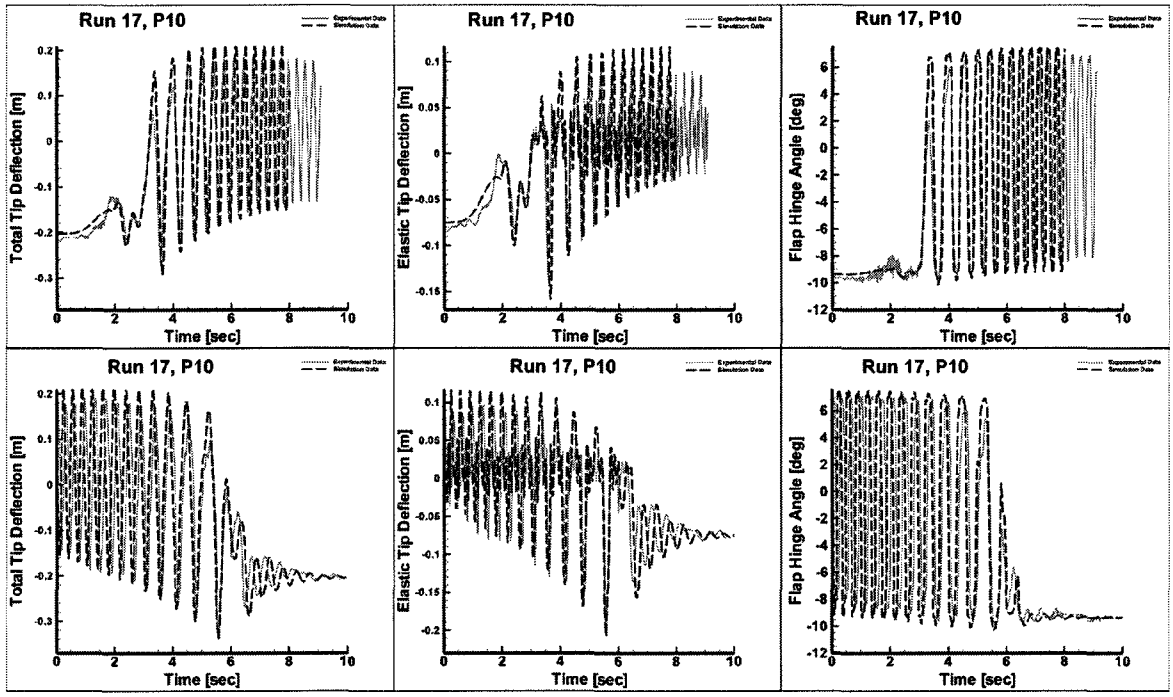

Figure F.7: Time histories of Run 17, P10 [Simulation: dashed line, Experiment: solid line].

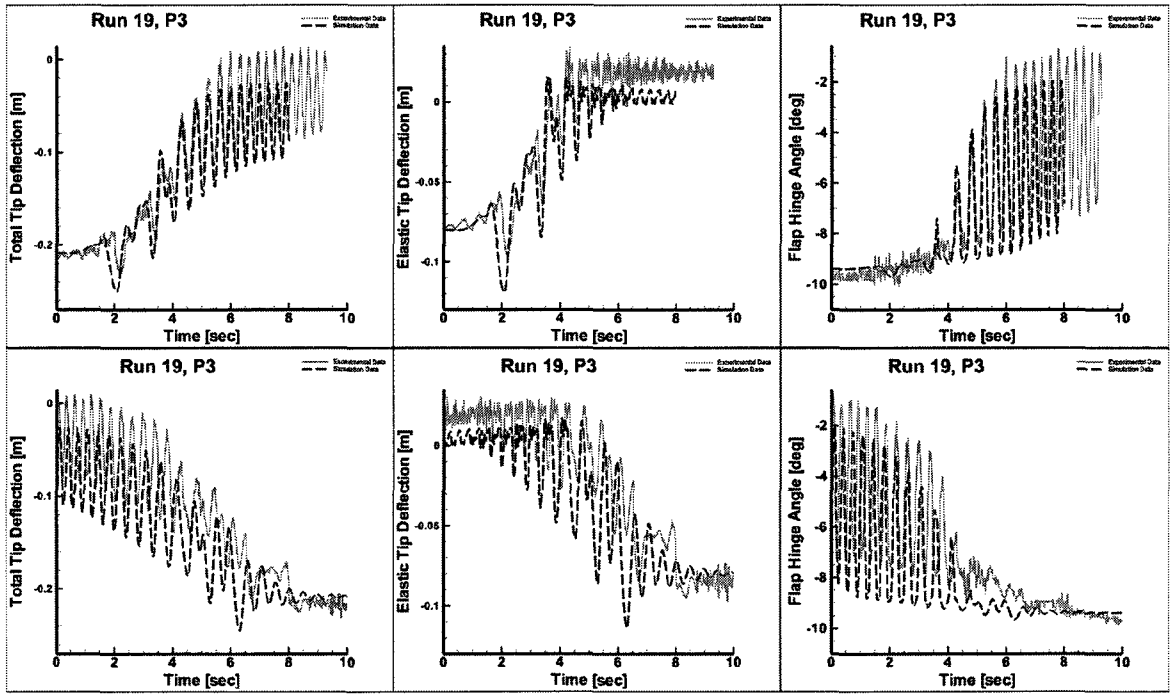

Figure F.8: Time histories of Run 19, P3 [Simulation: dashed line, Experiment: solid line].

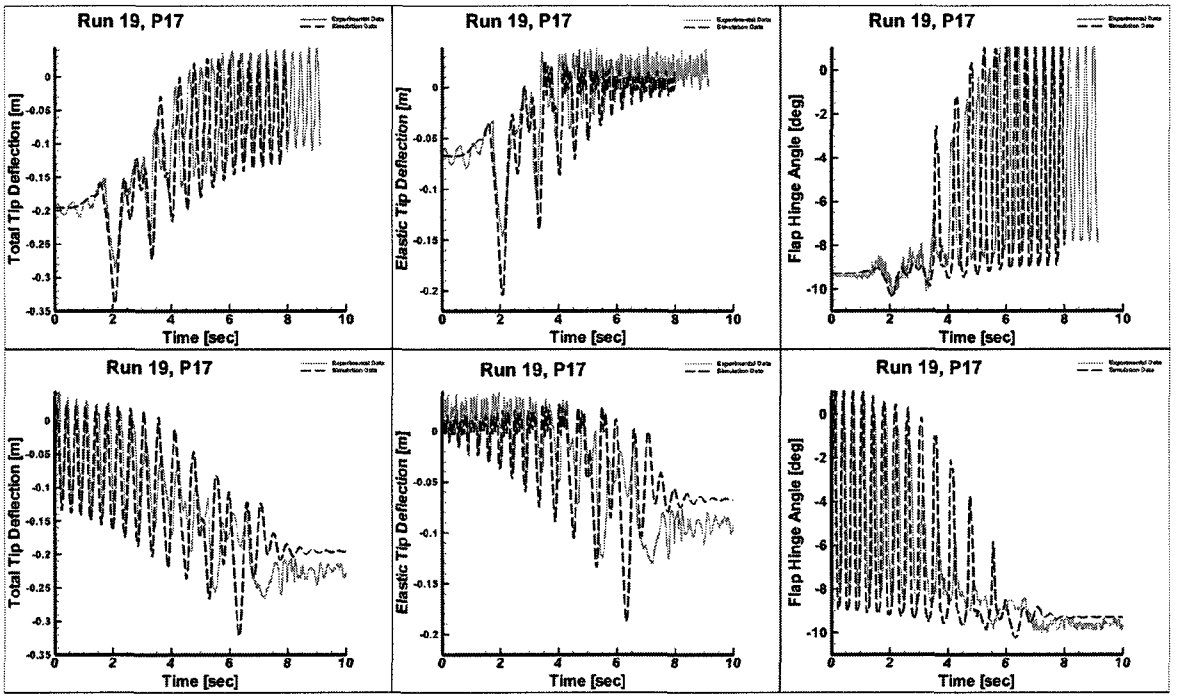

Figure F.9: Time histories of Run 19, P17 [Simulation: dashed line, Experiment: solid line].

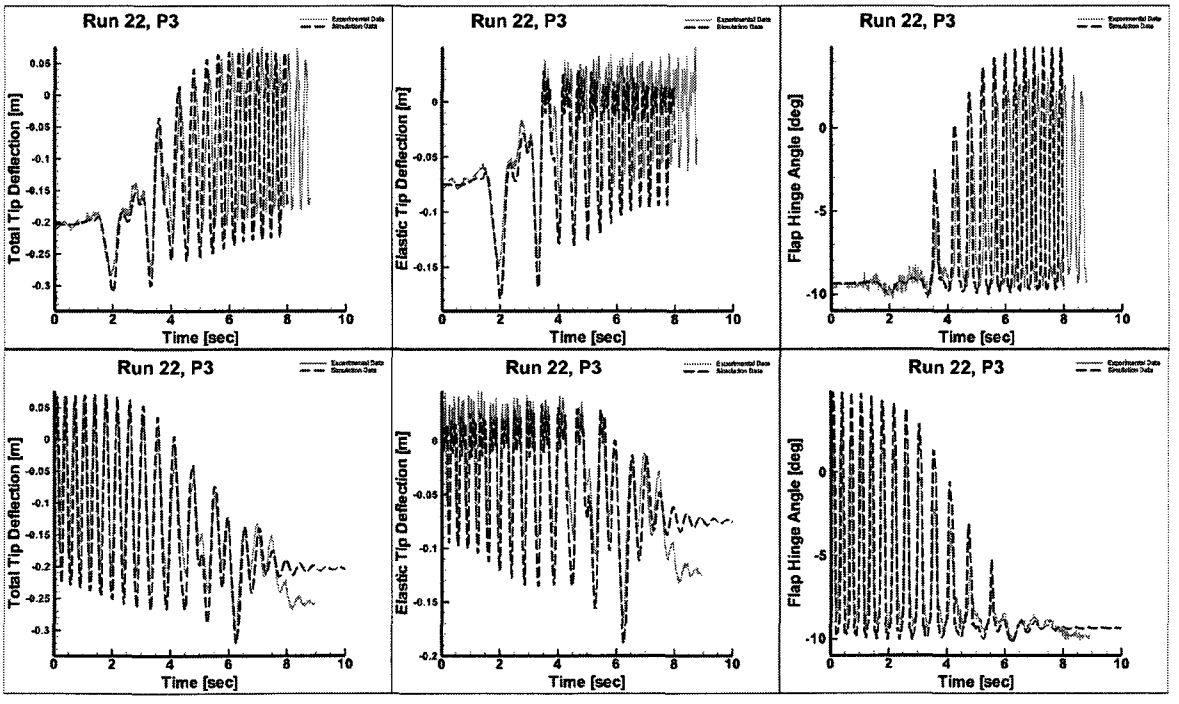

Figure F.10: Time histories of Run 22, P3 [Simulation: dashed line, Experiment: solid line].

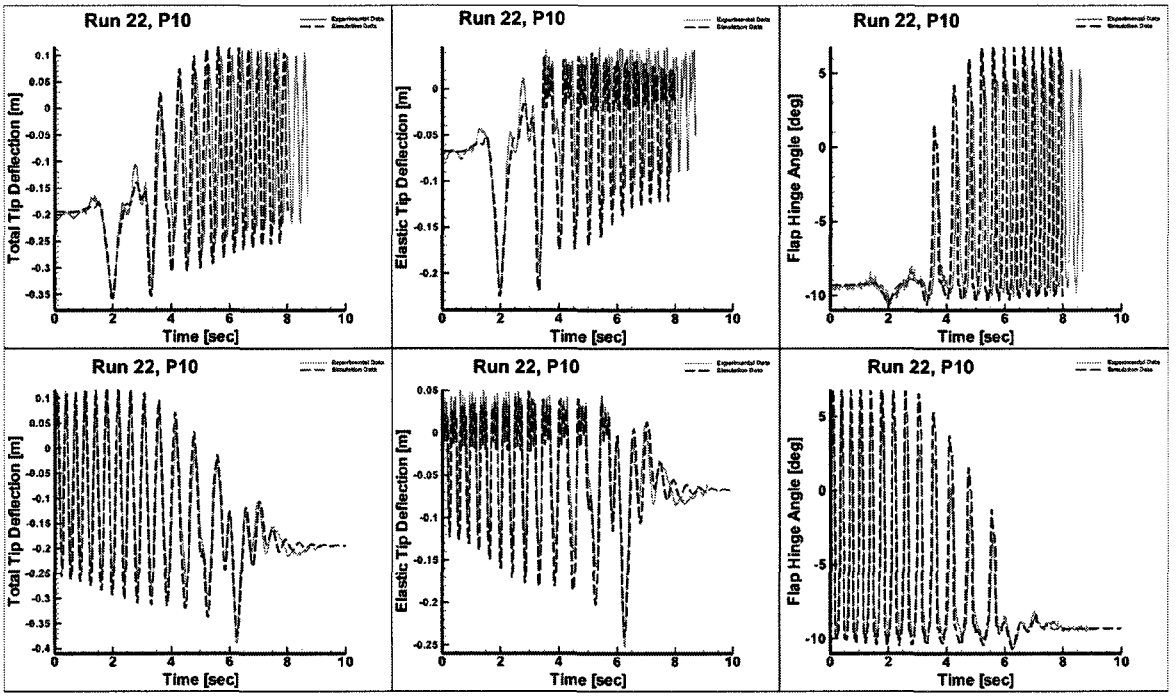

Figure F.11: Time histories of Run 22, P10 [Simulation: dashed line, Experiment: solid line].

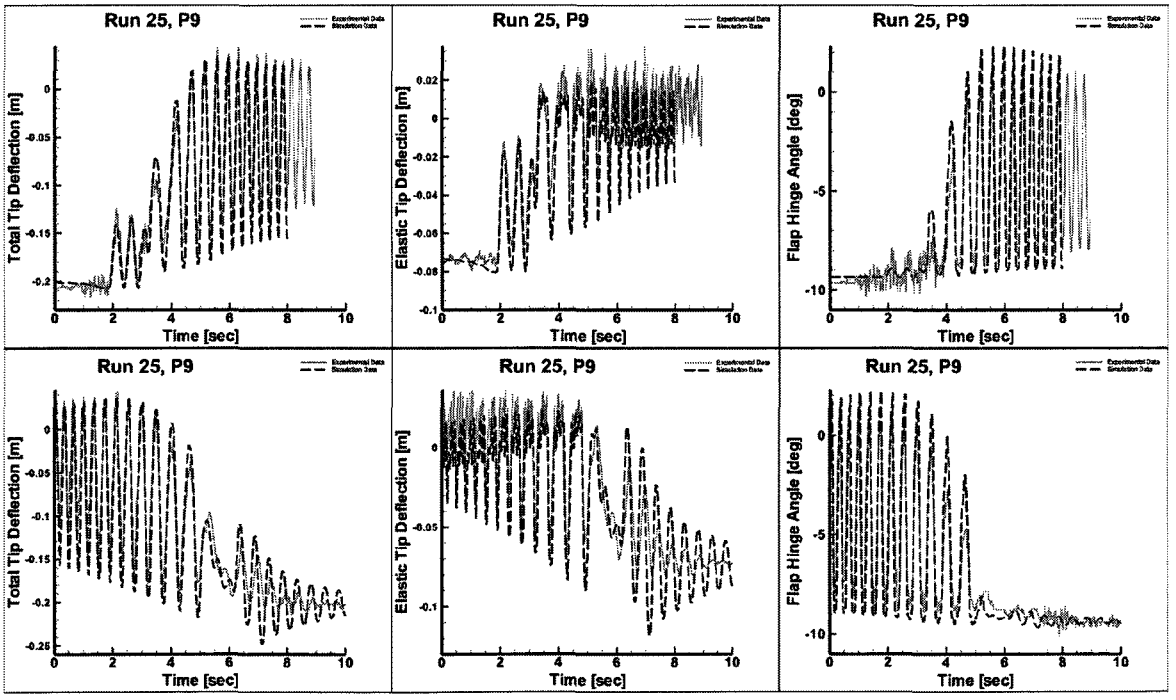

Figure F.12: Time histories of Run 25, P9 [Simulation: dashed line, Experiment: solid line].

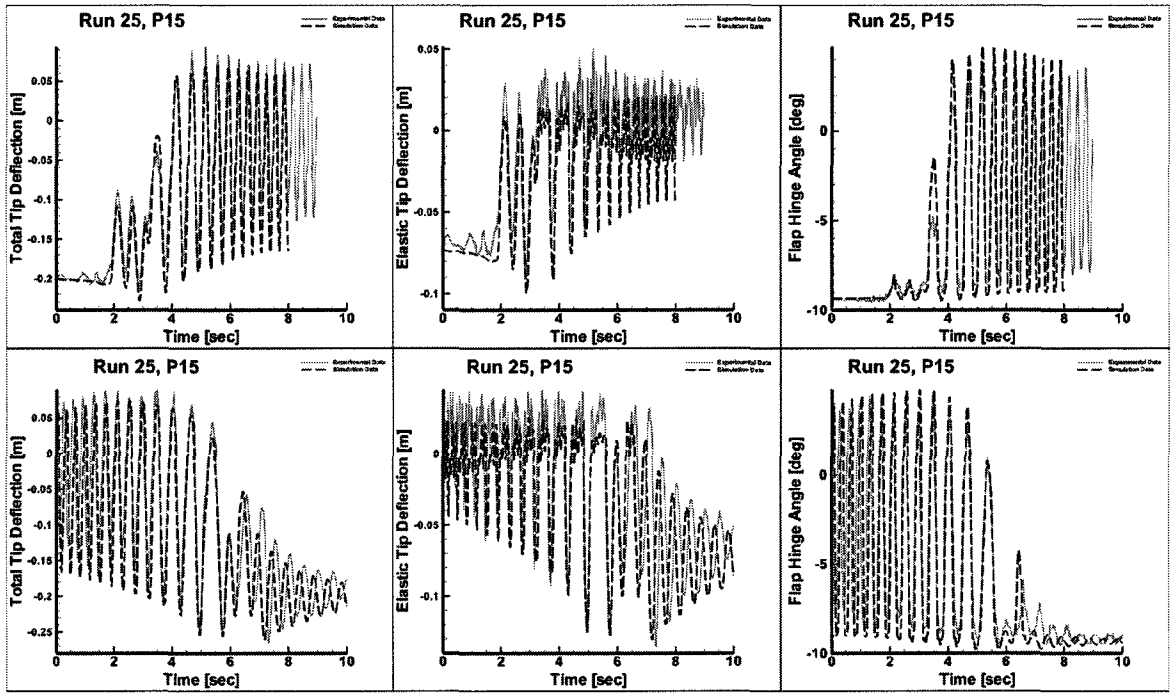

Figure F.13: Time histories of Run 25, P15 [Simulation: dashed line, Experiment: solid line].

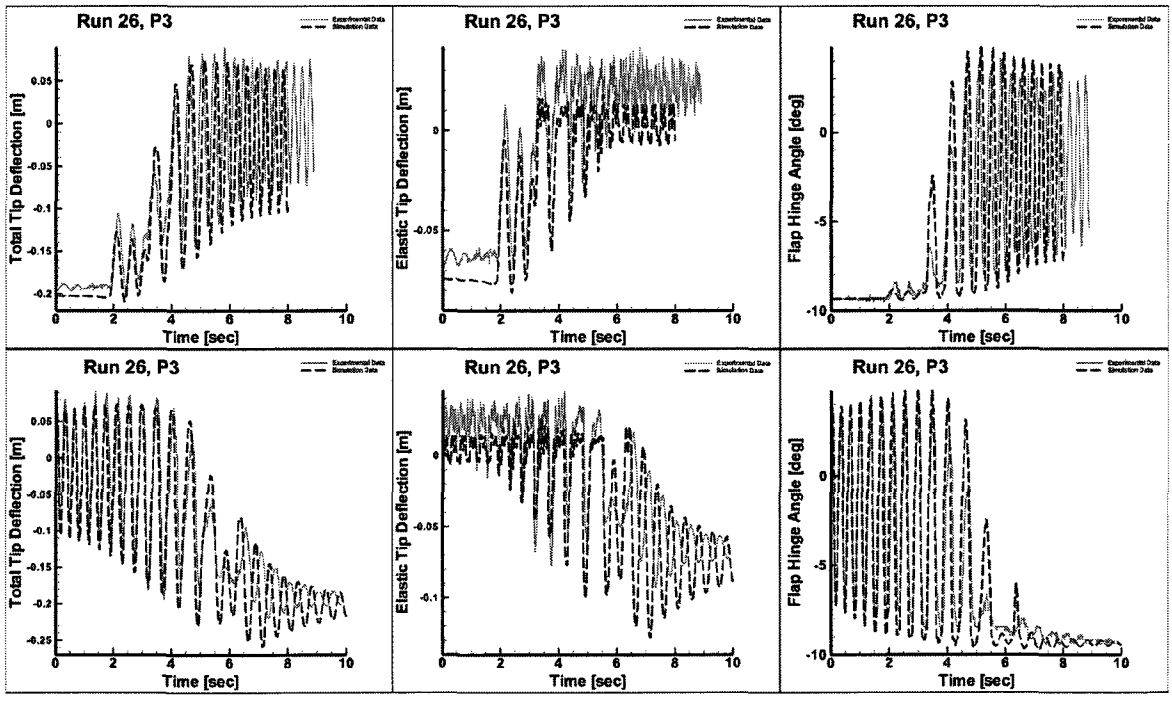

Figure F.14: Time histories of Run 26, P3 [Simulation: dashed line, Experiment: solid line].

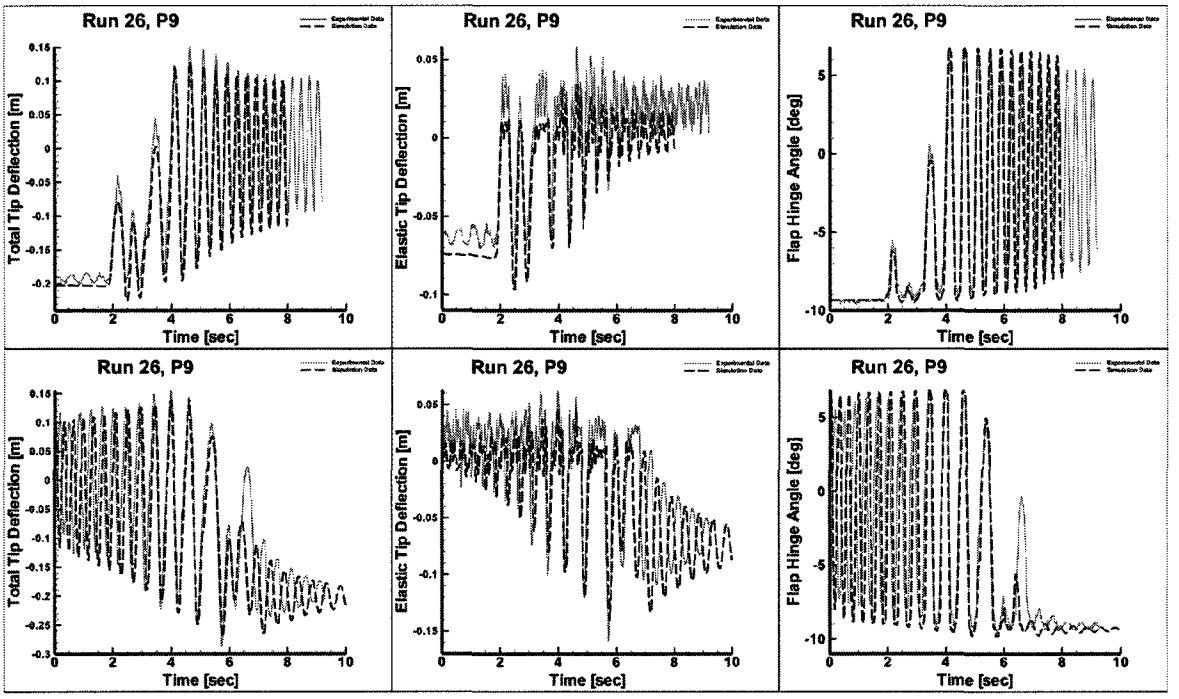

Figure F.15: Time histories of Run 26, P9 [Simulation: dashed line, Experiment: solid line].

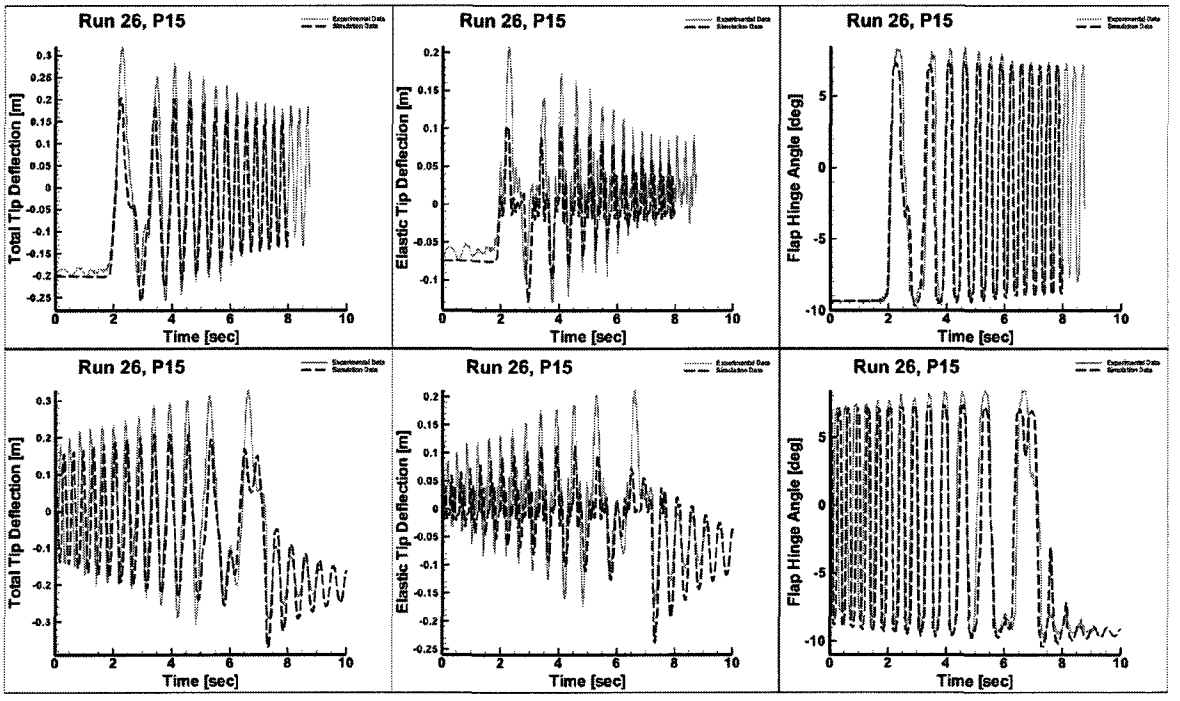

Figure F.16: Time histories of Run 26, P15 [Simulation: dashed line, Experiment: solid line].

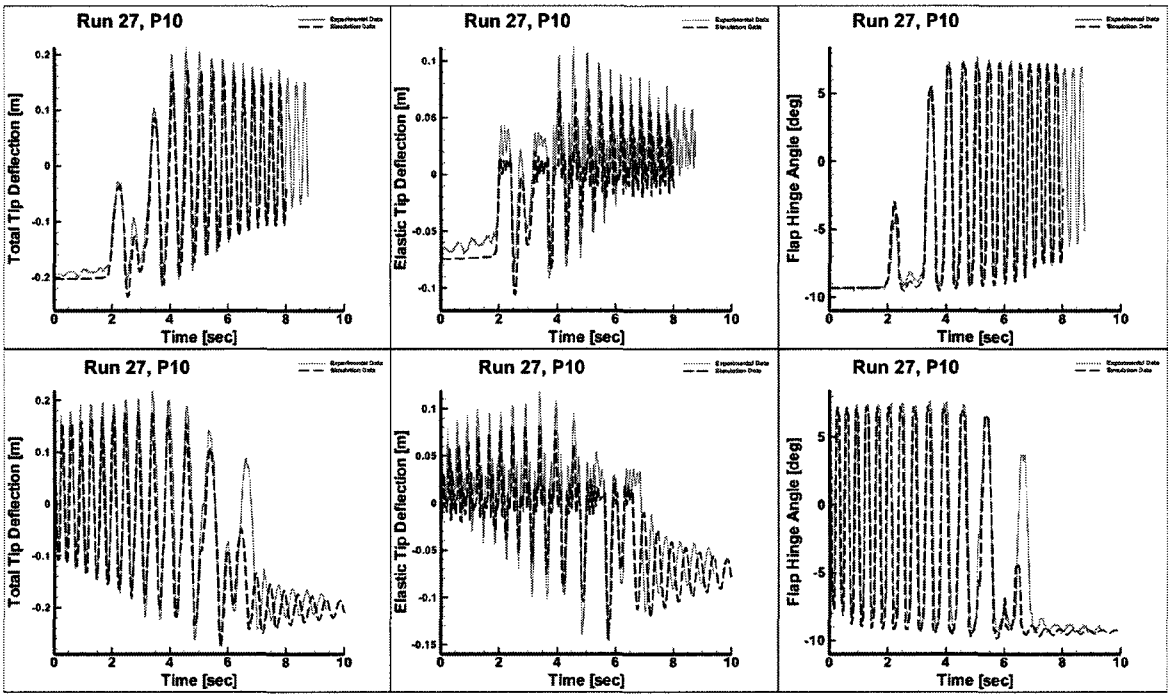

Figure F.17: Time histories of Run 27, P10 [Simulation: dashed line, Experiment: solid line].

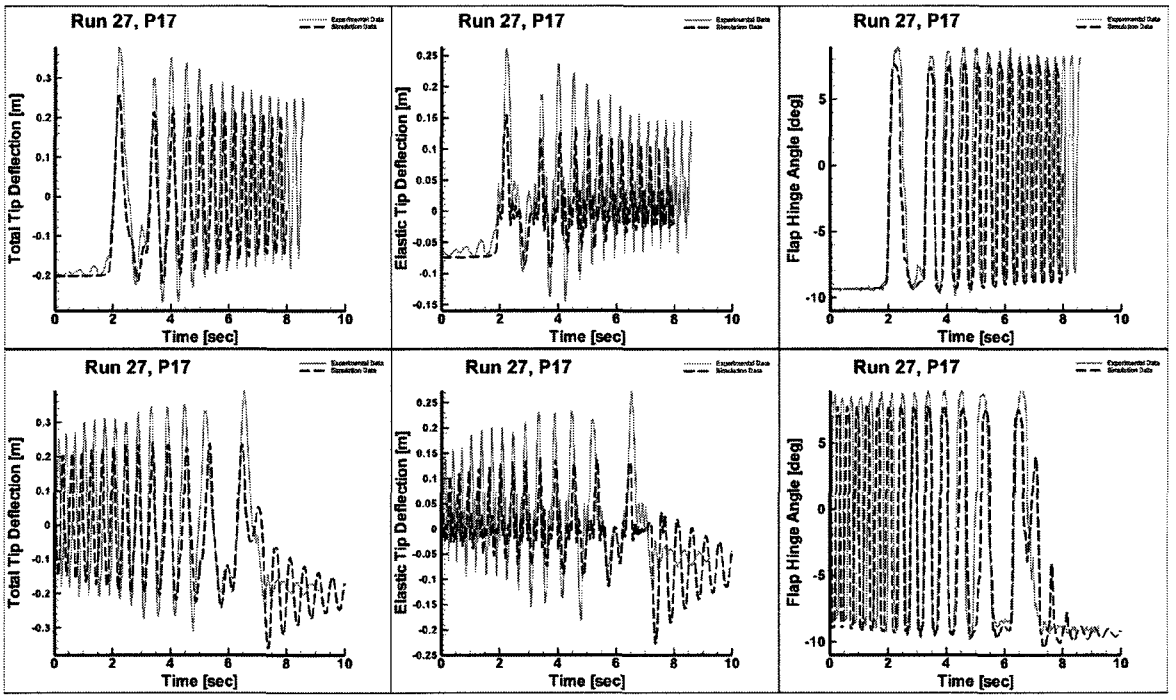

Figure F.18: Time histories of Run 27, P17 [Simulation: dashed line, Experiment: solid line].

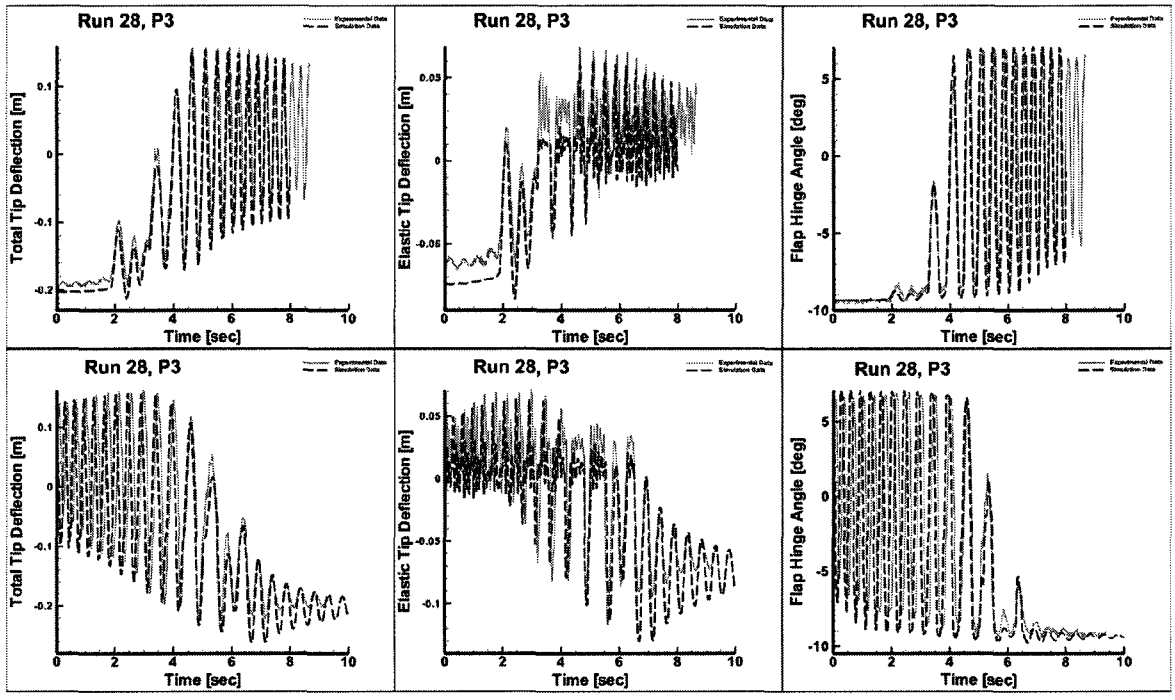

Figure F.19: Time histories of Run 28, P3 [Simulation: dashed line, Experiment: solid line].

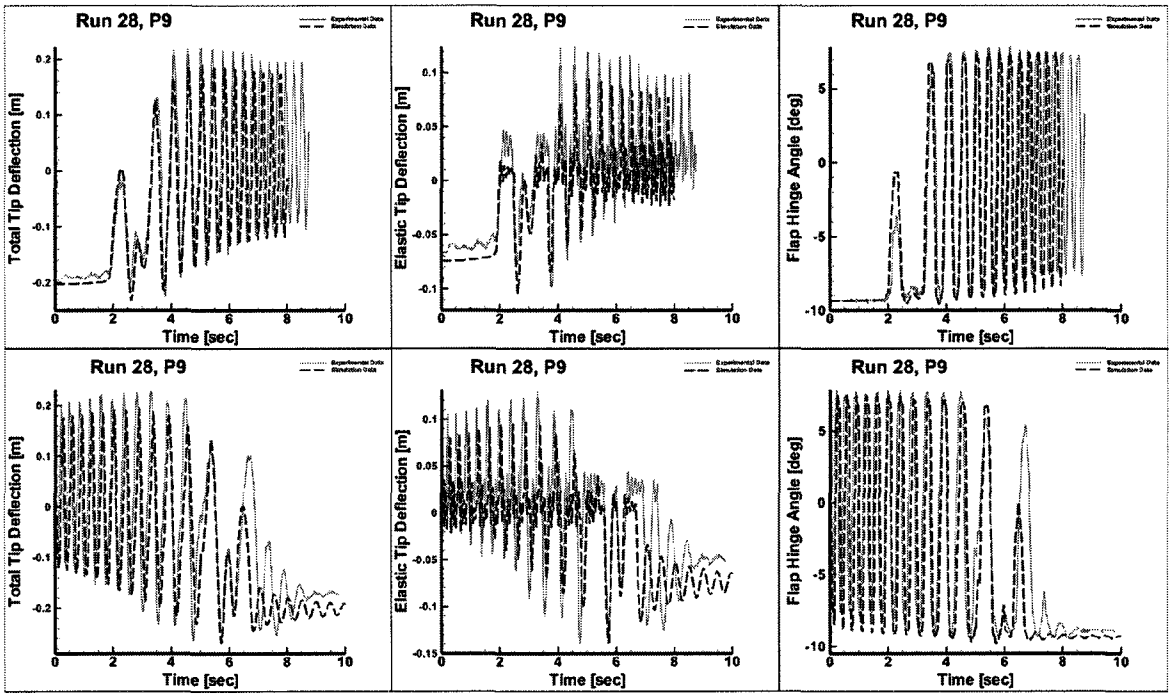

Figure F.20: Time histories of Run 28, P9 [Simulation: dashed line, Experiment: solid line].

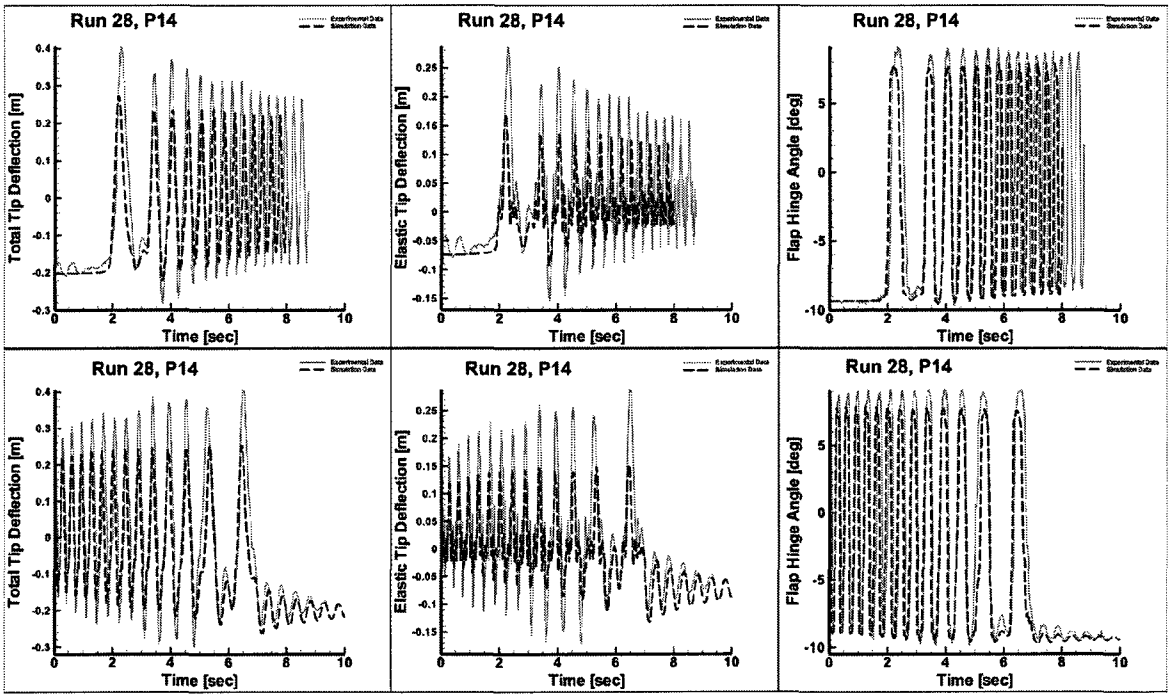

Figure F.21: Time histories of Run 28, P14 [Simulation: dashed line, Experiment: solid line].

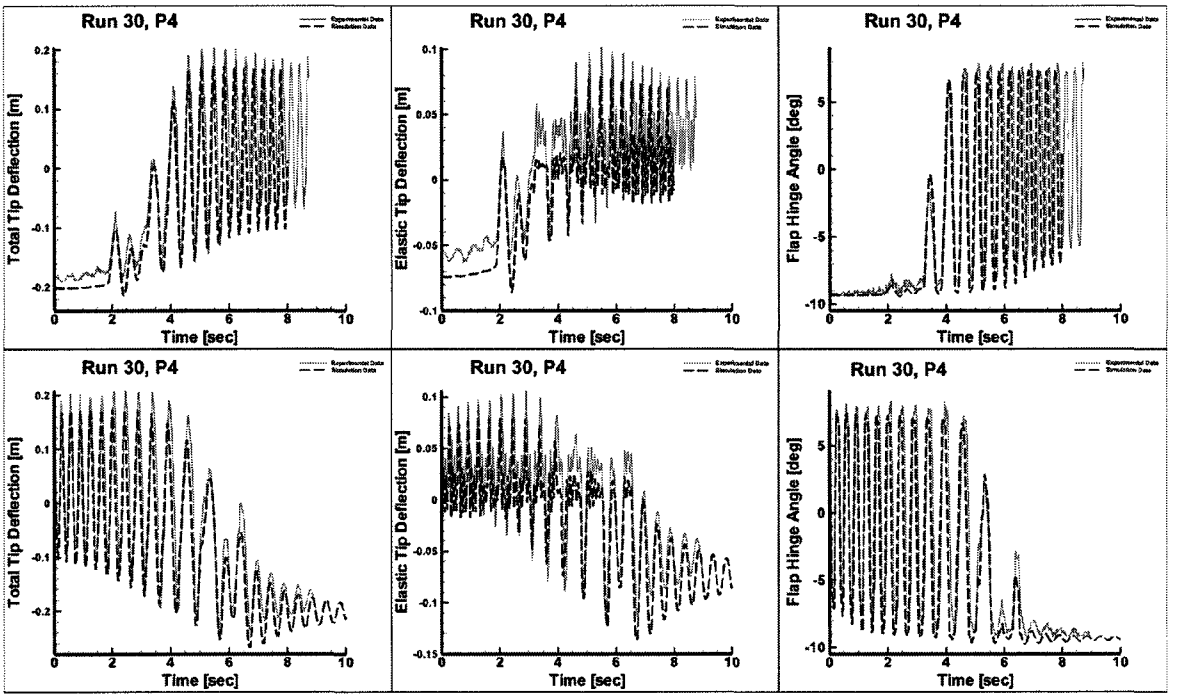

Figure F.22: Time histories of Run 30, P4 [Simulation: dashed line, Experiment: solid line].

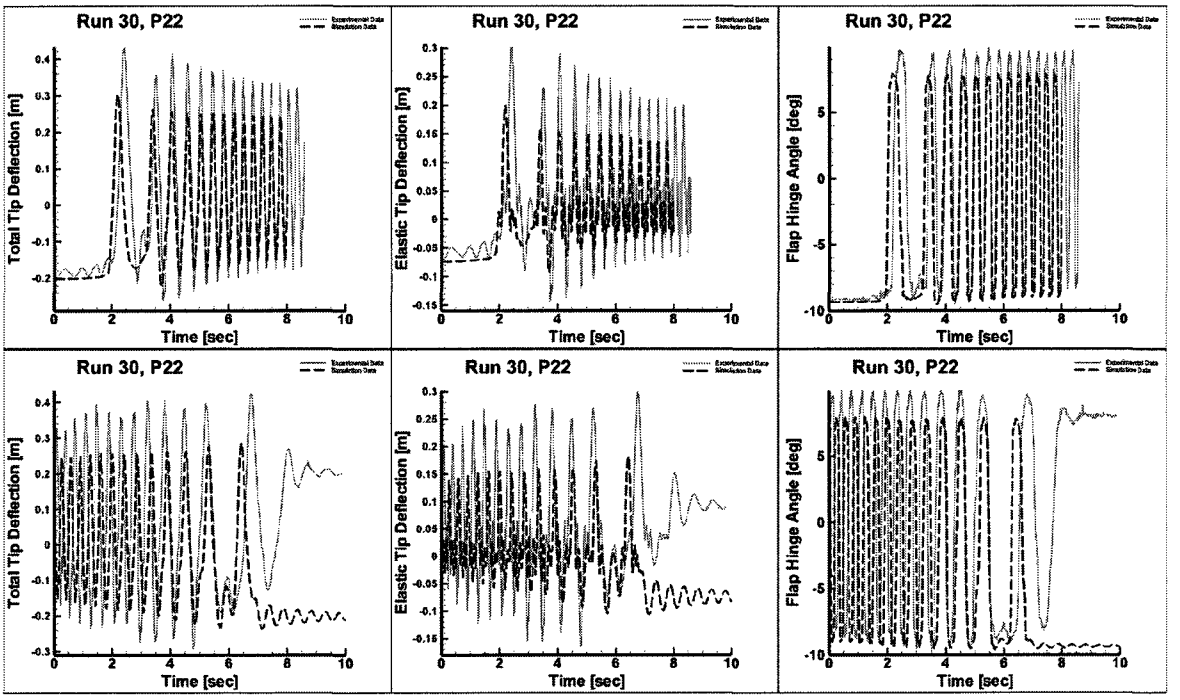

Figure F.23: Time histories of Run 30, P22 [Simulation: dashed line, Experiment: solid line].

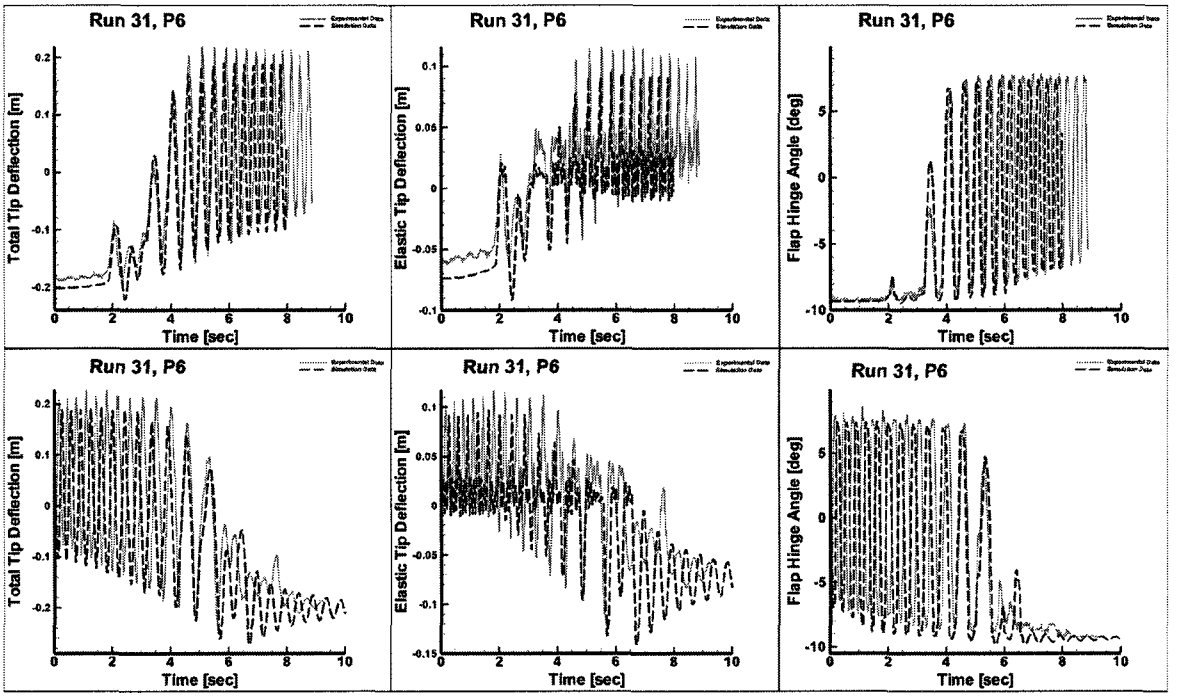

Figure F.24: Time histories of Run 31, P6 [Simulation: dashed line, Experiment: solid line].

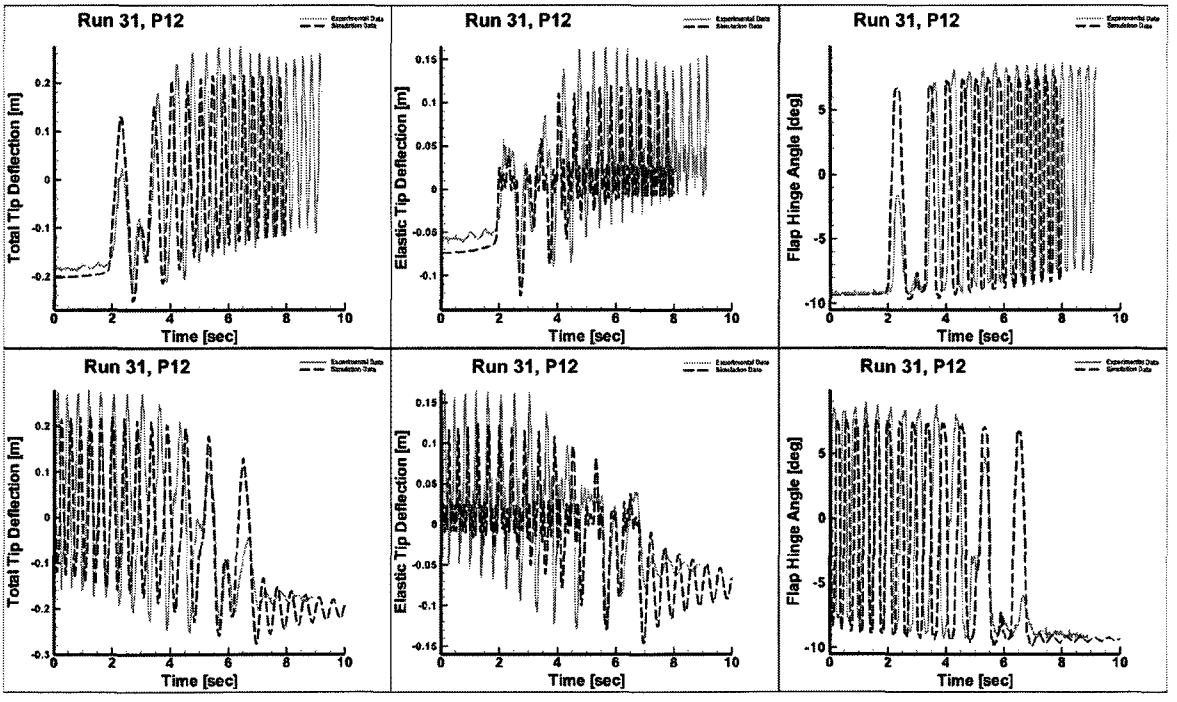

Figure F.25: Time histories of Run 31, P12 [Simulation: dashed line, Experiment: solid line].

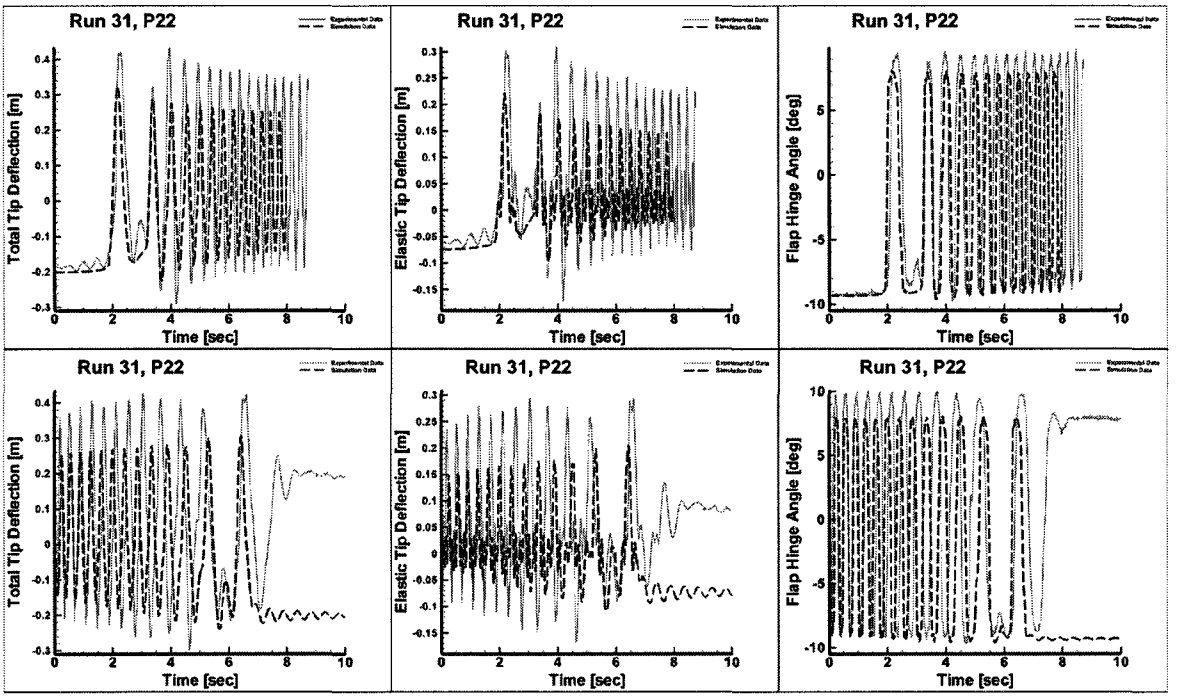

Figure F.26: Time histories of Run 31, P22 [Simulation: dashed line, Experiment: solid line].

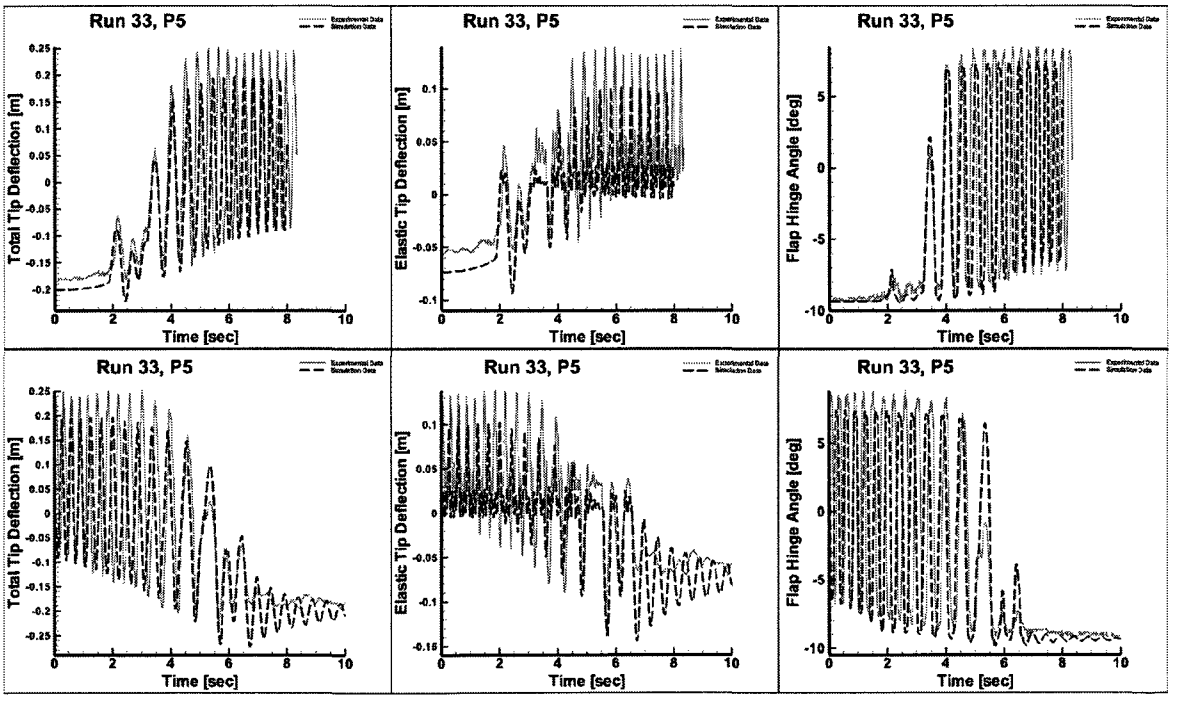

Figure F.27: Time histories of Run 33, P5 [Simulation: dashed line, Experiment: solid line].

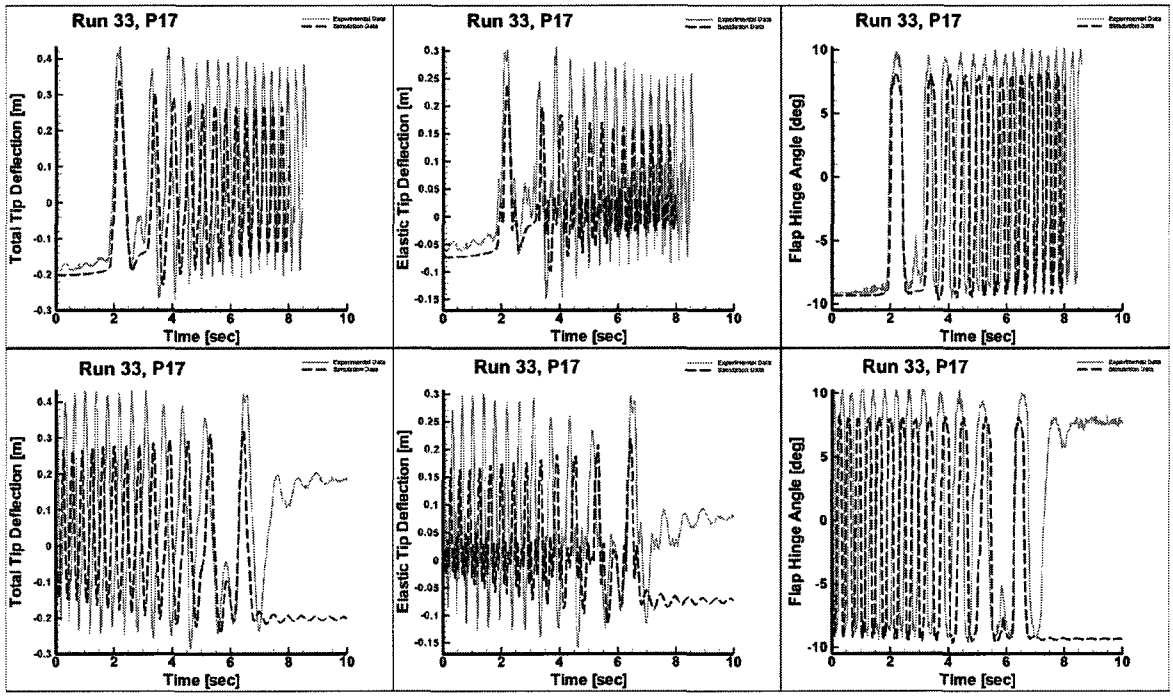

Figure F.28: Time histories of Run 33, P17 [Simulation: dashed line, Experiment: solid line].

Appendix G

G.1 Sample Time History of Representative $1/12^{th}$ Froude-Scaled Ship Motion

Scaled ship motion degrees of freedom and their time rate of change are provided for sea state 4_045_25 in Figs. G.1 through G.6.

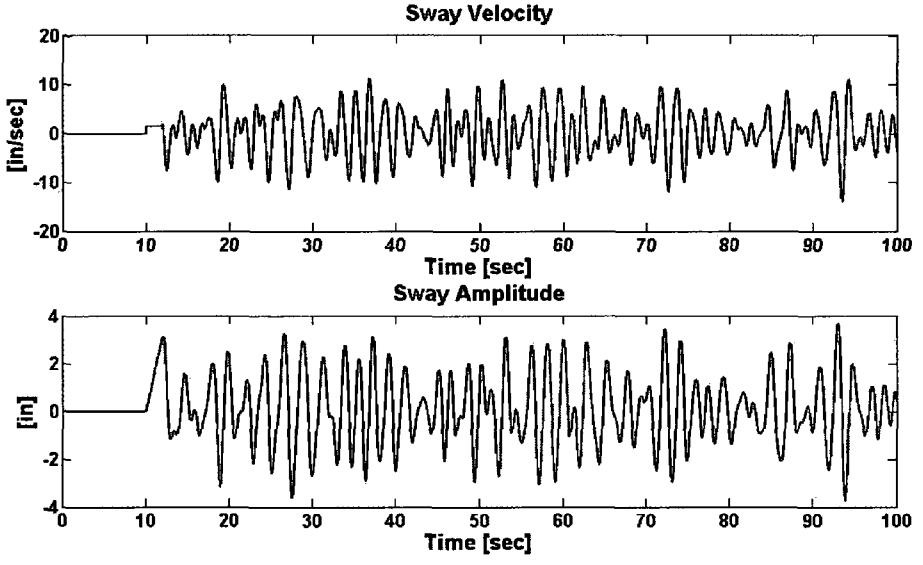

Figure G.1: Scaled sway and sway velocity of ship motion file 4_045_25.

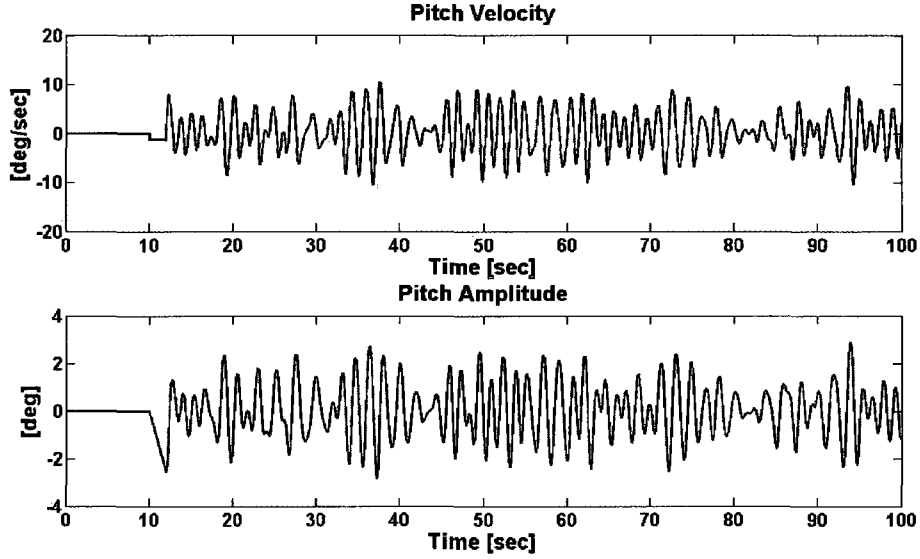

Figure G.2: Scaled pitch and pitch velocity of ship motion file 4_045_25.

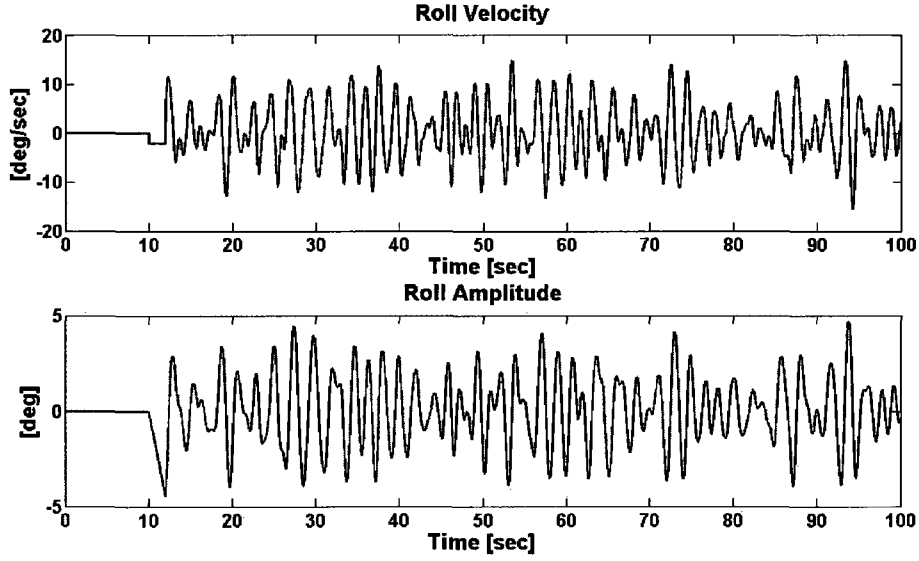

Figure G.3: Scaled roll and roll velocity of ship motion file 4_045_25.

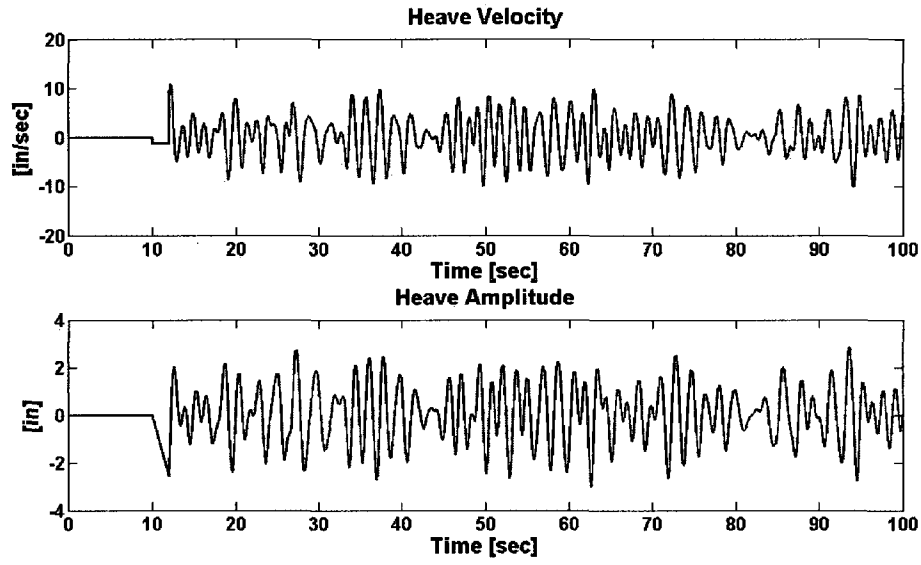

Figure G.4: Scaled heave and heave velocity of ship motion file 4_045_25.

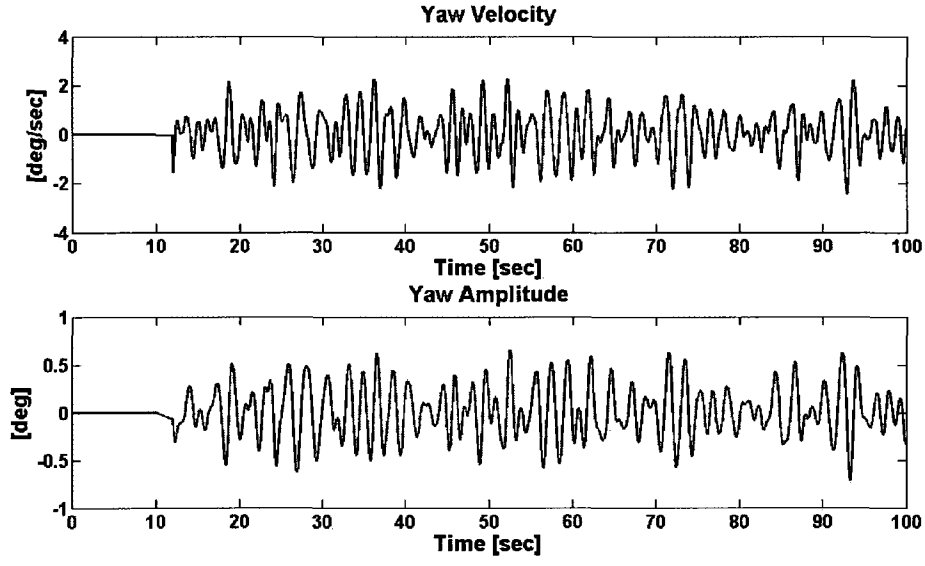

Figure G.5: Scaled yaw and yaw velocity of ship motion file 4_045_25.

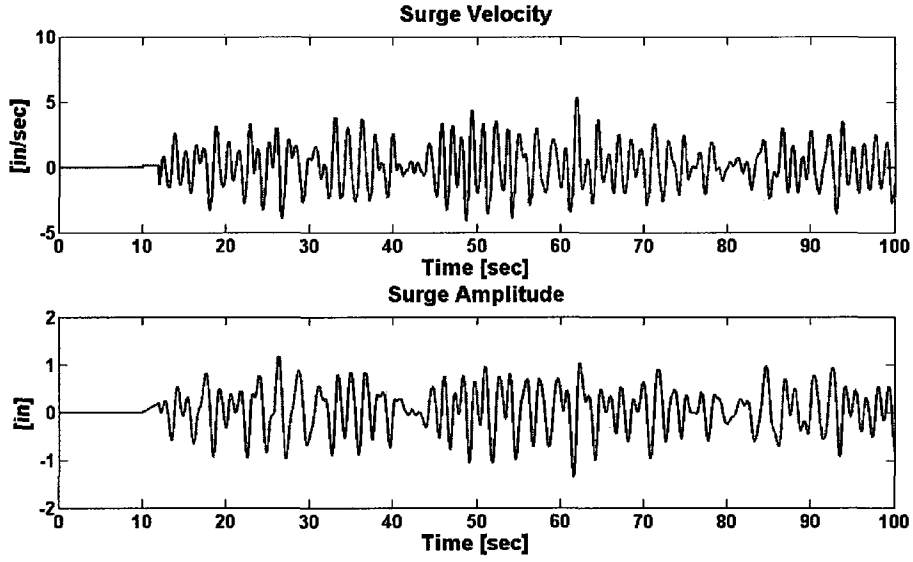

Figure G.6: Scaled surge and surge velocity of ship motion file 4_045_25.

Appendix H

H.1 Static Actuation

The results of the static actuation strategy using AFCs/MFCs for all wind speeds are shown in Fig. H.1 to Fig. H.2

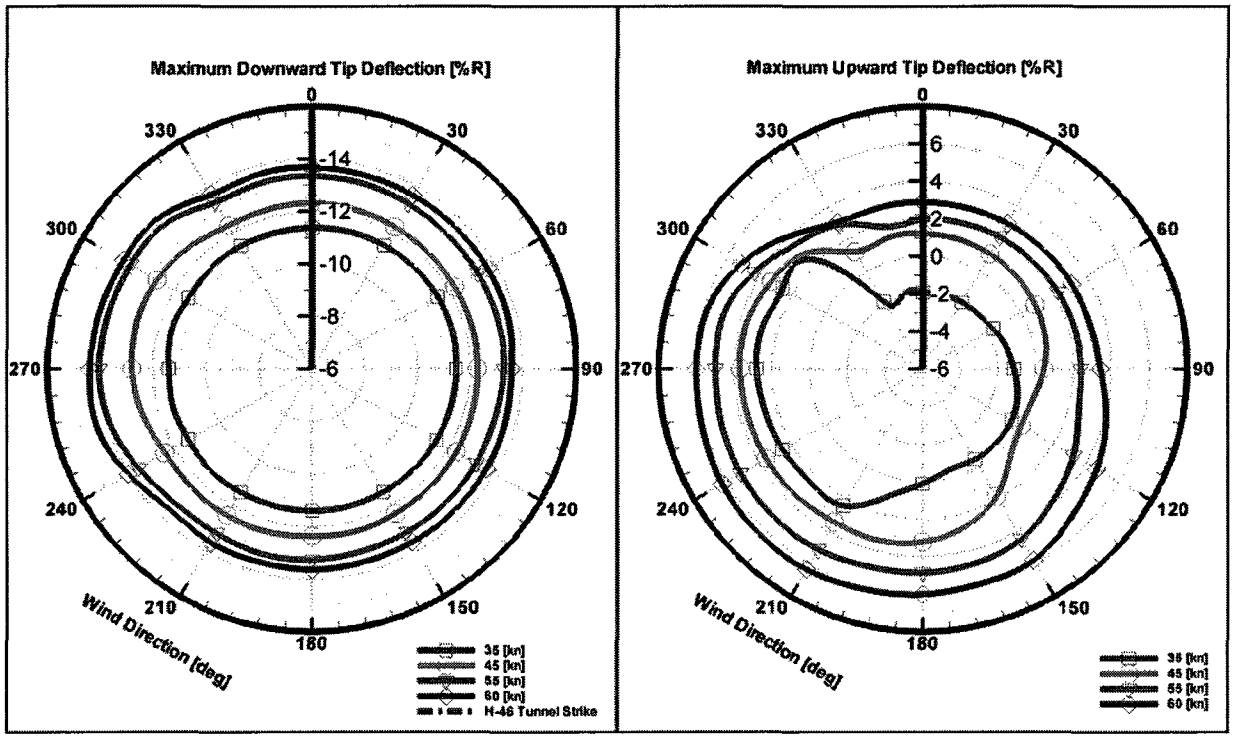

Figure H.1: Maximum downward and upward tip deflection of the engagement of the adopted IATR with DC actuation of the integrated AFCs.

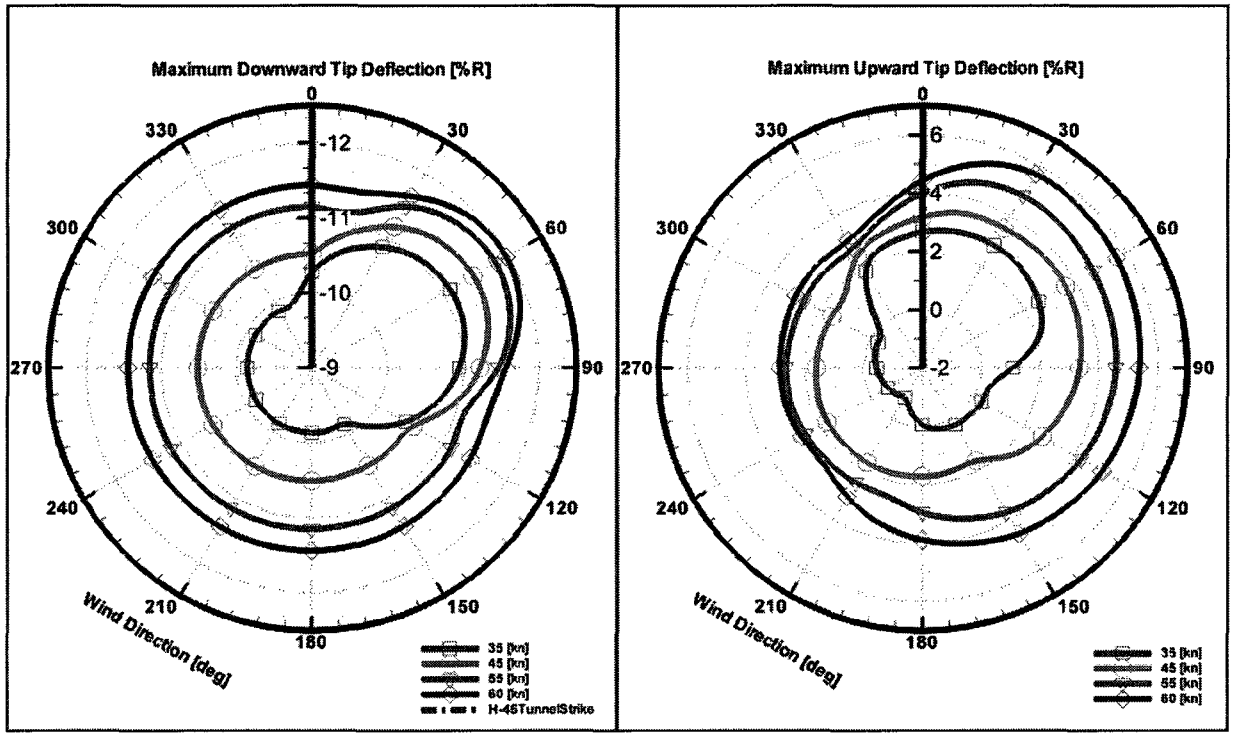

Figure H.2: Maximum downward and upward tip deflection of the disengagement of the adopted IATR with DC actuation of the integrated AFCs.

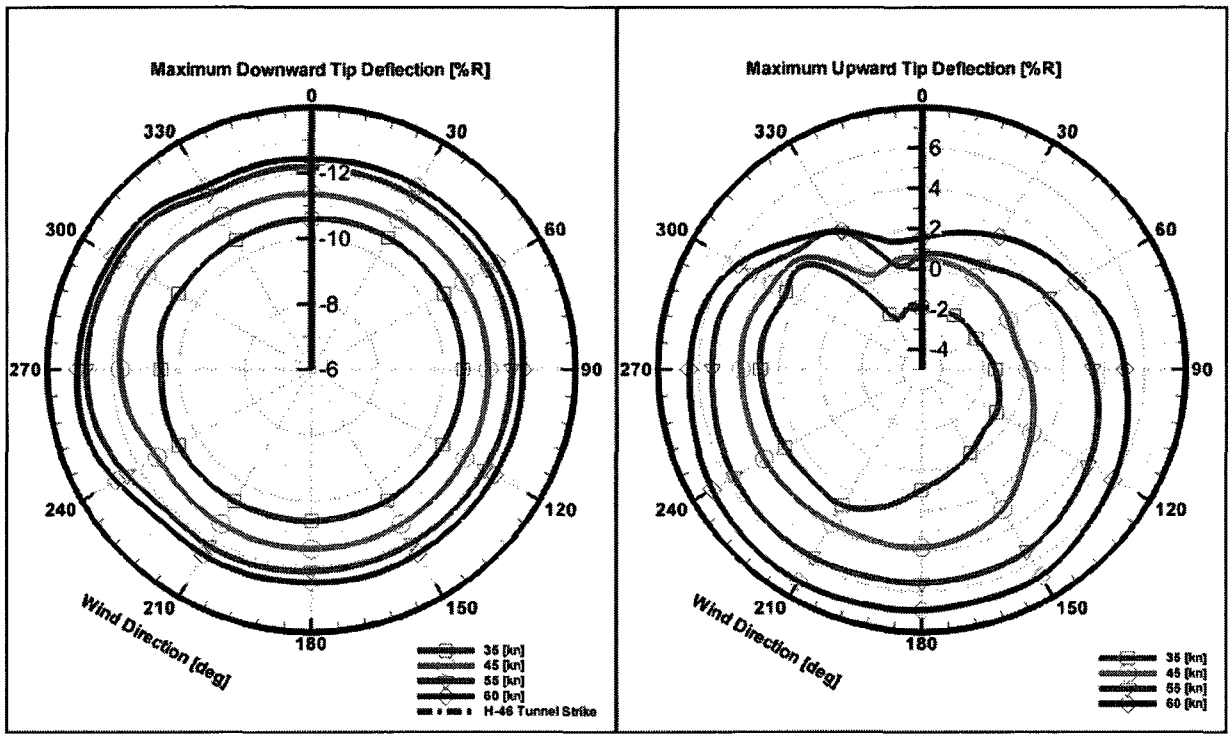

Figure H.3: Maximum downward and upward tip deflection of the engagement of the adopted IATR with DC actuation of the integrated MFCs.

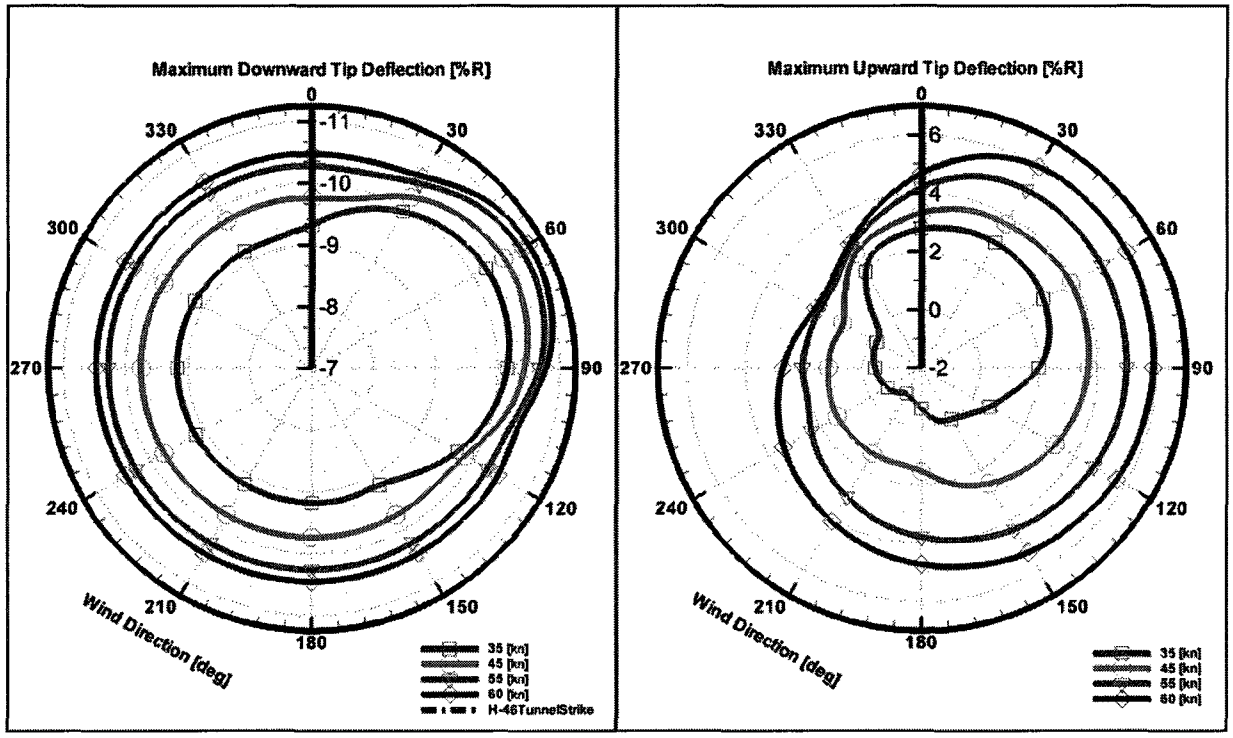

Figure H.4: Maximum downward and upward tip deflection of the disengagement of the adopted IATR with DC actuation of the integrated MFCs.

H.2 Dynamic Actuation

H.2.1 Test Temporal Points

The value of the transitional temporal points for the $0.75\Omega_{\text{critical}}$, $1.5\Omega_{\text{critical}}$, and $1.75\Omega_{\text{critical}}$ cases are given in Table. H.1 to Table. H.3

Table H.1: $0.75\Omega_{\text{critical}}$ and t_{critical} for a set of wind speeds and a gust factor of 0.25.

Wind Speed [kn]	$0.75\Omega_{\text{critical}}$ [rad/s]	% of Ω_{max}	t_{critical} [s]
35	13.98	7.77	3.599
45	16.23	9.02	3.647
55	18.72	10.39	3.697
60	19.98	11.10	3.721

Table H.2: $1.5\Omega_{\text{critical}}$ and t_{critical} for a set of wind speeds and a gust factor of 0.25.

Wind Speed [kn]	$1.5\Omega_{\text{critical}}$ [rad/s]	% of Ω_{max}	t_{critical} [s]
35	27.96	15.53	3.860
45	32.46	18.03	3.931
55	37.44	20.80	4.005
60	39.96	22.20	4.041

Table H.3: $1.75\Omega_{\text{critical}}$ and t_{critical} for a set of wind speeds and a gust factor of 0.25.

Wind Speed [kn]	$1.75\Omega_{\text{critical}}$ [rad/s]	% of Ω_{max}	t_{critical} [s]
35	32.62	18.12	3.933
45	37.87	21.04	4.011
55	43.68	24.27	4.093
60	46.62	25.90	4.133

The results of applying the actuation strategy of Eq. 9.11 and Eq. 9.12 at Ω_{critical} for AFCs and MFCs actuation are shown in Fig. H.5 to Fig. H.8

The results of examining all of the transitional temporal points for all considered wind speeds are shown in Fig. H.9 to Fig. H.14

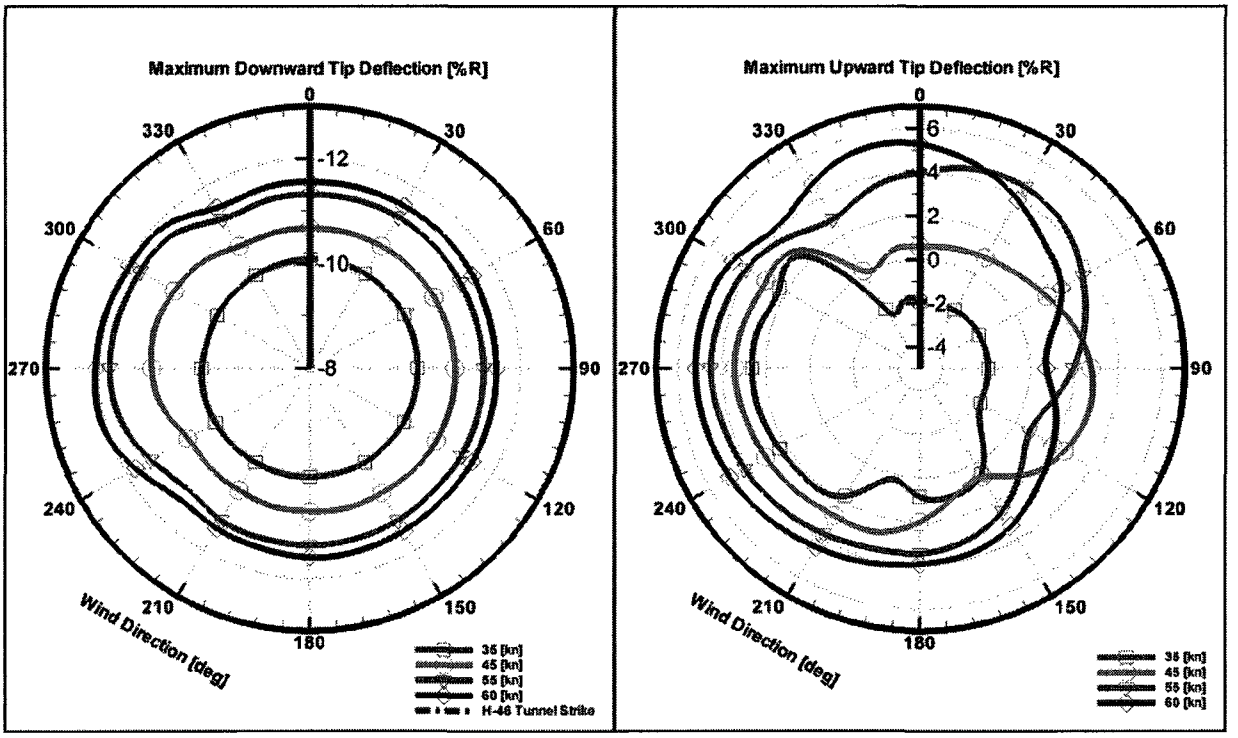

Figure H.5: Maximum downward and upward tip deflection of the engagement of the adopted IATR with dynamic actuation of the integrated AFCs for Ω_{critical}.

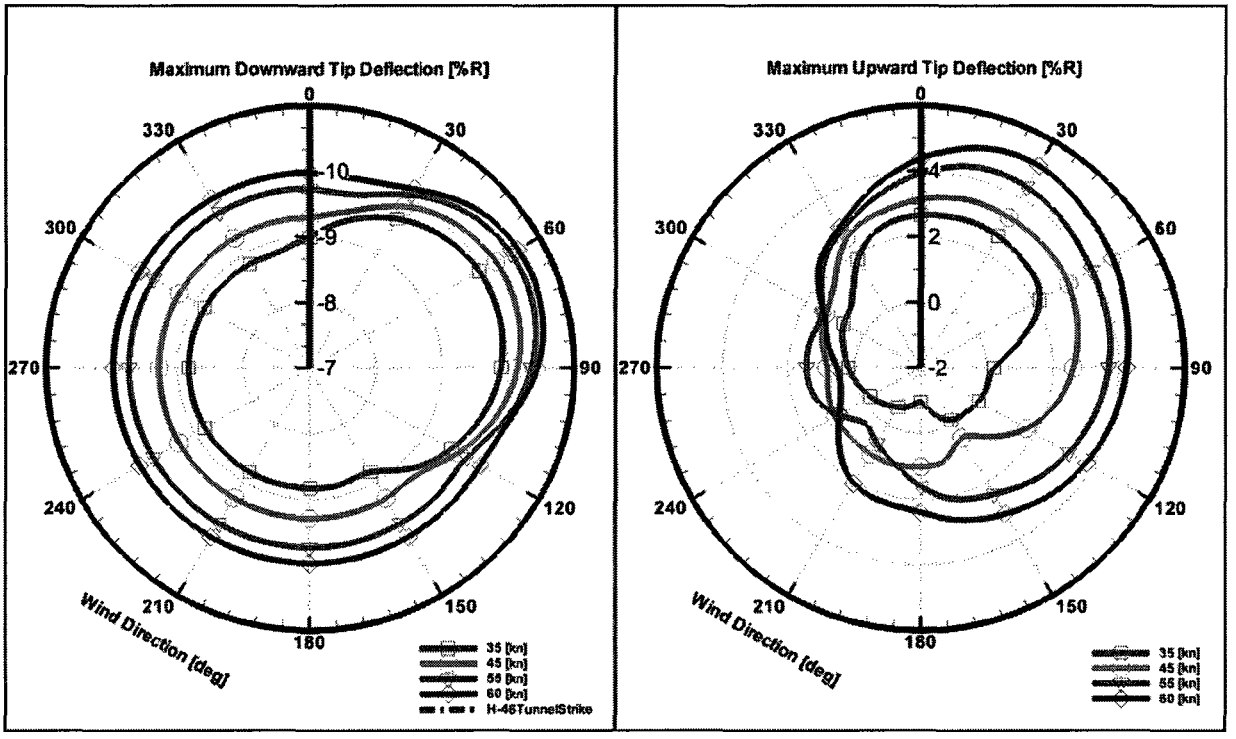

Figure H.6: Maximum downward and upward tip deflection of the disengagement of the adopted IATR with dynamic actuation of the integrated AFCs for Ω_{critical}.

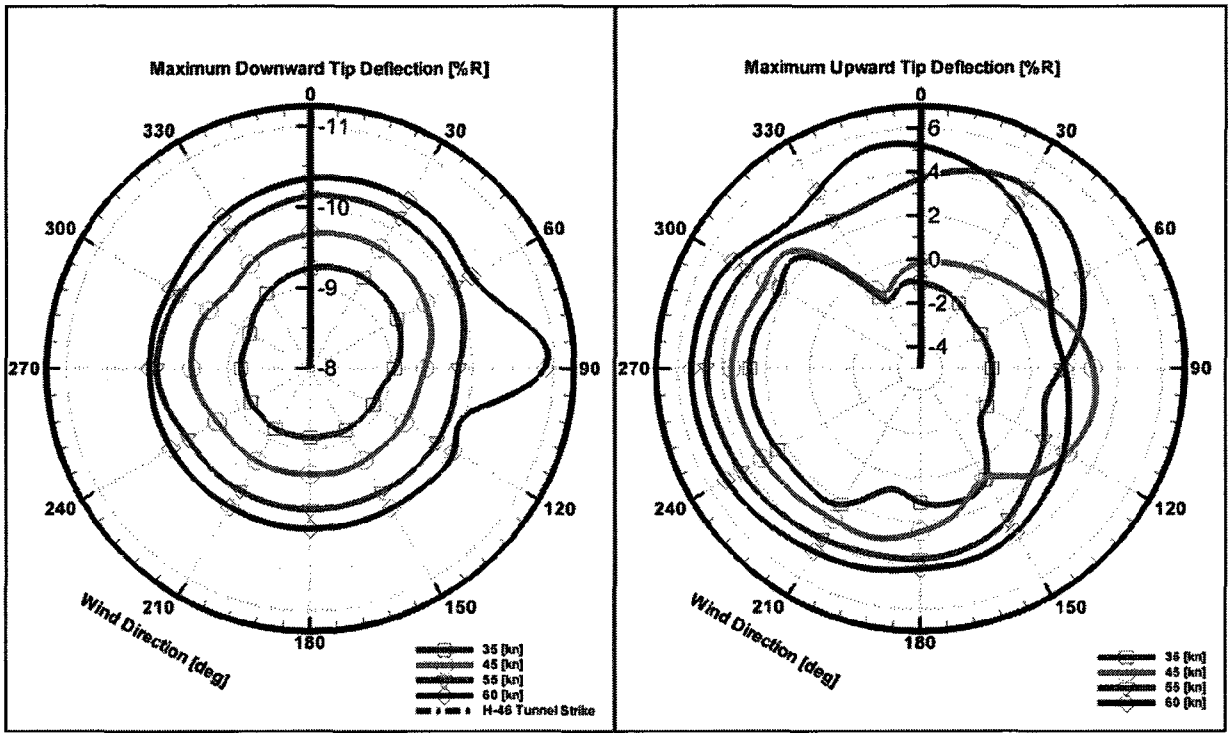

Figure H.7: Maximum downward and upward tip deflection of the engagement of the adopted IATR with dynamic actuation of the integrated MFCs for Ω_{critical}.

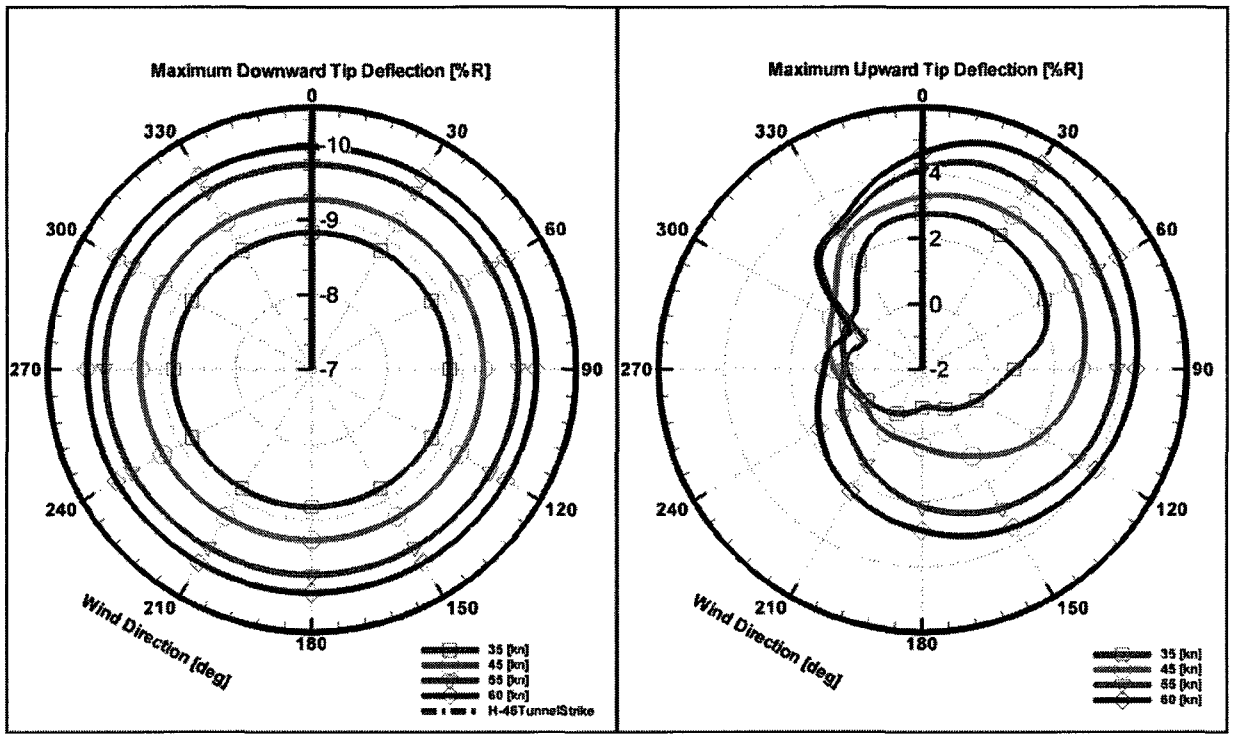

Figure H.8: Maximum downward and upward tip deflection of the disengagement of the adopted IATR with dynamic actuation of the integrated MFCs for Ω_{critical}.

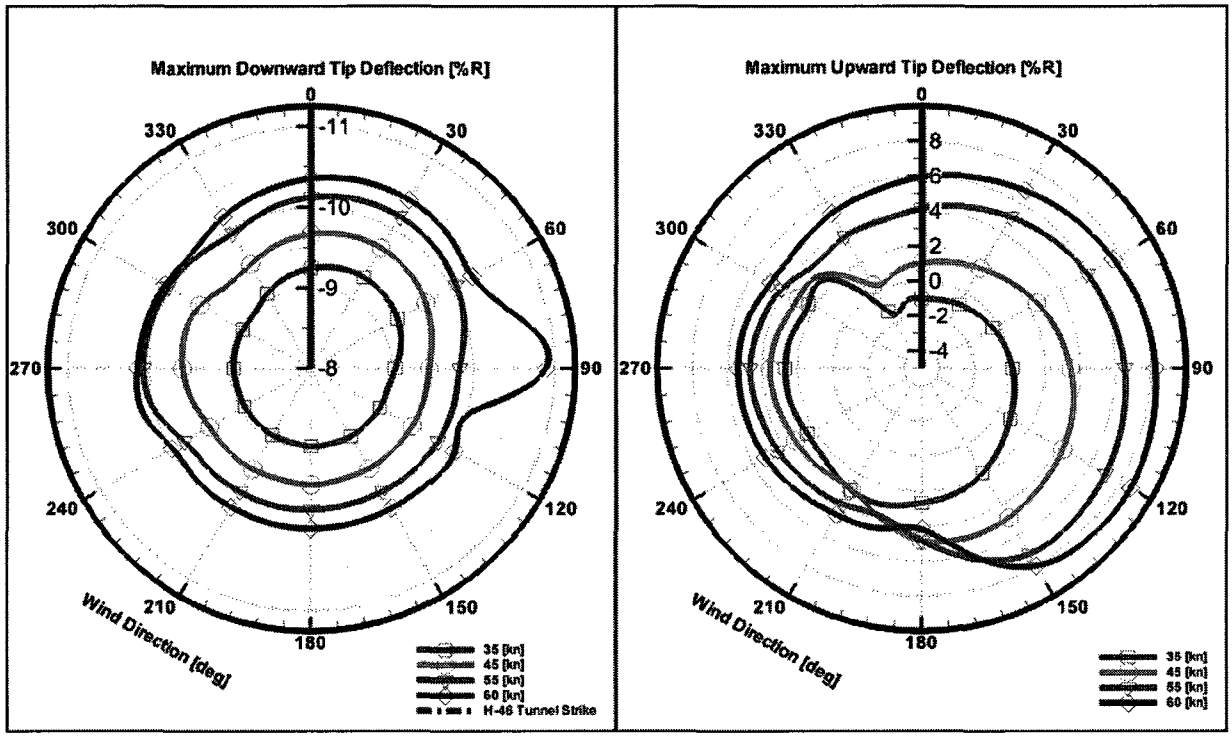

Figure H.9: Maximum downward and upward tip deflection of the engagement of the adopted IATR with dynamic actuation of the integrated MFCs for $0.5\Omega_{\text{critical}}$.

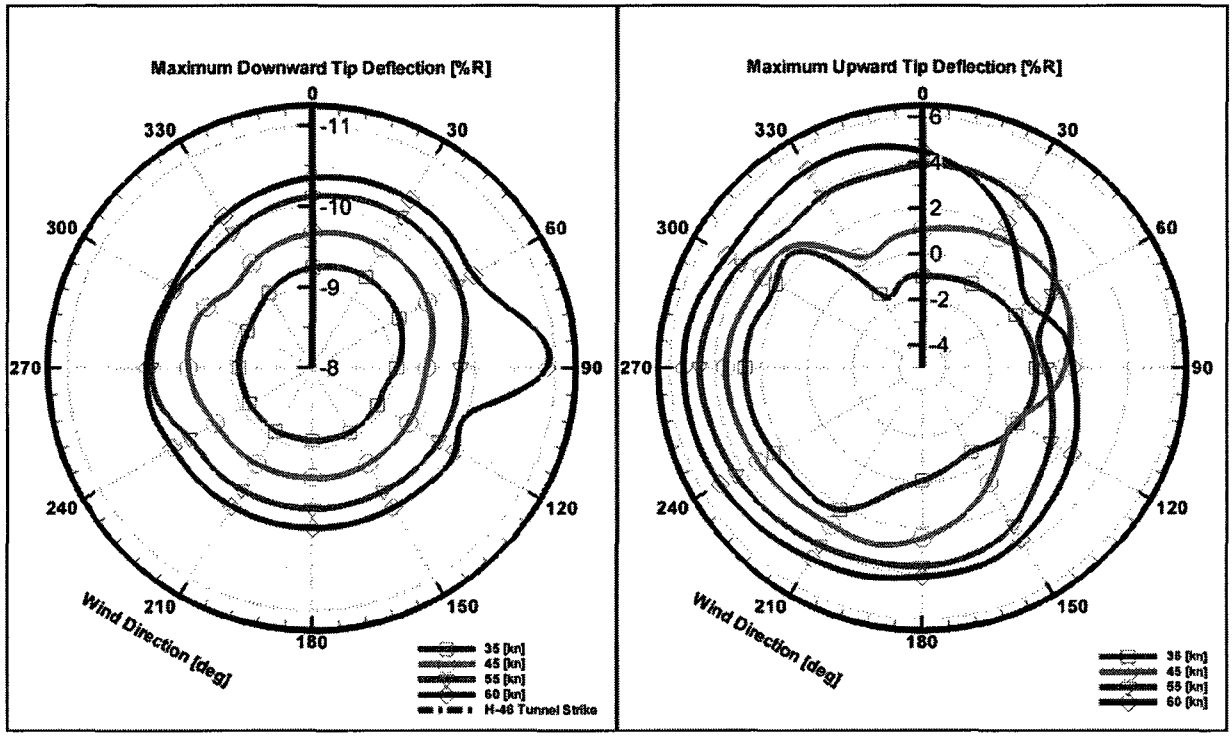

Figure H.10: Maximum downward and upward tip deflection of the engagement of the adopted IATR with dynamic actuation of the integrated MFCs for $0.75\Omega_{\text{critical}}$.

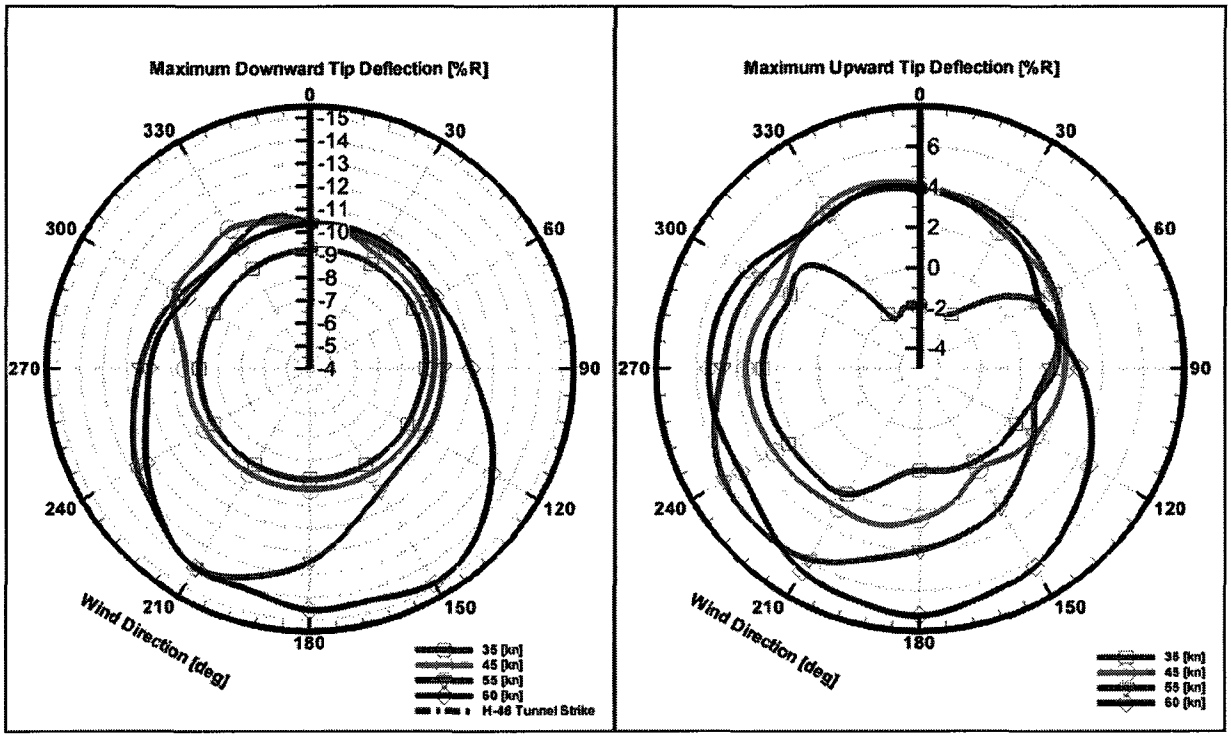

Figure H.11: Maximum downward and upward tip deflection of the engagement of the adopted IATR with dynamic actuation of the integrated MFCs for $1.25\Omega_{\text{critical}}$.

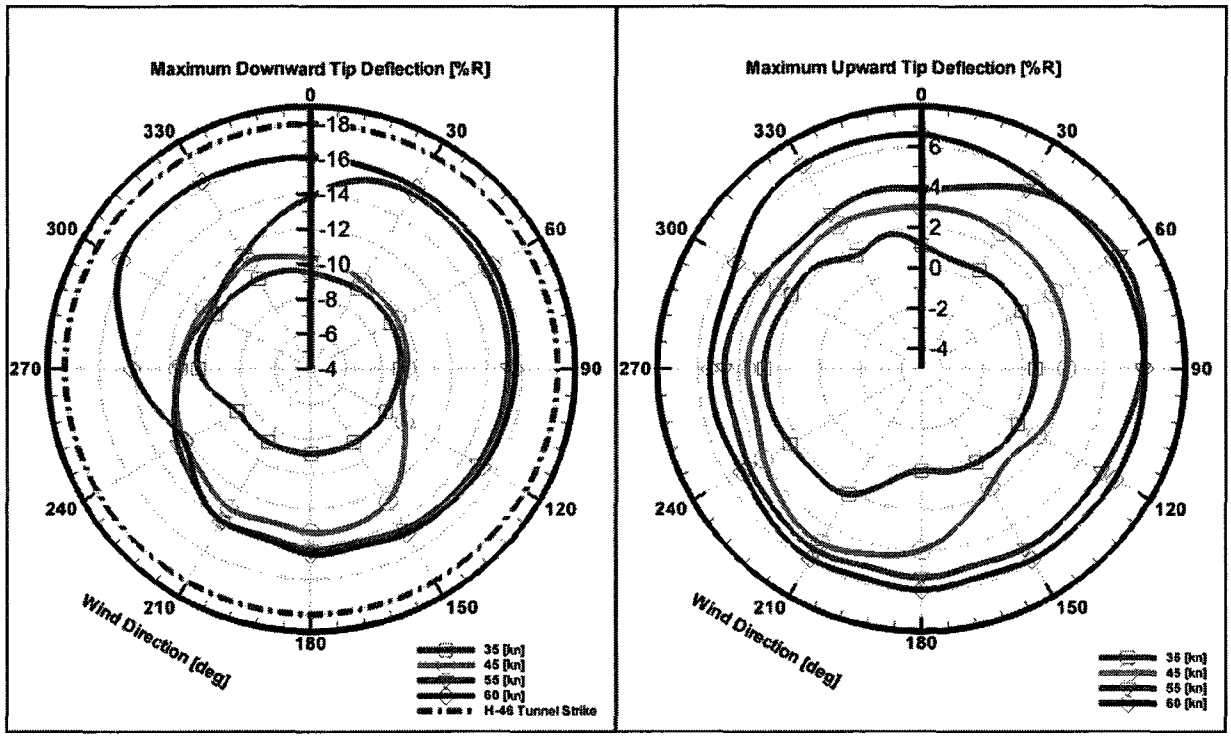

Figure H.12: Maximum downward and upward tip deflection of the engagement of the adopted IATR with dynamic actuation of the integrated MFCs for $1.5\Omega_{\text{critical}}$.

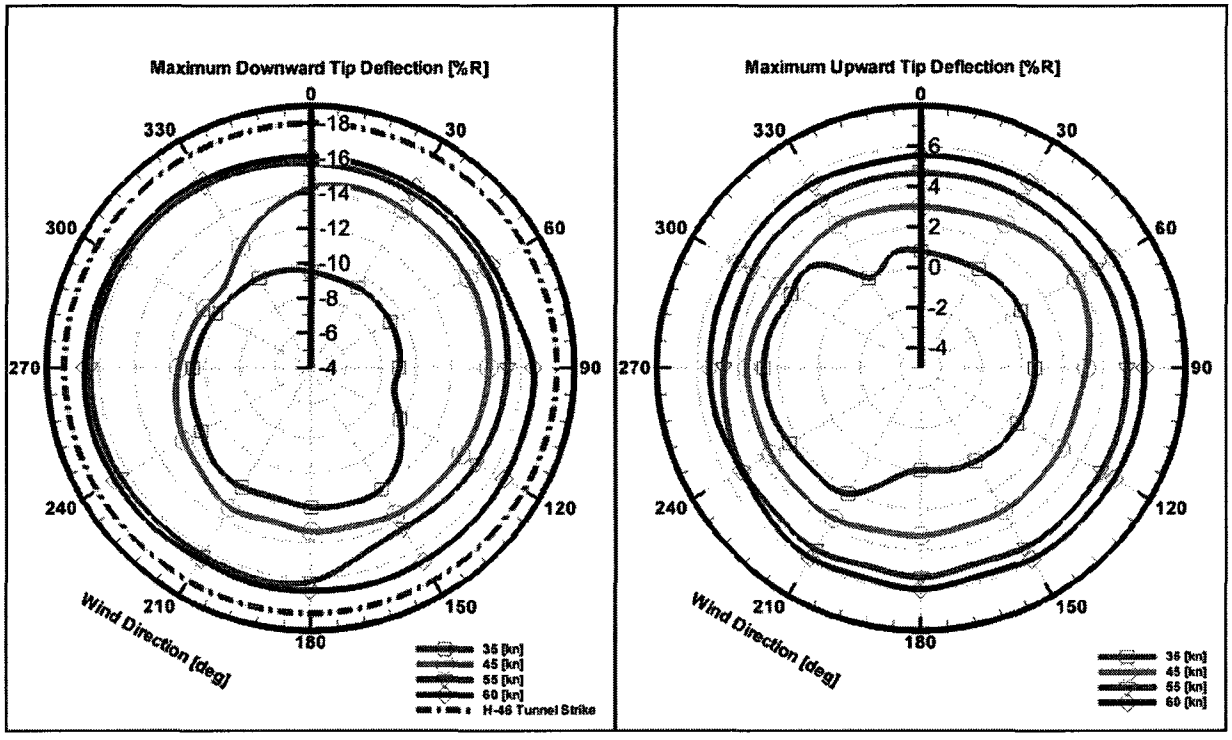

Figure H.13: Maximum downward and upward tip deflection of the engagement of the adopted IATR with dynamic actuation of the integrated MFCs for $1.75\Omega_{\text{critical}}$.

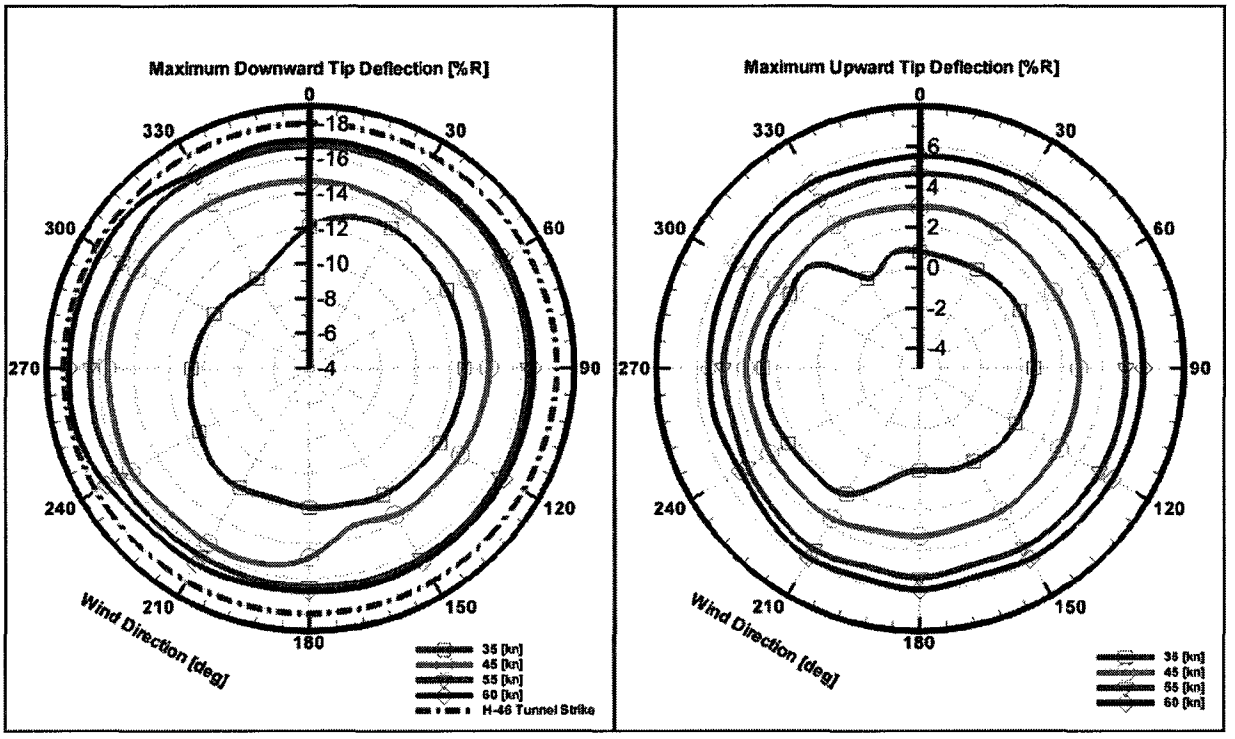

Figure H.14: Maximum downward and upward tip deflection of the engagement of the adopted IATR with dynamic actuation of the integrated MFCs for $2.0\Omega_{\text{critical}}$.

H.3 Effect of Ship Motion

The resulting maximum deflection response for the rotor engagement and disengagement for the 4_030_10 and 4_090_10 sea states coupled with the experimental and the linear deterministic airwake model is shown in Fig. H.15 to H.22 along with the effect of the dynamic actuation strategy.

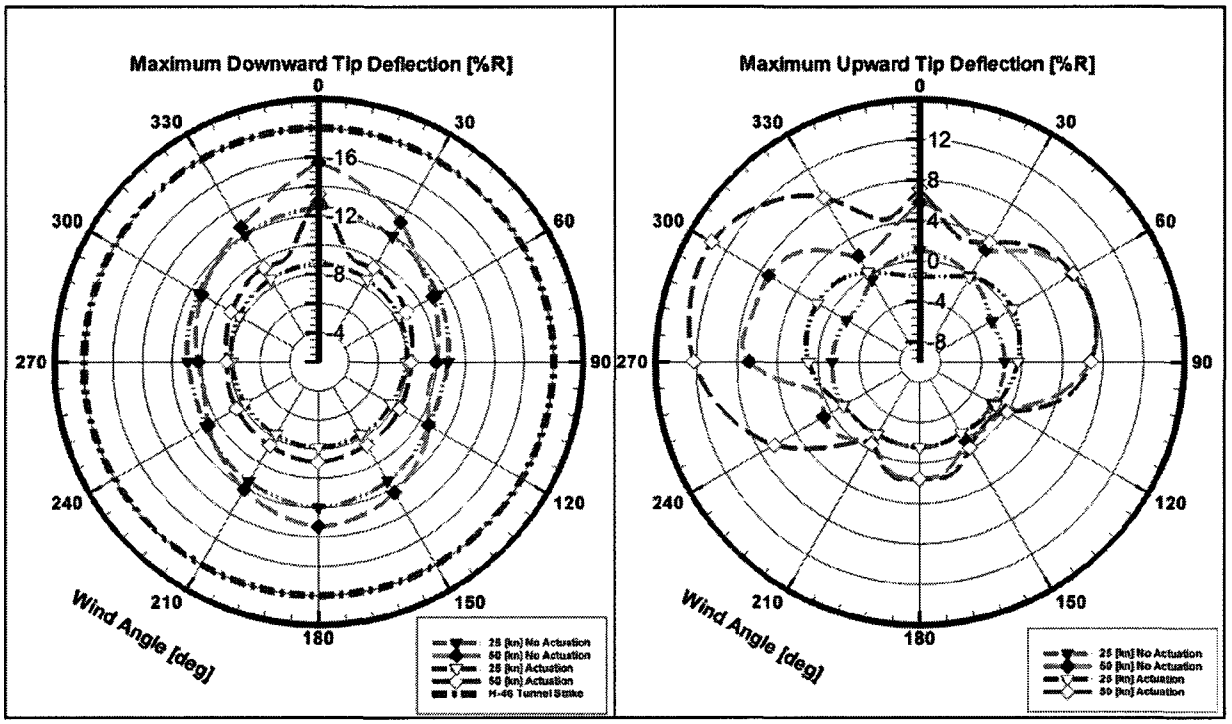

Figure H.15: Maximum downward and upward tip deflection of the engagement of the adopted IATR, sea state 4_030_10, experimental airwake.

The effectiveness of the proposed actuation strategy is further illustrated in selected time histories of the disengagement phase with ship motion for the experimental and the deterministic airwake model in Fig. H.23 to Fig. H.26

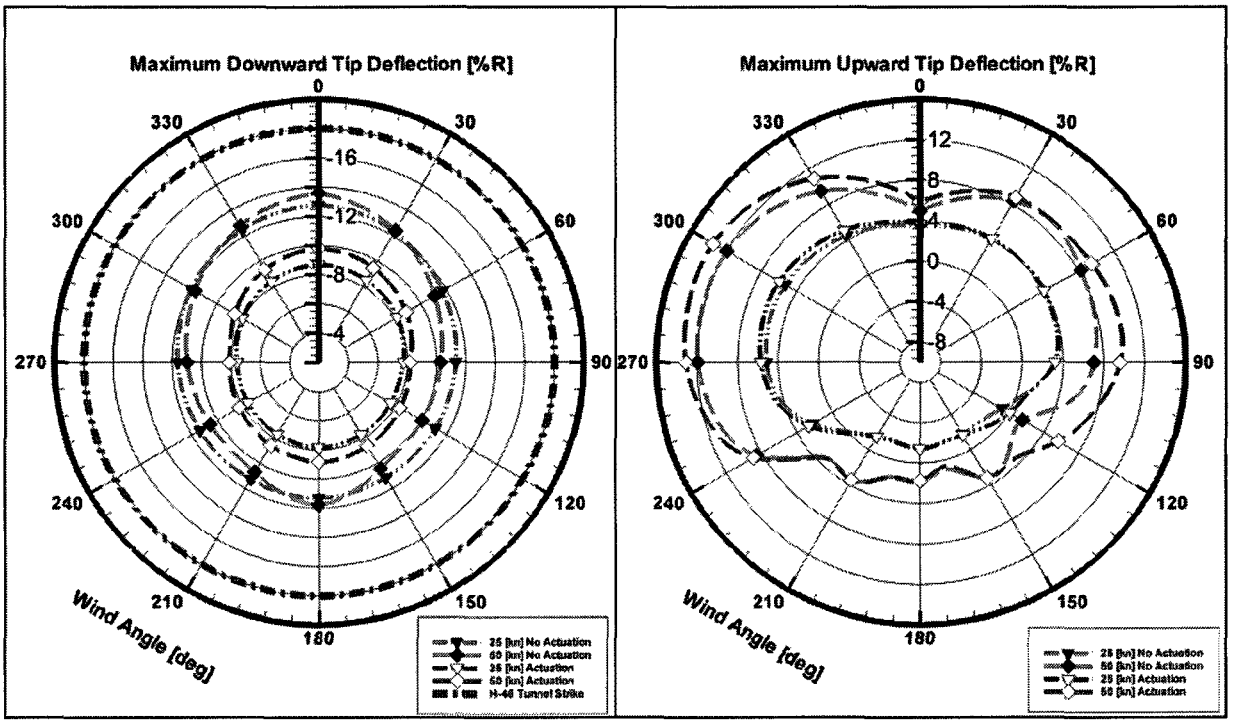

Figure H.16: Maximum downward and upward tip deflection of the disengagement of the adopted IATR, sea state 4_030_10, experimental airwake.

H.4 Effect of Turbulence

The effect of the perfectly correlated turbulence for the 60[kn] wind speed at various deck roll angles is shown in Fig. H.27 and Fig. H.28

The result of applying the actuation strategy on the maximum downward/upward tip displacement is shown in Fig. H.29 and Fig. H.30

Time histories of the rotor engagement phase with the perfectly correlated turbulence model included at the deck roll angles of -5°, 5° and wind speed of 45[kn] with the actuation strategy applied are shown in Fig. H.31 and Fig. H.32 respectively.

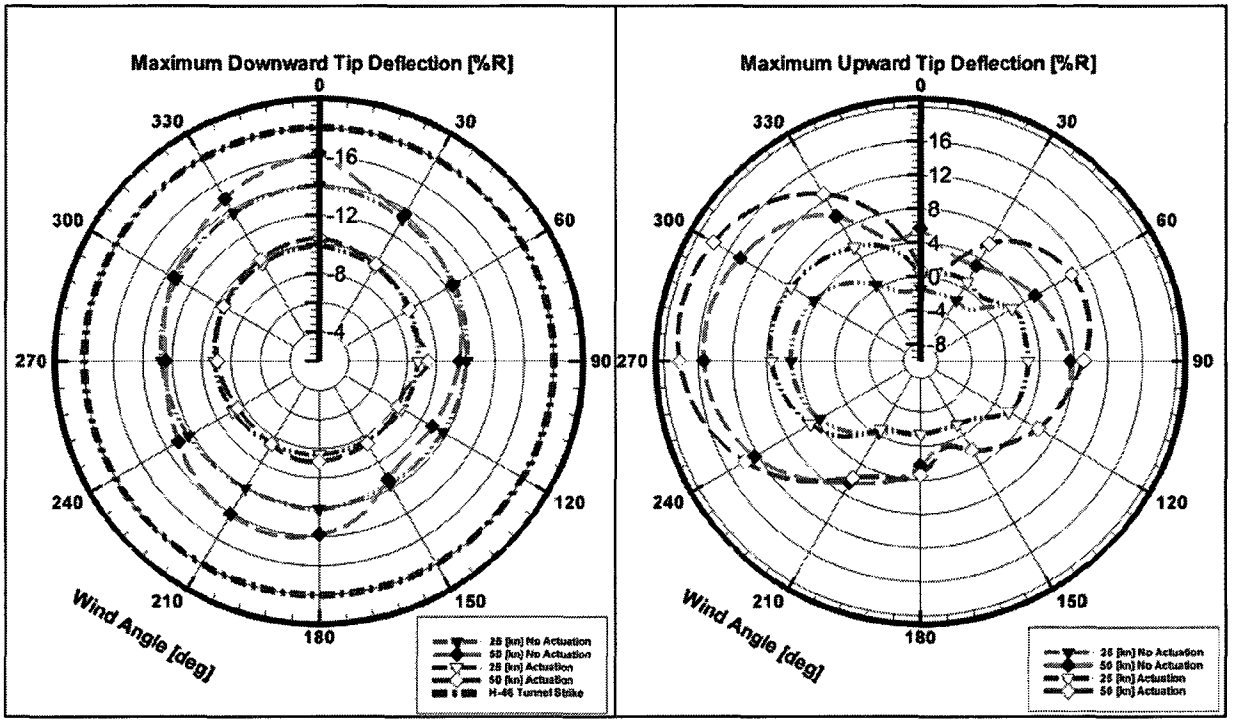

Figure H.17: Maximum downward and upward tip deflection of the engagement of the adopted IATR, sea state 4_090_10, experimental airwake.

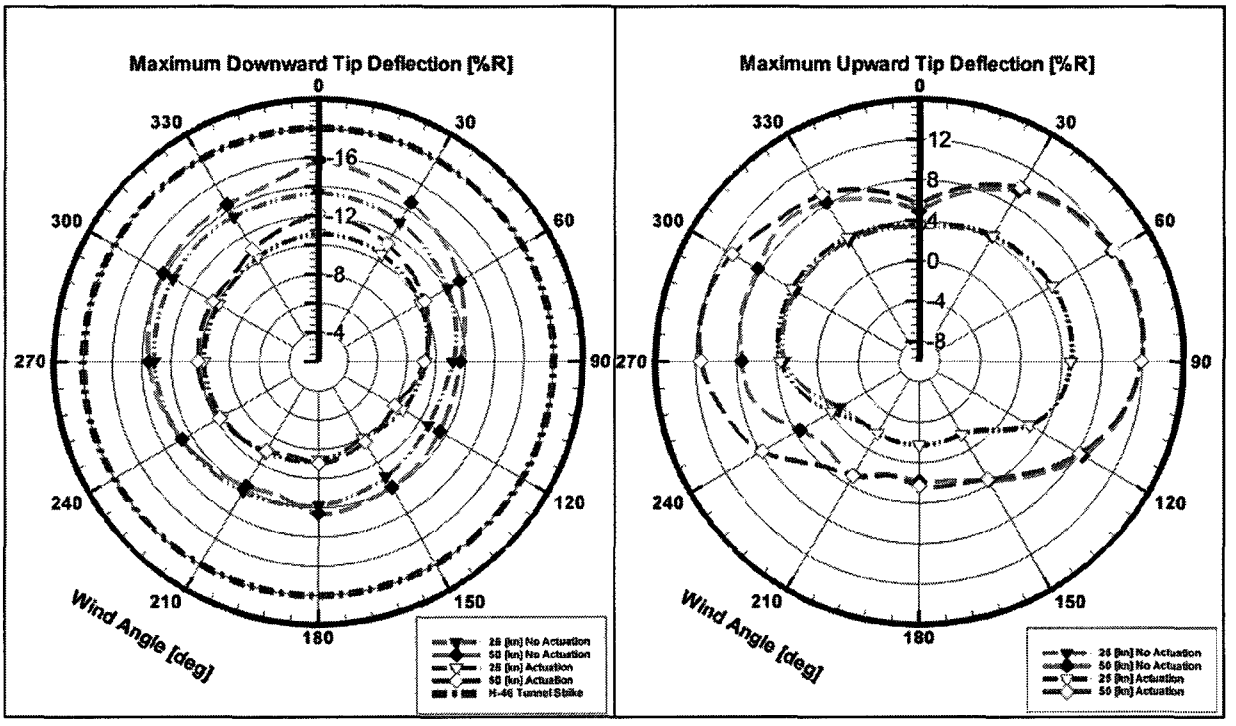

Figure H.18: Maximum downward and upward tip deflection of the disengagement of the adopted IATR, sea state 4_090_10, experimental airwake.

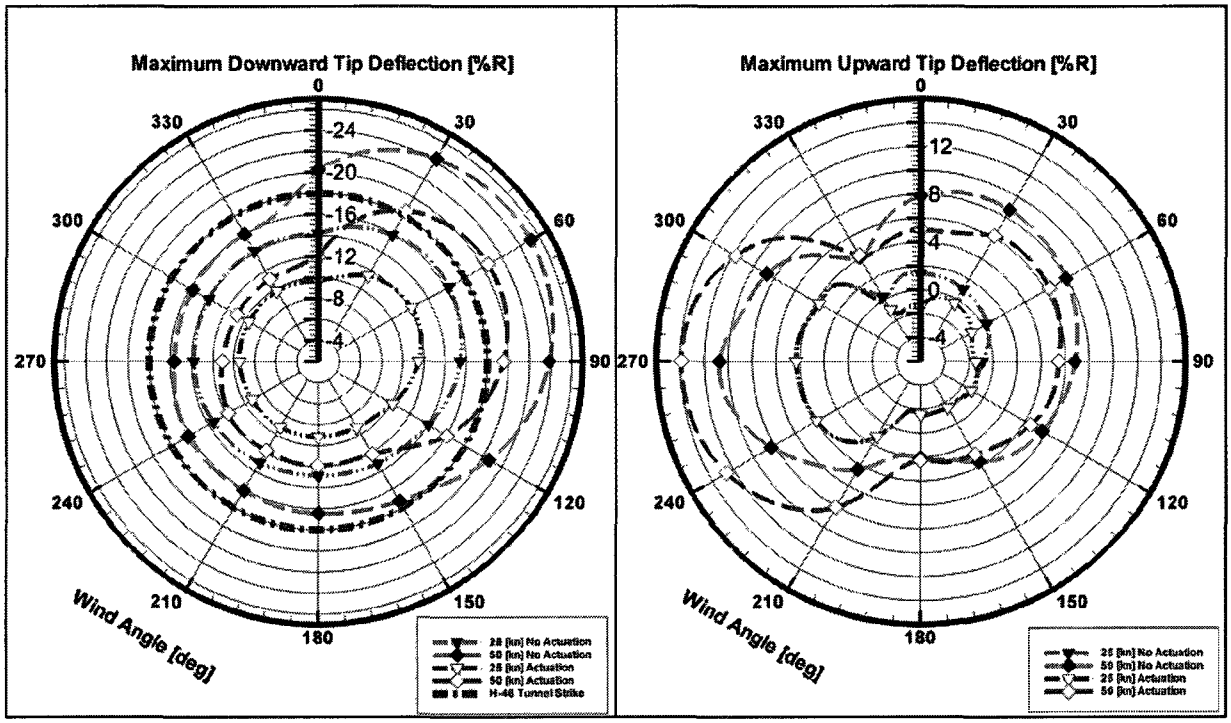

Figure H.19: Maximum downward and upward tip deflection of the engagement of the adopted IATR, sea state 4_030_10, deterministic airwake.

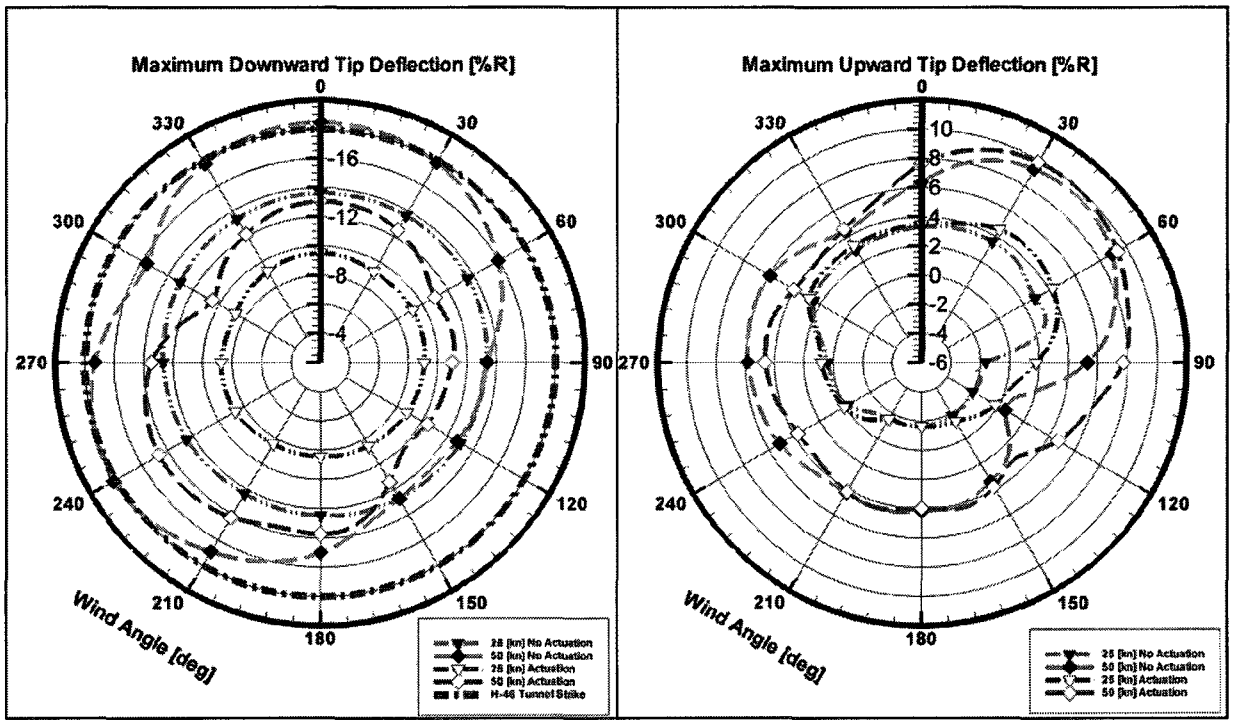

Figure H.20: Maximum downward and upward tip deflection of the disengagement of the adopted IATR, sea state 4_030_10, deterministic airwake.

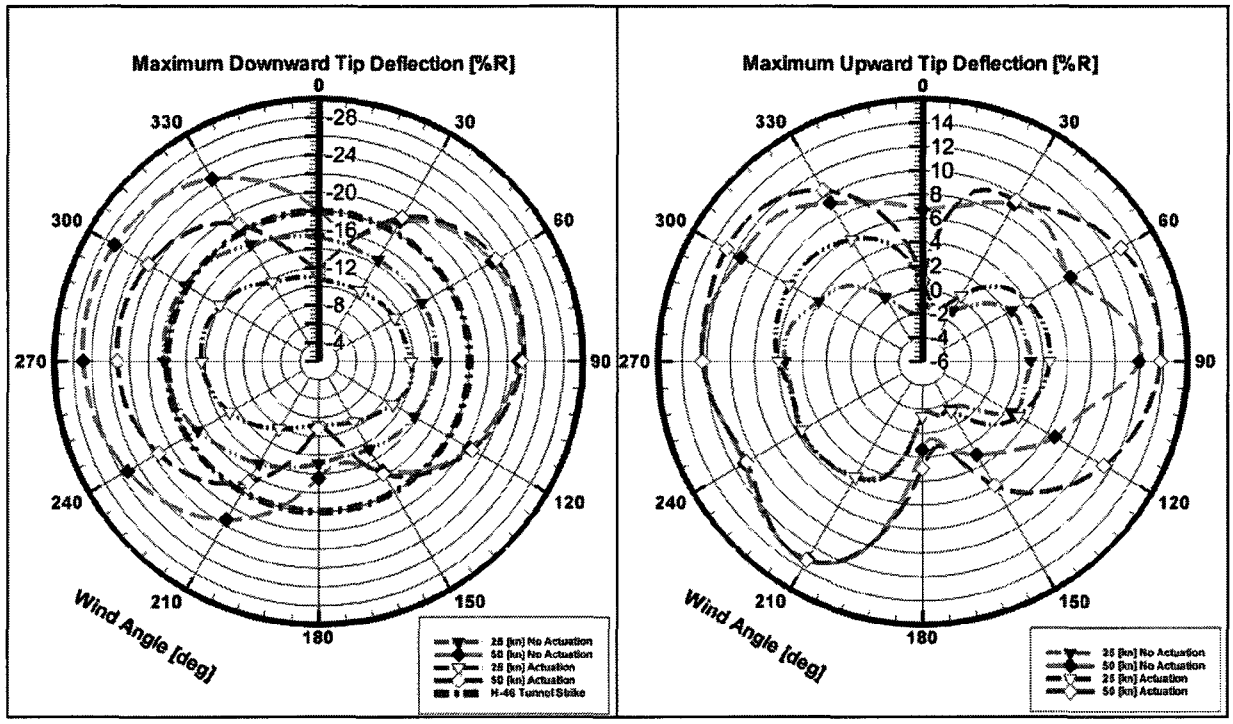

Figure H.21: Maximum downward and upward tip deflection of the engagement of the adopted IATR, sea state 4_090_10, deterministic airwake.

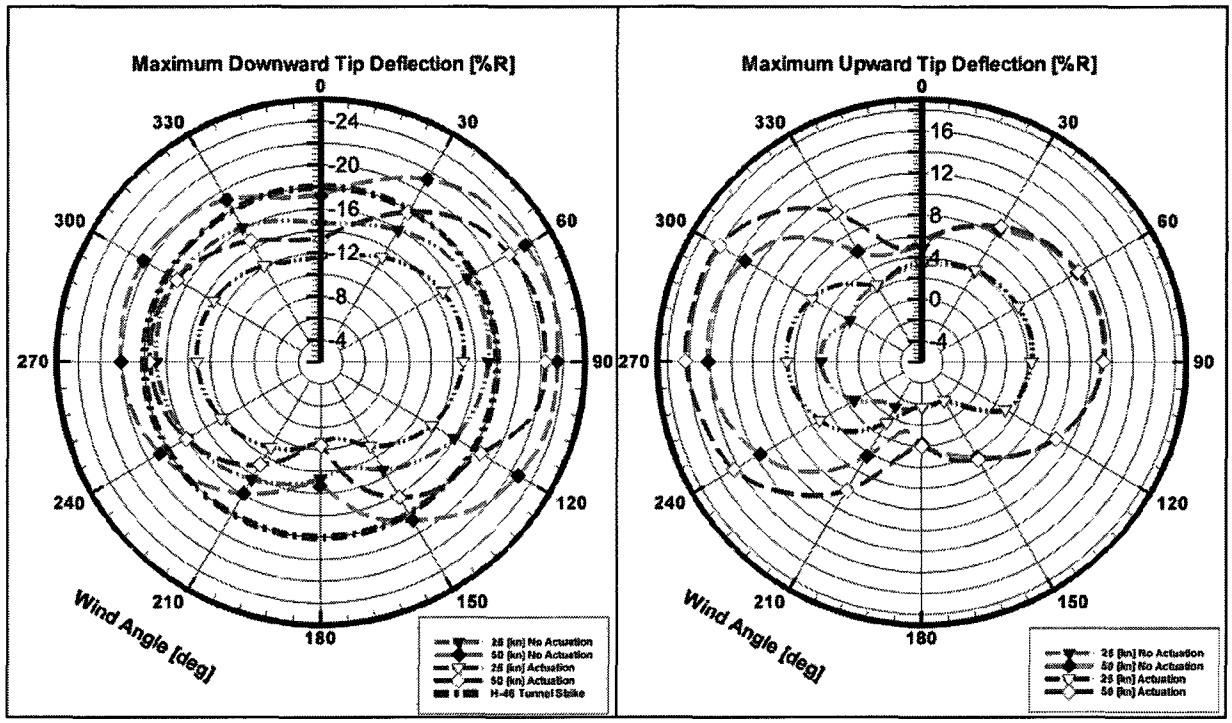

Figure H.22: Maximum downward and upward tip deflection of the disengagement of the adopted IATR, sea state 4_090_10, deterministic airwake.

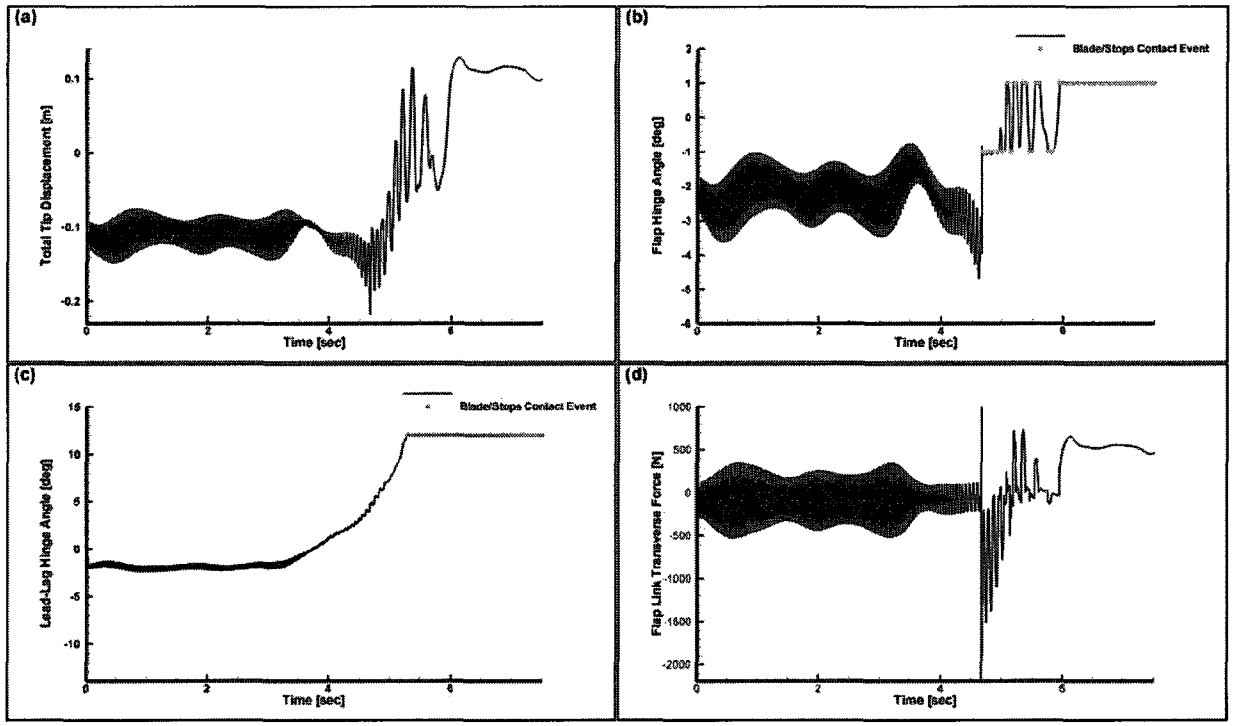

Figure H.23: Time history of the adopted IATR disengagement under the wind conditions of 50[kn], 300° WOD with 4_090_10 sea state using the experimental airwake model for:(a) Total tip displacement, (b) Flap hinge angle, (c) Lead-lag hinge angle, (d) Flap-link transverse force.

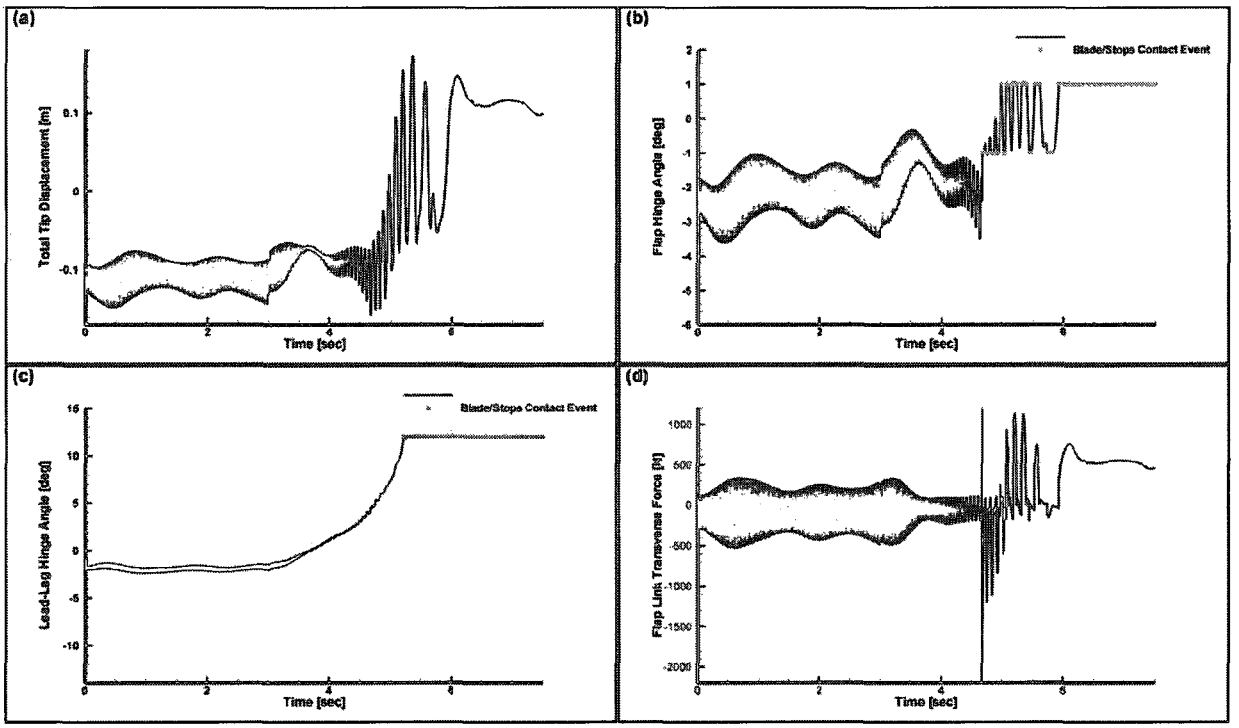

Figure H.24: Time history of the adopted IATR disengagement with the actuation strategy employed under the wind conditions of 50[kn], 300° WOD with 4_090_10 sea state using the experimental airwake model for:(a) Total tip displacement, (b) Flap hinge angle, (c) Lead-lag hinge angle, (d) Flap-link transverse force.

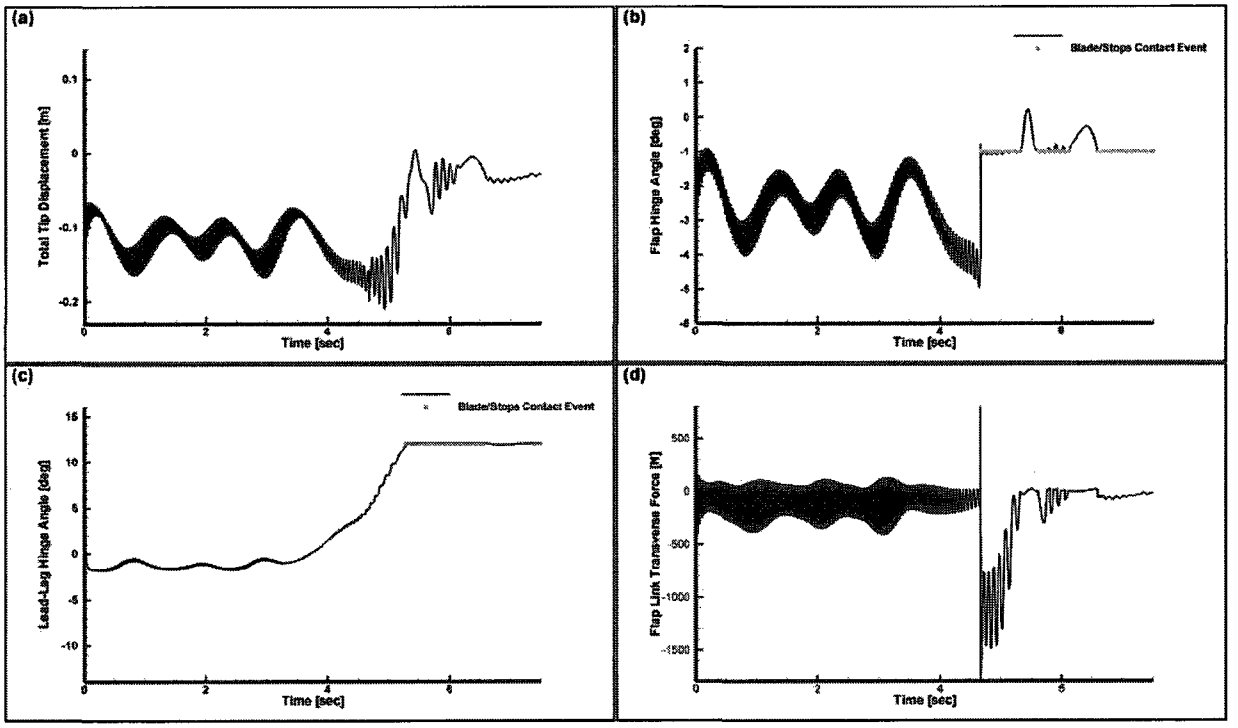

Figure H.25: Time history of the adopted IATR disengagement under the wind conditions of 25[kn], 270° WOD with 4_060_10 sea state using the linear deterministic airwake model for:(a) Total tip displacement, (b) Flap hinge angle, (c) Lead-lag hinge angle, (d) Flap-link transverse force.

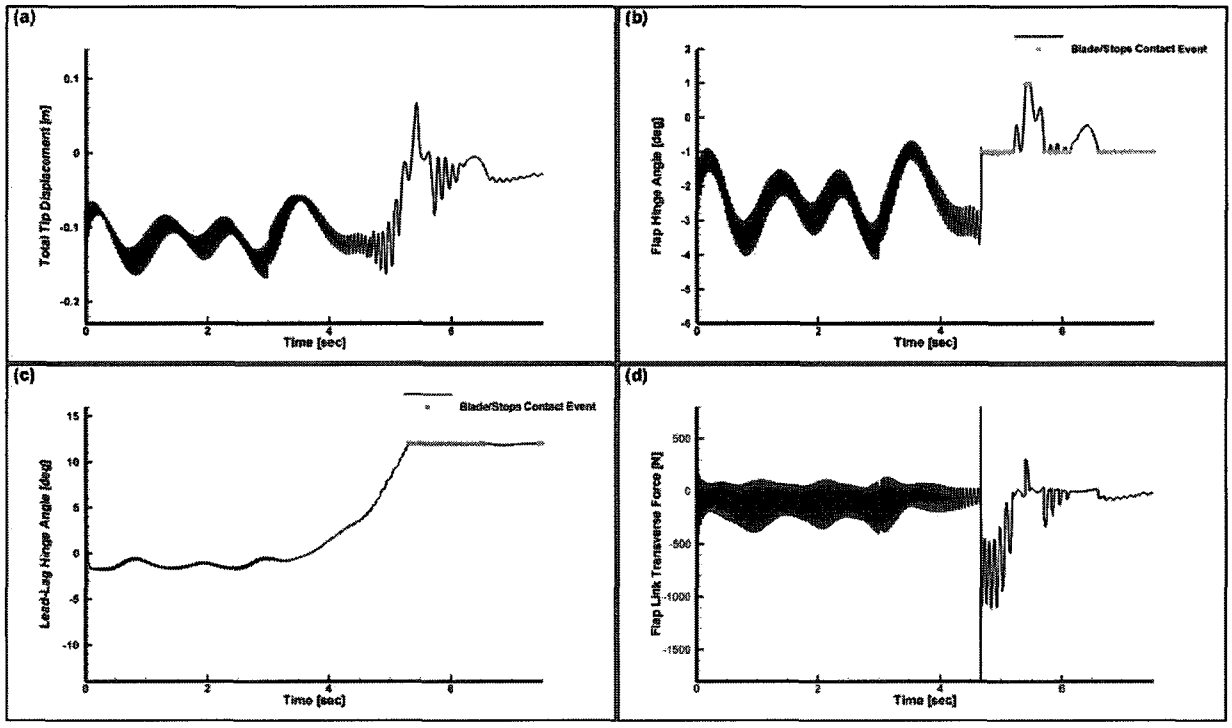

Figure H.26: Time history of the adopted IATR disengagement with the actuation strategy employed under the wind conditions of 25[kn], 270° WOD with 4_000_10 sea state using the linear deterministic airwake model for:(a) Total tip displacement, (b) Flap hinge angle, (c) Lead-lag hinge angle, (d) Flap-link transverse force.

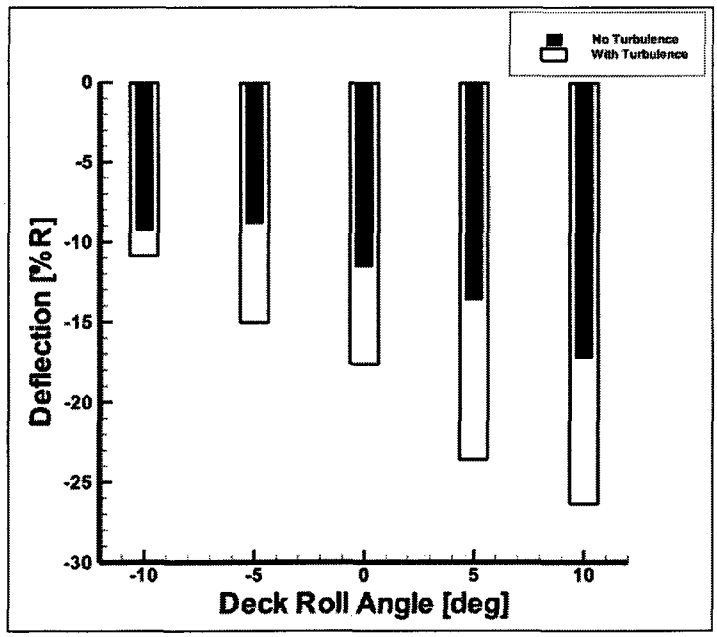

Figure H.27: Maximum downward tip deflections for various deck roll angles when the perfectly correlated turbulence is considered.

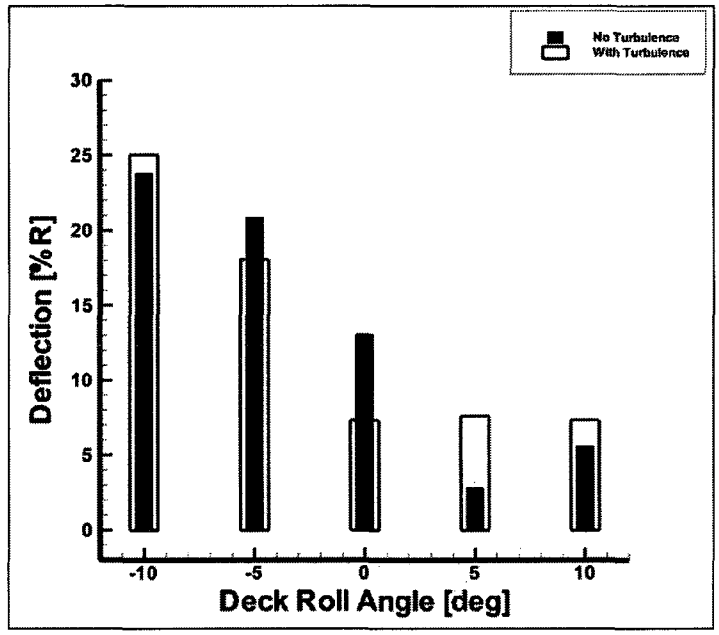

Figure H.28: Maximum downward tip deflections for various deck roll angles when the perfectly correlated turbulence is considered.

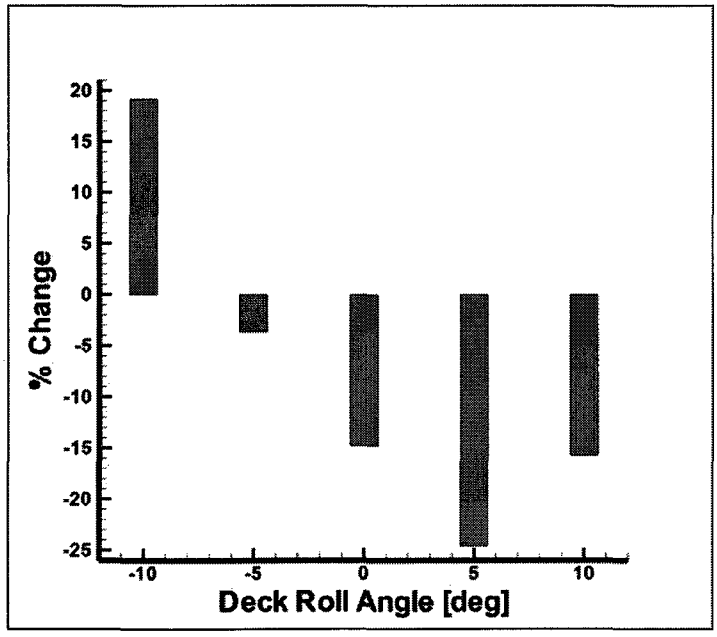

Figure H.29: Percent change in maximum downward tip deflections for various deck roll angles with the perfectly correlated turbulence model and the actuation strategy.

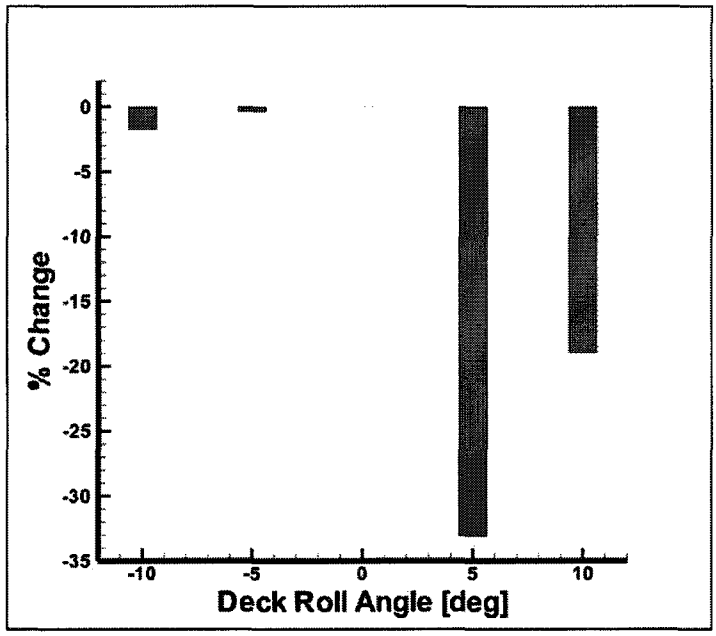

Figure H.30: Percent change in maximum upward tip deflections for various deck roll angles with the perfectly correlated turbulence model and the actuation strategy.

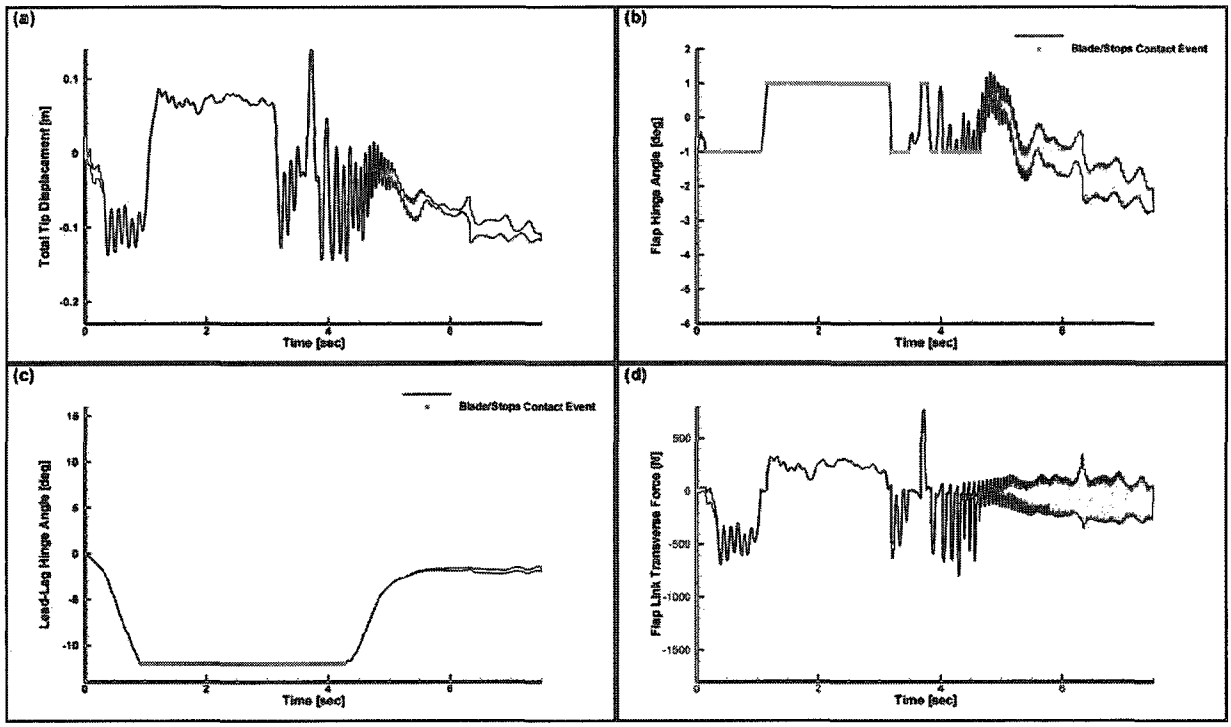

Figure H.31: Time history of the adopted IATR engagement with the actuation strategy employed under the wind conditions of 45[kn], beam wind, -5° deck roll angle, experimental airwake model with perfectly correlated turbulence for:(a) Total tip displacement, (b) Flap hinge angle, (c) Lead-lag hinge angle, (d) Flap-link transverse force.

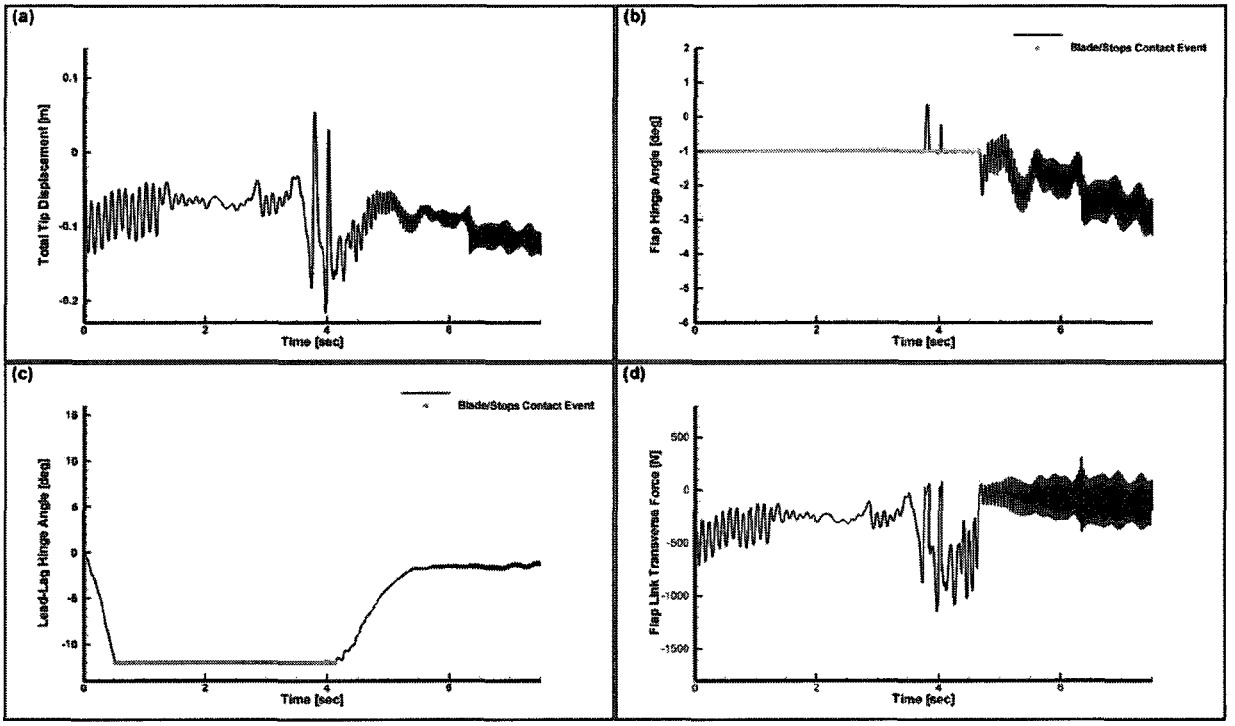

Figure H.32: Time history of the adopted IATR engagement with the actuation strategy employed under the wind conditions of 45[kn], beam wind, 5° deck roll angle, experimental airwake model with perfectly correlated turbulence for:(a) Total tip displacement, (b) Flap hinge angle, (c) Lead-lag hinge angle, (d) Flap-link transverse force.